*J. Fluid Mech.* (2020), *vol*. 905, A2.  
Published by Cambridge University Press

doi:10.1017/jfm.2020.692

# Bifurcation scenario in the two-dimensional laminar flow past a rotating cylinder

**J. Sierra[1,2], D. Fabre[1], V. Citro[2] and F. Giannetti[2,†]**

[1]Institut de Mécanique des Fluides de Toulouse (IMFT), Toulouse 31400, France

[2]Dipartimento di Ingegneria Industriale (DIIN), Universitá degli Studi di Salerno, Fisciano 84084, Italy

(Received 14 January 2020; revised 19 June 2020; accepted 12 August 2020)

The aim of this paper is to provide a complete description of the bifurcation scenario of a uniform flow past a rotating circular cylinder up to $Re = 200$. Linear stability theory is used to depict the neutral curves and analyse the arising unstable global modes. Three codimension-two bifurcation points are identified, namely a Takens–Bogdanov, a cusp and generalised Hopf, which are closely related to qualitative changes in orbit dynamics. The occurrence of the cusp and Takens–Bogdanov bifurcations for very close parameters (corresponding to an imperfect codimension-three bifurcation) is shown to be responsible for the existence of multiple steady states, as already observed in previous studies. Two bistability regions are identified, the first with two stable fixed points and the second with a fixed point and a cycle. The presence of homoclinic and heteroclinic orbits, which are classical in the presence of Takens–Bogdanov bifurcations, is confirmed by direct numerical simulations. Finally, a weakly nonlinear analysis is performed in the neighbourhood of the generalised Hopf, showing that above this point the Hopf bifurcation is subcritical, leading to a third range of bistability characterised by both a stable fixed point and a stable cycle.

**Key words:** bifurcation

## 1. Introduction

The flow past a circular cylinder is a classical configuration which has been widely adopted in the fluid dynamics community as a canonical model to investigate vortex shedding behind bluff bodies. In the case of a fixed cylinder, i.e. without rotation, the dynamics and the corresponding bifurcations are well known (Williamson 1996). The case of a rotating cylinder, which has implications for flow control using wall motion (Modi 1997; el Hak 2000), has recently received attention. A number of numerical studies in a two-dimensional framework have been conducted (Kang, Choi & Lee 1999; Stojković, Breuer & Durst 2002, 2003; Mittal 2004) and have revealed the existence of several steady and unsteady regimes. Linear stability approaches (Pralits, Brandt & Giannetti 2010; Pralits, Giannetti & Brandt 2013) have shown the existence of two separated regions

† Email address for correspondence: fgiannetti@unisa.it

of instability in the $(Re, \alpha)$ plane, where $\alpha$ is the dimensionless rotation rate and $Re$ is the Reynolds number. The so called Mode I becomes unstable via a supercritical Hopf bifurcation and it is present for $0 \leq \alpha \leq 2$. This mode is the one associated with the classical Bénard–von-Kármán vortex street, and characterised by the alternate shedding of vortices of opposite sign. At higher rotation rates, around $4.5 \leq \alpha < 6$ another unsteady mode exists, denoted as Mode II. The physical mechanism driving this mode is rather different, as it corresponds to a slow-frequency shedding of vortices with the same vorticity sign. Its onset is less well characterised than Mode I from the point of view of bifurcation theory: the fact that the frequency is very low suggests a more complex bifurcation scenario and its supercritical or subcritical nature is still unclear. The full characterisation of Mode II is complicated by the fact that, in approximately the same range of $(Re, \alpha)$ parameter space, a region where three steady-state solutions coexist has been evidenced (Pralits *et al.* 2010; Rao *et al.* 2013*a*). A more thorough characterisation of this phenomenon has been carried out by Thompson *et al.* (2014) who observed that the region of existence of multiple steady-state solutions grows with the Reynolds number. Note also that the picture is further complicated by the existence of three-dimensional (3-D) instabilities in this range. This point is outside of the range of the present paper which restricts to 2-D dynamics, but a brief review on 3-D stability properties of this flow can be found in appendix E.

To explain the existence of multiple steady states, Rao *et al.* (2013*a*) conjectured that they emerge from a cusp bifurcation point. Indeed, a cusp correctly explains the change in the number of steady states from one to three. However, a cusp is not generally associated with the existence of a Hopf bifurcation in the same range of parameters, so it cannot explain, alone, all the features discussed above. The fact that the frequency of Mode II is very small is an indicator of a second kind of codimension-two bifurcation, namely a $0^2$ or Takens–Bogdanov bifurcation (Kuznetsov 2013, chapter 8, p. 314) This bifurcation typically occurs when the frequency of a limit cycle vanishes. However, in the vicinity of a standard Takens–Bogdanov bifurcation, only two steady states generally exist, not three. This combination of features suggests that the picture could hide a codimension-three bifurcation point, also known as a generalised Hopf bifurcation. The unfolding of this generalised Takens–Bogdanov bifurcation has been studied by Dumortier *et al.* (2006) and Kuznetsov (2005) from a mathematical point of view, but to our knowledge such a feature has not yet been evidenced in a fluid dynamics system such as the one considered here.

The main purpose of the present work is to review the classification of the possible 2-D states in the $(Re, \alpha) \in [0, 200] \times [0, 10]$ parameter plane with the point of view of dynamical system theory. Firstly, we will characterise the nature of the codimension-one bifurcation curves (Hopf or saddle nodes). We give a cartography of the regions where multiple steady states exist and give a detailed description of these multiple states as well as their stability properties. We further identify three codimension-two points, namely a Takens–Bogdanov (TB) bifurcation, a cusp and a generalised Hopf (GH) bifurcation. We show that the two first are effectively located very close to each other and that the whole dynamics in this range of parameters is effectively described by the unfolding of a codimension-three bifurcation point.

The article is organised as follows: in § 2 the formulation of the problem is discussed together with the methodology adopted in the present analysis. Section 3 begins with a characterisation of the multiple steady states. A complete bifurcation diagram covering the range $(Re, \alpha) \in [0, 200] \times [0, 10]$ is then presented. The next subsections aim at clarifying the picture in the vicinity of the identified codimension-two points.

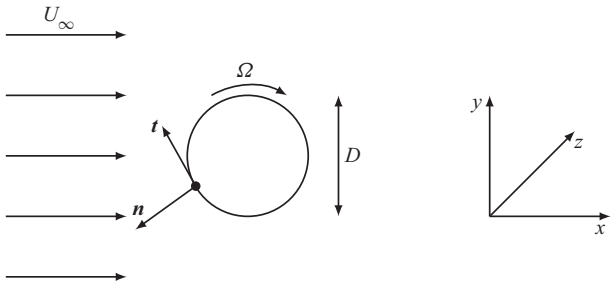


FIGURE 1. Sketch of a rotating cylinder immersed in a uniform flow.

## 2. Problem formulation and investigation methods

### 2.1. *Geometrical configuration and general equations*

The two-dimensional flow past a rotating circular cylinder is controlled by two parameters: the Reynolds number $Re = U_\infty D/\nu$ and the rotation rate $\alpha = \Omega D/2U_\infty$. Here, $\Omega$ is the dimensional cylinder angular velocity, $U_\infty$ is the free stream velocity, $D$ the diameter of the cylinder and $\nu$ the dynamic viscosity of the fluid. The fluid motion inside the domain is governed by the two-dimensional incompressible Navier–Stokes equations,

$$\frac{\partial \boldsymbol{U}}{\partial t} + \boldsymbol{U}\cdot\boldsymbol{\nabla}\boldsymbol{U} = -\boldsymbol{\nabla}P + \boldsymbol{\nabla}\cdot\tau(\boldsymbol{U}), \tag{2.1a}$$

$$\boldsymbol{\nabla}\cdot\boldsymbol{U} = 0, \tag{2.1b}$$

where $\boldsymbol{U}$ is the velocity vector whose components are $(U, V)$, $P$ is the reduced pressure and the viscous stress tensor $\tau(\boldsymbol{U})$ can be expressed as $\nu(\boldsymbol{\nabla}\boldsymbol{U} + \boldsymbol{\nabla}\boldsymbol{U}^{\mathrm{T}})$. The incompressible Navier–Stokes equations (2.1) are complemented with the following boundary conditions: on the cylinder surface, no-slip boundary conditions are set by $\boldsymbol{U}\cdot\boldsymbol{t} = \Omega D/2$ and $\boldsymbol{U}\cdot\boldsymbol{n} = 0$, where $(\boldsymbol{t}, \boldsymbol{n})$ are the director vectors of the surface in the plane $(x, y)$; in the far field, uniform boundary conditions are set $U \to (U_\infty, 0)$ when $r \to \infty$, where $r$ is the distance to the cylinder centre (see figure 1). In the discussion we consider clockwise rotation of the cylinder surface ($\alpha > 0$).

In the following, Navier–Stokes equations (2.1) and the associated boundary conditions will be written symbolically under the form $\mathcal{B}(\partial\boldsymbol{Q}/\partial t) = \mathcal{N}S(\boldsymbol{Q})$, where $\boldsymbol{Q} = (\boldsymbol{U}, P)$ is the state vector and $\mathcal{B}$ is a linear projection operator, meaning that the time derivatives apply only on the velocity components.

### 2.2. *Linear stability analysis*

Under the framework of linear stability analysis, we first need to identify base-flow solutions defined as the steady solutions $\boldsymbol{Q}_b$ of the (two-dimensional) Navier–Stokes equations, namely the solutions of $\mathcal{N}\mathcal{S}(Q_b) = 0$. We then characterise the dynamics of small-amplitude perturbations around this base flow by expanding them over the basis of linear eigenmodes, i.e.

$$\boldsymbol{Q}(x, y, t) = \boldsymbol{Q}_b(x, y) + \epsilon \sum_j \hat{\boldsymbol{q}}_j(x, y)\exp(\lambda_j t). \tag{2.2}$$

Here, $\epsilon$ is a small parameter, $\lambda_j$ the eigenvalues and $\hat{\boldsymbol{q}}_j$ the eigenmodes. The eigenpairs $[\lambda_j, \hat{\boldsymbol{q}}_j]$ have to be determined as the solutions of the following eigenvalue problem:

$$\lambda\hat{\boldsymbol{u}} + \boldsymbol{u}_b \cdot \boldsymbol{\nabla}\hat{\boldsymbol{u}} + \hat{\boldsymbol{u}} \cdot \boldsymbol{\nabla}\boldsymbol{u}_b = -\boldsymbol{\nabla}\hat{p} + \boldsymbol{\nabla} \cdot \tau(\hat{\boldsymbol{u}}) \tag{2.3a}$$

$$\boldsymbol{\nabla} \cdot \hat{\boldsymbol{u}} = 0. \tag{2.3b}$$

Which will be written in the following under the symbolic form $\lambda_j \mathcal{B}\hat{\boldsymbol{q}}_j + \mathcal{LNS}\hat{\boldsymbol{q}}_j = 0$. In the following we consider that eigenmodes $\hat{\boldsymbol{q}}(x, y)$ have been normalised, see appendix C for further details. Note that in (2.2), to fully represent the dynamics, the summation over eigenmodes may involve a continuous sum over the spectrum, i.e. the discrete and the continuous or essential spectra of the operator (see Kapitula & Promislow (2013) for a rigorous discussion). However, to determine global stability we only need to consider a limited number of eigenmodes, so we keep the summation as a discrete sum indexed by $j$.

Owing to the eigenvalues, two cases can be distinguished:

(i) If all eigenvalues $\lambda_j$ have negative real part the considered base flow is a stable solution.

(ii) If $n$ eigenvalues have positive real part, the considered base flow will be referred to as a $n$-unstable solution. Note that 1-unstable solutions are commonly referred to as saddle points because a projection of their dynamics in a 2-D plane (phase portrait) has an attractive direction and another repulsing one, while 2-unstable solutions are either unstable nodes or unstable foci depending if the leading eigenvalues are both real or complex conjugates.

The transition from stable to unstable (or from $n$-unstable to $n + 1$-unstable) is called a local bifurcation. The simplest bifurcations (such as saddle nodes and Hopf) are said to be codimension-one and occur along given curves in the parameter plane $(Re, \alpha)$. The intersection of two such curves tangentially is called a codimension-two bifurcation and generally leads to a rich dynamics in the vicinity of the intersection point.

### 2.3. *Notions of bifurcation theory*

From the viewpoint of dynamical system theory, the expression (2.2) can be generalised as a decomposition of the perturbations over the leading modes of the system

$$\boldsymbol{Q}(x, y, t) = \boldsymbol{Q}_b(x, y) + \sum_j A_j(t)\hat{\boldsymbol{q}}_j(x, y). \tag{2.4}$$

Then, the problem can be reduced to a low-dimensional system governing the amplitudes $A_j(t)$

$$\frac{\mathrm{d}}{\mathrm{d}t}A_j = \lambda_j A_j + (NL), \tag{2.5}$$

where $(NL)$ represent the nonlinear interactions between modes. Investigation of these nonlinear terms allows us to predict the dynamics in the vicinity of bifurcation points. Systematic methods exist to compute these nonlinear terms (such as weakly nonlinear expansions, centre manifold reduction or Lyapunov–Schmidt reduction). However, restricting ourselves to a qualitative point of view (up to a continuous change of coordinates with continuous inverse), it is also possible to predict a number of features by examining the generic normal form of the bifurcation, namely, a standard form to which the dynamical system can be reduced by a series of elementary manipulations

(see Wiggins (2003) for details). Particular forms of codimension-two bifurcations encountered in the rotating cylinder are discussed in §§ 3.5 and 3.6.

### 2.4. *Numerical methodology*

In the present manuscript, we adopt the same numerical methodology used in Fabre *et al.* (2020) and described in Fabre *et al.* (2019). The computation of the steady-state solutions, the resolution of the linear problems and the time stepping techniques are implemented using the open-source finite element software FreeFem++. Parametric studies and generation of figures are performed using Octave/Matlab thanks to the generic drivers of the StabFem project (see a presentation of these functionalities in Fabre *et al.* 2019). According to the philosophy of this project, codes reproducing parts of the results of the present paper are available from the StabFem website (https://gitlab.com/stabfem/StabFem). On a standard laptop, all the computations discussed below can be obtained in a few hours, except time stepping simulations which take longer. Results presented in § 3 are obtained with a computational domain $L_x = 120$ and $L_y = 80$ in the streamwise and cross-stream directions, respectively. The cylinder centre is located 40 diameters downstream of the inlet, symmetrically between the top and bottom boundaries. Numerical convergence issues are discussed in appendix D by a meticulous comparison between results obtained with different meshes, where domain dimension and grid density were varied.

Steady nonlinear Navier–Stokes equations are solved by a Newton method. In the degenerated cases, pseudo-arc length continuation is performed to be able to compute multiple steady-state solutions, as described in appendix A. The generalised eigenvalue problem (2.3) is solved by the Arnoldi method or by a simple inverse iteration algorithm. Finally, nonlinear unsteady Navier–Stokes equations are integrated forward in time with a second-order time scheme (Jallas, Marquet & Fabre 2017).

## 3. Results

### 3.1. *Characterisation of multiple steady-state solutions*

To introduce the existence of multiple steady states, we first characterise them by plotting in figure 2 the associated lift as function of the rotation rate $\alpha$, for four different values of $\alpha$. In these plots, stable solutions are indicated by continuous lines and unstable ones by dashed lines, following the usual convention in dynamical systems theory.

For $Re = 60$, as illustrated in figure 2($a$), only one steady state exists for all values of $\alpha$, for $Re = 60$. This state is stable except in the ranges $\alpha \lesssim 2$ (corresponding to the existence of Mode I), and $5.2 \lesssim \alpha \lesssim 5.5$ (corresponding to the existence of Mode II).

For higher Reynolds numbers, a small region of multiple solutions arises in a small-scale interval around $\alpha \approx 5$. This phenomenon is illustrated in figure 2($b$) for $Re = 100$ and is associated with an 's' shape of the curve, featuring two successive folds. Note that, before the first fold, the steady solution is 2-unstable (focus type); at the first fold it turns into 1-unstable (saddle type) and at the second fold it turns into stable. To detect these folds, pseudo-arc length continuation is carried out with $\alpha$ as a parameter and the horizontal force exerted on the cylinder surface $F_x$ as a monitor to track and distinguish multiple steady states (see appendix A for a more detailed discussion).

For larger values of the Reynolds number, as illustrated in figure 2($c$) for $Re = 170$, the interval of existence of multiple states for $\alpha \approx 5$ expands to $\alpha \in [4.75, 5.12]$. In addition, we observe a second range displaying multiple states for $\alpha > 5.87$. This second interval is associated with a fold bifurcation at $\alpha = 5.87$, giving rise to two additional and

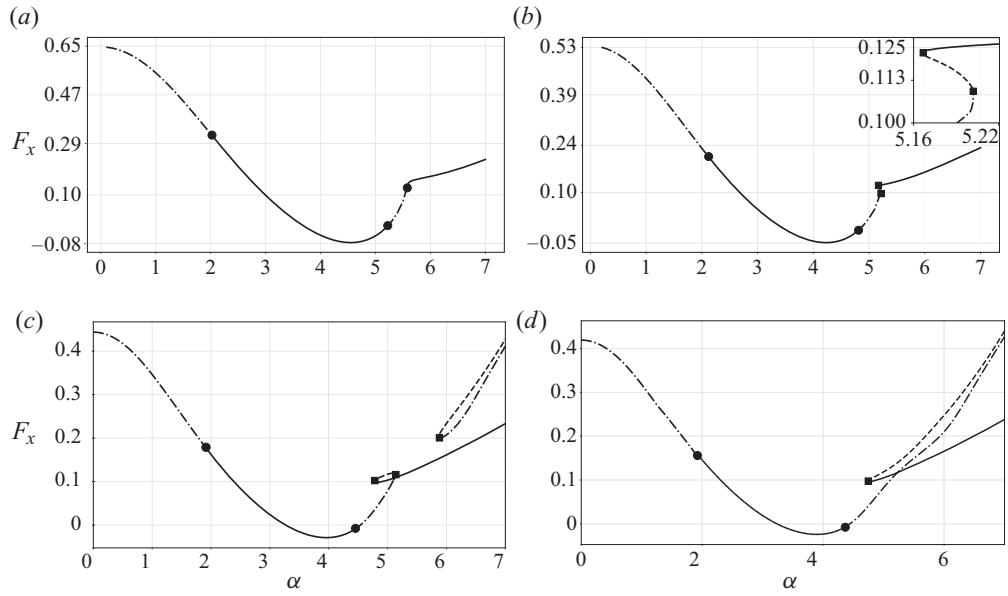


FIGURE 2. Evolution of the horizontal force $F_x$ as a function of the rotation rate $\alpha$ for four Reynolds numbers, (*a*) $Re = 60$, (*b*) $Re = 100$, (*c*) $Re = 170$ and (*d*) $Re = 200$. Solid lines ___ denote stable steady states, dashed-dotted lines _.-._.- denote unstable steady states of focus type or nodes, dashed lines _ _ _ are used for steady states of saddle type. Solid circles • denote Hopf bifurcations and solid squares ▪ denote saddle-node bifurcations.

disconnected steady solutions. Note that both these solutions are unstable, respectively of node and saddle types.

Finally, for $Re = 200$, as illustrated in figure 2(*d*), we observe that the two ranges of multiple steady states are merged into a single one. In this case there is a single saddle-node bifurcation around $\alpha = 4.75$ leading to two branches of steady states which are disconnected from the branch existing for lower values of $\alpha$. Here, one of these branches is stable and the second is unstable (saddle type).

### 3.2. *Topological description of steady-state solutions*

We now illustrate the spatial structure of some steady-state solutions, with emphasis on the topological structure of the corresponding flows. We restrict ourselves to the case $Re = 200$, as previously considered in figure 2(*d*).

Figure 3(*a*) corresponds to $\alpha = 1.8$, the value at which Mode I is re-stabilised. The corresponding flow is characterised by a stagnation point located beneath the cylinder axis, on the left side of the $y$-cylinder axis. Compared to the steady flow in the non-rotating case, which is characterised by a symmetrical recirculation region, the upper recirculating bubble is reduced whereas the lower one is moved downwards.

Further increasing the rotation speed, both recirculation bubbles shrink and eventually vanish. At $\alpha = 4.35$ (figure 3*b*) corresponding to the lower threshold for the existence of Mode II, recirculating bubbles have already disappeared and the vorticity wraps the cylinder. Stagnation point is located on the opposite side but downstream the cylinder vertical axis.

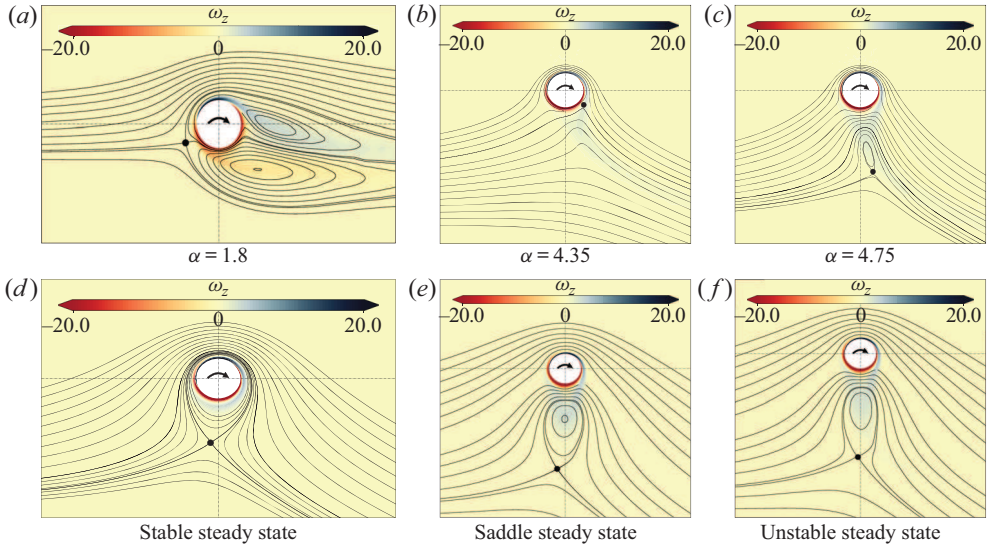


FIGURE 3. Steady flow around a rotating cylinder (vorticity levels and streamlines) for selected parameters. (*a*) $\alpha = 1.8$, $Re = 200$ (at the supercritical Hopf bifurcation threshold); (*b*) $\alpha = 4.35$, $Re = 200$ (at the Hopf bifurcation); (*c*) $\alpha = 4.75$, $Re = 200$ (at the fold bifurcation). (*d–f*) Correspond to three base-flow solutions existing in the range of multiple solutions, namely for $\alpha = 5.25$ and $Re = 200$. The circled dot shows the position of the hyperbolic stagnation point.

Figure 3(*c*) corresponds to the steady-state flow at the fold bifurcation observed for $\alpha = 4.75$ and giving rise to the disconnected states observed in figure 2(*d*). Compared to the previous state, the flow is topologically different as no stagnation point is observed along the wall of the cylinder. On the other hand, two stagnation points are observed within the flow. One of them is elliptic and located at the centre of the detached recirculation bubble. The other is hyperbolic and located along the streamline bounding the recirculation bubble.

Figure 3(*d–f*) displays the three coexisting steady states at $\alpha = 5.25$ and $Re = 200$. The topology of the streamlines of unstable and stable steady states differs. In the stable case (panel *d*) there is a single recirculation region encircling the cylinder and bounded by a hyperbolic stagnation point, as in the classical potential solution existing in this range of rotation rates. On the other hand, for both unstable states, the topology is similar to the case of figure 3(*c*). The recirculation region is detached from the cylinder and contains an elliptic stagnation point located approximately in the midpoint between the hyperbolic point and the bottom point of the cylinder surface. In the unstable steady state, the recirculating region is more stretched, as it can be seen in figure 3(*d–f*).

We highlight that even though topological changes in the streamlines of the steady states and bifurcations of the velocity field are in general independent events (see Brøns 2007), in some cases these two events occur in a small neighbourhood of the space of parameters (see Heil *et al.* 2017). In the current situation it has been confirmed that there is not a one-to-one relation between both phenomena. For instance, the transition between detached recirculation bubble (as in panel *c*) and recirculation bubble encircling the cylinder (as in panel *d*) along the stable branch occurs at some value of $\alpha$ in the range [4.75–5.25] where no dynamical bifurcation occurs. Yet, for larger Reynolds numbers,

i.e. $Re \gtrapprox 190$, successive creation and destruction of vortices seems to be relevant in the preservation of the disconnected branch of steady states.

### 3.3. *Analysis of the spatial structure of direct and adjoint eigenmodes*

To explain why the steady state displayed in figure 3($f$) is unstable, the two corresponding unstable modes (both associated with real eigenvalues) are displayed in figure 4 for $Re = 200$ and $\alpha = 5.25$. Direct modes are characterised by two recirculating regions of opposite vorticity. Vorticity is stronger and more localised in Mode IIa while Mode IIb displays a larger region with non-zero vorticity. Adjoint eigenvectors $\hat{\boldsymbol{q}}^\dagger$ for Mode IIa and Mode IIb are also displayed in figure 4. Adjoint fields (Luchini & Bottaro 2014) can be interpreted as a kind of Green's function for the receptivity of the global mode. Scalar product of the adjoint field with a forcing function or an initial condition provides the amplitude of the instability mode (see Giannetti & Luchini 2007). Therefore, Mode IIa is highly receptive in the upper right side of the near wake of the cylinder. The region of maximum receptivity extends from the close upper right region of the cylinder to a larger region at the bottom right of the cylinder and it is weaker than Mode IIa. Both modes present weak sensitivity to forcing upstream of the cylinder.

### 3.4. *Bifurcation diagram in the parameter plane* $(Re, \alpha)$

The bifurcation curves detected in the $\alpha < 10$, $Re < 200$ range by linear stability analysis of all steady-state solutions are depicted in figure 5.

Three Hopf bifurcation curves are detected and plotted with full lines. The first one encircles the range of existence of unsteady Mode I. The second one delimits the range of existence of unsteady Mode II in its lower and left parts, but not on its upper part. The third one (in grey) occurs along a steady state which is already unstable, and hence is not likely to be related to a bifurcation observable in DNS or experiments.

In addition, we have identified two bifurcation curves associated with saddle nodes or 'folds', here denoted $F_+$ and $F_-$. These curves delimit the range of existence of multiple two-dimensional steady states, displayed as a grey region in figure 5. Note that the extension of this region explains the difference between the cases $Re = 170$ and $Re = 200$ discussed in the previous paragraph; according to the figure a single interval of $\alpha$ is found for $Re \gtrsim 190$.

In figure 5, the two fold curves seem to merge with the Hopf curve existing for lower $Re$ at a point with coordinates $Re \approx 75$, $\alpha \approx 5.4$. Inspection shows that there are actually both a $0^2$ or TB bifurcation and a cusp (C) bifurcation in very close vicinity in this range of parameters. This region will be studied in § 3.5. Additionally, in another range of parameters located at the lower threshold of existence of the Mode II, we have identified the existence of a Bautin or GH bifurcation which splits the Hopf curve into supercritical ($Re < Re_{GH}$) and subcritical ($Re > Re_{GH}$). This region will be studied in § 3.6.

### 3.5. *Cusp–Takens–Bogdanov region*

#### 3.5.1. *Qualitative study of the normal form*

The transition occurring for $Re \approx 75$ and $\alpha \approx 5.4$ is characterised by the end of the Hopf curve ($H_-$) at a fold curve ($F_+$) (characteristic of a Takens–Bogdanov bifurcation), and a transition between one and three steady states (characteristic of a cusp). This suggests that the present situation is actually very close to a codimension-three bifurcation. The dynamical behaviour of the system can thus be expected to be well predicted using

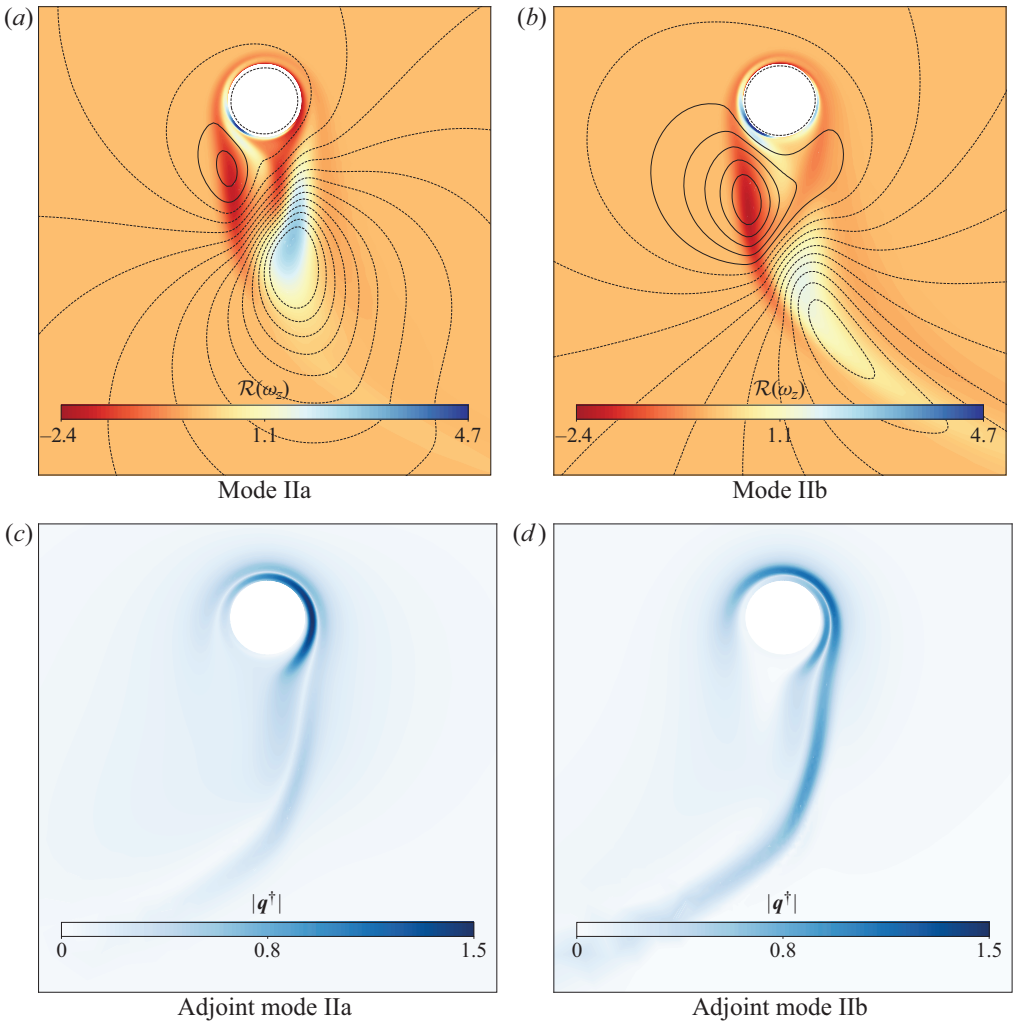


FIGURE 4. Contour plot of vorticity $\omega_z$ of Mode IIa and Mode IIb at $\alpha = 5.25$ and $Re = 200$ of the unstable steady state (*a*,*b*). The magnitude of adjoint modes (*c*,*d*).

the normal form describing the universal unfolding of the codimension-three planar bifurcation, also called a generalised TB bifurcation. This normal form has been studied by both Dumortier *et al.* (2006) and Kuznetsov (2013, chapter 8.3). The normal form can be written as follows:

$$\frac{\mathrm{d}y_1}{\mathrm{d}t} = y_2, \tag{3.1a}$$

$$\frac{\mathrm{d}y_2}{\mathrm{d}t} = \beta_1 + \beta_2 y_1 + \beta_3 y_2 + \epsilon y_1^3 + c_1 y_1 y_2 - y_1^2 y_2, \tag{3.1b}$$

where $\beta_1, \beta_2$ and $\beta_3$ are unfolding parameters (mapped from the physical parameters $(Re, \alpha)$), $c_1$, $\epsilon$ (which can be rescaled to $\pm 1$) are fixed coefficients which depend on the nonlinear terms of the underlying system. Note that this normal form generalises both the normal form of the standard TB bifurcation (which is recovered for $\beta_1(Re, \alpha) = 0$)

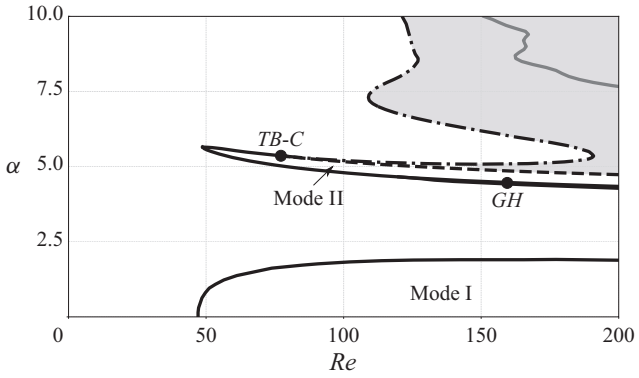


FIGURE 5. Bifurcation curves in the range $Re \in [0, 200]$ and $\alpha \in [0, 10]$. Black and grey lines are used to denote local bifurcations. Solid lines ——— indicate the presence of a Hopf bifurcation, dashed line - - - designates the first fold bifurcation curve, $F_-$, and dashed dotted line —·— denotes the second fold bifurcation, $F_+$. Grey region indicates the coexistence of three steady states. Solid grey line inside the grey region denotes a secondary Hopf bifurcation occurring on one of the unstable steady states.

and the one of the fold bifurcations (which is recovered for $\beta_3(Re, \alpha) = 0$). The occurrence of both these codimension-two conditions for very close values of the parameters is characteristic of an imperfect codimension-three bifurcation and justifies the relevance of the associated normal form.

The dynamics of the normal form (3.1) has been explored by Dumortier *et al.* (2006) who classified the possible phase portraits and the associated bifurcation diagrams as functions of the unfolding parameters $(\beta_1, \beta_2, \beta_3)$ along a spherical surface. They showed that all possible bifurcation diagrams fall into three possible categories, called focus, saddle and node according to the values of the coefficients $c_1$ and $\epsilon$. The situation $0 < c_1 < 2\sqrt{2}$ and $\epsilon = -1$ corresponds to the stable focus case and is found to lead to a bifurcation diagram consistent with the present situation, so we concentrate on this case.

Figure 6 illustrates all the possible behaviours of the dynamical system, sketched by sample phase portraits, along with their range of existence in the $(\beta_1, \beta_2)$ plane. This figure corresponds to a subset of the complete diagram displayed in Dumortier *et al.* (2006, chapter 1, pp. 6–8), restricted to a range of parameters which is sufficient to explain all the dynamical features of the present problem. The bifurcation diagram displays two codimension-two points, a cusp C and a TB. These codimension-two points result from the tangential intersection of two codimension-one curves: the cusp point C occurs when the two fold curves $F_+$ and $F_-$ collide, while the TB point arises from the intersection of the supercritical $H_-$ Hopf curve and the $F_+$ fold. In addition, the bifurcation diagram predicts a homoclinic global bifurcation along a curve $H_\infty$ originating from the TB point and terminating along the $F_-$ fold on a point denoted SNL (for saddle-node loop). Left from this point, the $F_-$ curve corresponds to a local saddle node while right from this point it corresponds to a homoclinic saddle-node bifurcation (appearance of two fixed points along a previously existing cycle). Note that the SNL point and the intersection of $H_-$ and $F_-$ are formally not codimension-two points (see Dumortier *et al.* 2006).

Phase portraits obtained in the various regions delimited by bifurcation boundaries are displayed in the panels of figure 6. One of the most interesting predictions is the existence of two regions characterised by the existence of two stable states, a bistability phenomenon. The first region (3), in the vicinity of the cusp, is characterised by two stable

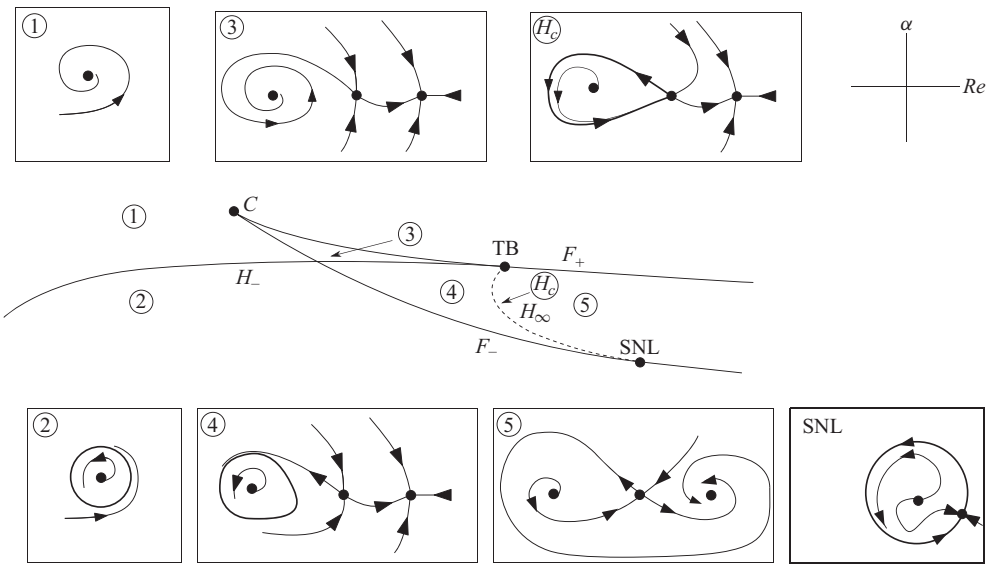


FIGURE 6. Bifurcation diagram predicted using the normal form 3.1 in the stable focus case (adapted from Dumortier *et al.* 2006), and qualitative phase portrait in regions (1), (2), (3), (4), (5) and along curve $H_\infty$. Note that in the qualitative phase portraits, focus and node points are not distinguished.

| Type | *Re* | $\alpha$ |
|---|---|---|
| TB | 77.6 | 5.36 |
| C | 75.6 | 5.38 |
| GH | 160 | 4.46 |

TABLE 1. Position of codimension-two bifurcation points.

steady states. The third region (4) is characterised by both a stable steady state and a stable cycle. In all other regions, there is a single stable solution which is either a steady state (in regions 1 and 5) or a cycle (in region 2).

Note that in these phase portraits nodes and foci are not distinguished. Distinguishing between these cases (Dumortier *et al.* 2006) leads to consideration of a larger number of subcases (for instance region 1 could be split in two subregions corresponding to a stable node and a stable focus ...) but the transitions between these subcases are not associated with bifurcations.

### 3.5.2. *Numerical results in the C–TB region*

In order to check the predictions of the normal form approach, we have conducted an accurate exploration of the range of parameters corresponding to the C–TB region. The exploration allowed us to confirm the existence of both a cusp and a Takens–Bogdanov point. The locations in the ($\alpha$, *Re*) plane are given in table 1.

Figure 7 displays 'zooms' of the full bifurcation diagram (figure 5) in two narrow ranges centred on the C and TB codimension-two points. The bifurcation curves and the regions

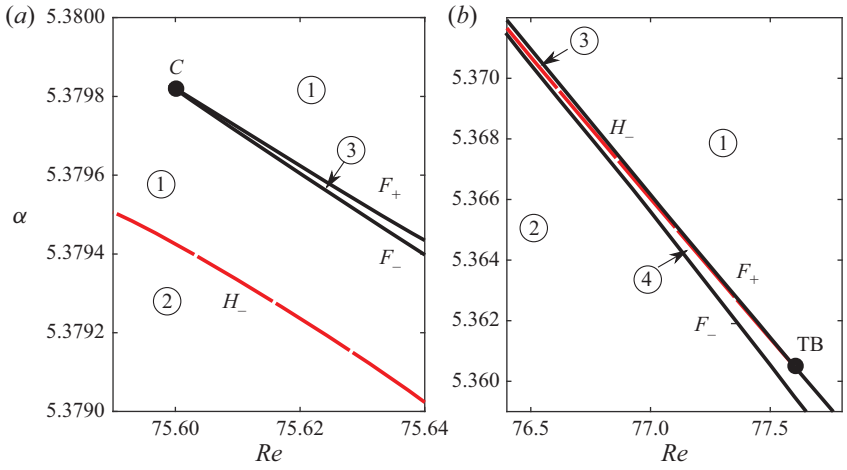


FIGURE 7. Zooms of figure 5 in the vicinity of the C and TB codimension-two points. Black solid lines denote fold bifurcations $F_{\pm}$, long dashed (red) line is used for the Hopf bifurcation line $H_{-}$ and short dashed (red) curve denotes the local change from stable focus to stable node. Numbers correspond to each phase portrait of figure 6(*a*). (*a*) Zoom in the region of cusp bifurcation. (*b*) Zoom in the region of Takens–Bogdanov bifurcation.

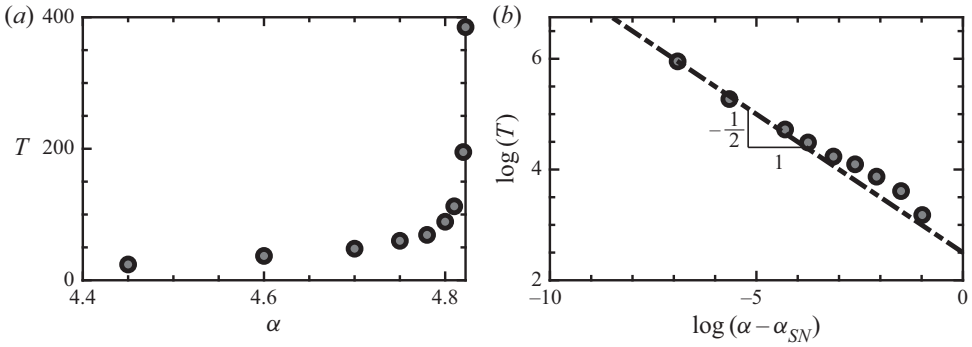


FIGURE 8. Evolution of the period of the limit cycle as it approaches the homoclinic connection. (*a*) Linear plot of the period $T$ as a function of the rotation rate $\alpha$ where $\alpha_{SN}$ is the rotation rate at the saddle node. (*b*) Logarithm of the period and the distance to the bifurcation point.

are numbered with the same convention as in figure 6. Although it is not possible to present all results in a single figure because the curves are very steep and close to each other, the numerical results fully confirm the predictions of the normal form. In particular, the numerical results allow us to confirm the coexistence of two stable states (in regions 3) and of a stable cycle and a stable state (in region 4). However, a precise mapping of the curve $H_{\infty}$ bounding the region 4 could not be achieved, but the occurrence of a global homoclinic bifurcation was confirmed (see § 3.5.3).

### 3.5.3. *Homoclinic bifurcation*

As explained in § 3.5, the normal form predicts a homoclinic curve $H_{\infty}$ and a homoclinic saddle-node bifurcation along the $F_{-}$ curve, right from the SNL point, corresponding to the appearance of two steady solutions along a previously existing cycle.

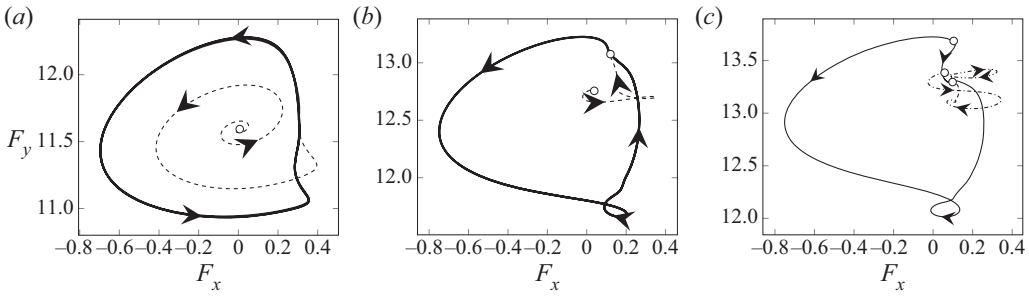


FIGURE 9. Phase portrait of the dynamics of the rotating cylinder at $Re = 170$ for three values of the rotation rate $\alpha$. Vertical (horizontal) axis is the lift force $F_y$ (drag force $F_x$) on the cylinder surface, empty dots denote steady-state solutions. (*a*,*b*) Limit sets (respectively transients) are depicted by a thick solid line (respectively thin dashed). (*c*) Heteroclinic connections between unstable–stable (respectively saddle–stable) are depicted by thin solid lines (respectively dashed dotted).

A generic feature of the imminent presence of a homoclinic saddle-node bifurcation is the divergence of the period of the limit cycle on which the saddle node appears. More precisely, the period is expected to scale as $\propto 1/\sqrt{\alpha_{SN} - \alpha}$ as $\alpha \to \alpha_{SN}$ (see Gasull, Mañosa & Villadelprat 2005). To check this prediction, time stepping simulations were conducted for $Re = 170$ and values of $\alpha$ just below the $F_-$ curve. As shown in figure 8 the period of the limit cycle effectively diverges as one approaches the bifurcation following the theoretical behaviour.

Dynamics near the threshold can be perfectly understood in a two-dimensional manifold. Phase portraits of the bifurcation are displayed in figure 9. These phase portraits were computed with an initial guess generated by a small linear perturbation to a steady state in the direction of its corresponding eigenmode. The initial guess is then integrated in time until it reaches its limit set, i.e. a periodic, homoclinic orbit or another steady state. Below the bifurcation threshold (figure 9*a*) a stable limit cycle exists, represented by a thick solid line. At the bifurcation threshold, a saddle node arises along this cycle, which ceases to exist, giving rise to a homoclinic connection (an approximation of this orbit is delineated by a thick solid line in figure 9*b*). Beyond the saddle-node bifurcation, the saddle node splits into two fixed points. Hence, three steady states exist, including a stable one (see figure 9*c*). There exist four stable heteroclinic connections, two between unstable–stable steady states represented by a dashed line in figure 9(*c*) and other two between saddle–stable steady states denoted by a solid line. This sequence of events is fully consistent to the sequence connecting phase portraits (2), (SNL) and (4) in figure 6.

### 3.6. *Generalised Hopf*

#### 3.6.1. *Normal form analysis*

Bautin bifurcation or GH is a codimension-two bifurcation where the equilibrium has purely imaginary eigenvalues $\lambda_{1,2} = \pm\omega_0$ with $\omega_0 > 0$, and the third-order coefficient of the normal form vanishes. Generalised Hopf bifurcation is thus a degenerate case of the generic Hopf bifurcation, where the cubic normal form is not sufficient to determine the nonlinear stability of the system. To unravel the dynamics near the Bautin bifurcation point

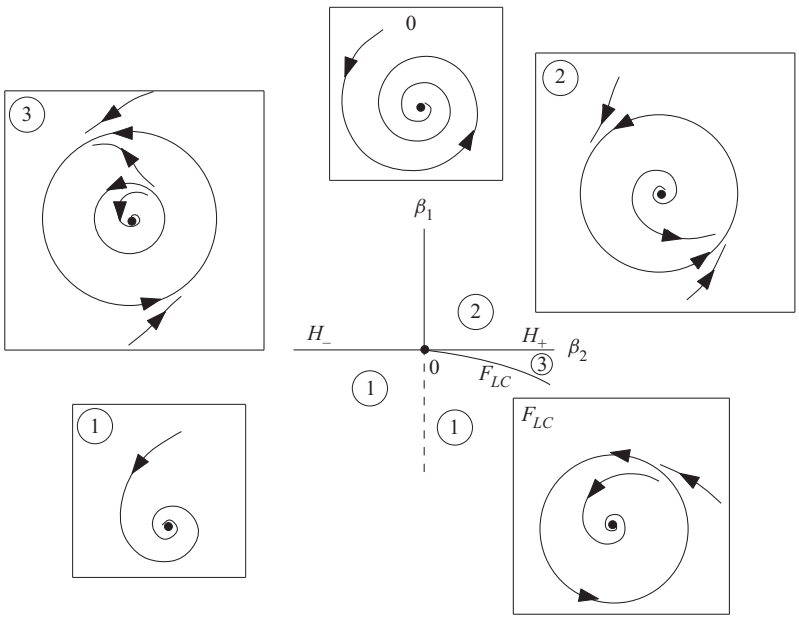


FIGURE 10. Qualitative bifurcation scenario in the vicinity of the GH bifurcation.

consider the normal form

$$\begin{cases} \dfrac{\mathrm{d}x_1}{\mathrm{d}t} = \beta_2 x_1 - x_2 + \beta_1 x_1 (x_1^2 + x_2^2) \pm x_1 (x_1^2 + x_2^2)^2. \\ \dfrac{\mathrm{d}x_2}{\mathrm{d}t} = \beta_2 x_2 + x_1 + \beta_1 x_2 (x_1^2 + x_2^2) \pm x_2 (x_1^2 + x_2^2)^2. \end{cases} \tag{3.2}$$

Three curves are of special interest:

(i) System (3.2) undergoes a supercritical Hopf bifurcation in the half-line $H_+ = \{(\beta_1, \beta_2) | \beta_2 > 0, \beta_1 = 0\}$. This curve separates a region containing a stable focus to a region containing an unstable focus plus a stable limit cycle.

(ii) System (3.2) undergoes a subcritical Hopf bifurcation in the half-line $H_- = \{(\beta_1, \beta_2) | \beta_2 < 0, \beta_1 = 0\}$. This curve separates a region containing an unstable focus, from one containing a stable focus and two limit cycles (one being stable and the other one being unstable).

(iii) System (3.2) undergoes a fold cycle bifurcation on the curve $F_{LC} = \{(\beta_1, \beta_2) | \beta_1^2 + 4\beta_2 = 0, \beta_1 < 0\}$. This curve separates a region containing two limit cycles from one which does not contain any limit cycle (a stable fixed point also exists in both regions).

The most notable feature of this bifurcation is the existence of a bistability region characterised by two stable states (a fixed point and a cycle). Therefore, hysteretic behaviour is expected as one successively crosses curves $H_-$ and $F_{LC}$. The bistability range is also characterised by the existence of an unstable limit cycle constituting the 'edge state' bounding the basins of attraction of the two stable states (figure 10).

3.6.2. *Weakly nonlinear analysis*

Unstable limit cycles are not easy to track, since they require stabilisation techniques, such as BoostConv (Citro *et al.* 2017) or edge-state tracking (Bengana *et al.* 2019), or the use of continuation techniques, such as harmonic balance (Fabre *et al.* 2019). Alternatively, we have performed a multiple-scale analysis up to fifth order (see appendix C). This method was previously used to study thermoacoustic bifurcations in the Rijke tube (Orchini, Rigas & Juniper 2016), displaying a good match with time stepping simulations with a much lower computational cost. By performing a weakly nonlinear analysis up to fifth order it is possible to determine a complex amplitude equation for the amplitude $A$ of the critical linear mode $\hat{\boldsymbol{q}}$. Here, the critical linear mode is normalised so that its $L^2\mathcal{B}$-norm (see appendix C), i.e. its kinetic energy, is unity, which corresponds to the same normalisation as in Mantič-Lugo, Arratia & Gallaire (2014). The governing equation is a Stuart Landau equation, depending on a small parameter $\epsilon^2 = Re_c(\alpha)^{-1} - Re^{-1}$

$$\frac{\mathrm{d}A}{\mathrm{d}t} = (\mathrm{i}\omega_0 + \epsilon^2\lambda_0 + \epsilon^4\lambda_1)A + (\nu_{1,0} + \epsilon^2\nu_{1,1})|A|^2A + \nu_{2,0}|A|^4A. \tag{3.3}$$

We remark that (3.3) is equivalent to (3.2) if separating real and imaginary parts. Searching for a solution under the form $A = |A|\,\mathrm{e}^{\mathrm{i}\omega t}$, and injecting into (3.3) leads to

$$\left.\begin{array}{c} |A| = \sqrt{-\dfrac{\nu_{1,r}}{2\nu_{2,r}} \pm \sqrt{\dfrac{\nu_{1,r}^2}{4\nu_{2,r}^2} - \dfrac{\lambda_r}{\nu_{2,r}}}} \\ \omega = \omega_0 + \nu_{1,i}|A| + \nu_{2,i}|A|^2 \end{array}\right\}, \tag{3.4}$$

where $\nu_1 = \nu_{1,0} + \epsilon^2\nu_{1,1}$, $\lambda = \epsilon^2\lambda_0 + \epsilon^4\lambda_1$, $\nu_2 = \nu_{2,0}$ and subscripts $r, i$ denote real and imaginary parts respectively. It turns out that $\nu_{2,r}$ is always negative while $\nu_{1,r}$ changes sign at $(Re, \alpha) = (Re_{GH}, \alpha_{GH})$. One can deduce the following consequences:

(i) If $Re < Re_{GH}$ (i.e. $\nu_{2r} < 0$), (3.4) has a single solution $|A|$ for $\lambda_r > 0$ (i.e. $Re > Re_c$) and none for $\lambda_r < 0$ (i.e. $Re < Re_c$). In this case, the Hopf bifurcation is supercritical.

(ii) If $Re > Re_{GH}$, (i.e. $\nu_{2r} > 0$), (3.4) has a single solution $|A|$ for $\lambda_r > 0$ (i.e. $Re > Re_c$), two solutions if $\lambda_c < \lambda_r < 0$ with $\lambda_c = \nu_{1,r}^2/4\nu_{2,r}$ and no solution if $\lambda_r < \lambda_c$. In this case, the Hopf bifurcation is subcritical. The condition $\lambda_r = \lambda_c$ defines a curve in the $(Re, \alpha)$ plane which corresponds to the fold cycle bifurcation associated with the emergence of the two limit cycles.

Figure 11 represents the amplitude and frequency of the limit cycles predicted by (3.4) for three values of $Re$. According to these results, the fold curve is predicted to be very close to the Hopf curve, i.e. within a few tenths of $Re$ up to $Re = 250$. This behaviour allows us to clarify the transition occurring at the GH point in figure 6. For $Re < Re_{GH}$, when increasing $Re$ for fixed $\alpha$ (or increasing $\alpha$ with fixed $Re$), the transition occurs via a supercritical Hopf bifurcation. On the other hand, for $Re > Re_{GH}$, the transition is predicted to be subcritical, involving the existence of a band where both steady state and Mode II coexist. Note that the width of the bistability band predicted by the weakly nonlinear analysis is very narrow, and could thus be difficult to evidence using direct numerical simulations.

## 4. Conclusion and discussion

The present study allowed us to clarify the bifurcation scenario in the two-dimensional flow past a rotating cylinder, especially concerning the range of parameters corresponding

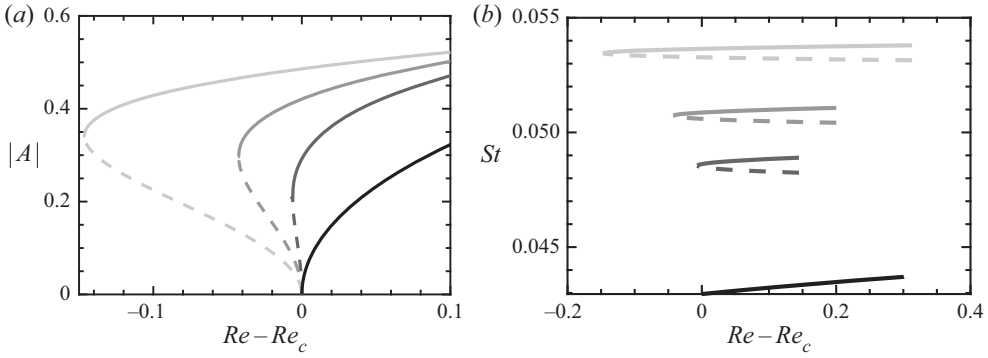


FIGURE 11. (*a*) Amplitudes of stable (solid line) and unstable (dashed line) limit cycles for four $Re_c = 100; 170; 200; 250$, where $Re_c$ denotes the Reynolds number at the Hopf bifurcation. Grey scale: darker curves designate quantities associated with a lower $Re$, i.e. black curve $Re = 100$ and light grey $Re = 250$. (*b*) Strouhal number of limit cycles.

to the onset of the 'Mode II' unsteady vortex shedding mode. Using steady-state calculation involving arclength continuation and linear stability analysis, we have been able to draw all bifurcation curves existing in the range of parameters corresponding to $Re < 200$ and $\alpha < 5$. Three codimension-two bifurcations have been identified along the border of the range of existence of this mode, namely a Takens–Bogdanov, a cusp and a generalised Hopf. The first two are located in close vicinity, in such a way that the whole dynamics can be understood using the normal form of the codimension-three bifurcation (for a generalised Takens–Bogdanov bifurcation). The analysis also allowed us to identify three ranges of parameters characterised by bistability, two of them located in the vicinity of the Takens–Bogdanov and cusp points, the third one emanating from the generalised Hopf point. Time stepping simulations and a weakly nonlinear analysis have confirmed these findings, and have also allowed us to characterise the homoclinic and heteroclinic orbits connecting the fixed points, in full accordance with the predictions of the normal form theory.

The most surprising result of the study is the existence of an almost perfect codimension-three bifurcation in a problem characterised by only two control parameters. Such a feature suggests that the problem could be quite sensible to any small perturbations in a way such that small perturbations could completely change the scenario. We have checked that the scenario is robust with respect to numerical discretisation issues (see appendix D). The dependency with respect to additional physical parameters is more interesting. The effect of compressibility is an interesting question which we expect to investigate in future studies. Preliminary results have shown that for a Mach number of order 0.1, the dynamics in the region of the near-codimension-three point is effectively greatly modified. Other additional parameters, such as for instance shear or confinement, could be added. Finally, one may question the relevance of the present findings for three-dimensional flows. A short review of three-dimensional stability properties of the rotating cylinder flow is given in appendix E. The discussion confirms that the most important results of the present study occur in range of parameters where no three-dimensional instabilities are present.

## Declaration of interests

The authors report no conflict of interest.

## Appendix A. Pseudo arc-length continuation

Arc-length continuation is a standard technique in dynamical systems theory. It allows for the continuation of a given solution branch through a turning or fold point. At the turning point the Jacobian of the system is singular; therefore, any iterative method based on the Jacobian is doomed to failure. To prevent the stall in the convergence of the Newton's method, an extra condition needs to be added to the system of equations. In the current study we have chosen a pseudo arc-length methodology, which is based in a predictor–corrector strategy. The extended system adds an extra equation which ensures the tangency to the branch of the solution. For that purpose, a parameter is chosen, here either $Re$ or $\alpha$, and a monitor of the variation, either the horizontal force acting on the cylinder surface $F_x$ or the vertical force $F_y$. The parameter and the monitor are parametrised by the length of the branch, here indicated by the parameter $s$. The current solution is varied by a given step $\Delta s$ tangent to the solution branch and later corrected by a orthogonal correction. Let us denote by the subscript $j$ the arc-length iteration and by the superscript $n$ the Newton iteration of the corrector step, where $N$ is used to denote the last step. In the description below, let us consider without loss of generality we have fixed the parameter $\alpha$ and the monitor $F_x$.

### A.1. *Predictor*

The predictor step consists in the determination of a initial guess $\alpha_j^0$ for the iteration $j$ of the arc length. The initial guess is determined from a tangent extrapolation of the solution branch.

$$\alpha_j^0 = \alpha_{j-1}^N + \frac{\mathrm{d}\alpha_{j-1}^N}{ds}\Delta s, \tag{A 1a}$$

$$\boldsymbol{q}_j^0 = \boldsymbol{q}_{j-1}^N + \frac{\mathrm{d}\boldsymbol{q}_{j-1}^N}{\mathrm{d}s}\Delta s \implies F_x(\boldsymbol{q}_j^0) = F_x(\boldsymbol{q}_{j-1}^N) + \frac{\mathrm{d}F_x(\boldsymbol{q}_{j-1}^N)}{\mathrm{d}s}\Delta s. \tag{A 1b}$$

In (A 1), $\mathrm{d}\alpha_{j-1}^N/\mathrm{d}s$ is the slope of the tangent in the $\alpha$ direction and $\mathrm{d}\boldsymbol{q}_{j-1}^N/\mathrm{d}s$ in the direction of the vector field. The tangent is computed from the differentiation of the stationary Navier–Stokes equations (2.1)

$$\frac{\mathrm{d}\boldsymbol{q}_{j-1}^N}{\mathrm{d}s} = -\left[\frac{\partial NS_{\boldsymbol{q}_{j-1}^N}}{\partial \boldsymbol{q}}\right]^{-1}\frac{\partial NS_{\boldsymbol{q}_{j-1}^N}}{\partial \alpha}, \tag{A 2}$$

where we have used the notation $NS_{\boldsymbol{q}_{j-1}^N} = 0$ to denote the steady incompressible Navier–Stokes equation whose solution is $\boldsymbol{q}_{j-1}^N$. The tangent is completed with a normalisation condition in the arc length

$$\left\|\frac{\mathrm{d}F_x(\boldsymbol{q}_{j-1}^N)}{\mathrm{d}s}\right\|_2^2 + \left\|\frac{\mathrm{d}\alpha_{j-1}^N}{\mathrm{d}s}\right\|_2^2 = 1. \tag{A 3}$$

### A.2. *Corrector*

This step consists in an orthogonal correction of the tangent guess. To do so one needs to solve the following system of equations

$$\begin{bmatrix} \frac{\partial NS_{q_j^n}}{\partial \boldsymbol{q}} & \frac{\partial NS_{q_j^n}}{\partial \alpha} \\ \frac{\mathrm{d}F_x(\boldsymbol{q}_{j1}^n)}{\mathrm{d}s}F_x(\cdot) & \frac{\mathrm{d}\alpha_j^n}{\mathrm{d}s} \end{bmatrix} \begin{bmatrix} \Delta \boldsymbol{q}_j^{n+1} \\ \Delta \alpha_j^{n+1} \end{bmatrix} = \begin{bmatrix} -NS(\boldsymbol{u}) \\ \Delta s - \frac{\mathrm{d}F_x}{\mathrm{d}s}F_x(\boldsymbol{q}_j^n - \boldsymbol{q}_{j-1}^N) - \frac{\mathrm{d}\alpha}{\mathrm{d}s}(\alpha_j^n - \alpha_{j-1}^N) \end{bmatrix}, \quad \text{(A 4)}$$

where the last equation of (A 4) comes from the differentiation of the normalisation condition (A 3) and considering that $\Delta\alpha_j = \Delta\alpha_j^{n+1} + \alpha_j^n - \alpha_{j-1}^N = \alpha_j^N - \alpha_{j-1}^N$ (similarly on $\boldsymbol{q}$).

## Appendix B. Weakly nonlinear analysis to determine the normal form of the saddle-node bifurcation

Saddle-node bifurcation and homoclinic saddle-node bifurcation are locally characterised by the normal form of the saddle-node bifurcation (see Kuznetsov 2013). In the generic case, when $a_2(Re, \alpha) \neq 0$ and $a_0(Re, \alpha) \neq 0$ the central manifold is unravelled by its second-order normal form

$$\frac{\mathrm{d}x_1}{\mathrm{d}t} = a_0(Re, \alpha) + a_2(Re, \alpha)x_1^2 + O(x_1^3). \quad \text{(B 1)}$$

Coefficients $a_2(Re, \alpha) \neq 0$ and $a_0(Re, \alpha) \neq 0$ can be obtained with aid of weakly nonlinear analysis. Let us consider the following transformations:

$$t = \tau_0 + \epsilon^2\tau_1, \quad \text{(B 2}a\text{)}$$

$$\frac{\mathrm{d}}{\mathrm{d}t} = \frac{\mathrm{d}}{\mathrm{d}\tau_0} + \epsilon^2\frac{\mathrm{d}}{\mathrm{d}\tau_1}, \quad \text{(B 2}b\text{)}$$

$$\boldsymbol{Q} = \boldsymbol{Q}_b + \epsilon\hat{\boldsymbol{q}} + \epsilon^2\boldsymbol{q}_2, \quad \text{(B 2}c\text{)}$$

where $\epsilon^2 = (1/Re_c) - (1/Re)$. The system at order $\epsilon^0$ is the incompressible Navier–Stokes system that provides the base flow. The system at order $\epsilon^1$ is identical to the linearised Navier–Stokes problem (2.3). At order $\epsilon^2$ secular term appears and solvability condition must be imposed

$$a_0 = \frac{\left\langle \hat{\boldsymbol{u}}^\dagger, -\tau(\boldsymbol{U}_b) \right\rangle}{\left\langle \hat{\boldsymbol{u}}^\dagger, \hat{\boldsymbol{u}} \right\rangle}, \quad \text{(B 3)}$$

$$a_2 = \frac{\left\langle \hat{\boldsymbol{u}}^\dagger, -\hat{\boldsymbol{u}}\nabla\hat{\boldsymbol{u}} \right\rangle}{\left\langle \hat{\boldsymbol{u}}^\dagger, \hat{\boldsymbol{u}} \right\rangle}. \quad \text{(B 4)}$$

Here, $\hat{\boldsymbol{u}}^\dagger$ denotes the adjoint or left eigenvector of linearised Navier–Stokes equations associated with the null eigenvalue.

## Appendix C. WNL to determine the normal form of the Hopf bifurcation degeneracy

Weakly nonlinear analysis has been used extensively in the case of Hopf bifurcations to unravel the frequency of the limit cycle near the bifurcation threshold

(see Gallaire *et al.* 2016) and to determine the validity of stability analysis on the mean flow (see Sipp & Lebedev 2007). In this article WNL analysis is used to determine the existence of a generalised Hopf bifurcation (see § 3.6). The starting point of the weakly nonlinear method is the decomposition of the flow field into multiple scales

$$\begin{aligned}\boldsymbol{Q} = \boldsymbol{Q}_b &+ \epsilon\left[A_{wnl}\hat{\boldsymbol{q}}\,\mathrm{e}^{\mathrm{i}\omega_0 t} + \mathrm{c.c.}\right]\\ &+ \epsilon^2\left[\boldsymbol{q}_{2,0} + |A_{wnl}|\boldsymbol{q}_{2,0}^{|A_{wnl}|} + (A_{wnl}^2\boldsymbol{q}_{2,2}\,\mathrm{e}^{2\mathrm{i}\omega_0 t} + \mathrm{c.c.})\right]\\ &+ \epsilon^3\left[A_{wnl}\,\mathrm{e}^{\mathrm{i}\omega_0 t}\left(\boldsymbol{q}_{3,1} + |A_{wnl}|^2\boldsymbol{q}_{3,1}^{|A_{wnl}|^2} + |A_{wnl}|^2\boldsymbol{q}_{3,1}^{A_{wnl}\bar{A}_{wnl}}\right) + A_{wnl}^3\,\mathrm{e}^{3\mathrm{i}\omega_0 t}\boldsymbol{q}_{3,3} + \mathrm{c.c.}\right]\\ &+ \epsilon^4\left[\boldsymbol{q}_{4,0} + |A_{wnl}|^2\boldsymbol{q}_{4,0}^{|A_{wnl}|^2} + |A_{wnl}|^4\boldsymbol{q}_{4,0}^{|A_{wnl}|^4}\right.\\ &\left.+A_{wnl}^2\,\mathrm{e}^{2\mathrm{i}\omega_0 t}\left(\boldsymbol{q}_{4,2} + |A_{wnl}|^2\boldsymbol{q}_{4,2}^{|A_{wnl}|^2}\right) + A_{wnl}^4\,\mathrm{e}^{4\mathrm{i}\omega_0 t}\boldsymbol{q}_{4,4} + \mathrm{c.c.}\right] + O(\epsilon^5),\end{aligned} \tag{C 1a}$$

where the complex amplitude $A_{wnl}$ depends upon a slow time scale $\tau = \epsilon^2 t$. The choice of the parameter $\epsilon$ is the same as in Fabre *et al.* (2019), $\epsilon^2 = 1/Re_c(\alpha) - 1/Re$, where the critical Reynolds $Re_c(\alpha)$ is a function of the rotation rate $\alpha$. When the ansatz (C 1) is substituted into the Navier–Stokes equations, at orders $O(\epsilon^3)$ and $O(\epsilon^5)$ solvability conditions need to be imposed due to the presence of secular terms which lead to a Stuart–Landau equation depending upon the slow time scale $\tau$

$$\frac{\partial A_{wnl}}{\partial \tau} = (\lambda_0 + \epsilon^2\lambda_1)A_{wnl} + (\nu_{1,0} + \epsilon^2\nu_{1,1})|A_{wnl}|^2 A_{wnl} + \epsilon^2\nu_{2,0}|A_{wnl}|^4 A_{wnl}. \tag{C 2}$$

If we take into account the definition of the slow time scale $\tau = \epsilon^2 t$, the fact that up to leading order $O(\epsilon)$ we have $\mathrm{d}A_{wnl}/\mathrm{d}t = \mathrm{i}\omega_0\epsilon A_{wnl}$ and we define a new amplitude which depends on $\epsilon$ as $A = \epsilon A_{wnl}$ we can rewrite (C 2) as

$$\frac{\mathrm{d}A}{\mathrm{d}t} = (\mathrm{i}\omega_0 + \epsilon^2\lambda_0 + \epsilon^4\lambda_1)A + (\nu_{1,0} + \epsilon^2\nu_{1,1})|A|^2 A + \nu_{2,0}|A|^4 A. \tag{C 3}$$

In the following we consider that the eigenmode $\hat{\boldsymbol{q}}$ and its adjoint $\hat{\boldsymbol{q}}^\dagger$ have been normalised so that $||\hat{\boldsymbol{q}}||_{\mathcal{B}}^2 = \langle\hat{\boldsymbol{q}}, \mathcal{B}\hat{\boldsymbol{q}}\rangle = \langle\hat{\boldsymbol{u}}, \hat{\boldsymbol{u}}\rangle = 1$ and $\left\langle\hat{\boldsymbol{q}}^\dagger, \mathcal{B}\hat{\boldsymbol{q}}\right\rangle = \left\langle\hat{\boldsymbol{u}}^\dagger, \hat{\boldsymbol{u}}\right\rangle = 1$. This normalisation is the same as that one used in the self-consistent methodology (see Mantič-Lugo *et al.* 2014): with this choice, $A$ is a real constant representing the amplitude of the linear mode with respect to its $L^2$ norm. In the following we will use the notation $\mathcal{LNS}_{\mathrm{i}\omega}\boldsymbol{q} = \mathrm{i}\omega\mathcal{B}\boldsymbol{q} - \mathcal{LNS}\boldsymbol{q}$ to denote the application of the linearised operator at a specific frequency $\omega$.

The ansatz (C 1) is substituted into the incompressible Navier–Stokes equations (2.1):

(i) Order $O(\epsilon^0)$ leads to the steady-state Navier–Stokes equations (2.1).
(ii) Order $O(\epsilon^1)$ leads to the linearised Navier–Stokes equations (2.3).
(iii) Order $O(\epsilon^2)$ contains three terms, which are computed as the solution of three linear systems:

$$\mathcal{LNS}_0\boldsymbol{q}_{2,0} = -2\boldsymbol{\nabla}\cdot(d(\boldsymbol{U}_b)), \tag{C 4a}$$

$$\mathcal{LNS}_0\boldsymbol{u}_{2,0}^{|A_{wnl}|} = -\hat{\boldsymbol{q}}\cdot\boldsymbol{\nabla}\bar{\hat{\boldsymbol{u}}} + \bar{\hat{\boldsymbol{u}}}\cdot\boldsymbol{\nabla}\hat{\boldsymbol{q}}, \tag{C 4b}$$

$$\mathcal{LNS}_{2\mathrm{i}\omega_0}\boldsymbol{u}_{2,2} = -\hat{\boldsymbol{u}}\cdot\boldsymbol{\nabla}\hat{\boldsymbol{u}}. \tag{C 4c}$$

(iv) At order $O(\epsilon^3)$ there are degenerate terms, i.e. terms corresponding to the frequency $\mathrm{i}\omega_0$. The operator $\mathcal{LNS}_{\mathrm{i}\omega_0}$ is not injective ($\hat{\boldsymbol{q}}$ belongs to its kernel) and it is not surjective because $\hat{\boldsymbol{q}}^\dagger$ belongs to the kernel of its adjoint and the operator is Fredholm in $L^2$. Therefore we need to impose solvability conditions in order to obtain terms $\boldsymbol{q}_{3,1}$, $\boldsymbol{q}_{3,1}^{|A_{wnl}|^2}$ and $\boldsymbol{q}_{3,1}^{A_{wnl}\bar{A}_{wnl}}$. Solvability conditions at $O(\epsilon^3)$ correspond to

$$\mu_1 = -\frac{\left\langle \hat{\boldsymbol{u}}^\dagger, \hat{\boldsymbol{u}}\cdot\nabla \boldsymbol{u}_{2,0}^{|A_{wnl}|} + \boldsymbol{u}_{2,0}^{|A_{wnl}|}\cdot\nabla\hat{\boldsymbol{u}}\right\rangle}{\left\langle \hat{\boldsymbol{u}}^\dagger, \hat{\boldsymbol{u}}\right\rangle}, \tag{C 5}$$

$$\mu_2 = -\frac{\left\langle \hat{\boldsymbol{u}}^\dagger, \bar{\hat{\boldsymbol{u}}}\cdot\nabla \boldsymbol{u}_{2,2} + \boldsymbol{u}_{2,2}\cdot\nabla\bar{\hat{\boldsymbol{u}}}\right\rangle}{\left\langle \hat{\boldsymbol{u}}^\dagger, \hat{\boldsymbol{u}}\right\rangle}, \tag{C 6}$$

$$\lambda_0 = -\frac{\left\langle \hat{\boldsymbol{u}}^\dagger, \hat{\boldsymbol{u}}\cdot\nabla \boldsymbol{u}_{2,0} + \boldsymbol{u}_{2,0}\cdot\nabla\hat{\boldsymbol{u}} + 2\nabla\cdot(d(\hat{\boldsymbol{u}}))\right\rangle}{\left\langle \hat{\boldsymbol{u}}^\dagger, \hat{\boldsymbol{u}}\right\rangle}, \tag{C 7}$$

where $\mu_1 + \mu_2 = \nu_{1,0}$. Additionally, given the fact that $L^2$ is a Hilbert space and the operator is Fredholm, the space can be decomposed into a direct sum of the range of the operator $\mathcal{LNS}_{\mathrm{i}\omega_0}$ and the kernel of its adjoint. This implies that secular terms are determined up to a constant in the direction of the eigenmode $\hat{\boldsymbol{q}}$, i.e. $\boldsymbol{q}_{3,1} \to \boldsymbol{q}_{3,1} + \delta_0\hat{\boldsymbol{q}}$, $\delta_0 \in \mathbb{R}$. This degree of freedom is fixed by considering $\delta_0 = 0$, i.e. each secular term is orthogonal to the linear adjoint mode $\hat{\boldsymbol{q}}^\dagger$ in the norm $\mathcal{B}$, i.e. $\left\langle \hat{\boldsymbol{q}}^\dagger, \mathcal{B}\boldsymbol{q}_{3,1}\right\rangle = 0$. This choice for the extra degree of freedom has been also used in Carini, Auteri & Giannetti (2015). This leads to

$$\begin{pmatrix} \mathcal{LNS}_{\mathrm{i}\omega_0} & -\mathcal{B}\hat{\boldsymbol{q}} \\ \hat{\boldsymbol{q}}^{\dagger H}\mathcal{B} & 0 \end{pmatrix}\begin{pmatrix} \boldsymbol{q}_{3,1} \\ \lambda_0 \end{pmatrix} = \begin{pmatrix} \boldsymbol{F}_{3,1} \\ 0 \end{pmatrix} \tag{C 8}$$

and similarly for pairs $(\boldsymbol{q}_{3,1}^{|A_{wnl}|^2}, \mu_1)$ and $(\boldsymbol{q}_{3,1}^{A_{wnl}\bar{A}_{wnl}}, \mu_2$ replacing $\boldsymbol{F}_{3,1}$ by $\boldsymbol{F}_{3,1}^{|A_{wnl}|^2}$ and $\boldsymbol{F}_{3,1}^{A_{wnl}\bar{A}_{wnl}}$ respectively. Please note that

$$\left.\begin{aligned} \boldsymbol{F}_{3,1} &= -\hat{\boldsymbol{u}}\cdot\nabla\boldsymbol{u}_{2,0} - \boldsymbol{u}_{2,0}\cdot\nabla\hat{\boldsymbol{u}} - 2\nabla\cdot(d(\hat{\boldsymbol{u}})) \\ \boldsymbol{F}_{3,1}^{|A_{wnl}|^2} &= -\hat{\boldsymbol{u}}\cdot\nabla\boldsymbol{u}_{2,0}^{|A_{wnl}|} - \boldsymbol{u}_{2,0}^{|A_{wnl}|}\cdot\nabla\hat{\boldsymbol{u}} \\ \boldsymbol{F}_{3,1}^{A_{wnl}\bar{A}_{wnl}} &= -\bar{\hat{\boldsymbol{u}}}\cdot\nabla\boldsymbol{u}_{2,2} - \boldsymbol{u}_{2,2}\cdot\nabla\bar{\hat{\boldsymbol{u}}} \end{aligned}\right\}. \tag{C 9}$$

The other non-resonant term is solved as usually,

$$\mathcal{LNS}_{3\mathrm{i}\omega_0}\boldsymbol{q}_{3,3} = \boldsymbol{F}_{3,3} = -\hat{\boldsymbol{u}}\cdot\nabla\boldsymbol{u}_{2,2} - \boldsymbol{u}_{2,2}\cdot\nabla\hat{\boldsymbol{u}}. \tag{C 10}$$

(v) At order $O(\epsilon^4)$ we find six terms which are solved by the resolution of the following linear systems

$$\left.\begin{aligned}
\mathcal{LNS}_0 \boldsymbol{q}_{4,0} &= \boldsymbol{F}_{4,0} \\
\mathcal{LNS}_0 \boldsymbol{q}_{4,0}^{|A_{wnl}|^2} &= \boldsymbol{F}_{4,0}^{|A_{wnl}|^2} \\
\mathcal{LNS}_0 \boldsymbol{q}_{4,0}^{|A_{wnl}|^4} &= \boldsymbol{F}_{4,0}^{|A_{wnl}|^4} \\
\mathcal{LNS}_{2\mathrm{i}\omega_0} \boldsymbol{q}_{4,2} &= \boldsymbol{F}_{4,2} \\
\mathcal{LNS}_{2\mathrm{i}\omega_0} \boldsymbol{q}_{4,2}^{|A_{wnl}|^2} &= \boldsymbol{F}_{4,2}^{|A_{wnl}|^2} \\
\mathcal{LNS}_{4\mathrm{i}\omega_0} \boldsymbol{q}_{4,4} &= \boldsymbol{F}_{4,4}
\end{aligned}\right\}, \tag{C 11}$$

where the right-hand side terms are

$$\boldsymbol{F}_{4,0} = -\boldsymbol{u}_{2,0}\cdot\nabla\boldsymbol{u}_{2,0} - 2\nabla\cdot d(\boldsymbol{u}_{2,0}), \tag{C 12}$$

$$\begin{aligned}
\boldsymbol{F}_{4,0}^{|A_{wnl}|^2} = &-\boldsymbol{u}_{3,1}\cdot\nabla\bar{\hat{\boldsymbol{u}}} - \bar{\hat{\boldsymbol{u}}}\cdot\nabla\boldsymbol{u}_{3,1} - \bar{\boldsymbol{u}}_{3,1}\cdot\nabla\hat{\boldsymbol{u}} - \hat{\boldsymbol{u}}\cdot\nabla\bar{\boldsymbol{u}}_{3,1} \\
&- \boldsymbol{u}_{2,0}\cdot\nabla\boldsymbol{u}_{2,0}^{|A_{wnl}|^2}\boldsymbol{u}_{2,0}^{|A_{wnl}|^2}\cdot\nabla\boldsymbol{u}_{2,0},
\end{aligned} \tag{C 13}$$

$$\begin{aligned}
\boldsymbol{F}_{4,0}^{|A_{wnl}|^4} = &-\boldsymbol{u}_{2,2}\cdot\nabla\bar{\boldsymbol{u}}_{2,2} - \bar{\boldsymbol{u}}_{2,2}\cdot\nabla\boldsymbol{u}_{2,2} - \boldsymbol{u}_{2,0}^{|A_{wnl}|^2}\cdot\nabla - \boldsymbol{u}_{2,0}^{|A_{wnl}|^2} \\
&- \boldsymbol{u}_{3,1}^{|A_{wnl}|^2}\cdot\nabla\bar{\hat{\boldsymbol{u}}} - \bar{\hat{\boldsymbol{u}}}\cdot\nabla\boldsymbol{u}_{3,1}^{|A_{wnl}|^2} - \bar{\boldsymbol{u}}_{3,1}^{|A_{wnl}|^2}\cdot\nabla\hat{\boldsymbol{u}} - \hat{\boldsymbol{u}}\cdot\nabla\bar{\boldsymbol{u}}_{3,1}^{|A_{wnl}|^2} \\
&- \boldsymbol{u}_{3,1}^{A_{wnl}\bar{A}_{wnl}}\cdot\nabla\bar{\hat{\boldsymbol{u}}} - \bar{\hat{\boldsymbol{u}}}\cdot\nabla\boldsymbol{u}_{3,1}^{A_{wnl}\bar{A}_{wnl}} - \bar{\boldsymbol{u}}_{3,1}^{A_{wnl}\bar{A}_{wnl}}\cdot\nabla\hat{\boldsymbol{u}} - \hat{\boldsymbol{u}}\cdot\nabla\bar{\boldsymbol{u}}_{3,1}^{A_{wnl}\bar{A}_{wnl}},
\end{aligned} \tag{C 14}$$

$$\begin{aligned}
\boldsymbol{F}_{4,2} = &-\boldsymbol{u}_{2,0}^{|A|^2_{wnl}}\cdot\nabla\boldsymbol{u}_{2,0} - \boldsymbol{u}_{2,0}\cdot\nabla\boldsymbol{u}_{2,0}^{|A|^2_{wnl}} - \boldsymbol{u}_{3,1}\cdot\nabla\hat{\boldsymbol{u}} - \hat{\boldsymbol{u}}\cdot\nabla\boldsymbol{u}_{3,1} \\
&- 2\nabla\cdot d(\boldsymbol{u}_{2,2}),
\end{aligned} \tag{C 15}$$

$$\begin{aligned}
\boldsymbol{F}_{4,2}^{|A_{wnl}|^2} = &-\boldsymbol{u}_{2,0}\cdot\nabla\boldsymbol{u}_{2,2} - \boldsymbol{u}_{2,2}\cdot\nabla\boldsymbol{u}_{2,0} - \boldsymbol{u}_{3,1}^{|A_{wnl}|^2}\cdot\nabla\hat{\boldsymbol{u}} - \hat{\boldsymbol{u}}\cdot\nabla\boldsymbol{u}_{3,1}^{|A_{wnl}|^2} \\
&- \boldsymbol{u}_{3,1}^{A_{wnl}\bar{A}_{wnl}}\cdot\nabla\hat{\boldsymbol{u}} - \hat{\boldsymbol{u}}\cdot\nabla\boldsymbol{u}_{3,1}^{A_{wnl}\bar{A}_{wnl}} - \boldsymbol{u}_{3,3}\cdot\nabla\bar{\hat{\boldsymbol{u}}} - \bar{\hat{\boldsymbol{u}}}\cdot\nabla\boldsymbol{u}_{3,3},
\end{aligned} \tag{C 16}$$

$$\boldsymbol{F}_{4,4} = -\boldsymbol{u}_{2,2}\cdot\nabla\boldsymbol{u}_{2,2} - \boldsymbol{u}_{3,3}\cdot\nabla\hat{\boldsymbol{u}} - \hat{\boldsymbol{u}}\cdot\nabla\boldsymbol{u}_{3,3}. \tag{C 17}$$

(vi) At order $O(\epsilon^5)$ we find three degenerate terms proportional to $A_{wnl}$, $A_{wnl}|A_{wnl}|^2$ and $A_{wnl}|A_{wnl}|^4$. As for the case of the third-order solvability conditions, they lead to the computation of coefficients $\lambda_1$, $\nu_{1,1}$ and $\nu_{2,0}$

$$\left.\begin{aligned}
\lambda_1 &= \left\langle \hat{\boldsymbol{u}}^\dagger, \boldsymbol{F}_{5,1} \right\rangle \\
\nu_{1,1} &= \left\langle \hat{\boldsymbol{u}}^\dagger, \boldsymbol{F}_{5,1}^{A_{wnl}|A_{wnl}|^2} \right\rangle \\
\nu_{2,0} &= \left\langle \hat{\boldsymbol{u}}^\dagger, \boldsymbol{F}_{5,1}^{A_{wnl}|A_{wnl}|^4} \right\rangle
\end{aligned}\right\}, \tag{C 18}$$

where $\boldsymbol{F}_{5,1}$, $\boldsymbol{F}_{5,1}^{|A_{wnl}|^2}$ and $\boldsymbol{F}_{5,1}^{|A_{wnl}|^4}$ are defined as follows:

$$\begin{aligned}\boldsymbol{F}_{5,1} = &-\boldsymbol{u}_{2,0}\cdot\nabla\boldsymbol{u}_{3,1} - \boldsymbol{u}_{2,0}\cdot\nabla\boldsymbol{u}_{3,1} - \boldsymbol{u}_{4,0}\cdot\nabla\hat{\boldsymbol{u}} - \hat{\boldsymbol{u}}\cdot\nabla\boldsymbol{u}_{4,0}\\ &- 2\nabla\cdot d(\boldsymbol{u}_{3,1}),\end{aligned} \tag{C 19}$$

$$\begin{aligned}\boldsymbol{F}_{5,1}^{A_{wnl}|A_{wnl}|^2} = &-\boldsymbol{u}_{2,0}\cdot\nabla\boldsymbol{u}_{3,0}^{|A_{wnl}|^2} - \boldsymbol{u}_{3,0}^{|A_{wnl}|^2}\cdot\nabla\boldsymbol{u}_{2,0}\\ &- \boldsymbol{u}_{2,0}\cdot\nabla\boldsymbol{u}_{3,0}^{A_{wnl}\bar{A}_{wnl}} - \boldsymbol{u}_{3,0}^{A_{wnl}\bar{A}_{wnl}}\cdot\nabla\boldsymbol{u}_{2,0}\\ &- \boldsymbol{u}_{2,0}^{|A_{wnl}|^2}\cdot\nabla\boldsymbol{u}_{3,1} - \boldsymbol{u}_{3,1}\cdot\nabla\boldsymbol{u}_{2,0}^{|A_{wnl}|^2}\\ &- \boldsymbol{u}_{2,2}\cdot\nabla\bar{\boldsymbol{u}}_{3,1} - \bar{\boldsymbol{u}}_{3,1}\cdot\nabla\boldsymbol{u}_{2,2}\\ &- \hat{\boldsymbol{u}}\cdot\nabla\boldsymbol{u}_{4,0}^{|A_{wnl}|^2} - \boldsymbol{u}_{4,0}^{|A_{wnl}|^2}\cdot\nabla\hat{\boldsymbol{u}}\\ &- \bar{\hat{\boldsymbol{u}}}\cdot\nabla\boldsymbol{u}_{4,0}^{A_{wnl}^2} - \boldsymbol{u}_{4,0}^{A_{wnl}^2}\cdot\nabla\bar{\hat{\boldsymbol{u}}}\\ &- 2\nabla\cdot d(\boldsymbol{u}_{3,0}^{|A_{wnl}|^2}) - 2\nabla\cdot d(\boldsymbol{u}_{3,0}^{A_{wnl}\bar{A}_{wnl}}),\end{aligned} \tag{C 20}$$

$$\begin{aligned}\boldsymbol{F}_{5,1}^{A_{wnl}|A_{wnl}|^4} = &-\boldsymbol{u}_{2,0}^{|A_{wnl}|^2}\cdot\nabla\boldsymbol{u}_{3,0}^{|A_{wnl}|^2} - \boldsymbol{u}_{3,0}^{|A_{wnl}|^2}\cdot\nabla\boldsymbol{u}_{2,0}^{|A_{wnl}|^2}\\ &- \boldsymbol{u}_{2,0}^{|A_{wnl}|^2}\cdot\nabla\boldsymbol{u}_{3,0}^{A_{wnl}\bar{A}_{wnl}} - \boldsymbol{u}_{3,0}^{A_{wnl}\bar{A}_{wnl}}\cdot\nabla\boldsymbol{u}_{2,0}^{|A_{wnl}|^2}\\ &- \boldsymbol{u}_{2,2}\cdot\nabla\bar{\boldsymbol{u}}_{3,0}^{|A_{wnl}|^2} - \bar{\boldsymbol{u}}_{3,0}^{|A_{wnl}|^2}\cdot\nabla\boldsymbol{u}_{2,2}\\ &- \boldsymbol{u}_{2,2}\cdot\nabla\bar{\boldsymbol{u}}_{3,0}^{A_{wnl}\bar{A}_{wnl}} - \bar{\boldsymbol{u}}_{3,0}^{A_{wnl}\bar{A}_{wnl}}\cdot\nabla\boldsymbol{u}_{2,0}\\ &- \boldsymbol{u}_{4,0}^{|A_{wnl}|^4}\cdot\nabla\bar{\hat{\boldsymbol{u}}} - \bar{\hat{\boldsymbol{u}}}\cdot\nabla\boldsymbol{u}_{4,0}^{|A_{wnl}|^4}\\ &- \boldsymbol{u}_{4,0}^{A_{wnl}^2|A_{wnl}|^2}\cdot\nabla\bar{\hat{\boldsymbol{u}}} - \bar{\hat{\boldsymbol{u}}}\cdot\nabla\boldsymbol{u}_{4,0}^{A_{wnl}^2|A_{wnl}|^2}\\ &- \bar{\boldsymbol{u}}_{2,2}\cdot\nabla\boldsymbol{u}_{3,3} - \boldsymbol{u}_{3,3}\cdot\nabla\bar{\boldsymbol{u}}_{2,2}.\end{aligned} \tag{C 21}$$

## Appendix D. Mesh convergence

Mesh independence of the solutions has been verified systematically. First, we have considered a given mesh refinement and varied the physical size of the domain, see table 2. We have observed that for a domain length of 80 diameters downstream the cylinder centre, 40 diameters upstream the cylinder centre and 40 in the cross-stream direction the solution is not affected by the imposition of boundary conditions. Secondly, we have looked at the effect of the mesh refinement on the properties of the solution. For that purpose a parametric study of eigenvalues, Hopf WNL coefficients and global monitors of a given steady-state solution have been carried out, see (table 3). The sensitivity to mesh convergence of cusp and Takens–Bogdanov bifurcation points has been also tested. Results show that each of them is found within $\Delta Re_c < 0.2$. Every mesh is computed by Delaunay triangulation. Mesh $M_1$ has been generated by blocks, as it is generally done with structured meshes; $M_2$ and $M_3$ have been computed following the mesh adaption procedure described in Fabre *et al.* (2019, appendix A), with respect to base flow only and with respect to base flow and direct mode structure; $M_4$ and $M_5$ are the consequence of successive division of each triangle edge by two and four respectively, with respect to mesh $M_3$. The mesh selected for this study is $M_1$ which provides results within the one per cent of relative error with respect to the finest mesh. One of the reasons that led us not to use mesh adaptation is the fact that the structure of the mode greatly changes within

| Mesh | $X_{min}$ | $X_{max}$ | $Y_{max}$ | Method |
|---|---|---|---|---|
| $M_1$ | −40 | 80 | 40 | Meshed by blocks |
| $M_2$ | −40 | 80 | 40 | Adapted BF |
| $M_3$ | −40 | 80 | 40 | Adapted BF + EM |
| $M_4$ | −40 | 80 | 40 | Adapted BF + EM + (split 2) |
| $M_5$ | −40 | 80 | 40 | Adapted BF + EM + (split 4) |
| $M_6$ | −20 | 40 | 20 | Meshed by blocks |

TABLE 2. Geometrical parameters of the physical domain of meshes $M_i$ and the method adopted for their generation.

| Mesh | $\omega_c$ | $\alpha_c$ | $F_x$ | $F_y$ | $\mu_1$ | $\mu_2$ | $N_p$ |
|---|---|---|---|---|---|---|---|
| $M_1$ | 0.3057 | 4.433 | −0.0107 | 10.712 | −0.0348 + 0.0669i | 0.0334 − 0.0231i | 32 291 |
| $M_2$ | 0.3035 | 4.447 | −0.0028 | 10.791 | −0.0442 + 0.0548i | 0.0469 − 0.0553i | 1966 |
| $M_3$ | 0.3067 | 4.429 | −0.0146 | 10.700 | −0.0351 + 0.0663i | 0.0330 − 0.0232i | 7682 |
| $M_4$ | 0.3075 | 4.424 | −0.0160 | 10.675 | −0.0349 + 0.0655i | 0.03290 − 0.0227i | 30 364 |
| $M_5$ | 0.3027 | 4.444 | −0.0142 | 10.772 | −0.0349 + 0.0691i | 0.0342 − 0.0240i | 120 728 |
| $M_6$ | 0.3078 | 4.4486 | −0.0575 | 10.7844 | −0.0343 + 0.0695i | 0.0324 − 0.0219i | 8089 |
| $M_7$ | 0.3053 | 4.4308 | −0.0226 | 10.7018 | −0.0354 + 0.0669i | 0.0336 − 0.0231i | 72 088 |

TABLE 3. Comparison of the performance of several meshes at $Re_c = 170$.

the parameter range $(Re, \alpha)$ investigated: this would have required many successive mesh adaptions.

## Appendix E: Three-dimensional stability of steady-state solutions

In this section, we review three-dimensional stability studies carried out by Pralits *et al.* (2013), Rao *et al.* (2013*a*,*b*), Radi *et al.* (2013) and Rao *et al.* (2015).

It is now well known the secondary three-dimensional transition from a two-dimensional unsteady flow towards a three-dimensional flow at $Re \approx 190$ and $\alpha = 0$, see Williamson (1996). Vortices in the wake of the fixed cylinder, i.e. $\alpha = 0$, develop spanwise waviness whose wavelength is approximatelyfour cylinder diameters. The rotation of the cylinder surface on this linear steady mode, denoted as Mode A in Rao *et al.* (2015), has a stabilising effect for rotation rates $\alpha < 1$, see figure 12.

Instead, if we consider the stability of an infinitesimal spanwise perturbation on a steady-state solution, the flow displays spanwise waviness at a much lower Reynolds number $Re \approx 100$ and $\alpha = 0$. The onset of instability of this stationary mode, denoted as Mode E in Rao *et al.* (2015), is shown in figure 12 as a function of $(Re, \alpha)$.

In the same region of existence of the unsteady two-dimensional Mode II, experimental evidence has shown the presence of a three-dimensional mode, see Linh (2011). A steady three-dimensional mode, here denoted as Mode II-3D, extends to lower Reynolds values than the two-dimensional threshold of the non-rotating cylinder, and for a larger interval in $\alpha$ than the two-dimensional Mode II. The instability mechanism of Mode II-3D is of hyperbolic nature, see Pralits *et al.* (2013).

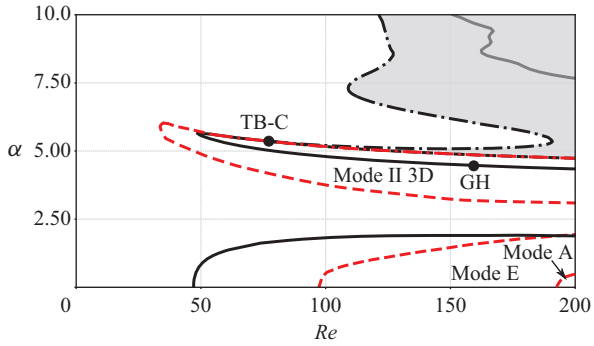


FIGURE 12. Neutral stability curves in the range $Re \in [0, 200]$ and $\alpha \in [0, 10]$. Black and grey lines are used to denote two-dimensional local bifurcations whereas red lines are used to designate the boundaries of three-dimensional local bifurcations. Dashed and point-dashed lines indicate the presence of a stationary bifurcation boundary, solid lines are used to designate unsteady bifurcation boundaries.

Finally, note that the occurrence of two unstable modes has also been documented in the flow past rotating spheres (Citro *et al.* 2016; Fabre *et al.* 2017). However, the spatial structure of the direct and adjoint modes for our geometrical configuration is very different with respect to the case of the rotating sphere flow.

## REFERENCES

BENGANA, Y., LOISEAU, J. CH., ROBINET, J. CH. & TUCKERMAN, L. S. 2019 Bifurcation analysis and frequency prediction in shear-driven cavity flow. *J. Fluid Mech.* **875**, 725–757.

BRØNS, M. 2007 Streamline topology: patterns in fluid flows and their bifurcations. *Adv. Appl. Mech.* **41**, 1–42.

CARINI, M., AUTERI, F. & GIANNETTI, F. 2015 Centre-manifold reduction of bifurcating flows. *J. Fluid Mech.* **767**, 109–145.

CITRO, V., LUCHINI, P., GIANNETTI, F. & AUTERI, F. 2017 Efficient stabilization and acceleration of numerical simulation of fluid flows by residual recombination. *J. Comput. Phys.* **344**, 234–246.

CITRO, V., TCHOUFAG, J., FABRE, D., GIANNETTI, F. & LUCHINI, P. 2016 Linear stability and weakly nonlinear analysis of the flow past rotating spheres. *J. Fluid Mech.* **807**, 62–86.

DUMORTIER, F., ROUSSARIE, R., SOTOMAYOR, J. & ZOLADEK, H. 2006 *Bifurcations of Planar Vector Fields: Nilpotent Singularities and Abelian Integrals*. Springer.

FABRE, D., CITRO, V., SABINO, D., FERREIRA, B. P., SIERRA, J., GIANNETTI, F. & PIGOU, M. 2019 A practical review to linear and nonlinear approaches to flow instabilities. *Appl. Mech. Rev.* **70** (6), 060802.

FABRE, D., LONGOBARDI, R., CITRO, V. & LUCHINI, P. 2020 Acoustic impedance and hydrodynamic instability of the flow through a circular aperture in a thick plate. *J. Fluid Mech.* **885**, A11.

FABRE, D., TCHOUFAG, J., CITRO, V., GIANNETTI, F. & LUCHINI, P. 2017 The flow past a freely rotating sphere. *Theor. Comput. Fluid Dyn.* **31**, 475–482.

GALLAIRE, F., BOUJO, E., MANTIC-LUGO, V., ARRATIA, C., THIRIA, B. & MELIGA, P. 2016 Pushing amplitude equations far from threshold: application to the supercritical Hopf bifurcation in the cylinder wake. *Fluid Dyn. Res.* **48** (6), 061401.

GASULL, A., MAÑOSA, V. & VILLADELPRAT, J. 2005 On the period of the limit cycles appearing in one-parameter bifurcations. *J. Differ. Equ.* **213** (2), 255–288.

GIANNETTI, F. & LUCHINI, P. 2007 Structural sensitivity of the first instability of the cylinder wake. *J. Fluid Mech.* **581**, 167–197.

EL HAK, M. G. 2000 *Flow Control: Passive, Active, and Reactive Flow Management*. Cambridge University Press.

HEIL, M., ROSSO, J., HAZEL, A. L. & BRØNS, M. 2017 Topological fluid mechanics of the formation of the Kármán-vortex street. *J. Fluid Mech.* **812**, 199–221.

JALLAS, D., MARQUET, O. & FABRE, D. 2017 Linear and nonlinear perturbation analysis of the symmetry breaking in time-periodic propulsive wakes. *Phys. Rev.* E **95** (6), 063111.

KANG, S., CHOI, H. & LEE, S. 1999 Laminar flow past a rotating circular cylinder. *Phys. Fluids* **11** (11), 3312–3321.

KAPITULA, T. & PROMISLOW, K. 2013 *Spectral and Dynamical Stability of Nonlinear Waves*, vol. 47. Springer.

KUZNETSOV, Y. A. 2005 Practical computation of normal forms on center manifolds at degenerate Bogdanov–Takens bifurcations. *Intl J. Bifurcation Chaos* **15** (11), 3535–3546.

KUZNETSOV, Y. A. 2013 *Elements of Applied Bifurcation Theory*, vol. 112. Springer Science & Business Media.

LINH, D. T. T. 2011 Flow past a rotating circular cylinder. PhD thesis, Department of Mechanical Engineering, National University of Singapore.

LUCHINI, P. & BOTTARO, A. 2014 Adjoint equations in stability analysis. *Annu. Rev. Fluid Mech.* **46**, 493–517.

MANTIČ-LUGO, V., ARRATIA, C. & GALLAIRE, F. 2014 Self-consistent mean flow description of the nonlinear saturation of the vortex shedding in the cylinder wake. *Phys. Rev. Lett.* **113** (8), 084501.

MITTAL, S. 2004 Three-dimensional instabilities in flow past a rotating cylinder. *Trans. ASME: J. Appl. Mech.* **71** (1), 89–95.

MODI, V. J. 1997 Moving surface boundary-layer control: a review. *J. Fluids Struct.* **11** (6), 627–663.

ORCHINI, A., RIGAS, G. & JUNIPER, M. P. 2016 Weakly nonlinear analysis of thermoacoustic bifurcations in the Rijke tube. *J. Fluid Mech.* **805**, 523–550.

PRALITS, J. O., BRANDT, L. & GIANNETTI, F. 2010 Instability and sensitivity of the flow around a rotating circular cylinder. *J. Fluid Mech.* **650**, 513–536.

PRALITS, J. O., GIANNETTI, F. & BRANDT, L. 2013 Three-dimensional instability of the flow around a rotating circular cylinder. *J. Fluid Mech.* **730**, 5–18.

RADI, A., THOMPSON, M. C., RAO, A., HOURIGAN, K. & SHERIDAN, J. 2013 Experimental evidence of new three-dimensional modes in the wake of a rotating cylinder. *J. Fluid Mech.* **734**, 567–594.

RAO, A., LEONTINI, J. S., THOMPSON, M. C. & HOURIGAN, K. 2013*a* Three-dimensionality in the wake of a rapidly rotating cylinder in uniform flow. *J. Fluid Mech.* **717**, 1–29.

RAO, A., LEONTINI, J. S., THOMPSON, M. C. & HOURIGAN, K. 2013*b* Three-dimensionality in the wake of a rapidly rotating cylinder in uniform flow. *J. Fluid Mech.* **730**, 379–391.

RAO, A., RADI, A., LEONTINI, J. S., THOMPSON, M. C., SHERIDAN, J. & HOURIGAN, K. 2015 A review of rotating cylinder wake transitions. *J. Fluids Struct.* **53**, 2–14.

SIPP, D. & LEBEDEV, A. 2007 Global stability of base and mean flows: a general approach and its applications to cylinder and open cavity flows. *J. Fluid Mech.* **593**, 333–358.

STOJKOVIĆ, D., BREUER, M. & DURST, F. 2002 Effect of high rotation rates on the laminar flow around a circular cylinder. *Phys. Fluids* **14** (9), 3160–3178.

STOJKOVIĆ, D., BREUER, M. & DURST, F. 2003 On the new vortex shedding mode past a rotating circular cylinder. *Phys. Fluids* **15** (5), 1257–1260.

THOMPSON, M. C., RAO, A., LEONTINI, J. S. & HOURIGAN, K. 2014 The existence of multiple solutions for rotating cylinder flows. In *19th Australasian Fluid Mechanics Conference, Melbourne, Australia December 8-11*. RMIT University.

WIGGINS, S. 2003 *Introduction to Applied Nonlinear Dynamical Systems and Chaos*, vol. 2. Springer Science & Business Media.

WILLIAMSON, C. H. K. 1996 Vortex dynamics in the cylinder wake. *Annu. Rev. Fluid Mech.* **28** (1), 477–539.

Journal of Computational Physics 440 (2021) 110403

Contents lists available at ScienceDirect

Journal of Computational Physics

www.elsevier.com/locate/jcp

# Adjoint-based sensitivity analysis of periodic orbits by the Fourier–Galerkin method

J. Sierra [a,b], P. Jolivet [c], F. Giannetti [b,*], V. Citro [b]

[a] Institut de m'ecanique des fluides de Toulouse (IMFT), Toulouse 31400, France
[b] Dipartimento di Ingegneria (DIIN), Universitá degli Studi di Salerno, Fisciano 84084, Italy
[c] CNRS-IRIT, 2 rue Charles Camichel, 31071 Toulouse Cedex 7, France

ARTICLE INFO

*Article history:*
Available online 13 May 2021

*Keywords:*
Sensitivity
Fourier–Galerkin method
Floquet stability analysis
Unstable periodic orbits

ABSTRACT

Sensitivity of periodic solutions of time-dependent partial differential equations is commonly computed using time-consuming direct and adjoint time integrations. Particular attention must be provided to the periodicity condition in order to obtain accurate results. Furthermore, stabilization techniques are required if the orbit is unstable. The present article aims to propose an alternative methodology to evaluate the sensitivity of periodic flows via the Fourier–Galerkin method. Unstable periodic orbits are directly computed and continued without any stabilizing technique. The stability of the periodic state is determined via Hill's method: the frequency-domain counterpart of Floquet analysis. Sensitivity maps, used for open-loop control and physical instability identification, are directly evaluated using the adjoint of the projected operator. Furthermore, we propose an efficient and robust iterative algorithm for the resolution of underlying linear systems. First of all, the new approach is applied on the Feigenbaum route to chaos in the Lorenz system. Second, the transition to a three-dimensional state in the periodic vortex-shedding past a circular cylinder is investigated. Such a flow case allows the validation of the sensitivity approach by a systematic comparison with previous results presented in the literature. Finally, the transition to a quasi-periodic state past two side-by-side cylinders is considered. These last two cases also served to test the performance of the proposed iterative algorithm.



## 1. Introduction

Steady and periodic states of continuous and discrete dynamical systems are the two simplest cases of invariant sets which are of fundamental importance to characterize dynamics and to design efficient control strategies. Limit cycles may be found in almost every field of physics and applied mathematics. Some complex structures of the phase space, such as invariant tori or some strange attractors, may be preceded by a stable periodic solution. The continuation of these periodic solutions beyond their domain of stability may help unravel some stochastic properties of these complex organizations, i.e., Lyapunov exponents, entropy, natural measure, etc., cf. Cvitanovic [1]. Stability and sensitivity calculations require robust and efficient numerical algorithms for their computation. Concerning uniquely the computation of the periodic orbits there exist two groups of methods: *local methods* which aim to determine a point of the periodic orbit and which is set as the

* Corresponding author.
*E-mail address:* fgiannetti@unisa.it (F. Giannetti).

https://doi.org/10.1016/j.jcp.2021.110403
0021-9991/

initial value for further integration, and *global methods* that aim to reconstruct the whole solution without time integration. Among local methods, one may find the direct integration of the governing equations and the shooting technique. The latter minimizes the distance to the periodic orbit via an iterative procedure, which leads to an improvement on the convergence rate with respect to the simple time integration. These methods, without further modifications, however, fail to compute unstable periodic orbits (UPO) and, in some cases, they are characterized by a low convergence rate. Some of the stabilization techniques applied to UPO are the recursive projection method (RPM) [2] or the residual recombination approach (BoostConv) [3]. Global methods, on the other hand, seek for direct representation of the sought solution on a given basis in a weighted residual approach. In this way, one may distinguish among trigonometric or orthogonal collocation, whose weight basis is composed of Dirac delta functions and its ansatz is either a Fourier or polynomial basis respectively, and Fourier–Galerkin or harmonic balance, whose weight and ansatz basis is composed of Fourier functions. Collocation methods are common in numerical continuation tools, such as AUTO [4] and MatCont [5,6], due to their robustness and generality. They are able to compute not only periodic solutions but also homoclinic or heteroclinic connections. Fourier–Galerkin uses trigonometric base functions as ansatz as well as weight functions. Fourier base functions possess interesting properties: they are by definition periodic, easy to compute, and provide rapid convergence whenever the solution is smooth.

Similarly, the stability of periodic orbits may be carried out in a local or global manner. In the local approach, the computation of Floquet multipliers is realized by a power iteration or Arnoldi algorithm via a matrix-free approach which reconstructs a faithful projection of the monodromy matrix. On the contrary, global methods directly reconstruct the monodromy matrix, either in the time or frequency domain, which generally allows more accurate results with faster convergence. The algorithm for the evaluation of sensitivity quantities is composed of two main building blocks: computation of a periodic solution and resolution of its direct and adjoint linear stability problems. Accordingly, efficient and simpler numerical techniques for the resolution of both problems imply faster and easier evaluations of sensitivity quantities. Such a constraint leads us to discard local methods due to their slow rate of convergence towards the periodic state. Furthermore, given that the nature of the orbit is periodic, every sensitivity equation shall also be. The periodicity requirement is critical in the calculation of accurate sensitivity maps, such as those computed by Giannetti et al. [7]. Therefore, a methodology that respects such a constraint seems a natural choice. The present study presents in a systematic manner the computation of stability and sensitivity of periodic solutions of discretizations of PDEs (resp. solutions to a system of ODE) via the Fourier–Galerkin method where the determination of its stability is carried out by Floquet or Hill's theory. Authors follow the new framework developed by Giannetti et al. [8] to investigate the sensitivity of periodic orbits. Giannetti et al. [8] studied the sensitivity of the three-dimensional secondary instability of the wake to a structural perturbation of the associated linear equations. The region of maximum coupling between the velocity components was found using the most unstable Floquet mode and its adjoint mode. The authors reported also the variation of this region in time by considering a structural perturbation that is impulsively applied in time at a given phase of the vortex-shedding process. The present approach can be considered an efficient and effective approximation of the framework proposed in Giannetti et al. [8,7].

The text is structured as follows: first, the methodology for the computation of a periodic orbit and the evaluation of its stability is introduced in section 2. The Fourier–Galerkin method is introduced in section 2.1 and section 2.2 is dedicated to the evolution equations with quadratic nonlinearities, e.g., Lorenz-like systems or Navier–Stokes equations. Floquet stability is reviewed in a general context in section 2.3, which is then particularized to the frequency domain in section 2.4. Sensitivity computations are later introduced in section 2.5. Section 2.6 addresses the numerical solution of the large algebraic systems in a parallel context via iterative methods. Finally, the study is concluded by some numerical examples. At first, we show the ability of the present methodology to track the route to chaos via period-doubling in the Lorenz system. Sections 3.2 and 3.3 are then dedicated to two fluid flow cases to discuss the performance of the methodology and to demonstrate the utility of sensitivity maps in the identification of physical instability mechanisms.

## 2. Methodology

### 2.1. Periodic boundary value problem

Let us start with a generic autonomous class of evolution equations of the form:

$$\mathbf{B}\frac{\partial \mathbf{q}}{\partial t} = \mathbf{F}(\mathbf{q}, \nu), \quad \mathbf{q}(t+T) = \mathbf{q}(t), \tag{1}$$

where $\mathbf{B}$ is a linear operator, $\mathbf{F}$ is a nonlinear operator on a Hilbert space $X$ with inner product $\langle \cdot, \cdot \rangle$, and $\nu \in \mathbb{R}^p$ the set of parameters. In this way, both differential algebraic problems (DAE) and evolutionary partial differential equations (PDE) are included. Natural Hilbert spaces for the infinite-dimensional case are Sobolev spaces, see Kapitula and Promislow [9], whereas in finite dimensions we will generally consider $\mathbb{R}^n$. In the following, we assume that the nonlinear operator $\mathbf{F}$ is of quadratic type, i.e., $\mathbf{F}(\mathbf{q}) = \mathbf{L}\mathbf{q} + \mathbf{N}(\mathbf{q}, \mathbf{q})$, where $\mathbf{L}$ and $\mathbf{N}(\cdot, \cdot)$ are linear and quadratic nonlinear operators, respectively. This choice will be clear later in section 2.2, however note that many analytical functions can be recast in this way, see Guillot et al. [10].

### 2.2. The Fourier–Galerkin method for periodic boundary problems

The solution of eq. (1) is $T$-periodic. Therefore, it seems a natural choice to parametrize any $T$-periodic orbit $\mathbf{q}^*$, in a $t \mod T$ basis, i.e., a Fourier basis. For that purpose, let us consider the Fourier–Galerkin method, also denoted harmonic balance (HB) in the literature, cf. [11,12]. Fourier–Galerkin can be seen as a weighted residual approach for a periodic ansatz and weight functions. Fourier base functions present the advantage of being easy to compute and provide fast convergence in smooth cases.

We start our analysis by introducing the Fourier–Galerkin projection operator $\pi_N$ onto the Fourier basis as follows:

$$\begin{aligned} \pi_N &: X \times \mathbb{R} \to X \times (\mathbb{Z}/(2N+1)\mathbb{Z}) \\ \pi_N(\mathbf{q}) &= \mathbf{q}_h(t) = \mathbf{q}_0 + \textstyle\sum_{n=1}^{N} \left[\mathbf{q}_{c,n}\cos(n\omega t) + \mathbf{q}_{s,n}\sin(n\omega t)\right] \\ &= \underbrace{\left[\mathbf{q}_0, \mathbf{q}_{1,c}, \mathbf{q}_{1,s}, ..., \mathbf{q}_{N,c}, \mathbf{q}_{N,s}\right]}_{(\mathbf{Q}^{(\tau,N)})^T} \underbrace{\left[1, \cos(\omega t), \sin(\omega t), ..., \cos(N\omega t), \sin(N\omega t)\right]}_{\mathcal{F}_\mathbf{N}}, \end{aligned} \tag{2}$$

where $\mathbf{Q}^{(\tau,N)}$ are the $2N+1$ Fourier coefficients of the approximated solution $\mathbf{q}_h$ and $\mathcal{F}_N$ is the Fourier basis in sine/cosine components. The ansatz $\mathbf{q}_h(t)$ and its derivative are smooth $T$-periodic functions.

The residual is defined as the difference between the nonlinear and the time-derivative term, which is expressed as follows:

$$\begin{aligned} &\mathbf{r} : X \times \mathbb{R} \to X \times \mathbb{R} \\ &\mathbf{r}(\mathbf{q}, \tfrac{\partial \mathbf{q}}{\partial t}, t) = \mathbf{B}\tfrac{\partial \mathbf{q}}{\partial t} - \mathbf{F}(\mathbf{q}). \end{aligned} \tag{3}$$

Following the Fourier–Galerkin or Bubnov–Galerkin method in the Fourier basis, the governing equations of HB are obtained by integrating the truncated residual equations weighted by the Fourier basis over a period $T = \frac{2\pi}{\omega}$. The obtained residual is called the *truncated residual*:

$$\begin{aligned} &\hat{\mathbf{r}}_h : X \times (\mathbb{Z}/(2N+1)\mathbb{Z}) \to X \times (\mathbb{Z}/(2N+1)\mathbb{Z}) \\ &\hat{\mathbf{r}}_h(\mathbf{Q}_N, \omega) = \textstyle\int_0^{\frac{2\pi}{\omega}} \mathbf{r}_h(\mathbf{q}_h, \tfrac{\partial \mathbf{q}_h}{\partial t}, t)^T \mathcal{F}_N \, dt = \mathbf{0}, \end{aligned} \tag{4}$$

where

$$\mathbf{r}_h(\mathbf{q}_h, \frac{\partial \mathbf{q}_h}{\partial t}, t) = \mathbf{B}\frac{\partial \mathbf{q}_h}{\partial t} - \mathbf{F}(\mathbf{q}_h). \tag{5}$$

Equation (5) provides $2N+1$ equations for $2N+2$ unknowns in the autonomous case. Autonomous systems present a continuous symmetry, i.e., $\mathbf{q}(t+\xi)$ is also a periodic solution with an arbitrary $\xi$ phase. The phase of the limit cycle remains to be fixed. This is usually done by imposing a condition at $t=0$, i.e., $g(\mathbf{q}, \frac{\partial \mathbf{q}}{\partial t}, 0) = 0$ or an orthogonality condition $\int_0^T \mathbf{F}(\mathbf{q}_h)^T \mathbf{q}_h dt = 0$. Equation (5) corresponds to balancing each harmonic individually, that is to have null Fourier coefficients of the truncated residual.

*Fourier–Galerkin equations* So far, the procedure to obtain a periodic orbit remains general. Now, without loss of generality, we shall consider the case where the nonlinear flow is of quadratic type. This constraint is far from being restrictive since many evolution problems can be recasted in this form, see Cochelin et al. [13] for the finite-dimensional case. Under these assumptions, eq. (5) takes the form:

$$\begin{aligned} 0 &= \mathbf{L}\mathbf{q}_0 + \mathbf{N}_0 \\ n\omega\mathbf{B}\mathbf{q}_{n,s} &= \mathbf{L}\mathbf{q}_{n,c} + \mathbf{N}_{n,c}, \quad n = 1, \dots, N \\ -n\omega\mathbf{B}\mathbf{q}_{n,c} &= \mathbf{L}\mathbf{q}_{n,s} + \mathbf{N}_{n,s}, \quad n = 1, \dots, N \\ g_h(\mathbf{q}_h) &= 0. \end{aligned} \tag{6}$$

For the sake of brevity, Fourier coefficients $\mathbf{N}_i$ are not developed as functions of $\mathbf{Q}^{(\tau,N)}$, see appendix A for an explicit description of these terms. Formally, eq. (6) will be denoted as:

$$\mathbf{0} = -\omega\tilde{\mathbf{B}}\mathbf{Q}^{(\tau,N)} + \tilde{\mathbf{L}}\mathbf{Q}^{(\tau,N)} + \tilde{\mathbf{N}}(\mathbf{Q}^{(\tau,N)}, \mathbf{Q}^{(\tau,N)}) = \tilde{\mathbf{r}}(\mathbf{Q}^{(\tau,N)}), \tag{7}$$

where operators $\tilde{\mathbf{B}}$, $\tilde{\mathbf{L}}$, and $\tilde{\mathbf{N}}(\cdot,\cdot)$ are detailed in appendix A and it is assumed that the phase of the limit cycle has been fixed.

**Remark 1.** It is here highlighted that if one desires to compute a $2T$-periodic solution $\tilde{\mathbf{q}}^*$, since a $2T$-periodic solution is also $T$-periodic, the current strategy requires some modifications. The methodology is adapted by doubling the number of harmonics to $2N$: the odd harmonics of the initial guess coincide with those of the $T$-periodic solution, and even modes are initialized to zero or to the Floquet mode associated with a period-doubling bifurcation, see section 2.4.

Finally, we briefly recall that Stokes [14] provided a dedicated theorem about the convergence of eq. (7). In particular, if the exact problem eq. (1) possesses a solution $\mathbf{q}^*$ of period $T = \frac{2\pi}{\omega}$, then the solution $[\mathbf{Q}^{\tau,N}, \omega^{\tau,N}]$ of the system eq. (7), for sufficiently large $N$, converges to the exact solution $\mathbf{q}^*$ if the monodromy matrix possesses a unique Floquet multiplier of multiplicity one.

**Remark 2.** In the original work of Stokes [14], where the theorem was originally proved, the main hypothesis was the *non-criticality* of the periodic solution, i.e., the periodic orbit is isolated in the phase space: the neutral Floquet multiplier is of multiplicity one.

### 2.3. Floquet-time stability theory

In this section, the Floquet theory of finite-dimensional systems in $\mathbb{R}^N$ is addressed. Unfortunately, there does not exist a general theory for time-periodic PDEs but some particular cases have been already tackled, see parabolic and hyperbolic evolution problems in Kuchement [15, Chapter 5] and references therein. For the sake of self-consistency, let us introduce a set of classical definitions in the study of dynamical systems.
For the sake of self-consistency, let us introduce a set of classical definitions in the study of dynamical systems.
Let $t \to \mathbf{q}^*(t)$ be a $T$-periodic solution of eq. (1) for a given set of parameters $\nu^* \in \mathbb{R}^p$. The associated *flow* of eq. (1) is denoted by $\varphi(t; \mathbf{q}_0)$, which solves $\mathbf{B}\frac{\partial \mathbf{q}}{\partial t} = \mathbf{F}(\mathbf{q}, \nu)$ with $\mathbf{q}(0) = \mathbf{q}_0$.
Furthermore, we consider a codimension one hypersurface $S$, chosen in such a way that every trajectory that crosses $S$ in a neighborhood of the intersection point $\mathbf{o} \in S$ of the periodic orbit with the surface $S$ intersects transversally and in the same direction, see Kuznetsov [16]. Such a section $S$ is denoted as *Poincaré section*. Thanks to the Poincaré section, let us define the *Poincaré map* or *return map* $\mathbf{P}(\mathbf{o})$:

$$\mathbf{P}(\mathbf{o}) := \mathbf{P}_S(\mathbf{o}) = \varphi(T_S(\mathbf{o}); \mathbf{o}), \tag{8}$$

where $T_S(\mathbf{o})$ is the return time and it coincides with the period $T$ of the periodic orbit when $\mathbf{o}^*$ is a fixed point, i.e., $\mathbf{o}^* = \mathbf{P}(\mathbf{o}^*)$:

$$\mathbf{o} \xrightarrow[\mathbf{q}\to\mathbf{q}^*]{} \mathbf{o}^* \quad \text{implies} \quad T_S(\mathbf{o}) \to T.$$

The linear stability of the $T$-periodic orbit $\mathbf{q}^*(t)$ can be studied by checking the evolution of the perturbed distance $\delta\mathbf{q}(t)$ to the $T$-periodic orbit $\mathbf{q}^*$:

$$\delta\mathbf{q}(t) = \varphi(t; \mathbf{q}^* + \delta\mathbf{q}_0) - \varphi(t; \mathbf{q}^*), \quad \text{with} \quad \delta\mathbf{q}(0) = \delta\mathbf{q}_0. \tag{9}$$

Measuring the distance after a period yields:

$$\delta\mathbf{q}(T) = \varphi(T; \mathbf{q}^* + \delta\mathbf{q}_0) - \varphi(T; \mathbf{q}^*) = \frac{\partial\varphi(T; \mathbf{q}^*)}{\partial\mathbf{q}}\delta\mathbf{q}_0 + O(||\delta\mathbf{q}_0||^2), \tag{10}$$

where in the last expression appears the *monodromy matrix* $\frac{\partial\varphi(T;\mathbf{q}^*)}{\partial\mathbf{q}}$. To find another representation of the monodromy matrix, consider the following evolution equation:

$$\mathbf{B}\frac{\partial}{\partial t}\frac{\partial\varphi(t; \mathbf{q}^*)}{\partial\mathbf{q}} = \frac{\partial\mathbf{F}(\varphi, \lambda^*)}{\partial\varphi}\frac{\partial\varphi(t; \mathbf{q}^*)}{\partial\mathbf{q}}, \quad \frac{\partial\varphi(0; \mathbf{q}^*)}{\partial\mathbf{q}} = \mathbf{I}. \tag{11}$$

Consequently, the monodromy matrix will be denoted by $\Phi(T) = \frac{\partial\varphi(T;\mathbf{q}^*)}{\partial\mathbf{q}}$, where the *fundamental solution matrix* $\Phi(t) \in \mathcal{M}(\mathbb{R})^{N\times N}$ satisfies the following matrix initial-value problem:

$$\mathbf{B}\frac{\partial\Phi}{\partial t} = \frac{\partial\mathbf{F}}{\partial\mathbf{q}}(\mathbf{q}^*, \lambda^*)\Phi, \quad \Phi(0) = \mathbf{I}. \tag{12}$$

The spectrum of the monodromy matrix is composed of an eigenvalue $\mu = 1$, due to the translation invariance of the periodic orbit and another set of $N-1$ eigenvalues. Due to the definition of the Poincaré map, it is not difficult to observe that the other $N-1$ eigenvalues of the Jacobian operator coincide with those of the derivative of the Poincaré map $DP(\mathbf{o}^*)$, see the book of Seydel [17] and references therein for a proof.

Thanks to Floquet's theorem, the perturbation $\delta\mathbf{q}(t)$ is written as:

$$\delta\mathbf{q}(t) = \sum_{n=1}^{N} c_n \delta\mathbf{q}_n(t),$$

where *fundamental solutions* $\delta\mathbf{q}_n$ can be rewritten in the Floquet's normal form:

$$\delta\mathbf{q}_n(t) = e^{\lambda_n t}\mathbf{p}_n(t), \tag{13}$$

where $\mathbf{p}_n$ is a $T$-periodic vector and $\lambda_n$ are called the *Floquet exponents*. They are related to the eigenvalues $\mu_n$ of the monodromy matrix, also called *Floquet multipliers*, by the following relation: $\lambda_n = \frac{\log(\mu_n)}{T} + ik\omega$ for $k \in \mathbb{Z}$. To see this relation, consider linear independence of fundamental solutions and let us substitute the Floquet's normal form into eq. (10). Then, we are left with the following expression:

$$\mu_n\mathbf{p}_n(0) = \frac{\partial\varphi(T;\mathbf{q}^*)}{\partial\mathbf{q}}\mathbf{p}_n(0) \iff \lambda_n\mathbf{B}\mathbf{p}_n = \Big[-\mathbf{B}\frac{\partial}{\partial t} + \frac{\partial\mathbf{F}(\mathbf{q}^*,\lambda)}{\partial\mathbf{q}}\Big]\mathbf{p}_n. \tag{14}$$

### 2.4. Hill's method

In section 2.3, we have carried out a brief review of the stability of periodic orbits. Here, we aim to determine an efficient algorithm for the solution of the Floquet stability eq. (14). Prior to the discussion of the algorithm, please note the following analogy between the HBM parametrization of the autonomous problem eq. (1) and the Poincaré map, introduced in eq. (8). Phase condition may be interpreted as the parametrization of a codimension one hypersurface. Then, the $T$-periodic solution $\mathbf{q}_h^*$ taken at $nT$ instants, $n \in \mathbb{N}$, is a fixed point of the Poincaré map. As discussed in section 2.3, eigenvalues of the derivative of the Poincaré map determine the stability of the periodic orbit, and these arise as a subproduct of the computation of the periodic orbit.

Nevertheless, this procedure to determine the Floquet stability would break the continuous symmetry, i.e., the phase is fixed, then the neutral Floquet multiplier, i.e., $\mu = 1$, would not be in the spectrum set. Therefore, in practice, the phase condition is left in the stability study.

The Fourier–Galerkin form of Floquet stability eq. (14) consists in the projection onto the finite Fourier space $X \times (\mathbb{Z}/(2N+1)\mathbb{Z})$, i.e., on a finite Fourier series.

The Floquet stability problem in the Fourier–Galerkin basis can be formally expressed with the following generalized eigenvalue problem:

$$\begin{aligned} \lambda^{(\tau,N)}\,\mathrm{diag}(\mathbf{B})_{2N+1}\mathbf{P}^{(\tau,N)} &= D\tilde{\mathbf{r}}(\mathbf{Q}^{(\tau,N)})\mathbf{P}^{(\tau,N)} \\ \text{where } D\tilde{\mathbf{r}}(\mathbf{Q}^{(\tau,N)})\mathbf{P}^{(\tau,N)} &= \Big[-\omega\tilde{\mathbf{B}} + \tilde{\mathbf{L}} + D\tilde{\mathbf{N}}(\mathbf{Q}^{(\tau,N)})\Big]\mathbf{P}^{(\tau,N)}, \end{aligned} \tag{15}$$

where $\mathbf{P}^{(\tau,N)} = \big[\mathbf{p}_0, \mathbf{p}_{1,c}, \mathbf{p}_{1,s}, ..., \mathbf{p}_{N,c}, \mathbf{p}_{N,s}\big]^T$ is the finite Fourier decomposition of the periodic eigenvector $\mathbf{p}(t)$ and $\lambda^{(\tau,N)}$ is the approximation of the Floquet exponent defined eq. (13).

Please note that the explicit definition of the derivative of the residual operator $D\tilde{\mathbf{r}}(\mathbf{Q}^{(\tau,N)})$ can be found in appendix A.

As depicted in Fig. 1, Floquet exponents are not unique in the complex field $\mathbb{C}$, nevertheless they are in $\mathbb{C}/i\omega\mathbb{R}$. Let us consider the finite-dimensional case, i.e., $\mathbf{q}^* \in \mathbb{R}^n$. In such a case, the Floquet spectrum is of dimension $n$, i.e., there are $n$ eigenvalues in $\mathbb{C}/i\omega\mathbb{R}$. Nonetheless, the dimension of the Floquet HBM problem is $(2N+1)n$, there are $2N+1$ in the same conjugacy class, i.e., $\lambda_k^\tau = \lambda_0^\tau + ik\omega, k \in \mathbb{Z}$, where $\lambda_0^\tau$ is the eigenvalue closest to the real axis in the complex plane.

This remark motivates the definition of the *truncated spectra* $\Lambda_N$: this set of converged eigenvalues is a compact set in $\mathbb{C}$ restricted to the strip $C_\omega \equiv \{z \in \mathbb{C} : \omega/2 \le \mathrm{Im}(z) \le \omega/2\}$ (Fig. 2).

*Notes on the convergence of the truncated spectra* Since eq. (15) is a spectral approximation of the continuous problem eq. (10), an important aspect of the methodology is whether or not the eigenvalue $\lambda$ and the eigenvector $\mathbf{P}_N$ converge to the actual eigenvalue and eigenmode respectively. Zhou et al. [18] have partially answered this query. They proved the convergence of the truncated problem in the strip $C_\omega \equiv \{z \in \mathbb{C} : \omega/2 \le \mathrm{Im}(z) \le \omega/2\}$ under the assumption that the nonlinear flow $F(\mathbf{q}, \nu)$ is piecewise $C^1[0,T]$. Likewise, Deconick et al. [19] proved the convergence of Hill's method in the Floquet–Bloch theory, i.e., periodicity in space, for compact subsets of $\mathbb{C}$. They proved the absence of spurious eigenvalues, i.e., an eigenvalue $\lambda_n$ which does not converge to any eigenvalue $\lambda$ of the problem eq. (14) as the number of harmonics $N \to \infty$. In the same reference, one may find for self-adjoint operators that for any eigenvalue $\lambda$ of the monodromy operator, there exists a sequence $\{\lambda_N\}_{N=1}^{\infty}$ such that $\lim_{N\to\infty}|\lambda_N - \lambda| \to 0$ and with a spectral rate of convergence, i.e., $|\lambda_N - \lambda| = O(N^{-p})$ for $p \ge 1$, which has been later extended for a larger family of periodic differential operators by Jonshon et al. [20].

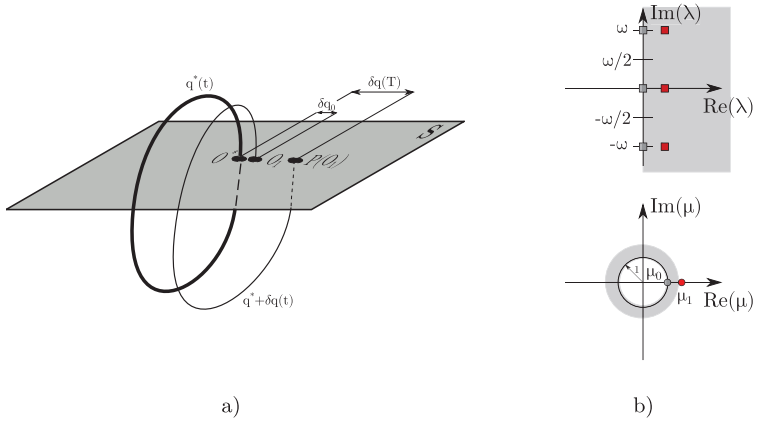


**Fig. 1.** a) An unstable periodic orbit $\mathbf{q}^*$ crossing the Poincaré section at point $\mathbf{o}^*$, and the evolution perturbed orbit $\mathbf{q}^* + \delta\mathbf{q}(t)$ from the point $\mathbf{o}_1$. b) Floquet spectrum in terms of Floquet multipliers $\mu_n$ (resp. Floquet exponents $\lambda_n$ on top figure) of an unstable periodic orbit $\mathbf{q}^*$. Red dots (square on the top figure) are associated to the unstable fundamental solution $\delta\mathbf{q}_1(t)$ whereas gray markers denote the neutral Floquet eigenvalue. (For interpretation of the colors in the figure(s), the reader is referred to the web version of this article.)

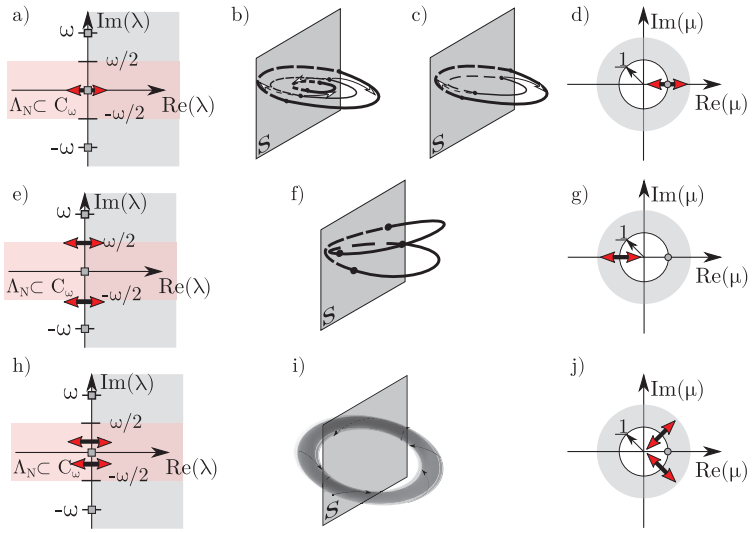


**Fig. 2.** Local bifurcations of codimension one of periodic orbits. Spectrum in terms of Floquet exponents a), e), and h). Spectrum in terms of Floquet multipliers d), g), and j). Pitchfork bifurcation in a), b), and d). Fold bifurcation in a), c), and d). Period-doubling bifurcation in e), f), and g). Neimark–Sacker in h), i), and j).

Finally, let us contemplate other choices for the selection of the set of converged eigenvalues. Bentvelsen et al. [21] compared different sorting algorithms to determine the set of converged eigenvalues and eigenmodes. They employed a sorting algorithm between elements in the same conjugacy class, i.e., $\lambda_n = \lambda_j + ik\omega$. Numerical experiments reported a faster numerical strategy to produce a set of converged eigenvalues, but such an approach is not yet rigorously justified. Such a sorting algorithm seems to be the preferred strategy for mechanical systems, see Lazarus et al. [22] and Guillot et al. [23].

For convenience, we introduce also the Floquet adjoint stability problem with respect to the natural inner product in the Fourier–Galerkin basis:

$$\begin{aligned} \bar{\lambda}^{(\tau,N)}\,\mathrm{diag}(\mathbf{B})_{2N+1}\mathbf{P}^{\dagger(\tau,N)} &= D\tilde{\mathbf{r}}^T(\mathbf{Q}^{(\tau,N)})\mathbf{P}^{\dagger(\tau,N)} \\ \text{where } D\tilde{\mathbf{r}}^T(\mathbf{Q}^{(\tau,N)})\mathbf{P}^{\dagger(\tau,N)} &= \Big[-\omega\tilde{\mathbf{B}}^T + \tilde{\mathbf{L}}^T + D\tilde{\mathbf{N}}^T(\mathbf{Q}^{(\tau,N)})\Big]\mathbf{P}^{\dagger(\tau,N)}, \end{aligned} \tag{16}$$

where $\mathbf{P}^{\dagger(\tau,N)} = \left[\mathbf{p}_0, \mathbf{p}^\dagger_{1,c}, \mathbf{p}^\dagger_{1,s}, \ldots, \mathbf{p}^\dagger_{N,c}, \mathbf{p}^\dagger_{N,s}\right]^T$ is the finite Fourier decomposition of the periodic adjoint eigenvector $\mathbf{p}^\dagger(t)$ and the conjugate eigenvalue $\bar{\lambda}^{(\tau,N)}$ is the approximation of the adjoint Floquet exponent.

### 2.5. Sensitivity analysis for periodic orbits

This section is an introduction to sensitivity computations near a bifurcation point of the periodic solution. Among possible applications to sensitivity theory, one may find passive control or identification of underlying physical mechanisms leading to the instability.
Let us consider the infinitesimal perturbed problem of eq. (1) with respect to the state variable $\mathbf{q}$:

$$\mathbf{B}\frac{\partial(\mathbf{q}^* + \delta\mathbf{q})}{\partial t} = \mathbf{F}(\mathbf{q}^* + \delta\mathbf{q}, \nu) + \delta\mathbf{H}(\mathbf{q}^* + \delta\mathbf{q}), \quad \mathbf{q}^*(t+T) = \mathbf{q}^*(t). \tag{17}$$

A force-feedback perturbation $\delta\mathbf{H}(\mathbf{q}^* + \delta\mathbf{q})$ leads to changes in dynamics. The original work of Giannetti et al. [8] analyzed the effect of a local force-feedback $\delta\mathbf{H}(\delta\mathbf{q})$. For that purpose, authors introduced the concept of *structural sensitivity* tensor $\mathsf{S}_s$ to the secondary instability, i.e., a bifurcation of the Poincaré map associated with a $T$-periodic solution, which is the extension of the structural sensitivity tensor of bifurcations from a steady-state solution, introduced by Giannetti et al. [24]. The structural sensitivity measures the variation of a Floquet exponent $\delta\lambda$ with respect to variations of the Floquet mode $\delta\mathbf{p}$. In a second article, the same authors [7] introduced the sensitivity to variations in the periodic orbit $\mathbf{q}^*$ itself. This tensor field is called *sensitivity to baseflow* variations, denoted as $\mathsf{S}_b$. Analogously to the structural sensitivity, the sensitivity to baseflow variations measures the effect of a localized force-feedback $\delta\mathbf{H}(\mathbf{q}^*)$. This leads to a variation in the Floquet exponent $\delta\lambda$ with respect to variations of the periodic solution $\delta\mathbf{q}^*$. $\mathsf{S}_b$ is evaluated following a similar procedure to $\mathsf{S}_s$. Nonetheless, one must take special care to ensure the uniqueness of $\mathsf{S}_b$. Uniqueness is guaranteed by construction and the Fredholm alternative. For the sake of clarity, $\mathsf{S}_b$ will not be rigorously introduced because it would lead to another set of definitions to overcome this technical issue, the interested reader is referred to [7].

Instead, we have decided to introduce another interesting sensitivity map $\mathsf{S}_\omega$, the sensitivity map to frequency variations of the limit cycle, which measures the variation of the frequency (resp. period) of the periodic state with respect to the introduction of a localized feedback. Furthermore, in the present section, authors introduce the novel harmonic sensitivity map $\mathsf{S}_s^n$ (resp. $\mathsf{S}_\omega^n$), which measures the effect of a structural harmonic perturbation. This last set of maps provides new insights into the harmonic nature of the instability. Each sensitivity quantity is directly computed in the frequency domain.

Let us begin with the averaged structural sensitivity tensor $\bar{\mathsf{S}}_s$ of a Floquet exponent $\lambda$:

$$\bar{\mathsf{S}}_s(\mathbf{x}) = \frac{\int_t^{T+t} \mathbf{Mp} \otimes \mathbf{Mp}^\dagger \mathrm{d}t}{\int_t^{T+t}\int_\Omega \mathbf{Mp}\cdot\mathbf{Mp}^\dagger \mathrm{d}\mathbf{x}\mathrm{d}t}. \tag{18}$$

It is the operator whose contraction with a generic infinitesimal localized feedback operator in space provides: $\delta\lambda = \mathsf{C}_1 : \bar{\mathsf{S}}_s(\mathbf{x}_0)$, where $\delta\mathbf{H}(\delta\mathbf{q}) = \delta(\mathbf{x}-\mathbf{x}_0)\mathsf{C}_1\cdot\delta\mathbf{q}$, where $\delta(\mathbf{x}-\mathbf{x}_0)$ is the Dirac distribution at $\mathbf{x}-\mathbf{x}_0$ and $\mathsf{C}_1$ is a generic constant feedback matrix. In the sensitivity paradigm, it is also helpful to consider phase details of the structural sensitivity which are retrieved by considering impulsive structural perturbations applied in time at a precise phase of the periodic solution, i.e., at $t = t_0$. This consideration leads to the instantaneous structural sensitivity $\mathsf{S}_s$:

$$\mathsf{S}_s(\mathbf{x}, t) = \frac{\mathbf{Mp} \otimes \mathbf{Mp}^\dagger}{\int_t^{T+t}\int_\Omega \mathbf{Mp}\cdot\mathbf{Mp}^\dagger \mathrm{d}\mathbf{x}\mathrm{d}t}. \tag{19}$$

In such a case, the variation of the Floquet exponent $\delta\lambda = \mathsf{C}_1 : \mathsf{S}_s(\mathbf{x}_0, t_0)$, where $\delta\mathbf{H}(\delta\mathbf{q}) = \delta\big((t \mod T) - t_0\big)\delta\big(\mathbf{x}-\mathbf{x}_0\big)\mathsf{C}_1\cdot\delta\mathbf{q}$, provides access to the phase. However, it fails to determine the harmonic nature of the instability. For such considerations, it is helpful to introduce a novel sensitivity map, the harmonic structural sensitivity $\mathsf{S}_s^n$, where $n$ indicates the harmonic number. The direct computation of the frequency spectra $\mathsf{S}_s^n$ is in general complex-valued. However, for the sake of self-consistency with the previous methodology, $\mathsf{S}_s^{n,\{s|c\}}$ is the real harmonic structural sensitivity:

$$\begin{aligned}
\mathsf{S}_s^{n,c}(\mathbf{x}) &= \frac{2}{T}\frac{\int_t^{T+t} \mathbf{Mp} \otimes \mathbf{Mp}^\dagger \cos(n\omega t)\mathrm{d}t}{\int_t^{T+t}\int_\Omega \mathbf{Mp}\cdot\mathbf{Mp}^\dagger \mathrm{d}\mathbf{x}\mathrm{d}t} \\
\mathsf{S}_s^{n,s}(\mathbf{x}) &= \frac{2}{T}\frac{\int_t^{T+t} \mathbf{Mp} \otimes \mathbf{Mp}^\dagger \sin(n\omega t)\mathrm{d}t}{\int_t^{T+t}\int_\Omega \mathbf{Mp}\cdot\mathbf{Mp}^\dagger \mathrm{d}\mathbf{x}\mathrm{d}t},
\end{aligned} \tag{20}$$

where the structural perturbation $\delta\mathbf{H}(\delta\mathbf{q}) = \frac{2}{T}\cos(n\omega t)\delta\big(\mathbf{x}-\mathbf{x}_0\big)\mathsf{C}_1\cdot\delta\mathbf{q}$ (resp. $\sin(n\omega t)$) provides a variation of the Floquet exponent $\delta\lambda = \mathsf{C}_1 : \mathsf{S}_s^{n,c}(\mathbf{x}_0)$ (resp. $\mathsf{S}_s^{n,s}(\mathbf{x}_0)$) due to a harmonic perturbation. The $\frac{2}{T}$ term is simply a normalization factor.

**Remark 3.** In the original work of Giannetti et al. [8], $\mathbf{M} = \mathbf{B}$. The inclusion of the matrix $\mathbf{M}$ in the definition of the structural sensitivity was done to consider a particular set of variables instead of the whole set of variables. We highlight that definition eqs. (18) to (20) are valid for PDEs. Finite-dimensional systems do not depend on spatial coordinates. Therefore, there is no need to introduce a localized feedback force, i.e., $\delta\mathbf{H}(\delta\mathbf{q}) = \mathsf{C}_1\cdot\delta\mathbf{q}$.

The averaged structural sensitivity $\bar{\mathsf{S}}_s^{(\tau,N)}$ associated to the Floquet exponent $\lambda^{(\tau,N)}$ in the Fourier–Galerkin basis can be expressed as:

$$\bar{\mathsf{S}}_s^{(\tau,N)}(\mathbf{x}) = \frac{\mathbf{M}\mathbf{p}_0 \otimes \mathbf{M}\mathbf{p}_0^\dagger + \frac{1}{2}\sum_{n=1}^{N} \mathbf{M}\mathbf{p}_{n,c} \otimes \mathbf{M}\mathbf{p}_{n,c}^\dagger + \mathbf{M}\mathbf{p}_{n,s} \otimes \mathbf{M}\mathbf{p}_{n,s}^\dagger}{\int_\Omega \mathbf{M}\mathbf{p}_0 \cdot \mathbf{M}\mathbf{p}_0^\dagger + \frac{1}{2}\sum_{n=1}^{N} \mathbf{M}\mathbf{p}_{n,c} \cdot \mathbf{M}\mathbf{p}_{n,c}^\dagger + \mathbf{M}\mathbf{p}_{n,s} \cdot \mathbf{M}\mathbf{p}_{n,s}^\dagger \mathrm{d}\mathbf{x}}. \tag{21}$$

Analogously, harmonic components may be written as:

$$\begin{aligned}
\mathsf{S}_s^{n,c;(\tau,N)}(\mathbf{x}) = \; & \frac{2}{T\int_t^{T+t}\int_\Omega \mathbf{M}\mathbf{p}\cdot\mathbf{M}\mathbf{p}^\dagger \mathrm{d}\mathbf{x}\mathrm{d}t}\Big(\big[\mathbf{M}\mathbf{p}_{i,c} \otimes \mathbf{M}\mathbf{p}_0^\dagger + \mathbf{M}\mathbf{p}_0 \otimes \mathbf{M}\mathbf{p}_{i,c}^\dagger\big] \\
& + \tfrac{1}{2}\sum_{j=1}^{i-1}\big[\mathbf{M}\mathbf{p}_{i,c} \otimes \mathbf{M}\mathbf{p}_{i-j,c}^\dagger - \mathbf{M}\mathbf{p}_{j,s} \otimes \mathbf{M}\mathbf{p}_{i-j,s}^\dagger\big] \\
& + \tfrac{1}{2}\sum_{j=i+1}^{N}\big[\mathbf{M}\mathbf{p}_{j,c} \otimes \mathbf{M}\mathbf{p}_{j-i,c}^\dagger + \mathbf{M}\mathbf{p}_{j-i,s} \otimes \mathbf{M}\mathbf{p}_{j,s}^\dagger\big] \\
& + \tfrac{1}{2}\sum_{j=i+1}^{N}\big[\mathbf{M}\mathbf{p}_{j-i,c} \otimes \mathbf{M}\mathbf{p}_{j,c}^\dagger + \mathbf{M}\mathbf{p}_{j,s} \otimes \mathbf{M}\mathbf{p}_{j-i,s}^\dagger\big]\Big) \\
\mathsf{S}_s^{n,s;(\tau,N)}(\mathbf{x}) = \; & \frac{2}{T\int_t^{T+t}\int_\Omega \mathbf{M}\mathbf{p}\cdot\mathbf{M}\mathbf{p}^\dagger \mathrm{d}\mathbf{x}\mathrm{d}t}\Big(\big[\mathbf{M}\mathbf{p}_{i,s} \otimes \mathbf{M}\mathbf{p}_0^\dagger + \mathbf{M}\mathbf{p}_0 \otimes \mathbf{M}\mathbf{p}_{i,s}^\dagger\big] \\
& + \tfrac{1}{2}\sum_{j=1}^{i-1}\big[\mathbf{M}\mathbf{p}_{i,c} \otimes \mathbf{M}\mathbf{p}_{i-j,s}^\dagger + \mathbf{M}\mathbf{p}_{j,s} \otimes \mathbf{M}\mathbf{p}_{i-j,c}^\dagger\big] \\
& - \tfrac{1}{2}\sum_{j=i+1}^{N}\big[\mathbf{M}\mathbf{p}_{j,c} \otimes \mathbf{M}\mathbf{p}_{j-i,s}^\dagger + \mathbf{M}\mathbf{p}_{j-i,s} \otimes \mathbf{M}\mathbf{p}_{j,c}^\dagger\big] \\
& + \tfrac{1}{2}\sum_{j=i+1}^{N}\big[\mathbf{M}\mathbf{p}_{j-i,c} \otimes \mathbf{M}\mathbf{p}_{j,s}^\dagger + \mathbf{M}\mathbf{p}_{j,s} \otimes \mathbf{M}\mathbf{p}_{j-i,c}^\dagger\big]\Big).
\end{aligned} \tag{22}$$

In a similar fashion, let us introduce the sensitivity tensor of frequency variations $\omega$, here denoted as $\bar{\mathsf{S}}_\omega$:

$$\bar{\mathsf{S}}_\omega(\mathbf{x}) = \frac{\int_0^T \mathbf{M}\mathbf{q}^* \otimes \mathbf{M}\mathbf{p}_h^\dagger \mathrm{d}t}{\int_0^T \int_\Omega \mathbf{M}\frac{\partial \mathbf{q}^*}{\partial t} \cdot \mathbf{M}\mathbf{p}_h^\dagger \mathrm{d}\mathbf{x}\mathrm{d}t}, \tag{23}$$

where $\mathbf{p}_h^\dagger$ is the adjoint Floquet mode associated to the neutral Floquet exponent $\lambda = 0$. $\bar{\mathsf{S}}_\omega$ is the operator whose contraction with a generic infinitesimal localized feedback operator in space provides the variation of the frequency $\delta\omega = \mathsf{C}_2 : \mathsf{S}_\omega$, where $\delta\mathbf{H}(\mathbf{q}^*) = \delta(\mathbf{x} - \mathbf{x}_0)\mathsf{C}_2 \cdot \mathbf{q}^*$.

The instantaneous sensitivity tensor to frequency variations $\mathsf{S}_\omega$ is defined as:

$$\mathsf{S}_\omega(\mathbf{x}) = \frac{\mathbf{M}\mathbf{q}^* \otimes \mathbf{M}\mathbf{p}_h^\dagger \mathrm{d}t}{\int_0^T \int_\Omega \mathbf{M}\frac{\partial \mathbf{q}^*}{\partial t} \cdot \mathbf{M}\mathbf{p}_h^\dagger \mathrm{d}\mathbf{x}\mathrm{d}t}, \tag{24}$$

where $\delta\omega = \mathsf{C}_2 : \mathsf{S}_\omega(\mathbf{x_0}, t_0)$ and $\delta\mathbf{H}(\delta\mathbf{q}) = \delta\big((t \mod T) - t_0\big)\delta\big(\mathbf{x} - \mathbf{x}_0\big)\mathsf{C}_2 \cdot \mathbf{q}^*$

Finally, let us introduce harmonic sensitivity to frequency variations maps $\mathsf{S}_\omega^{n,c}$ and $\mathsf{S}_\omega^{n,s}$. They provide further information for the open-loop control of the periodic solution with harmonic forcing. These quantities are a generalization of the weakly nonlinear expansion introduced by Sipp [25] to perform harmonic control near the onset of unsteadiness. These sensitivity maps are introduced as weighted products with the Fourier basis:

$$\begin{aligned}
\mathsf{S}_\omega^{n,c}(\mathbf{x}) &= \frac{2}{T}\frac{\int_0^T \mathbf{M}\mathbf{q}^* \otimes \mathbf{M}\mathbf{p}_h^\dagger \cos(n\omega t)\mathrm{d}t}{\int_0^T \int_\Omega \mathbf{M}\frac{\partial \mathbf{q}^*}{\partial t} \cdot \mathbf{M}\mathbf{p}_h^\dagger \mathrm{d}\mathbf{x}\mathrm{d}t} \\
\mathsf{S}_\omega^{n,s}(\mathbf{x}) &= \frac{2}{T}\frac{\int_0^T \mathbf{M}\mathbf{q}^* \otimes \mathbf{M}\mathbf{p}_h^\dagger \sin(n\omega t)\mathrm{d}t}{\int_0^T \int_\Omega \mathbf{M}\frac{\partial \mathbf{q}^*}{\partial t} \cdot \mathbf{M}\mathbf{p}_h^\dagger \mathrm{d}\mathbf{x}\mathrm{d}t},
\end{aligned} \tag{25}$$

where the structural perturbation $\delta\mathbf{H}(\delta\mathbf{q}) = \frac{2}{T}\cos(n\omega t)\delta\big(\mathbf{x} - \mathbf{x}_0\big)\mathsf{C}_2 \cdot \mathbf{q}^*$, resp. $\sin(n\omega t)$, provides a variation of oscillating frequency $\delta\omega = \mathsf{C}_2 : \mathsf{S}_\omega^{n,c}(\mathbf{x}_0)$, resp. $\mathsf{S}_\omega^{n,s}(\mathbf{x}_0)$, due to an harmonic perturbation. Eventually, the sensitivity of the frequency $\bar{\mathsf{S}}_\omega^{(\tau,N)}$ in the Fourier–Galerkin basis is computed as:

$$\bar{\mathsf{S}}_\omega^{(\tau,N)}(\mathbf{x}) = \frac{\mathbf{M}\mathbf{q}_0^* \otimes \mathbf{M}\mathbf{p}_{h;0}^\dagger + \frac{1}{2}\sum_{n=1}^{N} \mathbf{M}\mathbf{q}_{n,c}^* \otimes \mathbf{M}\mathbf{p}_{h;n,c}^\dagger + \mathbf{M}\mathbf{q}_{n,s}^* \otimes \mathbf{M}\mathbf{p}_{h;n,s}^\dagger}{\frac{\omega}{2}\int_\Omega \sum_{n=1}^{N} n\big[\mathbf{M}\mathbf{q}_{n,s}^* \cdot \mathbf{M}\mathbf{p}_{n,c}^\dagger - \mathbf{M}\mathbf{q}_{n,c}^* \cdot \mathbf{M}\mathbf{p}_{n,s}^\dagger\big]\mathrm{d}\mathbf{x}}, \tag{26}$$

and harmonic sensitivity tensors $\mathsf{S}_\omega^{n,c;(\tau,N)}$ and $\mathsf{S}_\omega^{n,s;(\tau,N)}$ in the Fourier–Galerkin basis:

$$
\begin{aligned}
\mathsf{S}_s^{n,c;(\tau,N)}(\mathbf{x}) = & \frac{2}{T\int_t^{T+t}\int_\Omega \mathbf{Mq}^*\cdot\mathbf{Mp}_h^\dagger \mathrm{d}\mathbf{x}\mathrm{d}t}\Big(\left[\mathbf{Mq}_{i,c}^*\otimes\mathbf{Mp}_{h;0}^\dagger + \mathbf{Mq}_0^*\otimes\mathbf{Mp}_{h;i,c}^\dagger\right] \\
& + \tfrac{1}{2}\sum_{j=1}^{i-1}\left[\mathbf{Mq}_{i,c}^*\otimes\mathbf{Mp}_{h;i-j,c}^\dagger - \mathbf{Mq}_{j,s}^*\otimes\mathbf{Mp}_{h;i-j,s}^\dagger\right] \\
& + \tfrac{1}{2}\sum_{j=i+1}^{N}\left[\mathbf{Mq}_{j,c}^*\otimes\mathbf{Mp}_{h;j-i,c}^\dagger + \mathbf{Mq}_{j-i,s}^*\otimes\mathbf{Mp}_{h;j,s}^\dagger\right] \\
& + \tfrac{1}{2}\sum_{j=i+1}^{N}\left[\mathbf{Mq}_{j-i,c}^*\otimes\mathbf{Mp}_{h;j,c}^\dagger + \mathbf{Mq}_{j,s}^*\otimes\mathbf{Mp}_{h;j-i,s}^\dagger\right]\Big) \\
\mathsf{S}_s^{n,s;(\tau,N)}(\mathbf{x}) = & \frac{2}{T\int_t^{T+t}\int_\Omega \mathbf{Mq}^*\cdot\mathbf{Mp}_h^\dagger \mathrm{d}\mathbf{x}\mathrm{d}t}\Big(\left[\mathbf{Mq}_{i,s}^*\otimes\mathbf{Mp}_{h;0}^\dagger + \mathbf{Mq}_0^*\otimes\mathbf{Mp}_{h;i,s}^\dagger\right] \\
& + \tfrac{1}{2}\sum_{j=1}^{i-1}\left[\mathbf{Mq}_{i,c}^*\otimes\mathbf{Mp}_{h;i-j,s}^\dagger + \mathbf{Mq}_{j,s}^*\otimes\mathbf{Mp}_{h;i-j,c}^\dagger\right] \\
& - \tfrac{1}{2}\sum_{j=i+1}^{N}\left[\mathbf{Mq}_{j,c}^*\otimes\mathbf{Mp}_{h;j-i,s}^\dagger + \mathbf{Mq}_{j-i,s}^*\otimes\mathbf{Mp}_{h;j,c}^\dagger\right] \\
& + \tfrac{1}{2}\sum_{j=i+1}^{N}\left[\mathbf{Mq}_{j-i,c}^*\otimes\mathbf{Mp}_{h;j,s}^\dagger + \mathbf{Mq}_{j,s}^*\otimes\mathbf{Mp}_{h;j-i,c}^\dagger\right]\Big).
\end{aligned}
\tag{27}
$$

### 2.6. Numerical methods

This section presents strategies for the resolution of eqs. (7) and (15). Efficient numerical techniques are required for the solution of linear systems composed of a large number of degrees of freedom. In particular, direct factorization becomes rapidly unfeasible due to the large memory requirements. Iterative methods with inner-outer preconditioning are proposed. Outer preconditioning improves the convergence of the Krylov method and inner preconditioning increases the efficiency of computation on blocks.

*Nonlinear problem eq.* (7) The solution of eq. (7) is performed via a Newton-like method:

$$
D\tilde{\mathbf{r}}(\mathbf{Q}_{(n)}^{(\tau,N)})\delta\mathbf{Q}_{(n+1)}^{(\tau,N)} = -\tilde{\mathbf{r}}(\mathbf{Q}_{(n)}^{(\tau,N)}). \tag{28}
$$

A Newton–Krylov strategy is chosen in the case $\tilde{\mathbf{r}}$ arises from semi-discretization in space of a PDE or via a Newton method if $\tilde{\mathbf{r}}$ is the vector field that stems from a differential system with a small number of degrees of freedom. The latter is common in the literature of mechanical systems and it is solved with dense matrices and direct linear solvers, for more information, the interested reader is referred to Krack et al. [12, Chapter 4].

*Eigenvalue problem* Arnoldi or shift-and-invert iteration are the chosen candidates for efficient extraction of leading Floquet exponents in eqs. (15) and (16).

*Linear systems* Preconditioning strategies are needed for an efficient resolution of linear systems from Newton iterations eq. (28) or Arnoldi iterations applied to eqs. (15) and (16). In the present study, we have considered three strategies for the outer preconditioning: block Jacobi, upper and lower triangular Gauss–Seidel. Solutions of inner systems, i.e., involving diagonal blocks of $D\tilde{\mathbf{r}}(\mathbf{Q}_{(n)}^{(\tau,N)})$, are computed using exact $LU$ factorizations or iterative solvers, e.g., additive Schwarz method (ASM). For other choices of inner block-factorization, the interested reader may consider, for example, the modified augmented Lagrangian method [26] as implemented by Moulin et al. [27]. The preconditioning step is coupled with an iterative Krylov method: the flexible GMRES [28].

## 3. Results

Numerical results presented in this section have been obtained with in-house codes. Results presented in section 3.1 have been calculated with a MATLAB code developed by the authors for the computation of limit cycles and the evaluation of their stability with the methodology shown in section 2. Numerical examples of sections 3.2 and 3.3 have been computed with FreeFEM, a finite element code for the resolution of PDEs in the variational form, cf. [29]. Navier–Stokes equations written in the weak formulation are discretized by projecting the flow field $(u, v, p)$ upon a basis of Taylor–Hood finite elements with piecewise quadratic velocities and piecewise linear pressure. The number of triangles of the discretized domain considered in sections 3.2 and 3.3 varies in a range of $\mathcal{O}(10^4) - \mathcal{O}(10^5)$ which results in around $\mathcal{O}(10^5) - \mathcal{O}(10^6)$ degrees of freedom per mode, that is $\mathcal{O}(n\cdot 10^5) - \mathcal{O}(n\cdot 10^6)$ with $n = 2N+1$ the number of modes retained in the Fourier basis. Linear systems and eigenvalue problems are solved by PETSc [30] and SLEPc [31]. For more information, the interested reader is referred to the recent review article in linear and nonlinear stability in fluid flows by Fabre et al. [32] and the StabFem project hosted at https://stabfem.gitlab.io/StabFem/. Results presented in section 3.1 provide numerical evidence of the capability of the Fourier–Galerkin methodology to continue stable and unstable branches of periodic solutions past period-doubling bifurcations and to accurately evaluate the stability of a periodic orbit. Evaluation of the performance of numerical techniques described in section 2.6 and an assessment of the accuracy of sensitivity quantities

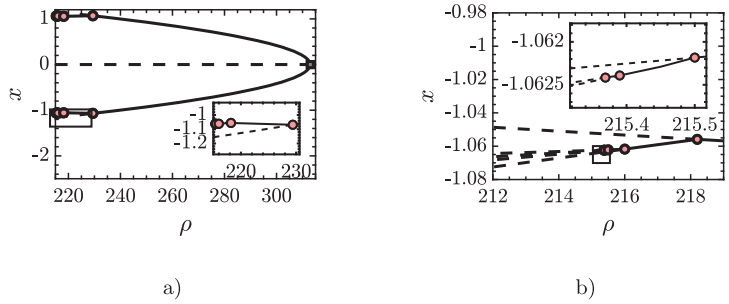


**Fig. 3.** a) Bifurcation diagram of the Lorenz system. b) Zoom into the interval of period-doubling bifurcations. Solid (resp. dashed) lines denote stable (resp. unstable) solutions. Red (resp. gray) markers denote a period-doubling bifurcation (resp. symmetry breaking).

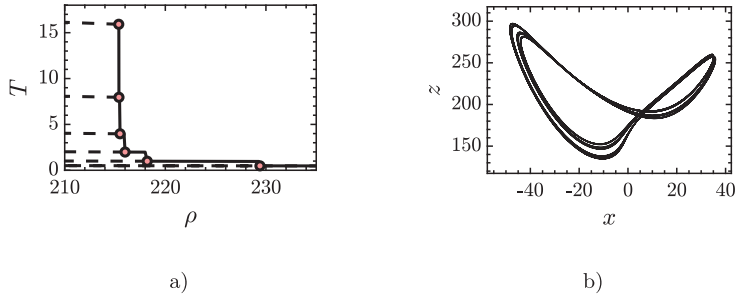


**Fig. 4.** a) Evolution of the period. b) $x-z$ slice of the stable solution at $\rho = 215.38$, before the sixth period-doubling bifurcation. Same legend as in Fig. 3.

detailed in section 2.5 is carried out in sections 3.2 and 3.3. The authors would like to compare the present methodology with respect to classical time-stepping techniques for the computation of sensitivity maps as in Giannetti et al. [7]. For that purpose, we consider an IMEX time-integration technique, e.g., explicit Runge–Kutta integration for the nonlinear terms and implicit Crank-Nicolson for the linear terms. The computation of the converged periodic solution, the direct and adjoint modes with time-stepping techniques require the solution of around $\mathcal{O}(MT)$ time units, with $M$ the number of periods required for convergence, which is usually of the order of few hundreds for the periodic solution and of thousands for the evaluation of the direct and adjoints modes to obtain accurate results, and $T$ the fundamental period. The evaluation of a period usually requires a number of time steps of the order of $N = \mathcal{O}(T/\Delta t)$, which is $N = \mathcal{O}(10^2)$ in the case of the wake flow past a cylinder, see [3, Sec. 7]. That results in a much larger total computation time than the one required for the evaluation of sensitivity maps with the current methodology. For instance, if we consider a coarse numerical domain, the mesh $\mathcal{M}_1$ of Table 1, the serial evaluation of Fourier–Galerkin methodology for the periodic solution, direct and adjoint eigenmodes are of the order of few minutes whereas the time-stepping methodology takes several hours, which is highly dependent on the time step which at the same time depends on the level of refinement. During the elaboration of this manuscript authors have compared the sensitivity maps computed with time-stepping techniques and Fourier–Galerkin method. Even if it is difficult to compare results that are coming from different numerical discretizations and different grids, [8] employed finite differences with a staggered grid, comparing the results we found that the sensitivity maps agree very well and the relative error is of few percents depending on the mesh and the physical parameters.

### 3.1. Lorenz system: the case of Feigenbaum route to chaos

Routes to chaos are of fundamental interest in the study of nonlinear dynamics. Most common routes to chaos are intermittency, crisis, quasiperiodicity, and period-doubling. The current section focuses on the latter. Period-doubling route is also denoted as *Feigenbaum* route to chaos and is characterized by an infinite number of period-doubling bifurcations in a finite interval of the parameter set. In particular, Feigenbaum noted that under mild assumptions of the nonlinear operator, the distance between consecutive bifurcations shrinks in a universal manner, see Collet et al. [33]:

$$\lim_{n\to\infty} \frac{\nu_{n+1} - \nu_n}{\nu_n - \nu_{n-1}} = \delta,$$

where $\delta \approx 4.6692016\ldots$ is the Feigenbaum constant for dissipative dynamical systems and it can be numerically evaluated from Figs. 3 and 4. Period-doubling arises as a pitchfork bifurcation of a fixed point of the associated Poincaré return map.

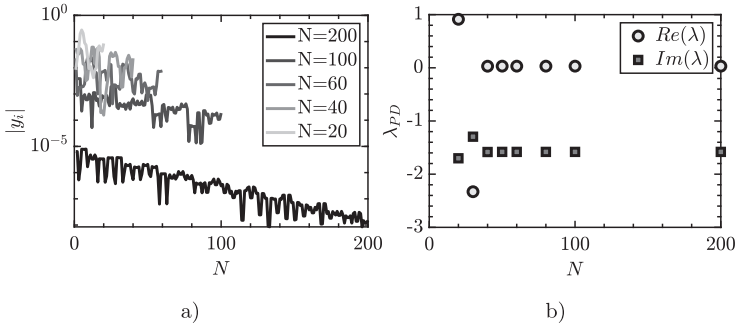


**Fig. 5.** a) Decay of Fourier modes of $y$ component for a periodic solution near the fourth period-doubling bifurcation. b) Evolution of the eigenvalue associated to the period-doubling mode.

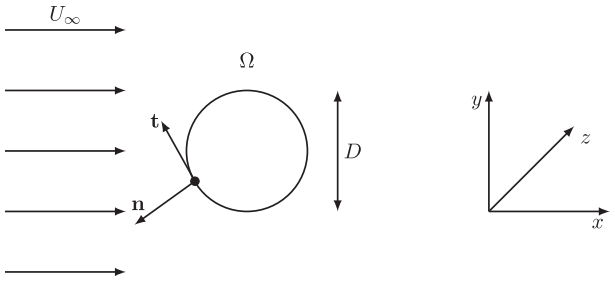


**Fig. 6.** Sketch of a cylinder immersed in a uniform flow.

In particular, here the Lorenz system illustrates the capability of the Fourier–Galerkin method to track period-doubling bifurcations and compute periodic solutions in a substantially nonlinear system. Let us first introduce Lorenz equations:

$$\begin{aligned} \dot{x} &= \sigma(y - x) \\ \dot{y} &= \rho x - y - xz \\ \dot{z} &= xy - bz, \end{aligned} \tag{29}$$

with parameters $b = \frac{8}{3}$, $\sigma = 10$, and $\rho \in (210, 320]$. In this range of parameters, there is a first bifurcation around $\rho \approx 312.9$, where the stable solution ceases to be symmetric via a pitchfork bifurcation due to the reflectional symmetry ($x \to -x$, $y \to -y$) of the system. These two branches remain stable up to $\rho \approx 229.4$, where a first period-doubling bifurcation occurs. It is then followed by an infinite number of them, of which the first six have been computed, see Fig. 3. The stable periodic orbit before the sixth period-doubling bifurcation is reported in Fig. 4 b). Fig. 4 a) illustrates the geometric growth of the period past successive period-doubling bifurcations. As pointed out in Remark 1, successive period-doubling solutions have been computed by doubling the number of harmonics of the truncated Fourier series.

The convergence of a periodic solution is evaluated a posteriori by the decay of Fourier modes and by the evolution of the leading eigenvalue. Fig. 5 shows, for a periodic solution at the onset of the fourth period-doubling bifurcation, the irregular decay of Fourier harmonics due to the strong nonlinearities. In addition, Fig. 5 shows that the methodology is able to accurately predict some parts of the spectrum even if the decay of Fourier modes is not smooth. Particularly, prior to the fourth period-doubling bifurcation Fig. 5, a minimum of around $N = 40$ is required for a correct evaluation of the leading Floquet exponent.

Finally, let us conclude this section with a remark concerning the number of Fourier modes retained for the reconstruction of a periodic solution past a period-doubling bifurcation. As stated in Remark 1, a periodic solution whose period is $2^m T$, i.e., the system has experienced $m$ period-doubling bifurcations, is also $2^{m-1}T$-periodic. The computation of a $2^m T$-periodic solution requires $2^m \tilde{N}$ Fourier modes, where $\tilde{N}$ is the length of the Fourier basis used for the computation of a $T$-periodic solution. As a consequence, the number of harmonics for a single $T$-period is $\tilde{N} = \frac{N}{2^m}$, which, for instance for $N = 40$ and $m = 3$, gives $\tilde{N} = 5$.

### 3.2. Flow past a two-dimensional circular cylinder

Let us consider a fluid mechanics example: a canonical case of the flow past a bluff body, i.e., the flow past a two-dimensional cylinder sketched in Fig. 6. Dynamics and the first two bifurcations are well known, see Williamson [34].

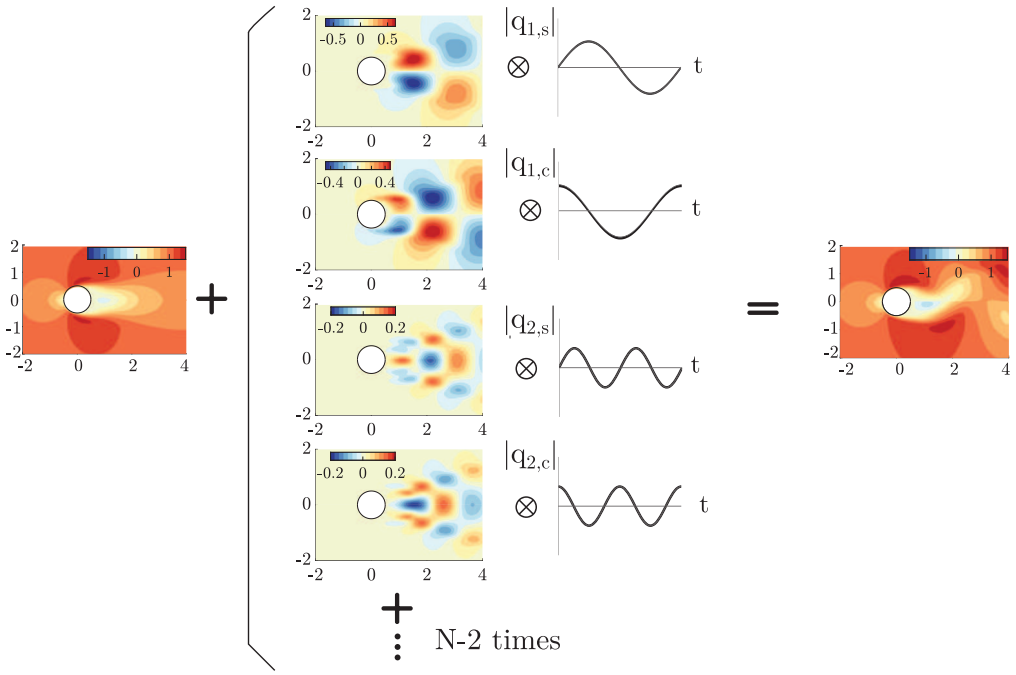


**Fig. 7.** Reconstruction of the streamwise velocity $U_x$ of the periodic oscillating vortex solution at $Re = 190$. The flow is reconstructed at $t = 0$ for $N = 6$.

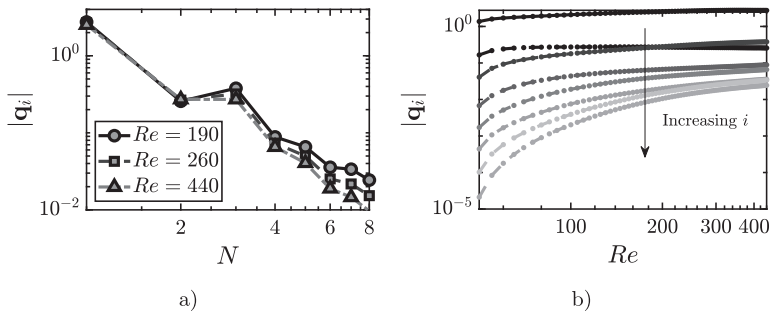


**Fig. 8.** a) Decay of Fourier spectrum for $Re = 190$, $Re = 260$, and $Re = 440$ b) Evolution of the amplitude of Fourier modes.

The governing equations are the incompressible Navier–Stokes equations which are of quadratic type, see appendix B, therefore they fit into the developed strategy.

*3.2.1. Computation of the baseflow*

The Fourier–Galerkin strategy reconstructs the periodic solution of the flow past a cylinder, as reported in Fig. 7. The approach is initialized with the unstable eigenmode at the threshold, $Re \approx 47$, and it is continued up to $Re = 450$, with at most $N = 10$ modes. In order to estimate the precision of the results obtained by the numerical procedure, two Reynolds numbers are selected, $Re = 190$ and $Re = 260$, and we run cross-comparison of the estimated Strouhal with the data available in the literature. At $Re = 190$ (resp. $Re = 260$), by retaining $N = 5$ harmonics, a Strouhal number $St = 0.1938$ (resp. $St = 0.2058$) has been obtained, a result in good agreement with the value $St = 0.1950$ (resp. $St = 0.2071$) reported by Barkley et al. [35]. These accurate results with a reduced Fourier basis are due to the rapid decay of the Fourier spectrum, which is displayed in Fig. 8 a). The Fourier spectrum displays a quadratic decay, with small dependence on the Reynolds number if sufficient modes are retained. To determine whether or not the number of retained modes is sufficient, one could evaluate a posteriori the evolution of the amplitude of each mode with respect to the parameter, i.e., $Re$. The amplitude of each Fourier mode grows exponentially until saturation, see Fig. 8 b). Therefore, an appropriate selection of $N$ could be to retain at least a mode that is not saturated or select the basis length $N$ so that the amplitude of the last mode is below a certain threshold.

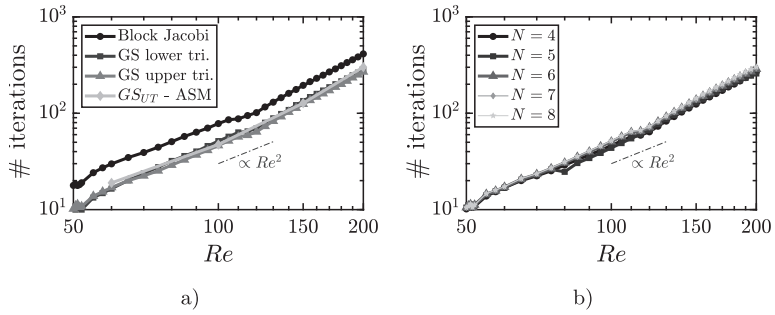


**Fig. 9.** Effect of Reynolds number, preconditioning technique and number of Fourier modes. a) Compares preconditioning techniques and b) the number of Fourier modes for a Gauss–Seidel upper triangular preconditioner.

**Table 1**
Average number of GMRES iterations per Newton iteration for three numerical domains $\mathcal{M}_1$, $\mathcal{M}_2$ and $\mathcal{M}_3$ at $Re = 100$ with upper triangular Gauss–Seidel. The tolerance of the Newton method is set to $10^{-8}$.

| Mesh ID | # elements | # GMRES iterations | | |
|---|---|---|---|---|
| | | $N = 1$ | $N = 2$ | $N = 3$ |
| $\mathcal{M}_1$ | $1.4 \cdot 10^4$ | 33 | 36 | 38 |
| $\mathcal{M}_2$ | $4.5 \cdot 10^4$ | 32 | 37 | 39 |
| $\mathcal{M}_3$ | $1.85 \cdot 10^5$ | 33 | 38 | 38 |

**Table 2**
Total number of GMRES iterations for the resolution of the nonlinear problem eq. (7) at $Re = 100$, $N = 4$ with the numerical domain $\mathcal{M}_1$, the upper triangular Gauss–Seidel as the outer preconditioning technique and inexact factorization with the ASM method for inner blocks. Variation of inner iterations and total GMRES iterations with respect to the relative tolerance in the inexact factorization of inner blocks. The tolerance of the Newton method is set to $10^{-8}$.

| ASM tolerance | $10^{-8}$ | $10^{-7}$ | $10^{-6}$ | $10^{-5}$ | $10^{-4}$ | $10^{-3}$ | LU |
|---|---|---|---|---|---|---|---|
| # total iterations | 344 | 310 | 278 | 246 | 267 | 369 | 238 |
| Average # inner iterations | 52 | 44 | 35 | 25 | 18 | 16 | – |

### *3.2.2. Performance evaluation of iterative methods*

Another important aspect to be addressed is the performance of methods used for numerical resolution. In particular, for the present case, authors have evaluated the dependency of the chosen iterative strategy, a flexible restarted GMRES, for the solution of linear systems such as eq. (28) on a set of parameters: Reynolds number, number of elements in the numerical domain, preconditioning techniques and number of modes of the Fourier basis.

Independently of the chosen preconditioning technique, the number of GMRES iterations for the resolution of the linear system eq. (28) increases quadratically with respect to the Reynolds number, see Fig. 9 a). As expected, triangular Gauss–Seidel preconditioning speeds up computations with respect to block Jacobi. However, the gain between choosing an upper or a lower triangular preconditioner is marginal. The second aspect that was studied is the influence of the number of iterations required to solve the linear system under a change of the total number of elements. Table 1 reports the average number of GMRES iterations, for three numerical domains $\mathcal{M}_i$, $i = 1, 2, 3$. It results that the number of GMRES iterations does scale with the total number of elements in the numerical domain. In addition, authors have studied the effect of an inexact factorization of the inner diagonal blocks. ASM is used to precondition the inner blocks with upper triangular GS as outer preconditioner. It is compared with exact $LU$ factorization for the diagonal blocks. Table 2 reports the variation of the total number of GMRES iterations required to solve the nonlinear problem eq. (7) and the averaged number of inner iterations for each inner diagonal block. It is concluded that inexact factorization of inner blocks hardly changes the number of GMRES iterations, as long as the relative tolerance is correctly tuned. The effect of the number of modes in the truncated Fourier basis is reported in Fig. 9 b). Similar conclusions can be drawn with respect to other preconditioners, the number of modes in the Fourier basis does not affect the iterative strategy, as long as $N$ is sufficient for convergence.

Finally, the performance of the parallel implementation is considered. For that purpose a strong scalability test has been carried out with a fine numerical domain composed of $1.85 \cdot 10^5$ elements. The number of modes is fixed to $N = 4$ and the preconditioning technique is the upper triangular Gauss–Seidel. Fig. 10 a) reports the evolution of the averaged time per Newton iteration with respect to the number of processes. The actual scaling time is degraded by around 35% with respect to perfect linear scaling, that is the average time per Newton iteration approximately evolves as # of processes$^{-0.65}$.

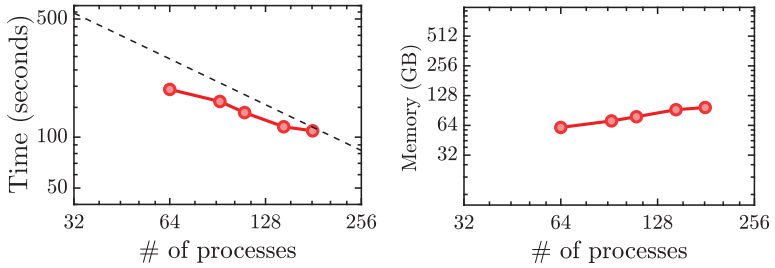


a) Average time per Newton iteration

b) Average memory consumption for the solution of eq. (28) in the Newton iteration.

**Fig. 10.** Performance of the linear solver with upper triangular Gauss–Seidel with a discretized domain composed of $1.85 \cdot 10^5$ elements and $N = 4$.

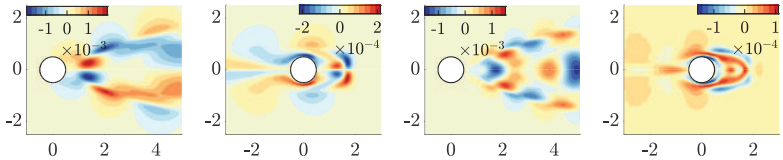


**Fig. 11.** Spanwise velocity component $U_z$ of *mode A* at $Re = 190$. a) and c), resp. b) and d), first and second sinus components of direct, resp. adjoint, Floquet modes.

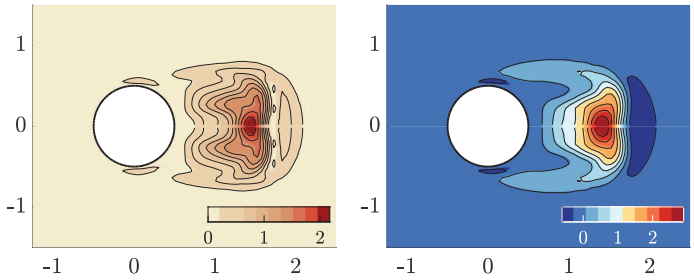


**Fig. 12.** Averaged structural sensitivity $\bar{S}_s^{(\tau,N)}$ of mode A at $Re = 190$, $k_z = 1.585$, and $N = 4$. a) Spectral norm. b) Trace.

Similarly, Fig. 10 b) reports the total memory consumption for the solution of the linear system eq. (28). It displays an increase of memory of around 20% each time the number of processes doubles.

In conclusion, GMRES iterations depend quadratically on Reynolds number and they are independent on the total number of mesh elements, the dimension of the Fourier basis as long as $N$ is sufficient to characterize the periodic solution. In a future study, authors will study other preconditioning techniques to attempt to reduce the dependency on $Re$.

### 3.2.3. Stability & sensitivity analysis

Beyond the threshold of the first instability, which is found at around $Re \approx 47$, a stable two-dimensional $T$-periodic solution exists up to $Re \approx 190$ where the stable solution ceases to be two-dimensional via a steady symmetry-breaking bifurcation of the spanwise homogeneous direction. The Floquet mode associated to this second instability, reported in Fig. 11, is commonly denoted as *mode A* whose wavenumber is $k_z = 1.585$, see Giannetti et al. [8].

Prior to the discussion of sensitivity quantities, let us point out their validity. The reported sensitivity maps in Figs. 12 and 13 are in perfect agreement with those presented in literature, cf. [7]. A common query in physics is: which are the underlying physical mechanisms responsible for the instability? Structural sensitivity allows to localize the core of the vortex-shedding instability, that is the sensitivity of the Floquet exponent to a generic structural perturbation of the linearized equations. Fig. 12 displays the compact support structure of the sensitivity for mode A, which translates to a localized instability in the near wake. Similarly, if one desires to shift the harmonic frequency $\omega$, the most efficient way is to act on the near wake in accordance with the map $S_\omega$, see Fig. 13.

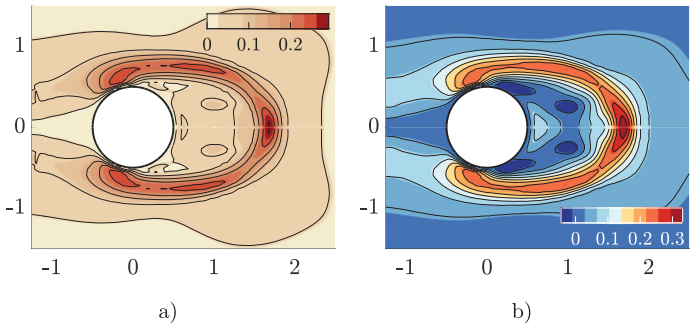


**Fig. 13.** Averaged sensitivity to frequency variations $\bar{\mathrm{S}}_{\omega}^{(\tau,N)}$ of mode A at $Re = 190$, $k_z = 1.585$, and $N = 4$. a) Spectral norm. b) Trace.

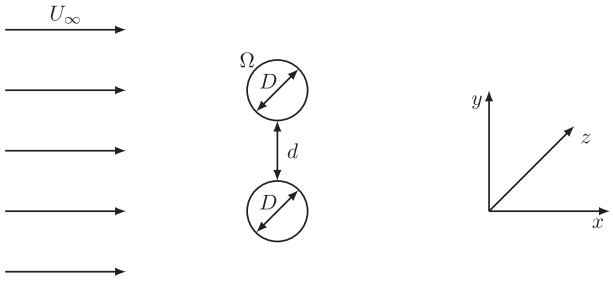


**Fig. 14.** Sketch of the two circular cylinders in a side-by-side arrangement immersed in a uniform flow.

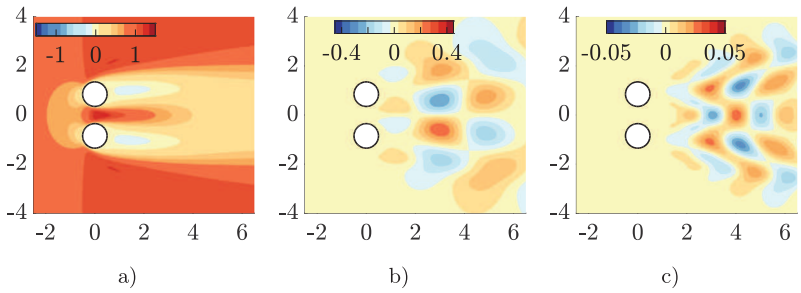


**Fig. 15.** Streamwise component $U_x$ of the periodic baseflow solution at $Re = 62$. a) Meanflow component. b) First cosinus component. c) Second cosinus component.

### 3.3. Flow past two cylinders in tandem

Let us explore a second fluid mechanics example: the flow past two side-by-side circular cylinders. The flow configuration, reported in Fig. 14, is governed by two dimensionless parameters, Reynolds number ($Re$) and the ratio of the distance between cylinders and their diameter ($g = \frac{d}{D}$). For some ranges of parameters, reported by Carini et al. [36], the two-dimensional flow pattern is characterized by an asymmetric unsteady wake with respect to the horizontal axis. Such a phenomenon, which has been denominated *flip-flop*, develops at low Reynolds numbers, $50 < Re < 90$, through a Neimark–Sacker bifurcation. In the following, the dimensionless distance between cylinders is fixed, $g = 0.7$, such that *flip-flop* instability appears.

#### 3.3.1. Computation of the baseflow

The periodic solution past two side-by-side cylinders is reconstructed by Fourier–Galerkin with $N = 4$ (Fig. 15). The method is initialized with the unstable in-phase eigenmode associated with the first supercritical Hopf bifurcation of the steady state, see section 3.2.3. The accuracy of baseflow computations were compared with reported results in the literature. At $Re = 62$, a $St \approx 0.111$ matches the one computed by Carini et al. [36].

#### 3.3.2. Memory requirements of linear solvers

Section 3.2.2 focuses on the performance of iterative methods by considering the influence of some parameters on the number of iterations required by the linear solver to solve eq. (28) with a relative tolerance of $10^{-5}$. Another important facet of linear solvers is their memory consumption. Particularly, the total memory consumption is expected to increases with

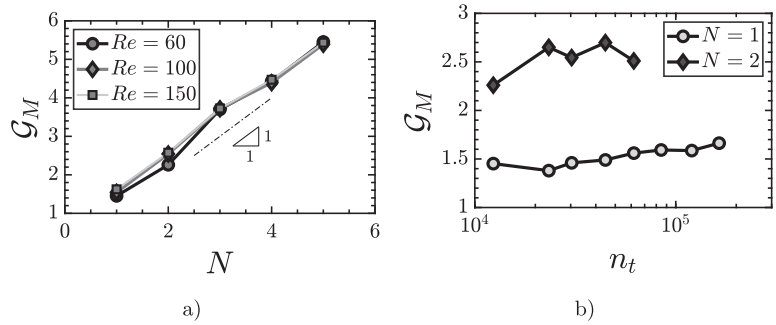


**Fig. 16.** a) Memory gain evolution w.r.t. number of Fourier modes (for a coarse mesh $n_t = 12354$ triangles) for three Reynolds numbers. b) Memory gain w.r.t. number of mesh triangles.

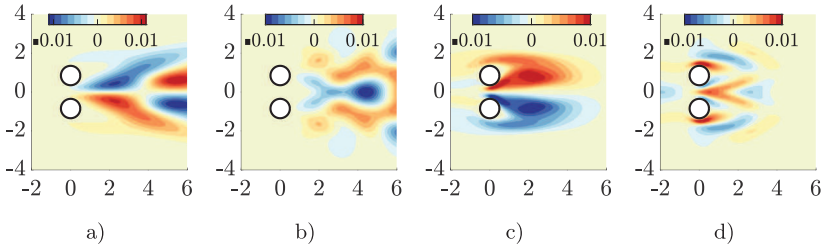


**Fig. 17.** *Mode IP* at $Re = 62$. a) and c), resp. b) and d), meanflow and first cosinus components of direct, resp. adjoint, Floquet modes.

the number of modes of the truncated Fourier basis and mesh refinement. We define the *memory gain*, $\mathcal{G}_M = \frac{\text{memory LU}}{\text{memory GMRES}}$, as the ratio of memory consumed by LU w.r.t. GMRES to solve a linear system whose linear operator is the Jacobian matrix defined in appendix A.3.

Tests have been run on an Intel cluster with 64 Intel(R) Xeon(R) CPU E5-4610 processors and 256 GB of memory. For a fixed mesh with $n_t = 12{,}354$ triangles, inner iterations of the Newton method are solved with varying $N$, with the upper triangular Gauss–Seidel preconditioner and $LU$ factorization. They have confirmed the linear memory gain, independently of $Re$, with respect to the number of elements kept in the Fourier basis, as reported in Fig. 16 a). Analogously, the effect of mesh size on memory storage is also studied. The memory gain is reported in Fig. 16 b) as a function of the number of triangles. Curves correspond to different lengths of the truncated Fourier basis. Clearly, memory gain is independent of the mesh size, regardless of $N$.

### 3.3.3. Stability & sensitivity analysis

The stability of the steady state has been studied by Mizushima et al. [37]. They reported three types of instabilities, a symmetry breaking of the steady state via a pitchfork bifurcation, an oscillatory in-phase via a Hopf bifurcation, and a third oscillatory instability far from the near wake. For the chosen configuration ($g = 0.7$) the primary instability is a supercritical Hopf bifurcation at $Re \approx 57.5$ whose most unstable eigenmode is the in-phase oscillatory, *mode IP* partially reported in Fig. 17. The Floquet analysis reveals a pair of complex-conjugate multipliers on the in-phase synchronized vortex shedding periodic solution between the two cylinders. Neimark–Sacker appears at $Re_c = 61.7$, which is in good agreement with the result $Re_c = 61.8$ reported by Carini et al. [36].

Structural sensitivity, reported in Fig. 18, shows a symmetric averaged core of the instability in the near wake that is larger than the sensitive instability core of the single cylinder reported in Fig. 12. In addition, amplitudes of harmonic sensitivity are displayed in the frequency $\omega$-axis. They provide further information about the origin of the flip-flop instability. Sensitive regions to harmonic structural perturbation are found for the first harmonic where it is possible to observe two sensitive regions around $y = \pm 2$ and a single one around $y = 0$ in the near wake for the second harmonic component. Remarkably, in this case, the instability is more sensitive to the second harmonic than the first one. The other sensitivity map, $\bar{S}_\omega$ reported in Fig. 19, is particularly concentrated in the zone between cylinders. Not surprisingly, previous results in the literature indicate large variations of baseflow frequency as the gap ratio $g$ is varied.

## 4. Conclusion

The computation of stability and sensitivity of periodic solutions provides access to inherent mechanisms leading to changes in dynamics. Efficient computational methods are essential for the computation of large-scale systems such as those arising from the semi-discretization of the governing equations. The spectral Fourier–Galerkin method is proposed for the efficient computation and continuation of autonomous problems. The methodology, though general, has been presented

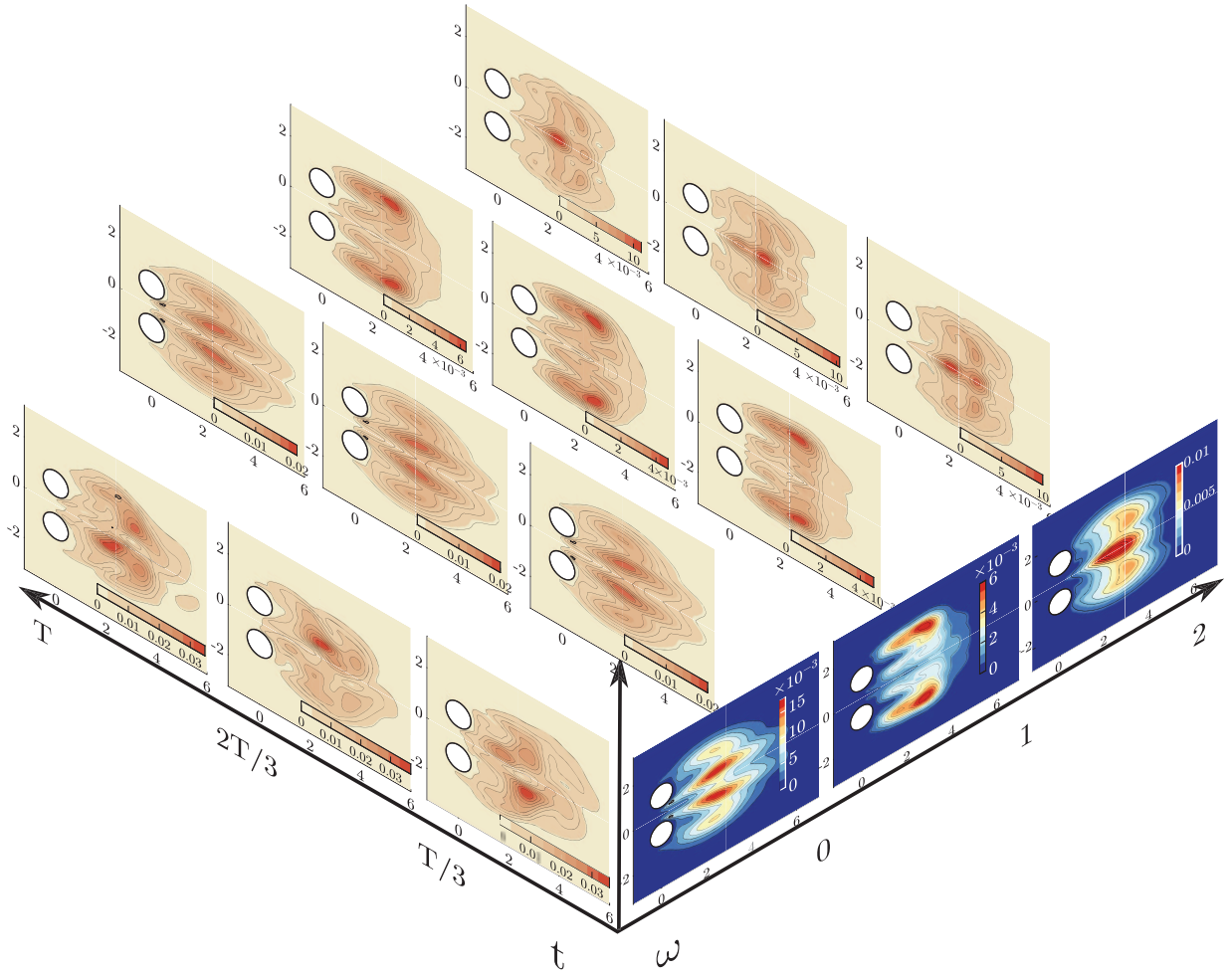


**Fig. 18.** Structural sensitivity $S_s^{(\tau,N)}$ for $Re = 62$ with $N = 2$. $t$-axis: reconstruction of the spectral norm of the instantaneous structural sensitivity $S_s^{(\tau,N)}(\mathbf{x}, t)$ at discrete instants $t = \{\frac{T}{3}, \frac{2T}{3}, T\}$. $\omega$-axis: spectral norm of the modulus of harmonic sensitivity $|S_s^{n;(\tau,N)}| = \sqrt{S_s^{n,c;(\tau,N)^2} + S_s^{n,s;(\tau,N)^2}}$ for harmonic components $n = \{0, 1, 2\}$. The spectral norm of the modulus of the harmonic sensitivity $|S_s^{n;(\tau,N)}|$ is reconstructed in time at discrete instants.

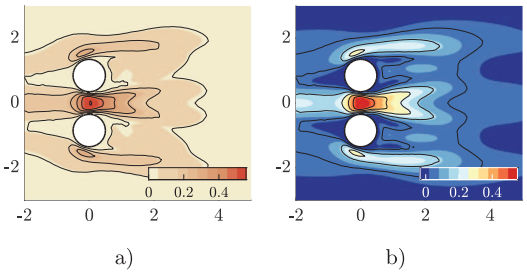


**Fig. 19.** Averaged sensitivity to frequency variations $\tilde{S}_\omega^{(\tau,N)}$ of mode A at $Re = 190$, $k_z = 1.585$, and $N = 4$. a) Spectral norm. b) Trace.

for quadratic nonlinearities, where the frequency transform has a simple form, see appendix A.1. In the case of finite systems with few degrees of freedom, quadratic recasting is an option ([10,13]). However, such a recast increases the computational burden. It multiplies the number of degrees of freedom by a factor, which is not acceptable in large-scale systems. In those cases, an exact Fourier transform of nonlinear terms is required, see for instance the cubic nonlinearity of the compressible Navier–Stokes equations in Sierra et al. [38].

The present methodology is used to analyze three different scenarios. First, a toy model: Lorenz equations are used to display some of the properties of the methodology. Fourier–Galerkin strategy is employed for the continuation of unstable periodic orbits through a series of period-doubling bifurcations in the Feigenbaum route to chaos. Such a situation, usually studied by collocation or shooting methods, proves to be one of the worst-case scenarios for this kind of spectral method

due to the lack of smoothness of the system of equations, see Moore [39]. Regardless, the approach proves to be capable to compute partially and accurately this route to chaos at least in small systems, the continuation of the period-doubling cascade in large systems is still an open challenge for future studies.
Two fluid mechanics cases, archetypal of bluff body flows, are studied with the presented machinery. The vortex-shedding periodic flow past a circular cylinder and the flip-flop instability of two circular cylinders side-by-side have been accurately reconstructed with a finite number of harmonics. Such a set of examples have been employed to test the performance of the numerical resolution. The number of GMRES iterations is independent of the number of harmonics and it depends quadratically on the Reynolds number. Similarly, the memory gain of iterative methods with respect to a direct factorization increases linearly with the length of the truncated basis and it is independent of the mesh size. Two kinds of instabilities are analyzed, the transition of a two-dimensional periodic solution towards a three-dimensional periodic state and the flip-flop instability through a Neimark–Sacker bifurcation. Both instabilities mechanisms have been examined with the aid of sensitivity maps developed in section 2.5. Structural sensitivity of the periodic solution allows the identification of physical mechanisms causing self-sustained instabilities. Two types of instabilities have been reported in section 3: the spatio-temporal symmetry breaking in the case of two circular cylinders in tandem configuration, or the transition to a three-dimensional flow in the single circular cylinder configuration. In addition, sensitivity to frequency variations identifies those regions of the space where open-loop control will be most effective to cause a change in frequency. To conclude, the authors would like to remark that these sensitivity maps are easily computed under this framework, which is also more computationally efficient than direct time-integration in the studied configurations.

## CRediT authorship contribution statement

The authors contributed equally to the submitted manuscript.

## Declaration of competing interest

The authors declare that they have no known competing financial interests or personal relationships that could have appeared to influence the work reported in this paper.

## Appendix A. Fourier–Galerkin equations

### A.1. Nonlinear operator

Fourier–Galerkin equations (6) are derived by averaging truncated residual equations over a period $T$. Given the orthogonality of the Fourier basis, linear terms depend only on a harmonic whereas Fourier coefficients of the quadratic term $\mathbf{N}_i$ may depend on several of them. Here a detailed description of the quadratic terms is given:

$$
\begin{aligned}
\mathbf{N}_0 = {} & \mathbf{N}(\mathbf{q}_0,\mathbf{q}_0) + \tfrac{1}{2}\textstyle\sum_{i=1}^{N} \mathbf{N}(\mathbf{q}_{i,s},\mathbf{q}_{i,s}) + \mathbf{N}(\mathbf{q}_{i,c},\mathbf{q}_{i,c}) \\
\mathbf{N}_{i,c} = {} & \left[\mathbf{N}(\mathbf{q}_{i,c},\mathbf{q}_0) + \mathbf{N}(\mathbf{q}_0,\mathbf{q}_{i,c})\right] \\
& + \tfrac{1}{2}\textstyle\sum_{j=1}^{i-1} \left[\mathbf{N}(\mathbf{q}_{j,c},\mathbf{q}_{i-j,c}) - \mathbf{N}(\mathbf{q}_{j,s},\mathbf{q}_{i-j,s})\right] \\
& + \tfrac{1}{2}\textstyle\sum_{j=i+1}^{N} \left[\mathbf{N}(\mathbf{q}_{j,c},\mathbf{q}_{j-i,c}) + \mathbf{N}(\mathbf{q}_{j-i,s},\mathbf{q}_{j,s})\right] \\
& + \tfrac{1}{2}\textstyle\sum_{j=i+1}^{N} \left[\mathbf{N}(\mathbf{q}_{j-i,c},\mathbf{q}_{j,c}) + \mathbf{N}(\mathbf{q}_{j,s},\mathbf{q}_{j-i,s})\right] \\
\mathbf{N}_{i,s} = {} & \left[\mathbf{N}(\mathbf{q}_{i,s},\mathbf{q}_0) + \mathbf{N}(\mathbf{q}_0,\mathbf{q}_{i,s})\right] \\
& + \tfrac{1}{2}\textstyle\sum_{j=1}^{i-1} \left[\mathbf{N}(\mathbf{q}_{j,c},\mathbf{q}_{i-j,s}) + \mathbf{N}(\mathbf{q}_{j,s},\mathbf{q}_{i-j,c})\right] \\
& - \tfrac{1}{2}\textstyle\sum_{j=i+1}^{N} \left[\mathbf{N}(\mathbf{q}_{j,c},\mathbf{q}_{j-i,s}) + \mathbf{N}(\mathbf{q}_{j-i,s},\mathbf{q}_{j,c})\right] \\
& + \tfrac{1}{2}\textstyle\sum_{j=i+1}^{N} \left[\mathbf{N}(\mathbf{q}_{j-i,c},\mathbf{q}_{j,s}) + \mathbf{N}(\mathbf{q}_{j,s},\mathbf{q}_{j-i,c})\right].
\end{aligned}
$$

### A.2. Residual notation

For the sake of a simpler presentation eq. (7) presents a series of operators, i.e., $\tilde{\mathbf{B}}, \tilde{\mathbf{L}}, \tilde{\mathbf{N}}$. Their definition is as follows:
*Time derivative matrix* $\tilde{\mathbf{B}}$

$$
\tilde{\mathbf{B}}\mathbf{Q}_N = \begin{bmatrix} \mathbf{0} & & & \\ & \mathbf{B}_1 & & \\ & & \ddots & \\ & & & \mathbf{B}_N \end{bmatrix} \begin{bmatrix} \mathbf{q}_0 \\ \mathbf{q}_1 \\ \vdots \\ \mathbf{q}_N \end{bmatrix} \text{ with } \mathbf{B}_n = \begin{bmatrix} \mathbf{0} & n\mathbf{B} \\ -n\mathbf{B} & \mathbf{0} \end{bmatrix} \text{ for } n = 1,\dots,N. \tag{A.1}
$$

*Linear operator* $\tilde{\mathbf{L}}$

$$\tilde{\mathbf{L}}\mathbf{Q}_N = \begin{bmatrix} \mathbf{L} & & & \\ & \mathbf{L} & & \\ & & \ddots & \\ & & & \mathbf{L} \end{bmatrix} \begin{bmatrix} \mathbf{q}_0 \\ \mathbf{q}_1 \\ \vdots \\ \mathbf{q}_N \end{bmatrix} \text{ with } \mathbf{q}_n = \begin{bmatrix} \mathbf{q}_{n,c} \\ \mathbf{q}_{n,s} \end{bmatrix} \text{ for } n = 1, \dots, N. \tag{A.2}$$

*Nonlinear operator* $\tilde{\mathbf{N}}$

$$\tilde{\mathbf{N}}(\mathbf{Q}_N, \mathbf{Q}_N) = \begin{bmatrix} \mathbf{N}_0 \\ \mathbf{N}_1 \\ \vdots \\ \mathbf{N}_N \end{bmatrix} \text{ with } \mathbf{N}_n = \begin{bmatrix} \mathbf{N}_{n,c} \\ \mathbf{N}_{n,s} \end{bmatrix} \text{ for } n = 1, \dots, N. \tag{A.3}$$

### *A.3. Jacobian operator*

Consider a small perturbation of $[\mathbf{Q}^{(\tau,N)}, \omega]^T$, here denoted as $[\delta\mathbf{Q}^{(\tau,N)}, \delta\omega]^T$, the linearized HBM equation is as follows:

$$\begin{aligned} \mathbf{0} &= -\delta\omega\tilde{\mathbf{B}}\mathbf{Q}_N - \omega\tilde{\mathbf{B}}\delta\mathbf{Q}^{(\tau,N)} + \tilde{\mathbf{L}}\delta\mathbf{Q}^{(\tau,N)} + D\tilde{\mathbf{N}}(\mathbf{Q}^{(\tau,N)})\delta\mathbf{Q}^{(\tau,N)} \\ &= -\delta\omega\tilde{\mathbf{B}}\mathbf{Q}^{(\tau,N)} + D\tilde{\mathbf{r}}(\mathbf{Q}^{(\tau,N)})\delta\mathbf{Q}^{(\tau,N)}, \end{aligned} \tag{A.4}$$

where the derivative of the quadratic operator is a dense block-symmetric matrix as follows:

$$D\tilde{\mathbf{N}}(\mathbf{Q}^{(\tau,N)}) = \begin{bmatrix} D\mathbf{N}^{(0)} & \dots & D\mathbf{N}^{(0,i)} & \dots & D\mathbf{N}^{(0,N)} \\ \vdots & \ddots & & & \vdots \\ D\mathbf{N}^{(i,0)} & \dots & D\mathbf{N}^{(i)} & \dots & D\mathbf{N}^{(i,N)} \\ \vdots & & & \ddots & \vdots \\ D\mathbf{N}^{(N,0)} & \dots & D\mathbf{N}^{(N,i)} & \dots & D\mathbf{N}^{(N)} \end{bmatrix}. \tag{A.5}$$

Let us consider the detailed description of each block. In the following, let us denote $D\mathbf{N}^{(\mathbf{q})} = \mathbf{N}(\cdot, \mathbf{q}) + \mathbf{N}(\mathbf{q}, \cdot)$, the linear operator of the derivative evaluated at $\mathbf{q}$.

*Diagonal blocks* $D\mathbf{N}^{(i)}$

$$D\mathbf{N}^{(0)} = D\mathbf{N}^{(\mathbf{q}_0)} \tag{A.6}$$

$$D\mathbf{N}^{(i)} = \begin{bmatrix} D\mathbf{N}^{(\mathbf{q}_0)} + \frac{1}{2}D\mathbf{N}^{(\mathbf{q}_{2i,c})} & \frac{1}{2}D\mathbf{N}^{(\mathbf{q}_{2i,s})} \\ \frac{1}{2}D\mathbf{N}^{(\mathbf{q}_{2i,s})} & D\mathbf{N}^{(\mathbf{q}_0)} - \frac{1}{2}D\mathbf{N}^{(\mathbf{q}_{2i,c})} \end{bmatrix} \text{ if } 0 < i \leq \frac{N}{2} \tag{A.7}$$

$$D\mathbf{N}^{(i)} = \begin{bmatrix} D\mathbf{N}^{(\mathbf{q}_0)} & \mathbf{0} \\ \mathbf{0} & D\mathbf{N}^{(\mathbf{q}_0)} \end{bmatrix} \text{ if } i > \frac{N}{2}. \tag{A.8}$$

*Off diagonal-blocks* $D\mathbf{N}^{(i,j)}$

$$D\mathbf{N}^{(0,j)} = \begin{bmatrix} \frac{1}{2}D\mathbf{N}^{(\mathbf{q}_{j,c})} & \frac{1}{2}D\mathbf{N}^{(\mathbf{q}_{j,s})} \end{bmatrix} \text{ if } j \neq 0, \tag{A.9}$$

$$D\mathbf{N}^{(i,0)} = \begin{bmatrix} \frac{1}{2}D\mathbf{N}^{(\mathbf{q}_{i,c})} \\ \frac{1}{2}D\mathbf{N}^{(\mathbf{q}_{i,s})} \end{bmatrix} \text{ if } i > 0. \tag{A.10}$$

If $i \neq j$, $j \neq 0$, $j < i$, $j + i \leq N$:

$$D\mathbf{N}^{(i,j)} = \begin{bmatrix} \frac{1}{2}D\mathbf{N}^{(\mathbf{q}_{i-j,c})} + \frac{1}{2}D\mathbf{N}^{(\mathbf{q}_{j+i,c})} & -\frac{1}{2}D\mathbf{N}^{(\mathbf{q}_{i-j,s})} - \frac{1}{2}D\mathbf{N}^{(\mathbf{q}_{j+i,s})} \\ \frac{1}{2}D\mathbf{N}^{(\mathbf{q}_{i-j,s})} + \frac{1}{2}D\mathbf{N}^{(\mathbf{q}_{j+i,s})} & \frac{1}{2}D\mathbf{N}^{(\mathbf{q}_{i-j,c})} + \frac{1}{2}D\mathbf{N}^{(\mathbf{q}_{j+i,c})} \end{bmatrix}. \tag{A.11}$$

If $i \neq j$, $j \neq 0$, $j < i$, $j + i > N$:

$$D\mathbf{N}^{(i,j)} = \begin{bmatrix} \frac{1}{2}D\mathbf{N}^{(\mathbf{q}_{i-j,c})} & -\frac{1}{2}D\mathbf{N}^{(\mathbf{q}_{i-j,s})} \\ \frac{1}{2}D\mathbf{N}^{(\mathbf{q}_{i-j,s})} & \frac{1}{2}D\mathbf{N}^{(\mathbf{q}_{i-j,c})} \end{bmatrix} \text{ if } i \neq j,\ j \neq 0,\ j < i, \tag{A.12}$$

otherwise $D\mathbf{N}^{(j,i)} = (D\mathbf{N}^{(i,j)})^T$.

## Appendix B. Navier–Stokes operators

In the studied configurations, the flow is controlled by the Reynolds number $Re = \frac{U_\infty D}{\nu}$, $U_\infty$ is the free stream velocity, $D$ the diameter of the cylinder and $\nu$ the dynamic viscosity of the fluid. The fluid motion inside the domain is governed by the two-dimensional incompressible Navier–Stokes equations,

$$\frac{\partial \mathbf{U}}{\partial t} + \mathbf{U} \cdot \nabla \mathbf{U} = -\nabla P + \nabla \cdot \tau(\mathbf{U}) \tag{B.1a}$$

$$\nabla \cdot \mathbf{U} = 0, \tag{B.1b}$$

where $\mathbf{q} = [\mathbf{U}, P]$, $\mathbf{U}$ is the velocity vector whose components are $(U, V)$, $P$ is the reduced pressure and the viscous stress tensor $\tau(\mathbf{u})$ can be expressed as $\nu(\nabla \mathbf{U} + \nabla \mathbf{U}^T)$. The incompressible Navier–Stokes equations (B.1) are complemented with the following boundary conditions: on the cylinder surface, no-slip boundary conditions, uniform boundary conditions are set $U \to (U_\infty, 0)$ and stress-free at the outlet.

In the main text, Navier–Stokes equations (B.1) and the associated boundary conditions are written under the form $\mathbf{B}\frac{\partial \mathbf{q}}{\partial t} = \mathbf{L}\mathbf{q} + \mathbf{N}(\mathbf{q}, \mathbf{q})$, where $\mathbf{N}(\mathbf{q}, \mathbf{q}) = \mathbf{U} \cdot \nabla \mathbf{U}$ is the convective term.

## References


[1] P. Cvitanović, Invariant measurement of strange sets in terms of cycles, Phys. Rev. Lett. 61 (24) (1988) 2729.
[2] G.M. Shroff, H.B. Keller, Stabilization of unstable procedures: the recursive projection method, SIAM J. Numer. Anal. 30 (4) (1993) 1099–1120.
[3] V. Citro, P. Luchini, F. Giannetti, F. Auteri, Efficient stabilization and acceleration of numerical simulation of fluid flows by residual recombination, J. Comput. Phys. 344 (2017) 234–246.
[4] E.J. Doedel, B. Oldeman, Auto-07p: Continuation and Bifurcation Software, 1998.
[5] A. Dhooge, W. Govaerts, Y.A. Kuznetsov, MATCONT: a MATLAB package for numerical bifurcation analysis of ODEs, ACM Trans. Math. Softw. 29 (2) (2003) 141–164.
[6] W. Govaerts, Y.A. Kuznetsov, V. De Witte, A. Dhooge, H. Meijer, W. Mestrom, A. Riet, B. Sautois, MATCONT and CL MATCONT: Continuation Toolboxes in Matlab, Gent University and Utrecht University, 2011.
[7] F. Giannetti, S. Camarri, V. Citro, Sensitivity analysis and passive control of the secondary instability in the wake of a cylinder, J. Fluid Mech. 864 (2019) 45–72.
[8] F. Giannetti, S. Camarri, P. Luchini, Structural sensitivity of the secondary instability in the wake of a circular cylinder, J. Fluid Mech. 651 (2010) 319–337.
[9] T. Kapitula, K. Promislow, Spectral and Dynamical Stability of Nonlinear Waves, vol. 185, Springer, 2013.
[10] L. Guillot, B. Cochelin, C. Vergez, A generic and efficient Taylor series-based continuation method using a quadratic recast of smooth nonlinear systems, Int. J. Numer. Methods Eng. 119 (4) (2019) 261–280.
[11] M. Urabe, Galerkin's procedure for nonlinear periodic systems, Arch. Ration. Mech. Anal. 20 (1965) 120–152.
[12] M. Krack, J. Gross, Harmonic Balance for Nonlinear Vibration Problems, Springer, 2019.
[13] B. Cochelin, C. Vergez, A high order purely frequency-based harmonic balance formulation for continuation of periodic solutions, J. Sound Vib. 324 (1–2) (2009) 243–262.
[14] A. Stokes, On the approximation of nonlinear oscillations, J. Differ. Equ. 12 (1972) 535–558.
[15] P. Kuchment, Floquet theory for hypoelliptic equations and systems in the whole space, in: Floquet Theory for Partial Differential Equations, Springer, 1993, pp. 103–123.
[16] Y.A. Kuznetsov, Elements of Applied Bifurcation Theory, vol. 112, Springer Science & Business Media, 2013.
[17] R. Seydel, Practical Bifurcation and Stability Analysis, vol. 5, Springer Science & Business Media, 2009.
[18] J. Zhou, T. Hagiwara, M. Araki, Spectral characteristics and eigenvalues computation of the harmonic state operators in continuous-time periodic systems, Syst. Control Lett. 53 (2) (2004) 141–155.
[19] C. Curtis, B. Deconinck, On the convergence of Hill's method, Math. Comput. 79 (269) (2010) 169–187.
[20] M.A. Johnson, K. Zumbrun, Convergence of Hill's method for non-self-adjoint operators, SIAM J. Numer. Anal. 50 (1) (2012) 64–78.
[21] B. Bentvelsen, A. Lazarus, Modal and stability analysis of structures in periodic elastic states: application to the Ziegler column, Nonlinear Dyn. 91 (2) (2018) 1349–1370.
[22] A. Lazarus, O. Thomas, A harmonic-based method for computing the stability of periodic solutions of dynamical systems, C. R., Méc. 338 (9) (2010) 510–517.
[23] L. Guillot, A. Lazarus, O. Thomas, C. Vergez, B. Cochelin, A purely frequency based Floquet–Hill formulation for the efficient stability computation of periodic solutions of ordinary differential systems, J. Comput. Phys. 416 (2020) 109477.
[24] F. Giannetti, P. Luchini, Structural sensitivity of the first instability of the cylinder wake, J. Fluid Mech. 581 (2007) 167–197.
[25] D. Sipp, Open-loop control of cavity oscillations with harmonic forcings, J. Fluid Mech. 708 (2012) 439.
[26] M. Benzi, M.A. Olshanskii, Z. Wang, Modified augmented Lagrangian preconditioners for the incompressible Navier–Stokes equations, Int. J. Numer. Methods Fluids 66 (4) (2011) 486–508.
[27] J. Moulin, P. Jolivet, O. Marquet, Augmented Lagrangian preconditioner for large-scale hydrodynamic stability analysis, Comput. Methods Appl. Mech. Eng. 351 (2019) 718–743.
[28] Y. Saad, Iterative Methods for Sparse Linear Systems, vol. 82, SIAM, 2003.
[29] F. Hecht, New development in FreeFem++, J. Numer. Math. 20 (3–4) (2012) 251–266.
[30] S. Balay, S. Abhyankar, M. Adams, J. Brown, P. Brune, K. Buschelman, L. Dalcin, A. Dener, V. Eijkhout, W. Gropp, et al., PETSc Users Manual, 2019.
[31] V. Hernandez, J.E. Roman, V. Vidal, SLEPc: a scalable and flexible toolkit for the solution of eigenvalue problems, ACM Trans. Math. Softw. 31 (3) (2005) 351–362.
[32] D. Fabre, V. Citro, D. Ferreira Sabino, P. Bonnefis, J. Sierra, F. Giannetti, M. Pigou, A practical review on linear and nonlinear global approaches to flow instabilities, Appl. Mech. Rev. 70 (6) (2018).
[33] P. Collet, J.-P. Eckmann, O. Lanford, Universal properties of maps on an interval, Commun. Math. Phys. 76 (3) (1980) 211–254.
[34] C.H.K. Williamson, Vortex dynamics in the cylinder wake, Annu. Rev. Fluid Mech. 28 (1) (1996) 477–539.
[35] D. Barkley, R.D. Henderson, Three-dimensional Floquet stability analysis of the wake of a circular cylinder, J. Fluid Mech. 322 (1996) 215–241.
[36] M. Carini, F. Giannetti, F. Auteri, On the origin of the flip-flop instability of two side-by-side cylinder wakes, J. Fluid Mech. 742 (2014) 552–576.

[37] J. Mizushima, Y. Ino, Stability of flows past a pair of circular cylinders in a side-by-side arrangement, J. Fluid Mech. 595 (2008) 491–507.
[38] J. Sierra, V. Citro, F. Giannetti, D. Fabre, Efficient computation of periodic compressible flows with spectral techniques, 2020, Manuscript submitted for publication.
[39] G. Moore, Floquet theory as a computational tool, SIAM J. Numer. Anal. 42 (6) (2005) 2522–2568.

*J. Fluid Mech.* (2022), *vol*. 942, A54, doi:10.1017/jfm.2022.395

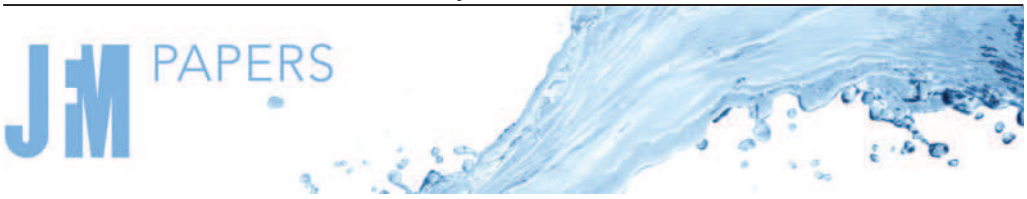


# Unveiling the competitive role of global modes in the pattern formation of rotating sphere flows

**J. Sierra-Ausín[1,2], M. Lorite-Díez[2,3], J.I. Jiménez-González[4,5,†], V. Citro[1] and D. Fabre[2]**

[1]Dipartimento di Ingegneria Industriale (DIIN), Università degli Studi di Salerno, Fisciano 84084, Italy

[2]Institut de Mécanique des Fluides de Toulouse (IMFT), Université de Toulouse and CNRS, Toulouse 31400, France

[3]Departamento de Ingeniería Mecánica, Térmica y de Fluidos, Universidad de Málaga, Málaga 29002, Spain

[4]Departamento de Ingeniería Mecánica y Minera, Universidad de Jaén, Jaén 23071, Spain

[5]Andalusian Institute for Earth System Research, Universidad de Jaén, Jaén 23071, Spain

(Received 11 September 2021; revised 28 February 2022; accepted 25 April 2022)

The wake flow past a streamwise rotating sphere is a canonical model of numerous applications, such as particle-driven flows, sport aerodynamics and freely rising or falling bodies, where the changes in particles' paths are related to the destabilization of complex flow regimes and associated force distributions. Herein, we examine the spatio-temporal pattern formation, previously investigated by Lorite-Díez & Jiménez-González (*J. Fluid Mech.*, vol. 896, 2020, A18) and Pier (*J. Fluids Struct.*, vol. 41, 2013, pp. 43–50), from a dynamical system perspective. A systematic study of the mode competition between rotating waves, which arise from the linearly unstable modes of the steady-state, exhibits their connection to previously observed helical patterns present within the wake. The organizing centre of the dynamics turns out to be a triple Hopf bifurcation associated with three non-axisymmetric, oscillating modes with respective azimuthal wavenumbers $m = -1, -1$ and $-2$. The unfolding of the normal form unveils the nonlinear interaction between the rotating waves to engender more complex states. It reveals that for low values of the rotation rate, the flow field exhibits a similar transition to the flow past the static sphere, but accompanied by a rapid variation of the frequencies of the flow with respect to the rotation. The transition from the single helix pattern to the double helix structure within the wake displays several regions with hysteric behaviour. Eventually, the interaction between single and double helix structures within the wake lead towards temporal chaos, which here is attributed to the Ruelle–Takens–Newhouse route. The onset of chaos is detected by the identification of an invariant state of the normal form constituted by three incommensurate frequencies. The evolution of the chaotic attractor is determined using of time-stepping

† Email address for correspondence: jignacio@ujaen.es

simulations, which were also performed to confirm the existence of bi-stability and to assess the fidelity of the computations performed with the normal form.

**Key words:** shear-flow instability, wakes

## 1. Introduction

The flow around a rotating sphere has drawn the attention of many researchers in recent years as it represents a canonical problem with many engineering and physics applications. For instance, such configuration may be found in multiple practical and natural phenomena like particle-driven flows (Shi & Rzehak 2019), fluidized bed combustion (Liu & Prosperetti 2010; Feng & Musong 2014), sports aerodynamics (Passmore *et al.* 2008; Robinson & Robinson 2013), seeds' flight (Barois *et al.* 2019; Rabault, Fauli & Carlson 2019) or free-falling/rising bodies (Ern *et al.* 2012; Auguste & Magnaudet 2018; Mathai *et al.* 2018), among others. In such applications, the instability of paths of the spherical bodies is shown to depend on the forces distributions acting on their surface and, therefore, on the flow regimes that are destabilized for different values of the Reynolds number and rotation rates. Consequently, a profound understanding of the physics of the flow around a rotating sphere and its instability features is required to predict the dynamics of rotating particles and evaluate possibilities of flow and path control.

The unstable flow regimes at the wake past a fixed sphere have been extensively characterized, as it represents a classical example of open flow leading to rich pattern formation and dynamical complexity. As reported by different numerical and stability analyses available in the literature, the flow experiences a complex sequence of laminar bifurcations as the Reynolds number $Re$ increases (see, e.g. Sakamoto & Haniu 1990; Johnson & Patel 1999; Fabre, Auguste & Magnaudet 2008; Fabre *et al.* 2017). For a static (non-rotating) sphere, the flow first experiences a steady bifurcation around $Re_{c1} \simeq 212$, leading to a steady, reflection-symmetric bifid wake (steady-state mode, Fabre *et al.* 2008), followed by a Hopf bifurcation at $Re_{c2} \simeq 272$ (Citro *et al.* 2017), leading to a periodic, vortex-shedding mode which preserves the axial reflection symmetry plane (RSP mode, Fabre *et al.* 2008). This reflection symmetry in the shedding process is lost around $Re_{c3} \simeq 375$, from which the wake starts to oscillate transversely (Chrust, Goujon-Durand & Wesfreid 2013).

When rotation is applied, the bifurcation scenario of the sphere wake is modified, generating even richer dynamics. In particular, as shown by Poon *et al.* (2010), the topology and frequency of the unstable flow regimes depend on the rotation rate $\Omega$ and the axis of rotation.

In general, the flow past streamwise rotating spheres has received considerably less attention than transversely rotating spheres (see, e.g. Citro *et al.* 2016), and their dynamics and controllability features are not yet fully understood. However, some numerical and experimental studies have focused on the flow topology and stability modifications produced in the sphere wake as the streamwise rotation speed increases (Kim & Choi 2002; Niazmand & Renksizbulut 2005; Skarysz *et al.* 2018) at low values of Reynolds number. The problem can be also studied under linear stability analysis perspective as in Pier (2013) and Jiménez-González, Manglano-Villamarín & Coenen (2019). Moreover, the influence of streamwise rotation is not only restricted to the sphere, and it has been also studied in wakes behind other axisymmetric geometries which follow a similar series of bifurcations, as in Jiménez-González *et al.* (2013) and Jiménez-González *et al.* (2014) for blunt-based bodies.

The introduction of streamwise rotation introduces unsteadiness and asymmetry in the sphere wake. The steady state is substituted by a frozen rotation with azimuthal wavenumber $m = -1$ symmetry (Kim & Choi 2002; Jiménez-González *et al.* 2019), the negative sign indicating that vortical structures wind in the direction opposite to the swirl motion. When either $Re$ or $\Omega$ increase, the periodic behaviour of this low-frequency frozen state diverges to quasiperiodic or even chaotic states. The quasiperiodicity can be caused by the appearance of a medium-frequency component, related to the RSP mode of the non-rotating situation, or to the appearance of a component with $m = -2$ symmetry in the flow, for $Re < 500$ and moderate $\Omega$ values (Skarysz *et al.* 2018; Lorite-Díez & Jiménez-González 2020). Moreover, in a more recent study, Lorite-Díez & Jiménez-González (2020) also identified very complex patterns close to chaotic behaviours, by performing direct numerical simulations (DNS). More precisely, with the help of dynamic mode decomposition tools, the nonlinear regimes are reported to be characterized by three fundamental frequency components (related to unstable structures displaying $m = -1$, $m = -1$ and $m = -2$ symmetries, respectively) and their interactions. However, the time-stepping simulations do not provide a clear insight about the origin of instability of these complex regimes and the fundamental nature of the incommensurate or derived frequency components, so that the use of adjoint stability tools seem advisable to isolate fundamental modes and identify mechanisms of receptivity to forcing or control.

Additionally, the time-stepping simulations of such complex dynamical systems are generally demanding in terms of computational cost, especially close to bifurcations thresholds, where long convergence times are usually required to obtain statistically relevant solutions. As a matter of fact, alternative weakly nonlinear approaches, as those based on bifurcation theory (Golubitsky & Langford 1988), may be more efficient to elucidate the pattern of transitions and major features of flow regimes with increasing values of the problem parameters (i.e. $Re$, $\Omega$), by taking advantage of the symmetry of the base flow and proximity between successive instability thresholds. That said, the transition scenarios of complex systems with underlying symmetries usually lead to a large variety of pattern formations.

Close to the onset of stability, these patterns may be caused by a single instability, or alternatively, the system can display instabilities where several modes are concomitantly accountable for the destabilization of the trivial state. Besides, flow configurations controlled by a diversity of parameters may lose stability in diverse manners. A large diversity of patterns may emerge in the entire parameter space, and, in particular, one can find specific regions displaying mode competition. The combination of symmetry with a parameter space whose dimension is higher than one is a classical scenario where mode interaction occurs. The organizing centre of such cases is denoted as a bifurcation of codimension $n$, with $n \in \mathbb{N}$. Codimension is herein loosely defined as the number of interacting modes, and also corresponds to the dimension of the low-order dynamical system model called the normal form capturing the essence of the dynamics. The interested reader can find more about pattern formation in symmetric systems in Golubitsky, Stewart & Schaeffer (2012), while the study of the normal form of bifurcations with codimension higher than one may be found in the books of Guckenheimer (2010) or Kuznetsov (2013). The passage from a high-dimensional system to a reduced one with a slow manifold takes advantage of the theoretical framework provided by the singular perturbation theory. For example, the geometric singular perturbation theory, reviewed by Verhulst (2007), is a powerful technique within the singular perturbation theory. In the bifurcation theory of autonomous systems, it is customary to employ centre manifold or normal form reduction. This procedure has been employed for the study of bifurcations from steady

states (Haragus & Iooss 2010), maps (respectively Poincaré maps associated with a limit-cycle solution) (Kuznetsov & Meijer 2005), homoclinic and heteroclinic connections (Homburg & Sandstede 2010). The most commonly used computational procedures to determine the centre manifold are weakly nonlinear analysis, multiple scales expansion or the homological equation. In the past, these approaches have been exploited to study mode interaction in thermally driven convective motions, e.g. the Rayleigh–Bénard (Varé *et al.* 2020) and Langmuir circulation (Allen & Moroz 1997), in the fluid flow between counter-rotating cylinders, e.g. the Taylor–Couette flow (Golubitsky & Langford 1988) and its variants (Renardy *et al.* 1996), in magnetoconvection (Rucklidge *et al.* 2000), in the flow past a rotating cylinder (Sierra *et al.* 2020*b*) and in swirling jets (Meliga, Gallaire & Chomaz 2012).

In light of the aforementioned studies, for the parameters considered herein, one can expect that a linear stability analysis (LSA) discriminates at least three unsteady unstable fundamental modes: two with azimuthal wavenumber $m = -1$ and a third one with $m = -2$; meaning that the organizing centre is a triple-Hopf bifurcation with $SO(2)$ symmetry. Despite the likely existence of three unstable modes, because the dimension of the parameter space is two, the triple-Hopf bifurcation is not expected to occur. Therefore, the approach followed herein for the study of the triple-Hopf bifurcation is based on the extension of the normal form obtained at codimension-two points to the codimension-three manifold. In practical terms, we determine a fifth-order truncation in terms of the expansion parameter of the normal form at codimension-two points, followed by a linear (respectively quadratic for linear coefficients) extension of normal form coefficients to a specific point in the parameter space. Such an approach is detailed in § 4 and it is similar to the centre-unstable manifold reduction, cf. Armbruster, Guckenheimer & Holmes (1989), Podvigina (2006*a*), Podvigina (2006*b*) and Meliga, Chomaz & Sipp (2009*a*). In any case, once the normal form is determined, one can analyse the bifurcation scenario, which displays a rich variety of patterns, among which one can expect: rotating waves, quasiperiodic mixed modes or chaotic solutions displaying multiple frequency components, along with bi-stable states stemming from the coexistence of two stable rotating waves, mixed modes and rotating waves, diverse mixed modes or mixed modes and chaotic attractor.

Some of these transition features and bi-stable dynamics had been confirmed via time-stepping numerical simulations undertaken by Lorite-Díez & Jiménez-González (2020) and Pier (2013) who reported a rich variety of spatio-temporal patterns. However, they did not perform an exhaustive analysis of the nature of the bifurcations between the distinct regimes. Therefore, the objective of the present research is twofold. The first objective is to undertake a global stability analysis to determine the connection between the observed patterns by Lorite-Díez & Jiménez-González (2020) and the linear stability of helical modes. The identification of these fundamental modes allows an identification of the underlying physical mechanisms responsible for the instabilities and the receptivity of the flow to forcing or control possibilities. Secondly, the analysis of the normal form associated with the organizing centre serves to provide a complete phase portrait of the flow attractors before the emergence of temporal chaos and to unravel the transition towards chaotic spatio-temporal dynamics observed by Lorite-Díez & Jiménez-González (2020) and Pier (2013).

The outline of the manuscript is as follows. First, the flow configuration and the numerical approach are presented in § 2. Second, we undergo a LSA in § 3, which identifies the most unstable global modes, their underlying physical mechanisms and sensitivity to forcing. Third, we introduce the methodology for the normal form reduction and we

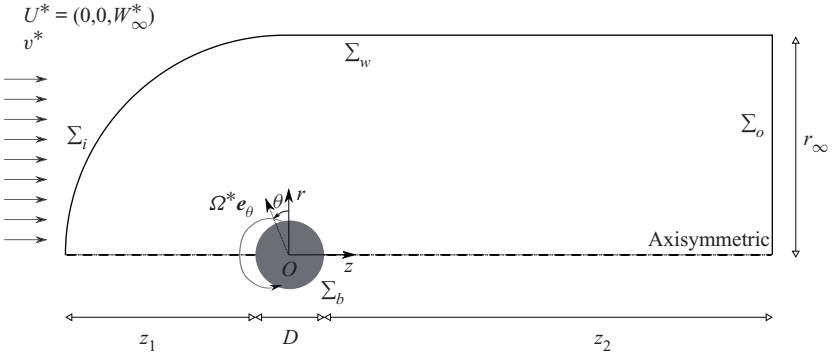


Figure 1. Sketch of the problem and geometric configuration.

illustrate it with a bifurcation diagram at constant rotation rate in § 4. Then, in § 5 we pursue the study by comparing the normal form predictions with DNS results and we provide a complete phase diagram of the stable attractors of the flow in the range $Re \leq 300$ and $\Omega < 4$. Finally, in § 6 we summarise the main findings and we argue of some future applications of the study.

## 2. Methodology

### 2.1. *Flow configuration – governing equations*

The flow past an axisymmetric rotating body is controlled by two parameters: the Reynolds number ($Re$) and the rotation rate ($\Omega$) which is defined as the ratio of the tangential velocity $\Omega^* D^*/2$ on the sphere surface to the inflow velocity $W^*_\infty$. The fluid motion inside the domain is governed by the incompressible Navier–Stokes equations written in cylindrical coordinates $(r, \theta, z)$,

$$\frac{\partial \boldsymbol{U}}{\partial t} + \boldsymbol{U} \cdot \boldsymbol{\nabla} \boldsymbol{U} = -\boldsymbol{\nabla} P + \boldsymbol{\nabla} \cdot \tau(\boldsymbol{U}), \quad \boldsymbol{\nabla} \cdot \boldsymbol{U} = 0, \tag{2.1a}$$

$$\text{with } \tau(\boldsymbol{U}) = \frac{1}{Re}(\boldsymbol{\nabla} \boldsymbol{U} + \boldsymbol{\nabla} \boldsymbol{U}^{\mathrm{T}}), \quad Re = \frac{W^*_\infty D^*}{\nu^*}, \quad \Omega = \frac{\Omega^* D^*}{2 W^*_\infty}, \tag{2.1b}$$

$$\boldsymbol{x} = \boldsymbol{x}^* \frac{1}{D^*}, \quad t = t^* \frac{W^*_\infty}{D^*}, \quad \boldsymbol{U} = \boldsymbol{U}^* \frac{1}{W^*_\infty} \quad P = P^* \left(\frac{1}{W^*_\infty}\right)^2. \tag{2.1c}$$

Dimensional quantities are identified with the upperscript symbol $^*$. Reference scales are specified in (2.1$c$). The dimensionless velocity vector $\boldsymbol{U} = (U, V, W)$ is composed of the radial, azimuthal and axial components, $P$ is the dimensionless reduced pressure and the viscous stress tensor, $\tau(\boldsymbol{U})$. For representation purposes, it is sometimes necessary to use the Cartesian coordinates $(x, y, z)$, here $z$ denotes the streamwise direction, $y$ the vertical crosswise direction and $x$ the direction that forms a direct trihedral with $z$ and $y$. The incompressible Navier–Stokes equations (2.1) are complemented with the following boundary conditions:

$$\boldsymbol{U} = (0, \Omega, 0) \text{ on } \Sigma_b \quad \boldsymbol{U} = (0, 0, 1) \text{ on } \Sigma_i. \tag{2.2}$$

No-slip boundary condition is set on the rotating sphere and a uniform boundary condition is set in the inlet, as shown in figure 1.

In the sequel, Navier–Stokes equations (2.1) and the associated boundary conditions will be written symbolically under the form

$$\boldsymbol{B}\frac{\partial \boldsymbol{Q}}{\partial t} = \boldsymbol{F}(\boldsymbol{Q}, \boldsymbol{\eta}) \equiv \boldsymbol{L}\boldsymbol{Q} + \boldsymbol{N}(\boldsymbol{Q}, \boldsymbol{Q}) + \boldsymbol{G}(\boldsymbol{Q}, \boldsymbol{\eta}), \tag{2.3}$$

where $\boldsymbol{B}$ is the projection matrix onto the velocity field with the flow state vector $\boldsymbol{Q} = [\boldsymbol{U}, P]^{\mathrm{T}}$, and the parameter vector $\boldsymbol{\eta} = [Re^{-1}, \Omega]^{\mathrm{T}}$. Such a form of the governing equations takes into account a linear dependency on the state variable $\boldsymbol{Q}$ through $\boldsymbol{L}$ and a quadratic dependency on parameters and the state variable through operators $\boldsymbol{N}(\cdot, \cdot)$ and $\boldsymbol{G}(\cdot, \cdot)$, which are detailed in Appendix A.

### 2.2. *Nomenclature*

Let us introduce some general concepts that will be employed throughout the study. Steady states, i.e. $\boldsymbol{Q}$ such that $\boldsymbol{F}(\boldsymbol{Q}, \boldsymbol{\eta}) = 0$, periodic orbits, i.e. $\boldsymbol{Q}(t) = \boldsymbol{Q}(t + T)$ for every $t \geq 0$, are the simplest invariants of (2.3). In general, an invariant set $V$ of the phase space of (2.3) is a set that is preserved under dynamics, i.e. for every initial solution $\boldsymbol{Q}(t_0) \in V$, we have $\boldsymbol{Q}(t) \in V$ for every $t \geq 0$. A $T^n$-quasiperiodic state, $n > 1$, $n \in \mathbb{N}^*$, is an invariant of the system (2.3) that can be decomposed as a finite sum of $n$ incommensurate frequencies $\omega_n$, i.e.

$$\boldsymbol{Q} = \boldsymbol{Q}_0 + \sum_{\ell=1}^{n} \left( \hat{\boldsymbol{Q}}_\ell \mathrm{e}^{\mathrm{i}\omega_\ell t} + \text{c.c.} \right). \tag{2.4}$$

Incommensurate frequencies are those that are linearly independent, i.e. for $k_\ell \in \mathbb{Z}$, we have $\sum_{\ell=1}^{n} k_\ell \omega_\ell = 0$ if and only if every $k_\ell = 0$. Here, we determine the incommensurate frequencies as those corresponding to the fundamental modes (least stable eigenmodes) identified by LSA.

A second important property is the attractiveness of an invariant set. We denote as basin of attraction the set of initial conditions leading to long-time behaviour that approaches the attractor. The celebrated manuscript of Newhouse, Ruelle & Takens (1978) states that $T^n$-quasiperiodic states, with $n \geq 3$, are unusual attractors, in the sense that every $T^n$-quasiperiodic state can be perturbed by an arbitrarily small amount to a new vector field with a chaotic attractor. In other words, for any $T^n$-quasiperiodic state of (2.3), one may observe a chaotic *Axiom A* attractor by experimental or numerical means. Here, *Axiom A* attractor denotes a class of dynamical systems where the non-wandering set is hyperbolic and the attractor has a dense set of periodic orbits, more details about hyperbolicity may be found, for instance, in the recent article by Ni (2019).

### 2.3. *Direct numerical simulation details*

The flow governed by (2.1) is solved by means of DNS, following a time-stepping approach using the finite-volume library OpenFOAM®. The domain shown in figure 1 consists of an upstream hemisphere of radius $r_\infty = 15D$ and a downstream tube extending $z_2 = 50D$ downstream of the body.

Regarding boundary conditions at the outlet, $\Sigma_o$, we impose an outflow condition that implements a Neumann condition for the velocity, $\boldsymbol{n} \cdot \nabla \boldsymbol{U} = 0$, where $\boldsymbol{n}$ is the outward normal, and a Dirichlet condition for the pressure, $P = 0$. The latter may be considered equivalent to setting a stress-free condition at the outlet for small values of the viscosity (as highlighted by Tomboulides & Orszag 2000). Finally, at the outer radial

boundary, $\Sigma_w$, we set a slip boundary condition, $\boldsymbol{n}\cdot\boldsymbol{U}=0$. Note that such domain size and boundary conditions have been selected according to previous numerical works on rotating axisymmetric bodies (see, e.g. Jiménez-González *et al.* 2013; Lorite-Díez & Jiménez-González 2020). Additionally, second-order schemes have been employed for spatial and time integration. Nevertheless, for the sake of conciseness, the reader is referred to Appendix A in Lorite-Díez & Jiménez-González (2020) for detailed information about the employed numerical schemes, convergence and validation studies. In the present simulations ∼2.6 millions of elements mesh, denoted #2 in table 1 (Appendix A) therein, is used.

The three-dimensional time-stepping simulations were computed in parallel. In particular, the DNS are carried out, once converged, for $T\sim 500$ convective units for periodic regimes, and until $T\sim 1000$ convective units for quasiperiodic and most complex regimes. The employed time step is $\Delta t=0.003$ for all simulations. In terms of computational cost, running on 16 Intel Xeon E5-2665 processors, a simulation lasting $T=1000$ convective time units corresponds to approximately 10 days.

## 3. Linear stability analysis

### 3.1. *Methodology*

As a first step of the reduction procedure, we identify the base flow solution, which is defined as the steady solution $\boldsymbol{Q}_b$ of the (axisymmetric) Navier–Stokes equations, namely the solution of $\boldsymbol{F}(\boldsymbol{Q}_b)=\boldsymbol{0}$. We then characterize the dynamics of small-amplitude perturbations around this base flow by expanding them over the basis of linear eigenmodes

$$\boldsymbol{Q}=\boldsymbol{Q}_b+\varepsilon\sum_{\ell}\boldsymbol{q}_{(\varepsilon)}(t,\tau)=\boldsymbol{Q}_b+\varepsilon\sum_{\ell}\left(z_\ell(\tau)\hat{\boldsymbol{q}}_{(z_\ell)}(r,z)\mathrm{e}^{\mathrm{i}(m_\ell\theta+\omega_\ell t)}+\mathrm{c.c.}\right),\quad \varepsilon\ll 1. \tag{3.1}$$

The eigenpairs $[\mathrm{i}\omega_\ell,\hat{\boldsymbol{q}}_{(z_\ell)}]$ are then determined as the solutions of the eigenvalue problem

$$\boldsymbol{J}_{(\omega_\ell,m_\ell)}\hat{\boldsymbol{q}}_{(z_\ell)}=\left(\mathrm{i}\omega_\ell\boldsymbol{B}-\left.\frac{\partial\boldsymbol{F}}{\partial\boldsymbol{q}}\right|_{\boldsymbol{q}=\boldsymbol{Q}_b,\Delta\boldsymbol{\eta}=\boldsymbol{0}}\right)\hat{\boldsymbol{q}}_{(z_\ell)}, \tag{3.2}$$

where $(\partial\boldsymbol{F}/\partial\boldsymbol{q}|_{\boldsymbol{q}=\boldsymbol{Q}_b,\Delta\boldsymbol{\eta}=\boldsymbol{0}})\hat{\boldsymbol{q}}_{(z_\ell)}=\boldsymbol{L}_{m_\ell}\hat{\boldsymbol{q}}_{(z_\ell)}+\boldsymbol{N}_{m_\ell}(\boldsymbol{Q}_b,\hat{\boldsymbol{q}}_{(z_\ell)})+\boldsymbol{N}_{m_\ell}(\hat{\boldsymbol{q}}_{(z_\ell)},\boldsymbol{Q}_b)+\boldsymbol{G}(\boldsymbol{Q}_b,\boldsymbol{\eta}_c)$, with $\boldsymbol{\eta}_c=[Re_c^{-1},\Omega_c]^{\mathrm{T}}$. The subscript $m_\ell$ indicates the azimuthal wavenumber used for the evaluation of the linearized Navier–Stokes operator $\boldsymbol{J}_{(\omega_\ell,m_\ell)}$. Please note that here, the term $\Delta\boldsymbol{\eta}=[Re_c^{-1}-Re^{-1},\Omega_c-\Omega]^{\mathrm{T}}$ denotes the departure from the critical condition attained at $[Re_c^{-1},\Omega_c]^{\mathrm{T}}$. In the following, we consider that eigenmodes $\hat{\boldsymbol{q}}_{(z_\ell)}(r,z)$ have been normalised in such a way that $\langle\hat{\boldsymbol{q}}_{(z_\ell)},\hat{\boldsymbol{q}}_{(z_\ell)}\rangle_{\boldsymbol{B}}=\langle\hat{\boldsymbol{u}}_{(z_\ell)},\hat{\boldsymbol{u}}_{(z_\ell)}\rangle=\int_\Omega\boldsymbol{u}(\boldsymbol{x})^{\mathrm{T}}\boldsymbol{u}(\boldsymbol{x})\,\mathrm{d}\boldsymbol{x}=1$.

#### 3.1.1. *Numerical methodology for stability tools*

Results presented herein follow the same numerical approach adopted by Fabre *et al.* (2018), Sierra, Fabre & Citro (2020*a*) and Sierra *et al.* (2020*b*). The calculation of the base flow, the eigenvalue problem and the normal form expansion are implemented in the open-source software FreeFem++. Parametric studies and generation of figures are collected by StabFem drivers, an open-source project available at https://gitlab.com/stabfem/StabFem. Results shown in §§ 3–5 have been computed with a numerical domain (see figure 1) of size $z_2=50D$, $z_1=20D$ and $r_\infty=20D$, in the streamwise and crosswise directions, respectively. For steady-state, stability and normal form computations, we set

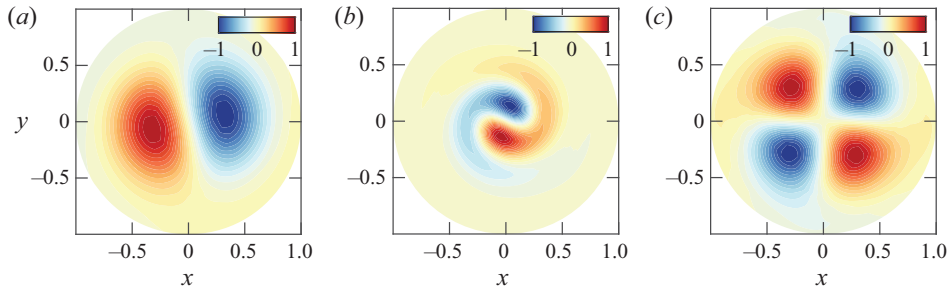


Figure 2. Cross-section view at $z = 3.5$ of the three unstable modes. The streamwise component of the vorticity vector $\varpi_z$ is visualized by colours. Results are shown for (*a*) $RW_1$ at point $(Re_A, \Omega_A) = (77, 2.24)$; (*b*) $RW_2$ at point $(Re_B, \Omega_B) = (188, 1.01)$; (*c*) $RW_3$ at point $(Re_A, \Omega_A)$.

the stress-free boundary condition at the outlet, which is the natural boundary condition in the variational formulation. Numerical convergence issues are discussed in Appendix D. The resolution of the steady nonlinear Navier–Stokes equations is tackled by means of the Newton method. While the generalized eigenvalue problem (3.2) is solved following the Arnoldi method with spectral transformations. The normal form reduction procedure of § 4 only requires us to solve a set of linear systems, which is also carried out within StabFem. On a standard laptop, every computation considered below can be attained within a few hours.

### 3.2. *Neutral curves of stability*

In the presence of supercritical self-sustained instabilities, rotating waves are predominant. These patterns prevail in axisymmetric flows, where the reflection symmetry regarding the azimuthal angle is broken. Here, the reflection symmetry is broken because of the rotation of the sphere, which induces a preferential direction of rotation. Consequently, bifurcations that lead to standing waves or to a symmetry breaking steady state do not occur generically. The existence of standing waves or a steady-state mode requires the matching between the phase speed of the helical pattern and the rotation of the body, which is another condition to be met. The global stability analysis of the flow past the sphere confirms that only rotating waves are linearly unstable for the range of Reynolds numbers $Re < 300$ and $\Omega < 4$. The parametric linear stability study of the flow past the rotating sphere shows the existence of three neutral curves, which are associated to the three least stable modes identified by global stability analysis. These correspond to rotating waves, named $RW_1$, $RW_2$ and $RW_3$, which are depicted in figure 2. Linear stability results (figure 3*a*) reveal that the axisymmetric steady state, referred in the following as a trivial state, is stable in the white shaded region and unstable in the grey shaded region. The neutral curve of stability displays two regions in the parameter space $(Re, \Omega)$ for which the first primary bifurcations are rotating waves of low frequency where the wake past the sphere displays a single helix ($RW_1$), depicted in figure 2(*a*). In the second region, the flow pattern of the wake displays a double helix ($RW_3$) with a high frequency, depicted in figure 2(*c*). The onset of instability of the third branch ($RW_2$) displaying a flow pattern of the wake with a single helix with a medium frequency, depicted in figure 2(*b*), turns out to be linearly unstable for $\Omega \leq 4$. Each pair of neutral curves intersects once, leading to three codimension-two points $(A, B, C)$, identified in table 1. Another aspect of importance is the evolution of frequencies of the instability. Frequencies at critical parameters are reported in figure 3(*b*) as a function of $\Omega$. The frequency evolution is divided into two regions, a

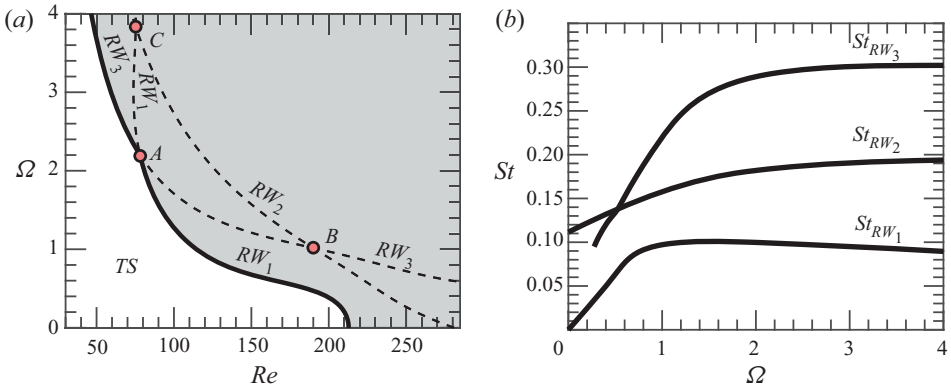


Figure 3. Linear stability properties of the rotating sphere configuration. (*a*) Neutral curve of stability: the onset of the primary instability is portrayed with a solid black line (—), whereas the continuation of the neutral curves is depicted with dashed black lines (- - -). (*b*) Frequency evolution with respect to $\Omega$ of linear modes at the critical Reynolds number ($Re_c(\Omega)$).

| Name | $Re$ | $\Omega$ | Mode inter. | $\theta_N$ | $\gamma$ |
|---|---|---|---|---|---|
| Static | 212 | 0 | $RW_1$ | 4° | 0.76 |
| $A$ | 77 | 2.24 | ($RW_1$, $RW_3$) | (4.6°, 8.0°) | (0.89, 0.98) |
| $B$ | 188 | 1.01 | ($RW_2$, $RW_3$) | (0.7°, 2.3°) | (0.82, 0.80) |
| $C$ | 73 | 3.95 | ($RW_1$, $RW_2$) | (3.8°, 9.9°) | (0.80, 0.68) |

Table 1. Location in the parameter space ($Re$, $\Omega$) and the pair of modes involved at the codimension-two points. It also lists the main properties of the primary bifurcation of the flow past the static sphere. The last two columns are related to non-normality effects and are defined in § 3.3.

first of rapid evolution for low rotation rates $\Omega < 1$ and a second where the frequency of the three modes hardly depends on the rotation rate.

The neutral curve of stability reveals that the static configuration ($\Omega = 0$) exhibits the largest critical Reynolds number. Then, the critical value of the Reynolds number is hardly modified by weak rotating speeds, in the range $\Omega < 0.3$. However, there is a clear threshold around $\Omega \approx 0.4$ where the critical Reynolds number passes from around $Re_c \approx 200$ to $Re_c \approx 100$ in a narrow interval $\Omega \in [0.4, 1.2]$. The critical Reynolds number remains approximately constant up to the point $A$, the point which divides the boundary of stability. Below the point $A$, that is, for $\Omega < \Omega_A$, the steady-state flow transits supercritically to a single helix rotating wave $RW_1$; above the point $A$, i.e. $\Omega > \Omega_A$, the steady-state flow transits supercritically to the double helix rotating wave, $RW_3$. Such a point corresponds to a double-Hopf bifurcation between modes 1 and 3, and its analysis is left to §§ 4 and 5. Other two double-Hopf bifurcation points exist, denoted $B$ and $C$, which characterize the interaction between modes 2 and 3, and 1 and 2, respectively. Yet, at points $B$ and $C$ the trivial state is already unstable, thus, instabilities associated with these points are not directly observed in experiments or numerical simulations. Instead, these organizing centres play a role in the pattern formation of secondary instabilities, which is left to §§ 4 and 5, where we interpret the subtle implications of these points in dynamics. In addition, authors have looked for the presence of a primary bifurcation that

leads to the $RW_2$ state. For the studied configuration, there does not exist such a region in the range $0 < \Omega < 6$.

### 3.3. *Properties of the axisymmetric steady state*

The analysis presented in this section studies the linear stability of the axisymmetric steady-state solution in the range $Re \leq 250$ and $\Omega \leq 4$. Typical axisymmetric steady-state solutions (TS) at codimension-two points are portrayed in figure 4, which shows the neutrally stable trivial state state at $(Re_A, \Omega_A) = (77, 2.24)$ and the two other unstable trivial states at $(Re_B, \Omega_B) = (188, 1.01)$ and $(Re_C, \Omega_C) = (73, 3.95)$, respectively. The flow visualization illustrates the recirculation region behind the sphere, delimited by the separatrix, which divides the recirculation bubble and the unperturbed flow field. Such a line, depicted with a thick solid line in figure 4 connects the separation point on the sphere surface and the stagnation point on the $r = 0$ axis. The development of the recirculation bubble can be measured using the maximum extent of the region

$$L_r = \max \left\{ z - \frac{D}{2} \mid W(r = 0, z) \leq 0 \right\}, \tag{3.3}$$

where $D$ is the diameter of the sphere. Figure 5($a$) displays the evolution of the length of the recirculation bubble by varying $\Omega$ and $Re$. The length of the bubble increases monotonically with the angular velocity $\Omega$ of the sphere as well as the largest negative values of the streamwise velocity behind the sphere, from around 40 % for $\Omega = 0$ to around 60 % for the largest values of $\Omega$ explored. A similar trend was identified by Kim & Choi (2002) at $Re$=100; however, we should consider that the trends observed in figure 5($a$) are only valid before bifurcation. After that, $L_r$ does not have to increase with $\Omega$, as seen by Lorite-Díez & Jiménez-González (2020) and Kim & Choi (2002). The results at the onset of stability of the steady state are synthesized in figure 5($b$), with a domain of existence of a stable steady state (white shaded) and another of an unstable steady state (grey shaded). In § 3.4 we identify the core of the $RW_1$ and $RW_3$ instabilities, which are found within the recirculation region. In particular, a passive control that shortens the recirculation region is an efficient technique to stabilize the flow. Therefore, it is not surprising that the neutrally stable flow is characterized by a shorter recirculation region with respect to the unstable steady state.

Finally, we briefly discuss the influence of non-normality mechanisms, lift-up and convective non-normality as they are partly related to recirculation region length. The main results are included in table 1, where we can see a lower influence of non-normality effects through the obtained values for $\gamma$ and $\theta_N$, with respect to the static sphere configuration. The estimator $\theta_N$ measures the importance of non-normality, the lower $\theta_N$ the more important non-normal effects are. On the other hand, the estimator $\gamma$ characterizes the relative contribution between the lift-up and the convective non-normality mechanisms to the total non-normality effects. A $\gamma$ value close to 0 indicates the dominance of the lift-up effect. The largest non-normal effects have been measured at point $B$ (lowest values of $\theta_N$), which corresponds to the point with the largest critical Reynolds number among the codimension-two points. The values of $\theta_N$ obtained at point $B$ are associated with a larger non-normality than the stationary mode (the case of $RW_1$ with $O(2)$ symmetry) and $RW_2$ at the threshold for ($\Omega = 0$, $Re = 281$), which was found by Meliga, Chomaz & Sipp (2009*b*) to be 1°. Thus, one may conclude that the rotation of the sphere increases the effect of non-normality, however, it induces an earlier transition with regard to the Reynolds number, which turns out to globally reduce the effect of non-normality. This previous

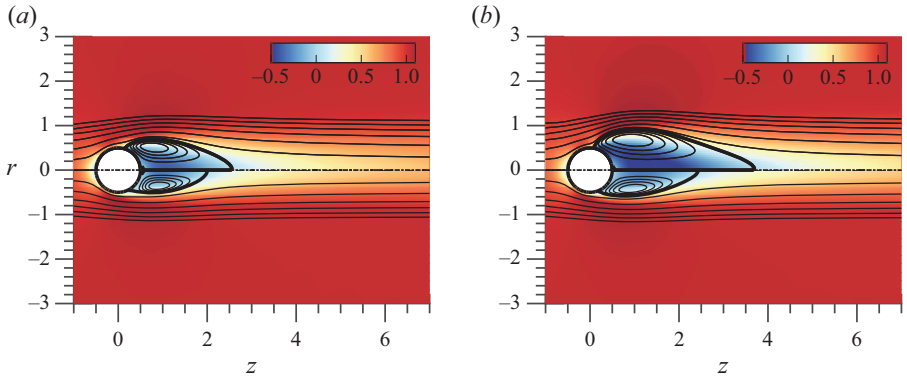


Figure 4. Spatial distribution of the streamwise velocity (contours) at the steady state along with flow streamlines (solid lines) and recirculation region separatrix (thick solid lines). Results are shown for (*a*) ($Re = 212$, $\Omega = 0$) in the upper half and ($Re_A$, $\Omega_A$) in the lower half; (*b*) ($Re_B$, $\Omega_B$) in the upper half and ($Re_C$, $\Omega_C$) in the bottom half. Points $A$, $B$ and $C$ are defined in table 1.

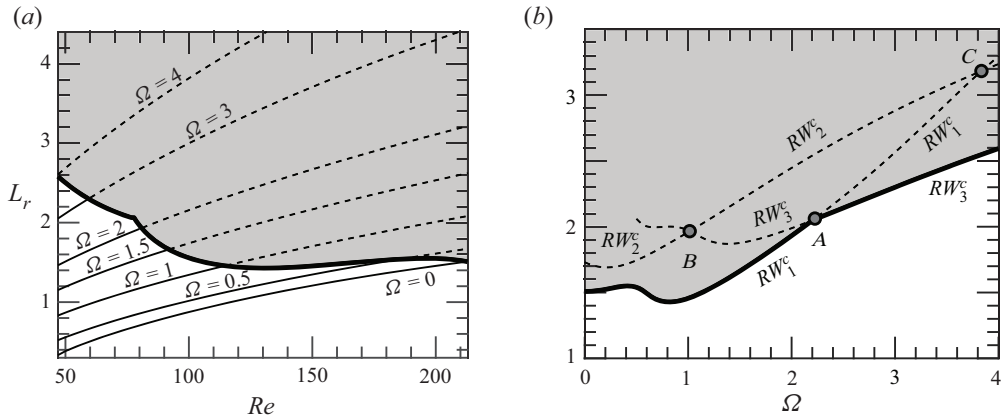


Figure 5. Evolution of the recirculating length $L_r$ in the plane ($Re$, $\Omega$). The unstable region is the grey-shaded area, delimited by a thick line. (*a*) The recirculating length of the stable solution is painted with solid lines, dashed lines are employed for the unstable steady state. (*b*) Length of the recirculating region at the onset of stability ($Re_c(\Omega)$).

statement can be also indirectly verified from the satisfactory comparison between normal form estimations and DNS results in § 5.1. Furthermore, the analysis of the direct global mode shows a dominant effect of the convective non-normality, which is responsible at most of around 90 % (mode $RW_1$) and 98 % (mode $RW_3$) at point $A$ and around 80 % for the remainder modes at points $B$ and $C$. In comparison, the stationary and oscillating modes of static configuration ($\Omega = 0$) displayed $\gamma = 0.76$ and $\gamma = 0.94$. More details about the non-normality study such as the definition of $\theta_N$ and $\gamma$ can be found in Appendix B.

### 3.4. *Identification of the physical mechanisms from a control perspective*

In this section we analyse the physical mechanisms leading to the $RW_1$ and $RW_3$ states at the point $A$. However, we do not discuss the $RW_2$ state as it will be seen in § 5, this state is not expected to be observed. First, we consider what is the effect of a steady axisymmetric forcing term, which represents the presence of a small obstacle, wall suction/blowing (as

the control applied in Niazmand & Renksizbulut 2005), etc. In this case the governing equations of the resulting flow are the same as (2.3) with the addition of a forcing term $\boldsymbol{H}_0 \equiv \hat{\boldsymbol{H}}_0$,

$$\boldsymbol{B}\frac{\partial \boldsymbol{Q}}{\partial t} = \boldsymbol{F}(\boldsymbol{Q}, \boldsymbol{\eta}) \equiv \boldsymbol{L}\boldsymbol{Q} + \boldsymbol{N}(\boldsymbol{Q}, \boldsymbol{Q}) + \boldsymbol{G}(\boldsymbol{Q}, \boldsymbol{\eta}) + \hat{\boldsymbol{H}}_0. \tag{3.4}$$

This case has been treated in the past by Marquet, Sipp & Jacquin (2008) in the case of the flow past a circular cylinder and by Sipp (2012) in the case of the open cavity flow. The introduction of the forcing induces a modification of the eigenvalue $\mathrm{i}\omega_\ell \mapsto \mathrm{i}\omega_\ell + \Delta\mathrm{i}\omega_\ell^0$, where $\Delta\mathrm{i}\omega_\ell^0 = \langle \boldsymbol{\nabla}_{\boldsymbol{H}_0}\mathrm{i}\omega_\ell, \hat{\boldsymbol{H}}\rangle$. Therefore, the control that induces the largest deviation of the growth rate (respectively frequency) of the mode $\ell$ is in the direction of $\boldsymbol{\nabla}_{\boldsymbol{H}_0}\mathrm{i}\omega_\ell$, which is defined as

$$\boldsymbol{\nabla}_{\boldsymbol{H}_0}\mathrm{i}\omega_\ell = \boldsymbol{B}^{\mathrm{T}}\boldsymbol{J}_{(0,0)}\boldsymbol{B}\boldsymbol{\nabla}_{\boldsymbol{U}_b}\mathrm{i}\omega_\ell \quad \text{for } \ell = 1, 2, 3. \tag{3.5}$$

Here $\boldsymbol{\nabla}_{\boldsymbol{U}_b}\mathrm{i}\omega_\ell$ is the sensitivity of the eigenvalue of the mode $\ell$ ($\ell = 1, 2, 3$) with respect to variations in the axisymmetric steady state, cf. (Marquet *et al.* 2008). The sensitivity of the $\ell^{th}$ eigenvalue $\boldsymbol{\nabla}_{\boldsymbol{H}_0}\lambda_\ell$ to the introduction of a steady axisymmetric forcing is represented in figure 6 for the two modes present in the codimension point $A$. The low-frequency mode ($RW_1$) is most sensitive to a steady axisymmetric forcing at the leftmost end of the recirculation region (see figure 6*a*,*b*). This forcing corresponds to one that accelerates the streamwise motion at the end of the recirculation region, thus reducing the counterclockwise motion of the recirculation zone, which would induce an effective decrease of the growth rate (respectively frequency). This is in accordance with the fact that the recirculation motion will be weaker, and the convective motion will be slower (note this is also the case for the sensitivity of the frequency $RW_3$ to steady forcing figure 6*d*). On the other hand, the high-frequency mode is most sensitive in a near wake region behind the sphere, close to the recirculation bubble (see figure 6*c*,*d*). In this case, a forcing that decelerates the clockwise motion within the recirculation region would cause the largest stabilization effect.

Second, let us consider the receptivity of the flow to the presence of localized feedbacks, as in Giannetti & Luchini (2007). The harmonic forcing $\boldsymbol{H} \equiv \boldsymbol{H}_{(z_\ell)}\exp(\mathrm{i}(\omega_\ell t + m_\ell\theta))$ is defined as

$$\boldsymbol{H}_{(z_\ell)} = \delta(\boldsymbol{x} - \boldsymbol{x}_0)\boldsymbol{C}_{(z_\ell)} \cdot \hat{\boldsymbol{u}}_{(z_\ell)}, \quad \ell = 1, 2, 3, \tag{3.6}$$

where $\boldsymbol{C}_{(z_\ell)}$ is a generic feedback matrix and $\delta(\boldsymbol{x} - \boldsymbol{x}_0)$ is the Dirac distribution centred at the point $\boldsymbol{x}_0 = (z_0, r_0, \theta_0)$. Thus, the variation of the eigenvalue due to the introduction of the localized feedback is

$$\Delta^u\mathrm{i}\omega_\ell = \langle \hat{\boldsymbol{q}}^\dagger_{(z_\ell)}, \delta\boldsymbol{H}_{(z_\ell)}\rangle = \boldsymbol{C}_{(z_\ell)} : \boldsymbol{S}_s^{(\ell)}(\boldsymbol{x}_0), \quad \ell \in \mathrm{I} \tag{3.7}$$

The rank two tensor of (3.7) is commonly designated as the structural sensitivity tensor, here denoted as $\boldsymbol{S}_s^{(\ell)}$,

$$\boldsymbol{S}_s^{(\ell)} \equiv \hat{\boldsymbol{u}}^\dagger_{(z_\ell)} \otimes \bar{\hat{\boldsymbol{u}}}_{(z_\ell)}, \quad \ell = 1, 2, 3. \tag{3.8}$$

The spectral norm of the structural sensitivity tensor for low- and high-frequency modes is depicted in figure 7. Similar to the receptivity to axisymmetric steady forcing, the recirculation bubble ($RW_3$) and the leftmost end of the recirculation region ($RW_1$) are the most sensitive regions of the flow.

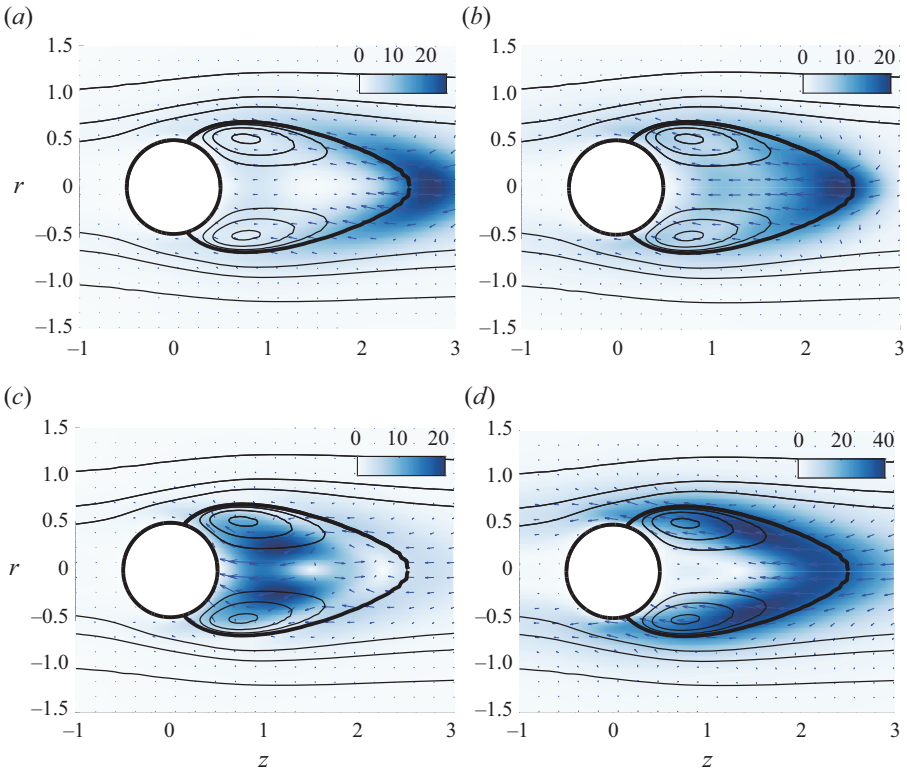


Figure 6. Steady forcing at codimension point $A$. Sensitivity of amplification rate to the steady axisymmetric forcing $\nabla_{H_0}\lambda_\ell$ for ($a$) the low-frequency mode, also known as $RW_1$, and ($c$) the high-frequency mode, also known as $RW_3$. Sensitivity of the frequency to the steady axisymmetric forcing $\nabla_{H_0}\lambda_\ell$ for ($b$) the low-frequency mode, $RW_1$, and ($d$) the high-frequency mode, $RW_3$. The magnitude of the growth rate and frequency sensitivities is pictured by colours and their orientation by arrows.

## 4. Normal form reduction

In this study bifurcations involving a steady-state mode uniquely exist for the static configuration ($\Omega = 0$). For such a reason, we will focus our attention on the codimension-two double-Hopf (Chossat, Golubitsky & Lee Keyfitz 1986) and the codimension-three triple-Hopf bifurcations, and we will characterize solutions based on the patterns allowed by these bifurcations. In our problem, the competition between two or more of the several rotating waves occurs in the neighbourhood of the primary bifurcation. For such a reason, the three double-Hopf points (depicted in figure 3$a$) are of special interest.

These points act as organizing centres of dynamics, and they provide some partial answers about the transition scenario. For instance, around the point $A$ there are regions of bi-stability where either $RW_1$ and $RW_3$ coexist. Nevertheless, these codimension-two points do not account for a third interaction. In each of the double-Hopf interactions, the competition with one of the leading modes is omitted. The full instability scenario is accounted by considering the unfolding of the triple-Hopf bifurcation. Yet, such an instability does not show up generally with only two parameters. And the search for a third parameter where such a bifurcation generically occurs is not a trivial task. Not to mention that even in the case one finds such a parameter, the flow configuration may be

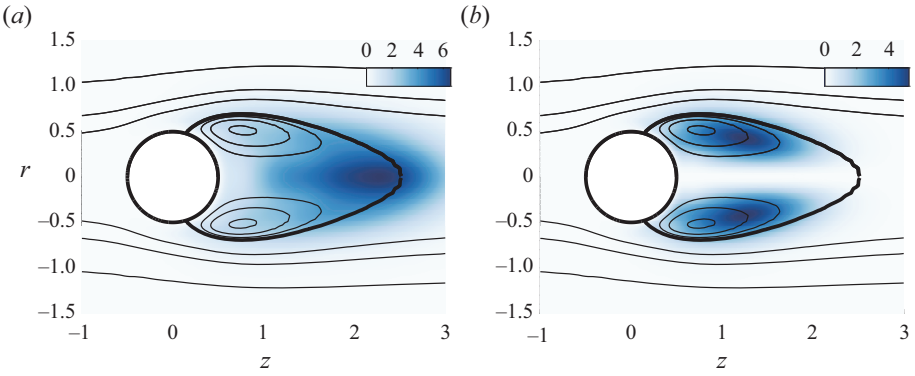


Figure 7. Spectral norm of the structural sensitivity tensor. (*a*) Low-frequency mode, (*b*) high-frequency mode.

considerably distinct from the one initially conceived. Therefore, in the current research, we adopt a similar strategy as the one conducted by Meliga *et al.* (2009*a*) on the wake flow past a disk. However, rather than performing a variation of the centre-unstable manifold reduction, which is an invariant procedure but without the attractiveness property of the centre manifold (Podvigina 2006*a*,*b*), we prefer to adopt a higher-order (up to fifth order) multiple scales expansion at each codimension-two point, and then we extend the coefficients to other locations in the parameter space. The chosen approach differentiates from other previous techniques because it allows an exact identification of the polynomial coefficients of the normal form at codimension-two points, where one can employ the Fredholm alternative to determine the normal form coefficients and remove the secular terms of the expansion. Other centre-unstable techniques determine the coefficients of the normal form at non-resonant conditions, which invalidates the use of the Fredholm alternative if one is far from the onset of instability. On the other hand, our technique does not provide an *a priori* knowledge of the error committed in the extension procedure from a codimension-two point to another point in the parameter space. Thus, as with other perturbative techniques, one needs to perform a cross-comparison with DNS in the region of interest of the parameter space, which is performed in § 5.1.

In the following, we briefly outline the main constituents in the study of pattern formation, a comprehensive explanation is left to Appendix A. Pattern formation is studied herein in the framework of bifurcation theory. Near the onset of the bifurcation, dynamics can be reduced to the centre manifold, whose algebraic expression is simplified via a series of topologically equivalent transformations into the normal form. The reduction to the normal form is carried out via a multiple scales expansion of the solution $\boldsymbol{Q}$ of (2.3). The expansion considers a two-scale development of the original time $t \mapsto t + \varepsilon^2\tau$, here $\varepsilon$ is the order of magnitude of the flow disturbances, assumed small $\varepsilon \ll 1$. In this study we carry out a normal form reduction via a weakly nonlinear expansion, where the small parameters are

$$\varepsilon_\Omega^2 = (\Omega_c - \Omega) \sim \varepsilon^2 \quad \text{and} \quad \varepsilon_\nu^2 = (\nu_c - \nu) = \left(Re_c^{-1} - Re^{-1}\right) \sim \varepsilon^2. \tag{4.1a,b}$$

The technique decomposes time into a fast time scale $t$ of the phase associated to the self-sustained instabilities and a slow time scale related to the evolution of the amplitudes $z_i(\tau)$, introduced in (4.3), for $i = 1, 2, 3$. The ansatz of the expansion is

$$\boldsymbol{Q}(t,\tau) = \boldsymbol{Q}_b + \varepsilon \boldsymbol{q}_{(\varepsilon)}(t,\tau) + \varepsilon^2 \boldsymbol{q}_{(\varepsilon^2)}(t,\tau) + \varepsilon^3 \boldsymbol{q}_{(\varepsilon^3)}(t,\tau) + \varepsilon^4 \boldsymbol{q}_{(\varepsilon^4)}(t,\tau) + O(\varepsilon^5). \tag{4.2}$$

In the following, we shall consider the normal form equation resulting from the interaction of three rotating wave modes identified by LSA, that is,

$$\begin{aligned}\boldsymbol{q}_{(\varepsilon)}(t,\tau) = &\left(z_1(\tau)\hat{\boldsymbol{q}}_{(z_1)}(r,z)\exp(\mathrm{i}(m_1\theta+\omega_1 t))+\mathrm{c.c.}\right)\\ &+\left(z_2(\tau)\hat{\boldsymbol{q}}_{(z_2)}(r,z)\exp(\mathrm{i}(m_2\theta+\omega_2 t))+\mathrm{c.c.}\right)\\ &+\left(z_3(\tau)\hat{\boldsymbol{q}}_{(z_3)}(r,z)\exp(\mathrm{i}(m_3\theta+\omega_3 t))+\mathrm{c.c.}\right).\end{aligned} \tag{4.3}$$

Note that the expansion of the left-hand side of (2.3) up to fifth order is

$$\varepsilon\boldsymbol{B}\frac{\partial\boldsymbol{q}_{(\varepsilon)}}{\partial t}+\varepsilon^2\boldsymbol{B}\frac{\partial\boldsymbol{q}_{(\varepsilon^2)}}{\partial t}+\varepsilon^3\left[\boldsymbol{B}\frac{\partial\boldsymbol{q}_{(\varepsilon^3)}}{\partial t}+\boldsymbol{B}\frac{\partial\boldsymbol{q}_{(\varepsilon)}}{\partial\tau}\right]+\varepsilon^4\boldsymbol{B}\frac{\partial\boldsymbol{q}_{(\varepsilon^4)}}{\partial t}+\varepsilon^5\left[\boldsymbol{B}\frac{\partial\boldsymbol{q}_{(\varepsilon^3)}}{\partial\tau}\right]+O(\varepsilon^5), \tag{4.4}$$

and the right-hand side respectively is

$$\boldsymbol{F}(\boldsymbol{q},\boldsymbol{\eta})=\boldsymbol{F}_{(0)}+\varepsilon\boldsymbol{F}_{(\varepsilon)}+\varepsilon^2\boldsymbol{F}_{(\varepsilon^2)}+\varepsilon^3\boldsymbol{F}_{(\varepsilon^3)}+\varepsilon^4\boldsymbol{F}_{(\varepsilon^4)}+\varepsilon^5\boldsymbol{F}_{(\varepsilon^5)}+O(\varepsilon^6). \tag{4.5}$$

Then, the problem truncated at order three is reduced to a low-dimensional system governing the complex amplitudes $z_j(t)$,

$$\left.\begin{aligned}\dot{z_1} &= z_1\left[\lambda_1+\nu_{11}|z_1|^2+\nu_{12}|z_2|^2+\nu_{13}|z_3|^2\right],\\ \dot{z_2} &= z_2\left[\lambda_2+\nu_{21}|z_1|^2+\nu_{22}|z_2|^2+\nu_{23}|z_3|^2\right],\\ \dot{z_3} &= z_3\left[\lambda_3+\nu_{31}|z_1|^2+\nu_{32}|z_2|^2+\nu_{33}|z_3|^2\right],\end{aligned}\right\} \tag{4.6}$$

where $\nu_{k\ell},\lambda_k\in\mathbb{C}$ for $k,\ell=1,2,3$. The real part of the linear terms, named $\lambda_k$, correspond to the growth rate of the $k^{th}$ mode. Respectively, the imaginary part of $\lambda_k$ is associated to the frequency variation of the $k^{th}$ mode with respect to the frequency of the neutral mode, i.e. with respect to the frequency $\omega_k$ determined from LSA. The terms $\nu_{k\ell}$ are the third-order self ($k=\ell$) and cross-interaction ($k\neq\ell$) coefficients. The coefficients of the normal form are estimated as

$$\left.\begin{aligned}\lambda_\ell &= \varepsilon_\nu^2\lambda_\ell^{(\varepsilon_\nu^2)}+\varepsilon_\Omega^2\lambda_\ell^{(\varepsilon_\Omega^2)}+\varepsilon_\nu^4\lambda_\ell^{(\varepsilon_\nu^4)}+\varepsilon_\Omega^4\lambda_\ell^{(\varepsilon_\Omega^4)}+\varepsilon_\Omega^2\varepsilon_\nu^2\lambda_\ell^{(\varepsilon_\nu^2\varepsilon_\Omega^2)},\\ \nu_{k\ell} &= \nu_{k\ell}^{(0)}+\varepsilon_\nu^2\nu_{k\ell}^{(\varepsilon_\nu^2)}+\varepsilon_\Omega^2\nu_{k\ell}^{(\varepsilon_\Omega^2)},\end{aligned}\right\} \tag{4.7}$$

where $\nu_{k\ell}^{(0)}$, $\nu_{k\ell}^{(\varepsilon_\nu^2)}$, $\nu_{k\ell}^{(\varepsilon_\Omega^2)}$, and the corresponding linear coefficients, are evaluated at the intersection point between the Hopf curves associated to mode $k$ and $\ell$. For instance, the coefficient $\nu_{13}^{(0)}$ is evaluated at point $A$. The distinct coefficients of (4.7) used for the evaluation of the coefficients of the normal form are listed in tables 4 and 5 (Appendix A).

### 4.1. *Classification of solutions*

In the following, the right-hand side of (4.6) is designated $\boldsymbol{f}(\boldsymbol{z})$ where $\boldsymbol{z}=(z_1,z_2,z_3)$. The reduced vector $\boldsymbol{f}$ is equivariant under the action of the group $\Gamma\equiv SO(2)\times\mathbb{T}^3$, with the

| Name | Representative | Isotropy group (complex) | Frequencies |
|---|---|---|---|
| TS (Trivial state) | $(0, 0, 0)$ | $SO(2) \times \mathbb{T}^3$ | 0 |
| RW (Rotating wave) | $(r_a, 0, 0)$ | $S(1, r, 0, 0) \times \mathbb{T}^2$ | 1 |
| MM (Mixed mode) | $(r_a, r_b, 0)$ | $S(1, r, l, 0) \times S^1$ | 2 |
| IMM (Interacting mixed mode) | $(r_a, r_b, r_c)$ | $\mathbb{1}$ | 3 |

Table 2. Nomenclature and symmetry group of fixed-point solutions of the system (4.9).

following action representation:

$$\left.\begin{aligned} \theta \cdot \boldsymbol{z} &\equiv (z_1 \mathrm{e}^{\mathrm{i}l\theta}, z_2 \mathrm{e}^{\mathrm{i}r\theta}, z_3 \mathrm{e}^{\mathrm{i}s\theta}), \\ (\psi_1, \psi_2, \psi_3) \cdot \boldsymbol{z} &\equiv (z_1 \mathrm{e}^{\mathrm{i}\psi_1}, z_2 \mathrm{e}^{\mathrm{i}\psi_2}, z_3 \mathrm{e}^{\mathrm{i}\psi_3}). \end{aligned}\right\} \tag{4.8}$$

Here $l, r, s \in \mathbb{Z}$, $\theta \in [0, 2\pi)$ and $\psi_i \in [0, 2\pi)$ for $i = 1, 2, 3$; $(\psi_1, \psi_2, \psi_3)$ and $\theta$ are the representations in $\mathbb{C}^3$ of the actions of the group $\Gamma$, which correspond to the time shift and rotational invariance, respectively. The substitution of the polar decomposition of $\boldsymbol{z} = \boldsymbol{r}\mathrm{e}^{\mathrm{i}\boldsymbol{\Phi}}$, with $\boldsymbol{r} = (r_1, r_2, r_3)$ and $\boldsymbol{\Phi} = (\phi_1, \phi_2, \phi_3)$, into (4.6) yields the following decoupled phase-amplitude system:

$$\left.\begin{aligned} \dot{r}_\ell &= r_\ell \left[ \Lambda_\ell^R + \mathcal{V}_{\ell k}^R r_k^2 \right], \quad k, \ell = 1, 2, 3, \\ \dot{\phi}_\ell &= \Lambda_\ell^I + \mathcal{V}_{\ell k}^I r_k^2, \quad k, \ell = 1, 2, 3. \end{aligned}\right\} \tag{4.9}$$

Here $\Lambda = \Lambda^R + \Lambda^I \equiv (\lambda_1, \lambda_2, \lambda_3)^{\mathrm{T}}$ and the matrix $\mathcal{V} = \mathcal{V}^R + \mathrm{i}\mathcal{V}^I$ is

$$\mathcal{V} \equiv \begin{pmatrix} \nu_{11} & \nu_{12} & \nu_{13} \\ \nu_{21} & \nu_{22} & \nu_{23} \\ \nu_{31} & \nu_{32} & \nu_{33} \end{pmatrix}. \tag{4.10}$$

To ease the presentation of the fixed-point solutions of (4.9), let us introduce the inverse of the linear operator $\mathcal{V}$, which can be written as

$$\mathcal{V}^{-1} = \frac{1}{\det \mathcal{V}} \begin{pmatrix} \det \mathcal{V}_{11} & \det \mathcal{V}_{21} & \det \mathcal{V}_{31} \\ \det \mathcal{V}_{12} & \det \mathcal{V}_{22} & \det \mathcal{V}_{32} \\ \det \mathcal{V}_{13} & \det \mathcal{V}_{23} & \det \mathcal{V}_{33} \end{pmatrix}, \tag{4.11}$$

where $\det \mathcal{V}_{k\ell}$ denotes the minor of the matrix $\mathcal{V}$, obtained by eliminating the line $k$ and the column $\ell$.

In the following, the notation $\dot{\boldsymbol{r}} = \boldsymbol{f}^R(\boldsymbol{r})$ will be adopted to denote the amplitude equation of the nonlinear system (4.9). The remainder of this subsection will be devoted to the study of the three fixed-point solutions of (4.9).

The classification of the solutions of the generic triple-Hopf bifurcation interaction with $SO(2)$ symmetry is based on maximal isotropy subgroups of the group $\Gamma$. This technique predicts the existence up to tertiary bifurcations of fixed points of the complex normal form (4.6). These isotropy subgroups correspond to the symmetries of the solutions within the fixed-point subspace of each isotropy group (cf. table 2).

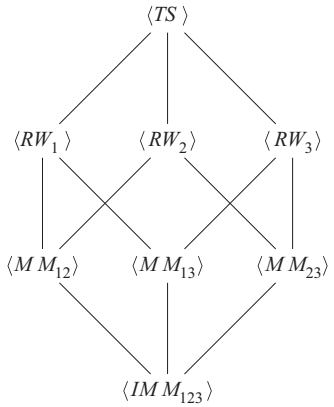


Figure 8. Isotropy lattice of the triple-Hopf bifurcation.

In our discussion, we identify the subgroups of $SO(2) \times \mathbb{T}^3$. Each element in the group has the form

$$(\theta, \psi_1, \psi_2, \psi_3) \in SO(2) \times \mathbb{T}^3. \tag{4.12}$$

Using this notation, the subgroup $S(k, l, r, s)$ of $SO(2) \times \mathbb{T}^3$ is defined as

$$S(k, l, r, s) = \{(k\theta, l\theta, r\theta, s\theta) | \theta \in S^1\}. \tag{4.13}$$

The conjugacy classes of isotropy subgroups of $SO(2) \times \mathbb{T}^3$ are documented with the representative of the fixed-point subspace in polar coordinates and the number of incommensurate frequencies in table 2. Additionally, a graphical representation of the isotropy lattice is displayed in figure 8 in terms of the class representative of the fixed-point subspace.

Rotating waves correspond to the simplest non-trivial fixed point of (4.9), which in the original set of equations is a periodic solution. They arise as the result of a supercritical Hopf bifurcation of the steady state (named trivial state in table 2) and they may eventually bifurcate into mixed modes; the eigenvalues of rotating waves may be found in the first row of table 3. Mixed modes, defined in table 3, are the result of the interaction between two rotating waves. A mixed mode has a representative in the normal form with two non-zero amplitude terms, thus, they correspond to a $T^2$-quasiperiodic state in the original system of equations. These states may experience two kinds of bifurcations. They may lose stability in the transversal direction or within their own subspace, these two conditions are listed in table 3. Eventually, a bifurcation in the transversal direction of a mixed mode may be associated with the appearance of an interacting mixed mode ($IMM_{123}$) attractor. An interacting mixed mode corresponds to a $T^3$-quasiperiodic state in the original system of equations, and it is represented by three non-zero amplitude terms. However, $T^3$-quasiperiodic states are hardly observed in numerical simulations of dissipative systems, as it is the case of Navier–Stokes equations (2.1), instead a chaotic attractor is usually detected. A more exhaustive analysis of the unfolding of the triple-Hopf bifurcation is left to Appendix C.

### 4.2. *Illustration of the procedure*

Let us detail the procedure followed to compute the bifurcation scenario, a procedure that is also followed in § 5 for the determination of the parametric portrait. For the sake of

| Name of solutions | Definition | Eigenvalues |
|---|---|---|
| $RW_i$ (for $i = 1, 2, 3$) | $r_i^{(RW)} = \sqrt{-\dfrac{\lambda_i^R}{\nu_{ii}^R}}$ | $-\lambda_i^R,\ \lambda_j^R - \nu_{ji}^R \dfrac{\lambda_i^R}{\nu_{ii}^R},$ for $j \neq i$ |
| $MM_{ij}$, $(i, j = 1, 2, 3)$ | $r_i^{(MM_{ij})} = \sqrt{\dfrac{\lambda_j^R \nu_{ij}^R - \lambda_i^R \nu_{jj}^R}{\det(\mathcal{V}_{kk})}}$ | $\dfrac{\nu_{ii}^R r_i^2 + \nu_{jj}^R r_j^2}{2} \pm \sqrt{(\nu_{ii}^R r_i^2 - \nu_{jj}^R r_j^2)^2/4 + \nu_{ij}^R \nu_{ji}^R r_i^2 r_j^2}$ |
| $(j \neq i, k \neq i, k \neq j)$ | $r_j^{(MM_{ij})} = \sqrt{\dfrac{\lambda_i^R \nu_{ji}^R - \lambda_j^R \nu_{ii}^R}{\det(\mathcal{V}_{kk})}}$ | $\dfrac{1}{\det(\mathcal{V}_{kk}^R)}[\lambda_k^R \det(\mathcal{V}_{kk}^R) + \lambda_i^R \det(\mathcal{V}_{ik}^R) + \lambda_j^R \det(\mathcal{V}_{jk}^R)]$ |
| $IMM_{123}$ | $(r_1^2, r_2^2, r_3^2)^{\mathrm{T}} = -(\mathcal{V}^R)^{-1} \Lambda^R$ | Eigs of $D\boldsymbol{f}^R$ |

Table 3. Defining equations and eigenvalues of the solutions of the polar third-order normal form (4.9).

simplicity, we first discuss the bifurcation diagram for a constant rotation rate $\Omega = 1.75$ in terms of the amplitudes $(r_1, r_2, r_3)$. We would like to remind the reader that the amplitudes $(r_1, r_2, r_3)$ are representative of the kinetic energy of the velocity fluctuations, based on the normalization choice of § 3.1. First, we need to determine the coefficients of the normal form, listed in tables 4 and 5, following the procedure of Appendix A. Then, one may evaluate the linear and cubic coefficients of the normal form at $\Omega = 1.75$ for a variable Reynolds number from the evaluation of (4.7). Please note that, for the evaluation of cross-diagonal cubic coefficients, the expansion parameter $\varepsilon_\Omega^2 = \Omega_c - \Omega$ depends on the location of the critical rotation rate $\Omega_c$, that is, to evaluate $\nu_{13}$ one evaluates $\varepsilon_{\Omega,A}^2 = \Omega_A - \Omega$ whereas to evaluate $\nu_{23}$ one evaluates $\varepsilon_{\Omega,B}^2 = \Omega_B - \Omega$. The diagonal cubic coefficients may be evaluated directly at the bifurcation point for every rotation rate $\Omega$ as a function of $\varepsilon_\nu^2$ or by considering the cubic coefficient of the nearest codimension-two point. In our procedure, we found good agreement with time-stepping simulations in the range $1 \leq \Omega \leq 3$ if we consider $\nu_{11} = \nu_{11}^A$, $\nu_{22} = \nu_{22}^B$ and $\nu_{33} = \nu_{33}^B$; the consideration of $\nu_{33}^A$ induces a small deviation in the transition from $MM_{23}$ to $IMM_{123}$ of few units of the Reynolds number. The corresponding coefficients for $\Omega = 1.75$ are listed in table 6 (Appendix A). Please note that the procedure illustrated herein corresponds to a method to determine the coefficients of the normal form; nonetheless, these coefficients can be estimated from numerical simulations as in Fabre *et al.* (2008) or following a data-driven approach, cf. Callaham, Brunton & Loiseau (2022), Loiseau & Brunton (2018) and Loiseau, Noack & Brunton (2018). Bifurcation events are designated by their corresponding value of the Reynolds number $Re_{state_a}^{state_b}$, where $state_a$ stands for the simplest state that exists before the bifurcation and $state_b$ stands for the resulting state after the bifurcation. In addition, the notation $Re_{state_a}^{\sigma_k,s}$ indicates a bifurcation of the $state_a$ where the eigenvalue $\sigma_k$ $(k = 1, 2, 3)$ has changed sign, $s$ indicates stabilization and $u$ indicates the change from stable to unstable of the referring eigenvalue/eigenmode pair. In the following, there is only a bifurcation of this kind, the one associated to the mixed mode $MM_{12}$ that is stabilized/destabilized because of a change of sign of the eigenvalue in the transversal direction $(r_3)$. Thus, we simplify the notation to $Re_{state_a}^s$ or $Re_{state_a}^u$.

Figure 9 displays the bifurcation diagram, with Reynolds number as the control parameter for $\Omega = 1.75$. There exist three primary bifurcations, i.e. bifurcations from the

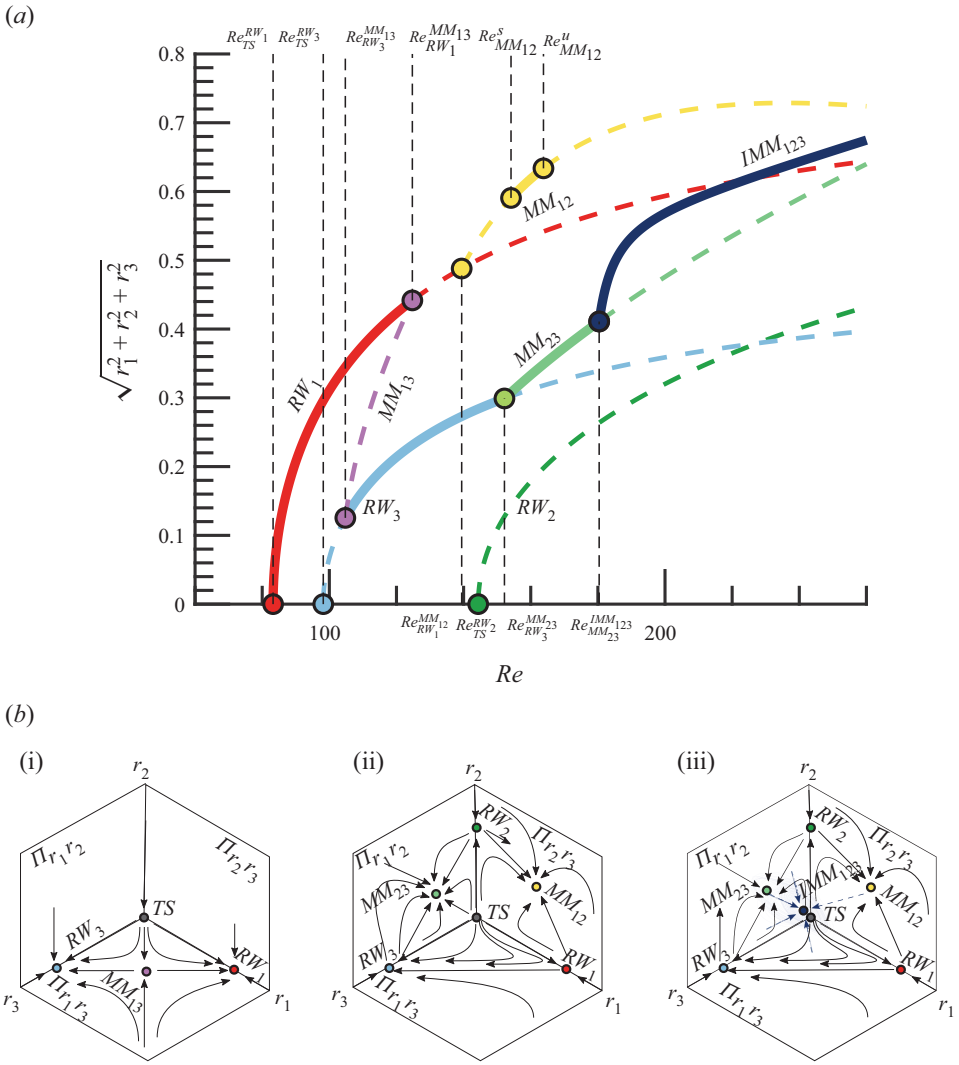


Figure 9. (*a*) Transition scenario at $\Omega = 1.75$. Attractors are depicted with solid lines, whereas unstable invariant states are represented with dashed lines.(*b*) Schematic representation of phase portraits. (i) Two stable rotating waves separated by a mixed-mode solution. (ii) Two stable mixed modes. (iii) An interacting mixed-mode attractor, the chaotic attractor that shadows the $IMM_{123}$ is sketched in a lighter blue colour.

axisymmetric steady state, located at $Re_{TS}^{RW_1}$, $Re_{TS}^{RW_2}$ and $Re_{TS}^{RW_3}$, respectively. However, the $RW_2$ branch remains unstable all along the analysed interval. The first transition to occur is a supercritical Hopf bifurcation leading to the $RW_1$ solution, which is then followed by another supercritical Hopf bifurcation leading to $RW_3$. For the range of Reynolds numbers $Re_{RW_1} < Re < Re_{RW_3}^{MM_{13}}$, there exists a single stable attractor, which corresponds to the limit cycle associated with the solution $RW_1$. At $Re_{RW_3}^{MM_{13}}$ the $RW_3$ branch experiences a Neimark–Sacker bifurcation that results in the appearance of the mixed-mode solution $MM_{13}$. In the interval $Re_{RW_3}^{MM_{13}} < Re < Re_{RW_1}^{MM_{13}}$ both primary solutions ($RW_1$ and $RW_3$) are stable under any arbitrary perturbation and in addition they are connected by the unstable

mixed mode $MM_{13}$, which is located on the separatrix of the basin of attraction of the two primary solutions, the phase portrait of this scenario is sketched in figure 9(*b* i). Eventually, the solution branch $MM_{13}$ terminates at $Re = Re_{RW_1}^{MM_{13}}$, which makes $RW_3$ the single attractor of the system for the interval $Re_{RW_1}^{MM_{13}} < Re < Re_{RW_3}^{MM_{23}}$. The $RW_3$ branch eventually bifurcates into the mixed-mode branch $MM_{23}$, which is a stable attractor within the interval $Re_{RW_3}^{MM_{23}} < Re < Re_{MM_{23}}^{IMM_{123}}$. The other primary branch, the unstable $RW_1$, undergoes another Neimark–Sacker bifurcation at $Re_{RW_1}^{MM_{12}}$ which results in the existence of the $MM_{12}$ branch, yet unstable for perturbations in the transversal direction of the mixed mode (in the $r_3$ direction). The $MM_{12}$ mixed-mode branch appears to be stable only within a small interval $Re_{MM_{12}}^{s} < Re < Re_{MM_{12}}^{u}$, where two bifurcations, which are associated to an instability in the transversal direction $r_3$, occur at the two limit values. We have employed $s$ and $u$ to denote the stable or unstable nature of the $MM_{12}$ regime. Thus, for $Re_{MM_{12}}^{s} < Re < Re_{MM_{12}}^{u}$, there is a second region with multiple stable attractors, which is schematically displayed in figure 9(*b* ii). The last bifurcation accounted by the normal form is the destabilization of the $MM_{23}$ branch at $Re = Re_{MM_{23}}^{IMM_{123}}$ that leads to the appearance of the $IMM_{123}$ branch, whose phase portrait is sketched in figure 9(*b* iii). Please note that despite the fact that $IMM_{123}$ is a fixed-point solution of the normal form, the Newhouse–Takens–Ruelle theorem indicates that the original system of equations may exhibit a chaotic attractors shadowing the $IMM_{123}$ solution.

## 5. Bifurcation scenario

### 5.1. *Comparison with DNS*

In this section we assess the validity of the normal form to characterize the bifurcation scenario, as well as its capability to predict accurately the frequencies and force coefficients of the flow. The estimations of the normal form are compared with DNS results, which are performed at constant rotation rate $\Omega = 1.75$, the scenario analysed in § 4.2. As a first guess, we show the accurate prediction of the fundamental frequencies of each of the invariant states from normal form analysis in figure 10(*a*) in comparison with DNS results (markers), which will be discussed below.

Direct numerical simulations have been carried out to confirm the existence of the bi-stability of full governing equations (2.1) at $Re = 110$. In particular, two families of time-stepping simulations have been performed with two distinct initial conditions, in such a way that, after a transient period, each of them converged towards different time-periodic solutions. On the one hand, we have used a static, axisymmetric base flow initially obtained at $Re = 70$, $\Omega = 0$ which is able to develop the $RW_1$ state (family I, grey markers). On the other hand, we have used the solution obtained by Lorite-Díez & Jiménez-González (2020) at $Re = 250$, $\Omega = 2.2$ as initial seed to find the $RW_3$ state (family II, blue markers), which in turn confirms the existence of multiple stable attractors at $Re = 110$.

To determine the observed regimes, we have computed the frequency components corresponding to $St_{RW_1}$ and $St_{RW_3}$, displayed in figure 10(*b*,*c*), using fast Fourier transform (FFT) spectra of pointwise streamwise and radial velocities in the near wake. The spectra are calculated using the oscillatory part of the velocity-time evolution, i.e. $U' = U - \bar{U}$ for the radial velocity component, where $\bar{\cdot}$ stands for the temporal averaging operator. The three-dimensional topology of the two rotating wave patterns are displayed by means of iso-surfaces of $Q$ quantity in figure 11, where single and double helices topologies are shown.

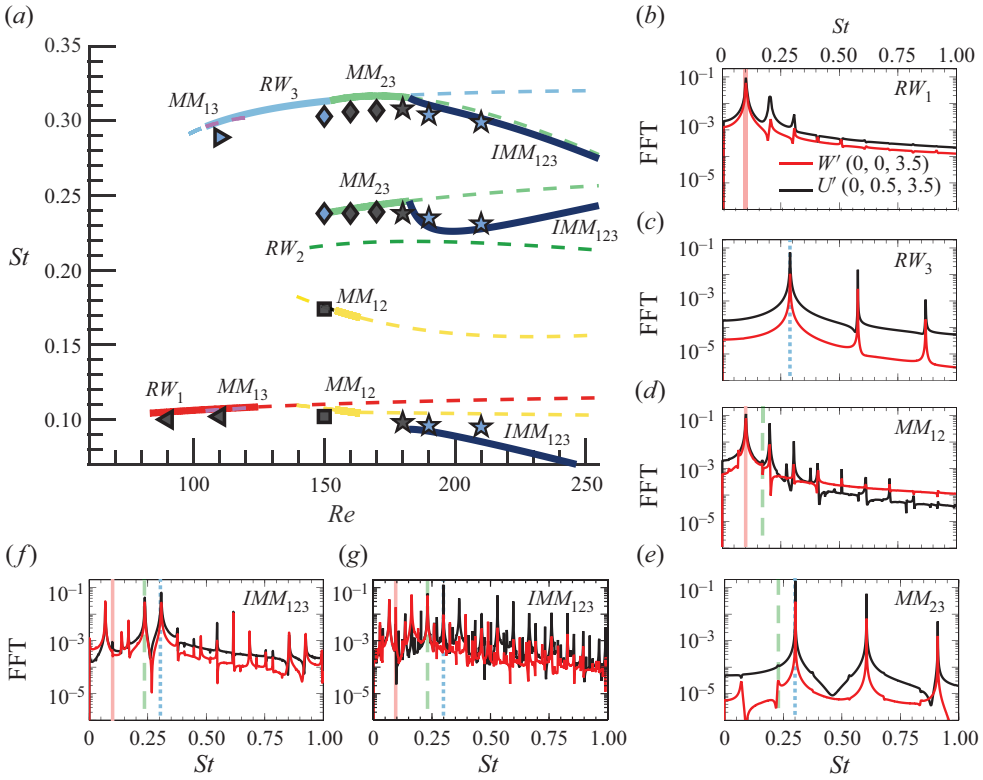


Figure 10. Frequency characterization of the flow at $\Omega = 1.75$. (*a*) Frequency evolution estimated from the normal form (continuous lines), where attractors are represented with continuous lines, whereas unstable invariant solutions are depicted with dashed lines. The markers of figure (*a*) denote the resulting pattern obtained from a time-stepping simulation; axisymmetric steady state ○, $RW_1$ ◁, $RW_3$ ▷, $MM_{12}$ □, $MM_{23}$ ♢, $IMM_{123}$ ⋆, the family of initial conditions is visualized by colours (family I: grey, family II: blue). Figures (*b–g*) display the FFT fluctuating velocity spectra for the different regimes obtained by means of DNS. Two velocity components: $W'$ (red solid line), $U'$ (black solid line) and locations (0, 0, 3.5) and (0, 0.5, 3.5), respectively, are selected to characterize all the frequencies in the wake. Unstable mode frequencies are included: low frequency (light red solid line), medium frequency (light green dashed line) and high frequency (light blue dotted line). Results are shown for (*b*) $Re = 110$, (*c*) $Re = 110$, (*d*) $Re = 150$, (*e*) $Re = 150$, (*f*) $Re = 181$, (*g*) $Re = 210$.

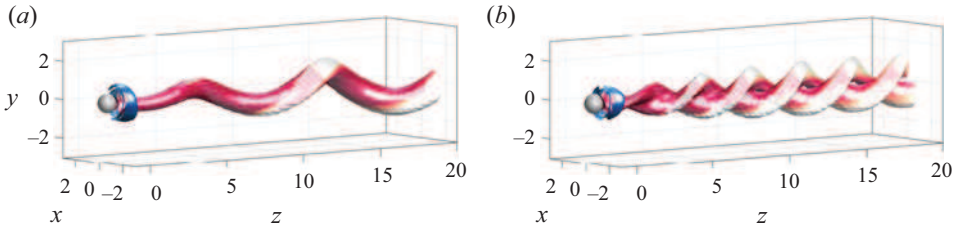


Figure 11. Three-dimensional structures of $RW_1$ (*a*) and $RW_3$ (*b*) at $Re = 110$ and $\Omega = 1.75$. We have used isosurfaces of Q-criterion, $Q = 0.001$, coloured by streamwise vorticity, $\varpi_z \in [-1, 1]$ (blue to red) to depict the flow structure.

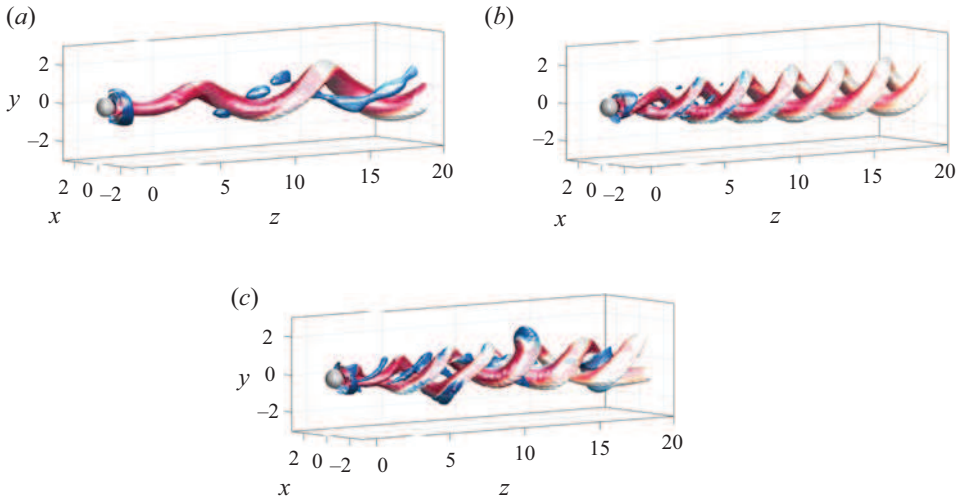


Figure 12. Three-dimensional structure of $MM_{12}$ (*a*), $MM_{23}$ (*b*) and $IMM_{123}$ (*c*) at $Re = 150$ (*a*,*b*) and $Re = 210$ (*c*) and $\Omega = 1.75$. We have used isosurfaces of Q-criterion, $Q = 0.001$, coloured by streamwise vorticity, $\varpi_z \in [-1, 1]$ (blue to red) to depict the flow structure.

Similarly, the existence of two stable mixed-mode attractors ($MM_{12}$ and $MM_{23}$) is confirmed at $Re = 150$. Two time-stepping simulations of the full governing equations at $Re = 150$ were performed, using $RW_1$ and $RW_3$ solutions as initial seeds, the resulting frequency spectra of these patterns are displayed in figure 10(*d*,*e*), where the different frequencies associated with $MM_{12}$ and $MM_{23}$ are identified. In particular, we can see that the appearance of the medium-frequency component originates quasiperiodic regimes. The mixed mode $MM_{12}$ has been detected only in a small interval of Reynolds numbers, which is faithfully captured by the normal form; however, the value of $Re^s_{MM_{12}} \approx 154$ slightly differs from the results of the DNS, which show a stable $MM_{12}$ for $Re = 150$. The corresponding patterns are displayed in figure 12(*a*,*b*).

The $T^3$-quasiperiodic state $IMM_{123}$ has been detected with DNS for Reynolds numbers $Re \approx 181$. Such a state seems to be the single stable attractor in the analysed range $181 < Re < 210$. A series of DNS were carried out with two families of initial conditions: the mixed modes $MM_{12}$ and $MM_{23}$, both obtained at lower Reynolds numbers. Eventually, every DNS converged to the $IMM_{123}$ state, which seems to confirm the claim that it is the single stable attractor. Their associated spectra is depicted in figure 10(*f*,*g*) and its complex topology can be seen in figure 12(*c*). The identification of the three main frequencies (low, medium and high) in the spectra, figure 10(*f*), along with the multiple nonlinear interactions between them is possible for Reynolds number values near the bifurcation value $Re^{IMM_{123}}_{MM_{23}} \simeq 181$. However, it rapidly departs from the $T^3$-quasiperiodic state towards a more irregular state ($Re = 210$) with a nearly continuous velocity spectrum, depicted in figure 10(*g*).

Globally, the good agreement between normal form analysis and DNS frequencies shows the predictive capability of the normal form within the range of Reynolds numbers studied (see figure 10*a*).

A further investigation of the dynamics of this attractor has been carried out by means of the $0-1$ test. Such a test was introduced by Gottwald & Melbourne (2004, 2009) to distinguish between regular and chaotic dynamics. More precisely, it corresponds to a dichotomy test where an estimate $K$, associated to an asymptotic growth of the dynamics,

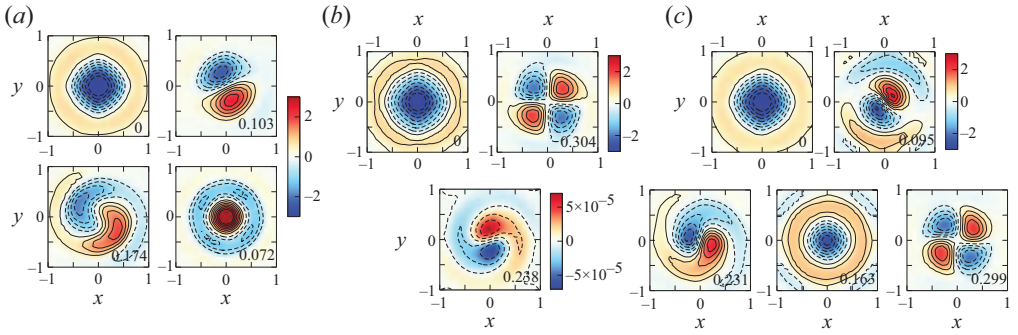


Figure 13. Nonlinear patterns identified through HODMD analysis. The patterns are depicted using streamwise vorticity contours, $\varpi_z$. Results are shown for (*a*) $MM_{12}$, (*b*) $MM_{23}$ and (*c*) $IMM_{123}$ regimes. Tags values inside the contours refer to the corresponding frequency of each mode, $St_i$.

takes discrete values [0, 1] which are associated with non-chaotic (0) and chaotic (1). Further details are given in Appendix F. The results corresponding to the application of the test to the local radial velocity $U'(0, 0.5, 3.5)$, obtained for the two families of computations, indicate a rapid departure towards chaotic dynamics, displayed in the Appendix (figure 16). These results confirm that the transition scenario is eventually ended by the Newhouse–Takens–Ruelle route to chaos.

Furthermore, DNS results can be used to illustrate the spatial pattern associated with each fundamental frequency (low, medium, high). To that aim, a high-order dynamic mode decomposition (HODMD) technique (see Vega & Le Clainche 2020, and references therein) has been applied to instantaneous fields of streamwise vorticity $\varpi_z$ located at $z = 2.5$ to isolate the spatial distributions of the main frequency components. More details about the HODMD technique and its application to present data can be found in Appendix E. In particular, the application of the technique to flow patterns $MM_{12}$, $MM_{23}$ and $IMM_{123}$ allowed the spatial characterization of the fundamental frequencies and their interactions. Apart from these frequencies, the methodology also provides the approximate contribution of each fundamental mode in the nonlinear state. The spatial patterns identified by HODMD are depicted using contours of spanwise vorticity without normalization. Thus, for the $MM_{12}$ state, the HODMD decomposition identifies four energetic modal contributions, corresponding to frequencies $St = 0, 0.103, 0.174$ and $0.072$, which are depicted in figure 13(*a*). The use of instantaneous snapshots of $\varpi_z$ allows identifying mean flow ($St = 0$) given by the constant streamwise rotation. Likewise, the low-frequency component ($St = 0.103$) displays a dipole $m = -1$ topology. Similarly, the medium-frequency component ($St = 0.174$), also features a $m = -1$ structure, although their topology resembles the Yin-Yang mode (Auguste, Fabre & Magnaudet 2010). Finally, an axisymmetric $m = 0$ topology is identified at $St = 0.072$, as the product of the interaction between low-frequency (LF) and medium-frequency (MF) modes, $St_{m_0} \simeq St_{MF} - St_{LF}$. Such a mode is specially energetic close to the longitudinal axis and even dominant in some locations. In Lorite-Díez & Jiménez-González (2020) the authors identified such a mode as a fundamental frequency of the flow, named $f_b$ therein. However, given the results from linear stability and normal form analysis, we have now identified this mode as a subproduct.

The same analysis for the $MM_{23}$ regime allows the identification of three main frequency components, depicted in figure 13(*b*). Apart from the mean flow ($St = 0$), the flow decomposition pinpoints a mode with high frequency (HF) $St_{HF} = 0.304$, that displays

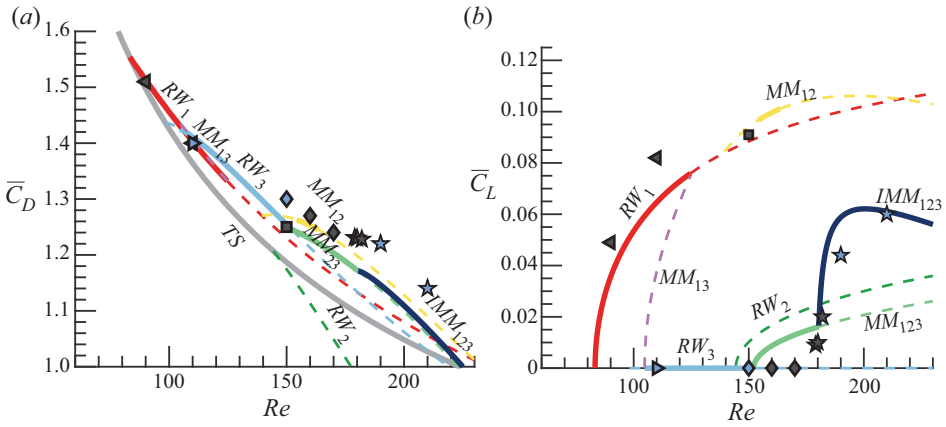


Figure 14. Evolution of the time-averaged forces with respect to Reynolds number for a constant rotation rate $\Omega = 1.75$. The force coefficients determined from the normal form analysis are represented by continuous lines. The force coefficients determined from DNS are depicted with markers. Same legend as in figure 10.

a $m = -2$ structure. In addition, the Yin-Yang mode is also retrieved but now with a frequency, $St_{MF} = 0.238$. Note that, the amplitude associated with this medium-frequency component is very small. The weak energy associated with such a medium-frequency mode in the $MM_{23}$ regime is also observable in the corresponding spectra in figure 10(*e*).

Furthermore, the HODMD analysis of the complex regime $IMM_{123}$, present at $Re = 210$ and $\Omega = 1.75$, is depicted in figure 13(*c*). The decomposition identifies the axisymmetric mean flow, the three fundamental frequencies and many interactions between them, although only five energetic components have been selected for depiction. For instance, the low-frequency and medium-frequency modes display $m = -1$ symmetries and respective frequencies $St_{LF} = 0.095$ and $St_{MF} = 0.231$, which are similar to those corresponding to the $MM_{12}$ and $MM_{23}$ regimes. Similarly, the frequency value of the high-frequency mode ($m = -2$) remains nearly constant with respect to previous regimes, $St_{HF} = 0.299$, indicating that the dependence of frequencies with $Re$ is small (as in figure 3*b*). Among the main subproducts, the axisymmetric pattern ($m = 0$) produced by the interaction of fundamental frequencies $St_{m0} \simeq St_{LF} + St_{HF} - St_{MF} = 0.163$ stands out. It should be noted that there is a small mismatch between the identified peaks in FFT and the frequencies obtained by HODMD that is produced by the different sampling period and the corresponding recording frequency during the simulation.

To complement the previous analysis, we next focus on the effect of the different flow states, shown in figure 11 and figure 12, on the sphere's aerodynamic forces. Thus, we present in figure 14(*a*) the evolution with respect to Reynolds number at $\Omega = 1.75$ of the time-averaged drag coefficient, $\overline{C_D} = \overline{C_z}$, and on figure 14(*b*) the total transverse force coefficient $\overline{C_L} = \overline{\sqrt{C_x^2 + C_y^2}}$ for normal form analysis and DNS.

The comparison between force coefficients obtained by means of normal form and DNS approaches is indeed fairly satisfactory. The method captures the main trends in the forces and, for most of the states, the prediction is reasonably similar, as it was with the different fundamental frequencies. More precisely, for simpler regimes, such as rotating waves, the normal form analysis and DNS provide the same results. At $Re = 150$, for mixed modes, both methods display a small discrepancy (below five percent). This seems to be related to a small nonlinear contribution of the medium-frequency mode identified by the DNS,

as it can be seen in the corresponding FFT spectra (see figure 10*d*,*e*). That said, the general trend of the mean drag $\overline{C_D}$ displays a general reduction with $Re$, which may be partly due to a smaller viscous drag contribution. Besides, the pressure drag component is likely to decrease as well, since $L_r$ is shown to increase with $Re$ (see figure 5*b*) for a given rotation rate, $\Omega$. In particular, as discussed by Roshko (1993) for three-dimensional bluff body wakes, an increase of the recirculating length leads to a decrease in the drag values on account of a pressure recovery associated to changes in the curvature of the separatrix line. Additionally, major changes in the trends are reported between different flow regimes, as expected from strong modifications in the near wake topology and flow separation (Lorite-Díez & Jiménez-González 2020).

Similarly, the agreement is also good for the mean total transverse coefficient, $\overline{C_L}$, although it displays small deviations for states $RW_1$ and $MM_{23}$ (see figure 14*b*). The value of $\overline{C_L}$ is strongly affected by the wake regime and the corresponding azimuthal symmetry. Therefore, the two families of simulations display quite a different evolution. Moreover, it should be noted that the high-frequency mode does not create a net component of transverse force due their symmetric wake topology, as it is seen for $RW_3$ and $MM_{23}$ regimes, where this mode is dominant, causing $\overline{C_L} \simeq 0$. In those cases, the wake structures net eccentricity is small, inducing a negligible transverse force. In view of such results, such regimes should be favoured in case of control if a stabilization of the trajectory is wished, e.g. for freely rising or falling rotating spheres, as the transverse displacement of the body might be limited. Conversely, $RW_1$, $MM_{12}$ and $IMM_{123}$ are likely to cause lateral shift and destabilization of the trajectory for freely moving bodies due to their greater mean lateral force and their corresponding eccentric wake structures.

### 5.2. *Parametric exploration*

Let us discuss the influence of the rotation rate in the dynamics of the flow past the rotating sphere. For that purpose, we determine the stable attractors of the normal form in the range $Re < 300$ and $\Omega < 4$. The cubic normal form coefficients are determined following the same procedure as in § 4.2. However, for low rotation rates ($\Omega < 0.8$), we found that the linear coefficients of the normal form were not correctly estimated. So, for these values of the rotation rate, the linear coefficients are determined exactly at the threshold of instability of each codimension-one bifurcation.

The flow past the static sphere ($\Omega = 0$), analysed by Fabre *et al.* (2008), experiences a symmetry breaking bifurcation that leads to the reflection-symmetric bifid wake (steady-state mode) and eventually a Hopf bifurcation that leads to the RSP. The phase diagram depicted in figure 15 shows that both the rotating wave $RW_1$ and the mixed mode $MM_{12}$ are the continuation in the parameter space of the steady-state and RSP mode, respectively. Thus, dynamics for low values of the rotation rate ($\Omega < 1$) are qualitatively similar to the flow past the static sphere. However, for rotation rate values slightly larger than $\Omega_B$, one starts detecting a wake with a double helix. This fact has been evidenced by the numerical simulations of Lorite-Díez & Jiménez-González (2020), Pier (2013) and the experimental work of Skarysz *et al.* (2018) who reported that at around $\Omega \approx 1.5$ for large Reynolds numbers ($Re > 250$) the quasiperiodic motion of the wake changes from a single to double helix pattern, which is consistent with the phase diagram in figure 15. However, if we look in detail at how the flow transits from a single helix to the double helix wake in terms of the rotation of the sphere, one can observe three bi-stable regions, between $RW_1$ and $RW_3$, between $RW_3$ and $MM_{12}$, and between $MM_{12}$ and $MM_{23}$. These bi-stable sections connect two regions of the parameter space with distinct attractors, the rotating waves $RW_1$ and $RW_3$ and the mixed modes $MM_{12}$ and $MM_{23}$. It is of interest that the formation of

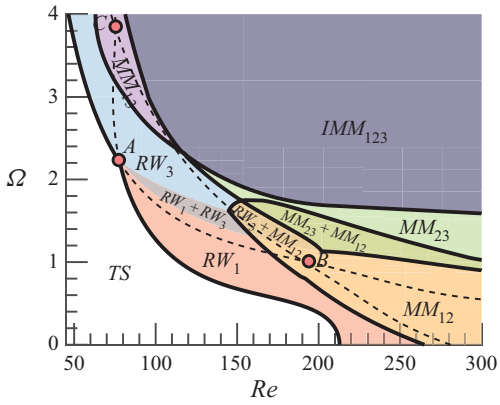


Figure 15. Phase diagram of the nonlinear patterns in the range $\Omega < 4$ and $Re < 300$, as predicted by the normal form (4.9). The axisymmetric state (TS) persists in the white region. Shaded regions indicate the existence of a stable pattern (respectively, stable patterns). Dashed lines illustrate unstable rotating waves neutral curves obtained by LSA.

these new states occurs near the codimension-two point $B$, which exhibits the importance of this bifurcation as an organizing centre, even though it occurs as a bifurcation for an already unstable trivial state. Furthermore, the importance of the codimension point $A$ is clearly evidenced by figure 15, which also acts as an organizing centre of dynamics. Around point $A$, one finds four distinct regions with inequivalent dynamics. If we move counterclockwise from point $A$, we have the left region where the trivial axisymmetric state is stable, the lower region where the $RW_1$ state is the single attractor, a region with two stable attractors ($RW_1$ and $RW_3$) and the upper region where the $RW_3$ is the single stable state. Finally, the significance of the other codimension-two bifurcation, the point $C$, is rather more subtle. This point is located in the only region where one can observe the mixed mode $MM_{13}$, which is only observed for very large rotation rates, and it connects the $RW_3$ state and the $T^3$-quasiperiodic state $IMM_{123}$.

Therefore, one may conclude that the rotation of the sphere has a mild effect on the bifurcation scenario for low rotation rates ($\Omega < 1$). Rotation rates between $1 < \Omega < 2$ favourise the appearance of a double helix wake and hysteresic behaviour, whereas large rotation rates ($\Omega > 2$) have a destabilizing effect which rapidly triggers the emergence of chaotic dynamics via a Ruelle–Takens–Newhouse route.

## 6. Conclusion

The present study conducts a complete study of the transition scenario of the flow past a rotating sphere, which is a canonical model of many industrial and natural phenomena like particle-driven flows, sport aerodynamics, bubble motion, plant seeds, etc. In such applications the changes in the paths of the particles are related to the destabilization of complex flow regimes and associated force distributions. To gain a deeper understanding of the underlying physics and evaluate possibilities of flow and path control, we have studied the mode competition involved in the formation of patterns in the flow past a rotating sphere, associated sensitivity to forcing and the effect of flow regimes on the force coefficients. This research aimed to structurally study the pattern formation previously examined by Lorite-Díez & Jiménez-González (2020), Pier (2013) and to determine from a dynamical perspective the fundamental building blocks of dynamics before and up to

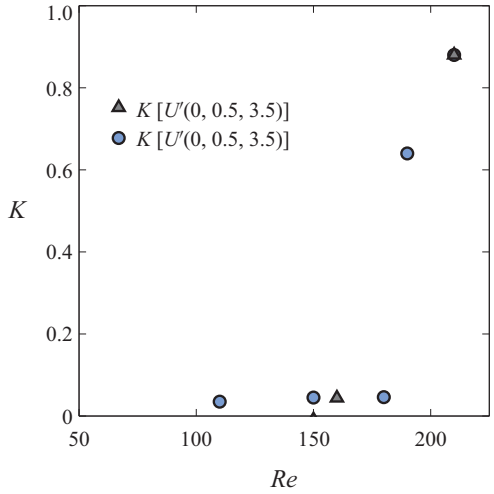


Figure 16. Asymptotic growth $K$ associated with the local radial velocity $U'(0, 0.5, 3.5)$ (same as in figure 10). Results are shown for the different initial seeds: $RW_1$ (grey triangles) and $RW_3$ (blue circles).

temporal chaos. In order to do that, we have employed LSA, normal form analysis and DNS.

Rotation of the sphere breaks the reflectional symmetry, thus inducing a preferential direction. This turns out to favourise the presence of rotating wave instabilities, instead of a steady symmetry breaking bifurcation, as it is the case for the flow past the static sphere. These instabilities exhibit a localized wavemaker within the recirculation zone, which is evidenced by the sensitivity maps. In addition, non-normality effects are weaker than in the flow past the static sphere, mainly because the primary bifurcation occurs at lower Reynolds number values. This might be an indication of a weaker transient growth of asymptotically stable perturbations for the rotating sphere wake flow (Chomaz 2005).

The bifurcation scenario is qualitatively distinct and it greatly varies with the rotation rate, as it has been discussed in § 5.2. The flow field displays a large variety of attractors from rotating waves, quasiperiodic mixed modes to $T^3$-quasiperiodic structures. In addition, one may find multiple attractors, which is associated to hysteresis, and it seems to be a common feature of many supercritical and subcritical flows, cf. (Subramanian, Sujith & Wahi 2013; Guo *et al.* 2018; Ren *et al.* 2021; Huang *et al.* 2018; Suckale *et al.* 2018). Eventually, for sufficiently large Reynolds numbers, Lorite-Díez & Jiménez-González (2020) and Pier (2013) identified irregular regimes for most rotation rates, which are associated to a $T^3$-quasiperiodic attractor. Nonetheless, such a state is just observed by means of DNS near its onset of existence. For larger Reynolds number values, the attractor is no longer quasiperiodic, but it is characterized by a continuous frequency spectra, that turns out to be chaotic. Indeed, such a chaotic attractor shadows the three frequency quasiperiodic state predicted by the normal form, which is evidenced by physical global features of the flow, e.g. the force acting on the surface of the sphere.

The analysis performed in this paper is able to accurately predict the fundamental modes of the wake flow, the bifurcation scenario and the forces acting on the sphere without the need of performing a fully nonlinear DNS. The results are compared against DNS computations at $\Omega = 1.75$ with an excellent agreement in regime zones, mode frequencies and force coefficients. Then, our procedure has been validated without

including non-normal and resonance effects in our analysis. In any case, their impact has been proven to be very reduced in this problem.

In the classification of the observed regimes, one may question which is the path or bifurcation scenario and how are they constituted, i.e. if it is possible to reconstitute the strange attractor with a sparse approximation. The identification of a $T^3$-quasiperiodic state, complemented with DNS results, allows the justification that the route to chaos is indeed the Ruelle–Takens–Newhouse. This has several consequences for further studies of this or similar flows. First, we have been able to identify the route to chaos and the fundamental building blocks, which are the three rotating waves. One could attempt to obtain further insight into the chaotic attractor and to investigate physically interesting properties such as mixing or the forces on the sphere from the information extracted from the three unstable periodic orbits associated with the fundamental rotating waves. In this case, it seems reasonable to construct a symbolic alphabet with the main fundamental modes being the rotating waves. Then, one may approximate average quantities or the eigenvalues of the Perron–Frobenius operator by cycle expansions, cf. (Cvitanovic *et al.* 2005), as it has been recently done by Yalnız & Budanur (2020); Yalnız, Hof & Budanur (2021) using algebraic topology techniques.

In addition, if ones attempt to design a control procedure to the quasiperiodic state or to prevent the presence of chaotic dynamics, the use of harmonic forcing, as in Sipp (2012), seems a promising option, and the implementation is straightforward from the information provided in §§ 4 and 5. Additionally, the sensitivity to base flow modifications and structural sensitivity have been presented for the low-frequency and high-frequency modes in § 3.4 to analyse harmonic and steady control possibilities. It has been shown that the low-frequency mode displays a strong sensitivity inside the recirculating region, suggesting a higher receptivity to control through surface rear blowing, in line with the results presented in Niazmand & Renksizbulut (2005). In principle, the attenuation of the amplitude of such a mode would imply a decrease in the mean drag and total lift coefficients (see figure 14), which could presumably prevent the path's instability in the case of freely rising bodies, as those analysed by Mathai *et al.* (2018). Therein, the tuning of rotational inertia is proposed to modify the wake and path's instabilities. The effect of changes in the moment of inertia may imply variations of the rotation rate, and consequently, changes in the regimes and associated forces. At that point, the force diagrams presented in figure 14 could be useful to guide such a tuning procedure and selectively set the regime of interest.

**Acknowledgements.** The authors are grateful to A. Chatterjee for useful discussions and the critical reading of the manuscript.

**Funding.** This work has been partially financed by the Junta de Andalucía, Universidad de Jaén, and European Funds under Project FEDER-UJA 1262764.

**Declaration of interests.** The authors report no conflict of interest.

**Author ORCIDs.**
J. Sierra-Ausín https://orcid.org/0000-0001-6036-5093;
M. Lorite-Díez https://orcid.org/0000-0002-7392-8622;
J.I. Jiménez-González https://orcid.org/0000-0001-6669-9000;
V. Citro https://orcid.org/0000-0003-2923-9157;
D. Fabre https://orcid.org/0000-0003-1875-6386.

| Coef. | $\lambda_\ell^{(\varepsilon_\nu^2)}$ | $\lambda_\ell^{(\varepsilon_\Omega^2)}$ | $\lambda_\ell^{(\varepsilon_\nu^4)}$ | $\lambda_\ell^{(\varepsilon_\Omega^2\varepsilon_\nu^2)}$ | $\lambda_\ell^{(\varepsilon_\Omega^4)}$ |
|---|---|---|---|---|---|
| $\lambda_1^A$ | $15-0.60\mathrm{i}$ | $(-1.8+8.2\mathrm{i})\times10^{-2}$ | $(-1.5-2.9\mathrm{i})\times10^{2}$ | $9.6-1.5\mathrm{i}$ | $(-38-2.9\mathrm{i})\times10^{-3}$ |
| $\lambda_3^A$ | $43-5.5\mathrm{i}$ | $(-22+5.8\mathrm{i})\times10^{-2}$ | $(-2.3-10\mathrm{i})10^{2}$ | $11-0.18\mathrm{i}$ | $(-1.6-1.6\mathrm{i})10^{-1}$ |
| $\lambda_2^B$ | $(11-3.2\mathrm{i})\times10^{1}$ | $(-2.6+1.64\mathrm{i})\times10^{-1}$ | $(-1.1+6.9\mathrm{i})\times10^{2}$ | $5.4+5.2\mathrm{i}$ | $(-3.4-18\mathrm{i})\times10^{-2}$ |
| $\lambda_3^B$ | $54-50\mathrm{i}$ | $0.36-0.58\mathrm{i}$ | $(4.2-6.9\mathrm{i})\times10^{3}$ | $64-22\mathrm{i}$ | $(-1.9-4.4\mathrm{i})\times10^{-1}$ |
| $\lambda_1^C$ | $9.1-3.7\mathrm{i}$ | $(1.1+11\mathrm{i})\times10^{-2}$ | $(-1.1-7.4\mathrm{i})\times10^{2}$ | $-0.80+3.8\mathrm{i}$ | $(18-4.4\mathrm{i})\times10^{-2}$ |
| $\lambda_2^C$ | $46-18\mathrm{i}$ | $(-1.2+1.7)\times10^{-2}$ | $(-2.7-18\mathrm{i})\times10^{2}$ | $16+10\mathrm{i}$ | $(-4.4-3.6\mathrm{i})\times10^{-2}$ |

Table 4. Linear coefficients of the normal form (4.9) evaluated at codimension-two points.

## Appendix A. Normal form reduction procedure for the triple-Hopf interaction

Before we detail the procedure for the reduction of the governing equations to the normal form (4.6), let us detail the terms that composed the compact notation of the governing equations (2.3), which is reminded here for the sake of conciseness,

$$\boldsymbol{B}\frac{\partial \boldsymbol{Q}}{\partial t} = \boldsymbol{F}(\boldsymbol{Q},\boldsymbol{\eta}) \equiv \boldsymbol{L}\boldsymbol{Q} + \boldsymbol{N}(\boldsymbol{Q},\boldsymbol{Q}) + \boldsymbol{G}(\boldsymbol{Q},\boldsymbol{\eta}). \tag{A1}$$

The operator $\boldsymbol{G}(\boldsymbol{Q},\boldsymbol{\eta}) = \boldsymbol{G}(\boldsymbol{Q},[\eta_1,0]^{\mathrm{T}}) + \boldsymbol{G}(\boldsymbol{Q},[0,\eta_2]^{\mathrm{T}})$, where $\boldsymbol{G}(\boldsymbol{Q},[\eta_1,0]^{\mathrm{T}}) = \eta_1\boldsymbol{\nabla}\cdot(\boldsymbol{\nabla}\boldsymbol{U}+\boldsymbol{\nabla}\boldsymbol{U}^{\mathrm{T}})$ and $\boldsymbol{G}(\boldsymbol{Q},[0,\eta_2]^{\mathrm{T}})$ expresses the imposition of the boundary condition $\boldsymbol{U}=(0,\eta_2,0)$ on $\Sigma_b$. The nonlinear operator $\boldsymbol{N}(\boldsymbol{Q}_1,\boldsymbol{Q}_2)=\boldsymbol{U}_1\cdot\boldsymbol{\nabla}\boldsymbol{U}_2$, and the linear operator accounts for the remaining terms that are linear on the state variable $\boldsymbol{Q}$, i.e. $\boldsymbol{L}\boldsymbol{Q}=[\boldsymbol{\nabla}P,\boldsymbol{\nabla}\cdot\boldsymbol{U}]^{\mathrm{T}}$. In addition, we consider the following splitting of the parameters $\boldsymbol{\eta}=\boldsymbol{\eta}_c+\Delta\boldsymbol{\eta}$, where $\boldsymbol{\eta}_c$ denotes the critical parameters $\boldsymbol{\eta}_c\equiv[Re_c^{-1},\Omega_c]^{\mathrm{T}}$ attained when the spectra of the Jacobian operator of the steady state posses at least an eigenvalue whose real part is zero, and $\Delta\boldsymbol{\eta}=[Re_c^{-1}-Re^{-1},\Omega_c-\Omega]^{\mathrm{T}}$ the departure from the critical condition.

The procedure followed in this manuscript consists of the determination of a fifth-order Taylor expansion of the centre manifold, also known as the normal form, of the three codimension-two-Hopf points ($A$, $B$, $C$), which enables a linear approximation of the cubic coefficients $\nu_{k\ell}$ and a quadratic approximation of the linear coefficients $\lambda_\ell$. The ultimate goal of this approach is the determination of the coefficients listed in tables 4–6. That is, to determine the cubic coefficient $\nu_{k\ell}$ values as

$$\nu_{k\ell} = \nu_{k\ell}^{(0)} + \varepsilon_\nu^2\nu_{k\ell}^{(\varepsilon_\nu^2)} + \varepsilon_\Omega^2\nu_{k\ell}^{(\varepsilon_\Omega^2)}, \tag{A2}$$

where $\nu_{k\ell}^{(0)}$, $\nu_{k\ell}^{(\varepsilon_\nu^2)}$ and $\nu_{k\ell}^{(\varepsilon_\Omega^2)}$ are determined at the two-Hopf point between mode $k$ and $\ell$. Similarly, the estimation of the linear coefficient is

$$\lambda_\ell = \varepsilon_\nu^2\lambda_\ell^{(\varepsilon_\nu^2)} + \varepsilon_\Omega^2\lambda_\ell^{(\varepsilon_\Omega^2)} + \varepsilon_\nu^4\lambda_\ell^{(\varepsilon_\nu^4)} + \varepsilon_\Omega^4\lambda_\ell^{(\varepsilon_\Omega^4)} + \varepsilon_\Omega^2\varepsilon_\nu^2\lambda_\ell^{(\varepsilon_\nu^2\varepsilon_\Omega^2)}. \tag{A3}$$

The reduction to the normal form is carried out via a multiple scales expansion of the solution $\boldsymbol{Q}$ of (2.3). The expansion considers a two-scale expansion of the original time, a fast time scale $t$ of the self-sustained instability and a slow time scale of the evolution of

| Coef. | $\nu_{k\ell}^{(0)}$ | $\nu_{k\ell}^{(\varepsilon_\nu^2)}$ | $\nu_{k\ell}^{(\varepsilon_\Omega^2)}$ |
|---|---|---|---|
| $\nu_{11}^A$ | $-0.46 + 0.16\mathrm{i}$ | $6.3 + 10.1\mathrm{i}$ | $(4.4 - 1.1\mathrm{i}) \times 10^{-2}$ |
| $\nu_{13}^A$ | $-3.0 + 0.73\mathrm{i}$ | $(4.6 - 2.3\mathrm{i}) \times 10^{2}$ | $-3.6 - 5.2\mathrm{i}$ |
| $\nu_{31}^A$ | $-0.73 + 1.07\mathrm{i}$ | $(2.2 - 8.6\mathrm{i}) \times 10^{1}$ | $(2.2 - 2.4\mathrm{i}) \times 10^{-1}$ |
| $\nu_{33}^A$ | $-1.5 + 2.1\mathrm{i}$ | $(-1.1 - 11\mathrm{i}) \times 10^{1}$ | $-0.56 - 0.30\mathrm{i}$ |
| $\nu_{22}^B$ | $-1.8 + 0.22\mathrm{i}$ | $(2.2 - 34\mathrm{i}) \times 10^{1}$ | $0.46 - 1.0\mathrm{i}$ |
| $\nu_{23}^B$ | $-1.9 - 0.2\mathrm{i}$ | $(2.9 - 1.4\mathrm{i}) \times 10^{2}$ | $2.6 + 2.4\mathrm{i}$ |
| $\nu_{32}^B$ | $(-34 - 3.1\mathrm{i}) \times 10^{-2}$ | $(3.0 - 10\mathrm{i}) \times 10^{2}$ | $-0.22 + 2.2\mathrm{i}$ |
| $\nu_{33}^B$ | $-1.7 + 0.9\mathrm{i}$ | $(1.0 - 11\mathrm{i}) \times 10^{2}$ | $0.30 - 1.54\mathrm{i}$ |
| $\nu_{11}^C$ | $-0.25 + 0.15\mathrm{i}$ | $34 - 2.1\mathrm{i}$ | $(5.2 - 10\mathrm{i}) \times 10^{-2}$ |
| $\nu_{12}^C$ | $0.58 - 0.58\mathrm{i}$ | $(-2.4 + 3.0\mathrm{i}) \times 10^{2}$ | $0.74 - 0.28\mathrm{i}$ |
| $\nu_{21}^C$ | $(4.6 - 26\mathrm{i}) \times 10^{-2}$ | $2.3 - 71\mathrm{i}$ | $(2.4 - 30\mathrm{i}) \times 10^{-2}$ |
| $\nu_{22}^C$ | $-1.9 + 3.1\mathrm{i}$ | $(4.7 - 10\mathrm{i}) \times 10^{2}$ | $-2.4 + 5.2$ |

Table 5. Cubic coefficients of the normal form (4.9) evaluated at codimension-two points.

| Coef. | | | Value | | |
|---|---|---|---|---|---|
| $\lambda_1$ | $(-0.019 + 0.038\mathrm{i})$ | $+$ | $(20.2 - 1.60\mathrm{i})\varepsilon_\nu^2$ | $+$ | $(-1.5 - 2.9\mathrm{i}) \times 10^{2}\varepsilon_\nu^4$ |
| $\lambda_2$ | $(0.1805 + 0.1107\mathrm{i})$ | $+$ | $(11 - 2.8\mathrm{i}) \times 10^{1}\varepsilon_\nu^2$ | $+$ | $(-1.1 + 6.9\mathrm{i}) \times 10^{2}\varepsilon_\nu^4$ |
| $\lambda_3$ | $(-0.13 + 0.003\mathrm{i})$ | $+$ | $(49 - 6.3\mathrm{i})\varepsilon_\nu^2$ | $+$ | $(-2.3 - 10\mathrm{i})10^{2}\varepsilon_\nu^4$ |
| $\nu_{11}$ | $(-0.44 + 0.15\mathrm{i})$ | $+$ | $(6.3 - 10\mathrm{i})\varepsilon_\nu^2$ | | |
| $\nu_{12}$ | $(2.2 - 1.2\mathrm{i})$ | $+$ | $(-2.4 + 3.0\mathrm{i}) \times 10^{2}\varepsilon_\nu^2$ | | |
| $\nu_{13}$ | $(-4.7 + 1.9\mathrm{i})$ | $+$ | $(4.6 - 2.3\mathrm{i}) \times 10^{2}\varepsilon_\nu^2$ | | |
| $\nu_{21}$ | $(0.10 + 0.43\mathrm{i})$ | $+$ | $(2.3 - 71\mathrm{i})\varepsilon_\nu^2$ | | |
| $\nu_{22}$ | $(-2.2 + 0.94\mathrm{i})$ | $+$ | $(2.2 - 34\mathrm{i}) \times 10^{1}\varepsilon_\nu^2$ | | |
| $\nu_{23}$ | $(-0.08 - 1.6\mathrm{i})$ | $+$ | $(2.9 - 1.4\mathrm{i}) \times 10^{2}\varepsilon_\nu^2$ | | |
| $\nu_{31}$ | $(-0.63 + 0.95\mathrm{i})$ | $+$ | $(2.2 - 8.6\mathrm{i}) \times 10^{1}\varepsilon_\nu^2$ | | |
| $\nu_{32}$ | $(-0.19 - 0.06\mathrm{i})$ | $+$ | $(3.0 - 10\mathrm{i}) \times 10^{2}\varepsilon_\nu^2$ | | |
| $\nu_{33}$ | $(-1.9 + 2.0\mathrm{i})$ | $+$ | $(1.0 - 11\mathrm{i}) \times 10^{1}\varepsilon_\nu^2$ | | |

Table 6. Cubic coefficients of the normal form (4.9) evaluated at $\Omega = 1.75$.

the amplitudes

$$t \mapsto t + \varepsilon^2\tau, \quad \varepsilon \ll 1, \tag{A4}$$

here $\varepsilon$ is the order of magnitude of the flow disturbances. The small parameters are

$$\varepsilon_\Omega^2 = (\Omega_c - \Omega) \sim \varepsilon^2 \quad \text{and} \quad \varepsilon_\nu^2 = (\nu_c - \nu) = \left(Re_c^{-1} - Re^{-1}\right) \sim \varepsilon^2. \tag{A5a,b}$$

The ansatz of the expansion is

$$\boldsymbol{Q}(t,\tau) = \boldsymbol{Q}_b + \varepsilon\boldsymbol{q}_{(\varepsilon)}(t,\tau) + \varepsilon^2\boldsymbol{q}_{(\varepsilon^2)}(t,\tau) + \varepsilon^3\boldsymbol{q}_{(\varepsilon^3)}(t,\tau) + \varepsilon^4\boldsymbol{q}_{(\varepsilon^4)}(t,\tau) + O(\varepsilon^5). \tag{A6}$$

Note that the expansion of the left-hand side of (2.3) up to fifth order is

$$\begin{aligned}&\varepsilon\boldsymbol{B}\frac{\partial\boldsymbol{q}_{(\varepsilon)}}{\partial t} + \varepsilon^2\boldsymbol{B}\frac{\partial\boldsymbol{q}_{(\varepsilon^2)}}{\partial t} + \varepsilon^3\left[\boldsymbol{B}\frac{\partial\boldsymbol{q}_{(\varepsilon^3)}}{\partial t} + \boldsymbol{B}\frac{\partial\boldsymbol{q}_{(\varepsilon)}}{\partial\tau}\right]\\ &\quad + \varepsilon^4\left[\boldsymbol{B}\frac{\partial\boldsymbol{q}_{(\varepsilon^4)}}{\partial t} + \boldsymbol{B}\frac{\partial\boldsymbol{q}_{(\varepsilon^2)}}{\partial\tau}\right] + \varepsilon^5\left[\boldsymbol{B}\frac{\partial\boldsymbol{q}_{(\varepsilon^5)}}{\partial t} + \boldsymbol{B}\frac{\partial\boldsymbol{q}_{(\varepsilon^3)}}{\partial\tau}\right],\end{aligned} \tag{A7}$$

respectively the right-hand side is

$$\boldsymbol{F}(\boldsymbol{q},\boldsymbol{\eta}) = \boldsymbol{F}_{(0)} + \varepsilon\boldsymbol{F}_{(\varepsilon)} + \varepsilon^2\boldsymbol{F}_{(\varepsilon^2)} + \varepsilon^3\boldsymbol{F}_{(\varepsilon^3)} + \varepsilon^4\boldsymbol{F}_{(\varepsilon^4)} + \varepsilon^5\boldsymbol{F}_{(\varepsilon^5)}. \tag{A8}$$

Then we are left with the determination of the forcing terms of (A8).

The reduction detailed in this appendix considers the interaction between two rotating wave solutions at a codimension-two point. In the following, we adopt the notation for the solutions $z_1$ and $z_2$, which correspond to point $C$. In order to proceed for the other two points, replace $z_1$ by $z_3$ or $z_2$ by $z_3$.

### A.1. *Notation*

Since the number of terms grows quickly with the order, in order to enhance readability, we define the set of vectors of linear, quadratic, cubic and fourth-order interactions as

$$\begin{aligned}
\boldsymbol{Z} &\equiv \{z_1, z_2\}, \quad \overline{\boldsymbol{Z}} = \{\bar{z}_1, \bar{z}_2\},\\
\boldsymbol{Z}^2 &\equiv \boldsymbol{Z}\otimes\boldsymbol{Z}\oplus\boldsymbol{Z}\otimes\overline{\boldsymbol{Z}} = \{z_1^2, z_1z_2, z_2^2, |z_1|^2, z_1\bar{z}_2, |z_2|^2\},\\
\boldsymbol{Z}^3 &\equiv \boldsymbol{Z}\otimes\boldsymbol{Z}^2\oplus\boldsymbol{Z}^2\otimes\overline{\boldsymbol{Z}}\\
&= \{z_1^3, z_1^2z_2, z_1z_2^2, z_2^3, z_1|z_1|^2, z_2|z_1|^2, z_2^2\bar{z}_1, \bar{z}_2z_1^2, z_1|z_2|^2, z_2|z_2|^2\},\\
\boldsymbol{Z}^4 &\equiv \boldsymbol{Z}^2\otimes\boldsymbol{Z}^2\oplus\boldsymbol{Z}\otimes\overline{\boldsymbol{Z}}^3\\
&= \{z_1^4, z_1^3z_2, z_1^2z_2^2, z_1z_2^3, z_2^4, z_1^2|z_1|^2, z_1z_2|z_1|^2, z_2^2|z_1|^2, z_1^2|z_2|^2,\\
&\quad z_1z_2|z_2|^2, z_2^2|z_2|^2, z_1\bar{z}_2|z_1|^2, z_1\bar{z}_2|z_2|^2, z_1^3\bar{z}_2, \bar{z}_1z_2^3\},
\end{aligned} \tag{A9}$$

where only unique elements are kept. We denote by $\boldsymbol{z}_\alpha^n$ any element of the family $\boldsymbol{Z}^n$, with $n\in\mathbb{N}^*$. In addition to these sets, we shall define the set of resonant terms

$$\boldsymbol{Z}_R \equiv \{z_1, z_2, z_1|z_1|^2, z_1|z_2|^2\}. \tag{A10}$$

### A.2. *Zeroth order*

The zeroth order corresponds to the steady-state problem of the governing equations evaluated at the threshold of instability, i.e. $\Delta\boldsymbol{\eta}=\boldsymbol{0}$,

$$\boldsymbol{0} = \boldsymbol{F}(\boldsymbol{Q}_b, \boldsymbol{0}), \tag{A11}$$

whose solution is the steady state $\boldsymbol{Q}_b$.

### A.3. *First order*

The first order corresponds to the resolution of a homogeneous linear system, i.e. the generalized eigenvalue problem evaluated at the threshold of instability, i.e. $\Delta\boldsymbol{\eta}=\boldsymbol{0}$. In such a case, the vector is expanded as

$$\boldsymbol{q}_{(\varepsilon)} = z_1\hat{\boldsymbol{q}}_{(z_1)}\exp(-\mathrm{i}(m_1\theta+\omega_1 t)) + z_2\hat{\boldsymbol{q}}_{(z_2)}\exp(-\mathrm{i}(m_2\theta+\omega_2 t)) + \text{c.c.} \tag{A12}$$

Then, the eigenpairs $[\mathrm{i}\omega_\ell, \hat{\boldsymbol{q}}_{(z_\ell)}]$ are determined as the solutions of the following eigenvalue problem:

$$\boldsymbol{J}_{(\omega_\ell,m_\ell)}\hat{\boldsymbol{q}}_{(z_\ell)} = \left(\mathrm{i}\omega_\ell\boldsymbol{B} - \frac{\partial\boldsymbol{F}}{\partial\boldsymbol{q}}|_{\boldsymbol{q}=\boldsymbol{Q}_b,\Delta\boldsymbol{\eta}=\boldsymbol{0}}\right)\hat{\boldsymbol{q}}_{(z_\ell)}. \tag{A13}$$

The eigenmode $\hat{\boldsymbol{q}}_{(z_\ell)}(r,z)$ is then normalised in such a way that $\langle\hat{\boldsymbol{u}}_{(z_\ell)}, \hat{\boldsymbol{u}}_{(z_\ell)}\rangle_{L^2} = 1$.

### A.4. *Second order*

The second-order expansion term $\boldsymbol{q}_{(\varepsilon^2)}(t,\tau)$ is determined by the resolution of a set of linear systems, where the forcing terms are evaluated from first- and zeroth-order terms. The expansion in terms of amplitudes $z_\ell(\tau)$ of $\boldsymbol{q}_{(\varepsilon^2)}(t,\tau)$ is assessed by collecting the second-order forcing terms. Nonlinear second-order terms in $\varepsilon$ are

$$\begin{aligned}\boldsymbol{F}_{(\varepsilon^2)} \equiv &\sum_{j,k=1}^{2}\left(z_j z_k \boldsymbol{N}(\hat{\boldsymbol{q}}_{(z_j)},\hat{\boldsymbol{q}}_{(z_k)})\exp(-\mathrm{i}(m_j+m_k)\theta)\exp(-\mathrm{i}(\omega_j+\omega_k)t)+\text{c.c.}\right)\\ &+\sum_{j,k=1}^{2}\left(z_j \bar{z}_k \boldsymbol{N}(\hat{\boldsymbol{q}}_{(z_j)},\hat{\boldsymbol{q}}_{(\bar{z}_k)})\exp(-\mathrm{i}(m_j-m_k)\theta)\exp(-\mathrm{i}(\omega_j-\omega_k)t)+\text{c.c.}\right)\\ &+\sum_{\ell=1}^{2}\eta_\ell \boldsymbol{G}(\boldsymbol{Q}_b,\boldsymbol{e}_\ell),\end{aligned} \tag{A14}$$

where $\boldsymbol{e}_\ell$ is an element of the orthonormal basis of $\mathbb{R}^2$. Then the second-order expansion of the flow variable is carried out so it matches the terms of the forcing (A14),

$$\boldsymbol{q}_{(\varepsilon^2)} \equiv \sum_{z_\alpha^2 \in \boldsymbol{Z}}\left(z_\alpha^2 \hat{\boldsymbol{q}}_{(z_\alpha^2)}\exp(-\mathrm{i}(m_\alpha\theta+\omega_\alpha t))+\text{c.c.}\right)+\sum_{\ell=1}^{2}\eta_\ell \boldsymbol{Q}_b^{(\eta_\ell)}. \tag{A15}$$

Terms $\hat{\boldsymbol{q}}_{(z_j^2)}$ are harmonics of the flow, $\hat{\boldsymbol{q}}_{(z_j z_k)}$ with $j\neq k$ are coupling terms, $\hat{\boldsymbol{q}}_{(|z_j|^2)}$ are harmonic base flow modification terms and $\boldsymbol{Q}_b^{(\eta_\ell)}$ are base flow corrections due to a modification of the parameter $\eta_\ell$ from the critical point. Then the second-order terms are determined from the resolution of the following systems of equations:

$$\boldsymbol{J}_{(\omega_j+\omega_k,m_j+m_k)}\hat{\boldsymbol{q}}_{(z_j z_k)} = \hat{\boldsymbol{F}}_{(z_j z_k)}. \tag{A16}$$

Here $\hat{\boldsymbol{F}}_{(z_j z_k)} \equiv \boldsymbol{N}(\hat{\boldsymbol{q}}_{(z_j)},\hat{\boldsymbol{q}}_{(z_k)})+\boldsymbol{N}(\hat{\boldsymbol{q}}_{(z_k)},\hat{\boldsymbol{q}}_{(z_j)})$ and

$$\boldsymbol{J}_{(0,0)}\boldsymbol{Q}_b^{(\eta_\ell)} = \boldsymbol{G}(\boldsymbol{Q}_b,\boldsymbol{e}_\ell). \tag{A17}$$

### A.5. *Third order*

At third order, we proceed as for previous orders, first the forcing term is expanded as

$$\begin{aligned}\boldsymbol{F}_{(\varepsilon^3)} &\sum_{z_\alpha\in\boldsymbol{Z},z_\beta^2\in\boldsymbol{Z}^2} z_\alpha\cdot z_\beta^2\left[\boldsymbol{N}(\hat{\boldsymbol{q}}_{(z_\beta^2)},\hat{\boldsymbol{q}}_{(z_\alpha)})+\boldsymbol{N}(\hat{\boldsymbol{q}}_{(z_\alpha)},\hat{\boldsymbol{q}}_{(z_\beta^2)})\right]\exp(\mathrm{i}(m_\alpha+m_\beta)\theta+\mathrm{i}(\omega_\alpha+\omega_\beta)t)\\ &+\sum_{j=1}^{2}\sum_{\ell=1}^{2}\left[z_j\eta_\ell\left[\boldsymbol{N}(\hat{\boldsymbol{q}}_{(z_j)},\boldsymbol{Q}_b^{(\eta_\ell)})+\boldsymbol{N}(\boldsymbol{Q}_b^{(\eta_\ell)},\hat{\boldsymbol{q}}_{(z_j)})\right]\exp(-\mathrm{i}m_j\theta)\exp(-\mathrm{i}\omega_j t)+\text{c.c.}\right]\\ &+\sum_{j=1}^{2}\sum_{\ell=1}^{2}\left[z_j\eta_\ell \boldsymbol{G}(\hat{\boldsymbol{q}}_{(z_j)},\boldsymbol{e}_\ell)\exp(-\mathrm{i}m_j\theta)\exp(-\mathrm{i}\omega_j t)+\text{c.c.}\right],\end{aligned} \tag{A18}$$

where $\omega_n$ and $m_n$ are defined as $\omega_n = \omega_j + \omega_k + \omega_\ell$, $m_n = m_j + m_k + m_\ell$ with $n = j + k + \ell$. Followed by the expansion of the state variable $\boldsymbol{q}_{(\varepsilon^3)}(t, \tau)$,

$$\boldsymbol{q}_{(\varepsilon^3)}(t,\tau) \equiv \sum_{z_\alpha^3 \in \boldsymbol{Z}} \left[ z_\alpha^3 \hat{\boldsymbol{q}}_{(z_\alpha^3)} \exp(-\mathrm{i}(m_\alpha\theta + \omega_\alpha t)) + \text{c.c.} \right] + \sum_{j=1}^{2} \sum_{\ell=1}^{2} \left[ z_j \eta_\ell \boldsymbol{Q}_{(z_j)}^{(\eta_\ell)} \exp(-\mathrm{i}m_j\theta) \exp(-\mathrm{i}\omega_j t) + \text{c.c.} \right]. \tag{A19}$$

At this order there exist resonance terms, which are associated with the singular Jacobian $\boldsymbol{J}_{(\omega_k, m_k)}$ for $k = 1, 2, 3$. To ensure the solvability of these terms, we must enforce compatibility conditions, i.e. the Fredholm alternative. The resonant terms are then determined from the resolution of the following set of bordered systems:

$$\begin{pmatrix} \boldsymbol{J}_{(\omega_k, m_k)} & \hat{\boldsymbol{q}}_{(z_k)} \\ \hat{\boldsymbol{q}}_{(z_k)}^\dagger & 0 \end{pmatrix} \begin{pmatrix} \hat{\boldsymbol{q}}_{(z_\alpha^{(R)})} \\ s \end{pmatrix} = \begin{pmatrix} \hat{\boldsymbol{F}}_{(z_\alpha^{(R)})} \\ 0 \end{pmatrix}, \; z_\alpha^{(R)} \in \boldsymbol{Z}_R. \tag{A20}$$

Here $s = \lambda_k^{(\varepsilon_\nu^2)}$ (respectively $s = \lambda_k^{(\varepsilon_\Omega^2)}$) for $z_\alpha^{(R)} = z_k$ and $s = \nu_{kl}^{(0)}$ for $z_\alpha^{(R)} = z_k |z_\ell|^2$. The non-resonant terms are then determined as at second order from the resolution of forced linear systems.

### A.6. *Fourth order*

At fourth order we proceed as at second order, we expand the forcing term $\boldsymbol{F}_{(\varepsilon^4)}$ as

$$\begin{aligned} \boldsymbol{F}_{(\varepsilon^4)} \equiv & \sum_{z_\alpha \in \boldsymbol{Z}, z_\beta^3 \in \boldsymbol{Z}^3} z_\alpha \cdot z_\beta^3 \left[ \boldsymbol{N}(\hat{\boldsymbol{q}}_{(z_\beta^3)}, \hat{\boldsymbol{q}}_{(z_\alpha)}) + \boldsymbol{N}(\hat{\boldsymbol{q}}_{(z_\alpha)}, \hat{\boldsymbol{q}}_{(z_\beta^3)}) \right] \exp(\mathrm{i}(m_\alpha + m_\beta)\theta + \mathrm{i}(\omega_\alpha + \omega_\beta)t) \\ & + \sum_{z_\alpha^2 \in \boldsymbol{Z}^2, z_\beta^2 \in \boldsymbol{Z}^2} z_\alpha^2 \cdot z_\beta^2 \left[ \boldsymbol{N}(\hat{\boldsymbol{q}}_{(z_\alpha^2)}, \hat{\boldsymbol{q}}_{(z_\beta^2)}) \right] \exp(\mathrm{i}(m_\alpha + m_\beta)\theta + \mathrm{i}(\omega_\alpha + \omega_\beta)t) \\ & + \sum_{\ell=1}^{2} \eta_\ell \sum_{z_\alpha^2 \in \boldsymbol{Z}^2} z_\alpha^2 \boldsymbol{G}(\hat{\boldsymbol{q}}_{(z_\alpha^2)}, \boldsymbol{e}_\ell) \exp(-\mathrm{i}(m_\alpha \theta \omega_\alpha t)) \\ & + \sum_{\ell,k=1}^{2} \eta_\ell \eta_k \left[ \boldsymbol{N}(\boldsymbol{Q}_b^{(\eta_k)}, \boldsymbol{Q}_b^{(\eta_\ell)}) \right] \\ & + \sum_{\ell=1}^{2} \eta_\ell \sum_{z_\alpha \in \boldsymbol{Z}, z_\beta \in \boldsymbol{Z}} z_\alpha \cdot z_\beta \left[ \boldsymbol{N}(\boldsymbol{Q}_{(z_\alpha)}^{(\eta_\ell)}, \hat{\boldsymbol{q}}_{(z_\beta)}) \right. \\ & \left. + \boldsymbol{N}(\hat{\boldsymbol{q}}_{(z_\beta)}, \boldsymbol{Q}_{(z_\alpha)}^{(\eta_\ell)}) \right] \exp(\mathrm{i}(m_\alpha + m_\beta)\theta + \mathrm{i}(\omega_\alpha + \omega_\beta)t), \end{aligned} \tag{A21}$$

and the state variable $\boldsymbol{q}_{(\varepsilon^4)}$ as

$$\boldsymbol{q}_{(\varepsilon^4)} \equiv \sum_{z_\alpha^4 \in \boldsymbol{Z}^4} \left( z_\alpha^4 \hat{\boldsymbol{q}}_{(z_\alpha^4)} \exp(-\mathrm{i}(m_\alpha \theta + \omega_\alpha t)) + \mathrm{c.c.} \right) + \sum_{\ell=1}^{2} \eta_\ell \sum_{z_\beta^2 \in \boldsymbol{Z}^2} z_\beta^2 \boldsymbol{Q}_{(z_\beta^2)}^{(\eta_\ell)} \exp(-\mathrm{i}(m_\beta \theta + \omega_\beta t)) + \sum_{\ell,k=1}^{2} \eta_k \eta_\ell \boldsymbol{Q}_b^{(\eta_\ell \eta_k)}, \tag{A22}$$

which are determined from the resolution of a forced linear system.

### A.7. *Fifth order*

At fifth order, we uniquely consider the resonant terms. These are the coefficients of members of $\boldsymbol{Z}_R$. The resonant forcing terms are

$$\begin{aligned}
\hat{\boldsymbol{F}}_{z_\ell}^{(\eta_j \eta_k)} &= \boldsymbol{N}(\hat{\boldsymbol{q}}_{(z_\ell)}, \boldsymbol{Q}_b^{(\eta_j \eta_k)}) + \boldsymbol{N}(\boldsymbol{Q}_b^{(\eta_j \eta_k)}, \hat{\boldsymbol{q}}_{(z_\ell)}) \\
&\quad + \left( \boldsymbol{G}(\boldsymbol{Q}_{(z_\ell)}^{(\eta_k)}, \boldsymbol{e}_j) + \boldsymbol{G}(\boldsymbol{Q}_{(z_\ell)}^{(\eta_j)}, \boldsymbol{e}_k) - \lambda_\ell^{(\eta_j)} \boldsymbol{B} \boldsymbol{Q}_{(z_\ell)}^{(\eta_k)} - \lambda_\ell^{(\eta_k)} \boldsymbol{B} \boldsymbol{Q}_{(z_\ell)}^{(\eta_j)} \right) \left( 1 - \frac{1}{2} \delta_{jk} \right), \\
\hat{\boldsymbol{F}}_{z_j |z_k|^2}^{(\eta_\ell)} &= \boldsymbol{N}(\hat{\boldsymbol{q}}_{(z_j)}, \boldsymbol{Q}_{(|z_k|^2)}^{(\eta_\ell)}) + \boldsymbol{N}(\boldsymbol{Q}_{(|z_k|^2)}^{(\eta_\ell)}, \hat{\boldsymbol{q}}_{(z_j)}) \\
&\quad + \boldsymbol{N}(\hat{\boldsymbol{q}}_{(\bar{z}_k)}, \boldsymbol{Q}_{(z_j z_k)}^{(\eta_\ell)}) + \boldsymbol{N}(\boldsymbol{Q}_{(z_j z_k)}^{(\eta_\ell)}, \hat{\boldsymbol{q}}_{(\bar{z}_k)}) \\
&\quad + \boldsymbol{N}(\hat{\boldsymbol{q}}_{(z_j |z_k|^2)}, \boldsymbol{Q}_b^{(\eta_\ell)}) + \boldsymbol{N}(\boldsymbol{Q}_b^{(\eta_\ell)}, \hat{\boldsymbol{q}}_{(z_j |z_k|^2)}) \\
&\quad + \boldsymbol{N}(\hat{\boldsymbol{q}}_{(|z_k|^2)}, \boldsymbol{Q}_{(z_j)}^{(\eta_\ell)}) + \boldsymbol{N}(\boldsymbol{Q}_{(z_j)}^{(\eta_\ell)}, \hat{\boldsymbol{q}}_{(|z_k|^2)}) \\
&\quad + \boldsymbol{N}(\hat{\boldsymbol{q}}_{(z_j z_k)}, \boldsymbol{Q}_{(\bar{z}_k)}^{(\eta_\ell)}) + \boldsymbol{N}(\boldsymbol{Q}_{(\bar{z}_k)}^{(\eta_\ell)}, \hat{\boldsymbol{q}}_{(z_j z_k)}) \\
&\quad + \left( \boldsymbol{N}(\hat{\boldsymbol{q}}_{(z_j \bar{z}_k)}, \boldsymbol{Q}_{(z_k)}^{(\eta_\ell)}) + \boldsymbol{N}(\boldsymbol{Q}_{(z_k)}^{(\eta_\ell)}, \hat{\boldsymbol{q}}_{(z_j \bar{z}_k)}) \right) (1 - \delta_{jk}) \\
&\quad + \left( \boldsymbol{N}(\hat{\boldsymbol{q}}_{(z_k)}, \boldsymbol{Q}_{(z_j \bar{z}_k)}^{(\eta_\ell)}) + \boldsymbol{N}(\boldsymbol{Q}_{(z_j \bar{z}_k)}^{(\eta_\ell)}, \hat{\boldsymbol{q}}_{(z_k)}) \right) (1 - \delta_{jk}) \\
&\quad - \left( \lambda_j^{(\eta_\ell)} + \lambda_k^{(\eta_\ell)} + \bar{\lambda}_j^{(\eta_\ell)} \right) \boldsymbol{B} \hat{\boldsymbol{q}}_{(z_j |z_k|^2)} - \nu_{jk}^{(0)} \boldsymbol{B} \boldsymbol{Q}_{(z_j)}^{(\eta_\ell)},
\end{aligned} \tag{A23}$$

with $j, k, \ell = 1, 2$ and $\delta_{jk}$ is the Kronecker symbol. Finally, the coefficients of the normal form are obtained as

$$\left.
\begin{aligned}
\lambda_\ell^{(\eta_j \eta_k)} &= \frac{\langle \hat{\boldsymbol{q}}_{(z_\ell)}^\dagger, \hat{\boldsymbol{F}}_{z_\ell}^{(\eta_j \eta_k)} \rangle}{\langle \hat{\boldsymbol{q}}_{(z_\ell)}^\dagger, \boldsymbol{B} \hat{\boldsymbol{q}}_{(z_\ell)} \rangle}, \\
\nu_{jk}^{(\eta_\ell)} &= \frac{\langle \hat{\boldsymbol{q}}_{(z_\ell)}^\dagger, \hat{\boldsymbol{F}}_{z_j |z_k|^2}^{(\eta_\ell)} \rangle}{\langle \hat{\boldsymbol{q}}_{(z_\ell)}^\dagger, \boldsymbol{B} \hat{\boldsymbol{q}}_{(z_\ell)} \rangle}
\end{aligned}
\right\} \tag{A24}$$

for $j, k, \ell = 1, 2$.

## Appendix B. Non-normality (lift-up and convective mechanisms)

In this section we explore the effect of the non-normal mechanisms on the instability. Two non-normal mechanisms were identified in the flow configuration of the static sphere

($\Omega = 0$), cf. Meliga *et al.* (2009*b*), the lift-up and convective non-normality mechanisms. The lift-up mechanism is associated with the transport of the steady-state solution by the perturbation, that is, to the component $\hat{\boldsymbol{u}} \cdot \boldsymbol{\nabla} \boldsymbol{U}_b$ of (3.2), cf. Marquet *et al.* (2009). On the other hand, the convective non-normality is due to the advection of disturbances by the steady state, that is, the term $\boldsymbol{U}_b \cdot \boldsymbol{\nabla}_m \hat{\boldsymbol{u}}$ of (3.2) and $-\boldsymbol{U}_b \cdot \boldsymbol{\nabla}_m \hat{\boldsymbol{u}}^\dagger$ for the adjoint operator. In physical terms, it corresponds to the convection of disturbances in opposite directions. In terms of direct $\hat{\boldsymbol{q}}$ and adjoint $\hat{\boldsymbol{q}}^\dagger$ global modes, the lift-up non-normality is characterized by the near orthogonality of the direct and adjoint components of velocity because they tend to concentrate in different components of velocity, even if both direct and adjoint modes are active in the same region of space. Instead, the convective non-normality is associated with direct and adjoint modes that tend to be orthogonal because they are localized in different regions of the space. The non-normality may be measured by the angle $\theta_N$ (Meliga *et al.* 2009*b*) defined as

$$\cos\left(\frac{\pi}{2} - \theta_N\right) = \frac{\langle \hat{\boldsymbol{q}}^\dagger_{(z_\ell)}, \boldsymbol{B}\hat{\boldsymbol{q}}_{(z_\ell)} \rangle}{\left(\langle \hat{\boldsymbol{q}}^\dagger_{(z_\ell)}, \boldsymbol{B}\hat{\boldsymbol{q}}^\dagger_{(z_\ell)} \rangle\right)^{1/2} \left(\langle \hat{\boldsymbol{q}}_{(z_\ell)}, \boldsymbol{B}\hat{\boldsymbol{q}}_{(z_\ell)} \rangle\right)^{1/2}}, \tag{B1}$$

where the direct and adjoint modes are normalised such that $\langle \hat{\boldsymbol{q}}^\dagger_{(z_\ell)}, \boldsymbol{B}\hat{\boldsymbol{q}}_{(z_\ell)} \rangle = 1$ and $\langle \hat{\boldsymbol{q}}_{(z_\ell)}, \boldsymbol{B}\hat{\boldsymbol{q}}_{(z_\ell)} \rangle = 1$. It thus measures the departure of $\theta_N$ from $\pi/2$ of the angle between direct and adjoint global modes, that is, the smaller the departure the larger the non-normality. However, such a quantity does not suffice to estimate the global effect of each non-normal mechanism, lift-up and convective non-normality. To overcome such an issue, Meliga *et al.* (2009*b*) proposed to introduce the estimator $\gamma$ defined as

$$\gamma = 1 - \frac{\langle |\hat{\boldsymbol{q}}^\dagger_{(z_\ell)}|, \boldsymbol{B}|\hat{\boldsymbol{q}}_{(z_\ell)}| \rangle}{\left(\langle \hat{\boldsymbol{q}}^\dagger_{(z_\ell)}, \boldsymbol{B}\hat{\boldsymbol{q}}^\dagger_{(z_\ell)} \rangle\right)^{1/2} \left(\langle \hat{\boldsymbol{q}}_{(z_\ell)}, \boldsymbol{B}\hat{\boldsymbol{q}}_{(z_\ell)} \rangle\right)^{1/2}}, \tag{B2}$$

where $|\hat{\boldsymbol{q}}_{(z_\ell)}|^2 = |\hat{\boldsymbol{u}}_{(z_\ell)}|^2 + |\hat{p}_{(z_\ell)}|^2 = |\hat{u}_{(z_\ell)}|^2 + |\hat{v}_{(z_\ell)}|^2 + |\hat{w}_{(z_\ell)}|^2 + |\hat{p}_{(z_\ell)}|^2$ stands for the Euclidean pointwise norm. Such an estimator is used to determine whether the non-normality is due to the lift-up effect or the convective non-normality and it is bounded $0 \leq \gamma \leq 1$. In the case of dominance of the lift-up effect $\gamma$ is close to 0, i.e. a similar spatial distribution of direct and adjoint modes. On the other hand, a value of $\gamma$ close to unity implies separation in the support of the adjoint and direct global modes.

## Appendix C. Unfolding of the triple-Hopf bifurcation

### C.1. *Classification of solutions*

The trivial axisymmetric steady-state solution transits into a rotating wave

$$RW_i = \{z_j = 0| \quad \forall j \neq i, \quad i, j = 1, 2, 3\} \tag{C1}$$

via Hopf-bifurcation. Each of the three types of rotating waves are potential candidates for a primary bifurcation, and they appear in distinct regions of the parameter space ($Re$, $\Omega$).

In addition, in the vicinity of the organizing centre of the type (Hopf-Hopf) one can predict the type of secondary bifurcation from each of the rotating waves. Secondary bifurcations of rotating axisymmetric bodies are of mixed-mode type $MM_{ij}$, $i, j = 1, 2, 3$,

$$MM_{ij} = \{z_\ell = 0| \quad \forall \ell \neq i, \ell \neq j, \quad i, j, \ell = 1, 2, 3\}. \tag{C2}$$

Mixed-mode solutions are quasiperiodic solutions with possibly different azimuthal patterns. The transition to a mixed-mode solution $MM_{12}$ is possible either from $RW_1$

or $RW_2$ but not from $RW_3$. Finally, near a triple-Hopf bifurcation point there may exist a mixed mode composed of three (incommensurate) frequencies, here denoted $IMM_{123}$. This branch can bifurcate from any of the two-frequency component mixed modes $MM_{ij}$, for distinct $i, j = 1, 2, 3$.

### C.2. *Unfolding amplitude equations – types of solutions*

#### C.2.1. *Rotating waves – RW*

Rotating waves $RW_i$ are fixed points of (4.9), where two modes are null, i.e. they satisfy

$$r_i^{(RW)} = \sqrt{-\frac{\lambda_i^R}{\nu_{ii}^R}}, \quad \text{for } i = 1, 2, 3. \tag{C3}$$

Rotating wave solutions are stable if

$$\lambda_i^R > 0, \quad \lambda_j^R - \nu_{ji}^R \frac{\lambda_i^R}{\nu_{ii}^R} < 0, \quad \text{for } j \neq i, \quad \text{for } i, j = 1, 2, 3. \tag{C4}$$

#### C.2.2. *Mixed modes – $MM_{ij}$*

Mixed-mode solutions $MM_{12}$ (respectively $MM_{13}$ or $MM_{23}$) are two-component solutions of (4.9) where $r_3 = 0$ (respectively $r_2 = 0$ or $r_1 = 0$) and the other two components are non-null. Amplitudes $r_i$, $r_j$ depend on parameters as follows:

$$r_i^{(MM_{ij})} = \sqrt{\frac{\lambda_j^R \nu_{ij}^R - \lambda_i^R \nu_{jj}^R}{\det(\mathcal{V}_{kk}^R)}}, \quad r_j^{(MM_{ij})} = \sqrt{\frac{\lambda_i^R \nu_{ji}^R - \lambda_j^R \nu_{ii}^R}{\det(\mathcal{V}_{kk}^R)}}. \tag{C5a,b}$$

Here $i, j, k = 1, 2, 3$ with $i \neq j$, $k \neq i$ and $k \neq j$.

The Jacobian matrix $D\boldsymbol{f}^R$ can be written in block-diagonal form, which simplifies the stability computations. It is composed of a $2 \times 2$ and a $1 \times 1$ block. The eigenvalue associated with the $1 \times 1$ block is stable if

$$\sigma_k \equiv \frac{1}{\det(\mathcal{V}_{kk}^R)} \left[ \lambda_k^R \det(\mathcal{V}_{kk}^R) + \lambda_i^R \det(\mathcal{V}_{ik}^R) + \lambda_j^R \det(\mathcal{V}_{jk}^R) \right] < 0. \tag{C6}$$

The $2 \times 2$ block is

$$D\boldsymbol{f}_{ij}^R = 2 \begin{pmatrix} \nu_{ii}^R (r_i^{(MM_{ij})})^2 & \nu_{ij}^R r_i^{(MM_{ij})} r_j^{(MM_{ij})} \\ \nu_{ji}^R r_i^{(MM_{ij})} r_j^{(MM_{ij})} & \nu_{jj}^R (r_j^{(MM_{ij})})^2 \end{pmatrix}, \tag{C7}$$

with $r_i^{(MM_{ij})} r_j^{(MM_{ij})} = \sqrt{\lambda_i^R \lambda_j^R [\nu_{ij}^R \nu_{ji}^R + \nu_{jj}^R \nu_{ii}^R] - [(\lambda_i^R)^2 \nu_{jj}^R \nu_{ji}^R + (\lambda_j^R)^2 \nu_{ii}^R \nu_{ij}^R]} / \det(\mathcal{V}_{kk}^R)$.

The eigenvalues that govern the stability of the mixed-mode solutions of kind $MM_{ij}$ are the roots of the characteristic polynomial

$$\sigma^2 - \mathrm{tr}\left(D\boldsymbol{f}^R_{ij}\right)\sigma + \det\left(D\boldsymbol{f}^R_{ij}\right) = 0, \tag{C8}$$

where

$$\mathrm{tr}\left(D\boldsymbol{f}^R_{ij}\right) = \nu^R_{ii}\left(r_i^{(MM_{ij})}\right)^2 + \nu^R_{jj}\left(r_j^{(MM_{ij})}\right)^2 \tag{C9}$$

and

$$\det\left(D\boldsymbol{f}^R_{ij}\right) = \left(r_i^{(MM_{ij})}\right)^2\left(r_j^{(MM_{ij})}\right)^2 \det\left(\mathcal{V}^R_{kk}\right). \tag{C10}$$

Therefore, one can express the pair of eigenvalues as

$$\sigma^{\pm}_{ij} \equiv \frac{\nu^R_{ii}r_i^2 + \nu^R_{jj}r_j^2}{2} \pm \sqrt{\left(\nu^R_{ii}r_i^2 - \nu^R_{jj}r_j^2\right)^2/4 + \nu^R_{ij}\nu^R_{ji}r_i^2r_j^2}, \tag{C11}$$

where, for ease of notation, the uperscript $MM_{ij}$ has been removed. A necessary condition for the Hopf bifurcation of the mixed-mode solutions to occur is that $\nu^R_{ii}\nu^R_{jj} < 0$ and $\nu^R_{ij}\nu^R_{ji} < 0$. In other words, a Hopf bifurcation from the mixed mode may occur if one of the rotating waves comprised in the mixed mode arises from a supercritical bifurcation whereas the other arises as a result of a subcritical bifurcation from the axisymmetric steady state. This case is discussed in detail in Kuznetsov (2013, § 8.6) and is denoted as the difficult case. The case where $\nu^R_{ii}\nu^R_{jj} > 0$ is denoted as the simple case, in such a case the mixed-mode solution is a sink or a source located in the separatrix of the basin of attraction of rotating waves.

### C.3. *Interacting mixed mode – $IMM_{123}$*

The $IMM_{123}$ mode is a 3-tori solution (phases $\phi_i$ are non-resonant) with their amplitudes determined as the solution of the following linear system:

$$\boldsymbol{r}^2 \equiv (r_1^2, r_2^2, r_3^2)^{\mathrm{T}} = -\left(\mathcal{V}^R\right)^{-1}\Lambda^R = \frac{-1}{\det\mathcal{V}^R}\begin{pmatrix} \det\mathcal{V}^R{}_{11}\lambda^R_1 + \det\mathcal{V}^R{}_{21}\lambda^R_2 + \det\mathcal{V}^R{}_{31}\lambda^R_3 \\ \det\mathcal{V}^R{}_{12}\lambda^R_1 + \det\mathcal{V}^R{}_{22}\lambda^R_2 + \det\mathcal{V}^R{}_{32}\lambda^R_3 \\ \det\mathcal{V}^R{}_{13}\lambda^R_1 + \det\mathcal{V}^R{}_{23}\lambda^R_2 + \det\mathcal{V}^R{}_{33}\lambda^R_3 \end{pmatrix}. \tag{C12}$$

The stability of the interacting mixed-mode solution is determined by the eigenvalues of the Jacobian $D\boldsymbol{f}^R$,

$$D\boldsymbol{f}^R \equiv 2\begin{pmatrix} \nu^R_{11}r_1^2 & \nu^R_{12}r_1r_2 & \nu^R_{13}r_1r_3 \\ \nu^R_{21}r_1r_2 & \nu^R_{22}r_2^2 & \nu^R_{23}r_3r_2 \\ \nu^R_{31}r_1r_3 & \nu^R_{32}r_3r_2 & \nu^R_{33}r_3^2 \end{pmatrix}. \tag{C13}$$

The eigenvalues of $D\boldsymbol{f}^R$ are roots of its characteristic polynomial denoted as $p(D\boldsymbol{f}^R)$,

$$\left.\begin{gathered} p(D\boldsymbol{f}^R) \equiv \sigma^3 - \mathbb{I}_1\sigma^2 + \mathbb{I}_2\sigma - \mathbb{I}_3 = 0, \\ \mathbb{I}_1 = \mathrm{tr}\left(D\boldsymbol{f}^R\right), \quad \mathbb{I}_2 = \frac{1}{2}\left[\left(\mathrm{tr}\left(D\boldsymbol{f}^R\right)\right)^2 - \mathrm{tr}\left([D\boldsymbol{f}^R]^2\right)\right], \quad \mathbb{I}_3 = \det\left(D\boldsymbol{f}^R\right). \end{gathered}\right\} \tag{C14}$$

The trace of the Jacobian can be expressed as a function of the square of the amplitudes $r_1^2$, $r_2^2$ and $r_3^2$ and the real part of the matrix of coefficients $\mathcal{V}$,

$$\mathrm{tr}\left(D\boldsymbol{f}^R\right) \equiv 2\left(\nu_{11}^R r_1^2 + \nu_{22}^R r_2^2 + \nu_{33}^R r_3^2\right), \tag{C15}$$

similarly the second invariant of the Jacobian

$$\frac{1}{2}\left[\left(\mathrm{tr}\left(D\boldsymbol{f}^R\right)\right)^2 - \mathrm{tr}\left([D\boldsymbol{f}^R]^2\right)\right] \equiv 4\left(r_1^2 r_2^2 \det \mathcal{V}_{33}^R + r_1^2 r_3^2 \det \mathcal{V}_{22}^R + r_2^2 r_3^2 \det \mathcal{V}_{11}^R\right), \tag{C16}$$

and the determinant

$$\det\left(D\boldsymbol{f}^R\right) = 8 r_1^2 r_2^2 r_3^2 \det \mathcal{V}^R. \tag{C17}$$

The characteristic polynomial (C14) is a cubic polynomial with real coefficients. Thus, the eigenvalues $\sigma$ of the Jacobian $D\boldsymbol{f}^R$ are either all real or one of them is real and the other two are complex conjugate. The nature of the eigenvalues depends on the discriminant of the cubic equation. A stationary bifurcation occurs when $\det(D\boldsymbol{f}^R) = 0$, which under the generic condition $\det \mathcal{V}^R \neq 0$ only occurs at the origin of the $IMM_{123}$.

A Hopf bifurcation arises when the following conditions are satisfied:

$$\left.\begin{aligned} &\mathrm{tr}\left(D\boldsymbol{f}^R\right) < 0, \quad \left[\left(\mathrm{tr}\left(D\boldsymbol{f}^R\right)\right)^2 - \mathrm{tr}\left([D\boldsymbol{f}^R]^2\right)\right] > 0 \\ \text{and} \quad &\left[\left(\mathrm{tr}\left(D\boldsymbol{f}^R\right)\right)^3 - \mathrm{tr}\left(D\boldsymbol{f}^R\right)\mathrm{tr}\left([D\boldsymbol{f}^R]^2\right)\right] = \det\left(D\boldsymbol{f}^R\right). \end{aligned}\right\} \tag{C18}$$

The condition $\mathrm{tr}\,(D\boldsymbol{f}^R) < 0$ ensures that Hopf bifurcation is the primary bifurcation of the $IMM_{123}$ solution, i.e. the real eigenvalue is negative. Such a condition holds true in the supercritical case, when $\nu_{ii} < 0$, for $i = 1, 2, 3$. Additionally, there is a change in the nature of the solution $IMM_{123}$ whenever the discriminant changes sign, it changes from sink to stable foci, from source to unstable foci, from saddle to saddle foci or vice versa. Even though these local changes in the nature of the fixed-point solution $IMM_{123}$ cannot be considered as a local bifurcation, they could be linked to global changes in dynamics, e.g. the appearance of a heteroclinic cycle as in the difficult case of a Hopf-Hopf bifurcation (Kuznetsov 2013, Ch. 8.7.). Finally, a necessary and sufficient condition for the stability of the asymptotic stability of the $IMM_{123}$ solution can be expressed in terms of the invariants of the Jacobian matrix

$$\mathbb{I}_1 < 0, \quad \mathbb{I}_2 > 0, \quad \mathbb{I}_3 < 0, \quad \mathbb{I}_1\mathbb{I}_2 > \mathbb{I}_3. \tag{C19}$$

Inspection of (C19) shows that the condition for the Hopf bifurcation indeed corresponds to the limit case of the condition $\mathbb{I}_1\mathbb{I}_2 \geq \mathbb{I}_3$.

## Appendix D. Mesh convergence

Mesh independent solutions have been verified systematically. First, we have considered a given mesh refinement, and we have varied the physical size of the domain. We have observed that, for a domain length of 50 diameters downstream of the sphere centre, 20 diameters upstream of the cylinder centre and 20 in the cross-stream direction, the effects of the boundary condition do not have an effect on the solution. Secondly, we

| | $M_1$ | $M_2$ | $M_3$ | $M_4$ |
|---|---|---|---|---|
| Num. tri. | $5.6 \times 10^3$ | $2.4 \times 10^4$ | $3.9 \times 10^4$ | $8.1 \times 10^4$ |
| $h_{max}$ | $3D$ | $2D$ | $1D$ | $0.25D$ |
| $h_{aniso}$ | 5 | 2 | 1 | 1 |
| Adaptation | Steady state | Steady state and modes | Same as $M_2$ | Same as $M_2$ |

Table 7. Properties of the meshes used in the study of mesh convergence.

| Coef. | $M_1$ | $M_2$ | $M_3$ | $M_4$ |
|---|---|---|---|---|
| $\nu_{22}^B$ | $-1.8 + 0.23\mathrm{i}$ | $-1.8 + 0.22\mathrm{i}$ | $-1.8 + 0.22\mathrm{i}$ | $-1.8 + 0.22\mathrm{i}$ |
| $\nu_{23}^B$ | $-2.1 - 0.26\mathrm{i}$ | $-2.0 - 0.27\mathrm{i}$ | $-1.9 - 0.21\mathrm{i}$ | $-1.9 - 0.0.22\mathrm{i}$ |
| $\nu_{32}^B$ | $-0.32 - 0.042\mathrm{i}$ | $-0.35 - 0.027\mathrm{i}$ | $-0.34 - 0.027\mathrm{i}$ | $-0.34 - 0.031\mathrm{i}$ |
| $\nu_{33}^B$ | $-1.6 + 0.91\mathrm{i}$ | $-1.6 + 0.87\mathrm{i}$ | $-1.7 + 0.89\mathrm{i}$ | $-1.7 + 0.89\mathrm{i}$ |

Table 8. Cubic coefficients of the normal form (4.9) evaluated at the codimension-two point $A$.

have looked at the effect of mesh refinement on the properties of the solution. For that purpose, we performed a parametric study of eigenvalues, normal form coefficients of the codimension-two point $B$ (table 8). Every mesh is initially computed by Delauny triangulation, and subsequently adapted to either base flow, eigenmode or both, following the methodology described in Fabre *et al.* (2018); and their properties are summarised in table 7.

## Appendix E. Higher-order dynamic mode decomposition

This analysis allows us to gain valuable insight on the dominant modes and associated spatio-temporal flow structures which govern the wake for the different regimes encountered in our transition scenario (figure 9). As detailed by Le Clainche & Vega (2017*a*), Vega & Le Clainche (2020), HODMD is an extension of the standard dynamic mode decomposition (DMD) technique (Schmid 2010), which has been proven useful to study flow structures associated with quasiperiodic (featuring a large number of frequencies) or transitional regimes (Le Clainche & Vega 2017*b*), where the classical DMD approach may fail, being therefore applicable to complex spectral and spatial cases, as the problem investigated herein. The number of modes identified by HODMD is determined by $M$, whose value is related to the spatial resolution of the input data, and $N$, determined by the temporal resolution.

Thus, the present HODMD tool has been applied to resolve the spatial structure related to dominant frequencies characterizing the different flow regimes identified from the DNS results. Typically, the input data consists of a set of $N = 2000$ streamwise vorticity, $\varpi_z$, snapshots interpolated in a $80 \times 80$ ($M = 6400$) rectangular grid whose domain is $(x, y) \in [-1, 1]$ located at $z = 2.5$. Moreover, it should be noted that the vorticity snapshots are equally spaced in time with a $\Delta t = 0.15$. Such temporal parameters allow us to resolve frequencies between $St_{min} = 0.003$ and $St_{max} = 3.33$, according to the Nyquist criterion. Given such input data, which satisfies the condition $N < M$, the values of the main HODMD parameters, i.e. order, $d$, and tolerance, $\epsilon$, have been calibrated and fixed at $d = 50$ and $\epsilon = 1e - 6$ to capture a great number of modes.

## Appendix F. The 0-1 test

The quantitative 0-1 method (Gottwald & Melbourne 2004) is used to evaluate the dynamic complexity and likely chaotic nature of the flow regimes. The method is directly applied to time series of any scalar, as the pointwise fluctuating radial velocity $U'$. In particular, given a set of data from velocity of $N$ samples, $U'(j)$ with $j = 1, \ldots, N$, a translation variable is defined as $p(m) = \Sigma_{j=1}^{m_s} U'(j)\cos(js)$, for $m = 1, \ldots, m_s$ and $s \in (0, \pi/5)$. The mean square displacement is defined as $M_c(m) = \lim_{N\to\infty}(1/N)\Sigma_{j=1}^{N}[p_c(j+m) - p(j)]^2$, which requires that $m_s \leq N$ (as in Gottwald & Melbourne (2004), we use $m_s = N/10$). Thus, the variable $M_c(m)$ is bounded when $p(j)$ is also bounded which is the case for regular dynamics. However, if the translation variable $p(m)$ is chaotic, $M_c(m)$ grows linearly with $m$, so that an asymptotic growth $K$ can be defined as

$$K = \lim_{m\to\infty} \frac{\log(M_c(m))}{\log(m)}, \tag{F1}$$

which will take the value of 1 for chaotic dynamics and 0 for regular dynamics. Further information and validation of the use of this estimate to evaluate the dynamic nature of complex flow regimes can be found in Lorite-Díez & Jiménez-González (2020).

## References


Allen, T. & Moroz, I.M. 1997 Hopf-Hopf and Hopf-steady mode interactions with O(2) symmetry in Langmuir circulations. *Geophys. Astrophys. Fluid Dyn.* **85** (3–4), 243–278.

Armbruster, D., Guckenheimer, J. & Holmes, P. 1989 Kuramoto–Sivashinsky dynamics on the center–unstable manifold. *SIAM J. Appl. Maths* **49** (3), 676–691.

Auguste, F., Fabre, D. & Magnaudet, J. 2010 Bifurcations in the wake of a thick circular disk. *Theor. Comput. Fluid Dyn.* **24**, 305–313.

Auguste, F. & Magnaudet, J. 2018 Path oscillations and enhanced drag of light rising spheres. *J. Fluid Mech.* **841**, 228–266.

Barois, T., Huck, P.D., Paleo, C., Bourgoin, M. & Volk, R. 2019 Probing fluid torque with a hydrodynamical trap: rotation of chiral particles levitating in a turbulent jet. *Phys. Fluids* **31** (12), 125116.

Callaham, J.L., Brunton, S.L. & Loiseau, J.-C. 2022 On the role of nonlinear correlations in reduced-order modelling. *J. Fluid Mech.* **938**, A1.

Chomaz, J.-M. 2005 Global instabilities in spatially developing flows: non-normality and nonlinearity. *Annu. Rev. Fluid Mech.* **37** (1), 357–392.

Chossat, P., Golubitsky, M. & Lee Keyfitz, B. 1986 Hopf-Hopf mode interactions with O(2) symmetry. *Dyn. Stab. Syst.* **1** (4), 255–292.

Chrust, M., Goujon-Durand, S. & Wesfreid, J.E. 2013 Loss of a fixed plane symmetry in the wake of a sphere. *J. Fluid Mech.* **41**, 51–56.

Citro, V., Siconolfi, L., Fabre, D., Giannetti, F. & Luchini, P. 2017 Stability and sensitivity analysis of the secondary instability in the sphere wake. *AIAA J.* **55**, 3661–3668.

Citro, V., Tchoufag, J., Fabre, D., Giannetti, F. & Luchini, P. 2016 Linear stability and weakly nonlinear analysis of the flow past rotating spheres. *J. Fluid Mech.* **807**, 62–86.

Cvitanovic, P., Artuso, R., Mainieri, R., Tanner, G., Vattay, G., Whelan, N. & Wirzba, A. 2005 Chaos: classical and quantum. *ChaosBook.org (Niels Bohr Institute, Copenhagen 2005)* **69**, 25.

Ern, P., Risso, F., Fabre, D. & Magnaudet, J. 2012 Wake-induced oscillatory paths of bodies freely rising or falling in fluids. *Annu. Rev. Fluid Mech.* **44** (1), 97–121.

Fabre, D., Auguste, F. & Magnaudet, J. 2008 Bifurcations and symmetry breaking in the wake of axisymmetric bodies. *Phys. Fluids* **20**, 051702.

Fabre, D., Citro, V., Ferreira Sabino, D., Bonnefis, P., Sierra, J., Giannetti, F. & Pigou, M. 2018 A practical review on linear and nonlinear global approaches to flow instabilities. *Appl. Mech. Rev.* **70** (6), 060802.

Fabre, D., Tchoufag, J., Citro, V., Giannetti, F. & Luchini, P. 2017 The flow past a freely rotating sphere. *Theor. Comput. Fluid Dyn.* **31**, 475–482.

Feng, Z.-G. & Musong, S.G. 2014 Direct numerical simulation of heat and mass transfer of spheres in a fluidized bed. *Powder Technol.* **262**, 62–70.

GIANNETTI, F. & LUCHINI, P. 2007 Structural sensitivity of the first instability of the cylinder wake. *J. Fluid Mech.* **581** (1), 167–197.

GOLUBITSKY, M. & LANGFORD, W.F. 1988 Pattern formation and bistability in flow between counterrotating cylinders. *Physica* D **32** (3), 362–392.

GOLUBITSKY, M., STEWART, I. & SCHAEFFER, D.G. 2012 *Singularities and Groups in Bifurcation Theory: Volume II*, vol. 69. Springer Science & Business Media.

GOTTWALD, G.A. & MELBOURNE, I. 2004 Proceedings of the Royal Society of London. Series A: mathematical and physical sciences. *Proc. R. Soc. Lond.* A **460** (2042), 603–611.

GOTTWALD, G.A. & MELBOURNE, I. 2009 Higher order dynamic mode decomposition and its applications. *SIAM J. Appl. Dyn. Syst.* **8** (1), 129–145.

GUCKENHEIMER, J. 2010 Bifurcations of dynamical systems. In *Dynamical Systems* (ed. C. Marchioro), pp. 5–123. Springer.

GUO, H., FAUCI, L., SHELLEY, M. & KANSO, E. 2018 Bistability in the synchronization of actuated microfilaments. *J. Fluid Mech.* **836**, 304–323.

HARAGUS, M. & IOOSS, G. 2010 *Local Bifurcations, Center Manifolds, and Normal Forms in Infinite-Dimensional Dynamical Systems*. Springer Science & Business Media.

HOMBURG, A.J. & SANDSTEDE, B. 2010 Homoclinic and heteroclinic bifurcations in vector fields. *Handb. Dyn. Syst.* **3**, 379–524.

HUANG, Y., RISTROPH, L., LUHAR, M. & KANSO, E. 2018 Bistability in the rotational motion of rigid and flexible flyers. *J. Fluid Mech.* **849**, 1043–1067.

JIMÉNEZ-GONZÁLEZ, J.I., SANMIGUEL-ROJAS, E., SEVILLA, A. & MARTÍNEZ-BAZÁN, C. 2013 Laminar flow past a spinning bullet-shaped body at moderate angular velocities. *J. Fluid Mech.* **43**, 200–219.

JIMÉNEZ-GONZÁLEZ, J.I., SEVILLA, A., SANMIGUEL-ROJAS, E. & MARTÍNEZ-BAZÁN, C. 2014 Global stability analysis of the axisymmetric wake past a spinning bullet-shaped body. *Intl J. Fluid Mech. Res.* **748**, 302–327.

JIMÉNEZ-GONZÁLEZ, J.I., MANGLANO-VILLAMARÍN, C. & COENEN, W. 2019 The role of geometry on the global instability of wakes behind streamwise rotating axisymmetric bodies. *Eur. J. Mech. B/Fluids* **76**, 205–222.

JOHNSON, T.A. & PATEL, V.C. 1999 Flow past a sphere up to Reynolds number of 300. *J. Fluid Mech.* **378**, 19–70.

KIM, D. & CHOI, H. 2002 Laminar flow past a sphere rotating in the streamwise direction. *J. Fluid Mech.* **461**, 365–386.

KUZNETSOV, Y.A. 2013 *Elements of Applied Bifurcation Theory*, vol. 112. Springer Science & Business Media.

KUZNETSOV, Y.A. & MEIJER, H.G.E. 2005 Numerical normal forms for codim 2 bifurcations of fixed points with at most two critical eigenvalues. *SIAM J. Sci. Comput.* **26** (6), 1932–1954.

LE CLAINCHE, S. & VEGA, J. 2017*a* Higher order dynamic mode decomposition. *SIAM J. Appl. Dyn. Syst.* **16** (2), 882–925.

LE CLAINCHE, S. & VEGA, J.M. 2017*b* Higher order dynamic mode decomposition to identify and extrapolate flow patterns. *Phys. Fluids* **29** (8), 084102.

LIU, Q. & PROSPERETTI, A. 2010 Wall effects on a rotating sphere. *J. Fluid Mech.* **657**, 1–21.

LOISEAU, J.-C. & BRUNTON, S.L. 2018 Constrained sparse galerkin regression. *J. Fluid Mech.* **838**, 42–67.

LOISEAU, J.-C., NOACK, B.R. & BRUNTON, S.L. 2018 Sparse reduced-order modelling: sensor-based dynamics to full-state estimation. *J. Fluid Mech.* **844**, 459–490.

LORITE-DÍEZ, M. & JIMÉNEZ-GONZÁLEZ, J.I. 2020 Description of the transitional wake behind a strongly streamwise rotating sphere. *J. Fluid Mech.* **896**, A18.

MARQUET, O., LOMBARDI, M., CHOMAZ, J.-M., SIPP, D. & JACQUIN, L. 2009 Direct and adjoint global modes of a recirculation bubble: lift-up and convective non-normalities. *J. Fluid Mech.* **622**, 1–21.

MARQUET, O., SIPP, D. & JACQUIN, L. 2008 Sensitivity analysis and passive control of cylinder flow. *J. Fluid Mech.* **615**, 221–252.

MATHAI, V., ZHU, X., SUN, C. & LOHSE, D. 2018 Flutter to tumble transition of buoyant spheres triggered by rotational inertia changes. *Nat. Commun.* **9**, 1792.

MELIGA, P., CHOMAZ, J.-M. & SIPP, D. 2009*a* Global mode interaction and pattern selection in the wake of a disk: a weakly nonlinear expansion. *J. Fluid Mech.* **633**, 159–189.

MELIGA, P., CHOMAZ, J.-M. & SIPP, D. 2009*b* Unsteadiness in the wake of disks and spheres: instability, receptivity and control using direct and adjoint global stability analyses. *J. Fluids Struct.* **25** (4), 601–616.

MELIGA, P., GALLAIRE, F. & CHOMAZ, J.-M. 2012 A weakly nonlinear mechanism for mode selection in swirling jets. *J. Fluid Mech.* **699**, 216–262.

NEWHOUSE, S., RUELLE, D. & TAKENS, F. 1978 Occurrence of strange axiom a attractors near quasi periodic flows on $t^m$, $m \geq 3$. *Commun. Math. Phys.* **64** (1), 35–40.
NI, A. 2019 Hyperbolicity, shadowing directions and sensitivity analysis of a turbulent three-dimensional flow. *J. Fluid Mech.* **863**, 644–669.
NIAZMAND, H. & RENKSIZBULUT, M. 2005 Flow past a spinning sphere with surface blowing and heat transfer. *Trans. ASME J. Fluids Engng* **127** (1), 163–171.
PASSMORE, M.A., TUPLIN, S., SPENCER, A. & JONES, R. 2008 Experimental studies of the aerodynamics of spinning and stationary footballs. *Proc. Inst. Mech. Engrs* C **222** (2), 195–205.
PIER, B. 2013 Periodic and quasiperiodic vortex shedding in the wake of a rotating sphere. *J. Fluids Struct.* **41**, 43–50.
PODVIGINA, O.M. 2006*a* The center manifold theorem for center eigenvalues with non-zero real parts. arXiv:physics/0601074.
PODVIGINA, O.M. 2006*b* Investigation of the abc flow instability with application of centre manifold reduction. *Dyn. Syst.* **21** (2), 191–208.
POON, E.K.W., OOI, A.S.H., GIACOBELLO, M. & COHEN, R.C.Z. 2010 Laminar flow structures from a rotating sphere: effect of rotating axis angle. *Intl J. Heat Fluid Flow* **31** (5), 961–972, 6th International Symposium on Turbulence, Heat and Mass Transfer, Rome, Italy, 14-18 September 2009.
RABAULT, J., FAULI, R.A. & CARLSON, A. 2019 Curving to fly: synthetic adaptation unveils optimal flight performance of whirling fruits. *Phys. Rev. Lett.* **122**, 024501.
REN, C., CHENG, L., XIONG, C., TONG, F. & CHEN, T. 2021 Bistabilities in two parallel kármán wakes. *J. Fluid Mech.* **929**, A5.
RENARDY, M., RENARDY, Y., SURESHKUMAR, R. & BERIS, A.N. 1996 Hopf-Hopf and steady-Hopf mode interactions in Taylor–Couette flow of an upper convected Maxwell liquid. *J. Non-Newtonian Fluid Mech.* **63** (1), 1–31.
ROBINSON, G. & ROBINSON, I. 2013 The motion of an arbitrarily rotating spherical projectile and its application to ball games. *Phys. Scr.* **88** (1), 018101.
ROSHKO, A. 1993 Perspectives on bluff body aerodynamics. *J. Wind Engng Ind. Aerodyn.* **49** (1), 79–100.
RUCKLIDGE, A.M., WEISS, N.O., BROWNJOHN, D.P., MATTHEWS, P.C. & PROCTOR, M.R.E. 2000 Compressible magnetoconvection in three dimensions: pattern formation in a strongly stratified layer. *J. Fluid Mech.* **419**, 283–323.
SAKAMOTO, H. & HANIU, H. 1990 A study on vortex shedding from spheres in a uniform flow. *Trans. ASME J. Fluids Engng* **112** (4), 386–392.
SCHMID, P.J. 2010 Dynamic mode decomposition of numerical and experimental data. *J. Fluid Mech.* **656**, 5–28.
SHI, P. & RZEHAK, R. 2019 Lift forces on solid spherical particles in unbounded flows. *Chem. Engng Sci.* **208**, 115145.
SIERRA, J., FABRE, D. & CITRO, V. 2020*a* Efficient stability analysis of fluid flows using complex mapping techniques. *Comput. Phys. Commun.* **251**, 107100.
SIERRA, J., FABRE, D., CITRO, V. & GIANNETTI, F. 2020*b* Bifurcation scenario in the two-dimensional laminar flow past a rotating cylinder. *J. Fluid Mech.* **905**, A2.
SIPP, D. 2012 Open-loop control of cavity oscillations with harmonic forcings. *J. Fluid Mech.* **708**, 439–468.
SKARYSZ, M., ROKICKI, J., GOUJON-DURAND, S. & WESFREID, J.E. 2018 Experimental investigation of the wake behind a rotating sphere. *Phys. Rev. Fluids* **3**, 013905.
SUBRAMANIAN, P., SUJITH, R.I. & WAHI, P. 2013 Subcritical bifurcation and bistability in thermoacoustic systems. *J. Fluid Mech.* **715**, 210–238.
SUCKALE, J., QIN, Z., PICCHI, D., KELLER, T. & BATTIATO, I. 2018 Bistability of buoyancy-driven exchange flows in vertical tubes. *J. Fluid Mech.* **850**, 525–550.
TOMBOULIDES, A.G. & ORSZAG, S.A. 2000 Numerical investigation of transitional and weak turbulent flow past a sphere. *J. Fluid Mech.* **416**, 45–73.
VARÉ, T., NOUAR, C., MÉTIVIER, C. & BOUTERAA, M. 2020 Stability of hexagonal pattern in Rayleigh–Bénard convection for thermodependent shear-thinning fluids. *J. Fluid Mech.* **905**, A33.
VEGA, J.M. & LE CLAINCHE, S. 2020 *Higher Order Dynamic Mode Decomposition and Its Applications*. Academic Press.
VERHULST, F. 2007 Singular perturbation methods for slow–fast dynamics. *Nonlinear Dyn.* **50** (4), 747–753.
YALNIZ, G. & BUDANUR, N.B. 2020 Inferring symbolic dynamics of chaotic flows from persistence. *Chaos* **30** (3), 033109.
YALNIZ, G., HOF, B. & BUDANUR, N.B. 2021 Coarse graining the state space of a turbulent flow using periodic orbits. *Phys. Rev. Lett.* **126** (24), 244502.

# Wake dynamics in buoyancy-driven flows: Steady-state–Hopf-mode interaction with math xmlns="http://www.w3.org/1998/Math/MathML">mi mathvariant="normal">O/mi>/math>(2) symmetry revisited

Javier Sierra-Ausin, David Fabre, and Edgar Knobloch

Phys. Rev. E **109**, 014216 — Published 12 January 2024

DOI: 10.1103/PhysRevE.109.014216

# Wake dynamics in buoyancy-driven flows: steady state–Hopf mode interaction with O(2) symmetry revisited

Javier Sierra-Ausin[1,2], David Fabre[1] and Edgar Knobloch[3]
[1] *UPS-IMFT, Allée du Professeur Camille Soula, 31000 Toulouse, France*
[2] *Università degli Studi di Salerno, 132 Via Giovanni Paolo II, 84084 Fisciano, Salerno, Italy and*
[3] *Department of Physics, University of California at Berkeley, Berkeley, California 94720, USA*
(Dated: November 14, 2023)

We present a detailed mathematical study of a truncated normal form relevant to the bifurcations observed in wake flow past axisymmetric bodies, with and without thermal stratification. We employ abstract normal form analysis to identify possible bifurcations and the corresponding bifurcation diagrams in parameter space. The bifurcations and the bifurcation diagrams are interpreted in terms of symmetry considerations. Particular emphasis is placed on the presence of attracting robust heteroclinic cycles in certain parameter regimes. The normal form coefficients are computed for several examples of wake flows behind buoyant disks and spheres, and the resulting predictions compared with the results of direct numerical flow simulations. In general, satisfactory agreement is obtained.

## I. INTRODUCTION

Bifurcation, defined here as a transition between two states with different symmetry, is a key concept in many fields of modern physics. Generally speaking, the larger the symmetry of a problem, the greater is the number of ways the symmetry may be broken, leading to the richest collections of bifurcation scenarios. *Equivariant bifurcation theory* [1] constitutes a mathematical framework for studying such problems, and predicts the possible states that may arise and the bifurcation routes between them. A key idea for the parameter space exploration of physical problems is the identification of points of *codimension two* (or greater), namely sets of parameters at which two (or more) bifurcations arise simultaneously. The richest range of possible behavior is usually encountered in the vicinity of such points. The theory also provides a systematic procedure for constructing truncated dynamical systems called *normal forms* that enable a classification of all admissible states near such codimension-two points and their stability properties. This classification depends only on the symmetry properties of the problem and is thus common to all problems involving the same symmetry.

Fluid mechanics has proved to be a particularly rich playground for the investigation of bifurcations [2]. The classical problems for which bifurcation theory has proved both relevant and helpful include, among others, Taylor–Couette flow (TCF, [3, 4]) and Rayleigh-Bénard convection (RBC, [5]). Bifurcation theory is also relevant to wake flows, with the wake of a fixed two-dimensional (2D) cylinder transverse to the flow providing the classic example. Here the wake experiences a Hopf bifurcation leading to the von Kármán vortex street beyond $\mathrm{Re} \approx 47$, where Re is a suitably defined Reynolds number. The case where the cylinder rotates was recently shown to give rise to a much richer range of behavior that was also successfully explained using bifurcation theory [6].

The present work is primarily devoted to transitions in *wake flows past axisymmetric objects* (WFA) within a homogeneous fluid. The geometry which attracted the largest number of studies is that of a sphere. Here, experiments [7, 8] and numerical investigations [9–11] reveal a primary steady state bifurcation resulting in the loss of axisymmetry, followed by a secondary bifurcation leading to reflection-symmetric periodic states. The case of a rotating sphere, recently analysed in [12], reveals a primary bifurcation leading to a rotating wave pattern. Secondary and tertiary bifurcations are therein interpreted as the result of an interaction between three rotating wave patterns. The cases of disks [13–15] and ellipsoids [15] have also been investigated, revealing a collection of new states and bifurcation scenarios involving the loss and recovery of planar symmetry.

Two other related classes of problems will also be considered here. The first is the path taken by objects in free motion, such as rising bubbles or falling solid disks (WFA-FO problem, see [16]). For falling or rising disks, experiments [16–19]) and simulations [20, 21] reveal a rich range of possible behavior. As shown in [22], linear stability analysis predicts correctly the primary bifurcations for these flows, while weakly nonlinear analysis [23] reproduces the zigzag path observed in experiments. The case of a rising bubble proved to be more challenging. For bubbles of a fixed ellipsoidal shape, linear stability analysis predicts correctly the destabilization of the path observed in experiments [24], while [25] conducted a linear stability analysis for a deformable bubble, leading to the conclusion that shape deformation plays little role in the resulting dynamics.

The last class of problems considered here is closely related to the two previous ones and corresponds to wake flows past fixed objects in a thermally stratified background involving mixed convection due to Prandtl number effects (WFA-MC). Motivated by interest in the transition to a turbulent wake in this system, the authors of Ref. [26] conducted a parameter study using numerical simulations at two different Prandtl numbers, $\mathrm{Pr} = 0.72$ and $\mathrm{Pr} = 7$. For both ellipsoids and disks [15], a large collection of states with various symmetry properties was

revealed, closely related to the states found in the two previous sets of problems.

Fabre et al. [13] were the first to recognize that equivariant bifurcation theory is relevant to these sets of problems, and to note that the relevant spatial symmetry (corresponding to the mathematical group $O(2)$) is the same as that in Taylor-Couette flow, thus highlighting an unexpected analogy between both systems. Fabre et al. thus reconsidered the normal form initially introduced in [3, 4] for the TCF problem, and showed that with an appropriate choice of the coefficients, the dynamics of the flow past a sphere and a thin disk are correctly reproduced. Auguste et al. [14] successfully applied the same approach to a thick disk. Subsequently, Meliga et al. [27] reconsidered the case of the sphere and the thick disk using a multiple scale analysis to determine the coefficients in the normal form. Their results are in agreement with the numerical simulations of [13], thereby confirming the relevance of the approach. However, their derivation method is not fully rigorous, as the problem is not strictly of codimension two. However, exact codimension-two points were detected in both the WFA-MC [26] and the WFA-FO [22] problems, indicating that in these problems a rigorous normal form derivation may be undertaken.

As previously mentioned, Golubitsky and collaborators [3, 28] investigated solutions of the normal form corresponding to the steady/Hopf interaction in the presence of $O(2)$ symmetry, with application to the TCF problem, exploring the dynamics up to secondary bifurcations. However, they do not provide a systematic study of the problem and many details are left to the reader. Their study also overlooks possible ternary bifurcation to states which are not observed in the TCF problem but are nonetheless relevant to the problems considered here. The purpose of this work is thus to revisit and extend these results and to explain how they can be applied to the TCF, WFA, and WFA-MC problems. Our method differs from that of Golubitsky et al. [3, 28] in several aspects:

- The study is restricted to a truncated problem where only third-order nonlinearities are considered.
- Two systems are introduced: a polar coordinate representation that eliminates the two continuous symmetries of the system and a second system written in its natural Hilbert basis which reduces the dynamics to its fundamental domain. These techniques, when systematically employed, reduce the six-dimensional system to four dimensions and the fixed-point solutions to a single representative of each group orbit and enable us to establish the presence of robust heteroclinic cycles in this system.
- The amplification rates $\lambda_s$ and $\lambda_h$ of the two primary modes are included explicitly in the unfolding of the problem. Golubitsky et al. considered the amplification rates as unspecified functions of a single control parameter only.

Our approach is thus much more in line with that used by Hirschberg and Knobloch [29, 30] for the related problem of interaction of two steady-state modes with $O(2)$ symmetry. There are strong similarities between these two situations, as emphasized in what follows.

The paper is organized as follows. Section II presents the normal form and introduces a reduction to polar coordinates that is used in what follows. Section III proposes a general nomenclature for the various solutions of the problem. Section IV reviews the fixed-point solutions of the normal form: pure modes, mixed modes, and possible bifurcations of higher order. Section V considers a degenerate case in which a number of details can be investigated analytically. Section VI presents a numerical exploration of various solutions of the truncated problem. Next, section VII explains how the various results can be used to construct consistent stability diagrams, while section VIII applies these results to the flow past a fixed axisymmetric object, in particular, a disk and a sphere. The paper concludes with a brief discussion in Section IX. Some technical details are relegated to a pair of Appendices. Background to the techniques we use and their application to problems arising in fluid mechanics may be found in [2].

## II. NORMAL FORM AND REDUCTION TO AMPLITUDE EQUATIONS

### A. Problem parametrization

The flow state $\mathbf{q} = [\mathbf{u}, p]$ is specified by the velocity field $\mathbf{u}$ and the hydrodynamic pressure $p$ (the WFA-MC also includes the temperature field $T$). Near the mode interaction (a codimension-two bifurcation) the flow state takes the form

$$\begin{aligned}\mathbf{q} = \; & \mathbf{Q}_0 + \mathrm{Re}\big[a_0(t)e^{-i\theta}\hat{\mathbf{q}}_s\big] \\ & + \mathrm{Re}\big[a_1(t)e^{-i\theta}\hat{\mathbf{q}}_{h,-1} + a_2(t)e^{i\theta}\hat{\mathbf{q}}_{h,1}\big] + \text{h.o.t.}\end{aligned} \tag{1}$$

Here $\mathbf{Q}_0$ is the steady-state flow state that is invariant under the action of the whole $O(2)$ group, $\hat{\mathbf{q}}_s$ is the steady mode and $\hat{\mathbf{q}}_h$ is the Hopf (unsteady) mode. The Ansatz in eq. (1) takes into account the continuous (translation or rotation) symmetry via the terms $e^{\pm i\theta}$, where $\theta \in S^1$ is an angle-like variable in the periodicity direction; for axisymmetric problems it corresponds to the azimuthal angle, while in the TCF it corresponds to the axial direction: $\theta \equiv -2\pi x/\Lambda$, where $\Lambda$ is the mode wavelength. Here without loss of generality the azimuthal wave number $m$ is taken to be $m = 1$. Both the steady-state flow and the eigenmodes are functions of other spatial variables (radial distance and azimuthal angle for the TCF; radial and axial distances for axisymmetric wake problems), but this dependence is not of importance here.

In the following we shall be interested in the dynamics arising from the interaction between the amplitude $a_0$ of the steady mode and the amplitudes $a_1$, $a_2$ of the left and right-rotating waves associated with the Hopf mode. All three amplitudes are in general complex functions of the time $t$ and their behavior near the mode interaction is described by normal form theory.

### B. Universal normal form

The normal form is obtained in a standard way: provided the original system of equations is $\Gamma$-equivariant under the group $\Gamma \equiv O(2) \times S^1$, the normal form must also be $\Gamma$-equivariant. The Hilbert–Weyl and Poénaru theorems, stated in [28, Ch 1], ensure the existence of a finite set of $\Gamma$-equivariant polynomials generating the $\Gamma$-equivariant Taylor expansion (at the origin) of any smooth mapping. The group $\Gamma$ acts on $\mathbb{C}^3$ which decomposes into irreducibles $\mathbb{C} \oplus \mathbb{C}^2$ corresponding to the steady and Hopf modes. The action of the group $\Gamma$ is generated by rotations $R_\alpha$, reflection $\kappa$, and the temporal phase shift $\Phi$ of the Hopf mode. The canonical representation of these actions is as follows:

$$\begin{array}{rl} R_\alpha & : (a_0, a_1, a_2) \to \big(a_0 e^{i\alpha}, a_1 e^{i\alpha}, a_2 e^{-i\alpha}\big) \\ \Phi & : (a_0, a_1, a_2) \to \big(a_0, a_1 e^{i\phi}, a_2 e^{i\phi}\big) \\ \kappa & : (a_0, a_1, a_2) \to \big(\overline{a}_0, a_2, a_1\big)\,. \end{array} \tag{2}$$

Based on these considerations, Golubitsky *et al.* [3, 28] show that the resulting normal form can be written as follows:

$$\begin{aligned} \begin{pmatrix} \dot{a_0} \\ \dot{a_1} \\ \dot{a_2} \end{pmatrix} &= \big(c^1 + i\delta c^2\big) \begin{pmatrix} a_0 \\ 0 \\ 0 \end{pmatrix} + \big(c^3 + i\delta c^4\big) \begin{pmatrix} \overline{a}_0 a_1 \overline{a}_2 \\ 0 \\ 0 \end{pmatrix} \\ &+ \big(p^1 + iq^1\big) \begin{pmatrix} 0 \\ a_1 \\ a_2 \end{pmatrix} + \big(p^2 + iq^2\big)\delta \begin{pmatrix} 0 \\ a_1 \\ -a_2 \end{pmatrix} \\ &+ \big(p^3 + iq^3\big) \begin{pmatrix} 0 \\ a_0^2 a_2 \\ \overline{a}_0^2 a_1 \end{pmatrix} + \big(p^4 + iq^4\big)\delta \begin{pmatrix} 0 \\ a_0^2 a_2 \\ -\overline{a}_0^2 a_1 \end{pmatrix}, \end{aligned} \tag{3}$$

where $\delta \equiv |a_2|^2 - |a_1|^2$, and the 12 real quantities $c^i$, $p^i$ and $q^i$, $i = 1, 2, 3, 4$, are functions of the control parameters and of the five generators of the ring of invariant polynomials under the action of the group $\Gamma$:

$$\begin{aligned} &\rho \equiv |a_0|^2, \quad N \equiv |a_1|^2 + |a_2|^2, \quad \Delta \equiv \big(|a_2|^2 - |a_1|^2\big)^2, \\ &\eta \equiv \mathrm{Re}\big(a_0^2 \overline{a}_1 a_2\big), \quad \xi \equiv \big(|a_2|^2 - |a_1|^2\big)\mathrm{Im}\big(a_0^2 \overline{a}_1 a_2\big)\,. \end{aligned} \tag{4}$$

Note that the term $\delta$ is not an invariant polynomial as its sign changes under the reflection $\kappa$. This feature is of importance when checking the equivariance properties of the normal form. That is, the terms of eq. (3) proportional to $\delta$ are $\Gamma$-equivariant.

### C. Normal form in polar coordinates

Using the polar representation of the complex amplitudes $a_j = r_j e^{i\phi_j}$ for $j = 0, 1, 2$, eq. (3) can be reduced to a system of four coupled equations governing the amplitudes $r_0$, $r_1$, $r_2$ and the phase $\Psi \equiv \phi_1 - \phi_2 - 2\phi_0$:

$$\begin{aligned} \dot{r}_0 &= \Big[c^1 + c^3 r_1 r_2 \cos\Psi - c^4 \delta r_1 r_2 \sin\Psi\Big] r_0 \\ \dot{r}_1 &= \Big[p^1 + \delta p^2\Big] r_1 \\ &\quad + \Big[\big(p^3 + \delta p^4\big)\cos\Psi + \big(q^3 + \delta q^4\big)\sin\Psi\Big] r_0^2 r_2 \\ \dot{r}_2 &= \Big[p^1 - \delta p^2\Big] r_2 \\ &\quad + \Big[\big(p^3 - \delta p^4\big)\cos\Psi - \big(q^3 - \delta q^4\big)\sin\Psi\Big] r_0^2 r_1 \\ \dot{\Psi} &= 2\big(q^2\delta - c^2\delta - c^3\sin\Psi - c^4\delta\cos\Psi\big) \\ &\quad + \tfrac{r_0^2}{r_1 r_2}\Big[\big(q^3 + Nq^4\big)\cos\Psi - \big(Np^3 + \Delta p^4\big)\sin\Psi\Big]\,. \end{aligned} \tag{5}$$

This system is four-dimensional owing to the two continuous symmetries of the system (3). Invariance under the action of the phase shift $\Phi$ reduces the three angle-like variables $(\phi_0, \phi_1, \phi_2)$ to two $(\phi_0,\ \phi_1 - \phi_2)$; invariance under the rotations $R_\alpha$ then leads to the single phase $\Psi$.

The polar system is equivariant under the action of the group $\Gamma_\rho$ which is isomorphic to the Pauli group $\Gamma_\rho \simeq D_4 \rtimes \mathbb{Z}_2$, where the symbol $\rtimes$ indicates the semi-direct product between groups. The generators of the group are the reflection $\kappa$ and $R_{\pi/2}\Phi_{\pi/2}$, the discrete rotation through $\pi/2$ with an equal time shift. For the sake of conciseness, let us introduce the action of the following group elements on the polar vector field:

$$\begin{array}{rl} \kappa & : \big(r_0, r_1, r_2, \Psi\big) \to \big(r_0, r_2, r_1, -\Psi\big) \\ R_{\pi/2}\Phi_{\pi/2} & : \big(r_0, r_1, r_2, \Psi\big) \to \big(r_0, -r_1, r_2, \Psi + \pi\big) \\ R_\pi \Phi_\pi & : \big(r_0, r_1, r_2, \Psi\big) \to \big(-r_0, r_1, r_2, \Psi\big) \\ R_{\pi/2}\Phi_{-\pi/2} & \big(r_0, r_1, r_2, \Psi\big) \to \big(r_0, r_1, -r_2, \Psi + \pi\big)\,, \end{array} \tag{6}$$

where $R_{\pi/2}\Phi_{-\pi/2} = \kappa \cdot \big(R_{\pi/2}\Phi_{\pi/2}\big)^3 \cdot \kappa$ and $R_\pi\Phi_\pi = (R_{\pi/2}\Phi_{\pi/2})^2$. In the next section, we present a classification of the various solutions based on the polar representation.

### D. Group-theoretic considerations

Branching of solutions is determined by the structure of the isotropy lattice acting on fixed points of the normal form (3). The isotropy subgroups of solutions that arise at primary bifurcations correspond to maximal isotropy subgroups of $\Gamma$, that is, isotropy subgroups that are not included in any other isotropy subgroup other than $\Gamma$ itself. Similarly, solutions arising at secondary bifurcations have isotropy subgroups that are maximal in a subgroup strictly smaller than $\Gamma$. This process continues until the trivial group is reached, corresponding to the most general fixed point subspace of the normal form.

Prior to the introduction of the isotropy lattice of the normal form (3), let us introduce the following notation to denote some isotropy subgroups of $\Gamma$: the group of rotations $\widetilde{SO(2)}$,

$$\widetilde{SO(2)} \equiv \{R_\phi \Phi_{-\phi} \mid \phi \in [0, 2\pi)\}, \tag{7a}$$

and the group $\mathbb{Z}_n(g)$, a cyclic subgroup generated by the element $g$, satisfying $g^n = \mathrm{Id}$. In Section III we use the information extracted from this lattice to determine the types of invariant solutions admitted by the normal form. In addition to the isotropy subgroups of the complex normal form, Table III lists the isotropy subgroups of the solutions of the polar system (5).

### E. Third order normal form

Here we do not deal with the general case, and instead consider a truncated form retaining only nonlinearities of third order. Such a truncated system can be expressed in the following explicit form:

$$\begin{aligned}\dot{a}_0 = \;& \lambda_s a_0 + l_0 a_0 |a_0|^2 + l_1\big(|a_1|^2 + |a_2|^2\big)a_0 \\ & + i l_2\big(|a_2|^2 - |a_1|^2\big)a_0 + l_3 \overline{a}_0 \overline{a}_2 a_1\end{aligned} \tag{8a}$$

$$\begin{aligned}\dot{a}_1 = \;& \big(\lambda_h + i\omega_h\big)a_1 + \big(B|a_1|^2 + \big(A+B\big)|a_2|^2\big)a_1 \\ & + C a_1 |a_0|^2 + D a_0^2 a_2\end{aligned} \tag{8b}$$

$$\begin{aligned}\dot{a}_2 = \;& \big(\lambda_h + i\omega_h\big)a_2 + \big(B|a_2|^2 + \big(A+B\big)|a_1|^2\big)a_2 \\ & + C a_2 |a_0|^2 + D \overline{a}_0^2 a_1\,,\end{aligned} \tag{8c}$$

where $l_0, l_1, l_2, l_3$ are real coefficients while $A, B, C, D$ are complex. The correspondence with the notation of Golubitsky *et al.* [3, 28] is reported in Tables I and II.

The system (8) thus corresponds to the polar equations

$$\begin{aligned}\dot{r}_0 = \big[\;& \lambda_s + l_0 r_0^2 + l_1\big(r_1^2 + r_2^2\big)\big] r_0 \\ & + l_3 r_0 r_1 r_2 \cos\Psi\end{aligned} \tag{9a}$$

$$\begin{aligned}\dot{r}_1 = \big[\;& \lambda_h + B_r r_1^2 + (A_r + B_r) r_2^2 + C_r r_0^2\big] r_1 \\ & + r_0^2 r_2\big(D_r \cos\Psi + D_i \sin\Psi\big)\end{aligned} \tag{9b}$$

$$\begin{aligned}\dot{r}_2 = \big[\;& \lambda_h + B_r r_2^2 + (A_r + B_r) r_1^2 + C_r r_0^2\big] r_2 \\ & + r_0^2 r_1\big(D_r \cos\Psi - D_i \sin\Psi\big)\end{aligned} \tag{9c}$$

$$\begin{aligned}\dot{\Psi} = \;& (A_i - 2l_2)(r_2^2 - r_1^2) - 2 l_3 r_1 r_2 \sin\Psi \\ & + r_0^2 D_i \cos\Psi\Big[\frac{r_2}{r_1} - \frac{r_1}{r_2}\Big] - r_0^2 D_r \sin\Psi\Big[\frac{r_2}{r_1} + \frac{r_1}{r_2}\Big]\,.\end{aligned} \tag{9d}$$

Interestingly, the polar system only involves 9 of the 13 original coefficients, namely: $l_0$, $l_1$, $l_3$, $A_r$, $B_r$, $C_r$, $D_r$, $D_i$ and $A_i - 2l_2$. The system (9) is decoupled from the evolution of the phase $\phi_0$ and the "mean phase" of the Hopf component $\phi_m = (\phi_1 + \phi_2)/2$, which evolve according to

$$\dot{\phi}_0 = l_2(r_2^2 - r_1^2) + l_3 r_1 r_2 \sin\Psi\,, \tag{10a}$$

$$\begin{aligned}\dot{\phi}_m = \;& \omega_h + \big(B_i + \tfrac{1}{2}A_i\big)(r_1^2 + r_2^2) + C_i r_0^2 \\ & + \frac{1}{2} r_0^2 D_i \cos\Psi\Big[\frac{r_2}{r_1} + \frac{r_1}{r_2}\Big] \\ & + \frac{1}{2} r_0^2 D_i \sin\Psi\Big[\frac{r_1}{r_2} - \frac{r_2}{r_1}\Big]\,.\end{aligned} \tag{10b}$$

In addition, we introduce a system whose coordinates are invariant under the group action, except for the reflection symmetry in $\Psi$. The resulting system is useful for studying a particular degenerate case considered in Section V. The advantage of such a system is that the dynamics occur in the "fundamental domain", that is, there is only one representative of each group orbit. The system is defined in terms of the invariants

$$R = r_0^2,\; S = r_1^2 + r_2^2,\; P = r_1 r_2,\; Q = \cos\Psi\,. \tag{11}$$

In terms of these coordinates, the evolution equations become

$$\dot{R} \;= 2\big[\lambda_s + l_0 R + l_1 S + l_3 P\big] R \tag{12a}$$

$$\begin{aligned}\dot{S} = \;& 2\big[\lambda_h + B_r S + C_r R\big] S \\ & + 4\big[A_r P + D_r Q R\big] P\end{aligned} \tag{12b}$$

$$\begin{aligned}\dot{P} = \;& \big[\lambda_h + B_r S + C_r R\big] P \\ & + 4\big[A_r P + D_r Q R\big] S - D_i R \sqrt{(1-Q^2)(S^2 - 4P^2)}\end{aligned} \tag{12c}$$

$$\begin{aligned}\dot{Q} = \;& \big[2l_3 + \tfrac{D_r R S}{P}\big](1 - Q^2) \\ & + \big[(A_i - 2l_2) - \tfrac{D_i R Q}{P}\big]\sqrt{(1-Q^2)(S^2 - 4P^2)}\,.\end{aligned} \tag{12d}$$

In the study that follows, we take the nonlinear coefficients $l_j$ $(j = 1, 2, 3, 4)$ and $A, B, C, D$ as constant and likewise for the frequency $\omega_h$ of the Hopf mode. The amplification rates $\lambda_s$ and $\lambda_h$ will be used as unfolding parameters. Our study provides predictions for the existence and stability of the possible solutions in the $(\lambda_s, \lambda_h)$ plane. To apply these results to the flows we are interested in, we have to specify the dependence of the amplification rates on the control parameters of the problem. The WFA problem employs a single control parameter

TABLE I: Correspondence of the real coefficients of the normal form (8) with the literature.

| | $\lambda_s$ | $\lambda_h$ | $\omega_h$ | $l_0$ | $l_1$ | $l_2$ | $l_3$ |
|---|---|---|---|---|---|---|---|
| [3, 28] | $c_\mu^1 \cdot \mu$ | $p_\mu^1 \cdot \mu$ | $q_0^1$ | $c_\rho^1$ | $c_N^1$ | $c_0^2$ | $c_0^3$ |
| [4] | $\alpha_0\mu + \beta_0\nu$ | $\alpha_1\mu + \beta_1\nu$ | $\omega_0$ | $c_0$ | $\mathrm{Re}(d_0)$ | $-\mathrm{Im}(d_0)$ | $f_0$ |

$R$ while the WFA-MC problem is specified by two control parameters $R_1$ and $R_2$ related to the magnitude of the incoming velocity and the temperature difference between the object and the background, respectively. In this case, the amplification rates can be assumed to have the following dependence:

$$\begin{aligned}\lambda_s &= \alpha_s(R_1 - R_1^*) + \beta_s(R_2 - R_2^*),\\ \lambda_h &= \alpha_h(R_1 - R_1^*) + \beta_h(R_2 - R_2^*)\,,\end{aligned} \tag{13}$$

where $R_1^*$ and $R_2^*$ are the threshold values given by the linear stability analysis of the axisymmetric steady state; for the WFA problem $\beta_s = \beta_h = 0$.

In the TCF problem $R_1, R_2$ are related to the angular velocities of the inner and outer cylinders; in the vicinity of the bicritical (codimension-two) point $(R_1^*,\ R_2^*)$ the amplification rates can be assumed to depend linearly on the distance to this point:

$$\begin{aligned}\lambda_s &= c^1_{R_1}(R_1 - R_1^*) + c^1_{R_2}(R_2 - R_2^*),\\ \lambda_h &= p^1_{R_1}(R_1 - R_1^*) + p^1_{R_2}(R_2 - R_2^*)\,.\end{aligned} \tag{14}$$

Numerical values for $(R_1^*, R_2^*)$ and for the parameters $c^1_{R_1}, c^1_{R_2}, p^1_{R_1}, p^1_{R_2}$ are tabulated in [3] for several values of the radius ratio $\eta < 1$ (i.e. the ratio of the radii of the inner and outer cylinders).

## III. CLASSIFICATION OF THE SOLUTIONS

The nomenclature used to classify the various solutions is given in Tables III and IV. We describe every possible solution, although emphasis will be put on solutions that arise generically in the third-order problem and in the degenerate case considered in Section V.

To illustrate the various solutions graphically, we project the four-dimensional phase space into a plane spanned either by the complex amplitude $A(t)$ or by $A'_j(t)$ for $j = 0, 1$, where

$$\begin{aligned}A(t) &\equiv a_0(t) + a_1(t) + \overline{a}_2(t),\\ A'_j(t) &\equiv \mathrm{A}(t)e^{-i\phi_j(t)},\ \text{for } j = 0, 1,\end{aligned} \tag{15}$$

hereafter referred to as the $A$-projection and the $A'$-projection, respectively.

The function $A$ provides a global measure of the dynamics of the system and combines contributions from both the steady and unsteady components. In the wake problem, the real and imaginary parts of $A$ can be identified with the leading order contribution to the lift forces in the $y$ and $z$ directions, respectively. In the TCF problem they represent, for example, the vorticity levels at two points located a quarter of a wavelength apart in the periodicity direction.

TABLE II: Correspondence of the complex coefficients of the normal form (8) with the literature.

| | $A$ | $B$ | $C$ | $D$ |
|---|---|---|---|---|
| [3, 28] | $2\big(p_0^2 + iq_0^2\big)$ | $(p_N^1 - p_0^2) + i(q_N^1 - q_0^2)$ | $p_\rho^1 + iq_\rho^1$ | $p_0^3 + iq_0^3$ |
| [4] | $e_1 - d_1$ | $d_1$ | $c_1$ | $f_1$ |

The solutions that are stationary in the polar representation are summarized in table III. The simplest solution is the trivial solution (TS: $(a_0, a_1, a_2) = (0, 0, 0)$). This solution corresponds to Couette flow in the TCF problem, and to the axisymmetric solution in the WFA and WFA-MC problems. In the $A$-projection this solution corresponds to the origin (Figure 1a). There are three primary solutions: steady-state modes (SS), rotating waves (RW) and standing waves (SW). The steady state mode (SS) takes the form $(a_0, 0, 0)$, $a_0 \neq 0$. This state corresponds to the Taylor Vortex state in the TCF problem and the Steady Shedding mode in the wake problems. In the $A$-projection, this state is represented by an off-center point (Figure 1b). As shown in Table V and in Figure 1b using a thin dashed-dotted line, there is a circle of such states related by the rotations $R_{\phi_0}$; each state is in addition reflection-symmetric.

The RW and SW solutions arise in a primary Hopf bifurcation of the trivial state. Because of the $O(2)$ symmetry, the eigenvalues at the Hopf bifurcation are doubled, and the Hopf bifurcation produces simultaneously a branch of rotating waves (RW: $(a_0, a_1, a_2) = (0, a_1, 0)$) and standing waves (SW: $(a_0, a_1, a_2) = (0, a_1, a_1)$). The RW break reflection symmetry; consequently, there are two RW, rotating in opposite directions and related by reflection. In contrast, the SW are reflection-symmetric oscillations with zero mean. In the TCF problem the RWs correspond to the Spiral Vortex state, while in the wake problem they correspond to the Spiral Shedding state, observed, for example, in the wake of a rising bubble [31]. In the $A$-projection, the RW state corresponds to a limit cycle centered at the origin (Figure 1c), while the SW state is represented by a radial oscillation through the origin (Figure 1d). In the TCF problem, the SWs correspond to the Ribbon state while in the wake problem they correspond to the Symmetric Periodic Shedding state observed, for example, in the wake of a disk when $R \approx 150$. As for SS, there is a circle of SW states related by rotations, see fig. 1d. Each of these solutions corresponds to a one-dimensional fixed point subspace spanned either by $a_0$ or $a_1$, and their presence is therefore guaranteed by the equivariant branching lemma.

Secondary bifurcations may lead to states with a higher-dimensional fixed point subspace. These states correspond to the next rung of the lattice of isotropy subgroups. An example is provided by mixed mode states that correspond to a (nonlinear) superposition of the SS and SW modes. There are two possible states of this type. The first is denoted by $\mathrm{MM}_0$, and corresponds, respectively, to a pattern called Twisted Vortices in the TCF problem and to the reflection symmetry-preserving mode (RSP) in the wake problem. In the $A$-projection the solution oscillates back and forth in the radial direction but now with non-zero mean (Figure 2a). The

TABLE III: Nomenclature and symmetry groups of the steady-state solutions of the system (5).

| Name | Representative | Isotropy group (complex) | Isotropy group (polar) | Frequencies |
|---|---|---|---|---|
| Pure modes: | | | | |
| TS | $(0,0,0,nd)$ | $O(2)\times S^1$ | $D_4 \rtimes \mathbb{Z}_2(\kappa)$ | 0 |
| SS | $(r_a,0,0,nd)$ | $\mathbb{Z}_2(\kappa)\times S^1$ | $\mathbb{Z}_2(\kappa)\times\mathbb{Z}_2(\Phi_\pi)$ | 0 |
| RW | $(0,r_a,0,nd)$ | $\widetilde{SO(2)}$ | $\mathbb{Z}_4(R_{\pi/2}\Phi_{\pi/2})$ | 1 |
| SW | $(0,r_a,r_a,nd)$ | $\mathbb{Z}_2(\kappa)\times\mathbb{Z}_2(R_\pi\Phi_\pi)$ | $\mathbb{Z}_2(\kappa)\times\mathbb{Z}_2(R_\pi\Phi_\pi)$ | 1 |
| Mixed modes: | | | | |
| $MM_0$ | $(r_a,r_b,r_b,0)$ | $\mathbb{Z}_2(\kappa)$ | $\mathbb{Z}_2(\kappa)$ | 1 |
| $MM_\pi$ | $(r_a,r_b,r_b,\pi)$ | $\mathbb{Z}_2\big(\kappa\cdot R_\pi\Phi_\pi\big)$ | $\mathbb{Z}_2\big(\kappa\cdot R_\pi\Phi_\pi\big)$ | 1 |
| MW | $(0,r_a,r_b,\Psi)$ | $\mathbb{Z}_2(R_\pi\Phi_\pi)$ | $\mathbb{Z}_2(R_\pi\Phi_\pi)$ | 2 |
| Precessing waves: | | | | |
| General | $(r_a,r_b,r_c,\Psi)$ | $\mathbb{1}$ | $\mathbb{1}$ | 2 |
| Type A | $(r_a,r_b,r_b,\Psi)$ | $\mathbb{1}$ | $\mathbb{1}$ | 2 |
| Type B | $(r_a,r_b,r_c,0$ or $\pi)$ | $\mathbb{1}$ | $\mathbb{1}$ | 2 |
| Type C | $(r_a,r_b,0,\Psi)$ | $\mathbb{1}$ | $\mathbb{1}$ | 2 |

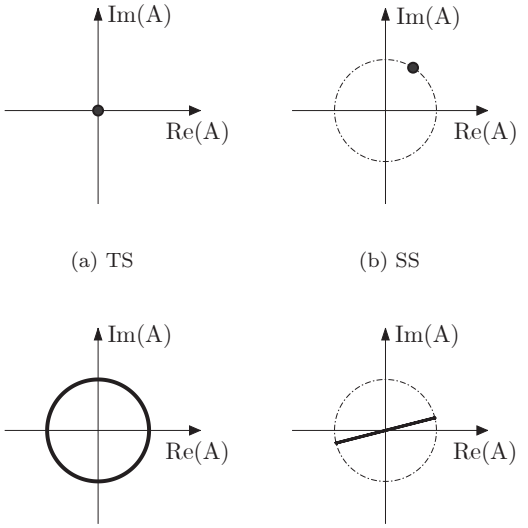


(a) TS (b) SS (c) RW (d) SW

FIG. 1: The trivial state TS and the primary branching solutions SS, RW and SW in the complex $A$ plane.

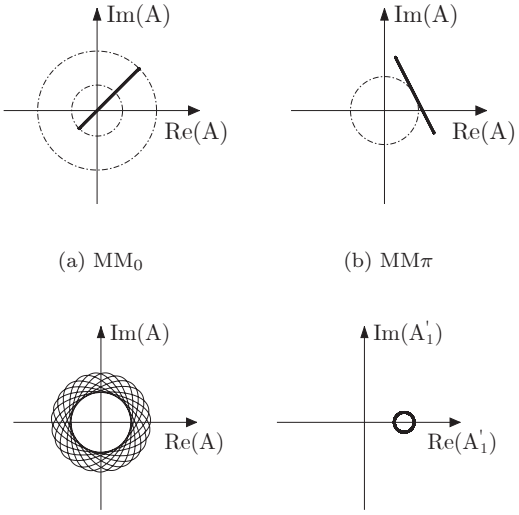


(a) $MM_0$ (b) $MM\pi$ (c) MW: $A$-projection (d) MW: $A_1'$-projection

FIG. 2: The secondary states (a) $MM_0$, (b) $MM_\pi$ and (c) MW in the complex $A$ plane. (d) The $A_1'$-projection of the MW state.

second mixed mode, $MM_\pi$, corresponds, respectively, to Wavy Vortices in the TCF problem and to the reflection symmetry-breaking mode (RSB) in the wake problem. In the $A$-projection, this solution corresponds to a back-and-forth along a line segment perpendicular to the radial direction (Figure 2b). The phase $\phi_0$ of both these states is arbitrary. In other words, there is a circle of solutions of each type, as indicated in fig. 2a) and fig. 2b). Finally, one can also find a mixed mode state involving the Hopf modes, referred to as a modulated wave state (MW), consisting of a (nonlinear) superposition of two rotating wave modes, and characterized in [32]. This state is referred to as the Modulated Spiral mode (MSP) in the TCF problem and the Modulated Wave mode (MW) in the wake problem. It is a state with two temporal frequencies, which are in general incommensurate, and so corresponds to a 2-torus as sketched in fig. 2c. This type of solution does not occur generically in the third-order system, although it arises in higher order normal forms or in the degenerate case corresponding to $A_r = 0$ [33].

The last solution type, that is, a state arising in a tertiary bifurcation, corresponds to a fixed point in the $(r_0, r_1, r_2, \Psi)$ coordinates with no further symmetry. According to eq. (10), in such states the phase $\phi_0$ of the steady mode generically precesses at a constant rate given by $\dot{\phi}_0$. Consequently, states of this type display two

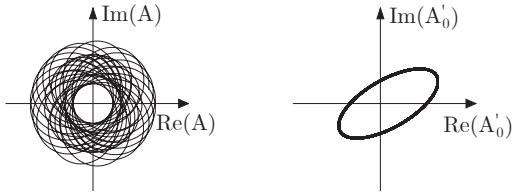


(a) $A$-projection of PrW (b) $A'_0$-projection of PrW

FIG. 3: The tertiary state PrW.

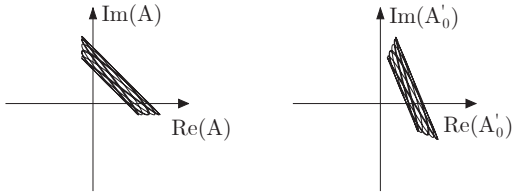


(a) $A$-projection of $\widetilde{\mathrm{MM}}_\pi$ (b) $A'_0$-projection of $\widetilde{\mathrm{MM}}_\pi$

FIG. 4: The Modulated Mixed Mode $\widetilde{\mathrm{MM}}_\pi$ in the complex $A$ plane.

frequencies, one of which is close to the critical Hopf frequency while the other is a low frequency given by eq. (10a). Such modes have been called "modulated rotating waves" in [3], but here we prefer to avoid the ambiguous word "modulated" which has been used to describe a large variety of very different states in the past. Instead, these solutions will be referred to as Precessing Waves (PrW) or "drifting waves".

The precession of these states is best appreciated in the $A'$-projection, showing the state in a frame of reference precessing with the steady-state component $a_0$. In this frame of reference, the PrW is periodic and takes the form of an ellipse (Figure 3b. Note that in this representation the polar coordinates $(r_0, r_1, r_2, \Psi)$ can be interpreted graphically: $r_0$ is the distance of the center of the ellipse to the origin, $(r_1 + r_2)/2$ and $(r_1 - r_2)/2$ are the major and minor axes, and $\Psi$ is twice the angle between the major axis of the ellipse and the direction of the steady-state component.

There are in fact four types of PrW as explained in Table III. The general solution, PrW General, occurs generically in the third order normal form and corresponds to the most general fixed-point solution of eq. (9). In addition, there are special PrW states. The first two, called PrW Type A and Type B, do not occur generically in the third order problem, but they are found in normal forms of higher order or in the degenerate case considered in section V. The third solution, PrW Type C is another degenerate solution that arises in the third order normal form but only when the three conditions $A_i - 2l_2 = D_r = D_i = 0$ are satisfied.

The solutions that are periodic in the polar representation are summarized in table IV. We distinguish three types of solutions. The first type is referred to as a Modulated Mixed Mode, since it displays the same spatial symmetries as the mixed modes already described. For example, in the $A$-projection the Modulated Mixed Mode state $\widetilde{\mathrm{MM}}_\pi$ evolves on a 2-torus, whose shape resembles that of $\mathrm{MM}_\pi$ (Figure 4a). The $A'_0$-projection (Figure 4b) yields an identical but rotated picture, indicating that the phase of the steady-state component remains constant. The related state $\widetilde{\mathrm{MM}}_0$ is not displayed, since its $A$-projection is identical to that of the $\mathrm{MM}_0$ state. Its modulus $|A|$, however, pulsates with two independent frequencies.

We also find periodic states we call Pulsating Waves (PuW). In such states, the polar coordinates $(r_0, r_1, r_2, \Psi)$ all oscillate periodically in time, but the pulsation retains a certain symmetry. Specifically, $\overline{r}_1 = \overline{r}_2$ and $\overline{\sin\Psi} = 0$, where the overbar indicates an average over the pulsation period. According to eq. (10) the phase $\phi_0$ of the steady-state component also pulsates periodically, but the average value of its derivative over one pulsation period vanishes. Consequently, the pattern does not precess. In the $A$-projection, the solution evolves on a 2-torus that remains confined within a given angular sector (Figure 6a), indicating the absence of net precession. The $A'_0$-projection (Figure 6b) also reveals a 2-torus, albeit of different form.

The last type of periodic solution corresponds to the case where the $(r_0, r_1, r_2, \Psi)$ variables are once again time-periodic, but the conditions $\overline{r}_1 = \overline{r}_2$ and $\overline{\sin\Psi} = 0$ are violated. In the $A$-projection, this state appears irregular (Figure 7a), while the $A'_0$-projection (Figure 7b) revels a 2-torus. In fact, this solution actually evolves on a 3-torus, owing to net drift in the phase $\phi_0$. We call these states Three-Frequency Waves (3FW), since they are characterized by a frequency near the critical Hopf frequency, the pulsation frequency, and finally the precession frequency.

The classification of the solutions of the generic steady-Hopf interaction with $O(2)$ symmetry presented by Golubitsky *et al.* [3, 28] and covered in Section II D is based on maximal isotropy subgroups of the symmetry group $O(2) \times S^1$ of the normal form. The isotropy lattice of the normal form (3) is represented in Figure 5. This technique predicts the existence up to tertiary bifurcations of fixed points of the complex normal form (3). These isotropy subgroups correspond to the symmetries of the solutions within the fixed point subspace of each isotropy group (cf. Table III). However, several of the states identified here have trivial symmetry (denoted by $\mathbb{1}$), and their existence cannot be established by group-theoretic arguments alone. Thus, the polar representation introduced here is helpful for the explicit computations required to establish the presence of these more complex states.

TABLE IV: Nomenclature and symmetry groups of limit cycle solutions of the system (5).

| Name of solution | Representative in polar coordinates | Isotropy group | Frequencies in primitive coordinates |
|---|---|---|---|
| $\widetilde{\mathrm{MM}}_{0,\pi}$ | $(r_a(t), r_b(t), r_b(t), 0 \text{ or } \pi)$ | $\mathbb{1}$ | 2 |
| IMM | $(0, r_b, r_c, \Psi(t))$ | $\mathbb{1}$ | 2 |
| PuW | $(r_a(t), r_b(t), r_c(t), \Psi(t))$ with $\overline{r}_b = \overline{r}_c$ and $\overline{\sin\Psi} = 0$ | $\mathbb{1}$ | 2 |
| 3-frequency waves: (3FW) | | | |
| General | $(r_a(t), r_b(t), r_c(t), \Psi(t))$ | $\mathbb{1}$ | 3 |
| Type A | $(r_a(t), r_b(t), r_b(t), \Psi(t))$ with $\overline{\sin\Psi} \neq 0$ | $\mathbb{1}$ | 3 |
| Type B | $(r_a(t), r_b(t), r_c(t), 0 \text{ or } \pi)$ with $\overline{r}_b \neq \overline{r}_c$ | $\mathbb{1}$ | 3 |
| Type C | $(0, r_b(t), r_c(t), \mathrm{nd})$ with $\overline{r}_b \neq \overline{r}_c$ | $\mathbb{1}$ | 3 |
| Type D | $(r_a(t), r_b(t), 0, \Psi(t))$ with $\overline{\sin\Psi} \neq 0$ | $\mathbb{1}$ | 3 |

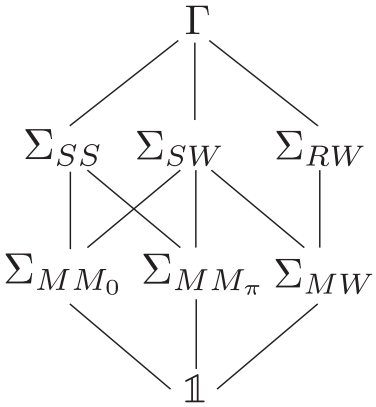


FIG. 5: Lattice of isotropy subgroups of the symmetry group $\Gamma$ (resp. $\Gamma_\rho$).

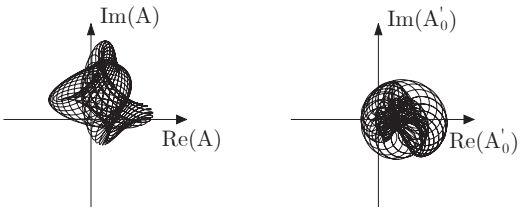


(a) $A$-projection of PuW (b) $A'_0$-projection of PuW

FIG. 6: The Pulsating Wave PuW in the complex $A$ plane.

## IV. DYNAMICS OF THE SOLUTIONS

In this section, we describe the various solutions of the truncated third-order system (8). We summarize not only the solutions but also their stability properties, assuming that all necessary nondegeneracy conditions hold.

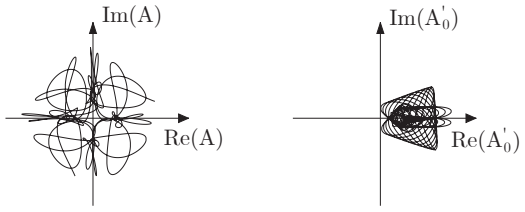


(a) $A$-projection of 3FW (b) $A'_0$-projection of 3FW

FIG. 7: The Three-Frequency Wave 3FW in the complex $A$ plane.

### A. Pure modes

Table V contains the definition and eigenvalues of the trivial state and of the pure modes. Since the polar angle $\Psi$ is undefined for these states, the results are obtained from the primitive amplitude equations (8). Therefore, six eigenvalues are listed for each branch. The condition for supercriticality of the primary branch is also given. This can be deduced from elementary considerations. For example, the SS branch is supercritical if $l_0 < 0$, as can be seen in both the equation for the branch (which is then defined for $\lambda_s > 0$) and the first non-zero eigenvalue (which is then negative, implying that stability has been transferred to the SS branch). The conditions for supercriticality also provide the conditions for the subcriticality (if the corresponding parameter has the opposite sign) and nondegeneracy (if the corresponding quantity is non-zero).

The bifurcation at $\lambda_h = 0$ is the standard Hopf bifurcation with $O(2)$ symmetry, and so gives rise simultane-

TABLE V: Defining equations and eigenvalues of primary branches in the third order normal form (8).

| Name of solutions (condition for supercriticality) | Definition | Eigenvalues | Notes |
|---|---|---|---|
| Pure modes: | | | |
| TS | $r_0 = r_1 = r_2 = 0$ | $\lambda_s$ (twice) | Bif. to SS |
| | | $\lambda_h \pm i\omega_h$ (twice each) | Bif. to SW and RW |
| SS | $r_0 = \sqrt{-\frac{\lambda_s}{l_0}} \equiv r_P$ | 0 | Inv. under rotation |
| $l_0 < 0$ | $\phi_0$ arbritrary | $2l_0 r_P^2$ | Bif. from TS |
| | $r_1 = r_2 = 0$ | $\lambda_h + i\omega_h + (C+D)r_P^2$ and c.c. | Bif. to $MM_0$ |
| | | $\lambda_h + i\omega_h + (C-D)r_P^2$ and c.c. | Bif. to $MM_\pi$ |
| SW | $r_1 = r_2 = \sqrt{-\frac{\lambda_h}{(2B_r+A_r)}} \equiv r_S$ | 0 | Inv. under time shift |
| $2B_r + A_r < 0$ | $r_0 = 0$ | 0 | Inv. under rotation |
| | $\phi_1 - \phi_2$ arbitrary | $(4B_r + 2A_r)r_S^2$ | Bif. from TS |
| | $\dot\phi_1 = \dot\phi_2 = \omega_h + (2B_i + A_i)r_S^2$ | $-2A_r r_S^2$ | Bif. to RW |
| | | $\lambda_s + (2l_1 + l_3)r_S^2$ | Bif. to $MM_0$ |
| | | $\lambda_s + (2l_1 - l_3)r_S^2$ | Bif. to $MM_\pi$ |
| RW | $r_1 = \sqrt{-\frac{\lambda_h}{B_r}} \equiv r_R$ | 0 | Inv. under time shift + rotation |
| $B_r < 0$ | $r_0 = r_2 = 0$ | $2B_r r_R^2$ | Bif. from TS |
| | $\dot\phi_1 = \omega_h + B_i r_R^2$ | $Ar_R^2$ and c.c. | Bif. to SW |
| | | $\lambda_s + (l_1 + il_2)r_R^2$ and c.c. | Bif. to PrW |

ously to branches of RW and SW. The RW rotate counterclockwise (clockwise) when $\omega_h > 0$ ($\omega_h < 0$). Reflection symmetry implies that for each RW $(r_1, r_2) = (r_1, 0)$ there is also a RW $(r_1, r_2) = (0, r_1)$ rotating in the opposite direction. The condition $A_r = 0$ represents a degeneracy that is analysed theoretically in [1, 2, 33, 34]. In the vicinity of this degeneracy, two-frequency states are present, and these are analyzed in Appendix B.

### B. Mixed modes

The defining equations for the mixed modes are given in Table VI. We differentiate between nondegenerate solutions of the third-order truncated normal form, which are the Mixed Modes of type $MM_{0,\pi}$, and degenerate solutions, which are the Modulated Wave modes MW briefly discussed in Appendix B. The nondegeneracy conditions for the existence of MM branches are $\Delta_\pm = (2B_r + A_r)l_0 - (2l_1 \pm l_3)(C_r \pm D_r) \neq 0$, with the positive sign for $MM_0$ and the negative sign for $MM_\pi$. Inspection shows that these states bifurcate supercritically from the SS branch if $\Delta_\pm l_0 < 0$ and from the SW branch if $\Delta_\pm(2B_r + A_r) < 0$. Modulated Wave modes MW are degenerate solutions of the third order normal form (9) and exist when $A_r = 0$ and $\Delta_b = l_3 \sin\Psi \neq 0$.

At this point, it is interesting to point out the similarities between the present problem and the related problem of the interaction between two steady-state modes with opposite parity analyzed by Hirschberg & Knobloch [29, 30]. The latter problem has two pure modes and two mixed modes, which are defined by equations similar to those defining our SS and SW pure modes and our mixed modes. So, if we restrict to the subspace generated by the SS and SW pure modes, all the results of Hirschberg & Knobloch [29, 30] can be directly applied to the present case. This is not so, however, within the system (8), which reveals the presence of additional secondary bifurcations (see below).

### C. Stability of mixed modes and tertiary bifurcations

Higher order bifurcations can be detected by linearizing the normal form (8) around the mixed modes in Table VI. Working with the primitive equations, as done in Golubitsky et al. [28], leads to the same results, but the procedure is more involved. Within the polar representation four eigenvalues need to be computed; the remaining eigenvalues are both zero owing to the two continuous symmetries representing the invariance of the mixed modes under rotation and time translation.

*Mixed modes*

To obtain the results listed in Table VI, consider the following expansion: $r_0 = r_a + x_0$, $r_1 = r_b + x_1$, $r_2 = r_b + x_2$ and $\Psi = \Psi_0 + \psi$, with either $\Psi_0 = 0$ for $MM_0$ or $\Psi = \pi$ for $MM_\pi$; in either case we suppose the perturbation is infinitesimal, $|x_0|, |x_1|, |x_2|, |\psi| \ll 1$. In terms of the quantities $\rho = x_1 - x_2$ and $x_M = (x_1 + x_2)/2$ the resulting liner stability problem is block-diagonal:

TABLE VI: Defining equations and eigenvalues of mixed modes in the third order normal form (8).

| Name of solutions (condition for supercriticality) | Definition | Eigenvalues | Notes |
|---|---|---|---|
| $\mathrm{MM}_0$ | $r_a^2 = \frac{(2l_1+l_3)\lambda_h-(2B_r+A_r)\lambda_s}{\Delta_+}$ | eigs of $M_a^+$ | Bif. to $\widetilde{\mathrm{MM}}_0$ |
| $\Delta_+ \neq 0$ | $r_b^2 = \frac{(C_r+D_r)\lambda_s-l_0\lambda_h}{\Delta_+}$ | eigs of $M_b^+$ | Bif. to PrW and/or PuW |
| | $\Delta_+ = (2B_r+A_r)l_0-(2l_1+l_3)(C_r+D_r)$ | | |
| $\mathrm{MM}_\pi$ | $r_a^2 = \frac{(2l_1-l_3)\lambda_h-(2B_r+A_r)\lambda_s}{\Delta_-}$ | eigs of $M_a^-$ | Bif. to $\widetilde{\mathrm{MM}}_\pi$ |
| $\Delta_- \neq 0$ | $r_b^2 = \frac{(C_r-D_r)\lambda_s-l_0\lambda_h}{\Delta_-}$ | eigs of $M_b^-$ | Bif. to PrW and/or PuW |
| | $\Delta_- = (B_r+A_r)l_0-(2l_1-l_3)(C_r-D_r)$ | | |
| MW | $r_a^2 = \frac{1}{2}\Big[-\frac{A_r}{2p_N^2}-\sqrt{\frac{\chi}{4p_\Delta^1 p_N^2}}\Big]$ | $-2r_{SW}^2\left(A_r+4r_{SW}^2p_N^2\right)$ | Bif. from/to SW |
| $2B_r+A_r<0$, $A_r>0$ | $r_b^2 = \frac{1}{2}\Big[-\frac{A_r}{2p_N^2}+\sqrt{\frac{\chi}{4p_\Delta^1 p_N^2}}\Big]$ | $-r_{RW}^2\left(A_r-2r_{RW}^2p_N^2\right)$ | Bif. from/to RW |
| $p_N^2<0$, $p_\Delta^1<0$ | | $\lambda_s - l_1\frac{A_r}{p_N^2}$ | Bif. to PrW or 3FW |
| Existence I: $A_r/p_N^2<0$ | | | |
| Existence II: $0<\frac{\chi}{p_\Delta^1 p_N^2}<\frac{A_r^2}{(p_N^2)^2}$ | $\chi = A_r(A_r+2B_r)-4p_N^2-A_r\frac{p_{N^2}^1}{p_N^2}\lambda_h$ | | |

$$\begin{pmatrix}\dot{x}_0\\ \dot{x}_M\end{pmatrix} = M_a^\pm \begin{pmatrix}x_0\\ x_M\end{pmatrix} \text{ with}$$

$$M_a^\pm = 2\begin{pmatrix} l_0 r_a^2 & (2l_1 \pm l_3) r_a r_b \\ (C_r \pm D_r) r_a r_b & (2B_r + A_r) r_b^2 \end{pmatrix},$$

$$\begin{pmatrix}\dot{\rho}\\ \dot{\psi}\end{pmatrix} = M_b^\pm \begin{pmatrix}\rho\\ \psi\end{pmatrix} \text{ with}$$

$$M_b^\pm = 2\begin{pmatrix} -A_r r_b^2 \mp D_r r_a^2 & \pm D_i r_a^2 r_b \\ (2l_2 - A_i) r_b \mp D_i r_a^2/r_b & \mp(D_r r_a^2 + l_3 r_b^2) \end{pmatrix}, \tag{16}$$

with the upper sign applying to $\mathrm{MM}_0$ and the lower one to $\mathrm{MM}_\pi$. The matrices $M_a^+$, $M_b^+$, $M_a^-$, $M_b^-$ correspond, respectively, to the matrices denoted $M_0$, $M_1$, $N_0$ and $N_1$ in Golubitsky et al. [28], but are obtained here in a much more straightforward way. The expressions are identical, except for the prefactor 2 which is missing in Golubitsky et al. and an overall change of sign in their matrix $M_1$.

Let us first discuss the situation in the subspace $(x_0, x_M)$, which is governed by the system (16a). This system is completely analogous to that studied by Hirschberg & Knobloch [29], since it involves perturbations within the SS/SW invariant subspace of the problem. In particular, the determinant of the matrix $M_a^\pm$ (i.e. the product of the eigenvalues) is $4r_a r_b \Delta_\pm$. It follows that a steady state bifurcation cannot occur along either mixed mode within the SS/SW subspace. This fact could have been anticipated by noting that this subspace does not admit symmetry-breaking bifurcations of these states. As a result, only Hopf bifurcations are possible. It follows that the eigenvalues of the matrix $M_a^\pm$ are either real with constant sign, or complex conjugate with a possible Hopf bifurcation. Inspection shows that the situation depends upon the signs of the quantities $l_0$, $2B_r + A_r$, and $\Delta_\pm$. If $\Delta_\pm < 0$, both eigenvalues are real and their product is negative. Therefore, one of the eigenvalues is stable and the other unstable. This means that the corresponding branch $\mathrm{MM}_{0,\pi}$ is always less stable than the primary SS and SW branches. In the case $\Delta_\pm > 0$, the product of the eigenvalues is positive, and their sum is given by the trace of the matrix, i.e. $2\big(l_0 r_a^2 + (2B_r + A_r) r_b^2\big)$. When $l_0 < 0$ and $2B_r + A_r < 0$, i.e., when both primary bifurcations are supercritical, the trace remains negative, indicating that both eigenvalues are stable along the whole mixed mode branch. Similarly, when $l_0 > 0$, and $2B_r + A_r > 0$, i.e. when both primary bifurcations are subcritical, the trace remains positive, indicating that both eigenvalues are unstable along the whole branch. The last possibility, $l_0(2B_r + A_r) < 0$, arises when one of the primary bifurcations is subcritical while the other is supercritical. In this case, the real part of the eigenvalues changes sign somewhere along the branch, signaling the occurrence of a Hopf bifurcation. The solution born at such a Hopf bifurcation is referred to here as a Modulated Mixed Mode ($\widetilde{\mathrm{MM}}_{\Psi_0}$, see Table IV). The frequency of oscillation of the Modulated Mixed Mode at the Hopf bifurcation is given by the determinant of the matrix $M_a^\pm$ and may be expressed in terms of $r_a^2$ as follows:

$$\omega_a^2 = -\frac{l_0 \Delta_\pm}{2B_r + A_r} r_a^4 . \tag{17}$$

According to Hirschberg & Knobloch [29], the corresponding bifurcation is degenerate within the third order truncation, and higher order terms are required to determine whether it is subcritical or supercritical.

Consider now the situation in the $(\rho, \psi)$ subspace, governed by the system (16b). Inspection shows that the matrix $M_b^\pm$ may have complex or real eigenvalues. So, in this subspace, each of the mixed modes can experience steady bifurcations (associated with the vanishing of a single eigenvalue of $M_b^\pm$) and/or Hopf bifurcations

(associated with the vanishing of the real part of a pair of complex eigenvalues of $M_b^{\pm}$). To discuss the nature of the solutions born at these tertiary bifurcations, it is useful to note that the phase drift $\dot{\phi}_0$ of the steady mode component is related to these quantities by the equation

$$\dot{\phi}_0 = -2l_2 r_b \rho \pm l_3 r_b^2 \psi + \mathcal{O}(\rho^3, \rho^2\psi, \psi^2\rho, \psi^3)\,, \qquad (18)$$

obtained from eq. (10a).

A steady state bifurcation will generically give rise to a branch with constant, nonzero $(\rho, \psi)$, and according to eq. (18) such a state will therefore precess at a constant angular velocity. The corresponding bifurcation will be referred to as a parity-breaking bifurcation, and the states produced as Precessing Waves (PrW, see Table III). On the other hand, a Hopf bifurcation will generically give rise to a limit cycle in the $(\rho, \psi)$ plane. Since this cycle is symmetric about $(\rho, \psi) = (0, 0)$, eq. (18) implies that the resulting state will drift back and forth with zero net drift. The result is a direction-reversing wave [35] and we refer here to states of this type as Pulsating Waves (PuW, see Table IV).

These predictions are in agreement with those of Golubitsky et al. except for their expectation that the symmetry-breaking Hopf bifurcation (i.e., the Hopf bifurcation in the $(\rho, \psi)$ subspace) gives rise to a 3-frequency state. We see that while the bifurcation is indeed associated with translations of the pattern and hence motion along a three-torus, this motion is in fact a two-frequency motion (in the original variables).

The eigenvalues of the matrix $M_b^{\pm}$ solve a quadratic equation which cannot be simplified easily, and generally has to be investigated on a case-by-case basis. However, it is instructive to consider the situation in the vicinity of the bifurcation points of the mixed modes from the pure modes. In the vicinity of the bifurcation from the SS mode one has $r_b \ll r_a$, and the eigenvalues of $M_b^{\pm}$ are, at leading order, $(\mp 2Dr_a^2, \mp\overline{D} r_a^2)$. Thus, if $D_r > 0$ (resp. $D_r < 0$), the $\mathrm{MM}_0$ is more (resp. less) stable than the $\mathrm{MM}_\pi$ mode in the vicinity of the bifurcation from the SS mode. Similarly, near the bifurcation from the SW mode, the requirement $r_a \ll r_b$ shows that the eigenvalues of $M_b^{\pm}$ are, at leading order, $(-2A_r r_b^2, \mp 2l_3 r_b^2)$. The first eigenvalue indicates stability for both $\mathrm{MM}_0$ and $\mathrm{MM}_\pi$ modes provided $A_r > 0$. Recall that the parameter $A_r$ also determines if the SW branch is more or less stable than the RW branch. Thus, the mixed modes inherit this property from the SW branch in the vicinity of the bifurcation point. The second eigenvalue likewise implies that if $l_3 > 0$ (resp. $l_3 < 0$), the $\mathrm{MM}_0$ is more (resp. less) stable than the $\mathrm{MM}_\pi$ in the vicinity of the bifurcation from the SW mode.

### D. Bifurcation from Rotating Waves to Precessing Waves

As indicated in Table III, the RW branch has a couple of complex eigenvalues, which may lead to a bifurcation to a Precessing Wave (PrW). This situation was investigated by Crawford et al. [36] using the primitive sixth-order system. The derivation was lengthy and required the demonstration of an extension of the Hopf theorem to complex equations. The use of the polar representation introduced here leads to substantial simplifications because, within this representation, this bifurcation is in fact a steady-state one, and the resulting Precessing Wave is a stationary solution of the polar equations.

We consider here the clockwise ($\omega_h > 0$) RW with $(r_1, r_2) \equiv (r_R, 0)$, where $r_R$ is given in Table III. According to the table, a bifurcation occurs along this branch when the bifurcation parameter, defined by

$$\sigma_R \equiv \lambda_s + l_1 r_R^2\,, \qquad (19)$$

vanishes. Inspection shows that the corresponding eigenvector breaks the symmetry of the mixed mode (i.e., it points in the $a_0$ direction). We expect, therefore, that the branch originating in this bifurcation will be characterized by $r_0 = \mathcal{O}(\sigma_R^{1/2})$. We further anticipate that $r_2 = \mathcal{O}(\sigma_R)$ and $r_1 = r_R + x_1$ with $x_1 = \mathcal{O}(\sigma_R)$. We also assume that $\Psi$ has a finite limit in the vicinity of the bifurcation point. With these assumptions, the stationary solutions of the polar system (12) obey the following equations at leading order:

$$\sigma_R + l_0 r_0^2 + 2l_1 r_R x_1 + l_3 r_R r_2 \cos\Psi = 0 \qquad (20a)$$

$$2B_r r_R x_1 + C_r r_0^2 = 0 \qquad (20b)$$

$$A_r r_R r_2 = -r_0^2\big(D_r \cos\Psi - D_i \sin\Psi\big) \qquad (20c)$$

$$(A_i - 2l_2) r_R r_2 = -r_0^2\big(D_i \cos\Psi + D_r \sin\Psi\big)\,. \qquad (20d)$$

To solve these equations, we add the squares of equations eqs. (20c) and (20d) to obtain

$$\Big[A_r^2 + (A_i - 2l_2)^2 r_R^2 r_2^2\Big] = |D|^2 r_0^4\,. \qquad (21)$$

This equation allows us to express $r_2$ in terms of $r_0$. Eliminating $\sin\Psi$ from eqs. (20c) and (20d) leads to

$$\cos\Psi = -\frac{D_r A_r + D_i\big(A_i - 2l_2\big)}{|D|\sqrt{A_r^2 + (A_i - 2l_2)^2}}\,. \qquad (22)$$

Finally, $x_1$ is easily expressed as a function of $r_0$ from eq. (20b). Introducing these expressions into eq. (20a) yields a classical branching equation which can be cast in the form

$$\begin{aligned} &\sigma_R + H^r r_0^2 = 0, \\ &\text{with } H^r = l_0 - l_1\frac{C_r}{B_r} - l_3\frac{D_r A_r + D_i(A_i - 2l_2)}{A_r^2 + (A_i - 2l_2)^2}\,. \end{aligned} \qquad (23)$$

It follows that in the vicinity of the bifurcation point, the Precessing Waves are given by the branching equation $r_0 \approx (-\sigma_R/H^r)^{1/2}$, and the bifurcation is then supercritical if $H_r < 0$.

The precession rate corresponding to this solution is given by eq. (10a) and reads

$$\begin{aligned}\dot{\phi}_0 &= -l_2 r_R^2 + H^i r_0^2 \\ \text{with } H^i &= l_2 \tfrac{C_r}{B_r} + l_3 \tfrac{D_i A_r - D_r(A_i - 2l_2)}{A_r^2 + (A_i - 2l_2)^2}\,.\end{aligned} \tag{24}$$

Note that the branching parameter $H^r$ and the term $H^i$ correspond, respectively, to the real and imaginary parts of the complex Hopf coefficient $H$ computed in [36], at the end of a much lengthier analysis.

### E. Robust heteroclinic cycles

As already mentioned, one may expect the presence of structurally stable or robust heteroclinic cycles in our system in view of its similarity to the mode interaction problem studied in [29, 30] when written in polar coordinates. More generally, a heteroclinic cycle is a set of trajectories $\{(\overline{r}_0^{(j)}(t), \overline{r}_1^{(j)}(t), \overline{r}_2^{(j)}(t), \overline{\Psi}^{(j)}(t))\}_{j=1,2,\ldots,m}$ that connect equilibrium solutions $\{(r_0^{(j)}, r_1^{(j)}, r_2^{(j)}, \Psi^{(j)})\}_{j=1,2,\ldots,m}$ with the property that $(\overline{r}_0^{(j)}(t), \overline{r}_1^{(j)}(t), \overline{r}_2^{(j)}(t), \overline{\Psi}^{(j)}(t))$ is backward asymptotic to $(r_0^{(j)}, r_1^{(j)}, r_2^{(j)}, \Psi^{(j)})$ and forward asymptotic to $(r_0^{(j+1)}, r_1^{(j+1)}, r_2^{(j+1)}, \Psi^{(j+1)})$ with the convention $(r_0^{(m+1)}, r_1^{(m+1)}, r_2^{(m+1)}, \Psi^{(m+1)}) = (r_0^{(1)}, r_1^{(1)}, r_2^{(1)}, \Psi^{(1)})$. Such cycles are *robust* if each connection is robust, i.e. cannot be destroyed by changing parameters. Robust heteroclinic cycles do not exist in general nonsymmetric vector fields. However, they may exist in symmetric systems such as ours. First examples of robust heteroclinic cycles connecting saddle points were found in [37, 38]. Afterwards, Melbourne, Krupa and collaborators [39, 40] established a general approach to the existence and stability of structurally stable heteroclinic cycles in Γ-equivariant systems. The existence of a robust heteroclinic cycle requires the following conditions:

- Each saddle solution sits on a flow-invariant line $l_j$, say, and each such line is the fixed-point subspace of the isotropy subgroup of the saddle solution, i.e. $l_j = \mathrm{Fix}(\Sigma_{j-1}) \cap \mathrm{Fix}(\Sigma_j)$.
- The isotropy subgroups of the invariant lines are maximal isotropy subgroups.
- The invariant plane containing the invariant line is the fixed point subspace of a maximal isotropy subgroup.

The proof of this result is based on the existence of cycles in the isotropy lattice, such as Figure 8 for the present case.

The isotropy lattice in Figure 8 suggests the existence of a robust heteroclinic cycle between the steady-state mode SS and the standing wave mode SW. Such a heteroclinic cycle possesses two connections that lie within the $\mathrm{Fix}(\mathbb{Z}(\kappa))$ and $\mathrm{Fix}(\mathbb{Z}(\kappa \cdot (\pi, \pi))$ subspaces. In our notation, the heteroclinic connections lie in the invariant subspaces of the two MM solutions. Melbourne et al. [41] found that in the supercritical case such a cycle exists whenever the steady-state mode SS is a saddle (resp. sink) in the fixed-point subspace $\mathrm{Fix}(\mathbb{Z}(\kappa))$ of the isotropy subgroup of the $\mathrm{MM}_0$ mode and a sink (resp. saddle) in the fixed-point subspace $\mathrm{Fix}(\mathbb{Z}(\kappa \cdot (\pi, \pi)))$ of the isotropy subgroup of the $\mathrm{MM}_\pi$ mode. Similarly, the SW mode must be a sink (resp. saddle) in $\mathrm{Fix}(\mathbb{Z}(\kappa))$ and a saddle (resp. sink) in $\mathrm{Fix}(\mathbb{Z}(\kappa \cdot (\pi, \pi))$. These conditions are satisfied if the first three existence conditions in Table VII are satisfied. In addition, no other fixed point solutions can be present in either of the fixed point subspaces and solutions starting in the neighborhood of the trivial mode are required to remain bounded, a condition that is satisfied if the last two existence conditions in Table VII hold.

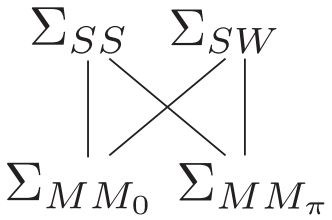


FIG. 8: Structure within in the isotropy lattice suggesting that there may exist of a robust heteroclinic cycle.

The necessary and sufficient conditions for the asymptotic stability of a particular type of robust heteroclinic cycle referred to as *Type A* are derived in [40]. This type of heteroclinic cycle is constructed in such a way that each trajectory connecting two fixed-point solutions lies within the fixed point subspace of an isotropy group isomorphic to $\mathbb{Z}_2$. Because of this the necessary and sufficient condition for asymptotic stability is

$$\prod_{j=1}^{m} \min\left(-\nu_j^c, \nu_j^e - \nu_j^t\right) > \prod_{j=1}^{m} \nu_j^e\,, \tag{25}$$

where $\nu_j^c$, $\nu_j^e$, $\nu_j^t$, $\nu_j^r$ denote the contracting, expanding, transversal and radial eigenvalues of the solution $j$. The *contracting* eigenvalue of the solution $j$ corresponds to the minimum eigenvalue (maximum $-\nu_j$) in the fixed point subspace of solution $j$; the *expanding* eigenvalue corresponds to the eigenvalue with the largest real part among the eigenvalues restricted to the fixed point subspace of the backward asymptotic heteroclinic connection; the *radial* eigenvalue is the eigenvalue with the smallest real part (largest $-\nu_j^r$) within the intersection between the two previous fixed point subspaces and the *transverse* eigenvalue correspond to the eigenvalue with the largest real part among the eigenvalues restricted to

TABLE VII: Definining conditions for structurally and asymptotically stable heteroclinic cycles connecting SS and SW. Here $\nu^{\pm}_{SS} \equiv \lambda_h + (C_r \pm D_r) r_P^2$ and $\nu^{\pm}_{SW} \equiv \lambda_s + (2l_1 \pm l_3) r_S^2$.

| Name of solution (condition for supercriticality) | Existence | Asymptotic stability (Asymp. stable if ii) and either i-a) or i-b) ) |
|---|---|---|
| $\mathrm{Het}_{SS-SW}$ | $\nu^{+}_{SS}\nu^{-}_{SS} < 0$ | i-a) $\nu^{+}_{SS}\nu^{-}_{SW} < -\nu^{-}_{SS}\min(-\nu^{+}_{SW}, \nu^{-}_{SW} + 2A_r r_s^2)$ |
| $l_0 > 0$ | $\nu^{+}_{SW}\nu^{-}_{SW} < 0$ | i-b) $\nu^{-}_{SS}\nu^{+}_{SW} < -\nu^{+}_{SS}\min(-\nu^{+}_{SW}, \nu^{+}_{SW} + 2A_r r_s^2)$ |
| $A_r + 2B_r > 0$ | $\nu^{+}_{SS}\nu^{-}_{SW} > 0$ | ii) $A_r > 0$ |
| | $\frac{\lambda_s}{\lambda_h}\frac{(C_r+D_r)}{l_0} + \frac{\lambda_h}{\lambda_s}\frac{(2l_1+l_0)}{(2B_r+A_r)} > -2$ | |
| | $\frac{\lambda_s}{\lambda_h}\frac{(C_r-D_r)}{l_0} + \frac{\lambda_h}{\lambda_s}\frac{(2l_1-l_0)}{(2B_r+A_r)} > -2$ | |

the orthogonal complement. The proof of the identity (25) is based on the use of a set of Poincaré return maps to obtain global estimates of stability from local ones. For more details, the reader is referred to [39, 40]. Application of eq. (25) to our case shows that the heteroclinic cycle $\mathrm{Het}_{SS-SW}$ is asymptotically stable provided condition ii) and either condition i-a) or i-b) in Table VII hold. This possibility was not considered in [28].

## V. THE DEGENERATE CASE $D_i = 0$, $A_i - 2l_2 = 0$

In this section, we consider the scenario where the parameters $D_i$ and $A_i - 2l_2$ both vanish. This situation arises when all the nonlinear coefficients in eq. (8) are real. This case is of basic theoretical interest since it corresponds to the case where an additional $\mathbb{Z}_2$ symmetry is present in the primitive amplitude equations. In this case eq. (8) reduces to a special case of the equations studied in generality by Silber & Knobloch [42] provided we also take $l_0 = A_r + 2B_r$, $\lambda_s = \lambda_h$.

In this case, the equations in polar coordinates take the form

$$\dot{r}_0 = \big[\lambda_s + l_0 r_0^2 + l_1\big(r_1^2 + r_2^2\big) + l_3 r_1 r_2 \cos\Psi\big] r_0 \tag{26a}$$

$$\dot{r}_2 + \dot{r}_1 = \big[\ \lambda_h + B_r(r_1^2 + r_2^2) + A_r r_1 r_2 + r_0^2(C_r + D_r\cos\Psi)\big](r_1 + r_2) \tag{26b}$$

$$\dot{r}_2 - \dot{r}_1 = \big[\ \lambda_h + B_r(r_1^2 + r_2^2) - A_r r_1 r_2 + r_0^2(C_r - D_r\cos\Psi)\big](r_2 - r_1) \tag{26c}$$

$$\dot{\Psi} = -\Big[2l_3 r_1 r_2 + D_r r_0^2 \frac{r_1^2 + r_2^2}{r_1 r_2}\Big]\sin\Psi\,, \tag{26d}$$

while $PQRS$ equations take the form

$$\dot{R} = 2\big[\lambda_s + l_0 R + l_1 S + l_3 PQ\big] R \tag{27a}$$

$$\dot{S} = \ 2\big[\lambda_h + B_r S + C_r R\big] S + 4\big[A_r P + D_r RQ\big] P \tag{27b}$$

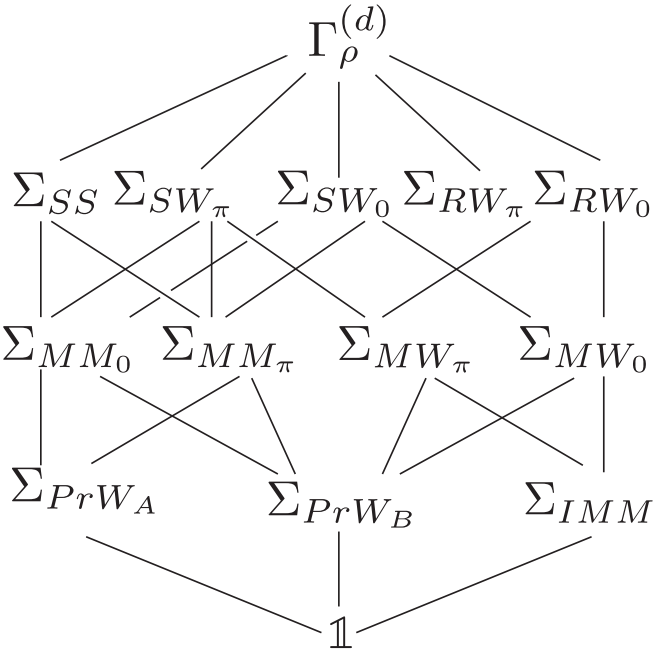


FIG. 9: Lattice of isotropy groups of the degenerate normal form.

$$\dot{P} = \ 2\big[\lambda_h + B_r S + C_r R\big] P + \big[A_r P + D_r RQ\big] S \tag{27c}$$

$$\dot{Q} = \ \big[2l_3 P^2 + D_r RS\big]\tfrac{1-Q^2}{P}\,. \tag{27d}$$

The former possess an additional reflection symmetry

$$\kappa_r : (r_0, r_1, r_2, \Psi) \to (r_0, r_2, r_1, \Psi) \tag{28}$$

responsible for a reflection symmetry in $\Psi$:

$$(\kappa_r \cdot \kappa)\cdot(r_0, r_1, r_2, \Psi) = (r_0, r_1, r_2, -\Psi).$$

This symmetry has several consequences. First, the isotropy group of the polar normal form is now $\Gamma_\rho^{(d)} \simeq \mathbb{Z}_2^2 \rtimes D_4 \simeq \mathbb{Z}_2^4 \rtimes \mathbb{Z}_2$. Its isotropy lattice, depicted in Figure 9, displays new isotropy groups whose fixed point subspaces are of dimension three, viz. $\Sigma_{PrW_A}$, $\Sigma_{PrW_B}$,

TABLE VIII: Nomenclature and symmetry groups of steady-state solutions of the system (26).

| Name | Representative | Isotropy group (polar) | Frequencies |
|---|---|---|---|
| Primary bifurcations: | | | |
| SS | $(r_a, 0, 0, nd)$ | $\mathbb{Z}_2(\kappa_r) \times \mathbb{Z}_2(\kappa) \times \mathbb{Z}_2(\Phi_\pi)$ | 0 |
| $\mathrm{RW}_0$ | $(0, r_a, 0, nd)$ | $D_4(R_{\pi/2}\Phi_{\pi/2}, \kappa \cdot \kappa_r)$ | 1 |
| $\mathrm{RW}_\pi$ | $(0, r_a, 0, nd)$ | $D_4(R_{\pi/2}\Phi_{\pi/2}, \kappa \cdot \kappa_r \cdot \Phi_\pi)$ | 1 |
| $\mathrm{SW}_0$ | $(0, r_a, r_a, nd)$ | $\mathbb{Z}_2(\kappa_r) \times \mathbb{Z}_2(\kappa) \times \mathbb{Z}_2(R_\pi\Phi_\pi)$ | 1 |
| $\mathrm{SW}_\pi$ | $(0, r_a, r_a, nd)$ | $\mathbb{Z}_2(\kappa_r\Phi_\pi) \times \mathbb{Z}_2(\kappa) \times \mathbb{Z}_2(R_\pi\Phi_\pi)$ | 1 |
| Secondary bifurcations: | | | |
| $\mathrm{MM}_0$ | $(r_a, r_b, r_b, 0)$ | $\mathbb{Z}_2(\kappa_r) \times \mathbb{Z}_2(\kappa)$ | 1 |
| $\mathrm{MM}_\pi$ | $(r_a, r_b, r_b, \pi)$ | $\mathbb{Z}_2(\kappa_r\Phi_\pi) \times \mathbb{Z}_2\big(\kappa \cdot R_\pi\Phi_\pi\big)$ | 1 |
| $\mathrm{MW}_0$ | $(0, r_a, r_b, 0)$ | $\mathbb{Z}_2(\kappa_r \cdot \kappa) \times \mathbb{Z}_2(R_\pi\Phi_\pi)$ | 1 |
| $\mathrm{MW}_\pi$ | $(0, r_a, r_b, \pi)$ | $\mathbb{Z}_2(\kappa_r \cdot \kappa \cdot \Phi_\pi) \times \mathbb{Z}_2(R_\pi\Phi_\pi)$ | 1 |
| Tertiary bifurcations: | | | |
| $\mathrm{PrW}_A$ | $(r_a, r_b, r_b, \Psi)$ | $\mathbb{Z}_2(\kappa_r)$ | 2 |
| $\mathrm{PrW}_B$ | $(r_a, r_b, r_c, 0 \text{ or } \pi)$ | $\mathbb{Z}_2(\kappa_r \cdot \kappa)$ | 2 |
| IMM | $(0, r_a, r_b, \Psi(t))$, $\Psi(t) = \phi_1(t) - \phi_2(t)$ | $\mathbb{Z}_2(R_\pi\Phi_\pi)$ | 2 |

$\Sigma_{\mathrm{IMM}}$. The fixed point subspaces $\mathrm{Fix}\big(\Sigma_{PrW_A}\big)$ and $\mathrm{Fix}\big(\Sigma_{PrW_B}\big)$ are characterized by $r_1 = r_2$ and $\sin\Psi = 0$, respectively, and are of dimension four in the space of complex amplitudes, i.e., they display two-frequency behavior, see Table VIII. In contrast, the fixed point subspace $\mathrm{Fix}\big(\Sigma_{\mathrm{IMM}}\big)$ is characterized by $r_0 = 0$. Strictly speaking this is not an invariant subspace of the cubic truncation (since $A_r \neq 0$) but it does become so when the truncation is extended to fifth order, cf. Appendix B. This subspace is also of dimension four, and is spanned by solutions of the form $(0, a_1, a_2)$, i.e., by $r_1 \neq r_2$ and the corresponding phases $(\phi_1, \phi_2)$.

In addition, it turns out that the isotropy subgroups associated to the Mixed Waves $\Sigma_{MW_0}$ and $\Sigma_{MW_\pi}$ are not conjugates of each other, i.e., these solutions are distinct, just as in the case of the Mixed modes $\mathrm{MM}_0$ and $\mathrm{MM}_\pi$. The reason behind the distinction between the subgroups $\Sigma_{SW_0}, \Sigma_{SW_\pi}$ (resp. $\Sigma_{RW_0}, \Sigma_{RW_\pi}$) is algebraic: these isotropy groups are not conjugate of each other, although their fixed point representatives are of the same type. This is because the phase $\Psi$ is undefined for either rotating waves and standing waves, a consequence of the fact that for these states $a_0 = 0$. However, we find it convenient to distinguish between $\mathrm{SW}_0$ and $\mathrm{SW}_\pi$ (resp. $\mathrm{RW}_0$ and $\mathrm{RW}_\pi$) based on the limiting behavior of the Mixed Modes (resp. Mixed Waves) as $r_0 \to 0$, as indicated in the isotropy lattice in Figure 9.

In this degenerate case the conditions for higher order bifurcations, as well as the complete definition of all possible branches of precessing waves, can be obtained explicitly. The corresponding results are tabulated in Table IX. It is found that there are at most three branches of precessing waves. The first two are denoted $\mathrm{PrW}_A$ and $\mathrm{PrW}_B$, while the third kind is generic with no additional symmetry and hence trivial isotropy, and is denoted $\mathrm{PrW}_G$.

### A. Bifurcations from Mixed Modes and Rotating Waves

Bifurcations from Mixed Modes are governed by the eigenvalues of the matrices $M_b^\pm$ defined in Section IV C (apart from the possible bifurcation to a modulated mixed mode if $l_0(2B_r + A_r) < 0$). In the present case, the matrix is diagonal with real eigenvalues. Therefore, symmetry-breaking bifurcations from MM can only lead to PrW (Precessing Waves), excluding the possibility of PuW (Pulsating Waves). The number of such bifurcations follows from the eigenvalues of $M_b^\pm$. The first of these is $2(-A_r r_b^2 \mp D_r r_a^2)$, and this quantity changes sign along the $\mathrm{MM}_0$ ($\mathrm{MM}_\pi$) branch. The second eigenvalue of $M_b^\pm$ is $\mp 2\big(l_3 r_b^2 + D_r r_a^2\big)$. Thus, if $l_3 D_r > 0$, this eigenvalue remains of one sign for both mixed modes. On the other hand, if $l_3 D_r < 0$, it changes sign somewhere along both branches. So, the number of branching points to Precessing Waves along the MM branches is either one (if $l_3 D_r > 0$) or three (if $l_3 D_r < 0$). These results are restated in the top part of Table IX, where the conditions for a zero eigenvalue are stated in terms of $\lambda_s$ and $\lambda_h$ instead of $r_a$ and $r_b$ using Table VI.

We also report in the table the branching point from the RW branch, investigated in Section IV D. This point exists generically, and the corresponding branch has $\Psi = 0$ (resp. $\Psi = \pi$) if $A_r D_r < 0$ (resp. $A_r D_r > 0$). We end up with a total number of either 2 or 4 bifurcation points to Precessing Waves.

The IMM solution is degenerate, as was the case already for the generic third order normal form. The addition of higher order terms, as done in Appendix B, leads to the existence of the solution IMM, which in this degenerate case is a heteroclinic connection between the Mixed Waves $\mathrm{MW}_0$ and $\mathrm{MW}_\pi$. This last statement follows from the integration of eq. (26d) with $r_0 = 0$, which leads to $\Psi \to 0$ as $t \to \infty$ and $\Psi \to \pi$ as $t \to -\infty$ if $l_3 r_a r_b > 0$ and to $\Psi \to \pi$ as $t \to \infty$ and $\Psi \to 0$ as $t \to -\infty$ if

$l_3 r_a r_b < 0$.

### B. The subspace $r_1 = r_2$

The dynamics within the invariant subspace $\mathrm{Fix}\big(\Sigma_{PrW_A}\big)$, defined in polar coordinates as

$$\mathrm{Fix}\big(\Sigma_{PrW_A}\big) = \{(r_0, r_1, r_2, \Psi) : r_1 = r_2\}, \tag{29}$$

take the form

$$\dot{r}_0 = \big[\ \lambda_s + l_0 r_0^2 + 2 l_1 r_1^2 + l_3 r_1^2 \cos\Psi\big] r_0 \tag{30a}$$

$$\dot{r}_1 = \big[\lambda_h + (A_r + 2B_r) r_1^2 + (C_r + D_r \cos\Psi) r_0^2\big] r_1 \tag{30b}$$

$$\dot{\Psi} = -2\Big[l_3 r_1^2 + D_r r_0^2\Big] \sin\Psi\,. \tag{30c}$$

The $RPQ$ coordinates can also be used in this subspace (which corresponds to $S = 2P$):

$$\dot{R} = 2\big[\lambda_s + l_0 R + (2l_1 + l_3 Q) P\big] R \tag{31a}$$

$$\dot{P} = \ 2\big[\lambda_h + (2B_r + A_r) P + (C_r + D_r Q) R\big] P \tag{31b}$$

$$\dot{Q} = \ 2\big[l_3 P + D_r R\big](1 - Q^2)\,. \tag{31c}$$

The resulting systems are formally identical to those governing the interaction of two steady-state modes with opposite parity studied by Hirschberg & Knobloch, eq. (10) of [29], given by the correspondence

$$\begin{array}{l} r_0 \equiv r, r_1 \equiv \rho, \Psi \equiv 2\Psi, \lambda_s \equiv \lambda, \lambda_h \equiv \mu, l_0 \equiv a, \\ 2l_1 \equiv b, l_3 \equiv e, 2B_r + A_r \equiv d, C_r \equiv c, D_r \equiv f. \end{array} \tag{32}$$

The results of [29, 30] can therefore be applied to the system eq. (30). We use these results to conclude that when $D_r l_3 < 0$ the two branches of mixed modes are connected by a tertiary branch of the form $r_0 \neq 0$, $r_1 = r_2 \neq 0$, $\sin\Psi \neq 0$. In the nomenclature of the present manuscript, this branch corresponds to a Precessing Wave of type A (see Table III). The defining equations for this solution are

$$R = r_0^2 = \frac{\sigma_{0A} - \sigma_{\pi A}}{2 D_r \Sigma_A}, \tag{33a}$$

$$P = r_1^2 = r_2^2 = -\frac{\sigma_{0A} - \sigma_{\pi A}}{2 l_3 \Sigma_A}, \tag{33b}$$

$$Q = \cos\Psi = \frac{\sigma_{\pi A} + \sigma_{0A}}{\sigma_{\pi A} - \sigma_{0A}}, \tag{33c}$$

where

$$\begin{array}{ll} \Sigma_A \equiv & (2B_r + A_r + 2l_1) D_r - l_3 (C_r + l_0) \neq 0, \\ \Sigma_A^a \equiv & D_r (A_r + 2B_r) - l_0 l_3, \\ H_A^{0,\pi} \equiv & (\Delta_+ + \Delta_-) - 4 D_r l_3 (1 - \Sigma_A / \Sigma_A^a), \\ \frac{1}{2}\big(\sigma_{0A} + \sigma_{\pi A}\big) \equiv & \big((2B_r + A_r) D_r - C_r l_3\big)\lambda_s \\ & + \big(2 D_r l_1 - l_0 l_3\big)\lambda_h, \\ \frac{1}{2}\big(\sigma_{0A} - \sigma_{\pi A}\big) \equiv & D_r l_3 (\lambda_s + \lambda_h), \end{array} \tag{33d}$$

as in eq. (17) of [29]. The range of existence of this connecting branch in the $(\lambda_s, \lambda_h)$ plane is obtained by imposing the requirement $\cos\Psi \in [-1, 1]$ on eq. (33c); the conditions obtained from $\cos\Psi = \pm 1$ are identical to the conditions obtained from the vanishing of the second eigenvalue of $M_b^{\pm}$ and displayed in Table IX, confirming that the $\mathrm{PrW}_A$ branch connects the two Mixed Mode branches.

The stability of all the solutions within the invariant subspace $\mathrm{Fix}\big(\Sigma_{PrW_A}\big)$ is determined as in Ref. [29]. The linearized dynamics within this subspace are governed by a $3\times3$ matrix with determinant $D_A$, trace $T_A$ and second invariant $I_A$ given below:

$$D_A \ = -\frac{4}{D_r \Sigma_A^2 l_3} \sigma_{\pi A} \sigma_{0A} \left(\sigma_{\pi A} - \sigma_{0A}\right), \tag{34a}$$

$$T_A \ = \frac{\Sigma_A^a \left(\sigma_{\pi A} - \sigma_{0A}\right)}{D_r l_3 \Sigma_A}, \tag{34b}$$

$$\begin{array}{rl} I_A = & -\dfrac{\Delta_+ \sigma_{\pi A}^2 + \Delta_- \sigma_{0A}^2}{D_r l_3 \Sigma_A^2} \\ & + \dfrac{(-4 D_r l_3 + \Delta_+ + \Delta_-)}{D_r l_3 \Sigma_A^2} \sigma_{\pi A} \sigma_{0A}. \end{array} \tag{34c}$$

Since $-1 < Q < 1$ along the $\mathrm{PrW}_A$ branch, the quantity $\sigma_{\pi A} - \sigma_{0A} \equiv -2 D_r l_3 (\lambda_s + \lambda_h)$ cannot vanish along it. As a consequence, $D_A$ only vanishes at the bifurcations to Mixed Modes (defined by $Q = \pm 1$), and no steady state bifurcations occurs within the invariant subspace $\Sigma_{\mathrm{PrW}_A}$ along the branch. The necessary and sufficient conditions for the stability of the branch within its fixed point subspace are $D_A < 0$, $T_A < 0$, $I_A > 0$ and $H_A \equiv I_A - D_A / T_A > 0$. Inspection of eq. (34a) shows that the determinant is negative (resp. positive) whenever $\sigma_{\pi A} - \sigma_{0A} > 0$, which occurs when $l_3 > 0$, $D_r < 0$ (resp. $l_3 < 0$, $D_r > 0$) corresponding to the bifurcation of $\mathrm{PrW}_A$ from the $\mathrm{MM}_\pi$ mode (resp. $\mathrm{MM}_0$). When the determinant is negative, the trace is negative if and only if $\Sigma_A \Sigma_A^a > 0$. If these two conditions are satisfied, the necessary and sufficient condition of the positivity of the second invariant $I_A$ all along the branch is that $\Delta_+ \geq 0$ and $\Delta_- \geq 0$ (defined in Table VI), since $\sigma_{0A} \sigma_{\pi A} \leq 0$ all along the branch. The fourth condition is as follows,

$$\begin{array}{rl} 0 < H_A \equiv & \dfrac{1}{D_r l_3 \Sigma_A^2} \Big[ -\Delta_+ \sigma_{\pi A}^2 - \Delta_- \sigma_{0A}^2 \\ & + \sigma_{\pi A} \sigma_{0A} (\Delta_+ + \Delta_- - 4 D_r l_3 (1 - \Sigma_A / \Sigma_A^a)\Big]. \end{array} \tag{35}$$

TABLE IX: Higher order bifurcations in the degenerate case $D_i = 0$, $A_i - 2l_2 = 0$. Note: [(1)]Results for bifurcations to modulated mixed modes hold in the generic case. [(2)]Results relevant to the PrW of type A also hold in the less degenerate case to $D_i = 0, A_i - 2l_2 \neq 0$. [(3)]The bifurcation from rotating waves leads to a $\mathrm{PrW}_B$ in the present case, and to a general PrW in the generic case. [(4)]The conditions listed for the existence of Hopf bifurcations ensure an odd number of Hopf lines (1 or 3). The condition for an odd number of Hopf lines in the case of a termination at the $\mathrm{MM}_\pi$ fixed point is $\Delta_+\Lambda_B^+ > 0$.

| Branch | New solution | Bifurcation point | Condition for existence |
|---|---|---|---|
| $\mathrm{MM}_0$ | $\mathrm{PrW}_A^{(2)}$ | $\sigma_{0A} \equiv \big[l_3(C_r + D_r) - D_r(2B_r + A_r)\big]\lambda_s + \big[(2l_1 + l_3)D_r - l_0 l_3\big]\lambda_h = 0$ | $l_3 D_r < 0$ |
| | $\mathrm{PrW}_B$ | $\sigma_{0B} \equiv -\big[A_r C_r - 2B_r D_r\big]\lambda_s + \big[A_r l_0 - D_r(2l_1 + l_3)\big]\lambda_h = 0$ | $A_r D_r < 0$ |
| | $\widetilde{MM}_0^{(1)}$ | $2(B_r + A_r)(C_r + D_r - l_0)\lambda_s + l_0(2l_1 + l_3 - 2B_r - A_r)\lambda_h = 0$ | $(2B_r + A_r)l_0 < 0$ |
| $\mathrm{MM}_\pi$ | $\mathrm{PrW}_A^{(2)}$ | $\sigma_{\pi A} \equiv \big[l_3(C_r - D_r) - D_r(2B_r + A_r)\big]\lambda_s + \big[(2l_1 - l_3)D_r - l_0 l_3\big]\lambda_h$ | $l_3 D_r < 0$ |
| | $\mathrm{PrW}_B$ | $\sigma_{\pi B} \equiv -[A_r C_r + 2B_r D_r]\lambda_s + [A_r l_0 + D_r(2l_1 - l_3)]\lambda_h = 0$ | $A_r D_r > 0$ |
| | $\widetilde{MM}_\pi^{(1)}$ | $(2B_r + A_r)(C_r + D_r - l_0)\lambda_s + l_0(2l_1 + l_3 - 2B_r - A_r)\lambda_h = 0$ | $(2B_r + A_r)l_0 < 0$ |
| RW | $\mathrm{PrW}_B^{(1,3)}$ | $\sigma_R \equiv \lambda_s - l_1\lambda_h/B_r = 0$ | Generic |
| $\mathrm{PrW}_A$ | $\mathrm{PrW}_G$ | $\sigma_{AG} \equiv \big(l_3(\sigma_{0A} + \sigma_{\pi A}) - A_r(\sigma_{\pi A} - \sigma_{0A})\big)/\big(\Sigma_A l_3\big) = 0$ | $l_3 D_r < 0$, $A_r^2 < l_3^2$ |
| | 3FW(A) | $H_A = 0$ | eq. (38). |
| $\mathrm{PrW}_B$ | $\mathrm{PrW}_G$ | $\sigma_{BG} \equiv [2l_3 B_r D_r - A_r^2 C_r]\lambda_s + [A_r^2 l_0 - 2l_1 l_3 D_r - l_3 A_r D_r]\lambda_h = 0$ | If $A_r D_r < 0$, $A_r^2 - A_r l_3 < 0$, If $A_r D_r > 0$, $A_r^2 + A_r l_3 < 0$ |
| | 3FW(B)[(4)] | $H_B = 0$ | eq. (49) |
| $\mathrm{PrW}_G$ | 3FW | $\Omega^4 - I I_G \Omega^2 + D_G = 0, \qquad T_G\Omega^2 - I_G = 0$ | – |

Thus, if the previous three conditions are satisfied, the necessary and sufficient condition for $H_A > 0$ all along the branch is

$$\Big|\big(1 - \frac{\Sigma_A}{\Sigma_A^a}\big) - \frac{\Delta_+ + \Delta_-}{4D_r l_3}\Big| \geq -\frac{\sqrt{\Delta_+\Delta_-}}{2D_r l_3}, \qquad (36)$$

which is immediately satisfied if $0 < \Sigma_A/\Sigma_A^a < 1$. Summarizing, the necessary and sufficient condition for the stability of the branch within the invariant subspace $\Sigma_{\mathrm{PrW}_A}$ all along its existence is

$$\Delta_+ > 0, \quad \Delta_- > 0, \quad 0 < \frac{\Sigma_A^a}{\Sigma_A} < 1, \quad l_3 > 0\,. \qquad (37)$$

The condition $\frac{\Sigma_A}{\Sigma_A^a} < 1$ can be replaced by eq. (36).

The quantity $H_A(\sigma_{0,A}, \sigma_{\pi,A})$ can be interpreted as the distance to a Hopf bifurcation of the $\mathrm{PrW}_A$ branch, which is located at $H_A(\sigma_{0,A}, \sigma_{\pi,A}) = 0$. In particular, because the trace $T_A$ divides $D_A$, we have at most two Hopf bifurcations. There is a supercritical Hopf from the $\mathrm{PrW}_A$ branch leading to a stable 3FW if the following conditions are satisfied:

$$\begin{aligned} &\Delta_+ > 0, \quad \Delta_- > 0, \quad l_3 D_r < 0, \\ &\frac{\sqrt{\Delta_+\Delta_-}}{2D_r l_3} \leq \big(1 - \frac{\Sigma_A}{\Sigma_A^a}\big) - \frac{\Delta_+ + \Delta_-}{4D_r l_3} \leq -\frac{\sqrt{\Delta_+\Delta_-}}{2D_r l_3}. \end{aligned} \qquad (38)$$

The case of a single Hopf bifurcation arises when the following two degeneracy conditions hold, $\Delta_-\Delta_+ = 0$ and $\Sigma_A = \Sigma_A^a$. Therefore, whenever eq. (38) is satisfied and $\Delta_+\Delta_- \neq 0$ we have two Hopf bifurcations in the $(\sigma_{0,A}, \sigma_{\pi,A})$ plane, located at

$$\begin{aligned} \sigma_{\pi A} &= K_{A,H}^{\pm}\sigma_{0A}, \\ K^{\pm} &\equiv \tfrac{H_A^{0,\pi}}{2\Delta_+} \pm \tfrac{1}{\Delta_+}\big((H_A^{0,\pi})^2 - 4\Delta_+\Delta_-\big)^{\frac{1}{2}}, \end{aligned} \qquad (39)$$

with $H_A^{0,\pi}$ defined in eq. (33d).

In the present situation, we also need to determine one additional eigenvalue that describes the stability in the $r_2 - r_1$ direction. This eigenvalue, hereafter $\sigma_{AG}$, is given by

$$\begin{aligned} \sigma_{AG} &\equiv 2P\,(l_3 Q - A_r) \\ &= \frac{l_3(\sigma_{0A} + \sigma_{\pi A}) - A_r(\sigma_{\pi A} - \sigma_{0A})}{\Sigma_A l_3}\,. \end{aligned} \qquad (40)$$

A necessary and sufficient condition ensuring the existence of a steady state bifurcation associated with the vanishing of $\sigma_{AG}$ is that the signs of $\sigma_{AG}$ at either end of the branch are opposite. This leads to the condition reported in the last column of Table IX.

### C. The subspace $\sin\Psi = 0$

The second fixed point subspace corresponds to $\sin\Psi = 0$. At first glance, this subspace corresponds to two distinct cases, $\Psi = 0$ and $\Psi = \pi$. However, because of the symmetry of the polar equations, a jump in $\Psi$ by $\pi$ is equivalent to a change of sign of either $r_1$ or $r_2$. As a consequence, to investigate this subspace, we may set $\Psi = 0$ but allow arbitrary signs of $r_1$ and $r_2$. Both Mixed Mode solutions belong to this subspace ($\mathrm{MM}_\pi$ corresponds to $\Psi = 0$, $r_2 = -r_1$). The pure modes can also be considered as part of this subspace, even though $\Psi$ is not defined for these branches. Within this subspace, the equations take the form:

$$\dot{r}_0 = \big[\lambda_s + l_0 r_0^2 + l_1\big(r_1^2 + r_2^2\big) + l_3 r_1 r_2\big]r_0 \qquad (41a)$$

$$\dot{r}_1 = \big[\begin{array}{l} \lambda_h + B_r r_1^2 + (A_r + B_r)r_2^2 + C_r r_0^2\big]r_1 \\ \quad + D_r r_0^2 r_2 \end{array} \qquad (41b)$$

$$\dot r_2 = \big[\ \lambda_h + B_r r_2^2 + (A_r + B_r) r_1^2 + C_r r_0^2\big] r_2 + D_r r_0^2 r_1 \tag{41c}$$

$$\dot R = 2\big[\lambda_s + l_0 R + l_1 S + l_3 P\big] R \tag{42a}$$

$$\dot S = 2\big[\lambda_h + B_r S + C_r R\big] S + 4\big[A_r P + D_r R\big] P \tag{42b}$$

$$\dot P = 2\big[\lambda_h + B_r S + C_r R\Big] P + \big[A_r P + D_r R] S\,. \tag{42c}$$

To detect the existence of Precessing Waves in the present subspace, we look for steady solutions of the above equations. From eqs. (42b) and (42c) we obtain the conditions

$$\lambda_h + B_r S + C_r R = 0, \qquad A_r P + D_r R = 0. \tag{43}$$

The Precessing Waves in question belong to this subspace, leading to

$$R = r_0^2 = -\frac{A_r}{D_r}\frac{\sigma_{0B} - \sigma_{\pi B}}{4\Sigma_B}, \tag{44a}$$

$$S = r_1^2 + r_2^2 = -\frac{\sigma_{0B} + \sigma_{\pi B}}{2\Sigma_B}, \tag{44b}$$

$$P = r_1 r_2 = \frac{\sigma_{0B} - \sigma_{\pi B}}{4\Sigma_B}, \tag{44c}$$

$$\begin{aligned} \text{where}\quad & \Sigma_B \equiv B_r(A_r l_0 - D_r l_3) - l_1(A_r C_r) \neq 0, \\ & \sigma_R \equiv \lambda_s - \frac{l_1}{B_r}\lambda_h, \\ & \sigma_{0B} + \sigma_{\pi B} \equiv 2\Big[\big(A_r C_r\big)\lambda_s + \big(l_3 D_r - A_r l_0\big)\lambda_h\Big], \\ & \sigma_{0B} - \sigma_{\pi B} \equiv 4 B_r D_r \sigma_R\,. \end{aligned} \tag{44d}$$

These expressions define a single branch of Precessing Waves, referred to as the $\mathrm{PrW}_B$ branch. One may check that the conditions obtained on imposing $P = 0$ and $S = 2|P|$ yield, respectively, the conditions listed in Table IX for the bifurcation from Rotating Waves and the relevant Mixed Mode, confirming that the $\mathrm{PrW}_B$ branch connects these two branches. Note that the sign of $P$ is given by $A_r D_r$. So, had we adopted the convention that both $r_1$ and $r_2$ are positive and $\Psi$ is either 0 or $\pi$ we would have arrived at the conclusion that $\mathrm{PrW}_B$ is associated with $\Psi = 0$ if $A_r D_r < 0$ and $\Psi = \pi$ if $A_r D_r > 0$. Note that the precession frequency given by eq. (10a) vanishes when $l_2 = 0$. In this case, the resulting mode will actually be singly periodic in the primitive variables, instead of a two-frequency wave. However, this property is not visible when working with the polar variables.

The stability of the $\mathrm{PrW}_B$ branch within its invariant subspace $\mathrm{Fix}\,(\Sigma_{PrW_B})$ can be determined by studying its characteristic polynomial in a similar manner as done for $\mathrm{PrW}_A$ in Section V B. The invariants of the $3\times3$ stability matrix are the determinant $D_B$, trace $T_B$ and $I_B$ given below:

$$\begin{aligned} D_B &= -4\Sigma_B R(2P - S)(2P + S) \\ &= \frac{A_r}{D_r \Sigma_B^2}\sigma_{\pi B}\sigma_{0B}\left(\sigma_{\pi B} - \sigma_{0B}\right) \end{aligned} \tag{45a}$$

$$\begin{aligned} T_B &= 2 l_0 R + (A_r + 2B_r)\, S \\ &= \frac{A_r l_0\big(\sigma_{\pi B} - \sigma_{0B}\big) - D_r(A_r + 2B_r)\big(\sigma_{0B} + \sigma_{\pi B}\big)}{2 D_r \Sigma_B} \end{aligned} \tag{45b}$$

$$\begin{aligned} I_B &= R\big(\Delta_+(2P + S) + \Delta_-(-2P + S)\big) \\ &\quad + 2A_r B_r\left(S^2 - 4P^2\right) \\ &= \frac{A_r}{4 D_r \Sigma_B^2}\big(\Delta_-\sigma_{\pi B}^2 - \Delta_+\sigma_{0B}^2\big) \\ &\quad + \frac{A_r}{4 D_r \Sigma_B^2}\big(8 B_r D_r + \Delta_+ - \Delta_-\big)\sigma_{0B}\sigma_{\pi B}\,. \end{aligned} \tag{45c}$$

The vanishing of $\sigma_R$ coincides with the origin of the $\mathrm{PrW}_B$ branch along the RW branch. Note that the vanishing of $\sigma_R$ implies $\sigma_{0B} = \sigma_{\pi B}$. Similarly, one of the quantities $\sigma_{0B}$ or $\sigma_{\pi B}$ vanishes at the termination of the $\mathrm{PrW}_B$ branch on one of the mixed modes. One may verify that the third point where $D_B$ vanishes is located outside the existence interval of the branch, confirming that no parity-breaking bifurcation occurs along the branch. In addition, one may confirm that $\sigma_{0B}\sigma_{\pi B} > 0$, except at the termination point.

The necessary conditions for stability within the $\mathrm{Fix}(PrW_B)$ subspace are $D_B < 0$, $T_B < 0$, $I_B > 0$ and $H_B \equiv I_B - D_B/T_B > 0$. From eq. (45a) one may easily verify that the determinant is negative if and only if $\Sigma_B < 0$. Similarly, the trace has a negative sign if $A_r + 2B_r < 0$ and $l_0 < 0$, which are the conditions for the supercriticality of Standing Waves and the Steady-State mode, respectively. If instead $l_0(A_r + 2B_r) < 0$, then the trace changes sign within the region of existence of the $\mathrm{PrW}_B$ solution. Analogously, the necessary conditions for a positive sign of the second invariant $I_B$ everywhere along the branch are

$$\begin{aligned} A_r B_r > 0 \quad & \text{and } \Delta_+ > 0 \text{ if } A_r D_r < 0 \\ & \text{or } \Delta_- > 0 \text{ if } A_r D_r > 0\,. \end{aligned} \tag{46}$$

The first condition ensures that the second invariant is positive at its birth from the RW branch, while the second condition ensures that $I_B$ is positive at its termination on the corresponding MM branch. To ensure that $I_B > 0$ along the whole $\mathrm{PrW}_B$ branch it suffices to have $\Delta_- > -C_+$ if $A_r D_r < 0$, a condition that depends only on $\Delta_+$ and $B_r D_r$, or $\Delta_+ > -C_-$ if $A_r D_r > 0$ for $C_- > 0$, a condition that depends only on $\Delta_-$ and $B_r D_r$.

The $\mathrm{PrW}_B$ branch is stable when $H_B > 0$. If $H_B$ changes sign along the $\mathrm{PrW}_B$ branch, a Hopf bifurcation with frequency $\Omega$ takes place ($H_B = 0$), characterized by the following set of conditions

$$T_B \Omega^2 - D_B = 0, \qquad \Omega^2 - I_B = 0\,. \tag{47}$$

These equations yield the conditions for the presence of a Hopf bifurcation along the $\mathrm{PrW}_B$ branch stated above. In terms of the eigenvalues $\sigma_{0B}(\lambda_s,\lambda_h)$ and $\sigma_{\pi B}(\lambda_s,\lambda_h)$ of the Mixed Modes the Hopf distance $H_B$ is given by

$$\begin{aligned} H_B \;\equiv& -\frac{A_r}{8D_r^2\Sigma_B^3}\Big(\Delta_-\Lambda_B^-\sigma_{\pi B}^3-\Delta_+\Lambda_B^+\sigma_{0B}^3 \\ &+\Big[\Lambda_B^+\big(8B_rD_r-\Delta_-\big)+2A_rl_0\Delta_+-8D_r\Sigma_B\Big]\sigma_{\pi B}\sigma_{0B}^2 \\ &+\Big[\Lambda_B^-\big(8B_rD_r+\Delta_+\big)+2A_rl_0\Delta_--8D_r\Sigma_B\Big]\sigma_{\pi B}^2\sigma_{0B}\Big) \\ \Lambda_B^\pm \;\equiv& D_r(A_r+2B_r)\pm A_rl_0\,. \end{aligned} \tag{48}$$

The condition $H_B=0$ describes a planar cubic algebraic curve in $(\sigma_{0B},\sigma_{\pi B})$. A possible procedure is to determine the type of the planar curve isomorphic to one of the five canonical forms [43], and then determine the number of solutions from it. Instead of following this procedure, we prefer to provide a sufficient condition for the appearance of a Hopf bifurcation along this branch. Provided eq. (46) holds, the frequency $\Omega$ is real, and there exists an odd number (one or three) of Hopf bifurcations whenever $H_B$ has opposite signs at the two endpoints of the branch. This occurs when

$$\Delta_-\Lambda_B^-<0\quad(\mathrm{MM}_0),\qquad \Delta_+\Lambda_B^+>0\quad(\mathrm{MM}_\pi)\,. \tag{49}$$

When eq. (49) does not hold, the number of Hopf bifurcations is even (none or two). In such a case one can distinguish between the different scenarios using, for instance, the Descartes sign rule for positive roots.

In addition to the three eigenvalues governing the stability of the $\mathrm{PrW}_B$ branch within the $\sin\Psi=0$ subspace discussed above, there is a fourth eigenvalue governing the stability in the orthogonal direction, given by

$$\sigma_{BG}=-(2l_3P-A_rS). \tag{50}$$

The vanishing of this eigenvalue leads to the birth of a branch of General Precessing Waves. The resulting condition in terms of $\lambda_s$ and $\lambda_h$ is listed in Table IX. A condition ensuring that such a bifurcation occurs somewhere along the branch is that $\sigma_{BG}$ has opposite signs at its termination points on RW and the relevant MM. This leads to the condition reported in the last column of Table IX. This condition is the same as for the bifurcation from $\mathrm{PrW}_A$.

### D. The third branch of precessing waves

As demonstrated in the previous sections, two bifurcations can occur along the precessing waves of type A and B giving rise to a precessing wave with no symmetry called $\mathrm{PrW}_G$. Here we investigate this branch as well as its stability. We look for a steady solution of the polar equations with $r_0\neq0$, $r_1\neq r_2$ and $\sin\Psi\neq0$, cf. Table VIII. The same manipulations as before lead to the following conditions:

$$\begin{aligned} 0 &= PQl_3+Rl_0+Sl_1+\lambda_s, \\ 0 &= B_rS+C_rR+\lambda_h, \\ 0 &= A_rP+D_rQR, \\ 0 &= D_rRS+2P^2l_3\,. \end{aligned} \tag{51}$$

The solution of this system yields the conditions for the presence of the $\mathrm{PrW}_G$ branch:

$$\begin{aligned} R &= \frac{2B_r\lambda_s-(2l_1+A_r)\lambda_h}{\Sigma_G}, \\ S &= 2\frac{C_r\lambda_s-l_0\lambda_h}{\Sigma_G}, \\ P &= \frac{-1}{l_3\Sigma_G}\Big(D_rl_3\big(B_r\lambda_s-(2l_1+A_r)\lambda_h\big)\big(C_r\lambda_s-l_0\lambda_h\big)\Big)^{\frac12}, \\ Q &= A_r\Big(\frac{C_r\lambda_s-l_0\lambda_h}{D_rl_3[2B_r\lambda_s-(2l_1+A_r)\lambda_h]}\Big)^{\frac12}, \\ &\text{where } \Sigma_G=C_r(A_r+2l_1)-2B_rl_0\neq0. \end{aligned} \tag{52}$$

These expressions define a single solution branch. One may check that imposing $Q^2=1$ and $S=2|P|$ yields, respectively, the same conditions as found for the steady bifurcations from the $\mathrm{PrW}_A$ and $\mathrm{PrW}_B$ branches listed in table IX, confirming that the $\mathrm{PrW}_G$ solution indeed links these two branches.

The invariants of the stability matrix are

$$\begin{aligned} T_G &= 2Rl_0+S\,(A_r+2B_r) \\ &= \frac{2\,(\sigma_S\,(A_r+2B_r)+l_0\sigma_R)}{\Sigma_G}, \\ D_G &= 8\Sigma_GD_rl_3R^2(4P^2-S^2)(Q^2-1) \\ &= \frac{32}{\Sigma_G^3l_3}\sigma_S\sigma_R\left(A_r^2\sigma_S+D_rl_3\sigma_R\right)\left(D_r\sigma_R+\sigma_Sl_3\right), \\ I_G &= \frac{4A_r}{\Sigma_G^2}\Big(2(B_r-A_r)\sigma_S^2-D_r^2\sigma_R^2\Big) \\ &\quad+\frac{\sigma_S\sigma_R}{\Sigma_G^2l_3}\big(4D_r(2A_rB_r-3l_3^2)+4l_0l_3(A_r+2B_r)\big) \\ &\quad-4\frac{\sigma_S\sigma_R}{\Sigma_G^2l_3}\big((A_r+2l_1)(A_rD_r+C_rl_3)\big), \\ II_G &= -\frac{8}{\Sigma_G^3}\big(D_r^2l_0\sigma_R^3+4A_r^2B_r\sigma_S^3\big) \\ &\quad+\frac{8D_r\sigma_S\sigma_R^2}{\Sigma_G^3l_3}\big(2\Sigma_B+l_3(\Sigma_A-4B_rD_r)-l_0(A_r^2+l_3^2)\big) \\ &\quad+\frac{8\sigma_S^2\sigma_R}{\Sigma_G^3l_3}\Big(A_rl_3\Sigma_G-6B_rD_rl_3^2\Big) \\ &\quad+\frac{8\sigma_S^2\sigma_R}{\Sigma_G^3l_3}A_r^2\Big(D_rA_r+2D_r(l_1-B_r)-2l_3l_0\Big)\,. \end{aligned} \tag{53}$$

The determinant $D_G$ only vanishes at the termination points, that is, whenever $Q^2=1$ or $S=2|P|$, which rules out the possibility of a steady state bifurcation. Thus there can only be Hopf bifurcations along the $\mathrm{PrW}_G$ branch. The frequency $\Omega$ solves the following equations obtained from the characteristic polynomial

$$\Omega^4-II_G\Omega^2+D_G=0,\qquad T_G\Omega^2-I_G=0\,, \tag{54}$$

leading to the following sixth order equation in terms of $\lambda_s$ and $\lambda_h$:

$$II_G^2 - II_G I_G T_G + T_G^2 D_G = 0\,. \tag{55}$$

### E. A robust heteroclinic cycle

The isotropy lattice (see Figure 9) of the degenerate case under discussion suggests the possibility that new heteroclinic cycles may exit. One of the most intriguing possibilities is a connection between the isotropy subspace of Mixed Modes and the subspaces of Precessing Waves A and B, corresponding to a cycle of type C in the classification of Krupa and Melbourne [40]. The conditions for the existence of a robust heteroclinic cycle connecting Mixed Modes consists in demanding that $\mathrm{MM}_0$ is a saddle whose unstable manifold is of dimension one (resp. sink) within $\Sigma_{PrW_B}$ and a sink (resp. saddle) within $\Sigma_{PrW_A}$. Then $\mathrm{MM}_\pi$ would need to be a sink (resp. saddle) within $\Sigma_{PrW_B}$ and a saddle (resp. sink) within $\Sigma_{PrW_A}$. However, for the mixed mode $\mathrm{MM}_\pi$ to be a saddle within $\Sigma_{PrW_A}$ and the mixed mode $\mathrm{MM}_0$ to be a sink it is necessary that $\sigma_{\pi_A} - \sigma_{0_A} < 0$ with $D_r l_3 < 0$, conditions that indicate that there is a fixed point within the invariant subspace $\Sigma_{PrW_A}$, i.e., $\mathrm{PrW}_A$ (resp. $\mathrm{PrW}_B$). Despite the existence of a fixed point within the invariant subspace $\Sigma_{PrW_A}$ (resp. $\Sigma_{PrW_B}$), a robust heteroclinic cycle may still exist, cf. [44] In the case of an invariant fixed point subspace of dimension two the existence of heteroclinic cycles relies on the use of the Poincaré-Bendixson theorem, see for instance [41]. In this case, the fixed-point subspace is required to be free of any other fixed point other than those connected by the heteroclinic cycle. Instead, when the dimension is three, one may use the invariant sphere theorem, or more generally a Lyapunov functional to establish attraction. In our case, the presence of a robust heteroclinic cycle requires that the coefficients $C_r \pm D_r$ and $2l_1 \pm l_3$ should both be positive, since otherwise the Precessing Waves A and B are globally attracting except possibly within a ball of size $\mathcal{O}(\lambda_s, \lambda_h)$ in the subspace $R, P, S$. These conditions are listed in Table X. Note that our reasoning does not exclude the existence of a small heteroclinic cycle within the $\mathcal{O}(\lambda_s, \lambda_h)$ ball near PrW, although such a state (if it exists) would require a larger set of defining conditions and would be restricted to a small region of phase space.

If the conditions listed in Table X are satisfied then there exists a robust heteroclinic cycle between the Mixed Modes, which bifurcates to a 3FW in the case $A_i - 2l_2 \neq 0$ and $D_i = 0$, and to a PuW or 3FW in the case with $A_i - 2l_2 \neq 0$ and $D_i \neq 0$, see Figure 10. Finally, the application of the theory of Krupa and Melbourne [40] also allows one to establish the existence of heteroclinic cycles between standing waves and mixed modes, whose existence and stability conditions are listed in Table X. As for the heteroclinic cycles between mixed modes, these

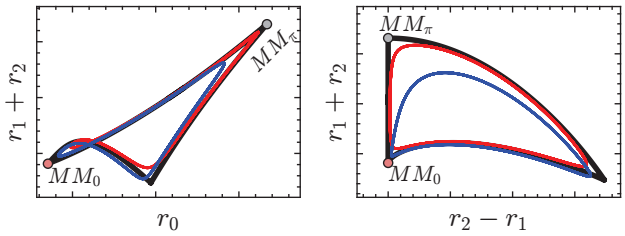


(a) $A$-projection of PuW (b) $A_0'$-projection of PuW

FIG. 10: Heteroclinic cycle between $\mathrm{MM}_0$ and $\mathrm{MM}_\pi$ in the polar normal form (9) with $A_i - 2l_2 = D_i = \sin\Psi = 0$ (black line) and corresponding results when $A_i - 2l_2 \neq 0$ and $D_i = 0$ (red line) or $D_i \neq 0$ and $A_i - 2l_2 = 0$ (blue line).

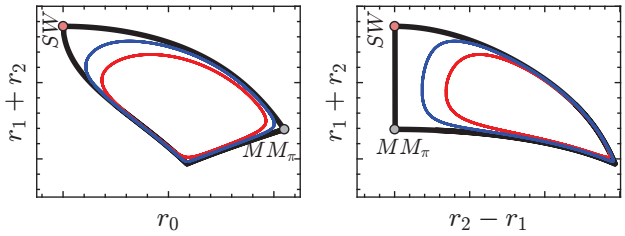


(a) $A$-projection of PuW (b) $A_0'$-projection of PuW

FIG. 11: Heteroclinic cycle (black) between $\mathrm{MM}_\pi$ and SW in the polar normal form (9) with $A_i - 2l_2 = D_i = \sin\Psi = 0$ (black line) and corresponding results with $A_i - 2l_2 \neq 0$ (red line) or $D_i \neq 0$ (blue line).

heteroclinic cycles persist in the form of limit cycles of the polar normal form when the degeneracy conditions are not satisfied, see Figure 11.

## VI. NUMERICAL EXPLORATION OF THE THIRD-ORDER NORMAL FORM (9)

Section V has shown the existence of multiple fixed points with additional symmetries, e.g., $\mathrm{PrW}_A$ and $\mathrm{PrW}_B$, in the degenerate case (equivariant under the group $O(2) \times \mathbb{Z}_2 \times S^1$). The additional $\mathbb{Z}_2$ symmetry is characteristic of mode interactions in $O(2)$ symmetric systems with strong resonance conditions (1:2 [44], 1:3 [45]). Departure from the degeneracy conditions ($A_i - 2l_2 = D_i = 0$) breaks this additional $\mathbb{Z}_2$ symmetry and may be responsible for destroying the $\mathrm{Het}_{SS-SW}$ heteroclinic cycle, leading to more complex dynamics. This section is devoted to the numerical exploration of the degenerate case $A_i - 2l_2 = D_i = 0$ and the implications of the departure from this condition ($A_i - 2l_2 \neq 0$ and/or $D_i \neq 0$). For this purpose, we choose generic values for the normal form coefficients, listed in Table XI. These coefficients are chosen in such a way that primary bifur-

TABLE X: Defining conditions for structurally and asymptotically stable heteroclinic cycles connecting Mixed Modes or Standing Waves and a Mixed Mode.

| Name of solution (comments) | Existence conditions | Asymptotic stability (Asymp. stable if either i-a) or i-b) ) |
|---|---|---|
| $\mathrm{Het}_{MM_0-MM_\pi}$ | | |
| Stable radial dir. | $\Delta_+ > 0, \quad \Delta_- > 0,\ l_0 < 0, \quad A_r + 2B_r < 0$ | i-a) $\sigma_{\pi A} + \sigma_{\pi B} < 0$, |
| Sink-saddle conditions | $\sigma_{0A}\sigma_{0B} > 0, \quad \sigma_{\pi A}\sigma_{\pi B} < 0,\ l_3 D_r < 0, \quad A_r D_r > 0,$ | i-b) $\sigma_{0A} - \sigma_{0B} > 0$ |
| Non-attractivity of PrW | $2l_1 \pm l_3 > 0, \quad C_r \pm D_r > 0$ | |
| $\mathrm{Het}_{SW-MM_\pi}$ | | |
| Stable radial dir. | $\Delta_- > 0,\ l_0 < 0,\ A_r + 2B_r < 0,\ A_r > 0$ | i-a) $2\big(2B_r + A_r\big)\lambda_s - \big(2l_1 - A_r\big)\lambda_h > 0$ |
| SW saddle in $\mathrm{Fix}(\Sigma_{MM_\pi})$ | $\sigma^-_{SW} > 0,\ \sigma^+_{SW} < 0$ | i-b) $\sigma_{\pi A} + \sigma_{\pi B} < 0$ |
| $\mathrm{MM}_\pi$ saddle in $\mathrm{Fix}(\Sigma_{PrW_B})$ | $\sigma_{\pi A}\sigma_{\pi B} < 0,\ A_r D_r > 0$ | |
| $\mathrm{Het}_{SW-MM_0}$ | | |
| Stable radial dir. | $\Delta_+ > 0,\ l_0 < 0,\ A_r + 2B_r < 0,\ A_r > 0$ | i-a) $2\big(2B_r + A_r\big)\lambda_s - \big(2l_1 - A_r\big)\lambda_h > 0$ |
| SW saddle in $\mathrm{Fix}(\Sigma_{MM_0})$ | $\sigma^-_{SW} < 0,\ \sigma^+_{SW} > 0$ | i-b) $\sigma_{\pi A} - \sigma_{\pi B} > 0$ |
| $\mathrm{MM}_0$ saddle in $\mathrm{Fix}(\Sigma_{PrW_B})$ | $\sigma_{0A}\sigma_{0B} > 0,\ A_r D_r < 0$ | |

cations, i.e., bifurcations leading to SS, SW and RW are supercritical, and the flow is globally stable, that is, there is no finite-time blow-up.

As the bifurcation parameter, we have selected the polar angle $\theta$ such that the unfolding parameters are $\lambda_S = \rho\cos\theta$ and $\lambda_H = \rho\sin\theta$, with $\rho = (0,\infty)$ and $\theta \in [0, 2\pi)$. In contrast to [44] the bifurcation diagram barely depends on $\rho$, and we have fixed the value of $\rho$ at $\rho = 0.5$. The numerical continuation of the polar normal form is carried out with the numerical continuation software MATCONT [46]. In the following, we show the bifurcation diagrams associated to the degenerate and nondegenerate cases. There are two major differences. First, the two connected branches of symmetric Precessing Waves ($\mathrm{PrW}_A$ and $\mathrm{PrW}_B$) are a characteristic feature of the degenerate case (symmetry $O(2)\times\mathbb{Z}_2\times S^1$). In the nondegenerate case, these two branches split into two disconnected branches of general Precessing Waves $\mathrm{PrW}_G$. Secondly, in the degenerate case we observe $\mathrm{Het}_{SS-SW}$ cycles, which break apart as the orbit intersects the invariant subspace $r_1 = r_2$. Instead, in the nondegenerate case, we have identified complex heteroclinic cycles around $\mathrm{Het}_{PrW_A}$. Such a feature was also observed by Porter and Knobloch [44], who concluded that the transition from $\mathrm{Het}_{SS-SW}$ cycles to this second set is a characteristic of systems with $O(2)\times\mathbb{Z}_2$ symmetry where the $\mathbb{Z}_2$ symmetry is weakly broken.

### A. The degenerate case $A_i - 2l_2 = D_i = 0$

Figure 12 shows the bifurcations of the fixed point branches of the polar normal form with the parameters listed in Table XI and the degeneracy conditions $A_i - 2l_2 = D_i = 0$. Along this particular path, the trivial state first loses stability at $\theta = -\pi/2$ in a primary pitchfork bifurcation to the SS mode, which terminates at $\theta = \pi/2$. The SS mode gives birth to the $\mathrm{MM}_0$ branch when $\theta = \arctan(C_r + D_r)/l_0 \approx -1.15$ and to the $\mathrm{MM}_\pi$ branch when $\theta = \arctan(C_r - D_r)/l_0 \approx 0.77$ (Table V). The mixed mode $\mathrm{MM}_0$ subsequently produces the $\mathrm{PrW}_A$ branch in a symmetry-breaking bifurcation when $\sigma_{0A} = 0$ (Table IX) and then terminates on the SW branch. A magnified visualization is displayed in Figure 13(a), where we can observe the $\mathrm{PrW}_A$ which terminates on the $\mathrm{MM}_\pi$ branch and eventually gives birth to a general precessing wave $\mathrm{PrW}_G$ via a symmetry-breaking bifurcation when $\sigma_{AG} = 0$. The $\mathrm{PrW}_G$ mode experiences a Hopf bifurcation that leads to a 3FW (blue point in Figure 12); Figure 14 illustrates the stable periodic orbit (3FW) with a thick black line and the stable manifold of $\mathrm{PrW}_A$ with a thin gray line. The existence of a global attractor ($\mathrm{PrW}_A$) in the invariant subspace $r_1 = r_2$ prevents the existence of a true heteroclinic cycle $\mathrm{Het}_{SS-SW}$, but allows the existence of shadowing stable periodic or-

TABLE XI: Cubic coefficients of the normal form.

| $l_0$ | $l_1$ | $l_3$ | $A_r$ | $B_r$ | $C_r$ | $D_r$ |
|---|---|---|---|---|---|---|
| −6.19 | −1.4 | −1.7 | 0.96 | −1.08 | 4 | 10 |

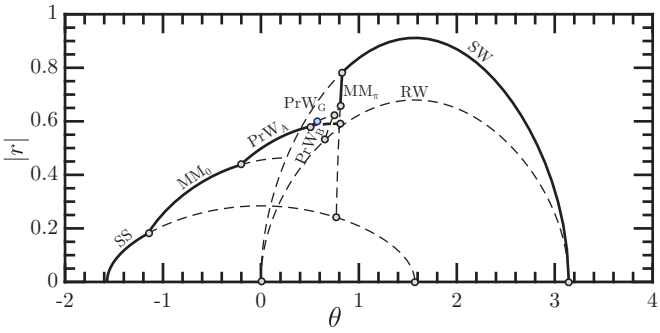


FIG. 12: Bifurcation diagram in the degenerate case when $\rho = 0.5$, showing $|r| = \sqrt{r_0^2 + r_1^2 + r_2^2}$ as a function of the angle $\theta$.

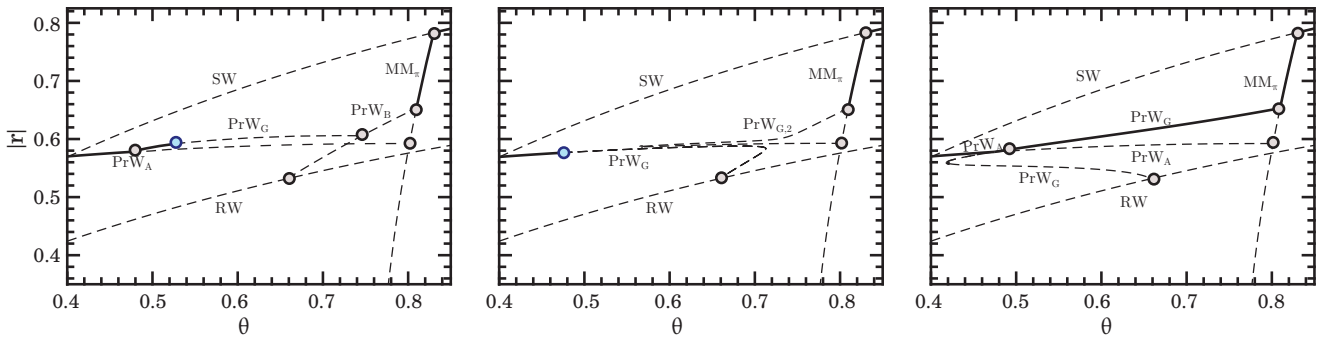


(a) $A_i$-2$l_2$ = 0, $D_i$ = 0 (b) $A_i$-2$l_2$ = 0, $D_i$ = 0.35 (c) $A_i$-2$l_2$ = -1, $D_i$ = 0

FIG. 13: Bifurcation diagram in the degenerate case when $\rho = 0.5$, showing $|r| = \sqrt{r_0^2 + r_1^2 + r_2^2}$ as a function of the angle $\theta$. Legend: Solid (dashed) lines correspond to stable (unstable) fixed points. Symmetry-breaking bifurcations are illustrated with gray points, and Hopf bifurcations with blue points. Note: in (a) as well as in Figure 12 the PrW$_G$ branch has been artificially displaced upwards to visually differentiate it from the PrW$_A$ branch.

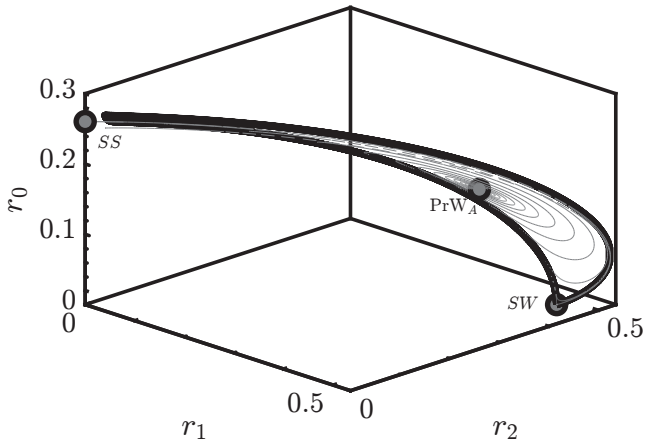


FIG. 14: Example of the heteroclinic cycle SS-SW (thick line). The gray line corresponds to the stable manifold of PrW$_A$.

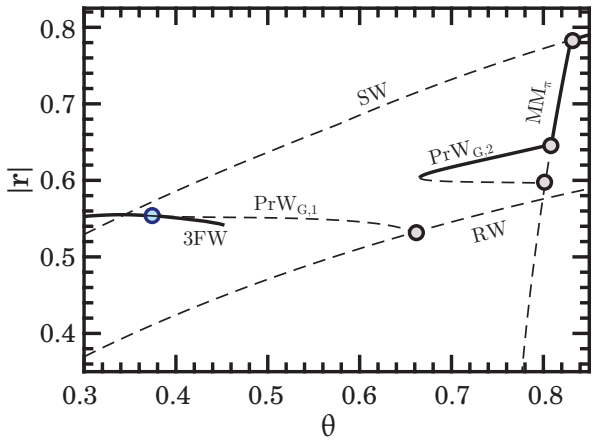


FIG. 15: Bifurcation scenario in the nondegenerate case, showing $|r| = \sqrt{r_0^2 + r_1^2 + r_2^2}$ as a function of the angle $\theta$ with the same legend as in Figure 13. The end point of $PrW_{G,1}$ is located at $\theta \approx 0.6581$ (gray point), i.e., below $\theta_{SN}$ but above the global bifurcation at $\theta \approx 0.6454$ (not shown). Note: The blue point and the associated 3FW branch have been artificially displaced, so the crossing point between the SW and PrW$_{G,1}$ and the blue Hopf point do not coincide.

bits that approximate it, see Figure 14. These orbits exist in $0.52 < \theta < 0.592$ and collapse in a global bifurcation when the limit cycle intersects the invariant subspace $r_1 = r_2$ at $\theta \approx 0.592$. Once a trajectory intersects the $r_1 = r_2$ subspace, it is trapped within it and so is attracted to the only attractor in this subspace, i.e., the PrW$_A$ state. The same phenomenon occurs in the small region of coexistence of MM$_\pi$ and the heteroclinic cycle, $0.78 < \theta < 0.82$. The PrW$_G$ branch terminates on the PrW$_B$ branch, which connects RW and MM$_\pi$. Finally, the MM$_\pi$ branch is stable between its endpoint on the SW branch and its symmetry-breaking bifurcation that leads to the PrW$_B$ branch. For $0.82 < \theta \leq \pi$ the only stable state is the SW branch.

### B. Nondegenerate case $A_i - 2l_2 = -1$, $D_i = 0.35$

The general picture of the bifurcation scenario, depicted in Figure 12, remains qualitatively unchanged. However, the Precessing Wave branches are modified. We first examine the case when one of the two degeneracy conditions is still satisfied. The case $A_i - 2l_2 = 0$ but $D_i \neq 0$ is illustrated in Figure 13(b) and reveals the existence of two distinct PrW$_G$ branches. This case corresponds to an imperfect bifurcation, where the two symmetry-breaking pitchfork bifurcations leading to the

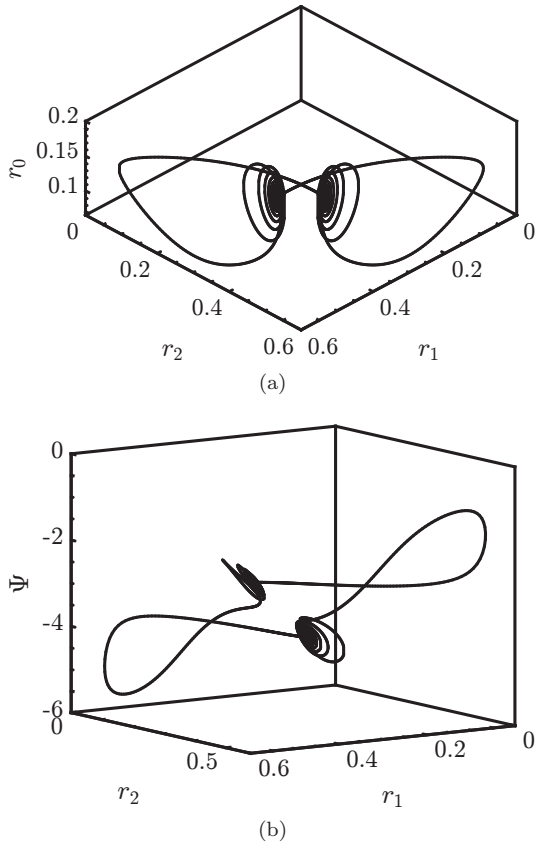


FIG. 16: Heteroclinic cycle at $\theta_{SN} \approx 0.663445$.

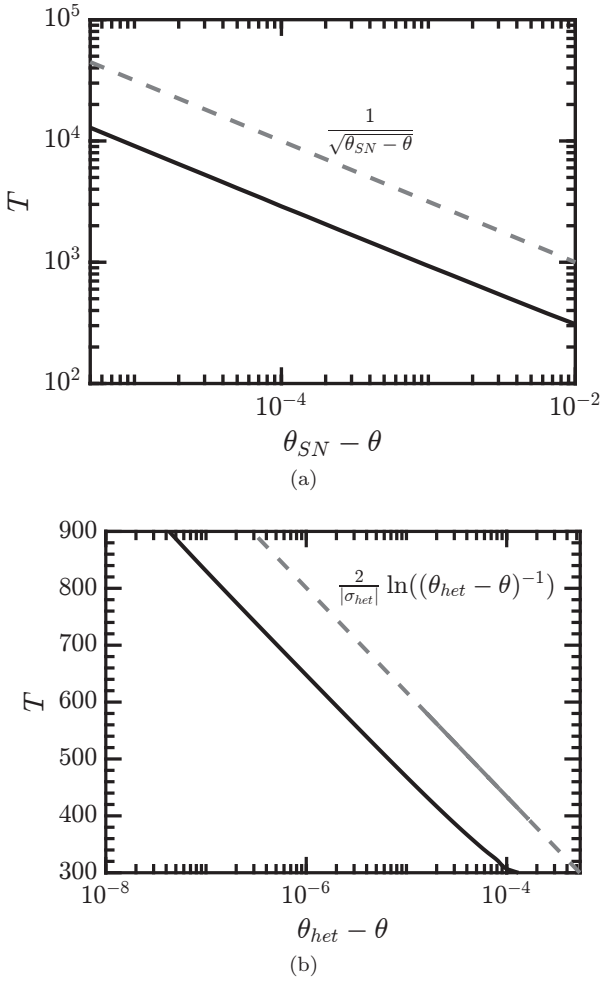


FIG. 17: (a) Evolution of the period of the stable limit cycles shadowing the heteroclinic cycle as a function of the distance $\theta_{SN} - \theta$ to the saddle-node bifurcation. (b) Evolution of the period near the heteroclinic bifurcation at $\theta_{het}$, where $\sigma_{het} = -0.0251$ is the leading stable eigenvalue of the $\mathrm{PrW}_{G,1}$ fixed point.

$\mathrm{PrW}_G$ branch in the degenerate case are replaced by a saddle-node bifurcation on each branch. The second case, $D_i = 0$ but $A_i - 2l_2 \neq 0$, illustrated in Figure 13(c), shows the presence of $\mathrm{PrW}_A$ and $\mathrm{PrW}_G$ branches, the latter replacing the symmetric $\mathrm{PrW}_B$ branch. These branches connect via a transcritical bifurcation, which is responsible, in this case, for the stability of the whole upper section of the $\mathrm{PrW}_G$ branch since no Hopf bifurcation takes place.

We next turn our attention to the nondegenerate case $A_i - 2l_2 \neq 0$, $D_i \neq 0$. The bifurcation diagram of the fixed points of the polar normal form is depicted in Figure 15. The figure displays two disconnected branches of general Precessing Waves $\mathrm{PrW}_G$. The first of these, referred to as $\mathrm{PrW}_{G,1}$ in the figure, becomes unstable through a Hopf bifurcation, leading to a 3FW branch (not shown). The second $\mathrm{PrW}_G$ branch, labeled $\mathrm{PrW}_{G,2}$, bifurcates from and terminates on the $\mathrm{MM}_\pi$ branch with a saddle-node bifurcation in between: the upper section is stable, whereas the lower is unstable. Because of the symmetry under the reflection $\kappa$, there is in fact a pair of such saddle-node bifurcations, $\mathrm{PrW}^{\pm}_{G,2}$, both occurring at $\theta = \theta_{SN} \approx 0.663445$. Moreover, each is of Saddle-Node-in-a-Periodic-Orbit (SNIPER) type but with complex leading eigenvalues at the fold points $\mathrm{PrW}^{\pm}_{G,2}$: $(0, -0.6795, -0.0182 \pm 0.4418i)$. For a study of this situation in the absence of $\kappa$ symmetry, see [47]. In the presence of this symmetry, this case can either lead to a pair of symmetry-related homoclinics to $\mathrm{PrW}^{\pm}_{G,2}$ or, as in this case, to a heteroclinic cycle connecting $\mathrm{PrW}^{+}_{G,2}$ to $\mathrm{PrW}^{-}_{G,2}$ and vice versa, a consequence of the intertwined nature of the stable and unstable manifolds of $\mathrm{PrW}^{\pm}_{G,2}$. In the former case the near-homoclinic orbit to the left of $\mathrm{PrW}^{\pm}_{G,2}$ contains a certain number of decreasing oscillations as it approaches and leaves $\mathrm{PrW}^{\pm}_{G,2}$, the number of these oscillations depending on the speed with which the trajectory passes through the $\mathrm{PrW}^{\pm}_{G,2}$ neighborhood, and hence on the distance of $\theta$ from $\theta_{SN}$. In the latter case the unstable manifold associated with the degenerate eigenvalue injects the trajectory into the image fold point and the same local behavior there leads to reinjection back into the original fold, generating a $\kappa$-

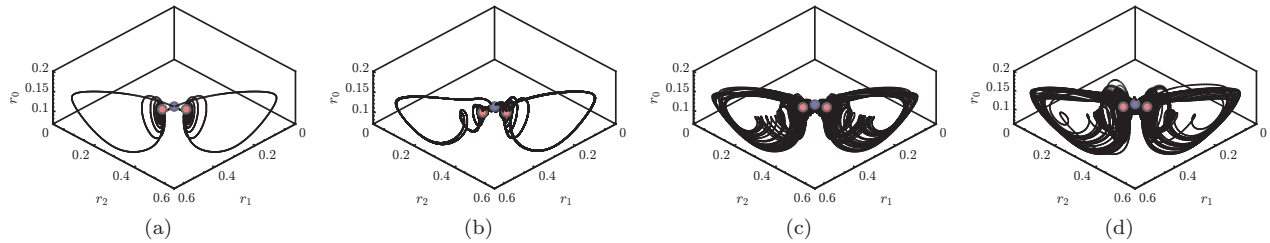


FIG. 18: Stable attractors in a $(r_0, r_1, r_2)$ projection for (a) $\theta = 0.663$ (symmetric periodic orbit); (b) $\theta = 0.647$ (asymmetric orbit); (c) $\theta = 0.645$ (asymmetric orbit); (d) $\theta = 0.643$ (asymmetric orbit). The symmetry-related $\mathrm{PrW}_{G,2}$ fixed points corresponding to the saddle-node at $\theta \approx 0.663445$ are indicated by red points, with the $\mathrm{PrW}_A$ point (present in the degenerate case only) depicted as a blue point; these are shown for orientation only.

symmetric heteroclinic cycle, cf. [48]. Figure 16 shows such an orbit in two projections, computed for $\theta$ just below $\theta_{SN} \approx 0.663445$. At this $\theta$ the $\mathrm{PrW}^{\pm}_{G,2}$ points are absent and the orbit shown is actually a long period periodic orbit. Figure 17a shows the period of such orbits as a function of $\theta_{SN} - \theta$, confirming the expected relation $T \sim (\theta_{SN} - \theta)^{-1/2}$. This divergence is a consequence of a slowdown of the trajectory in the vicinity of the phase space location where the $\mathrm{PrW}_{G,2}$ appear when $\theta$ increases through $\theta_{SN}$, resulting in increased accumulation of turns as this point is approached. Note that these orbits inherit the stability of the (upper) $\mathrm{PrW}_{G,2}$ branch (cf. Figure 15) and hence represent attractors of the system.

Figure 18 shows sample attractors found on decreasing $\theta$ further. Figure 18a shows a stable symmetric orbit at $\theta = 0.663$, followed by asymmetric chaotic attractors (with a positive Lyapunov exponent) generated with increasing distance from $\theta_{SN}$. The absence of chaotic states near $\theta_{SN}$ is a consequence of the fact the flow in this region is locally contracting.

To understand the origin of these states, we examine the behavior of a typical periodic orbit associated with the SNIPER bifurcation. As already explained this orbit depends sensitively on the value of $\theta < \theta_{SN}$. In Figure 19a we show the period $T$ of this orbit as a function of $\theta$ obtained using numerical continuation. This period diverges as $\theta \to \theta_{SN}$ from below and the orbit approaches the heteroclinic cycle shown in Figure 16. As $\theta$ decreases, the period $T$ decreases, although this decrease is interrupted by a series of back-to-back folds. Each such pair is responsible for the elimination of one small amplitude turn of the trajectory (not shown), resulting in a gradual unwinding of the trajectory. As $\theta$ decreases towards the leftmost fold and beyond, the trajectory develops small loops in the vicinity of $\mathrm{PrW}_{G,1}$ (Figure 20) and its period begins to diverge again, this time logarithmically (Figure 17b), indicating approach to a heteroclinic connection involving $\mathrm{PrW}_{G,1}$ and located at $\theta = \theta_{het} \approx 0.6454$. Since the leading unstable eigenvalues of $\mathrm{PrW}_{G,1}$ at this parameter values are complex, $0.2446 \pm 0.3661i$, while the leading stable eigenvalue is real, $-0.0251$, these points are both saddle-foci. The complex unstable eigenvalues account for the oscillatory approach to the global bifurcation at $\theta \approx 0.6454$ while the fact that the flow near $\mathrm{PrW}_{G,1}$ is locally expanding implies that we should expect stable chaotic dynamics near this parameter value, as in the classical example of Shil'nikov where the signs of the eigenvalues are reversed [49–51].

In Figure 19a the solid line tracks the period of the $\kappa$-symmetric orbit. As $\theta \to \theta_{het} \approx 0.6454$ from above, this orbit collides with $\mathrm{PrW}_{G,1}$, forming a heteroclinic connection from $\mathrm{PrW}_{G,1}$ to its image under $\kappa$ and back again. Near $\theta_{het}$ this orbit is accompanied by back-to-back symmetry-breaking bifurcations, generating asymmetric periodic orbits (Figure 19b). These asymmetric orbits are free to period-double into chaos, resulting in 'bubbles' of chaotic behavior, as described in [52] and references therein. Close to the primary heteroclinic bifurcation, these bubbles 'burst' via the formation of pairs of subsidiary homoclinic orbits. The red dashed and thin solid lines in Figure 19b show examples of this generic behavior in our problem; Figure 19c compares the homoclinic orbit at the green dashed asymptote with the corresponding period-doubled orbit on the red dashed branch at the same $\theta$ value. Further details are omitted. Thus, the primary symmetric periodic orbit is associated with a number of chaotic intervals located around subsidiary homoclinic orbits originating in global bifurcations of asymmetric orbits associated with it, cf. Figure 18. In particular, stable chaotic motion is also observed for $\theta$ *below* the primary heteroclinic bifurcation at $\theta_{het} \approx 0.6454$.

We mention that the periodic orbit originating from the Hopf point on the $\mathrm{PrW}_{G,1}$ branch ($\theta \approx 0.3841$, blue point in Figure 15) is stable from the Hopf point to $\theta \approx 0.4518$, where the first of several Neimark-Sacker bifurcations takes place. These are interspersed with additional global bifurcations and intervals of chaos as $\theta$ increases towards $\theta_{het} \approx 0.6454$. Some sample solutions are shown in Figure 21 to whet appetite. The details depend on the parameters used and are omitted.

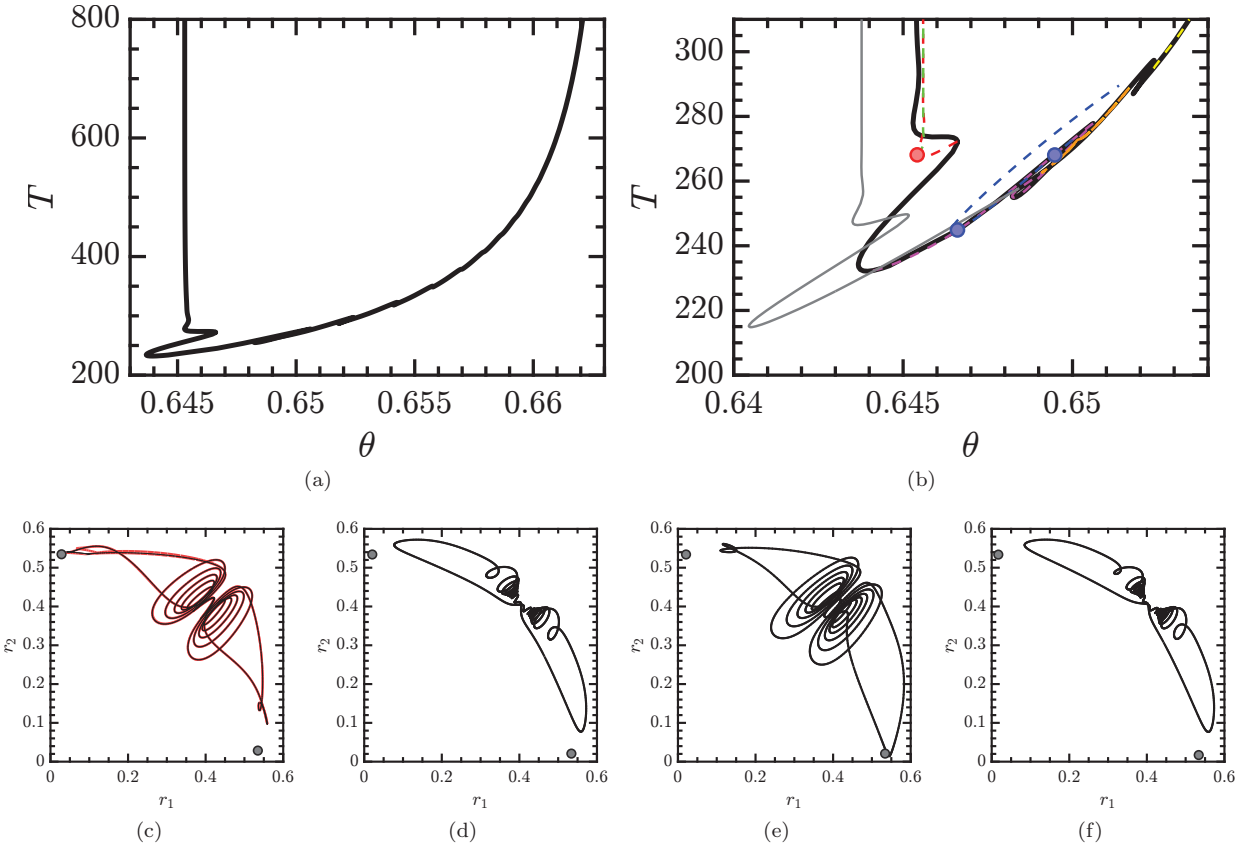


FIG. 19: (a) Evolution of the period $T$ of a symmetric periodic orbit born in the SNIPER bifurcation $\theta \approx 0.663445$ and terminating in a heteroclinic bifurcation at $\theta \approx 0.6454$ (thick solid line). Secondary branches of asymmetric states are displayed in thin lines: solid line for the branch whose period diverges at $\theta \approx 0.64377$ and dashed lines for the other branches, see panel (b) for more detail. The secondary branches are accompanied by back-to-back period-doubling cascades (three period-doubling points are indicated with solid circles of the same color as the branch) which open up via the formation of subsidiary homoclinic orbits as in panel (c), black line; the superposed red curve shows an accompanying period-doubled solution. Portraits (d-f) display the $(r_1, r_2)$ projection at $\theta = 0.65$ for the dashed magenta, blue, and orange branches in (b) showing a symmetric and two asymmetric periodic orbits, respectively. The location of $\mathrm{PrW}_{G,1}$ is indicated with a small circle in (c-f). Only (c) is close to homoclinic; the proximity of orbit (e) to the lower fixed point is a projection effect.

## VII. NORMAL FORM REDUCTION

The process of reducing the governing equations to normal form near a multiple bifurcation is based on center manifold reduction followed by a series of near-identity variable changes to simplify the dynamical equations on the center manifold. The resulting equations are then *unfolded* by introducing parameters that break apart the multiple bifurcation in a generic way. In infinite-dimensional problems, such as those arising in fluid mechanics, it is preferable to employ multiple scales techniques to compute both the normal form and the coefficients within it as part of the same calculation. We employ here this technique to determine all the coefficients in the third-order normal form (8).

First, let us introduce the following formal expression for the governing equations on a domain $\Omega$:

$$\begin{aligned} \mathbf{B}\frac{\partial \mathbf{q}}{\partial t} &= \mathbf{F}(\mathbf{q},\boldsymbol{\eta}) \equiv \mathbf{L}\mathbf{q} + \mathbf{N}(\mathbf{q},\mathbf{q}) + \mathbf{G}(\mathbf{q},\boldsymbol{\eta}),\ \mathbf{x} \in \Omega\,, \\ \mathbf{D}_{bc}\mathbf{q}(\mathbf{x}) &= \mathbf{q}_{\partial\Omega},\ \mathbf{x} \in \partial\Omega\,. \end{aligned} \tag{56}$$

Here $\partial\Omega$ represents the domain boundary. This form of the governing equations takes into account a linear dependence on the state variable $\mathbf{q}$ through $\mathbf{L}$ and a quadratic dependence on the state variable and the parameters $\boldsymbol{\eta}$ through the operators $\mathbf{G}(\cdot,\cdot)$ and $\mathbf{N}(\cdot,\cdot)$. Equation (56) formally includes the incompressible Navier–Stokes equations written in cylindrical coordinates for the TCF and WFA problems, whereas for WFA-MC one must consider the Boussinesq approximation of the incompressible Navier–Stokes equations written in cylindrical coordinates as well. For this set of

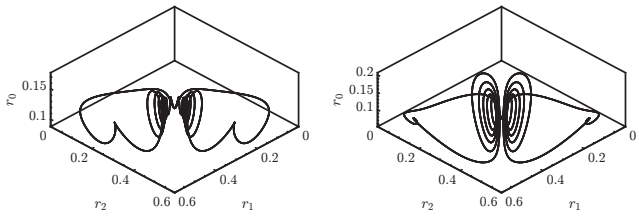


FIG. 20: The periodic orbit at the seventh and eighth folds from the right in Figure 19b, with a period-doubling bubble in between (not shown). (a) $\theta = 0.6437$. (b) $\theta = 0.6466$.

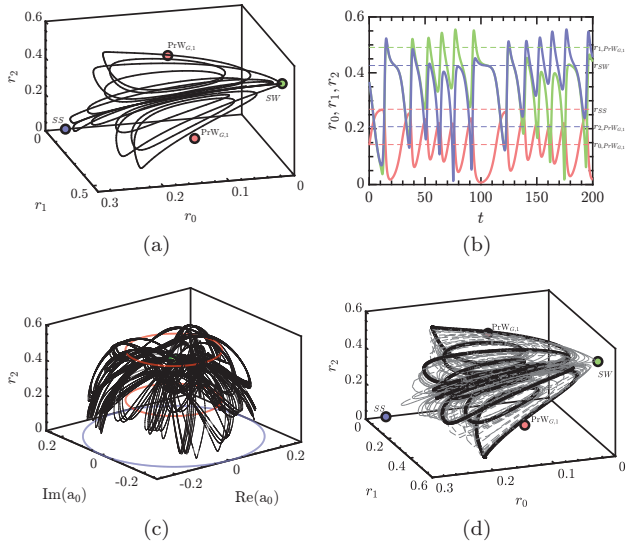


FIG. 21: (a) Phase portrait of a near-homoclinic orbit to the SW state in the $(r_0, r_1, r_2)$ space at $\theta = 0.452$, and (b) the corresponding time series showing $r_0(t)$ (red), $r_1(t)$ (green) and $r_2(t)$ (blue). Near the homoclinic connection $r_1$ approaches $r_2$ and $r_0$ falls to zero. (c) A trajectory at $\theta = 0.457$ in the $(\mathrm{Re}(a_0), \mathrm{Im}(a_0), r_2)$ space showing that the trajectory intermittently visits SW states with different phases $\phi$, each visit resulting in a switch between an oscillation about one $\mathrm{PrW}_{G,1}$ state to an oscillation about the other; red circles represent the group orbit of the two $\mathrm{PrW}_{G,1}$ states while the blue circle represents the group orbit of the SS states [53]. (d) Chaotic attractor at $\theta = 0.49$ (thin dashed grey line) together with an (unstable) $\kappa$-symmetric periodic orbit computed at $\theta \approx 0.4896$.

equations, the operators in eq. (56) take the following form,

$$\begin{aligned}
\mathbf{L}\mathbf{q} &= \begin{pmatrix} -\nabla P \\ \nabla \cdot \mathbf{U} \\ 0 \end{pmatrix}, \\
\mathbf{N}(\mathbf{q}_1, \mathbf{q}_2) &= -\begin{pmatrix} \mathbf{U}_1 \cdot \nabla \mathbf{U}_2 \\ 0 \\ \mathbf{U}_1 \cdot \nabla T \end{pmatrix}, \\
\mathbf{G}(\mathbf{q}, \boldsymbol{\eta}) &= \begin{pmatrix} \frac{1}{\mathrm{Re}} \nabla \cdot \left( \nabla \mathbf{U} + (\nabla \mathbf{U})^T \right) + \mathrm{Ri}\, T \mathbf{e}_z \\ 0 \\ \frac{1}{\mathrm{Re}\,\mathrm{Pr}} \nabla^2 T \end{pmatrix}.
\end{aligned} \tag{57}$$

In red color we have included the modification for the WFA-MC problem with respect to the WFA problem. The set of parameters $\boldsymbol{\eta} \in \mathbb{R}^{N_p}$, where $N_p$ is the number of parameters, is composed of the two dimensionless angular velocities of the cylindrical annulus for TCF, the inverse Reynolds number for WFA, and the inverse Reynolds number together with the Richardson and Prandtl numbers for WFA-MC. In the following, we will consider the most general case, that is, the WFA-MC case where the vector of parameters takes the form $\boldsymbol{\eta} \equiv [\eta_0, \eta_1, \eta_2] = [\mathrm{Re}^{-1}, \mathrm{Ri}, \mathrm{Pr}]^T$. The Reynolds number is defined as the ratio of inertial and viscous forces, i.e., $\mathrm{Re} = \frac{U_\infty D}{\nu}$, with $U_\infty$ the uniform velocity at the far field, $D$ the diameter of the bluff body and $\nu$ the kinematic viscosity; the Prandtl number, $\mathrm{Pr} = \frac{\nu}{\kappa}$, is the ratio of viscosity and the thermal diffusivity $\kappa$. The Richardson number is defined as $\mathrm{Ri} = -\frac{\beta(\mathbf{e}_{U_\infty} \cdot \mathbf{g})(T_b - T_\infty)D}{U_\infty^2}$, with $\beta$ the thermal expansion coefficient, $\mathbf{e}_{U_\infty} = \mathbf{U}_\infty / U_\infty$ the unit vector in the direction of the far field velocity, $\mathbf{g}$ the gravitational acceleration, and $T_b$ and $T_\infty$ the temperature of the bluff body and in the far field, respectively. Finally, we suppose that the dependence of the solution restricted to the boundary of the domain is linear, i.e., we take $\mathbf{D}_{bc}$ to be a linear boundary condition operator. One can also consider the dependence of the boundary conditions on parameters, that is either $\mathbf{D}_{bc}(\boldsymbol{\eta})$ or $\mathbf{q}_{\partial\Omega}(\boldsymbol{\eta})$, which may be used, for instance, for modelling of a moving wall. For the sake of simplicity this possibility is not considered.

The multiple scales expansion of the solution $\mathbf{q}$ of eq. (56) consists of an expansion of eq. (1) in powers of a small parameter $\varepsilon \ll 1$:

$$\mathbf{q}(t, \tau) = \mathbf{Q}_0 + \varepsilon \mathbf{q}_{(\varepsilon)}(t, \tau) + \varepsilon^2 \mathbf{q}_{(\varepsilon^2)}(t, \tau) + \mathcal{O}(\varepsilon^3)\,. \tag{58}$$

The departure $\boldsymbol{\eta} - \boldsymbol{\eta}_c$ of the parameters from criticality is assumed to be of second order, i.e., $\eta_i - \eta_{i,c} = \mathcal{O}(\varepsilon^2)$ for $i = 0, 1, 2$. The expansion (58) encompasses a two-scale expansion of the original time, $t \mapsto t + \varepsilon^2 \tau$, that incorporates the fast time scale $t$ of the self-sustained instability and the slow time scale $\tau$ of the evolution of the amplitudes $a_i(\tau)$ in eq. (1), for $i = 0, 1, 2$. The resulting expansion of the left side of eq. (56) up to third order is given by

$$\varepsilon \mathbf{B} \frac{\partial \mathbf{q}_{(\varepsilon)}}{\partial t} + \varepsilon^2 \mathbf{B} \frac{\partial \mathbf{q}_{(\varepsilon^2)}}{\partial t} + \varepsilon^3 \left[ \mathbf{B} \frac{\partial \mathbf{q}_{(\varepsilon^3)}}{\partial t} + \mathbf{B} \frac{\partial \mathbf{q}_{(\varepsilon)}}{\partial \tau} \right] \tag{59}$$

while the right side is

$$\mathbf{F}(\mathbf{q},\boldsymbol{\eta}) = \mathbf{F}_{(0)} + \varepsilon\mathbf{F}_{(\varepsilon)} + \varepsilon^2\mathbf{F}_{(\varepsilon^2)} + \varepsilon^3\mathbf{F}_{(\varepsilon^3)}\,. \tag{60}$$

The resulting problem is solved order by order.

### 1. Order $\varepsilon^0$

The leading order solution $\mathbf{Q}_0$ of the multiple scales expansion (58) is the steady state of the governing equations evaluated at the threshold of instability, i.e., $\boldsymbol{\eta} = \boldsymbol{\eta}_c$,

$$\begin{array}{ll} \mathbf{0} & = \mathbf{F}(\mathbf{Q}_0,\mathbf{0})\,, \quad \mathbf{x}\in\Omega\,, \\ \mathbf{D}_{bc}\mathbf{Q}_0(\mathbf{x}) & = \mathbf{Q}_{0,\partial\Omega}\,, \quad \mathbf{x}\in\partial\Omega\,. \end{array} \tag{61}$$

### 2. Order $\varepsilon^1$

The first order correction $\mathbf{q}_{(\varepsilon)}(t,\tau)$ in the multiple scales expansion (58) is composed of the eigenmodes of the linearized system

$$\begin{aligned} \mathbf{q}_{(\varepsilon)}(t,\tau) \equiv\ & \mathrm{Re}\big(a_0(\tau)e^{-im_0\theta}\hat{\mathbf{q}}_0\big) \\ & + \mathrm{Re}\big(a_1(\tau)e^{-i\omega t}e^{-im_1\theta}\hat{\mathbf{q}}_1\big) \\ & + \mathrm{Re}\big(a_2(\tau)e^{-i\omega t}e^{i-m_2\theta}\hat{\mathbf{q}}_2\big)\,, \end{aligned} \tag{62}$$

where the reflection symmetry in $O(2)$ imposes the requirement $m_2 = -m_1$.

Each term $\hat{\mathbf{q}}_\ell$ in the first order expansion (62) solves the corresponding linear problem:

$$\begin{array}{ll} \mathbf{J}_{(\omega_\ell,m_\ell)}\hat{\mathbf{q}}_\ell & = \Big(i\omega_\ell\mathbf{B} - \frac{\partial\mathbf{F}}{\partial\mathbf{q}}|_{\mathbf{q}=\mathbf{Q}_0,\boldsymbol{\eta}=\boldsymbol{\eta}_c}\Big)\hat{\mathbf{q}}_\ell = \mathbf{0}, \quad \mathbf{x}\in\Omega, \\ \mathbf{D}_{bc}\hat{\mathbf{q}}_\ell(\mathbf{x}) & = 0, \quad \mathbf{x}\in\partial\Omega\,, \end{array} \tag{63}$$

where $\frac{\partial\mathbf{F}}{\partial\mathbf{q}}|_{\mathbf{q}=\mathbf{Q}_0,\boldsymbol{\eta}=\boldsymbol{\eta}_c}\hat{\mathbf{q}}_\ell = \mathbf{L}_{m_\ell}\hat{\mathbf{q}}_\ell + \mathbf{N}_{m_\ell}(\mathbf{Q}_0,\hat{\mathbf{q}}_\ell) + \mathbf{N}_{m_\ell}(\hat{\mathbf{q}}_\ell,\mathbf{Q}_0)$. The subscript $m_\ell$ indicates the azimuthal wavenumber used for the evaluation of the operator.

### 3. Order $\varepsilon^2$

The second order expansion term $\mathbf{q}_{(\varepsilon^2)}(t,\tau)$ is determined from the resolution of a set of forced linear systems, with the forcing terms evaluated in terms of the (known) zeroth and first order terms. The expansion in terms of amplitudes $a_i(\tau)$ of $\mathbf{q}_{(\varepsilon^2)}(t,\tau)$ is assessed from term-by-term identification of the forcing terms at the second order. The nonlinear second order terms are

$$\begin{aligned} \mathbf{F}_{(\varepsilon^2)} \equiv\ & \sum_{\substack{j,k=0 \\ k\le j}}^{2} \Big(a_j a_k \mathbf{N}(\hat{\mathbf{q}}_j,\hat{\mathbf{q}}_k)e^{-i(m_j+m_k)\theta}e^{-i(\omega_j+\omega_k)t} + \text{ c.c.}\Big) \\ & + \sum_{\substack{j,k=0 \\ k\le j}}^{2} \Big(a_j\overline{a}_k \mathbf{N}(\hat{\mathbf{q}}_j,\overline{\hat{\mathbf{q}}}_k)e^{-i(m_j-m_k)\theta}e^{-i(\omega_j-\omega_k)t} + \text{ c.c.}\Big) \\ & + \sum_{\ell=0}^{2} \Delta\eta_\ell \mathbf{G}(\mathbf{Q}_0,\mathbf{e}_\ell)\,, \end{aligned} \tag{64}$$

where $\mathbf{e}_\ell$ is an element of the orthonormal basis of $\mathbb{R}^{N_p}$, a vector composed of zeros except at the position $\ell$ where it is equal to unity.

Since no quadratic combination of elements in eq. (62) results in resonant terms, the second order term can be expanded as

$$\mathbf{q}_{(\varepsilon^2)} \equiv \sum_{\substack{j,k=0 \\ k\le j}}^{2} \big(a_j a_k \hat{\mathbf{q}}_{j,k} + a_j\overline{a}_k\hat{\mathbf{q}}_{j,-k} + \text{ c.c. }\big) + \sum_{\ell=0}^{2}\Delta\eta_\ell\mathbf{Q}_0^{(\eta_\ell)}\,, \tag{65}$$

with the rules $\hat{\mathbf{q}}_{j,k} = \hat{\mathbf{q}}_{k,j}$ and $\hat{\mathbf{q}}_{-j,-k} = \overline{\hat{\mathbf{q}}}_{j,k}$. Note the slight abuse of notation with $\hat{\mathbf{q}}_{-0} = \overline{\hat{\mathbf{q}}}_0$. Terms $\hat{\mathbf{q}}_{j,j}$ are harmonics of the flow, $\hat{\mathbf{q}}_{j,k}$ with $j\neq k$ are coupling terms, $\hat{\mathbf{q}}_{j,-j}$ are harmonic base flow modification terms and $\mathbf{Q}_0^{(\eta_\ell)}$ are base flow corrections due to the assumed departure of the parameter $\Delta\eta_\ell = \eta_{\ell_c} - \eta_\ell$ from the critical point measured by $\varepsilon$.

Finally, the second-order terms are computed by solving the following nonresonant system of equations,

$$\mathbf{J}_{(\omega_j+\omega_k,m_j+m_k)}\hat{\mathbf{q}}_{j,k} = \hat{\mathbf{F}}_{(\varepsilon^2)}^{(j,k)}\,, \tag{66}$$

where $\hat{\mathbf{F}}_{(\epsilon^2)}^{(j,k)} \equiv \mathbf{N}(\hat{\mathbf{q}}_j,\hat{\mathbf{q}}_k) + \mathbf{N}(\hat{\mathbf{q}}_k,\hat{\mathbf{q}}_j)$ and

$$\mathbf{J}_{(0,0)}\mathbf{Q}_0^{(\eta_\ell)} = \mathbf{G}(\mathbf{Q}_0,\mathbf{e}_\ell). \tag{67}$$

### 4. Order $\varepsilon^3$

At third order resonant terms are generated and these lead to secular (nonperiodic) terms in the expansion. We eliminate these terms by imposing a solvability condition on the system via the Fredholm alternative. This condition determines the required normal form at third order in $\varepsilon$. Specifically, the linear terms $\lambda_s$ and $\lambda_h$ are determined as follows

$$\lambda_s = \frac{\langle\hat{\mathbf{q}}_0^\dagger,\hat{\mathbf{F}}_{(\epsilon^3)}^{(a_0)}\rangle}{\langle\hat{\mathbf{q}}_0^\dagger,\mathbf{B}\hat{\mathbf{q}}_0\rangle},\ \lambda_h = \frac{\langle\hat{\mathbf{q}}_1^\dagger,\hat{\mathbf{F}}_{(\epsilon^3)}^{(a_1)}\rangle}{\langle\hat{\mathbf{q}}_1^\dagger,\mathbf{B}\hat{\mathbf{q}}_1\rangle} = \frac{\langle\hat{\mathbf{q}}_2^\dagger,\hat{\mathbf{F}}_{(\epsilon^3)}^{(a_2)}\rangle}{\langle\hat{\mathbf{q}}_2^\dagger,\mathbf{B}\hat{\mathbf{q}}_2\rangle}\,, \tag{68}$$

while the (real) cubic coefficients $l_i$ for $i = 0,1,2,3$ are given by

$$\begin{aligned} l_0 &= \frac{\langle\hat{\mathbf{q}}_0^\dagger,\hat{\mathbf{F}}_{(\epsilon^3)}^{(a_0|a_0|^2)}\rangle}{\langle\hat{\mathbf{q}}_0^\dagger,\mathbf{B}\hat{\mathbf{q}}_0\rangle}, & l_3 &= \frac{\langle\hat{\mathbf{q}}_0^\dagger,\hat{\mathbf{F}}_{(\epsilon^3)}^{(\overline{a}_0a_1\overline{a}_2)}\rangle}{\langle\hat{\mathbf{q}}_0^\dagger,\mathbf{B}\hat{\mathbf{q}}_0\rangle} \\ l_1 - il_2 &= \frac{\langle\hat{\mathbf{q}}_0^\dagger,\hat{\mathbf{F}}_{(\epsilon^3)}^{(a_0|a_1|^2)}\rangle}{\langle\hat{\mathbf{q}}_0^\dagger,\mathbf{B}\hat{\mathbf{q}}_0\rangle}, & l_1 + il_2 &= \frac{\langle\hat{\mathbf{q}}_0^\dagger,\hat{\mathbf{F}}_{(\epsilon^3)}^{(a_0|a_2|^2)}\rangle}{\langle\hat{\mathbf{q}}_0^\dagger,\mathbf{B}\hat{\mathbf{q}}_0\rangle}\,. \end{aligned} \tag{69}$$

Finally, the complex coefficients $A, B, C$ and $D$ are given by

$$\begin{aligned} B &= \frac{\langle\mathbf{q}_1^\dagger,\hat{\mathbf{F}}_{(\epsilon^3)}^{(a_1|a_1|^2)}\rangle}{\langle\hat{\mathbf{q}}_1^\dagger,\mathbf{B}\hat{\mathbf{q}}_1\rangle}, & A+B &= \frac{\langle\mathbf{q}_1^\dagger,\hat{\mathbf{F}}_{(\epsilon^3)}^{(a_1|a_2|^2)}\rangle}{\langle\hat{\mathbf{q}}_1^\dagger,\mathbf{B}\hat{\mathbf{q}}_1\rangle}, \\ C &= \frac{\langle\mathbf{q}_1^\dagger,\hat{\mathbf{F}}_{(\epsilon^3)}^{(a_1|a_0|^2)}\rangle}{\langle\hat{\mathbf{q}}_1^\dagger,\mathbf{B}\hat{\mathbf{q}}_1\rangle}, & D &= \frac{\langle\mathbf{q}_1^\dagger,\hat{\mathbf{F}}_{(\epsilon^3)}^{(a_0^2a_2)}\rangle}{\langle\hat{\mathbf{q}}_1^\dagger,\mathbf{B}\hat{\mathbf{q}}_1\rangle}\,. \end{aligned} \tag{70}$$

The forcing terms associated with the solvability conditions in eqs. (68) to (70) are detailed in Appendix A 1.

## VIII. CONSTRUCTION OF BIFURCATION DIAGRAMS

We now explain how the results derived in the previous section can be used to construct consistent bifurcation diagrams. The method is similar to that used in Hirschberg & Knobloch [29] and is explained in Figure 22. As illustrated in this figure, the conditions for the occurrence of the various bifurcations can be interpreted as lines in the $(\lambda_s, \lambda_h)$ plane. For example, the primary steady-state bifurcation occurs along the line $\lambda_s = 0$, which is the horizontal axis in this representation. Similarly, the primary Hopf bifurcation occurs along the line $\lambda_h = 0$, which is the vertical axis. The conditions relevant to the birth of mixed modes also correspond to straight lines, as displayed in the figure. For both the wake problem (WFA or WFA-MC) and the TCF problem, variation of the base-flow parameters defines a path in the $(\lambda_s, \lambda_h)$ plane. The bifurcation diagram can then be constructed by considering the successive crossings of this path with the lines defining the bifurcations.

Let us consider first the bifurcation scenario of the WFA-MC case as a function of Reynolds numbers $\eta_{\mathrm{Re}}$ and $\eta_{\mathrm{Ri}}$, at a constant distance in terms of the second parameter from the organizing centre. We denote by $\eta_{\mathrm{Re}}|_{\mathrm{Ri}=\mathrm{Ri}_c}$ the path followed at a constant Richardson number equal to that at which the unsteady and steady modes become simultaneously unstable. Similarly, we denote by $\eta_{\mathrm{Re}}|_{\mathrm{Ri}=0}$ the straight line path from quadrant *III* (defined by $\lambda_s < 0$, $\lambda_h < 0$), traversing quadrant *IV* ($\lambda_s > 0$, $\lambda_h < 0$), and then crossing into quadrant *I* ($\lambda_s > 0$, $\lambda_h > 0$). This path is relevant to the wake problem (WFA) for increasing Reynolds number if we assume a linear dependence of the form (13). When following this path, the first bifurcation is the primary bifurcation leading to the SS mode. There are two possible secondary bifurcations on this branch, leading to $\mathrm{MM}_0$ and $\mathrm{MM}_\pi$ and these occur along the lines $-l_0\lambda_h + (C_r \pm D_r)\lambda_s = 0$ with positive sign for $\mathrm{MM}_0$ and negative sign for $\mathrm{MM}_\pi$. The sign of $D_r$ indicates which of these bifurcations occurs first along the given path. For example, if $D_r < 0$, as displayed on the figure, the bifurcation to $\mathrm{MM}_\pi$ occurs first. Moreover, if $\Delta_- > 0$ (as assumed in the figure), this bifurcation is supercritical and gives rise to a stable branch. The bifurcation from SS to $\mathrm{MM}_\pi$ may occur subsequently, as found in the figure, but the branch born at this bifurcation is necessarily unstable, according to the considerations in Section IV C.

Similarly, the lines $-(2B_r + A_r)\lambda_s + (l_1 \pm l_3)\lambda_h = 0$ indicate secondary bifurcations from SW to $\mathrm{MM}_0$ (positive sign) and $\mathrm{MM}_\pi$ (negative sign). Starting from the pure SW mode and following the prescribed path backward, the sign of $l_3$ lets us distinguish which of these lines will be crossed first. For example, if $l_3 < 0$, as displayed in the figure, the bifurcation to $\mathrm{MM}_\pi$ occurs first, leading to a stable branch if $\Delta_- > 0$.

Figure 22b exhibits the case corresponding to $l_3 < 0$, $D_r < 0$, $\Delta_+ > 0$, $\Delta_- > 0$, the situation relevant to wake flow past a fixed disk. The figure displays the bifurcation diagram for a disk of aspect ratio $\chi = 10$. For details, see Section VIII B.

In the following, we analyze the predicted transition behavior of the flow past a fixed sphere and a fixed disk. In some figures, we use the lift coefficient to illustrate the bifurcation diagram; this is defined as $C_L = \frac{L}{\frac{1}{2}\rho_\infty U_\infty^2 D}$, with $L$ the lift force, $\rho_\infty$ and $U_\infty$ the density and velocity in the far field (assumed equal to unity) and $D$ the diameter of the object.

### A. Mixed convection in the flow past a sphere

Let us revisit the problem of pattern formation behind a sphere falling through a thermally stratified fluid. In our formulation the sphere is held fixed, with upward flow past it (the WFA-MC problem). Specifically, a sphere of diameter $D$ is held at a constant temperature $T_b$ subject to upward flow characterized by a constant velocity $U_\infty$ and temperature $T_\infty$ far from the body. The problem is specified by the Reynolds number as $\mathrm{Re} = \frac{U_\infty D}{\nu}$ and the Richardson number $\mathrm{Ri} = -\frac{\beta(\mathbf{e}_{U_\infty}\cdot\mathbf{g})(T_b - T_\infty)D}{U_\infty^2}$. This problem has many practical applications in engineering such as cooling, heating [26], sedimentation [54], melting [55], combustion [56], and vaporization [57]. A hot sphere represents a heat source embedded within the physical domain, where the solid body is subjected to forces of hydrodynamic and thermal origin. There are two main cases of interest. The case of a hot falling sphere where the fluid within the wake is accelerated with respect to the spherical body is called the *assisting* case and is characterized by a positive Richardson number ($\mathrm{Ri} > 0$). The opposite case, where the wake of a hot ascending spherical particle is decelerated by buoyancy effects, is referred to as the *opposing* case and corresponds to a negative Richardson number ($\mathrm{Ri} < 0$). Kotouc et al. [26] studied numerically both configurations for two Prandtl numbers, $\mathrm{Pr} = 0.72$ and $\mathrm{Pr} = 7$. The assisting flow case displays an organising center of Hopf-Hopf type with azimuthal wavenumbers $m = 1$ and $m = 2$. The opposing flow configuration exhibits instead a point in the $(\mathrm{Re}, \mathrm{Ri})$ parameter space where a steady-state mode and a pair of unsteady modes with azimuthal wavenumber $m = \pm 1$ are simultaneously unstable, cf. Figure 22.

The opposing flow case at $\mathrm{Pr} = 0.72$ displays a large variety of patterns. The codimension-two point at $(\mathrm{Re}_c, \mathrm{Ri}_c)$ point, see Tables XII and XIII, splits the parameter space in the following sense: for $\mathrm{Ri}_c < \mathrm{Ri} < 0$ the primary bifurcation breaks the axisymmetry of the steady-state solution, i.e., it corresponds to a steady-state mode (state I in Kotouc et al. [26]); for $\mathrm{Ri} < \mathrm{Ri}_c$ the primary branch is a standing wave (state XIV in Ko-

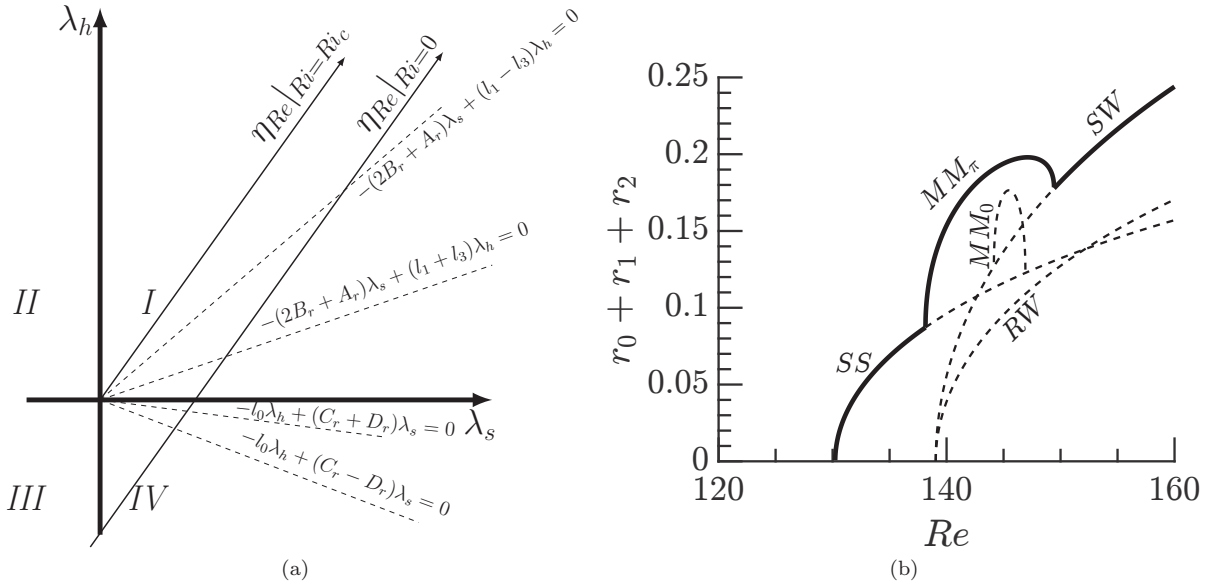


FIG. 22: Construction of the stability diagram for the WFA problem with a fixed disk of aspect ratio $\chi = 10$. (a) The unfolding plane $(\lambda_s, \lambda_h)$. Dashed lines indicate the loci of bifurcations from SS and SW to $\mathrm{MM}_{0,\pi}$. The paths labeled $\eta_{\mathrm{Re}}|_{\mathrm{Ri}=\mathrm{Ri}_c}$ and $\eta_{\mathrm{Re}}|_{\mathrm{Ri}=0}$ are the paths followed in this plane for $\mathrm{Ri} = \mathrm{Ri}_c$ and $\mathrm{Ri} = 0$, respectively. For this case $\mathrm{Ri}_c < 0$ and so increasing Ri destabilizes the system. (b) Bifurcation diagram corresponding to the $\eta_{\mathrm{Re}}|_{\mathrm{Ri}=0}$ path. See Section VIII B for details.

TABLE XII: Location of the codimension-two point and the corresponding Strouhal number ($\mathrm{Sr}_c$) at unsteady onset, together with the linear coefficients in the normal form for the WFA-MC flow past a sphere or a disk.

| Case | $\mathrm{Re}_c$ | $\mathrm{Ri}_c$ | $\mathrm{Sr}_c$ | $\lambda_s$ | $\lambda_h$ |
|---|---|---|---|---|---|
| Sphere | 172 | $-0.13$ | $8.5 \cdot 10^{-2}$ | $86.7 \cdot \eta_{\mathrm{Re}} + 0.82 \cdot \eta_{\mathrm{Ri}}$ | $\left(84.7 - 67.9i\right) \cdot \eta_{\mathrm{Re}} + \left(2.19 - 3.31i\right) \cdot \eta_{\mathrm{Ri}}$ |
| Disk $\chi = 10$ | 129.4 | $-0.069$ | $1.07 \cdot 10^{-1}$ | $76.8 \cdot \eta_{\mathrm{Re}} + 0.057 \cdot \eta_{\mathrm{Ri}}$ | $\left(66.0 - 25.2i\right) \cdot \eta_{\mathrm{Re}} + \left(0.52 - 1.10i\right) \cdot \eta_{\mathrm{Ri}}$ |
| Disk $\chi = 3$ | 152.9 | $-0.079$ | $9.5 \cdot 10^{-2}$ | $95.3 \cdot \eta_{\mathrm{Re}} + 0.37 \cdot \eta_{\mathrm{Ri}}$ | $\left(92.5 - 40.0i\right) \cdot \eta_{\mathrm{Re}} + \left(1.10 - 1.48i\right) \cdot \eta_{\mathrm{Ri}}$ |

touc et al. [26]), i.e., a solution with mean-zero lift force preserving the symmetry plane. For Richardson numbers $\mathrm{Ri} < \mathrm{Ri}_c$ the observed transition to more complex spatiotemporal patterns is explained by the interaction between the unsteady pair of modes. In this regime the cubic truncation is degenerate, as already explained, and in order to lift the degeneracy between the modulated wave states MW and IMM (these states are labelled XX in Kotouc et al. and not distinguished) one must either include higher order terms in the normal form or introduce terms that break the $O(2)$ symmetry, see Appendix B. These modulated wave states then bifurcate further, generating general Precessing Waves. In the study of Kotouc et al. [26], the authors did not observe $\mathrm{PrW}_G$, and instead identified aperiodic states, i.e., states that did not display any particular spatiotemporal symmetry. This finding could be explained by a subsequent bifurcation towards a 3FW, although this is not taken into account in the normal form.

TABLE XIII: Cubic and quintic coefficients of the normal form for the WFA-MC flow past a sphere.

| $l_0$ | $l_1$ | $l_2$ | $l_3$ | $p^1_\Delta$ |
|---|---|---|---|---|
| $-10.57$ | $-4.57$ | $-0.078$ | $0.27$ | $-201.1$ |
| $A$ | $B$ | $C$ | $D$ | $p^2_N$ |
| $1.07 + 0.75i$ | $-2.8 + 3.54i$ | $-3.78 + 3.02i$ | $0.79 - 1.0i$ | $-18.10$ |

When $\mathrm{Ri} > \mathrm{Ri}_c$ a large variety of states exist. The axisymmetric steady state loses stability with respect to a nonaxisymmetric steady-state mode, thereby losing axisymmetry. The resulting SS state then transitions into a mixed mode $\mathrm{MM}_0$ that preserves reflection symmetry and is associated with a nonzero mean lift. The $\mathrm{MM}_0$ state further transitions into a general Precessing Wave ($\mathrm{PrW}_G$), i.e., a state without a symmetry plane and slowly rotating mean lift, which in turn bifurcates into a 3FW and finally to a Pulsating Wave state. These three states are located within small regions of the parameter space. However, they have been numerically determined: $\mathrm{PrW}_G$ was numerically observed by Kotouc et al. [26] for $\mathrm{Ri} > -0.1$ (state XIII) and the 3FW (or PuW) state was identified for $\mathrm{Ri} \approx -0.1$ (state XIX), which is a state that

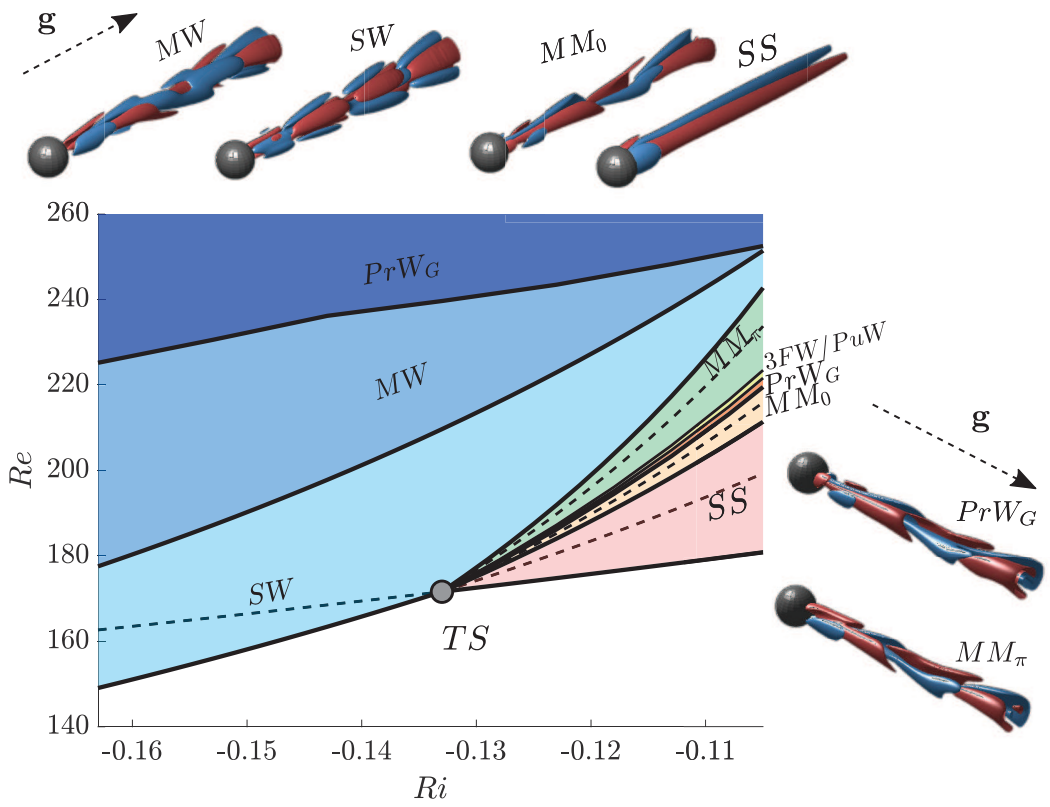


FIG. 23: Predicted flow patterns for flow past a hot sphere (the opposing case of mixed convection) in parameter space. Snapshots of the reconstructed states are included. The direction of gravity $\boldsymbol{g}$ is represented by a dashed line parallel to the axis of revolution and points from the sphere towards the wake when $T_b - T_\infty > 0$.

displays a temporary symmetry plane and at least two frequency components. The Pulsating Wave state eventually transitions into $\mathrm{MM}_\pi$, i.e., a mixed mode without a symmetry plane (see also state XIII in [26]). This series of bifurcations is followed either by SW or MW (or a Precessing Wave), in qualitative accordance with the study of Kotouc et al.

### B. Mixed convection in the flow past a disk

Let us now examine the transition scenario for axisymmetric wake flow past a disk, focusing again on the *opposing flow* case under mixed convection conditions.

TABLE XIV: Cubic and quintic coefficients of the normal form for the WFA-MC flow past a disk with $\chi = 10$.

| $l_0$ | $l_1$ | $l_2$ | $l_3$ | $p^1_\Delta$ |
|---|---|---|---|---|
| $-4.45$ | $-5.94$ | $0.92$ | $-2.28$ | $-50$ |
| $A$ | $B$ | $C$ | $D$ | $p^2_N$ |
| $0.1 - 1.29i$ | $-2.14 + 1.69i$ | $-0.64 - 2.35i$ | $-1.05 + 1.10i$ | $-1$ |

This problem depends on three control parameters, the Reynolds number Re, the Richardson number Ri, and the aspect ratio of the disk $\chi$, where $1/\chi$ is the dimensionless thickness.

The WFA problem for $\mathrm{Ri} = 0$ and $1/\chi \approx 0$ has already been studied by Fabre et al. [13] using numerical simulations and normal form coefficients fitted from the simulations. The case $\chi = 3$ was studied in detail by Auguste et al. [14]. A more rigorous study via multiple-scale analysis was performed by Meliga et al. [27]. Later, Chrust et al. [15] explored the flow dependence on the parameters $(\mathrm{Re}, \chi)$ using numerical simulations and proposed a classification of the patterns observed. These studies demonstrated the importance of the disk thickness on the transition scenario. Chrust et al. observed that, when the thickness $1/\chi$ is large, for instance $\chi = 1$, the symmetry plane is preserved for large values of the Reynolds number, i.e., only $SS$ and $\mathrm{MM}_0$ (possibly with modulated mixed modes or precessing waves) are observed before spatio-temporal chaos appears. In the limit of zero thickness, when $1/\chi \approx 0$, we will see that the transition scenario starts with the formation of a SS pattern followed by the breaking of the symmetry plane, leading to a $\mathrm{MM}_\pi$ mode and eventually to standing waves SW. At intermediate values of the thickness, a large variety of

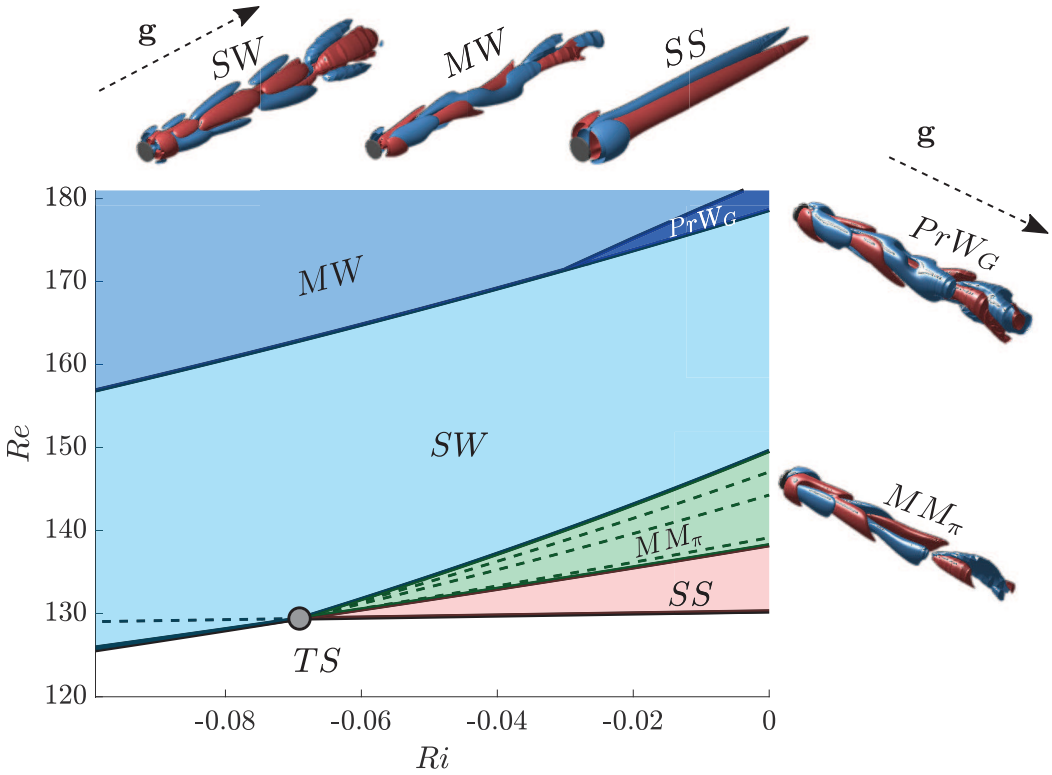


FIG. 24: Predicted flow patterns for flow past a hot disk with $\chi = 10$ (the opposing case of mixed convection) in parameter space. Snapshots of the reconstructed states are included. The direction of gravity $\boldsymbol{g}$ is represented by a dashed line parallel to the axis of revolution pointing from the disk towards the wake when $T_b - T_\infty > 0$.

spatio-temporal patterns may be observed, as highlighted by the study of Auguste et al. In the present study, we shall look for the connections between the *opposing flow* case in mixed convection and the situation at Ri $= 0$, in terms of the spatio-temporal patterns observed in the flow.

Figure 25 displays the location of the codimension-two point corresponding to the Hopf-Steady State bifurcation, obtained by varying $1/\chi \in [0, 1]$. The top panels show the corresponding temperature distribution in space and the growing extent of the recirculation bubble in the steady states associated with two distinct values of the aspect ratio $\chi$ of the disk. In the range of aspect ratios considered here, the critical Reynolds number grows linearly with the thickness $1/\chi$ of the disk, as previously observed by Fernandes et al. [18]. In addition, the critical Richardson number displays a maximum around $1/\chi \approx 0.1$ followed by a linear decrease. In the following, we shall discuss in detail the two cases $\chi = 10$ and $\chi = 3$. The case $\chi = 10$ corresponds to a case with a relatively simple transition scenario, similar to that explained by Meliga et al. [27]. On the other hand, the case $\chi = 3$ displays a larger number of spatio-temporal structures, and is qualitatively similar to the case of the sphere discussed in Section VIII A.

The parameter space summarizing the normal form predictions for $\chi = 10$ is displayed in Figure 24. In this case, to the left of the codimension-two point (gray point in the diagram), the trivial steady state transitions to standing waves and the subsequent bifurcations are uniquely explained by the unsteady modes. To the right of the codimension-two point the primary bifurcation breaks the axisymmetry of the steady state, i.e., it generates the SS state, followed by a periodic state with no reflection symmetry and nonzero mean lift, i.e., the $\mathrm{MM}_\pi$ state. The mixed mode $\mathrm{MM}_\pi$ state eventually bifurcates into a standing wave solution, which finally bifurcates to MW via the effect of higher order terms.

The dynamics near the organizing center for the flow

TABLE XV: Cubic and quintic coefficients of the normal form for the WFA-MC flow past a disk with $\chi = 3$.

| $l_0$ | $l_1$ | $l_2$ | $l_3$ | $p^1_\Delta$ |
|---|---|---|---|---|
| $-6.19$ | $-4.86$ | $0.47$ | $-2.76$ | $-50$ |
| $A$ | $B$ | $C$ | $D$ | $p^2_N$ |
| $0.56 - 0.38i$ | $-2.3 + 2.3i$ | $-1.7 + 0.32i$ | $0.79 + 0.52i$ | $-6$ |

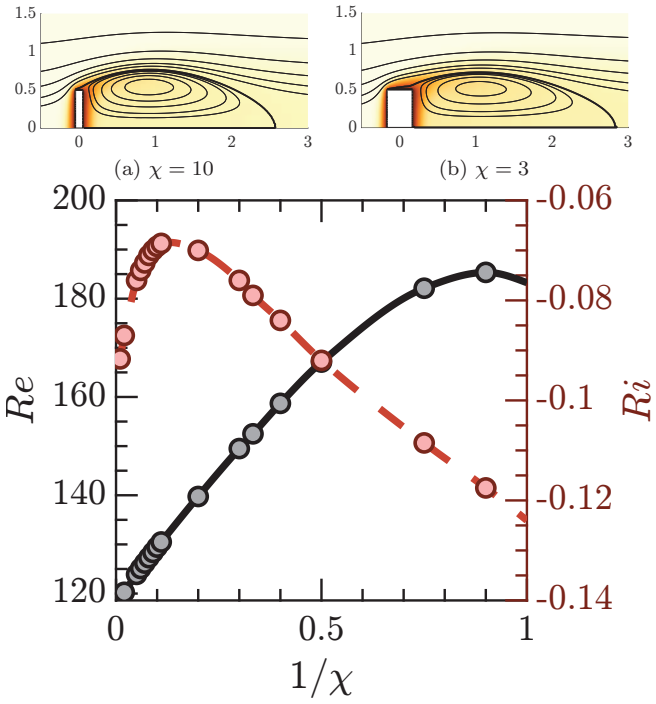


FIG. 25: The location of the codimension-two Hopf-Steady State bifurcation in the (Re, Ri) plane as a function of the aspect ratio $\chi$ of the disk (Re: black line; Ri: red line). The color-coded symbols refer to the points obtained in numerical computations. Top: temperature distribution in the trivial steady state at (a) $1/\chi = 0.1$ (Re $\approx 130$, Ri $\approx -0.068$), (b) $1/\chi \approx 0.33$ (Re $\approx 150$, Ri $\approx -0.078$).

past a disk with thickness $1/\chi = 1/3$ is richer. As in the previous cases, to the left of the organizing center the transition scenario is based on the initial formation of standing waves, followed by modulated waves and a possible tertiary bifurcation, not taken into account in the normal form, leading to temporal chaos. To the right of the organizing center, the transition scenario is qualitatively similar to that of the sphere (compare Section VIII A and Figure 26), although in the present case the codimension-two point is sufficiently close for the theory to provide quantitative predictions of the transition scenario. In other words, the transition scenario in the simple WFA problem of the disk with aspect ratio $\chi = 3$ is constrained by the dynamical structures emanating from the organizing center at Ri $\neq 0$, something that is not the case for the sphere, see Kotouc et al. [26, Fig 4]. Figure 27 displays the reconstruction of the lift coefficient from the normal form at Ri $= 0$, in comparison to the results obtained numerically by Auguste et al. in [14]. It distinguishes five regions, with the *Knit-Knot* (KK) region among them. The transition begins at Re $\approx 159.4$ (Re $\approx 159.8$ [14]) via the formation of a steady-state pattern (SS), which eventually bifurcates into a mixed mode (MM$_0$) at around Re $\approx 182.5$ (Re $\approx 179.9$ in [14]). The MM$_0$ state loses stability at around Re $\approx 184.5$. Quantitatively, up to this point, the sequence of bifurcations is reasonably well predicted with regard to the data reported in [14]. The Knit-Knot region in our analysis covers a large variety of states with similar characteristics in terms of the frequency components (at least two), and the lift coefficient $C_L$. Auguste et al. [14] identified this motion as temporally quasiperiodic motion resulting from spontaneously broken reflection symmetry. The temporal dynamics of the KK state may be described as the composition of a state with frequency $\omega_h$ and a low frequency state, whose frequency experiences large variation within its region of existence (from $T_p \approx 96\frac{2\pi}{\omega_h}$ at Re $= 185$ to $T_p \approx 48\frac{2\pi}{\omega_h}$ at Re $= 187$ and then to $T_p \approx 54\frac{2\pi}{\omega_h}$ at Re $= 190$, cf. Figure 29). This bifurcation sequence is followed by the appearance of the MM$_\pi$ state, estimated to be around Re $\approx 198.5$ (Re $\approx 190.4$ in [14]) which connects to the standing wave branch at around Re $\approx 214$ (Re $\approx 215.2$ in [14]). According to theory, this sequence of bifurcations should be followed by the formation of a modulated wave branch and precessing waves. However, we do not discuss these patterns here due to the lack of simulation data to compare with and because these patterns can only be described using the fifth order normal form whose coefficients we have not computed. For more information, see Figure 26.

Let us return to the discussion of the Knit-Knot region. In our more detailed analysis, this state is actually composed of several simpler states, see Figure 28. The MM$_0$ bifurcates into a precessing wave PrW$_G$ at Re $\approx 184.5$. This precessing wave is stable up to Re $\approx 186.3$, where a saddle-node bifurcation takes place leading to a $3FW$, denoted as 3FW$_A$ in Figure 28. The three-frequency wave is observable only in a small interval, however, and eventually reconnects to a Pulsating Wave via a global homoclinic bifurcation at around Re $\approx 186.9$. This Pulsating Wave is stable up to around Re $\approx 191.9$. At this stage, we can observe two other bifurcations leading to three-frequency waves with 3FW$_B$ (unstable) and 3FW$_C$ (stable); both of these branches reconnect to the main branch (PuW) following a saddle node bifurcation of limit cycles. The pulsating wave state finally reconnects with the symmetry-breaking mixed mode (MM$_\pi$) branch.

## IX. DISCUSSION & CONCLUSION

In this article, we have analyzed the properties of the normal form and the bifurcation scenario relevant to the bifurcations observed in axisymmetric wakes described by the Navier-Stokes equation. We have shown that near the onset of instability, it is possible to reduce the dynamics via center manifold reduction to a normal form, i.e., an ordinary differential equation, whose unfolding fully captures the local behavior of the Navier-Stokes equation. Such normal forms inherit the discrete and con-

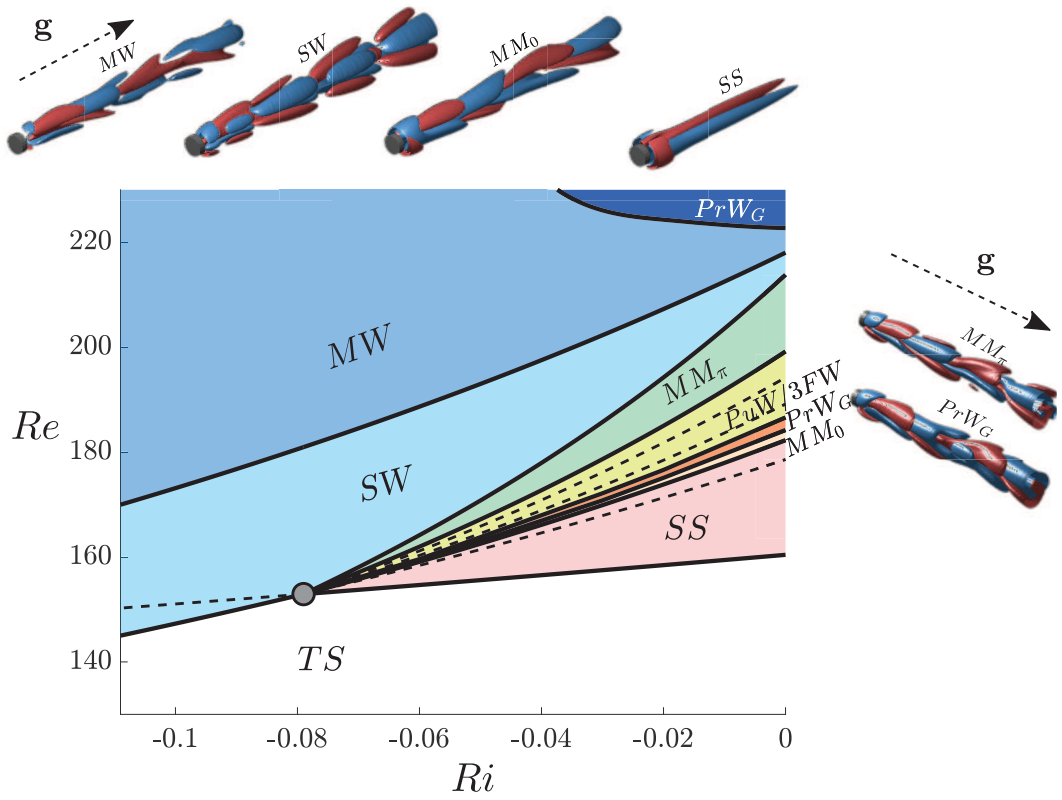


FIG. 26: Predicted flow patterns for flow past a hot disk with $\chi = 3$ (the opposing case of mixed convection) in parameter space. Snapshots of the reconstructed states are included. The direction of gravity $\boldsymbol{g}$ is represented by a dashed line parallel to the axis of revolution pointing from the disk towards the wake when $T_b - T_\infty > 0$.

tinuous symmetries of the system, in the present case $O(2)$ symmetry. We have shown that this approach, carried out in the vicinity of a steady state-Hopf interaction, suffices to predict much of the observed behavior.

Our analysis of the generic steady state-Hopf case relied on a reduction to polar coordinates. The fixed point solutions of the normal form, e.g. the pure modes and the mixed modes, have been observed in a variety of fluid flows, including Taylor-Couette and wake flows. Here, we have attempted to provide a complete description of the fixed point solutions of the normal form, as well as the possible bifurcations to periodic solutions of the polar normal form corresponding to two- and three-frequency waves.

Particularly noteworthy is our discovery of robust, potentially attracting, heteroclinic cycles in this mode interaction. In previous studies [58, 59], self-sustained processes have been related to a three-step process involving rolls advecting streamwise velocity, leading to streaks which once unstable lead to wavy perturbations whose nonlinear interaction with itself feeds the rolls. In terms of the mode interaction, the self-sustained cycle described by Dessup *et al.* [58] corresponds to a $\mathrm{Het}_{SS-SW}$ cycle or to an orbit that shadows it. In this sense, one could expect that other, more complex dynamics, for instance a $\mathrm{Het}_{PrW_A}$ cycle, may also be observed in the bifurcation scenario of real fluid systems. We mention that the indefinite increase in period associated with the approach to an attracting robust heteroclinic cycle cannot in general be seen in numerical integration of the normal form, on account of rounding error. Instead, the solution trajectory settles into a statistical limit cycle with a finite mean period [60]. This is even more so for partial differential equations [61] and in experiments where the presence of noise prevents approach to such a cycle [62]. This fact points to the importance of fluctuations in applications of the theory to fluid dynamics problems, as also emphasized in [48] in connection with the SNIPER bifurcation.

We have applied here the general theory to several distinct fluid flows and used it to explore the bifurcation scenario of wake flows behind a sphere or disk falling through either a constant density fluid or a vertically stratified fluid (problems WFA and WFA-MC, respectively). In particular, in Section VII, we determined the normal form coefficients for these problems on the assumption that each object is held fixed, and used these results in Section VIII to construct consistent stability diagrams for these flows, comparing the predicted bifurcation scenarios for mixed-convection flow past a fixed axisymmetric object, a disk or a sphere, with the results of

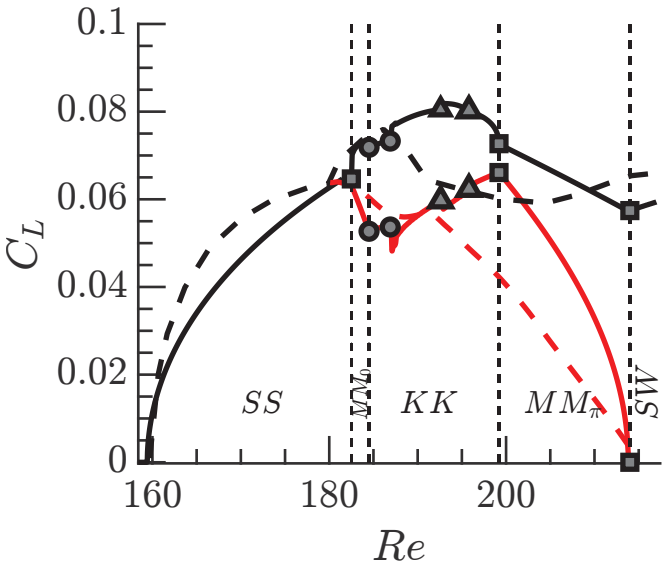


FIG. 27: Bifurcation diagram for a disk with $\chi = 3$ in terms of the lift coefficient $C_L$ for the WFA problem (Ri = 0). Solid lines were computed from the normal form, dashed lines were extracted from [14]. Black lines denote $C_{L,max}$ and red lines denote the average of $C_L$. See legend in Figure 28 for a description of the markers.

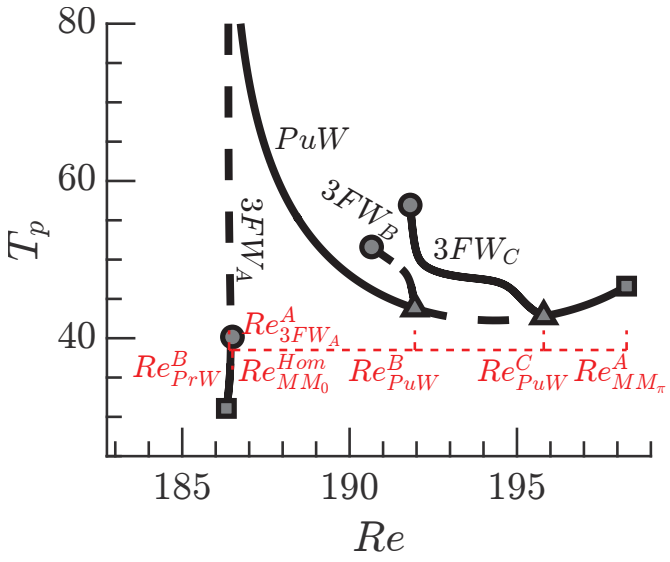


FIG. 28: Bifurcation diagram in the *Knit-Knot* region of Figure 27 in terms of the period $T_p$ of the low frequency modulation. Square markers: Hopf bifurcation. Circles: saddle-node bifurcation. Triangles: Neimark-Sacker bifurcation.

direct numerical simulations of these flows. These results enabled us to rationalize the results of previous numerical studies including those in the complicated Knit-Knot region of Auguste *et al.* [14] for the WFA problem for a disk of thickness $\chi = 3$ and the WFA-MC problem for a sphere of Kotouč *et al.* [26], states XIII or XIX, thereby demonstrating the utility of our bifurcation-theoretic approach. Unfortunately, neither of these cases predicts the presence of structurally stable heteroclinic cycles, although such states may arise for other parameter values.

**Acknowledgement**. The work of EK was supported in part by the National Science Foundation under Grant No. DMS-1908891.

## Appendix A: Normal form reduction

### 1. Third order forcing terms

The third order forcing terms are obtained from the substitution of the Ansatz (58) into $\mathbf{F}(\mathbf{q}, \boldsymbol{\eta})$. The general expression of the third order forcing term $\mathbf{F}_{(\varepsilon^3)}$ is as follows:

$$\begin{aligned}\mathbf{F}_{(\varepsilon^3)} \equiv & \sum_{\substack{j=-2\\k,\ell=-2}}^{2} a_j a_k a_\ell \big[\mathbf{N}(\hat{\mathbf{q}}_j, \hat{\mathbf{q}}_{k,\ell}) + \mathbf{N}(\hat{\mathbf{q}}_{k,\ell}, \hat{\mathbf{q}}_j)\big] e^{-im_n\theta} e^{-i\omega_n t} \\ & + \sum_{j=-2,\ell=0}^{2} a_j \Delta\eta_\ell \big[\mathbf{N}(\hat{\mathbf{q}}_j, \mathbf{Q}_0^{(\eta_\ell)}) + \mathbf{N}(\mathbf{Q}_0^{(\eta_\ell)}, \hat{\mathbf{q}}_j)\big] e^{-im_j\theta} e^{-i\omega_j t} \\ & + \sum_{j=-2,\ell=0}^{2} a_j \Delta\eta_\ell \mathbf{G}(\hat{\mathbf{q}}_j, \mathbf{e}_\ell) e^{-im_j\theta} e^{-i\omega_j t}\,,\end{aligned} \tag{A1}$$

with a slight abuse of notation such that $\hat{\mathbf{q}}_j = \overline{\hat{\mathbf{q}}}_{-j}$, $\hat{\mathbf{q}}_{k,j} = \overline{\hat{\mathbf{q}}}_{-k,-j}$ and $a_j = \overline{a}_{-j}$. Therefore, the azimuthal wave number and the frequency associated with a negative index are both considered to be of the opposite sign, i.e., $\omega_{-j} = -\omega_j$ and $m_{-j} = -m_j$. Finally, $\omega_n$ and $m_n$ are defined by the relations $\omega_n = \omega_j + \omega_k + \omega_\ell$, $m_n = m_j + m_k + m_\ell$, where $n = j + k + \ell$.

Resonant terms are those for which $(\omega_n, m_n)$ is equal to either $(0, m_0)$, $(\omega_1, m_1)$ or $(\omega_1, -m_1)$ (plus the complex conjugate pairs). The remaining terms only play a role in higher-order truncations.

Hierarchically, the first class of third-order forcing terms consists of those that are linear with respect to the amplitudes $a_j$ for $j = 0, 1, 2$,

$$\hat{\mathbf{F}}^{(a_j)}_{(\varepsilon^3)} \equiv \sum_{\ell=0}^{2} \Delta\eta_\ell \Big( \big[\mathbf{N}(\hat{\mathbf{q}}_j, \mathbf{Q}_0^{(\eta_\ell)}) + \mathbf{N}(\mathbf{Q}_0^{(\eta_\ell)}, \hat{\mathbf{q}}_j)\big] + \mathbf{G}(\hat{\mathbf{q}}_j, \mathbf{e}_\ell) \Big). \tag{A2}$$

The second type of resonant forcing terms are those used to compute the real coefficients $l_j$ for $j = 0, 1, 2, 3$.

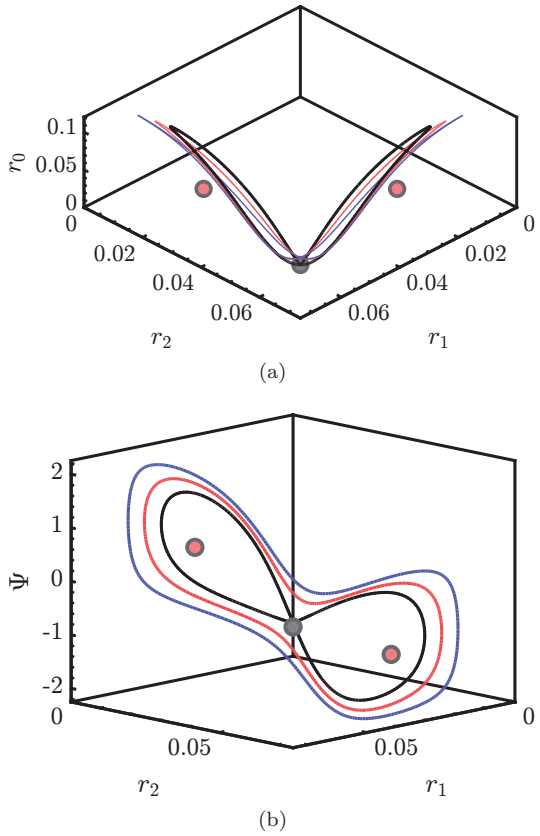


FIG. 29: The homoclinic orbit $\mathrm{Re}^{\mathrm{Hom}}_{MM_0}$ (gray line) at $\mathrm{Re} = 186.4$ of Figure 28. The gray dot is the location of $\mathrm{MM}_0$ while the red markers indicate the location of the $\mathrm{PrW}_G$ states. The red and blue trajectories represent limit cycles for higher values of Re; the period of these states diverges logarithmically as $\mathrm{Re} \to 186.4$ from above (not shown).

These are proportional to the cubic terms in the first equation of the complex normal form (8), and are given by

$$\begin{aligned}\hat{\mathbf{F}}^{(a_0|a_0|^2)}_{(\varepsilon^3)} \equiv& \left[\mathbf{N}(\hat{\mathbf{q}}_0, \hat{\mathbf{q}}_{0,-0}) + \mathbf{N}(\hat{\mathbf{q}}_{0,-0}, \hat{\mathbf{q}}_0)\right] \\ &+\left[\mathbf{N}(\hat{\mathbf{q}}_{-0}, \hat{\mathbf{q}}_{0,0}) + \mathbf{N}(\hat{\mathbf{q}}_{0,0}, \hat{\mathbf{q}}_{-0})\right],\end{aligned} \tag{A3}$$

with the notation $\hat{\mathbf{q}}_{-0} = \overline{\hat{\mathbf{q}}}_0$. Similarly, the terms $\hat{\mathbf{F}}^{(a_0|a_j|^2)}_{(\varepsilon^3)}$ for $j = 1, 2$ are given by

$$\begin{aligned}\hat{\mathbf{F}}^{(a_0|a_j|^2)}_{(\varepsilon^3)} \equiv& \left[\mathbf{N}(\hat{\mathbf{q}}_0, \hat{\mathbf{q}}_{j,-j}) + \mathbf{N}(\hat{\mathbf{q}}_{j,-j}, \hat{\mathbf{q}}_0)\right] \\ &+\left[\mathbf{N}(\hat{\mathbf{q}}_{-j}, \hat{\mathbf{q}}_{0,j}) + \mathbf{N}(\hat{\mathbf{q}}_{0,j}, \hat{\mathbf{q}}_{-j})\right] \\ &+\left[\mathbf{N}(\hat{\mathbf{q}}_j, \hat{\mathbf{q}}_{0,-j}) + \mathbf{N}(\hat{\mathbf{q}}_{0,-j}, \hat{\mathbf{q}}_j)\right],\end{aligned} \tag{A4}$$

while $\hat{\mathbf{F}}^{(\overline{a}_0 a_1 \overline{a}_2)}_{(\varepsilon^3)}$ is expressed as

$$\begin{aligned}\hat{\mathbf{F}}^{(\overline{a}_0 a_1 \overline{a}_2)}_{(\epsilon^3)} \equiv& \left[\mathbf{N}(\hat{\mathbf{q}}_{-0}, \hat{\mathbf{q}}_{1,-2}) + \mathbf{N}(\hat{\mathbf{q}}_{1,-2}, \hat{\mathbf{q}}_{-0})\right] \\ &+\left[\mathbf{N}(\hat{\mathbf{q}}_1, \hat{\mathbf{q}}_{-0,-2}) + \mathbf{N}(\hat{\mathbf{q}}_{-0,-2}, \hat{\mathbf{q}}_1)\right] \\ &+\left[\mathbf{N}(\hat{\mathbf{q}}_{-2}, \hat{\mathbf{q}}_{-0,1}) + \mathbf{N}(\hat{\mathbf{q}}_{-0,1}, \hat{\mathbf{q}}_{-2})\right].\end{aligned} \tag{A5}$$

The third class of forcing terms are those used for the computation of the complex coefficients $A, B, C$ and $D$. These are $\hat{\mathbf{F}}^{(a_j|a_j|^2)}_{(\varepsilon^3)}$ for $j = 1, 2$:

$$\begin{aligned}\hat{\mathbf{F}}^{(a_j|a_j|^2)}_{(\varepsilon^3)} \equiv& \left[\mathbf{N}(\hat{\mathbf{q}}_j, \hat{\mathbf{q}}_{j,-j}) + \mathbf{N}(\hat{\mathbf{q}}_{j,-j}, \hat{\mathbf{q}}_j)\right] \\ &+\left[\mathbf{N}(\hat{\mathbf{q}}_{-j}, \hat{\mathbf{q}}_{j,j}) + \mathbf{N}(\hat{\mathbf{q}}_{j,j}, \hat{\mathbf{q}}_{-j})\right],\end{aligned} \tag{A6}$$

$\hat{\mathbf{F}}^{(a_j|a_k|^2)}_{(\epsilon^3)}$ for $j = 1, 2$ and $k = 0, 1, 2$ with $j \neq k$,

$$\begin{aligned}\hat{\mathbf{F}}^{(a_j|a_k|^2)}_{(\varepsilon^3)} \equiv& \left[\mathbf{N}(\hat{\mathbf{q}}_j, \hat{\mathbf{q}}_{k,-k}) + \mathbf{N}(\hat{\mathbf{q}}_{k,-k}, \hat{\mathbf{q}}_j)\right] \\ &+\left[\mathbf{N}(\hat{\mathbf{q}}_{-k}, \hat{\mathbf{q}}_{j,k}) + \mathbf{N}(\hat{\mathbf{q}}_{j,k}, \hat{\mathbf{q}}_{-k})\right] \\ &+\left[\mathbf{N}(\hat{\mathbf{q}}_k, \hat{\mathbf{q}}_{j,-k}) + \mathbf{N}(\hat{\mathbf{q}}_{j,-k}, \hat{\mathbf{q}}_k)\right].\end{aligned} \tag{A7}$$

Finally, the term $\hat{\mathbf{F}}^{(a_0 a^2)}_{(\epsilon^3)}$ is expressed as

$$\begin{aligned}\hat{\mathbf{F}}^{(a_0 a^2)}_{(\varepsilon^3)} \equiv& \left[\mathbf{N}(\hat{\mathbf{q}}_0, \hat{\mathbf{q}}_{0,2}) + \mathbf{N}(\hat{\mathbf{q}}_{0,2}, \hat{\mathbf{q}}_0)\right] \\ &+\left[\mathbf{N}(\hat{\mathbf{q}}_2, \hat{\mathbf{q}}_{0,0}) + \mathbf{N}(\hat{\mathbf{q}}_{0,0}, \hat{\mathbf{q}}_2)\right].\end{aligned} \tag{A8}$$

## Appendix B: Modulated wave mode

The modulated wave mode is a degenerate solution of the normal form (8) truncated at third order. Crawford & Knobloch [33] analyzed the unfolding of the three simplest degeneracy conditions: (i) $A_r + 2B_r = 0$, (ii) $B_r = 0$ and (iii) $A_r = 0$. Here we briefly summarize some of their results, and list sufficient conditions for the branching and stability of the modulated wave solution.

The existence of the MW solution is subject to the following conditions

$$\begin{aligned}p^1(0, r_1^2 + r_2^2, (r_2^2 - r_1^2)^2, 0, 0, \lambda) \equiv 0 \\ p^2(0, r_1^2 + r_2^2, (r_2^2 - r_1^2)^2, 0, 0, \lambda) \equiv 0\,.\end{aligned} \tag{B1}$$

Hill and Stewart [63] observed that the condition $p^2 \equiv 0$ is a degeneracy condition if one evaluates the polynomial $p^2$ at the origin, i.e. $p^2(0,0,0,0,0,0) \equiv A_r$. Since, to fifth order,

$$\begin{aligned}&p^1(0, r_1^2 + r_2^2, (r_2^2 - r_1^2)^2, 0, 0, \lambda) \equiv \\ &\lambda_h + (\tfrac{1}{2}A_r + B_r)(r_1^2 + r_2^2) \\ &+p^1_\Delta (r_2^2 - r_1^2)^2 + p^1_N (r_1^2 + r_2^2)^2\,, \\ &p^2(0, r_1^2 + r_2^2, (r_2^2 - r_1^2)^2, 0, 0, \lambda) \equiv \\ &\tfrac{1}{2}A_r + p^2_N (r_1^2 + r_2^2) + p^2_\Delta (r_2^2 - r_1^2)^2\,,\end{aligned} \tag{B2}$$

the $\{r_1, r_2\}$ evolution is given by

$$\begin{aligned}\dot{r}_1 =& \; r_1\Big[\lambda_h + B_r r_1^2 + (A_r + B_r) r_2^2 \\ &+(p^1_\Delta + p^1_{N^2} - p^2_N) r_1^4 + (p^1_\Delta + p^1_{N^2} + p^2_N) r_2^4 \\ &+2(p^1_{N^2} - p^1_\Delta) r_2^2 r_1^2 + p^2_\Delta (r_2^2 - r_1^2)^3\Big], \\ \dot{r}_2 =& \; \kappa \cdot \dot{r}_1,\end{aligned} \tag{B3}$$

where $\kappa \cdot \dot{r}_1$ stands for the action of the reflection symmetry, defined in eq. (6), and $p^2_\Delta = 0$ to restrict the equation

to fifth order. Inspection of eq. (B3) shows that the fixed points $r_a, r_b$ satisfy

$$\begin{aligned} r_a^2 &= \frac{1}{2}\Big[ -\frac{A_r}{2p_N^2} - \sqrt{\frac{\chi}{4p_N^2 p_\Delta^1}}\Big] \\ r_b^2 &= \frac{1}{2}\Big[ -\frac{A_r}{2p_N^2} + \sqrt{\frac{\chi}{4p_N^2 p_\Delta^1}}\Big], \end{aligned} \tag{B4}$$

where the symbol $\chi$, which is a function of the parameter $\lambda_h$, is defined in Table VI. Evidently, the MW states exist when $A_r/p_N^2 < 0$ and $0 < \chi/(p_N^2 p_\Delta^1) < A_r^2/(p_N^2)^2$.

The stability within the MW subspace, i.e., with respect to perturbations in $\{r_1, r_2\}$ only, can be analyzed in terms of the determinant and trace of the Jacobian stability matrix restricted to this subspace:

$$\det(M^{MW}) = \; 32 p_N^2 p_\Delta^1 r_a^2 r_b^2 \left(r_a - r_b\right)^2 \left(r_a + r_b\right)^2, \tag{B5a}$$

$$\begin{aligned} \mathrm{tr}(M^{MW}) = \; & \frac{A_r}{p_N^2}\Big[\frac{A_r p_{N^2}^1}{p_N^2} - \frac{1}{2}(A_r + 2B_r)\Big] \\ & + \big(r_a^2 - r_b^2\big)^2 \big(4p_\Delta^1 - 2p_N^2\big), \end{aligned} \tag{B5b}$$

In view of eq. (B5a), the determinant vanishes when $r_a r_b = 0$ corresponding to the rotating wave branch and when $r_a = r_b$ corresponding to the standing wave branch. Therefore, the modulated wave branch connects the branches of rotating and standing waves. The standing waves changes stability when $\sigma_{SW} \equiv -2r_{SW}^2(A_r + 4r_{SW}^2 p_N^2)$ changes sign, which can happen if $A_r p_N^2 < 0$. The corresponding standing wave amplitude is given by $r_{SW}^2 = -\dfrac{A_r}{4p_N^2}$. The standing wave emerges as a stable (resp. unstable) solution within the $\{r_1, r_2\}$ subspace if $A_r > 0$ (resp. $A_r < 0$) and it becomes unstable (resp. stable) when $r_{SW}^2 = -\dfrac{A_r}{4p_N^2}$. The stability of the rotating wave within the $\{r_1, r_2\}$ subspace is determined by the eigenvalue $\sigma_{RW} \equiv -r_{RW}^2(A_r - 2r_{RW}^2 p_N^2)$ which is stable (resp. unstable) if $A_r < 0$ (resp. $A_r > 0$). The corresponding amplitude is $r_{RW}^2 = -\dfrac{A_r}{2p_N^2}$.

The conditions on the determinant show that the MW branch does not experience steady bifurcations, except at the two end points. The MW solution is stable if $\det(M^{MW}) > 0$, that is, $p_N^2 p_\Delta^1 > 0$, and the trace is negative. It is sufficient to ensure that the trace is negative at the end points, a condition equivalent to $A_r > 0$, $p_N^2 < 0$, $p_\Delta^1 < 0$ and $B_r + A_r < 0$. Otherwise, the MW branch may experience a Hopf bifurcation leading to a 3FW.

Let us now focus on the stability of the MW branch with respect to perturbations in the variable $r_0$. We see that the MW can bifurcate into a Precessing Wave solution whenever

$$\lambda_s - l_1 \frac{A_r}{p_N^2} \geq 0\,.$$

In the supercritical case, the PrW connects in parameter space a Mixed Mode with a Modulated Wave. Finally, a possible scenario for a bifurcation from PrW towards a three-frequency wave arises whenever eq. (9d) does not possess a fixed point.


[1] M. Golubitsky and M. Roberts, A classification of degenerate Hopf bifurcations with O(2) symmetry, Journal of Differential Equations **69**, 216 (1987).

[2] J. D. Crawford and E. Knobloch, Symmetry and symmetry-breaking bifurcations in fluid mechanics, Annual Review of Fluid Mechanics **23**, 341 (1991).

[3] M. Golubitsky and W. Langford, Pattern formation and bistability in flow between counterrotating cylinders, Physica D: Nonlinear Phenomena **32**, 362 (1988).

[4] P. Chossat and G. Iooss, *The Couette-Taylor Problem*, Vol. 102 (Springer Science & Business Media, 2012).

[5] M. Golubitsky, J. Swift, and E. Knobloch, Symmetries and pattern selection in Rayleigh-Bénard convection, Physica D: Nonlinear Phenomena **10**, 249 (1984).

[6] J. Sierra, D. Fabre, V. Citro, and F. Giannetti, Bifurcation scenario in the two-dimensional laminar flow past a rotating cylinder, Journal of Fluid Mechanics **905**, A2 (2020).

[7] D. Ormières and M. Provansal, Transition to turbulence in the wake of a sphere, Physical Review Letters **83**, 80 (1999).

[8] K. Gumowski, J. Miedzik, S. Goujon-Durand, P. Jenffer, and J. Wesfreid, Transition to a time-dependent state of fluid flow in the wake of a sphere, Physical Review E **77**, 055308 (2008).

[9] R. Natarajan and A. Acrivos, The instability of the steady flow past spheres and disks, Journal of Fluid Mechanics **254**, 323 (1993).

[10] B. Ghidersa and J. Dušek, Breaking of axisymmetry and onset of unsteadiness in the wake of a sphere, Journal of Fluid Mechanics **423**, 33 (2000).

[11] A. G. Tomboulides and S. A. Orszag, Numerical investigation of transitional and weak turbulent flow past a sphere, Journal of Fluid Mechanics **416**, 45 (2000).

[12] J. Sierra-Ausin, M. Lorite-Diez, J. Jimenez-Gonzalez, V. Citro, and D. Fabre, Unveiling the competitive role of global modes in the pattern formation of rotating sphere flows, Journal of Fluid Mechanics **942** (2022).

[13] D. Fabre, F. Auguste, and J. Magnaudet, Bifurcations and symmetry breaking in the wake of axisymmetric bodies, Physics of Fluids **20**, 051702 (2008).

[14] F. Auguste, D. Fabre, and J. Magnaudet, Bifurcations in the wake of a thick circular disk, Theoretical and Computational Fluid Dynamics **24**, 305 (2010).

[15] M. Chrust, G. Bouchet, and J. Dušek, Parametric study of the transition in the wake of oblate spheroids and flat cylinders, Journal of Fluid Mechanics **665**, 199 (2010).

[16] P. Ern, F. Risso, D. Fabre, and J. Magnaudet, Wake-induced oscillatory paths of bodies freely rising or falling in fluids, Annual Review of Fluid Mechanics **44**, 97

(2012).
[17] P. Fernandes, P. Ern, F. Risso, and J. Magnaudet, On the zigzag dynamics of freely moving axisymmetric bodies, Physics of Fluids **17**, 098107 (2005).
[18] P. C. Fernandes, F. Risso, P. Ern, and J. Magnaudet, Oscillatory motion and wake instability of freely rising axisymmetric bodies, Journal of Fluid Mechanics **573**, 479 (2007).
[19] P. C. Fernandes, P. Ern, F. Risso, and J. Magnaudet, Dynamics of axisymmetric bodies rising along a zigzag path, Journal of Fluid Mechanics **606**, 209 (2008).
[20] F. Auguste, J. Magnaudet, and D. Fabre, Falling styles of disks, Journal of Fluid Mechanics **719**, 388 (2013).
[21] M. Chrust, S. Goujon-Durand, and J. E. Wesfreid, Loss of a fixed plane symmetry in the wake of a sphere, Journal of Fluid Mechanics **41**, 51 (2013).
[22] J. Tchoufag, D. Fabre, and J. Magnaudet, Global linear stability analysis of the wake and path of buoyancy-driven disks and thin cylinders, Journal of Fluid Mechanics **740**, 278 (2014).
[23] J. Tchoufag, D. Fabre, and J. Magnaudet, Weakly nonlinear model with exact coefficients for the fluttering and spiraling motion of buoyancy-driven bodies, Physical Review Letters **115**, 114501 (2015).
[24] J. Tchoufag, J. Magnaudet, and D. Fabre, Linear instability of the path of a freely rising spheroidal bubble, Journal of Fluid Mechanics **751**, R4 (2014).
[25] P. Bonnefis, D. Fabre, and J. Magnaudet, When, how, and why the path of an air bubble rising in pure water becomes unstable, Proceedings of the National Academy of Sciences **120**, e2300897120 (2023).
[26] M. Kotouč, G. Bouchet, and J. Dušek, Transition to turbulence in the wake of a fixed sphere in mixed convection, Journal of Fluid Mechanics **625**, 205 (2009).
[27] P. Meliga, J.-M. Chomaz, and D. Sipp, Global mode interaction and pattern selection in the wake of a disk: a weakly nonlinear expansion, Journal of Fluid Mechanics **633**, 159 (2009).
[28] M. Golubitsky, I. Stewart, and D. G. Schaeffer, *Singularities and Groups in Bifurcation Theory: Volume II*, Vol. 69 (Springer Science & Business Media, 2012).
[29] P. Hirschberg and E. Knobloch, Zigzag and varicose instabilities of a localized stripe, Chaos: An Interdisciplinary Journal of Nonlinear Science **3**, 713 (1993).
[30] P. Hirschberg and E. Knobloch, A robust heteroclinic cycle in an steady-state mode interaction, Nonlinearity **11**, 89 (1998).
[31] G. Mougin and J. Magnaudet, Path instability of a rising bubble, Physical Review Letters **88**, 014502 (2001).
[32] D. Rand, Dynamics and symmetry. Predictions for modulated waves in rotating fluids, Archive for Rational Mechanics and Analysis **79**, 1 (1982).
[33] E. Knobloch, On the degenerate Hopf bifurcation with O(2) symmetry, Contemporary Mathematics **56**, 193 (1986).
[34] S. A. van Gils and J. Mallet-Paret, Hopf bifurcation and symmetry: travelling and standing waves on the circle, Proceedings of the Royal Society of Edinburgh, Section A: Mathematics **104**, 279 (1986).
[35] A. S. Landsberg and E. Knobloch, Direction-reversing traveling waves, Physics Letters A **159**, 17 (1991).
[36] J. D. Crawford, M. Golubitsky, and W. F. Langford, Modulated rotating waves in O(2) mode interactions, Dynamics and Stability of Systems **3**, 159 (1988).
[37] M. J. Field, Equivariant dynamical systems, Transactions of the American Mathematical Society **259**, 185 (1980).
[38] J. Guckenheimer and P. Holmes, Structurally stable heteroclinic cycles, Mathematical Proceedings of the Cambridge Philosophical Society **103**, 189 (1988).
[39] M. Krupa and I. Melbourne, Asymptotic stability of heteroclinic cycles in systems with symmetry, Ergodic Theory and Dynamical Systems **15**, 121 (1995).
[40] M. Krupa and I. Melbourne, Asymptotic stability of heteroclinic cycles in systems with symmetry II, Proceedings of the Royal Society of Edinburgh, Section A: Mathematics **134**, 1177 (2004).
[41] I. Melbourne, P. Chossat, and M. Golubitsky, Heteroclinic cycles involving periodic solutions in mode interactions with O(2) symmetry, Proceedings of the Royal Society of Edinburgh, Section A: Mathematics **113**, 315 (1989).
[42] E. Knobloch and M. Silber, Oscillatory convection in a rotating layer, Physica D: Nonlinear Phenomena **63**, 213 (1993).
[43] D. A. Weinberg, Canonical forms for symmetric tensors, Linear algebra and its applications **57**, 271 (1984).
[44] J. Porter and E. Knobloch, New type of complex dynamics in the 1:2 spatial resonance, Physica D: Nonlinear Phenomena **159**, 125 (2001).
[45] J. Porter and E. Knobloch, Complex dynamics in the 1:3 spatial resonance, Physica D: Nonlinear Phenomena **143**, 138 (2000).
[46] W. Govaerts, Y. A. Kuznetsov, H. Meijer, B. Al-Hdaibat, V. De Witte, A. Dhooge, W. Mestrom, N. Neirynck, A. Riet, and B. Sautois, *MATCONT: Continuation toolbox for ODEs in Matlab* (2019).
[47] M. K. S. Yeung and S. H. Strogatz, Nonlinear dynamics of a solid-state laser with injection, Physical Review E **58**, 4421 (1998).
[48] F. Pétrélis, S. Fauve, E. Dormy, and J.-P. Valet, Simple mechanism for reversals of Earth's magnetic field, Physical Review Letters **102**, 144503 (2009).
[49] L. P. Shil'nikov, A case of the existence of a countable number of periodic motions, Soviet Math. Doklady **6**, 163 (1965).
[50] P. Glendinnning and C. Sparrow, Local and global behaviour near homoclinic orbits, Journal of Statistical Physics **35**, 645 (1984).
[51] L. P. Shilnikov and A. Shilnikov, Shilnikov bifurcation, Scholarpedia **2**, 1891 (2007), revision #194931.
[52] E. Knobloch, D. R. Moore, J. Toomre, and N. O. Weiss, Transitions to chaos in double-diffusive convection, Journal of Fluid Mechanics **166**, 409 (1986).
[53] E. Knobloch and D. R. Moore, Minimal model of binary fluid convection, Physical Review A **42**, 4693 (1990).
[54] H. Gan, J. Chang, J. J. Feng, and H. H. Hu, Direct numerical simulation of the sedimentation of solid particles with thermal convection, Journal of Fluid Mechanics **481**, 385 (2003).
[55] P. Mcleod, D. S. Riley, and R. S. J. Sparks, Melting of a sphere in hot fluid, Journal of Fluid Mechanics **327**, 393 (1996).
[56] S. S. Sadhal, P. S. Ayyaswamy, and J. N. Chung, *Transport phenomena with drops and bubbles* (Springer Science & Business Media, 2012).
[57] C. H. Chiang and W. A. Sirignano, Interacting, convecting, vaporizing fuel droplets with variable properties, International Journal of Heat and Mass Transfer **36**, 875

(1993).
[58] T. Dessup, L. S. Tuckerman, J. E. Wesfreid, D. Barkley, and A. P. Willis, Self-sustaining process in Taylor-Couette flow, Physical Review Fluids **3**, 123902 (2018).
[59] Y. Bengana and L. S. Tuckerman, Spirals and ribbons in counter-rotating Taylor-Couette flow: Frequencies from mean flows and heteroclinic orbits, Physical Review Fluids **4**, 044402 (2019).
[60] F. H. Busse, Transition to turbulence in Rayleigh-Bénard convection, in *Hydrodynamic Instabilities and the Transition to Turbulence* (Springer-Verlag, Berlin, New York, 1981) pp. 97–137.
[61] I. Mercader, J. Prat, and E. Knobloch, Robust heteroclinic cycles in two-dimensional Rayleigh-Bénard convection without Boussinesq symmetry, International Journal of Bifurcation and Chaos **12**, 2501 (2002).
[62] E. Stone and P. Holmes, Random perturbations of heteroclinic attractors, SIAM Journal on Applied Mathematics **50**, 726 (1990).
[63] A. Hill and I. Stewart, Hopf-steady-state mode interactions with O(2) symmetry, Dynamics and Stability of Systems **6**, 149 (1991).

*J. Fluid Mech.* (2024), *vol*. 980, A19, doi:10.1017/jfm.2024.19

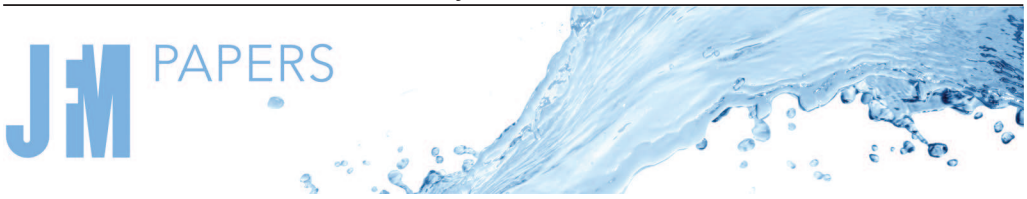


# Path instability of deformable bubbles rising in Newtonian liquids: a linear study

**Paul Bonnefis**[1], **Javier Sierra-Ausin**[1], **David Fabre**[1] **and Jacques Magnaudet**[1],†

[1]Université de Toulouse; INPT, UPS; IMFT (Institut de Mécanique des Fluides de Toulouse), Allée Camille Soula, F-31400 Toulouse, France

(Received 12 October 2023; revised 20 December 2023; accepted 29 December 2023)

The first stages of the path instability phenomenon affecting the buoyancy-driven motion of gas bubbles rising in weakly or moderately viscous liquids are examined using a recently developed numerical approach designed to assess the global linear stability of incompressible flows involving freely evolving interfaces. Predictions for the critical bubble size and frequency of the most unstable mode are found to agree well with reference data obtained in ultrapure water and in several silicone oils. By varying the bubble size, stability diagrams are built for several specific fluids, revealing three distinct regimes with different bifurcation sequences. The spatial structure of the unstable modes is analysed, together with the variations of the bubble shape, position and orientation. For this purpose, displacements of the bubble surface are split into rigid-body components and volume-preserving deformations, allowing us to determine how the relative magnitude of the latter varies with the fluid properties and bubble size. Predictions obtained with freely deformable bubbles are compared with those found by maintaining the bubble shape determined in the base state frozen during the stability analysis. This comparison reveals that deformations leave the phenomenology of the first bifurcations unchanged in low-viscosity fluids, especially water. Hence, in such fluids, bubbles behave essentially as freely moving rigid bodies submitted to constant-force and zero-torque constraints, at the surface of which the fluid obeys a shear-free condition. In contrast, deformations change the nature of the primary bifurcation in oils slightly more viscous than water, whereas, somewhat surprisingly, they leave the near-threshold phenomenology unchanged in more viscous oils.

**Key words:** bubble dynamics, instability

† Email address for correspondence: magnau@imft.fr

## 1. Introduction

A great deal of effort has been invested since the middle of the last century to elucidating the origin and predicting the characteristics of the intriguing path instability phenomenon affecting the buoyancy-driven motion of millimetre-sized gas bubbles rising in weakly or moderately viscous liquids. Attempts were mostly experimental during the first decades, before numerical simulation techniques became mature enough to shed some new light on this puzzling phenomenon. Among them, linear stability analyses have kept pace with advances in the computational techniques required to determine efficiently the discretized form of the stationary solutions of the Navier–Stokes equations subjected to appropriate boundary conditions, and to solve subsequently the large-size generalized eigenvalues problems giving access to the possibly linearly unstable eigenmodes.

Early studies considered bubbles with a frozen shape held fixed in a uniform stream. Assuming an oblate spheroidal shape with an arbitrary aspect ratio (the ratio of the major and minor axes lengths, hereinafter denoted as $\chi$), with the short axis of the spheroid aligned with the incoming flow, conditions under which the axisymmetric wake becomes unstable, the nature of the corresponding first bifurcations and the structure of the associated unstable modes could be explored (Yang & Prosperetti 2007; Tchoufag, Magnaudet & Fabre 2013). It was eventually concluded that wake instability occurs within a finite range of Reynolds number when $\chi \gtrsim 2.21$, in agreement with predictions provided by the numerical solution of the full Navier–Stokes equations in the same configuration (Magnaudet & Mougin 2007). The first bifurcation is stationary, i.e. the corresponding eigenvalue is real. Beyond this bifurcation, the stationary wake exhibits a pair of counter-rotating trailing vortices which are responsible for a non-zero lift force. For larger aspect ratios, increasing the Reynolds number beyond the primary threshold while keeping $\chi$ fixed or *vice versa*, a second bifurcation of Hopf type takes place. The wake keeps the previous planar symmetry unchanged beyond the corresponding threshold but vortices are periodically shed downstream, resulting in periodic oscillations of the lift force about a non-zero mean. This transition scenario, with the axisymmetric wake becoming unstable through a stationary bifurcation and the resulting non-axisymmetric stationary wake undergoing a Hopf bifurcation, is similar to that obeyed by the wake of rigid spheres and discs (Natarajan & Acrivos 1993).

Compared with the actual problem of buoyancy-driven rising bubbles, the configuration contemplated in the above studies is purely academic, as the bubble is held fixed despite the existence of a non-zero lift force. An important step towards physically realistic conditions was achieved during the last decade, starting with global linear stability studies of the flow past freely moving buoyancy/gravity-driven rigid bodies with various shapes. In this situation, the body motion is subjected to two additional constraints, since the hydrodynamic force must balance the net body weight at all times (implying that the horizontal force remains null whatever the body orientation and velocity), and the hydrodynamic torque must also remain zero, provided that the body density is uniform. Therefore, disturbances in the body velocity or orientation modify the velocity and pressure distributions in the surrounding fluid, which in turn induce changes in the force and torque acting on the body that must respect the above constraints. Two-dimensional plates and rods were considered by Fabre, Assemat & Magnaudet (2011) and Assemat, Fabre & Magnaudet (2012). The former study focused on 'heavy' bodies with a density much larger than that of the fluid. An asymptotic approach could then be employed and revealed the existence of four 'aerodynamic' modes distinct from the 'fluid' (or 'wake') modes associated with wake instability (qualitatively similar modes are encountered in flight dynamics, and those evidenced in the above studies were coined after them). Two

of these aerodynamic modes have real negative eigenvalues, i.e. they are always stable. In contrast, the other two are associated with a pair of complex conjugate eigenvalues, hence with a Hopf bifurcation. The corresponding oscillations are slow compared with those typical of vortex shedding in two-dimensional wakes, and their frequency varies as the inverse square root of the body-to-fluid density ratio, $m^*$, thus becoming vanishingly small for very heavy bodies. Existence of these modes was confirmed for arbitrary $m^*$ in the global linear stability analysis (hereinafter abbreviated as GLSA) performed numerically by Assemat *et al.* (2012), and the corresponding thresholds were compared with those of the fluid modes for thin plates and square rods. Increasing the Reynolds number, it was observed that, for infinitely thin plates, the primary wake mode always becomes unstable first, no matter what the value of $m^*$ is. The same conclusion was found to hold for square rods as long as the density ratio exceeds 1.22. In contrast, for lower $m^*$, the aerodynamic oscillatory mode is destabilized first and exhibits a frequency (corresponding to a fluttering of the falling/rising rod about the vertical) smaller than that of the wake mode by approximately a factor of two. Similar conclusions were previously obtained through fully resolved numerical simulations by Alben (2008) with light two-dimensional ellipses, and the critical Reynolds number at which the fluttering motion sets in was found to be approximately half that corresponding to the onset of wake instability. The two-dimensional GLSA approach of Assemat *et al.* (2012) was extended to axisymmetric bodies by Tchoufag, Fabre & Magnaudet (2014*a*), who considered the stability of rising/falling discs and short cylinders. Whatever the body aspect ratio, they found the aerodynamic low-frequency mode to be always the most unstable beyond a critical $\chi$-dependent $m^*$ (note the difference with two-dimensional square rods for which the same happens below a critical $m^*$). For lower $m^*$, the most unstable mode is either the one associated with the wake (here characterized by weak deviations of the path in the presence of sustained fluid oscillations at the back of the body), or a stationary mode in which the body follows an inclined path and its wake is made of a pair of steady counter-rotating streamwise vortices. Based on these findings, Tchoufag *et al.* (2014*a*) concluded that the first deviation of the path of such freely moving axisymmetric bodies cannot in general be predicted by considering the instability of the sole wake. Rather, the instability of their path results under most conditions from the intrinsic coupling between the body and fluid implied by the constant-force and zero-torque conditions.

Tchoufag, Magnaudet & Fabre (2014*b*) applied the GLSA approach to freely rising spheroidal bubbles with a prescribed oblateness. They observed that the vertical path becomes unstable within a finite range of Reynolds number when the bubble oblateness exceeds 2.15, which is slightly lower than the wake instability threshold determined for a fixed bubble (Magnaudet & Mougin 2007; Tchoufag *et al.* 2013). The unstable Reynolds number range widens as $\chi$ increases. For $2.15 < \chi < 2.25$, increasing the Reynolds number, i.e. the bubble size, while maintaining the oblateness fixed, the path first becomes unstable within a narrow Reynolds number range through a low-frequency mode similar to the aerodynamic mode encountered with heavy short cylinders and discs. Increasing the Reynolds number further, a stationary mode yielding an inclined path and growing much faster than the previous low-frequency mode becomes dominant. This situation prevails within an intermediate Reynolds number range, beyond which the low-frequency mode becomes dominant again. Last, the system restabilizes beyond a fourth critical Reynolds number. For instance, the path of a bubble with $\chi = 2.22$ becomes oscillatory through a low-frequency mode in the two separate ranges $310 \lesssim Re \lesssim 340$ and $450 \lesssim Re \lesssim 980$, while it takes a non-zero stationary inclination with respect to the vertical in the intermediate range $340 \lesssim Re \lesssim 450$, the Reynolds number $Re$ being based on the bubble

rise speed and equivalent diameter. Obviously, the description provided by this simplified model suffers from the fact that the bubble shape is not allowed to vary with the Reynolds number, in contrast to what happens under real conditions. Nevertheless, as will become apparent later, the first half of the above scenario, i.e. the succession of a low-frequency mode becoming unstable first and a stationary mode taking over it, is relevant to the case of deformable bubbles rising in low-viscosity high-surface-tension fluids, especially water.

A somewhat more sophisticated track was followed by Cano-Lozano *et al.* (2016*a*). Rather than prescribing arbitrarily an oblate spheroidal shape, they computed the actual bubble shape and rise speed corresponding to the stationary axisymmetric base state, using the open software Gerris (Popinet 2003, 2007). Then, they introduced this shape and speed into the GLSA solver of Tchoufag *et al.* (2014*b*), keeping the shape frozen despite the possible development of flow and path instabilities. With this approach, they could determine for a wide variety of Newtonian fluids (characterized by their density, viscosity and surface tension), the critical Reynolds number, i.e. the critical bubble size, beyond which the vertical path of a bubble with a nearly realistic shape becomes unstable. They could also compare these predictions with those corresponding to 'pure' wake instability, obtained by holding the same bubble fixed in a uniform stream. For low-viscosity high-surface-tension fluids, they found that, in agreement with the conclusions of Tchoufag *et al.* (2014*b*), the system first becomes unstable through a Hopf bifurcation leading to low-frequency path oscillations. At the corresponding Reynolds number, the wake of the same bubble held fixed is still stable, which proves that the mechanism responsible for path instability is intimately linked to the constant-force and torque-free conditions that constrain the dynamics of the coupled fluid–body system. For liquids with a viscosity 5 to 10 times larger than water and a surface tension 3–4 times smaller, they observed that path instability first arises through an oscillatory mode with a frequency 4–5 times higher than that found in low-viscosity high-surface-tension liquids. However, the picture looked dramatically different in the intermediate range corresponding to 'moderate' liquid viscosities and surface tensions. In particular, the instability thresholds of freely moving and fixed bubbles were found to be identical in that range. Hence, the first unstable mode is stationary, similar to that observed for fixed spheroidal bubbles (Magnaudet & Mougin 2007; Yang & Prosperetti 2007; Tchoufag *et al.* 2013). When compared with reference experiments carried out in ultrapure water (Duineveld 1995; De Vries 2002) or silicone oils (Zenit & Magnaudet 2008; Sato 2009), these predictions experience mixed successes. In low-viscosity high-surface-tension fluids, they properly capture the low-frequency oscillatory nature of the incipient path instability, and slightly over-predict the size of the smallest bubble whose path becomes unstable. The same conclusion holds for the 'high'-frequency path oscillations observed in oils 5–10 times more viscous than water. In contrast, for oils with an intermediate viscosity, experimental observations provide evidence that the first instability of the system keeps a similar oscillatory nature, at odds with the above predictions.

This blatant disagreement points to the role of transient bubble deformations not accounted for in the above studies. It provided one of the main motivations that decided us to undertake the development of a more general linear stability approach capable of dealing with free gas–liquid boundaries, thanks to which the fate of time-dependent deformations of the bubble–fluid interface may be predicted together with that of flow and path disturbances. The corresponding method was successfully developed and validated by Bonnefis (2019); other groups have pursued similar objectives in parallel (Zhou & Dusek 2017; Herrada & Eggers 2023). These efforts may be considered as the third and final step on the long route to the linear stability analysis of the flow past rising bubbles.

To summarize, in the first step, the bubble shape was frozen, its centroid was assumed to remain fixed and only the stability of the wake was assessed (Yang & Prosperetti 2007; Tchoufag *et al.* 2013). In the next step, the bubble shape was still frozen but the bubble centroid was allowed to move freely under the effect of buoyancy, being only constrained by the constant-force and zero-torque conditions (Tchoufag *et al.* 2014*b*; Cano-Lozano *et al.* 2016*a*). Most of the investigations performed in these first two steps assumed the bubble to keep an exact oblate spheroidal shape, except the last of them, in which this shape was obtained as part of the stationary solution of the full Navier–Stokes equations. The time-dependent adjustment of the bubble shape to its possibly non-straight unsteady motion was the last ingredient missing to reach a fully realistic description of the bubble–flow interaction. This is what the third step, achieved by Bonnefis (2019), enables. The purpose of this paper is to present and discuss the predictions provided by this approach across a wide range of fluids, from low-viscosity high-surface-tension liquid metals to oils with a viscosity typically ten times larger and a surface tension four times smaller than those of water, and to compare them with reference data when available. Predictions obtained in the specific case of water were already summarized by Bonnefis, Fabre & Magnaudet (2023) and are discussed in more detail here.

The numerical approach, already described by Sierra-Ausin *et al.* (2022), is summarized in § 2. The characteristics of the base state are presented in § 3, before the neutral curves resulting from the linear stability analysis are discussed in § 4, and the nature and sequencing of the first unstable modes are examined in § 5. Then, the relative magnitude of deformations of the bubble–fluid interface with respect to the lateral drift of the bubble centroid are discussed in § 6. Section 7 summarizes the main findings of the study and discusses the respective roles of wake, bubble deformation and fluid–bubble hydrodynamic couplings in the different regimes encountered by varying the physical properties of the carrying liquid.

## 2. Problem formulation and numerical approach

We assume that a single gas bubble with volume $\mathcal{V}$ and equivalent diameter $D = ((6/\pi)\mathcal{V})^{1/3}$ rises through a large expanse of a Newtonian liquid with density $\rho$, viscosity $\mu$ and surface tension $\gamma$ under the effect of gravity $g$. The liquid is at rest at infinity and the disturbance flow induced by the bubble ascent is assumed incompressible. The bubble is initially axisymmetric and is released with its symmetry axis aligned with gravity. Considering that the density and viscosity of the gas enclosed in the bubble are negligibly small compared with those of the surrounding liquid, the problem depends on two dimensionless parameters, namely the Bond number $Bo = \rho g D^2/\gamma$ and the Galilei number $Ga = \rho(gD^3)^{1/2}/\mu$. These characteristic numbers compare the gravitational force $\rho g D^3$ driving the bubble ascent with the capillary force $\gamma D$ and the viscous force $\mu(gD^3)^{1/2}$, respectively. Whatever the bubble size, a given liquid placed in a given gravitational environment is entirely characterized by the value of the so-called Morton number $Mo = Bo^3 Ga^{-4} = g\mu^4/(\rho\gamma^3)$. By defining the visco-gravitational diffusion length scale $l_\mu = [\mu^2/(\rho^2 g)]^{1/3}$ (the length over which viscosity diffuses a disturbance within a $[\mu/(\rho g^2)]^{1/3}$-long period of time) and the capillary length scale $l_\gamma = [\gamma/(\rho g)]^{1/2}$, it is seen that $l_\mu/l_\gamma = Mo^{1/6}$. Hence, the Morton number characterizes the ratio of these two length scales. The bubble diameter, $D$, the gravitational time, $(D/g)^{1/2}$, and their ratio, $(gD)^{1/2}$, will be used throughout the paper to make lengths, frequencies and velocities dimensionless. Once the bubble rise speed $u_b$ is known, the non-dimensional rise speed, $U = u_b/(gD)^{1/2}$ allows the bubble Reynolds number, $Re = Ga\,U$, and Weber number, $We = Bo\,U^2$, to be evaluated.

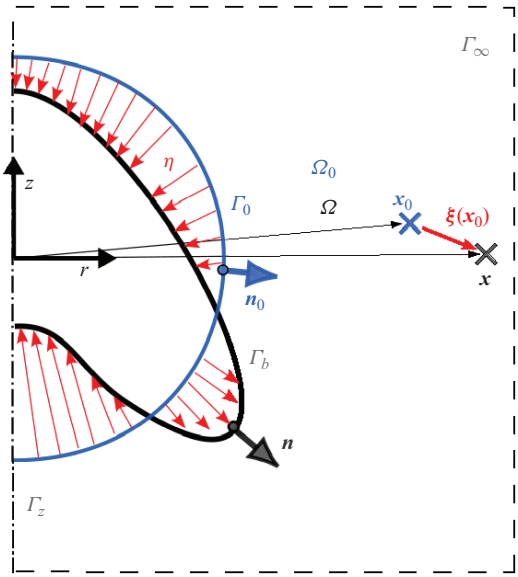


Figure 1. Flow domain and geometrical transformation involved in the L-ALE approach. The black line represents the current bubble–fluid interface $\Gamma_b(t)$ bounding internally the physical fluid domain $\Omega(t)$, while the blue line corresponds to the initial interface $\Gamma_0$ bounding the reference domain $\Omega_0$. Both domains exhibit a rotational symmetry about the $\Gamma_z$ axis.

The stability of the coupled fluid–bubble motion is examined with the help of the linearized arbitrary Lagrangian–Eulerian approach, hereinafter abbreviated as L-ALE, developed by Bonnefis (2019) and described by Sierra-Ausin *et al.* (2022). Here, we only summarize the main steps of this approach, referring readers to the above references for more details. The key idea is to solve the governing equations of the problem, which hold on a time-deforming domain $\Omega(t)$ since the bubble–fluid interface $\Gamma_b(t)$ experiences time-dependent deformations, on a prescribed reference domain $\Omega_0$ bounded internally by a fixed surface $\Gamma_0$ representing the reference position of the interface (figure 1). In addition to $\Gamma_0$, $\Omega_0$ is bounded by a fixed external surface $\Gamma_\infty$ on which suitable far-field conditions are imposed, and $\Gamma_0$ and $\Gamma_\infty$ are connected by the vertical axis, $\Gamma_z$, about which the base state exhibits an axial symmetry. The L-ALE approach is grounded on the explicit building of the bijective mapping connecting the instantaneous position $\boldsymbol{x}$ of a given geometrical point in the deforming domain to its position $\boldsymbol{x}_0$ in $\Omega_0$. In other words, this approach relies on the determination of the infinitesimal displacement field $\boldsymbol{\xi}(\boldsymbol{x}_0)$ such that $\boldsymbol{x} = \boldsymbol{x}_0 + \boldsymbol{\xi}(\boldsymbol{x}_0)$ everywhere in $\Omega_0 \cup \Gamma_0 \cup \Gamma_z \cup \Gamma_\infty$. On $\Gamma_0$, the unit normal of which is $\boldsymbol{n}_0$, the normal component of the displacement, $\boldsymbol{\xi} \cdot \boldsymbol{n}_0$, must equal the displacement of the bubble–fluid interface, $\eta$. In contrast, $\boldsymbol{\xi}$ may be arbitrarily chosen anywhere else. To ensure a smooth distribution of the displacement field, we assume that $\boldsymbol{\xi}$ obeys the Cauchy–Navier equation of elastostatics with unit Lamé coefficients in $\Omega_0$, together with a suitable symmetry condition on $\Gamma_z$ and a Dirichlet condition $\boldsymbol{\xi} = \boldsymbol{0}$ on $\Gamma_\infty$.

Knowing $\boldsymbol{\xi}(\boldsymbol{x}_0)$ and its gradients everywhere, the time and space derivatives involved in the governing equations written in $\Omega(t)$ may be expressed in $\Omega_0$ and linearized consistently with respect to $\boldsymbol{\xi}$, together with the variations of the unit normal and local mean curvature of $\Gamma_b(t)$. Governing equations in $\Omega_0$ were detailed in Sierra-Ausin *et al.* (2022). They consist of the continuity and Navier–Stokes equations, while the kinematic (no-penetration) and dynamic boundary conditions must be enforced on $\Gamma_0$. Owing to

the negligible viscosity of the gas enclosed in the bubble, the tangential component of the dynamic boundary condition reduces to a shear-free condition that must be satisfied on $\Gamma_0$ by the gradients of the liquid velocity field, $\boldsymbol{u}$. Since the gas density is also negligible, the momentum balance implies that the pressure is uniform (but possibly time dependent) within the bubble. Consequently, the normal component of the dynamic boundary condition on $\Gamma_0$ expresses the fact that the difference between the uniform pressure $p_b$ inside the bubble and the local pressure $p$ in the liquid (from which the hydrostatic component has been subtracted) balances the difference between the local capillary pressure and the normal viscous stress in the liquid. Last, two integral conditions have to be added to ensure that the volume of the bubble does not change over time, and that the vertical position of its geometrical centroid does not vary once the problem has been expressed in a reference frame translating with the bubble rise speed, $u_b$.

A key feature of the L-ALE approach is that the entire set of equations governing the evolution of the state vector $\boldsymbol{q} = [\boldsymbol{u}, p, \eta, \boldsymbol{\xi}, u_b, p_b]^{\mathrm{T}}$ ($^{\mathrm{T}}$ denoting the transpose) is solved simultaneously (such an approach is frequently referred to as 'monolithic'). Starting from an arbitrary initial solution $\boldsymbol{q}_0 = [\boldsymbol{u}_0, p_0, 0, \boldsymbol{0}, u_{b0}, p_{b0}]^{\mathrm{T}}$ (here assumed to be axisymmetric) and dropping time derivatives in the Navier–Stokes equations and in the no-penetration condition, a Newton algorithm is used to obtain the stationary base state through a series of global iterations in which the state vector and the reference domain are iteratively updated. For this purpose, we express the problem in weak form and make use of the finite element software FreeFem++ (Hecht 2012) to build and invert the various matrices involved. The volume fields $(\boldsymbol{u}, p, \boldsymbol{\xi})$ are discretized on the finite element basis suitable for each of them, while the normal displacement of the interface, $\eta$, is discretized on the local Fourier basis. Provided that $\boldsymbol{q}_0$ is chosen 'not too far' from the stationary solution (i.e. within its basin of attraction), the above algorithm converges quadratically in a few iterations. Moreover, compared with time-marching algorithms, it has the decisive advantage that unstable steady solutions may also be captured, allowing the features of the corresponding branches (if any) of the bifurcation diagram to be studied in detail; see, e.g. Sierra-Ausin *et al.* (2022).

Once the state vector and the shape of the bubble–fluid interface defining the axisymmetric base state have been obtained, the linear stability of this solution is assessed in the Galilean reference frame translating with the corresponding rise speed. For this purpose, we consider a cylindrical coordinate system $(r, \theta, z)$ whose axis $r = 0$ and cross-sectional plane $z = 0$ correspond to the symmetry axis and vertical position of the bubble geometrical centroid in the base state, respectively. Then we compute the complex eigenvalues $\lambda = \lambda_r + \mathrm{i}\lambda_i$ associated with disturbances of the form $\boldsymbol{q}'(r, \theta, z, t) = [(\hat{\boldsymbol{u}}, \hat{p}, \hat{\eta}, \hat{\boldsymbol{\xi}})\mathrm{e}^{\mathrm{i}m\theta}, \hat{p}_b]^{\mathrm{T}}\mathrm{e}^{\lambda t}$, with $m$ denoting the azimuthal wavenumber and $\theta$ the azimuthal angle, the hatted amplitudes $(\hat{\boldsymbol{u}}, \hat{p}, \hat{\eta}, \hat{\boldsymbol{\xi}})$ depending on both $r$ and $z$ (owing to the choice of the reference frame, $\hat{u}_b \equiv 0$, so that the instantaneous position of the bubble centroid no longer necessarily coincides with the origin of the reference frame). In what follows, we shall be primarily interested in the family of non-axisymmetric modes $|m| = 1$ which are those associated with the first deviations of the bubble path from the vertical, and in modes $m = 0$ and $|m| = 2$ associated with the oscillations of the bubble shape. The eigenvector $\boldsymbol{q}'$ is obtained via the Newton algorithm already employed to determine the base state. The set of equations to be solved is similar, except that the momentum equation and the no-penetration condition now involve terms proportional to $\lambda$ since the sought solution is time dependent; the reference state vector and domain to be considered are those corresponding to the base state. The complex eigenvalues are finally obtained using a Krylov–Shur projection method available in the SLEPc library.

Obviously, the accuracy with which the base state and the eigenvalues are determined depends critically on the finite element triangulation of $\Omega_0$, especially along the bubble–fluid interface $\Gamma_0$ and within the boundary layer and wake regions. The position of the fictitious outer boundary $\Gamma_\infty$ with respect to the bubble is also important, the computational domain having to be large enough to avoid spurious confinement effects. It must also be kept in mind that, in low-Morton-number fluids such as water ($Mo \approx 2.54 \times 10^{-11}$ under standard conditions) and even more in liquid metals, such as Galinstan ($Mo \approx 1.4 \times 10^{-13}$), the onset of path instability takes place in regimes where the bubble Reynolds number $Re = \rho u_b D/\mu$ is of the order of $10^3$ ($\approx$670 in water, $\approx$2100 in Galinstan, see figure 7 below). To ensure that the flow is still fully resolved in the thin boundary layers encountered in such regimes, we design an initial grid in which 18 nodes are distributed across a $5 \times Re^{-1/2}$-thick layer surrounding the bubble. Along the bubble surface, the number of nodes $N_D$ over a $D$-long arc length is approximately $7.2 \times Re^{1/2}$, with at least $N_D = 64$ when $Re$ becomes less than 80. Since $u_b$, hence $Re$, is not known *a priori*, once an approximate steady state has been computed on the initial grid, a new grid is generated following an adaptive mesh refinement procedure. This new grid is designed based on the previous steady-state solution, with some constraints ensuring that the boundary layer remains sufficiently resolved. This procedure is repeated a few times until the solution becomes grid independent. Extensive tests were carried out to evaluate the sensitivity of the base state (appreciated for instance through the variations of $Re$, $\chi$, $\lambda_r$ and $\lambda_i$) to factors such as the domain size, distance from the bubble to the downstream boundary and density of nodes along the bubble surface. For instance, in the case of a bubble with $Bo = 0.6$ rising in water, it was found that relative variations of these indicators for the non-axisymmetric modes $m = \pm 1$ are all less than 0.1 % provided that $N_D \gtrsim 70$ and the distance from the bubble centroid to the downstream end of the domain is at least $30D$, the upstream end and the lateral surface being both located $15D$ away from this centroid (Bonnefis 2019).

## 3. Base state

### 3.1. *Bubble shapes*

Figure 2 shows how the equilibrium shape of the bubble changes with the Bond number in three different fluids. As the Morton number keeps a constant value in each fluid, increasing $Bo$ (or $Ga$) in a given series amounts to increasing the bubble size; since $Bo \propto D^2$, the volume of the bubble grows as $Bo^{3/2}$. In each series, starting from nearly spherical shapes at low Bond number, bubbles take oblate spheroidal shapes when finite-$Bo$ effects become significant. The figure makes it clear that the properties of the carrying fluid have a major influence on the range of sizes in which this geometric approximation is valid: while the shape of a bubble with $Bo = 3$ is still close to a spheroid in silicone oil DMS-T05 ($Mo = 6.2 \times 10^{-7}$, see table 1 for the physical properties of the various fluids discussed below), a bubble with $Bo = 0.5$ is seen to already exhibit a significant fore–aft asymmetry in water. Beyond that range, the front part of the bubble flattens increasingly as its size increases, while its rear part becomes more and more rounded. As indicated by the change in colour of the bubble contour in the figure, the transition between these two 'regimes' corresponds approximately to the onset of path instability. Although they do not rise in a straight line, bubbles with a mildly convex front and a pronounced rounded rear are routinely observed in experiments. In contrast, bubbles with an almost flat or even concave front such as those shown in the figure for $Bo \gtrsim 5$ in DMS-T05 or $Bo \gtrsim 0.7$ in water are not. The obvious reason is that such bubbles actually experience large shape oscillations, so that the present stationary solution makes little sense in these regimes.

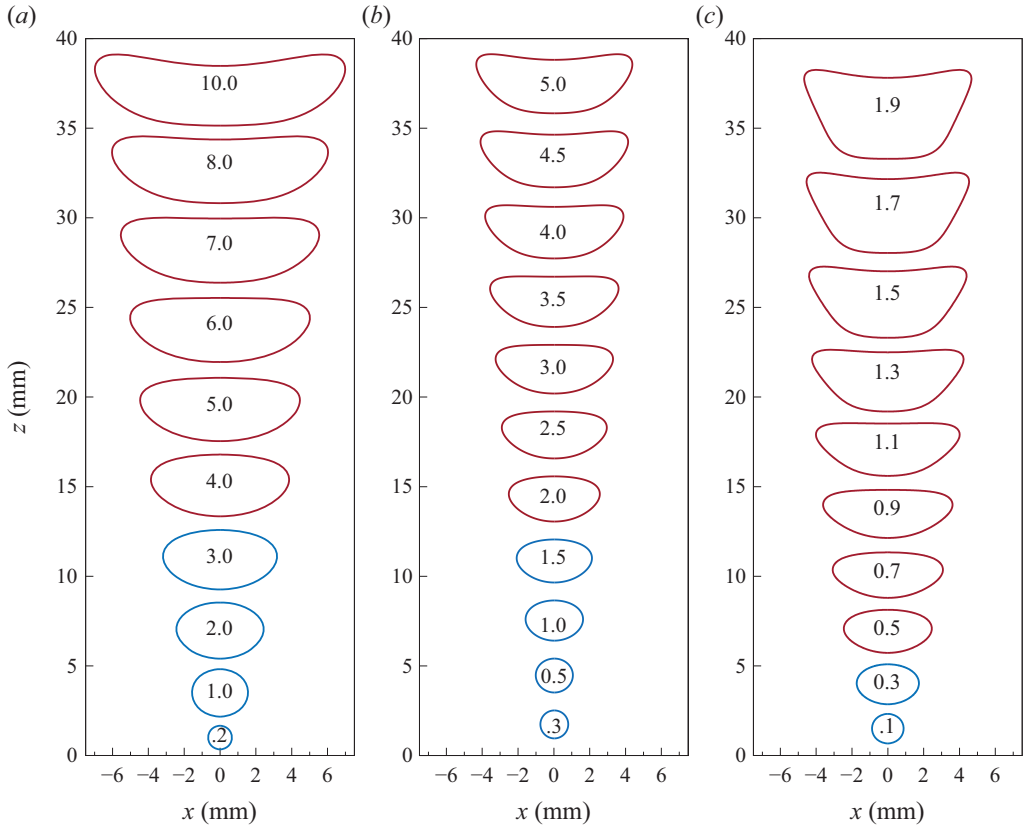


Figure 2. Equilibrium shapes of bubbles with various Bond numbers in three different fluids; the Bond number is specified within each contour. Contours represent different bubbles; their centroids are arbitrarily shifted in the vertical direction for readability, making the local value of $z$ irrelevant. Blue and red contours refer to stable and unstable configurations, respectively. (*a*) Silicone oil DMS-T05 ($Mo = 6.2 \times 10^{-7}$); (*b*) silicone oil DMS-T02 ($Mo = 1.6 \times 10^{-8}$); (*c*) water at 20 °C ($Mo = 2.54 \times 10^{-11}$).

| Liquid | $\rho$ (kg m$^{-3}$) | $\mu$ (mPa s) | $\gamma$ (mN m$^{-1}$) | $Mo = g\mu^4/(\rho\gamma^3)$ |
|---|---|---|---|---|
| Galinstan | 6440 | 2.40 | 718 | $1.4 \times 10^{-13}$ |
| Water (28 °C, 1 atm) | 996 | 0.80 | 71.0 | $1.13 \times 10^{-11}$ |
| Water (20 °C, 1 atm) | 1000 | 1.00 | 72.8 | $2.54 \times 10^{-11}$ |
| DMS-T00 | 761 | 0.49 | 15.9 | $1.8 \times 10^{-10}$ |
| DMS-T02 | 873 | 1.75 | 18.7 | $1.6 \times 10^{-8}$ |
| DMS-T05 | 918 | 4.59 | 19.7 | $6.2 \times 10^{-7}$ |
| DMS-T11 | 935 | 9.35 | 20.1 | $9.9 \times 10^{-6}$ |

Table 1. Physical properties of some specific fluids considered in this study. Note that the surface tension of Galinstan may vary from 535 to 718 mN m$^{-1}$, depending on the exact alloy composition.

### 3.2. *Rise speed*

Variations of the equilibrium rise speed with the bubble size and liquid properties are displayed in figure 3 in the form of a $Re(Bo)$ diagram. Comparison with experimental data reveals an excellent agreement in most fluids, especially in the most challenging case

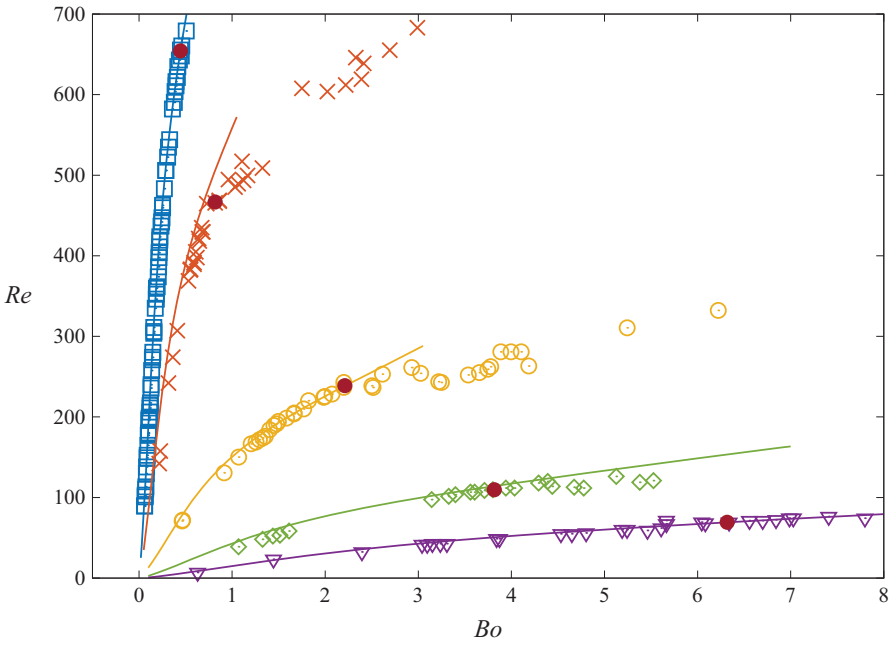


Figure 3. Rise Reynolds number vs the Bond number in several fluids. Solid lines: present predictions; symbols: experimental data, with ⊡ (blue): ultrapure water at 20 °C ($Mo = 2.54 \times 10^{-11}$) (Duineveld 1995), × (orange): silicone oil DMS-T00 ($Mo = 1.8 \times 10^{-10}$), ⊙ (yellow): DMS-T02 ($Mo = 1.6 \times 10^{-8}$), ⟐ (green): DMS-T05 ($Mo = 6.2 \times 10^{-7}$), and ▽ (purple): DMS-T11 ($Mo = 9.9 \times 10^{-6}$) (data for all four series taken from Zenit & Magnaudet 2008). Red bullets mark the onset of path instability detected experimentally in each series.

of water. A consistent 10 % over-estimate may be noticed in the least viscous silicone oil, DMS-T00, presumably because of some variation in the actual viscosity or surface tension of the sample used in the experiments with respect to the reference values provided by the manufacturer (Zenit & Magnaudet 2008). In each series, the location of the incipient path instability detected in the experiments is specified with a bullet in the figure. The threshold Reynolds number is seen to vary by nearly one order of magnitude from water to the most viscous oil, DMS-T11, 9.4 times more viscous than water. As the three intermediate series make clear, the predicted Reynolds number departs from that determined in the experiments beyond the threshold. This is no surprise, since part of the potential energy of zigzagging or spiralling bubbles is transferred to the radial and azimuthal fluid motions, yielding a decrease in the rise speed compared with the rectilinear regime.

Data reported in figure 3 may also be used to shed some light on the influence of the bubble shape and properties of the carrying fluid on the bubble rise speed. To this end, the above numerical predictions for the rise Reynolds number are replotted against the Galilei number in figure 4. This figure reveals the succession of two distinct behaviours in each fluid. First, at low enough $Ga$, all data collapse onto a master curve following the power law $Re \propto Ga^{5/3}$. This behaviour corresponds to the regime in which the bubble rise speed does not depend on surface tension, hence on the Morton number. In this regime, the bubble shape remains close to a sphere, i.e. its aspect ratio $\chi$ is close to unity. For low enough $We$, departures from sphericity are known to increase linearly with the Weber number according to the law $\chi = 1 + \frac{9}{64}We$ (Moore 1965). Since $We = Re^2 Mo^{1/3} Ga^{-2/3}$, the lower $Mo$ the wider the $Re$ range pertaining to this first regime, which extends up

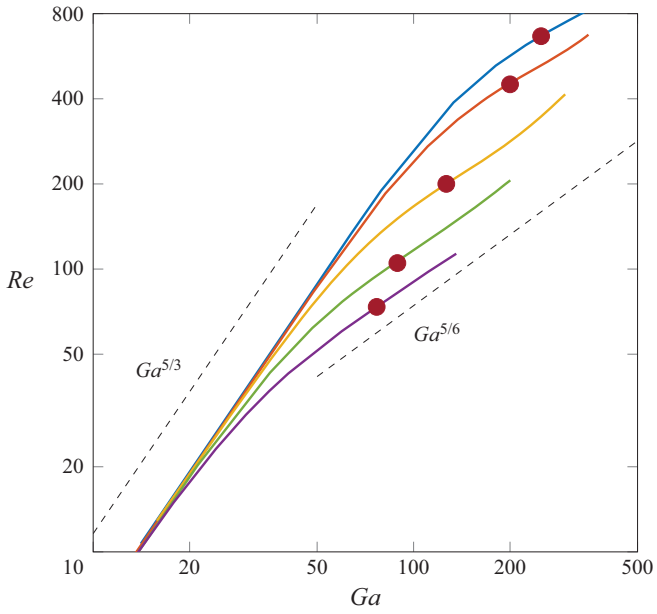


Figure 4. Numerical predictions for the rise Reynolds number, plotted vs the Galilei number. The colour code and the meaning of the red bullets are similar to those of figure 3.

to $Re \approx 200$ in water. Bubbles become flatter as $We$, hence $Re$, increases, opposing a larger resistance to the fluid. This makes their rise speed grow more slowly with $Ga$ when the Weber number becomes of order unity. Since their frontal area depends on $We$, which itself depends on $Mo$, the Reynolds number is no longer independent of the Morton number in this second regime. To further examine the two behaviours, one has to refer to the force balance on the bubble which, in non-dimensional form, reads $C_D(Re)Re^2 = \frac{4}{3}Ga^2$, with $C_D(Re)$ the usual drag coefficient. The drag coefficient of a spherical bubble is known to vary from $16Re^{-1}$ at low Reynolds number to $48Re^{-1}$ in the limit of very large Reynolds number (Batchelor 1967). Hence, for nearly spherical bubbles, the force balance implies $k(Re)Re = \frac{1}{12}Ga^2$, with $k(Re \ll 1) = 1$, $k(Re \gg 1) = 3$. The slow increase of $k(Re)$ in between these two limits, which follows approximately the power law $k(Re) \sim Re^{1/5}$ up to Reynolds numbers of a few hundreds, is the reason why the Reynolds number grows slightly more slowly than $Ga^2$ in the first regime. Bubbles are significantly distorted in the second regime, which corresponds to the intermediate range $We = O(1)$ ($We \approx 0.62$ at $Re = 200$ in water). Assuming that their frontal area, which is proportional to $\chi^{2/3}$, grows approximately linearly with the Weber number in that range yields $C_D(Re) \sim k(Re)Re^{-1}We \sim Re^{6/5}Mo^{1/3}Ga^{-2/3}$. The force balance then implies $Re \sim Ga^{5/6}Mo^{-5/48}$, a prediction supported by the numerical data for the various fluids in the $Ga$ range where path instability occurs.

### 3.3. *Flow structure*

The flow structure in the base state reveals several interesting features. Figure 5 displays the azimuthal vorticity (left half of each panel) and pressure (right half) and distributions past a bubble rising in three different fluids in the $Bo$-range where the path instability threshold will later be shown to lie. With no surprise, the near-surface pressure distribution

reaches its minimum very close to the equatorial plane, defined as the horizontal plane in which the longest axis of the bubble lies. This is a mere consequence of the increase of the fluid velocity along the interface from the apex of the bubble down to its equatorial plane. The norm of the azimuthal vorticity also reaches its maximum in that plane because this quantity is proportional to the product of the interface curvature in the vertical diametrical plane and the relative fluid velocity along the interface (Batchelor 1967), both of which are maximum there. This vorticity results directly from the shear-free condition obeyed by the fluid at the interface and is responsible for the existence of a boundary layer that encapsulates the bubble and turns into a wake downstream of it (Moore 1963, 1965). The wake structure is found to depend dramatically on the Bond number and, for a given $Bo$, on the fluid properties (compare panels ($a$,$f$), both for $Bo = 3$). In water, all streamlines are open for $Bo = 0.4$ (panel $g$) and they remain so up to $Bo \approx 0.5$. Beyond this point, a standing eddy exists and grows sharply with the Bond number, its length becoming of the same order as that of the long bubble axis for $Bo = 0.8$ (panel $i$). Qualitatively similar trends are observed in the more viscous fluids. However, for a given $Bo$, the normalized rise speed $U = u_b/(gD)^{1/2}$ is significantly smaller, and so is the Weber number $We \equiv \rho u_b^2 D/\gamma = Bo\, U^2$. Indeed, keeping $Bo$ unchanged, the Weber numbers in two different fluids, 1 and 2, obey the relation $We_2/We_1 = (Re_2/Re_1)^2(Mo_2/Mo_1)^{1/2}$. Hence, in the nearly five times more viscous silicone oil DMS-T05 for instance, the Weber number of a bubble with $Bo = 0.5$ is eight times smaller than in water, leaving it nearly spherical. Consequently, compared with water, much larger $Bo$ are required for the tangential fluid velocity and interface curvature to be large enough for a standing eddy to develop at the back of the bubble. In the case of DMS-T05, the required conditions are achieved only for $Bo \gtrsim 2.4$.

The above information regarding the existence of a standing eddy in the various liquids is summarized in figure 6. This plot shows the critical curve separating the upper region of the ($Bo$, $Ga$) plane where a standing eddy exists, from the lower region in which no such structure takes place; the two insets display an example of each situation. Present predictions are seen to be in excellent agreement with those of the fully resolved axisymmetric simulations carried out with Gerris by Cano-Lozano *et al.* (2013). It will become clear in the next section that, in low-$Mo$ fluids, path instability arises for ($Ga$, $Bo$) pairs located below this critical curve. This finding is of special importance in that it establishes that the existence of a standing eddy is not a prerequisite for the path of a freely rising bubble to become unstable, unlike the case of a fixed bubble (Tchoufag *et al.* 2013). More generally, it is well established that the initial 'seed' leading to global wake instability past bluff bodies held fixed in a uniform stream is the growth of disturbances in the core of the standing eddy (Chomaz 2005). That path instability may happen in the absence of such a near-wake structure proves that, in the relevant $Mo$-range, the mechanism that governs this instability is not driven by wake instability *per se*. This confirms the findings of Cano-Lozano *et al.* (2016*a*) who established that, for $Mo \lesssim 10^{-9}$, the path of bubbles with a frozen but realistic shape becomes unstable while their wake is still stable, the low-frequency 'aerodynamic' mode being destabilized first.

## 4. Neutral curves

### 4.1. *Critical bubble size*

Using the procedure described in § 2, we selected a set of $Mo$ values, some of which correspond to specific liquids. For each of these values, we increased the bubble size, i.e. the Bond and Galilei numbers, until the real part of one of the eigenvalues associated with

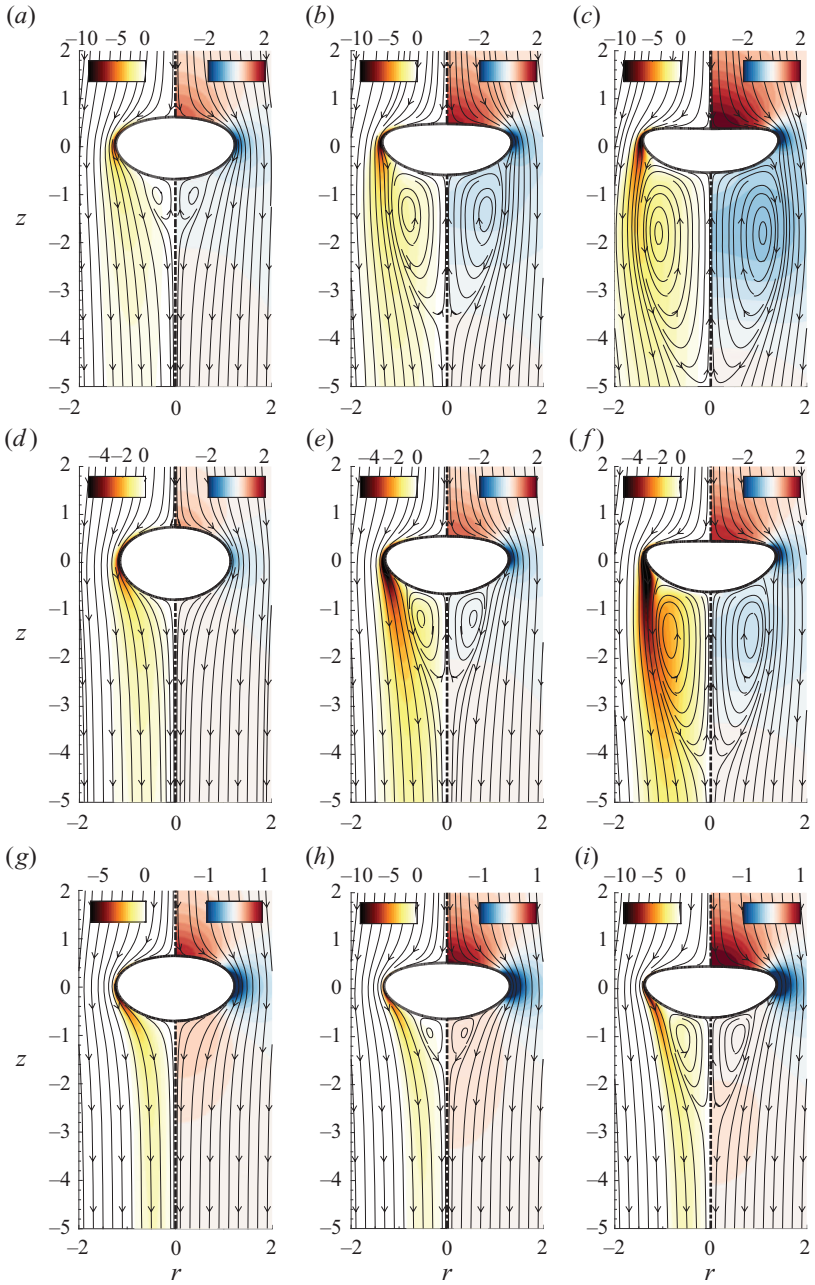


Figure 5. Base flow past bubbles rising in three different liquids: (*a–c*) DMST05 ($Mo = 6.2 \times 10^{-7}$), with, from left to right, $Bo = 3$, 5 and 7; (*d–f*) DMST02 ($Mo = 1.6 \times 10^{-8}$), with $Bo = 1$, 2 and 3; (*g–i*) water at 20 °C ($Mo = 2.54 \times 10^{-11}$), with $Bo = 0.4$, 0.6 and 0.8. The left and right halves of each panel display the azimuthal vorticity and pressure distributions, respectively. The thin lines are the streamlines in the reference frame rising with the bubble.

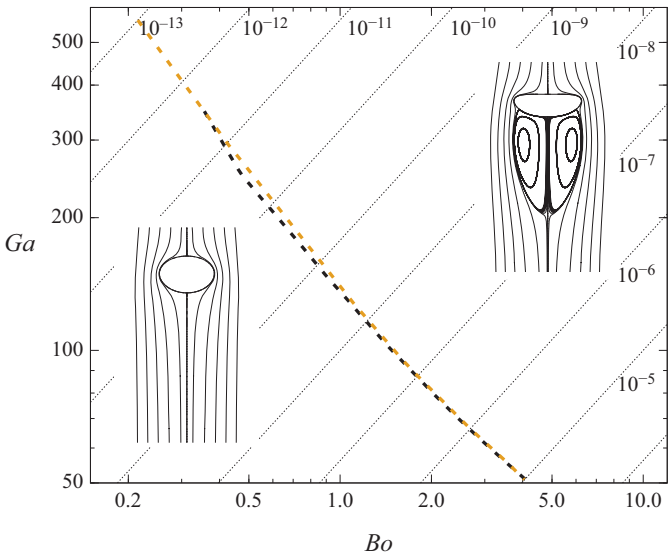


Figure 6. Critical curve corresponding to the onset of a recirculating region at the back of the bubble in the ($Bo$, $Ga$) plane. Yellow line: present results; black dashed line: predictions of Cano-Lozano, Bohorquez & Martinez-Bazán (2013). The left and right insets show some streamlines around a bubble with $Bo = 0.3$ in water and a bubble with $Bo = 6.5$ in DMS-T05, respectively. The thin dotted lines correspond to constant values of the Morton number, i.e. to a given liquid; $Mo$ values are specified along the upper and right sides of the figure.

the non-axisymmetric modes $m = \pm 1$ changes sign, which determines the threshold of path instability. The resulting neutral curve, obtained by linking these thresholds, is shown in figure 7. Together with figure 8, this is presumably the most important result of the present study with respect to the original physical problem. For each fluid characterized by a Morton number in the range $10^{-13}$–$10^{-5}$, this curve readily provides the size of the smallest bubble whose vertical path becomes linearly unstable. For instance, the path of a bubble rising in water at a temperature of 20 °C becomes unstable at $Bo = 0.463$ and $Ga = 250$, yielding a critical diameter $D \approx 1.854$ mm (Bonnefis 2019; Bonnefis *et al.* 2023). Similarly, the critical Bond numbers for Galinstan ($Mo = 1.4 \times 10^{-13}$) and DMS-T11 ($Mo = 9.9 \times 10^{-6}$) are 0.19 and 6.85, respectively. Therefore, the critical bubble sizes for these two fluids located close to the bounds of the $Mo$-interval considered here are 1.48 mm and 3.875 mm, respectively.

In figure 7 we also report some experimental data obtained under controlled conditions, ensuring that the carrying fluid obeys a shear-free condition at the gas–liquid interface. The reference data of Duineveld (1995) in ultrapure water at 20 °C yield a critical bubble diameter close to 1.82 mm, which differs by less than 2 % from the present prediction. De Vries (2002) also determined the onset of path instability in a tank of ultrapure water with an average temperature of 28 °C ($Mo = 1.13 \times 10^{-11}$). However, a 1.1 °C m$^{-1}$ stabilizing temperature gradient was established to visualize the wake thanks to optical index gradients. The influence of this stratification on path instability is unknown and might be at the origin of the 8 % difference between the experimentally determined critical bubble size and the present prediction. Comparisons with data obtained with four different silicone oils (Zenit & Magnaudet 2008) and with three other silicone oils in which photochromic dye was added to visualize the wake (Sato 2009) prove satisfactory in the sense that the neutral curve lies generally within the ($Bo$, $Ga$)-interval whose lower

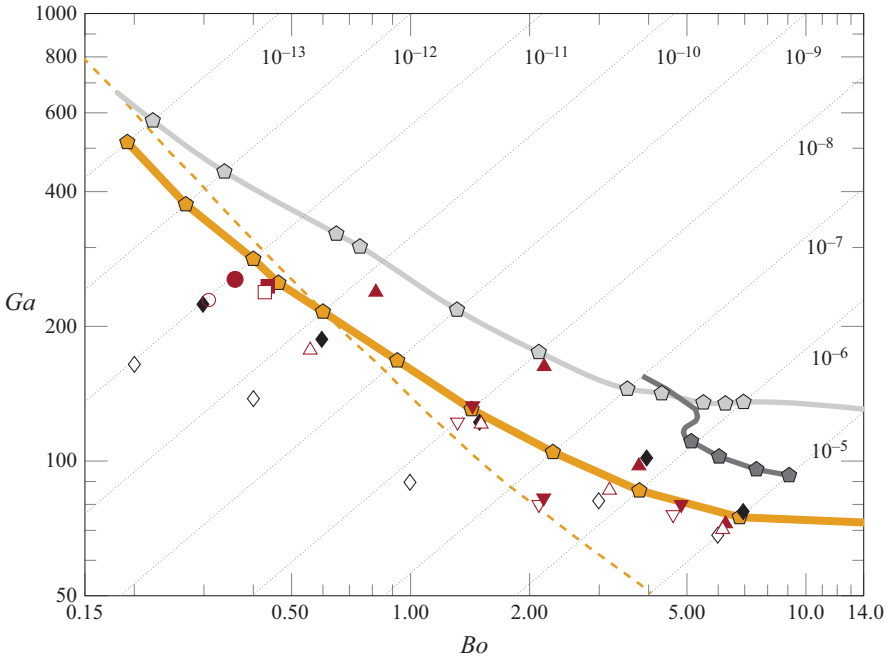


Figure 7. Neutral curve in the (*Bo*, *Ga*) plane, obtained by connecting the ⬠ (orange) symbols at which the threshold was determined. The pale and dark grey lines are the two branches of the neutral curve obtained by considering the same base state but keeping the bubble shape frozen in the stability analysis; the thin yellow dashed line is the critical curve of figure 6 beyond which a standing eddy exists at the back of the bubble in the base state. The thin dotted lines are iso-Morton-number lines corresponding to a given liquid; *Mo* values are specified along the upper and right sides of the figure. In a given fluid, open (respectively closed) symbols indicate stable (respectively unstable) paths observed in the simulations of Cano-Lozano *et al.* (2016*b*) (⟐, ⧫ black), in the experiments of De Vries (2002) (⊙, ●, purple) and Duineveld (1995) (⊡, ■ purple) with ultrapure water (performed at temperatures of 28 °C and 20 °C, respectively), and in those of Zenit & Magnaudet (2008) (◬,▲ purple) and Sato (2009) (▽,▼ purple) with various silicone oils.

(respectively upper) bound corresponds to the largest (respectively smallest) bubble for which a stable (respectively unstable) path could be identified experimentally. The only two exceptions correspond to a probable outlier in Sato's data for $Mo = 2.35 \times 10^{-7}$, and to DMS-T11 (the most viscous oil) in which the path of a bubble 4 % smaller than the critical size predicted here was found to be unstable. Numerical data obtained by Cano-Lozano *et al.* (2016*b*) with Gerris in the transition region (but not necessarily in the close vicinity of the threshold) are also reported. These data are seen to be in good agreement with present predictions for fluids with $Mo \gtrsim 10^{-8}$. In contrast, as the authors anticipated in their conclusions, these simulations underestimate the critical bubble size in fluids having a lower Morton number. The lower *Mo* the larger the underestimate, which makes the critical diameter in water under-predicted by 15 %–20 %. Since these simulations made use of an adaptive grid with 128 cells per bubble diameter on both sides of the interface, this significant underestimate helps appreciate how demanding fully resolved simulations of bubbly flows in low-viscosity fluids are.

In figure 7 we also reported the critical curve of figure 6 corresponding to the onset of a recirculating region at the back of the bubble in the base flow (yellow dashed line). The yellow solid and dashed lines are seen to cross each other at $Mo \approx 10^{-10}$. For lower *Mo*, the critical bubble size at which the path destabilizes first is such that no standing

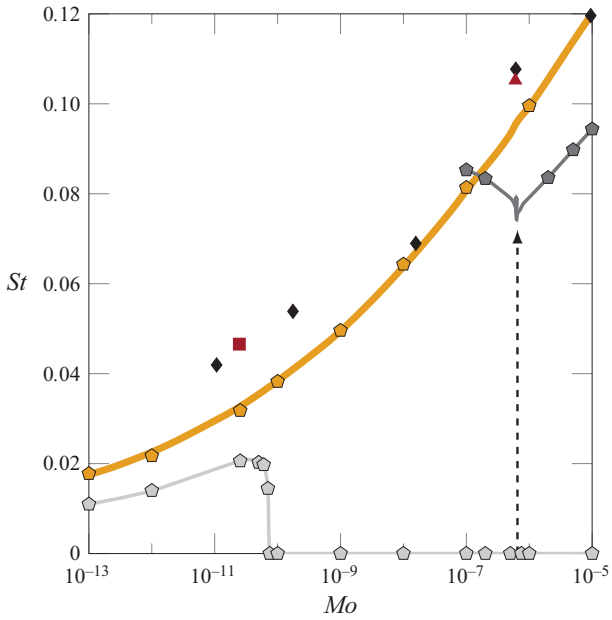


Figure 8. Variation of the reduced frequency $St = \lambda_i D/(2\pi u_b)$ at the threshold vs the Morton number. The yellow curve was obtained by connecting the ⬠ (orange) symbols at which the frequency was determined. The pale and dark grey lines correspond to the predictions along the two branches of the neutral curve predicted by the FSA using the same base state (for readability, only five of the computed points are highlighted with a marker on the dark grey line). The vertical arrow at $Mo = 2.7 \times 10^{-7}$ indicates the frequency jump associated with the switching from the stationary mode to the oscillatory mode predicted by FSA. ⧫ (black): numerical predictions of Cano-Lozano *et al.* (2016*b*); ■ (purple): experimental data of Duineveld (1994) for $Bo = 0.54$ in ultrapure water; ▲ (purple): experimental data of Zenit & Magnaudet (2009) for $Bo = 3.92$ in DMS-T05.

eddy exists in the base state. For the reasons discussed in the previous section, this leads to the conclusion that wake instability cannot be responsible for path instability in such low-*Mo* fluids. The pale and dark grey lines in the figure also provide interesting insight into the role of time-dependent bubble deformations. To obtain the neutral curve resulting from these two lines, we considered the same base state as above, and imported the corresponding interface shape and rise speed in the stability code used by Tchoufag *et al.* (2014*b*) and Cano-Lozano *et al.* (2016*a*). In this code, the interface shape is kept frozen, i.e. the bubble can only move as a rigid body. A similar neutral curve was computed by Cano-Lozano *et al.* (2016*a*) (black line in their figure 7), using a base state obtained with Gerris, instead of the present global Newton method. Their neutral curve is similar to that based on the two grey lines in figure 7 but the critical *Ga* they found at a given *Bo* stands consistently below that determined here, with differences ranging from 5 % for $Bo \geqslant 5$ to 15 % for $Bo = 0.5$. Again, the reasons for these differences are to be found in the limited spatial resolution of the Gerris-based computations in high-*Ga* low-*Bo* configurations.

Since the yellow and grey lines in figure 7 are based on strictly identical base states, time-dependent deformations not accounted for in the stability analysis used to produce the second of them are entirely responsible for the differences observed in the fate of the imposed disturbances. As the comparison of the thresholds predicted by the two approaches in a given fluid evidences, deformations always lower the threshold, i.e. they promote path instability. However, for fluids with Morton numbers less than $\approx 5 \times 10^{-7}$, the lower *Mo* the weaker this influence. For instance, the 'frozen-shape' approximation,

hereinafter referred to as FSA, over-predicts the critical bubble size by nearly 23 % for $Mo = 10^{-7}$, but this overestimate is reduced by a factor of three in the case of Galinstan. The FSA actually predicts that the neutral curve involves two distinct modes intersecting at $Mo \approx 2.8 \times 10^{-7}$. In the narrow range $4 \times 10^{-7} \lesssim Mo \lesssim 6.5 \times 10^{-7}$, the mode that becomes most unstable beyond this intersection (dark grey line) exhibits a S shape, implying a destabilization–restabilization scenario. In contrast, the neutral curve resulting from the stability analysis carried out with freely deforming bubbles remains single valued throughout the whole range of Morton number. For larger $Mo$, the FSA prediction based on this second mode is also quite good, with for instance a 16 % over-prediction of the critical bubble size in DMS-T11.

At this point it is also worth mentioning that Cano-Lozano *et al.* (2016*a*) established that the neutral curve predicted by FSA and that corresponding to the onset of 'pure' wake instability for a bubble with the same frozen shape held fixed in a uniform stream coincide in the range $10^{-9} \lesssim Mo \lesssim 6 \times 10^{-7}$. Outside of this range, the threshold values of the Bond and Galilei numbers corresponding to the onset of wake instability in a given fluid are consistently larger than those at which FSA predicts the occurrence of path instability. For $Mo \lesssim 10^{-9}$, the difference between the two thresholds increases gradually as $Mo$ is decreased. For $Mo \gtrsim 6 \times 10^{-7}$, the threshold of wake instability coincides with the upper neutral branch captured by FSA (here the pale grey line). In other words, depending on the Morton number, the threshold corresponding to the onset of wake instability past a fixed bubble is either identical to or larger than that of the path instability predicted by FSA. These findings, combined with the fact that figure 7 reveals that FSA overestimates the threshold of path instability whatever $Mo$, establish that the wake of a fixed bubble with a frozen shape is always stable at the actual onset of path instability. Hence, path instability cannot be explained on the sole basis of the mechanism responsible for wake instability.

### 4.2. *Frequency at threshold*

The most spectacular qualitative difference between the predictions of the present approach and those of FSA is seen in figure 8. This figure displays the Strouhal number, or reduced frequency, corresponding to the first unstable mode at the onset of the instability, computed as $St = \lambda_i D/(2\pi u_b)$, with $\lambda_i$ the imaginary part of the unstable eigenvalue at the threshold. As the yellow curve evidences, the present approach predicts that the most unstable mode of the system is always oscillatory, in line with experimental observations. The reduced frequency increases continuously with the Morton number, ranging from $St \approx 0.02$ for $Mo = 10^{-13}$ to $St \approx 0.12$ for $Mo = 10^{-5}$. The FSA predicts that the first non-vertical path of the bubble is associated with 'low-frequency' oscillations in low-$Mo$ liquids ($Mo \lesssim 7 \times 10^{-11}$) and with 'high-frequency' oscillations in liquids with $Mo \gtrsim 3 \times 10^{-7}$, in agreement with the conclusions of Cano-Lozano *et al.* (2016*a*). Present findings with deformable bubbles are qualitatively consistent with these predictions in both ranges. The reduced frequencies determined in both approaches for low-$Mo$ liquids are even in fairly good quantitative agreement. This confirms that deformations do not bring major changes in the dynamics of isolated bubbles rising in such liquids, which extends to all low-$Mo$ fluids the conclusions drawn by Bonnefis *et al.* (2023) in the specific case of water. More surprisingly, the agreement is still reasonable in fluids with $Mo \gtrsim 3 \times 10^{-7}$, where the FSA neutral curve (now corresponding to the dark grey line) underestimates the reduced frequency by only roughly 20 %. In contrast, the two approaches dramatically disagree in the intermediate $Mo$-range, where FSA predicts that the most unstable mode (pale grey line) is stationary. Hence, one has to conclude that, in

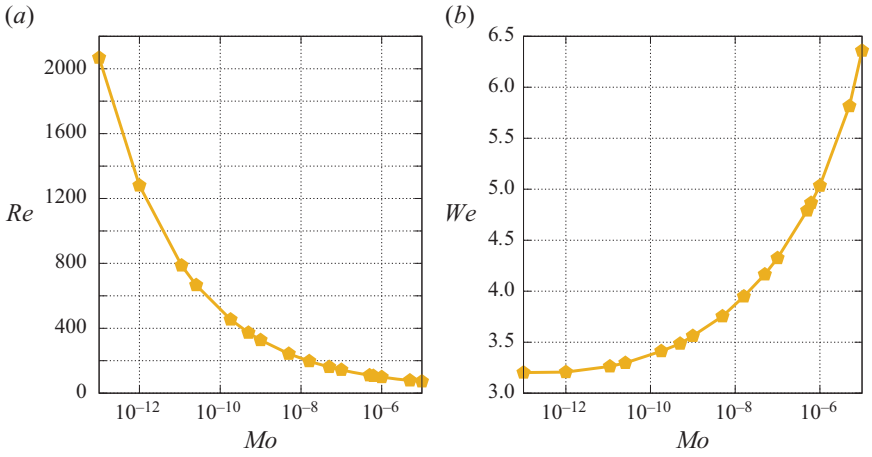


Figure 9. Influence of the fluid properties on (*a*) the critical Reynolds number and (*b*) the critical Weber number.

the linear framework adopted here, time-dependent deformations promote the instability of the oscillatory mode and succeed in making it more unstable than the stationary mode in this intermediate range, while only the latter mode may become unstable if these deformations are ignored. Some experimental and numerical data are also reported in figure 8. Most of them were obtained significantly above the threshold, which explains why the corresponding frequencies lie above present predictions (for instance, the bubble size is 8 % beyond the threshold value in the two experimental determinations). Only the two numerical determinations of Cano-Lozano *et al.* (2016*b*) in silicone oils DMS-T02 ($Mo = 1.6 \times 10^{-8}$) and DMS-T11 ($Mo = 9.9 \times 10^{-6}$) correspond to near-threshold conditions according to figure 7. The corresponding two $St$ values are seen to agree very well with present predictions.

Having determined the normalized rise speed in the base state, we can re-plot the neutral curve of figure 7 in two different forms, to make the variations of the critical Reynolds number, $Re = Ga\,U$, and Weber number, $We = Bo\,U^2$, with the liquid properties apparent. Figure 9(*a*) shows that the critical Reynolds number decreases sharply as $Mo$ increases, from ≈2070 for $Mo = 10^{-13}$ to 70 for $Mo = 10^{-5}$, via $Re = 668$ for water at 20 °C. Conversely, the critical Weber number (figure 7*b*) is seen to increase gradually from 3.20 for $Mo = 10^{-13}$ to 6.36 for $Mo = 10^{-5}$, via $We = 3.30$ for water. The above values for water are to be compared with those reported by Duineveld (1995), namely $Re = 658$, $We = 3.275$, from which they only differ by 1.5 % and 0.75 %, respectively.

## 5. Unstable modes: order of occurrence and physical nature

In this section, we examine the variations of the most unstable eigenvalues of the coupled bubble–fluid system as the size of the bubble (here measured through the Bond number) is varied in the vicinity of the primary threshold. We also analyse the spatial structure of the associated global modes. It will soon become apparent that the order in which the unstable modes follow one another as the Bond number increases, and even in some cases the way the nature of a given mode varies, depends dramatically on the range of fluid properties under consideration, the complexity of the picture increasing as the Morton number is decreased. For this reason, we discuss these features in descending order of $Mo$.

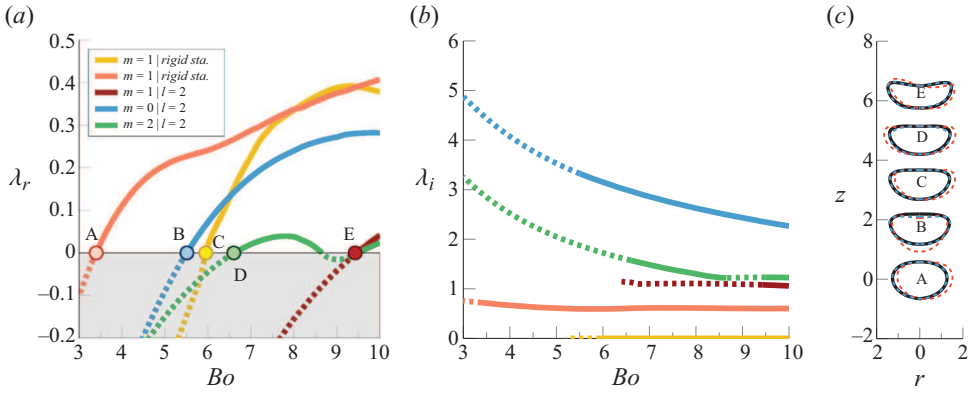


Figure 10. Variation of the first five unstable eigenvalues with the Bond number for bubbles rising in DMS-T05 ($Mo = 6.2 \times 10^{-7}$). (*a*) Growth rate ($\lambda_r$), normalized by the gravitational time $(D/g)^{1/2}$; (*b*) radian frequency ($\lambda_i$) normalized similarly; (*c*) equilibrium shapes at the threshold (labels refer to the transition points marked with bullets in *a*). In (*a*,*b*), dashed (respectively solid) lines represent the stable (respectively unstable) part of the various branches. In (*c*), the bubble contour in the vertical diametrical plane is shown at the threshold of each of the five successive modes in the base state (black solid line) and, with an arbitrary amplitude of the disturbance, for $t = 0$ (red dashed line) and $t = \pi/(2\lambda_i)$ (blue dashed line); bubble centroids are arbitrarily shifted in the $z$ direction for readability.

### 5.1. *Silicone oil DMS-T05 ($Mo = 6.2 \times 10^{-7}$)*

#### 5.1.1. *First unstable eigenvalues: thresholds and nature of the associated modes*

Figure 10 displays the variations of the first five eigenvalues whose real part becomes positive as the Bond number, hence the size, of a bubble rising in silicone oil DMS-T05 is increased. All but one of these eigenvalues have a non-zero imaginary part, indicating that the corresponding instabilities arise through Hopf bifurcations. The threshold of path instability is encountered at $Bo = 3.4$. This first unstable mode, associated with azimuthal wavenumbers $|m| = 1$, has a dimensionless frequency $\lambda_i/2\pi \approx 0.115$ at the threshold (throughout this section, eigenvalues are normalized using the gravitational time scale $(D/g)^{1/2}$). As panel (*c*) suggests, this mode is essentially associated with a lateral drift of the bubble centroid accompanied by some rigid-body rotation. Time-dependent deformations are small: it will be shown in § 6 that their maximum magnitude is barely 3 % of that of the horizontal displacement of the bubble centroid. For this reason, we refer to this mode as 'rigid'.

We continue to track this mode and other possible ones beyond this primary threshold by computing the base flow, still assumed axisymmetric, at the relevant Bond number. The growth rate of the rigid oscillatory mode continues to increase with *Bo*, and a second mode becomes unstable at $Bo \approx 5.5$ (point *B* in figure 10*a*). This mode is axisymmetric and oscillatory, with a dimensionless frequency approximately 5.5 times higher than that of the rigid mode. Examination of the corresponding successive contours in panel (*c*) reveals that this mode is associated with shape oscillations known as $l = 2, m = 0$, or $(2, 0)$, in the terminology of spherical harmonics, i.e. the associated interface displacements leave the interface position unchanged at two angular positions located on both sides of the equatorial plane. We shall show in § 6 that these deformations have a magnitude of the same order as the vertical displacement of the bubble centroid with respect to its reference position in the base state. For these reasons, we refer to this mode and those sharing similar properties as 'shape' modes. By further increasing *Bo*, a third unstable mode is encountered at point *C* ($Bo \approx 5.9$). Its growth rate increases strongly beyond the threshold

so that this mode would quickly become dominant, were its amplitude similar to that of the primary oscillatory mode. Panel (*b*) reveals that this mode is stationary and, since its azimuthal wavenumber is $|m| = 1$, it is also asymmetric. These two properties imply that this mode induces an inclined path of the bubble centroid. Moreover, panel (*c*) indicates that the corresponding interface deformations are weak compared with those associated with the previous 'shape' mode, so that this stationary mode can be considered 'rigid', just like the primary mode. Therefore, two rigid modes coexist in the system beyond $Bo \approx 5.9$, but one is oscillatory while the other is stationary. To the best of our knowledge, steady oblique bubble paths have never been reported in experiments, suggesting that this second rigid mode never becomes dominant. Nonlinearities not being taken into account here, i.e. the fact that the actual base flow at point *C* is no longer axisymmetric due to the nonlinear corrections brought by the primary oscillatory mode and is presumably even not stationary owing to the shape oscillations associated with the (2, 0) shape mode, are likely the reason for this.

A fourth mode becomes unstable at point *D* ($Bo \approx 6.6$), and restabilizes itself within the narrow interval $8.65 \lesssim Bo \lesssim 9.45$ before becoming unstable again at larger *Bo*. This mode has much in common with the (2, 0) shape mode, except that it is not axisymmetric. Rather, it is associated with azimuthal wavenumbers $|m| = 2$ and, in the *Bo*-range under consideration, its frequency is nearly half that of the (2, 0) mode. That the frequencies of two modes with the same $l$ but different $m$ differ in this context is no surprise, since spherical harmonics are no longer the eigenmodes with which a bubble oscillates when its undisturbed shape is not spherical (Meiron 1989). Here, the Bond number is large, and it is only in the small-*Bo* limit that the two frequencies are expected to get close to each other. Due to the symmetries preserved by angular variations of the form $\mathrm{e}^{\pm 2\mathrm{i}\theta}$, this (2, 2) mode does not induce any lateral displacement of the bubble. Last, at point *E* ($Bo \approx 9.45$), a third shape mode with a frequency close to that of the (2, 2) mode becomes unstable. Deformations associated with this mode share the same characteristics as those induced by modes (2, 0) and (2, 2) on both sides of the bubble equatorial plane. In contrast, as panel (*c*) makes clear, the two halves of the bubble deform in an asymmetric manner at every instant of time in the vertical diametrical plane, one half becoming more pointed while the other becomes more rounded. These characteristics identify this mode as the (2, 1) shape mode. Unlike those associated with $m = 0$ and $|m| = 2$, this mode may contribute to the lateral drift of the bubble at large enough Bond numbers, owing to its azimuthal asymmetry. It must be stressed that the full sequence described above is kept unchanged when the Morton number is increased up to $10^{-5}$.

#### 5.1.2. *Spatial structure of the first unstable mode*

Figure 11 shows the spatial structure of the first unstable mode slightly above the threshold. The real and imaginary parts of a given mode may be thought of as the associated disturbance at two different instants of time a quarter of a period apart, i.e. shifted by an interval $\tau = (\pi/2)\lambda_i^{-1}$. Therefore, if the bubble is zigzagging in a vertical plane (as it does if the two disturbances associated with modes $m = +1$ and $m = -1$ have the same amplitude), the real part corresponds to the time instant by which the bubble reaches its maximal lateral excursion (red contours in figures 11(*a*) and 10(*c*)), while the imaginary part corresponds to that by which it crosses the midline of its path (blue contours in figures 11(*b*) and 10(*c*)). The streamlines pattern evidences the antisymmetric nature of the disturbance flow. An alternation of positive and negative vorticity zones may be noticed in the wake, both in every horizontal plane (varying $r$) and at every radial position from the axis of the base flow (varying $z$). This pattern is indicative of a vortex shedding

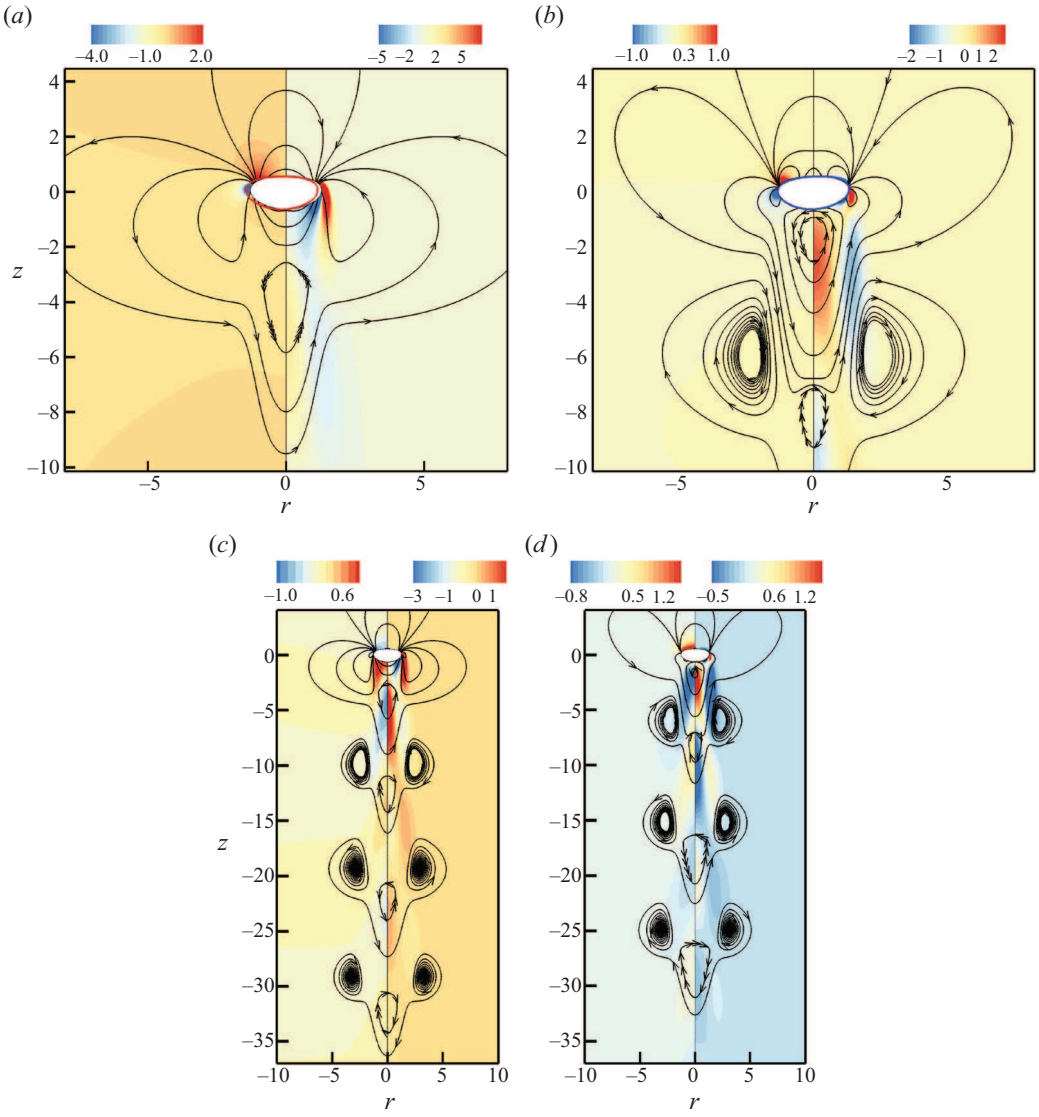


Figure 11. Structure of the first unstable mode past a bubble rising in DMS-T05 at $Bo = 3.7$. (*a*,*c*) Real part of the mode near the bubble and further downstream in the wake, respectively; (*b*,*d*) same for the imaginary part. The left and right halves in (*a*,*b*) display the pressure and azimuthal vorticity iso-levels, respectively; those in (*c*,*d*) display the azimuthal velocity and vorticity iso-levels, respectively; some streamlines defined in the reference frame of the base configuration are also shown. Black, red and blue bubble contours correspond to the base state, and the real and imaginary parts of the interface disturbance ($\hat{\eta}$), respectively.

process. A specific structure in which fluid particles rotate clockwise on both sides of the axis of the base flow is visible near the bottom of panel (*b*); in a three-dimensional representation, this structure would look like a pair of crescents connected through their horns in the vertical plane $\theta = \pm\pi/2$, with fluid particles rotating in the same direction in every azimuthal plane. As panels (*c*,*d*) make clear, this structure is actually the first of a series that develops further downstream in the wake, with alternating positive and negative directions of rotation.

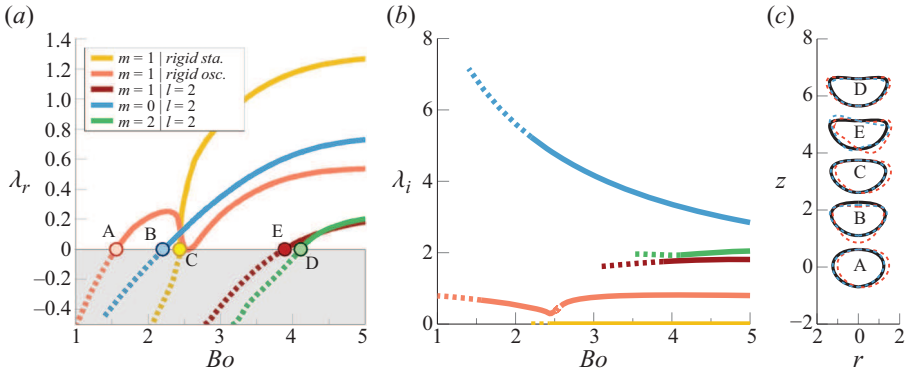


Figure 12. Same as figure 10 for bubbles rising in DMS-T02 ($Mo = 1.6 \times 10^{-8}$).

### 5.2. *Silicone oil DMS-T02 ($Mo = 1.6 \times 10^{-8}$)*

We now move to silicone oil DMS-T02 which is 2.6 times less viscous than DMS-T05 and has almost the same surface tension. Figure 12 shows how the first five eigenvalues yielding unstable modes vary with the Bond number in this case. The beginning of the sequence is similar to that described for DMS-T05. That is, path instability first arises through an oscillatory 'rigid' mode that becomes unstable at $Bo = 1.56$ (point $A$ in panel $a$). Then the shape mode $(2, 0)$ becomes unstable at point $B$ ($Bo = 2.2$), followed by the stationary rigid mode at point $C$ ($Bo = 2.43$). Further increasing $Bo$, the $(2, 1)$ and $(2, 2)$ shape modes become unstable at points $E$ ($Bo = 3.89$) and $D$ ($Bo = 4.12$), respectively. Note that, compared with the case of DMS-T05, these last two modes emerge in reverse order.

Nevertheless, the main originality of the present bifurcation diagram compared with that of DMS-T05 is that the growth rate of the primary mode starts to decrease slightly beyond point $B$, and becomes even very weakly negative within a tiny interval around $Bo \approx 2.55$, before turning positive again and growing continuously up to the upper bound of the explored Bond number range. This non-monotonic behaviour is to be related to the fact that DMS-T02 stands in the middle of the $Mo$-range where FSA predicts the emergence of path instability through a stationary bifurcation instead of a Hopf bifurcation, being unable to detect that the oscillatory rigid mode becomes actually unstable first. This failure is presumably closely connected with the fact that, although interface deformations succeed in making the oscillatory mode unstable first, the growth rate of this mode remains quite low throughout the interval bounded by points $A$ and $C$. We shall come back to this point in § 7.

### 5.3. *Water at 20 °C ($Mo = 2.54 \times 10^{-11}$)*

#### 5.3.1. *First unstable eigenvalues: thresholds and nature of the associated modes*

We finally consider the case of bubbles rising in pure water maintained at a temperature of 20 °C. Variations of the eigenvalues leading to the first five unstable modes are shown in figure 13. Again, the sequence begins with the emergence of an oscillatory rigid mode that becomes unstable at $Bo = 0.463$ with a dimensionless frequency $\lambda_i/2\pi = 0.088$, followed by the $(2, 0)$ shape mode at $Bo = 0.525$. However, the next steps differ deeply from those encountered in the previous two cases. The primary mode grows continuously until $Bo \approx 0.64$. There, this mode splits into two separate branches, both of which are

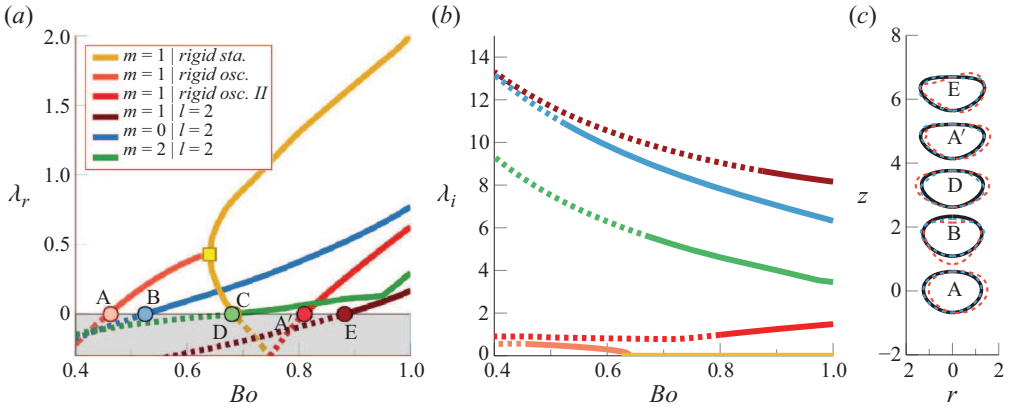


Figure 13. Same as figure 10 for bubbles rising in water at 20 °C ($Mo = 2.54 \times 10^{-11}$). In (*a*), the square indicates the codimension-two 'exceptional' point at which the pair of complex conjugate eigenvalues associated with the first unstable mode turns into a pair of real eigenvalues.

stationary. Therefore, at the point (marked with a square in the figure) where the three branches meet, the pair of complex eigenvalues associated with the oscillatory mode turns into a pair of real eigenvalues. Such a codimension 2 singular point is referred to as 'exceptional' in the theory of non-Hermitian Hamiltonian systems (Bergholtz, Budich & Kuns 2021). In the present case, this exceptional point, at which the two eigenvalues change their nature, corresponds to a Takens–Bogdanov bifurcation with $O(2)$-symmetry (Dangelmayr & Knobloch 1987). Beyond this point, the upper stationary branch exhibits a rapid and continuous growth. Conversely, the growth rate of the lower branch decreases sharply with the distance to the exceptional point, until it becomes negative at $Bo = 0.685$ (point $C$ in the figure). Similar to the cases of DMS-T02 and DMS-T05, and undoubtedly for the same reasons, inclined paths corresponding to the above stationary modes have not been observed in experiments carried out in water, irrespective of the bubble size.

Next, figure 13 indicates that the mode (2, 2) becomes unstable at $Bo = 0.68$ (point $D$ in the figure) and then grows slowly with the Bond number. Then, a fourth mode becomes unstable at $Bo = 0.809$ (point $A'$) with a dimensionless frequency $\lambda_i/2\pi = 0.162$. This mode (identified as *rigid osc. II* in the legend of figure 13*a*) is associated with an azimuthal wavenumber $|m| = 1$, exhibits low-frequency oscillations (panel *b*), and is not accompanied by significant shape oscillations (panel *c*). These characteristics point to another rigid mode. Hence, similar to the right part of figures 10 and 12, two rigid modes coexist in the case of water beyond point $A'$. In all three cases, the most amplified of them is stationary (yellow curve in figure 13) while the other (red curve) exhibits slow oscillations. Finally, figure 13 indicates that a fifth eigenvalue crosses the real axis at $Bo \approx 0.88$ (point $E$). As panels (*b*,*c*) make clear, this eigenvalue corresponds to the asymmetric shape mode (2, 1) already encountered with DMS-T02 and DMS-T05. One may notice that the mode (2, 1) becomes unstable at a larger $Bo$ than the mode (2, 2) in the cases of water and DMS-T05, while the reverse is true for DMS-T02. It is also worth noting that, among the three shape modes revealed by figure 13, the mode (2, 2) is the one with the lowest frequency in the range of Bond numbers relevant here, say $Bo \gtrsim 0.4$, followed by the mode (2, 0) and then the mode (2, 1). This is in line with the conclusions obtained by Meiron (1989) assuming an inviscid potential flow. In contrast, figures 10 and 12 show that modes (2, 1) and (2, 2) have nearly equal frequencies, both significantly lower than that of the mode (2, 0), in DMS-T05 and DMS-T02. This suggests that vortical effects not accounted

for in the above reference significantly modify the dynamics of shape oscillations of strongly deformed bubbles, even in low-viscosity fluids. Indeed, although the viscosity of DMS-T02 is less than twice that of water, its surface tension is four times lower, so that the relevant Bond numbers in DMS-T02 are typically larger than 3.0, while those in water are less than 1.0.

To finish with figure 13, it is important to stress that the succession of modes it reveals is the canonical sequence encountered throughout the low-$Mo$-range, say for $Mo \lesssim 10^{-9}$. For instance, the same first five modes become unstable in the same order in the case of DMS-T00 ($Mo = 1.8 \times 10^{-10}$), with the low-frequency rigid mode splitting into two stationary modes at an exceptional point, just as in figure 13. Only the thresholds and frequencies differ, with points $A$–$B$ then located at $Bo = 0.66$ and 0.805, followed by points $C$ and $D$ almost coincident at $Bo = 0.98$, and finally points $A'$ and $E$ located at $Bo = 1.135$ and 1.42, respectively.

5.3.2. *Spatial structure of rigid and shape modes*

Figure 14 displays the structure of the three successive rigid modes encountered in the sequence analysed above. Panels (*a*,*b*) look qualitatively similar to their counterparts in figure 11. However, the 'double-crescent' structure identified in the bottom part of the latter is not present here. The reason is that the Strouhal number of the primary low-frequency mode is approximately three times lower in water (see figure 8). For this reason, the vertical distance separating vortices shed in the wake is much larger, so that the double-crescent structure closest to the bubble is located further downstream. Panels (*c*,*e*) compare the wake structure of the primary and secondary oscillatory rigid modes. They evidence the higher vortex shedding frequency of the latter, in line with the nearly twice as large dimensionless frequency noticed at point $A'$ in figure 13 compared with that at point $A$. In the case of the stationary mode displayed in panel (*d*), the azimuthal vorticity and velocity disturbances are seen to keep a constant sign all along the wake (the real part of the azimuthal velocity is null in this case, which is why the imaginary part is shown in the figure). This is the generic hallmark of wakes associated with stationary inclined paths of axisymmetric bodies; e.g. Tchoufag *et al.* (2014*a*, *b*). No vortex shedding takes place in that situation, the inclination of the body path resulting from the constant lift force generated by a pair of semi-infinite counter-rotating streamwise vortices.

Figure 15 reveals the structure of the $(2, 0)$ and $(2, 1)$ shape modes at $Bo = 0.54$ and $Bo = 0.9$, respectively. The axial symmetry of the flow field is obvious in panels (*a*,*b*), with a succession of toroidal eddies of alternate signs shed downstream of the bubble. The red and blue contours evidence the fact that the bubble alternatively 'inflates' and 'deflates' along its axis while simultaneously shortening or lengthening in its equatorial plane. The streamlines in panels (*c*,*d*) make the antisymmetry of the mode $(2, 1)$ just as obvious. The wake is dominated by a series of double-crescent structures qualitatively similar to those identified in figure 11. The wavelength separating two consecutive structures is slightly shorter than that of the toroidal eddies in panels (*a*,*b*), although the dimensionless frequency of the mode $(2, 1)$ at $Bo = 0.9$ is approximately 30 % lower than that of the mode $(2, 0)$ at $Bo = 0.54$ according to figure 13(*b*). However, these structures are advected downstream by the base flow, so that their wavelength is determined by the Strouhal number $St = \lambda_i/(2\pi U)$, not directly by $\lambda_i$. Therefore, what the comparison of the wavelengths for the two modes indicates is that the normalized rise speed $U$ decreases by slightly more than 30 % from $Bo = 0.54$ to $Bo = 0.9$, owing to the progressive flattening of the bubble (in the regime where bubbles keep an approximate oblate spheroidal shape, $U$ is known to vary approximately as $Bo^{-1/2}$ for $Bo \ll 1$ and $Bo^{-1}$ for $Bo \gg 1$; see equation (7-3) and the associated figure in Clift, Grace & Weber 1978).

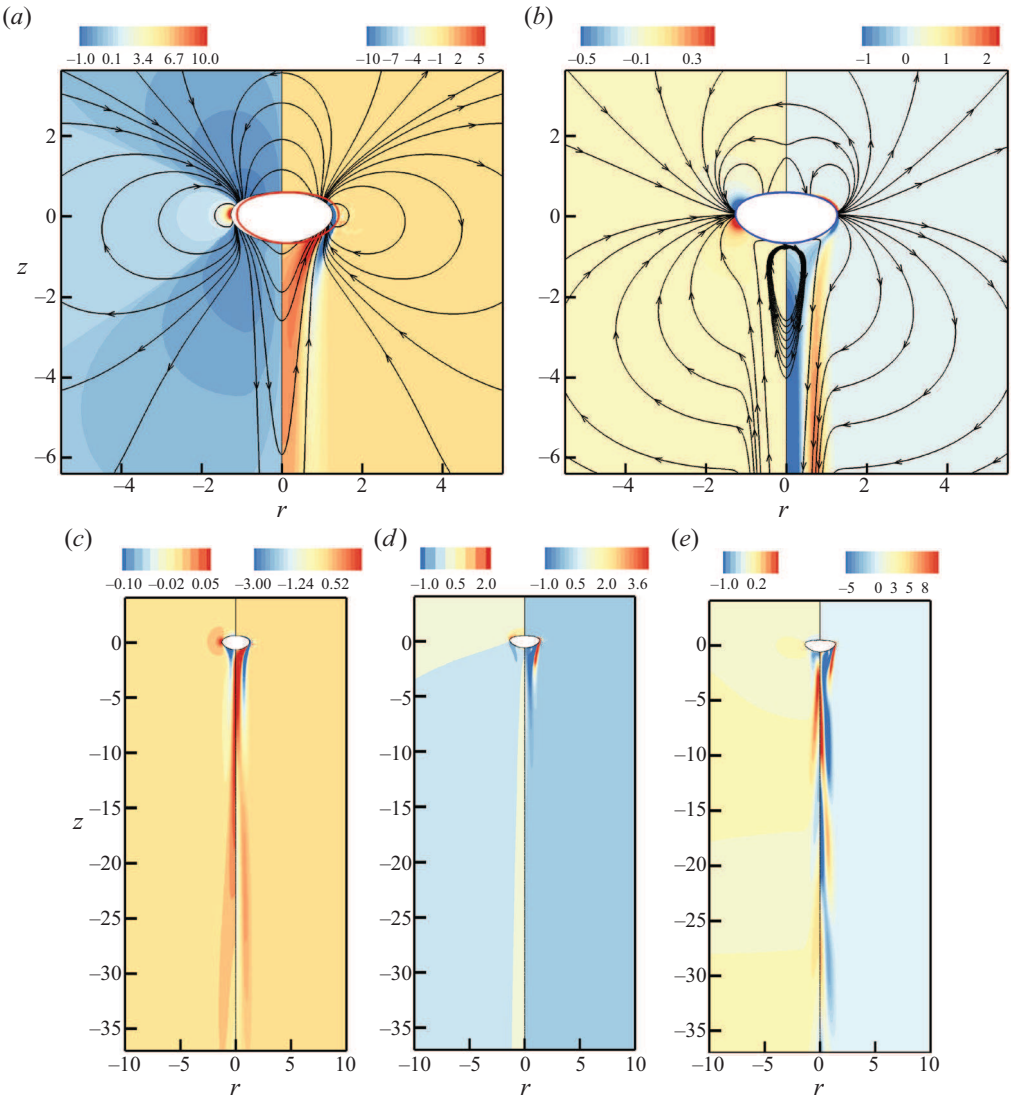


Figure 14. Structure of the rigid modes past a bubble rising in water. (*a*,*b*) Primary low-frequency mode at $Bo = 0.48$ in the bubble vicinity, with the real and imaginary parts shown in (*a*,*b*), respectively. The left and right halves of the two panels display the pressure and azimuthal vorticity iso-levels, respectively; some streamlines defined in the reference frame of the base configuration are also shown. Black, red and blue bubble contours correspond to the base state, and the real and imaginary parts of the interface disturbance, respectively. (*c*–*e*) Wake structure of the successive rigid modes. (*c*) Primary low-frequency mode at $Bo = 0.48$; (*d*) most amplified stationary mode at $Bo = 0.75$; (*e*) secondary oscillating mode at $Bo = 0.85$. The right half of each panel displays the real part of the azimuthal vorticity iso-levels; the left half of (*c*,*e*) (respectively *d*) displays the real (respectively imaginary) part of the azimuthal velocity iso-levels.

## 6. Respective magnitudes of rigid-body motions and time-dependent deformations

### 6.1. *Decomposition technique*

In the previous section, we identified ‘rigid’ and ‘shape’ modes qualitatively, stating that the former leave the bubble shape almost unchanged while the latter are associated with significant time-dependent shape oscillations. However, this distinction deserves a more

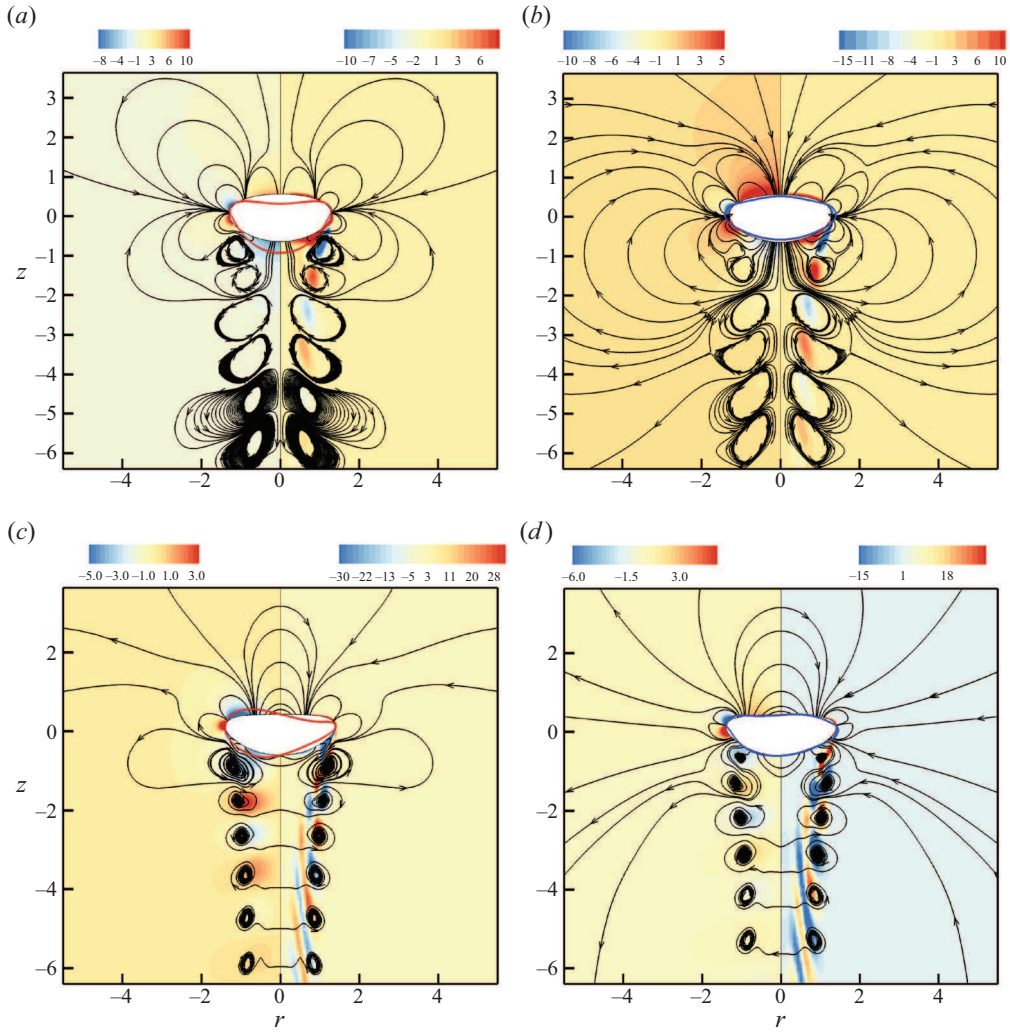


Figure 15. Structure of the first axisymmetric and asymmetric shape modes past a bubble rising in water. (*a*,*b*) Axisymmetric (2, 0) mode at $Bo = 0.54$, with the real and imaginary parts shown in (*a*,*b*), respectively. (*c*,*d*) Same for the asymmetric (2, 1) mode at $Bo = 0.90$. For caption see figures 11 and 14.

quantitative basis. Moreover, determining how large the deformations at the threshold of path instability are, compared with the lateral drift of the bubble, is key to clarifying the relative role of the various possible causes of instability present in the system. In order to quantify time-dependent deformations, we define a $(x, y, z)$ Cartesian coordinate system, the origin of which stands at the centroid of the bubble in the base state. We assume that the bubble performs planar zigzags in the vertical $(x, z)$ plane corresponding to the plane $\theta = (0, \pi)$ in the cylindrical $(r, \theta, z)$ system defined in § 2. At any position $\boldsymbol{x}_0$ on the undisturbed bubble–fluid interface, the normal displacement of the interface, $\hat{\eta}(\boldsymbol{x}_0)$, may be decomposed into a rigid motion inducing a lateral (respectively vertical) displacement $\hat{T}_x$ (respectively $\hat{T}_z$) about the $x$ (respectively $z$) axis and an inclination $\hat{\psi}$ resulting from a rotation about the $y$ axis, augmented by a local volume-preserving deformation $\hat{\zeta}(\boldsymbol{x}_0)$ in the normal direction. Projecting this decomposition onto the local normal unit vector $\boldsymbol{n}_0$,

one has

$$\hat{\eta}(\boldsymbol{x}_0) = \hat{T}_x(\boldsymbol{e}_x \cdot \boldsymbol{n}_0) + \hat{T}_z(\boldsymbol{e}_z \cdot \boldsymbol{n}_0) + \hat{\psi}(\boldsymbol{x}_0 \times \boldsymbol{n}_0) \cdot \boldsymbol{e}_y + \hat{\zeta}(\boldsymbol{x}_0), \tag{6.1}$$

with $\boldsymbol{e}_x, \boldsymbol{e}_y, \boldsymbol{e}_z$ the unit vectors in the $x, y, z$ directions, respectively. Odd modes $m = \pm 1$ do not induce any translation in the vertical direction, so that $\hat{T}_z = 0$ for such modes. Conversely, the lateral displacement $\hat{T}_x$ and the inclination $\hat{\psi}$ of the bubble remain null for even modes $m = -2, 0, 2$. To determine the non-zero displacement and inclination associated with a given mode, we make use of a least-squares fitting technique. That is, we define the local functional $\mathcal{F}_{\hat{T}_x, \hat{T}_z, \hat{\psi}}(\boldsymbol{x}_0) \equiv \{\hat{\eta} - [\hat{T}_x(\boldsymbol{e}_x \cdot \boldsymbol{n}_0) + \hat{T}_z(\boldsymbol{e}_z \cdot \boldsymbol{n}_0) + \hat{\psi}(\boldsymbol{x}_0 \times \boldsymbol{n}_0) \cdot \boldsymbol{e}_y]\}^2$, integrate it over the entire bubble contour and minimize the corresponding residue with respect to the non-zero components of the triplet $(\hat{T}_x, \hat{T}_z, \hat{\psi})$. Given the linear framework of the present study, the magnitude of the displacements is arbitrary, and only their relative magnitudes with respect to a common reference makes sense. This is why we normalize the local displacement $\hat{\eta}(\boldsymbol{x}_0)$ by $\hat{T}_x$ for odd modes and $\hat{T}_z$ for even modes, in order to make the translational displacement of the bubble centroid unity in all cases.

Thanks to this procedure, the evolution of the bubble shape and the relative magnitude of the interface displacements induced by the rigid-body rotation and volume-preserving deformations may be tracked along each branch of the bifurcation diagram. To save space, we do not discuss shape evolutions here (examples are provided by Bonnefis 2019), and focus on the relative variations of the different contributions and their physical origin.

### 6.2. *Variations of the inclination/deformation-induced contributions and path styles*

Figure 16(*a*) considers the case of the most amplified rigid mode for a bubble rising in water at 20 °C, i.e. the low-frequency oscillating mode up to $Bo \approx 0.64$, followed by the upper branch of the stationary mode for higher $Bo$ (figure 13). It shows how the maximum over the bubble contour of the three contributions to $\hat{\eta}$ varies with the Bond number. In the vicinity of the threshold ($Bo = 0.463$), the inclination-induced displacement is seen to be essentially in quadrature with the lateral drift, which is the expected behaviour in a planar zigzagging motion if the bubble axis remains aligned with the path (i.e. its inclination is maximum when the bubble reaches the centreline of its zigzagging path). The relative magnitude of the maximum normal displacement resulting from this inclination is $7 \times 10^{-2}$ and experiences little variation up to $Bo \approx 0.55$. At the threshold, the maximum of the volume-preserving deformation is almost in phase with the lateral drift. This is because the rise speed reaches a maximum at each extremity of the zigzag (Mougin & Magnaudet 2006), resulting in some flattening of the bubble. Conversely, the rise speed is minimum when the bubble crosses the centreline of the zigzag, which slightly reduces its oblateness, yielding the small non-zero imaginary component of the deformation (dashed green line in figure 16*a*). The relative magnitude of the deformation does not exceed $3 \times 10^{-3}$ in this $Bo$ range. This provides the confirmation that time-dependent deformations are extremely weak at the onset of path instability for bubbles rising in low-$Mo$ liquids. These findings also validate the 'rigid' qualification employed for the primary low-frequency mode throughout § 5. Conversely, the relative magnitude of deformations in modes $(2, 0)$ and $(2, 1)$ (not shown) is almost unity at their respective thresholds. The real (respectively imaginary) part of the displacements associated with the bubble inclination (respectively deformation) is typically one order of magnitude smaller than its imaginary (respectively real) counterpart. These weak components exhibit abrupt variations close to the threshold (and for one of them around

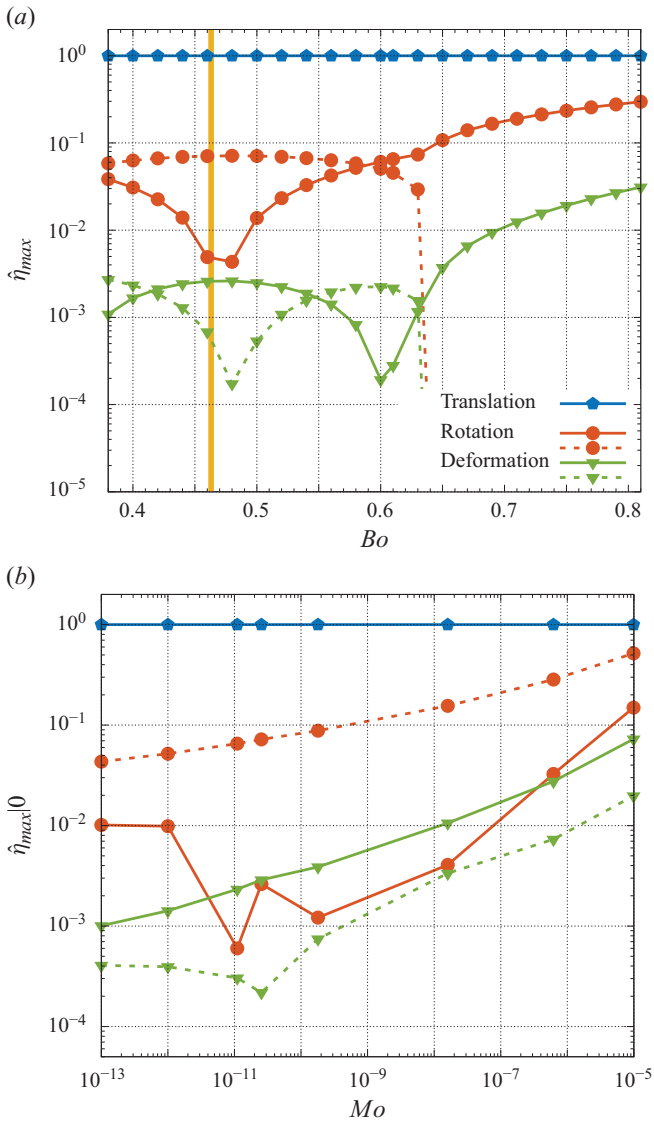


Figure 16. Decomposition of the normal displacement of the bubble surface into a horizontal uniform translation, an inclination-induced displacement resulting from a rigid-body rotation, and a volume-preserving deformation. (*a*) Variation with *Bo* for the most amplified rigid mode $|m| = 1$ in the case of a bubble rising in water at 20 °C; the yellow vertical line indicates the threshold of path instability; (*b*) variation with the fluid properties at the path instability threshold. Each line figures the maximum of the corresponding component over the bubble contour; for each component, the solid and dashed lines refer to the real and imaginary parts, respectively.

$Bo = 0.6$), presumably because such low-magnitude quantities are only determined with a limited accuracy by the least-squares technique.

These two weak components increase sharply with *Bo* and become dominant for $Bo \gtrsim 0.55$, marking a change in the style of the bubble ascent. In particular, the real part of the displacement associated with the bubble inclination exceeds the imaginary part for $Bo \geqslant 0.59$. This behaviour indicates that the bubble now exhibits a non-zero

inclination at the extremities of its zigzagging path, so that its minor axis is no longer aligned with its velocity. In between two successive extremities of the zigzag, the bubble now glides along its path rather than facing it. This makes the part of its surface pointing in the direction of the lateral drift slightly more pointed, while the opposite part becomes slightly more rounded. This is the reason why the imaginary part of the deformation is significant in this second style of zigzagging motion. Conversely, owing to the non-zero bubble inclination at the extremities of the zigzag, the rise speed is slightly lower than in the previous zigzag style. This mitigates the flattening of the bubble, thus reducing the real part of the volume-preserving deformation, as observed on the solid green line of figure 16(*a*) in the range $0.5 \lesssim Bo \lesssim 0.6$.

At $Bo = 0.64$, the imaginary parts of the rotation- and deformation-induced contributions fall to zero, a consequence of the change in nature of the primary rigid mode at the exceptional point revealed by figure 13. Beyond this point, the rigid mode is stationary, yielding a non-oscillatory inclined path. When the Bond number increases in the range 0.6–0.8, the bubble gradually flattens and the size of the standing eddy at its back grows significantly, as panels (*h*,*i*) of figure 5 show. This makes the strength of the trailing vortices that set in at the path instability threshold increase with $Bo$, which translates directly into an increase of the lift force acting on the bubble, hence an increase of its inclination with the Bond number. This scenario is confirmed by the solid red line in figure 16(*a*), which shows that the maximum displacement associated with the bubble inclination increases by a factor of four from $Bo = 0.64$ to $Bo = 0.8$. The larger the bubble inclination, the lower its rise speed, which in turn makes its oblateness reduce compared with that in the base state. This is the origin of the sharp increase of the real part of the volume-preserving deformation (solid green line in figure 16*a*), which gains two orders of magnitude between $Bo = 0.6$ and $Bo = 0.8$. Nevertheless, deformations remain small compared with the lateral drift, reaching only a relative magnitude of $3 \times 10^{-2}$ at $Bo = 0.8$.

Figure 16(*b*) shows how the relative magnitude of the three contributions to $\hat{\eta}$ vary with the Morton number at the path instability threshold, i.e. along the neutral curve of figure 7. Since the corresponding unstable mode is always oscillatory, one expects the relative magnitude of the different contributions to behave qualitatively in the same way as in the case of water in the vicinity of the primary threshold. Indeed, in line with the behaviours noticed above, deformation-induced displacements are essentially in phase with the bubble lateral drift throughout the eight decades of $Mo$ explored here, while those associated with the bubble inclination are almost in quadrature. Again, we attribute the non-smooth variations of the weak real (respectively imaginary) component of the inclination-induced (respectively deformation-induced) contribution observed for $Mo \lesssim 10^{-10}$ to the limitations of the minimization technique. In contrast, the dominant component of these two contributions is seen to increase smoothly with the Morton number. The relative deformation-induced displacements, say $\hat{\eta}^{def}_{max}|_0$, follow the approximate power law $\hat{\eta}^{def}_{max}|_0 \sim Mo^{0.23}$, increasing by two orders of magnitude from Galinstan ($\hat{\eta}^{def}_{max}|_0 \approx 10^{-3}$) to DMS-T11 ($\hat{\eta}^{def}_{max}|_0 \approx 7 \times 10^{-2}$). The relative inclination-induced displacements only grow by one order of magnitude, from $4 \times 10^{-2}$ to $5 \times 10^{-1}$, in between the same two limits. Nevertheless, the fact that these displacements reach 50 % of the lateral drift for DMS-T11 (to be compared with 7 % in the case of water) indicates that bubbles wobble significantly when their path becomes unstable in liquids having a Morton number four to five orders of magnitude higher than that of water.

## 7. Summary and final discussion

### 7.1. *Main findings*

Thanks to an innovative numerical approach allowing the linear stability of the viscous flow past freely rising and deforming bubbles to be assessed accurately, even when the rise Reynolds number is large, we explored the conditions under which the path of such bubbles deviates from a straight vertical line and the physical nature of the underlying instability modes over a wide range of properties of the carrying liquids. Present results extend over eight orders of magnitude of the Morton number. Over this range, the critical Bond number increases by a factor of 35 from Galinstan to silicone oil DMS-T11 (yielding an increase by a factor of 2.6 of the critical bubble size), whereas the critical Reynolds number decreases by a factor of 30, from $\approx 2100$ to 70, in between the same two liquids. We showed that path instability always arises through the destabilization of a non-axisymmetric oscillatory mode associated with weak time-dependent changes of the bubble shape. Increasing the bubble size in a given fluid, the nature of this primary 'rigid' mode stays unchanged if the Morton number is large enough, say $Mo \gtrsim 10^{-7}$. Conversely, this mode gives birth to two stationary modes if the Morton number is low enough ($Mo \lesssim 10^{-9}$). In the intermediate range $10^{-9} \lesssim Mo \lesssim 10^{-7}$, this mode remains oscillatory even far from the primary threshold but its growth rate varies non-monotonically with the bubble size, and it may even re-stabilize within a narrow size range. A second rigid mode, which turns to be stationary for intermediate and 'high' Morton numbers but oscillatory for low Morton numbers also arises further away from the primary threshold. 'Shape' modes distinct from the previous rigid modes in that they exhibit much larger oscillations of the bubble surface also become unstable as the bubble size is increased.

Comparison of present predictions with reference experimental and numerical data revealed a very good agreement, both on the threshold (most often measured through the Bond or Galilei number, or alternatively the rise Reynolds number) and the reduced frequency of path oscillations (measured through a Strouhal number). This agreement fully supports the view that the path instability of real gas bubbles results from a linear mechanism associated with a Hopf bifurcation. In contrast, oblique paths which are the hallmark of stationary modes have not been reported in experiments, nor in fully resolved simulations. We see their absence as an indication that the changes introduced in the base flow by the primary non-axisymmetric oscillatory mode are significant enough to alter the next steps of the actual bifurcation sequence compared with the predictions of the linear approach.

To better quantify time-dependent bubble deformations and their influence on the path instability mechanisms and characteristics, we employed two additional and complementary tools. First, a least-squares minimization technique allowed us to split the displacements of the bubble–fluid interface into contributions associated with a rigid-body motion and volume-preserving deformations. By doing so, we could among other things establish how the amplitude of the deformations varies with the Morton number at the onset of path instability. It turned out that the ratio of the maximum deformation to the maximum lateral drift of the bubble centroid is always much smaller than unity. In particular, this ratio is approximately $10^{-3}$ for Galinstan and $3 \times 10^{-3}$ for water. It exceeds 1 % only for liquids with $Mo \gtrsim 1.5 \times 10^{-8}$, reaching 7 % for DMS-T11 ($Mo = 9.9 \times 10^{-6}$). Second, we took advantage of the base states computed with the present numerical technique to update the predictions obtained in the framework of the FSA by Cano-Lozano *et al.* (2016*a*). With this procedure, any difference in the nature of the primary bifurcation or/and the corresponding threshold may be ascribed to effects of time-dependent bubble deformations. We found that, despite their weak magnitude,

these deformations lower significantly the threshold whatever the Morton number. Hence, a general conclusion of the present study is that deformations always promote path instability in the linear framework. Differences between the predicted critical size of deformable and non-deformable bubbles increase gradually from 8 % at $Mo \approx 10^{-13}$ to 23 % at $Mo \approx 6 \times 10^{-7}$, before decreasing sharply to nearly 15 % for larger $Mo$. For $Mo \lesssim 7 \times 10^{-11}$, FSA correctly predicts that the most unstable mode is a 'low-frequency' one with $St = O(0.01)$ at the threshold. Similarly, it rightly predicts that path instability arises through a 'high-frequency' mode with $St = O(0.1)$ at the threshold for $Mo \gtrsim 3 \times 10^{-7}$. The predicted reduced frequencies lie 20 to 30 % below those obtained with deformable bubbles, but their variations with the Morton number are qualitatively similar. In contrast, FSA dramatically fails to detect that the most unstable mode is still oscillatory in the intermediate-Morton-number range $7 \times 10^{-11} \lesssim Mo \lesssim 3 \times 10^{-7}$.

### 7.2. *Discussion*

To better understand the above issue and gain some insight into the subtle balances involved in the various regimes encountered by varying the fluid properties, it is useful to put the first stages of the bifurcation diagrams obtained with deformable bubbles in perspective with those determined by Tchoufag *et al.* (2014*b*) who assumed a perfectly oblate spheroidal bubble with a frozen shape. By increasing the geometrical aspect ratio $\chi$ in the range [2.21, 2.30] they identified three successive phenomenologies summarized in their figures 1 and 2. For $2.21 \leqslant \chi \leqslant 2.23$, the system first becomes unstable through a low-frequency mode which, by increasing the bubble size (i.e. the Reynolds number in their case), turns into a pair of stationary modes, one of which is quickly damped as the bubble size is increased further while the other gets strongly amplified (their figure 1). Present findings summarized in figure 13 indicate that this is exactly what happens with deformable bubbles rising in water and more generally in low-$Mo$ liquids. That the scenario relevant to frozen spheroidal bubbles remains unchanged in the case of freely deforming bubbles rising in low-$Mo$ liquids strongly supports the view that time-dependent deformations do not play any causal role in the mechanisms governing the first stages of path instability in such fluids, although they lower the critical bubble size by 18 % for water and increase the reduced frequency by nearly 30 %, as may be deduced from the two neutral curves in figures 7 and 8 for $Mo = 2.54 \times 10^{-11}$. The wake alone is not the source of the instability, since it is still stable at the FSA threshold (Cano-Lozano *et al.* 2016*a*). Therefore, as already stated by Bonnefis *et al.* (2023) in the case of water, the key explanation of path instability in low-Morton-number fluids lies in the specific physical processes accounted for in FSA, namely the degrees of freedom allowed by the rigid-body buoyancy-driven motion of the bubble, and the back reaction imposed by the fluid to this motion by the constant-force and zero-torque constraints.

Increasing the bubble aspect ratio to the range $2.23 \leqslant \chi \leqslant 2.25$, Tchoufag *et al.* (2014*b*) observed that, although it is still present, the low-frequency mode is no longer unstable, its growth rate keeping weak negative values. In the approximation they used, path instability then arises through a stationary bifurcation, similar to what the FSA neutral curves (pale grey lines) in figures 7 and 8 indicate for $7 \times 10^{-11} \lesssim Mo \lesssim 3 \times 10^{-7}$. The corresponding stationary mode is that associated with the wake instability observed when the bubble is held fixed in a uniform stream. Hence, one has to conclude that the additional degrees of freedom offered by the free motion of a frozen-shape bubble are not sufficient to change qualitatively the overall dynamics of the system in that range. The yellow neutral curve $St = f(Mo)$ in figure 8 proves that, despite their weak relative magnitude (from 0.4 % for DMS-T00 to 2 % for $Mo = 3 \times 10^{-7}$ according to figure 16*b*), deformations are able

to restore the instability of the oscillatory mode and to make it more unstable than the stationary mode, keeping the near-threshold path instability phenomenology unchanged with respect to the one prevailing in the low-$Mo$ range. Nevertheless, expanding the growth rate in the form $\lambda_r \approx \alpha(Mo)(Bo - Bo_c(Mo))$, with $Bo_c$ the threshold Bond number, and considering variations of $\alpha(Mo)$ from water (figure 13*a*) to DMS-T02 (figure 12*a*) via DMS-T00 (not shown), one finds $\alpha(Mo) \sim Mo^{-0.15}$. Hence, the larger $Mo$ the slower the increase of the growth rate of the oscillatory mode with the distance to the threshold, despite the fact that the magnitude of surface deformations at the threshold increases as $Mo^{0.23}$ (figure 16*b*). This confirms that the damping mechanism predicted by FSA, be it with the schematic spheroidal shape prescribed by Tchoufag *et al.* (2014*b*) or with the more realistic shape corresponding to the actual base state, is still active in this intermediate $Mo$-range in the case of deformable bubbles. The reasons for this damping are not obvious. For a non-deforming body, the eigenvalues of the system depend directly on the drag and torque associated with a small edgewise translation or a slow rotation about the major axis perpendicular to the plane of motion (Fabre *et al.* 2011). We believe that, when the bubble geometrical anisotropy is varied, small changes in the structure of the base flow, especially in the near wake, make these loads vary in a non-monotonic manner with $\chi$, hence with $Mo$, which makes eventually the real part of the eigenvalues associated with the oscillatory mode be positive in some ranges of the parameter space but slightly negative in others.

Last, for $\chi \geqslant 2.25$, Tchoufag *et al.* (2014*b*) found the first unstable mode to be oscillatory again. Similar to what is noticed on the FSA neutral curve in figure 8, the corresponding oscillations are much faster than those observed for $2.21 \leqslant \chi \leqslant 2.23$, the two oscillatory modes predicted by FSA in the two subdomains being distinct (pale and dark grey lines in figures 7 and 8). Deformation effects totally smooth out this abrupt change by allowing the frequency to increase gradually throughout the intermediate $Mo$-range discussed above. Increasing the Reynolds number at a given $\chi$, i.e. the bubble size in a given fluid, Tchoufag *et al.* (2014*b*) found that the next mode that becomes unstable is the stationary mode associated with wake instability. The FSA prediction obtained with the actual base flow confirms this conclusion. For instance, the dark grey line in figure 7 shows that, for DMS-T05, the 'high-frequency' mode becomes unstable at $Bo \approx 5.0$. Then the stationary mode (pale grey line) becomes unstable in turn at $Bo = 5.85$, i.e. for a bubble only 8 % larger than at the primary threshold. This sequence subsists when the bubble deforms freely, but the gap between the two thresholds increases considerably, with the oscillatory and stationary modes becoming unstable at $Bo = 3.4$ and $Bo = 5.95$, respectively. Moreover, the influence of deformation manifests itself through the emergence of the (2, 0) axisymmetric shape mode that becomes unstable in between these two thresholds. The above comparisons establish that the role of bubble deformations on the most unstable non-axisymmetric mode responsible for path instability deeply differs among the three $Mo$-ranges identified by FSA. This role is limited to mere, albeit significant, quantitative changes in the critical bubble size and oscillations frequency in the low- and 'high'-$Mo$ regimes, whereas it induces a complete change in the nature of the most unstable mode in the intermediate-$Mo$ regime.

A weakly nonlinear approach inspired by those developed by Fabre, Tchoufag & Magnaudet (2012) and Tchoufag, Fabre & Magnaudet (2015) for buoyancy/gravity-driven rigid bodies is desirable to extend present predictions to slightly supercritical bubble sizes. By incorporating nonlinear corrections to the base state resulting from the primary non-axisymmetric unstable mode, this extension may in particular allow the disappearance of the stationary mode at any Morton number to be rationalized. Such a weakly nonlinear approach would also settle the question of the supercritical or subcritical nature of the

primary bifurcation in each Morton-number range, which the present linear approach cannot answer. Another more modest but much cheaper approach worth exploring is the extension to bubbles (and more generally to rigid bodies with a moderate or low body-to-fluid density ratio) of the 'aerodynamic' reduced-order model derived by Fabre *et al.* (2011) for heavy freely falling two-dimensional bodies. This model should be able to predict accurately the most unstable or least stable eigenvalues of the system for bubbles with a frozen shape, provided that the drag and torque coefficients associated with a small edgewise translation and a slow rotation of the bubble are computed in the relevant base flow. This is the route to be followed to quantify the influence of base flow variations resulting from slight changes in the interface geometry on the hydrodynamic reaction experienced by bubbles close to the threshold of path instability.

**Declaration of interests.** The authors report no conflict of interest.

**Author ORCIDs.**
Paul Bonnefis https://orcid.org/0000-0003-2825-2974;
Javier Sierra-Ausin https://orcid.org/0000-0001-6036-5093;
David Fabre https://orcid.org/0000-0003-1875-6386;
Jacques Magnaudet https://orcid.org/0000-0002-6166-4877.

## References

Alben, S. 2008 An implicit method for coupled flow-body dynamics. *J. Comput. Phys.* **227**, 4912–4933.
Assemat, P., Fabre, D. & Magnaudet, J. 2012 The onset of unsteadiness of two-dimensional bodies falling or rising freely in a viscous fluid: a linear study. *J. Fluid Mech.* **690**, 173–202.
Batchelor, G.K. 1967 *An Introduction to Fluid Dynamics*. Cambridge University Press.
Bergholtz, E.J., Budich, J.C. & Kuns, F.K. 2021 Exceptional topology of non-Hermitian systems. *Rev. Mod. Phys.* **93**, 015005.
Bonnefis, P. 2019 Etude des instabilités de sillage, de forme et de trajectoire de bulles par une approche de stabilité linéaire globale. PhD thesis, Inst. Nat. Polytech. Toulouse, Toulouse, France (available online at https://hal.science/tel-03982380).
Bonnefis, P., Fabre, D. & Magnaudet, J. 2023 When, how, and why the path of an air bubble rising in pure water becomes unstable. *Proc. Natl Acad. Sci. USA* **120**, e2300897120.
Cano-Lozano, J.C., Bohorquez, P. & Martinez-Bazán, C. 2013 Wake instability of a fixed axisymmetric bubble of realistic shape. *Intl J. Multiphase Flow* **51**, 11–21.
Cano-Lozano, J.C., Martinez-Bazán, C., Magnaudet, J. & Tchoufag, J. 2016*b* Paths and wakes of deformable nearly spheroidal rising bubbles close to the transition to path instability. *Phys. Rev. Fluids* **1**, 053604.
Cano-Lozano, J.C., Tchoufag, J., Magnaudet, J. & Martinez-Bazán, C. 2016*a* A global stability approach to wake and path instabilities of nearly oblate spheroidal rising bubbles. *Phys. Fluids* **28**, 014102.
Chomaz, J.M. 2005 Global instabilities in spatially developing flows: non-normality and nonlinearity. *Annu. Rev. Fluid Mech.* **37**, 357–392.
Clift, R., Grace, J.R. & Weber, M.E. 1978 *Bubbles, Drops and Particles*. Academic.
Dangelmayr, G. & Knobloch, E. 1987 The Takens–Bogdanov bifurcation with $O(2)$-symmetry. *Phil. Trans. R. Soc. Lond.* A **322**, 243–279.
De Vries, A. 2002 Path and wake of a rising bubble. PhD thesis, Twente University.
Duineveld, P.C. 1994 Bouncing and coalescence of two bubbles in water. PhD thesis, Twente University.
Duineveld, P.C. 1995 The rise velocity and shape of bubbles in pure water at high Reynolds number. *J. Fluid Mech.* **292**, 325–332.
Fabre, D., Assemat, P. & Magnaudet, J. 2011 A quasi-static approach to the stability of the path of heavy bodies falling within a viscous fluid. *J. Fluids Struct.* **27**, 758–767.
Fabre, D., Tchoufag, J. & Magnaudet, J. 2012 The steady oblique path of buoyancy-driven disks and spheres. *J. Fluid Mech.* **707**, 24–36.
Hecht, F. 2012 New development in FreeFem++. *J. Numer. Maths* **20**, 251–265.
Herrada, M.A. & Eggers, J. 2023 Path instability of an air bubble rising in water. *Proc. Natl Acad. Sci. USA* **120**, e2216830120.

MAGNAUDET, J. & MOUGIN, G. 2007 Wake instability of a fixed spheroidal bubble. *J. Fluid Mech.* **572**, 311–337.
MEIRON, D.I. 1989 On the stability of gas bubbles rising in an inviscid fluid. *J. Fluid Mech.* **198**, 101–114.
MOORE, D.W. 1963 The boundary layer on a spherical gas bubble. *J. Fluid Mech.* **16**, 161–176.
MOORE, D.W. 1965 The velocity of rise of distorted gas bubbles in a liquid of small viscosity. *J. Fluid Mech.* **23**, 749–766.
MOUGIN, G. & MAGNAUDET, J. 2006 Wake-induced forces and torques on a zigzagging/spiralling bubble. *J. Fluid Mech.* **567**, 185–194.
NATARAJAN, R. & ACRIVOS, A. 1993 The instability of the steady flow past spheres and disks. *J. Fluid Mech.* **254**, 323–344.
POPINET, S. 2003 Gerris: a tree-based adaptive solver for the incompressible Euler equations in complex geometries. *J. Comput. Phys.* **190**, 572–600.
POPINET, S. 2007 The Gerris flow solver. http://gfs.sourceforge.net/wiki/index.php.
SATO, A. 2009 Deformation, wake and collision of rising bubbles. PhD thesis, Kyushu University.
SIERRA-AUSIN, J., BONNEFIS, P., FABRE, D. & MAGNAUDET, J. 2022 Dynamics of a gas bubble in a straining flow: deformation, oscillations, self-propulsion. *Phys. Rev. Fluids* **7**, 113603.
TCHOUFAG, J., FABRE, D. & MAGNAUDET, J. 2014*a* Global linear stability analysis of the wake and path of buoyancy-driven disks and thin cylinders. *J. Fluid Mech.* **740**, 278–311.
TCHOUFAG, J., FABRE, D. & MAGNAUDET, J. 2015 Weakly nonlinear model with exact coefficients for the fluttering and spiraling motion of buoyancy-driven bodies. *Phys. Rev. Lett.* **115**, 114501.
TCHOUFAG, J., MAGNAUDET, J. & FABRE, D. 2013 Linear stability and sensitivity of the flow past a fixed oblate spheroidal bubble. *Phys. Fluids* **25**, 054108.
TCHOUFAG, J., MAGNAUDET, J. & FABRE, D. 2014*b* Linear instability of the path of a freely rising spheroidal bubble. *J. Fluid Mech.* **751**, 1–12.
YANG, B. & PROSPERETTI, A. 2007 Linear stability of the flow past a spheroidal bubble. *J. Fluid Mech.* **582**, 53–78.
ZENIT, R. & MAGNAUDET, J. 2008 Path instability of rising spheroidal air bubbles. *Phys. Fluids* **20**, 061702.
ZENIT, R. & MAGNAUDET, J. 2009 Measurements of the streamwise vorticity in the wake of an oscillating bubble. *Intl J. Multiphase Flow* **35**, 195–203.
ZHOU, W. & DUSEK, J. 2017 Marginal stability curve of a deformable bubble. *Intl J. Multiphase Flow* **89**, 218–227.

*Under consideration for publication in J. Fluid Mech.*

Banner appropriate to article type will appear here in typeset article

# Exceptional points in Fluid-Structure interaction

**Javier Sierra-Ausin [1] and Olivier Marquet[2]**

[1]DMPE, ONERA, Université de Toulouse, 31055 Toulouse, France

[2]DAAA, ONERA, Institut Polytechnique de Paris, 92190 Meudon, France

**Corresponding author:** Javier Sierra-Ausin, javier.sierra_ausin@onera.fr

(Received xx; revised xx; accepted xx)

The linear stability analysis of fluid-structure interaction (FSI) systems, governed by inherently non-Hermitian operators, can exhibit spectral singularities known as exceptional points (EPs). This study demonstrates the existence and topological consequences of EPs across three canonical aeroelastic configurations: vortex-induced vibration of a spring-mounted cylinder, flutter of a thin plate, and transonic flutter of an OAT15a airfoil. A unified numerical framework is employed, coupling the compressible Navier–Stokes equations with structural dynamics. Stability is analysed via a characteristic equation constructed from fluid transfer functions, efficiently interpolated into the complex plane using the Loewner framework. Results reveal second-order EPs ($EP_2$) where two eigenmodes coalesce, leading to characteristic eigenvalue veering and mode-swapping phenomena governed by a half-integer winding number. In the transonic case, the interaction of three modes (fluid/buffet, pitching, heaving) is organised by a third-order EP ($EP_3$), a codimension-four singularity where three eigenvalues and eigenvectors coalesce. These findings establish EPs as fundamental features in FSI, providing a novel topological perspective on stability transitions, with implications for predicting and controlling phenomena like flutter and the transonic dip.

**Key words:** Authors should not enter keywords on the manuscript, as these must be chosen by the author during the online submission process and will then be added during the typesetting process (see Keyword PDF for the full list). Other classifications will be added at the same time.

## 1. Introduction

The mathematical description of dissipative and open systems frequently necessitates a departure from the conservative, Hermitian framework that underpins much of classical physics. In fluid mechanics, this is the rule rather than the exception: the Navier-Stokes equations are inherently dissipative, and the linearised operators that arise in the study of stability, acoustics, and wave propagation are often non-normal (Trefethen *et al.* 1993). This non-normality leads to rich phenomena such as transient growth and sensitivity to perturbations, which are crucial for understanding the transition to turbulence (Schmid

2007) and the dynamics of coherent structures. A powerful and generalised framework for analysing such open systems has emerged from the study of non-Hermitian quantum mechanics and optics, where the spectrum of the governing non-self-adjoint operator is complex. Within this framework, a paramount feature is the existence of exceptional points (EPs)—spectral singularities where not only the eigenvalues but also the corresponding eigenvectors of the system coalesce (Heiss 2012; Bergholtz *et al.* 2021).

The topology of the complex energy Riemann surface around an EP leads to a host of counter-intuitive phenomena with no direct analogue in Hermitian systems. These include the chiral behaviour of state populations when an EP is dynamically encircled (Doppler *et al.* 2016), that is, encircling an EP in a clockwise or a counter-clockwise direction results in different final states. We also find the breakdown of the conventional bulk-boundary correspondence (Bergholtz *et al.* 2021), and the non-Hermitian skin effect—a phenomenon where a macroscopic number of states localise at a system's boundary, as first rigorously characterized in quantum systems (Yao & Wang 2018) and since explored in photonic (Zhou *et al.* 2018) and acoustic (Zhu *et al.* 2018) metamaterials. The implications of EPs are now being explored across a wide range of classical wave systems, including nanophotonics for light manipulation (Miri & Alu 2019), in single-mode lasers to decrease the fluctuating level of lasers Feng *et al.* (2014) or in augmenting the quality of sensors (Wiersig 2020) and in the design of electrical circuits (Helbig *et al.* 2020) where they have been shown to enable novel functionalities such as unidirectional invisibility, topological lasing, and enhanced sensing.

The exploration of non-Hermitian physics and EPs has attracted some interest in acoustics and thermoacoustics. In acoustics, where the concepts of gain and loss can be engineered with some precision, we find the seminal work by Shi *et al.* (2016) who demonstrated the accessibility of EPs in parity-time (PT) symmetric acoustic systems, revealing phenomena like unidirectional transparency.The role of EPs has since been elucidated in sound absorption, with Achilleos *et al.* (2017) showing how they govern the behavior of non-Hermitian acoustic metamaterials, and Xiong *et al.* (2017) optimizing sound attenuation in metaporous materials by tuning them to an EP. The extension of these ideas to systems with background flow was established by Aurégan & Pagneux (2017), who explored PT-symmetric scattering in flow ducts. More recently, studies have continued to explore the implications of EPs in complex scattering scenarios (Matsushima & Yamada 2025) and in achieving extreme wave phenomena like asymmetric absorption in elastic structures (Li *et al.* 2022).

In the field of thermoacoustics Mensah *et al.* (2018) established the existence of EPs in a prototypical thermoacoustic system, demonstrating their signature infinite eigenvalue sensitivity. The interplay between different types of modes, such as those of pure acoustic origin and Intrinsic Thermoacoustic (ITA) modes, was further shown by Orchini *et al.* (2020) to generate EPs that govern the stability landscape by acting as spectral root loci. The profound implications for practical systems were highlighted by Ghani & Polifke (2021) who identified an EP in a combustion experiment, showing how its branch-switching characteristic can facilitate a sudden jump from strong instability to stable operation. This real-world impact underscores the critical need to understand EPs, as their presence can fundamentally affect the reliability of stability analyses, a point rigorously examined by Schaefer *et al.* (2021). The understanding of EPs is now being leveraged to develop innovative design methods for stable combustion systems. Recent research by Casel & Ghani (2024*a*,*b*) has introduced the Exceptional Point-based Thermoacoustic Design (EPTD) method. This conceptual framework, detailed in two parts, uses the relation between mode origins, encoded in the EP's position and parameters, to strategically shift the entire thermoacoustic spectrum toward stability. The EPTD method has been successfully

demonstrated in lab-scale combustors, stabilizing originally unstable laminar and turbulent flame configurations. Concurrently, the role of system symmetries in organizing these non-Hermitian degeneracies has been advanced by Humbert & Orchini (2025), who demonstrated how symmetry-breaking induces EPs in the complex spectra of annular combustors. This collective body of work represents a paradigm shift from traditional stability analysis toward actively designing stability maps using the topological features of EPs.

In hydrodynamics, the concepts underpinning non-Hermitian physics have long been in the analysis of linear stability and global modes (Chomaz 2005). However, EPs have scarcely been clearly identified and only recently their importance has been highlighted. Recently, Jouin *et al.* (2024) identified different types of EPs as the result of the interaction between cross-flow vortices with opposite spanwise wavenumber and different spanwise wavenumber. Kern *et al.* (2024) documented the formation of subharmonic eigenvalue orbits in the periodic spectrum of pulsating plane Poiseuille flow as the pulsation amplitude is increase, due to the coalescence of eigenvalues at exceptional points. Similarly, in the context of a rising bubble immersed in a liquid Bonnefis *et al.* (2024) identified a EP which results from the interaction of two symmetry breaking modes, the inclination-induced displacement and the lateral drift of the trajectory.

A particularly fertile and complex domain for the application of this non-Hermitian framework is the field of fluid-structure interaction (FSI). FSI systems are open and dissipative, characterised by a strong, often non-linear, coupling between a deformable or moving structure and a surrounding fluid flow. The linearised operators governing the stability of these coupled systems—such as in flutter of airfoils, vortex-induced vibrations, or the dynamics of flags and membranes—are inherently non-Hermitian. The spectral properties of these coupled fluid-structure operators are known to give rise to complex phenomena like mode coalescence in flutter bifurcations, which bears the hallmark of an EP. We posit that the confluence of two distinct non-normal subsystems—the fluid and the structure—creates a rich environment for the emergence and manipulation of EPs. Understanding these points in FSI is not merely a formal exercise; it holds the potential to unravel the mechanisms behind hard-to-predict instabilities, to design novel strategies for their suppression, and to exploit the unique spectral properties of EPs for applications in energy harvesting and flow control. In this paper, we therefore seek to elucidate the role of exceptional points in fluid-structure interaction, exploring their manifestation, topological consequences, and the distinctive physical phenomena they govern in this fundamentally coupled context.

We have selected three aeroelastic configurations in order to show the importance of EPs in fluid-structure interaction, these are: (a) the flow past a spring-mounted cylinder, which exhibits Vortex-Induced-Vibrations (VIV), (b) the flow past a thin plate at zero angle of attack, which exhibits flutter and (c) the transonic flow past an airfoil which exhibits transonic flutter. The last two configurations are the two-dimensional representation of the flutter dynamics of a wing-section, where the bending mode is represented as the heaving motion, while the torsion is modeled by the pitching motion. Both structural degrees of freedom are treated as a spring-mass-damper system: heaving is emulated by a vertical spring, and pitching by a torsional spring, as shown in fig. 1 (a).

## 2. Methods

We numerically integrate the conservative variables $\mathbf{Q} = \left(\rho, \mathbf{m}, \rho E\right)^T$, $\rho$ the density field, $\mathbf{m} \equiv \rho\mathbf{u}$ the momentum field with $\mathbf{u}$ the velocity field, and $\rho E$ the total energy, according to the compressible Navier–Stokes equations. The governing equations are written in the

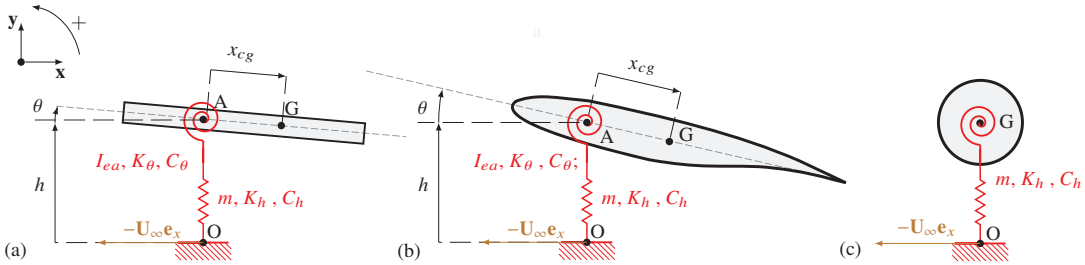


Figure 1. Diagram of the three aeroelastic configurations (a) Two-degrees of freedom spring-mounted plate. (b) Two degrees of freedom OAT15a airfoil. (c) Spring-mounted cylinder.

moving frame of reference using the absolute velocity formulation (Mougen and Magnaudet 2002), which can be written in compact form as follows:

$$\partial_t \mathbf{Q} + \nabla \cdot \mathbf{F}_c(\mathbf{Q}) - \nabla \cdot \mathbf{F}_v(\mathbf{Q}, \nabla \mathbf{Q}) = \mathbf{S}. \tag{2.1}$$

In eq. (2.1) the convective flux $\mathbf{F}_c(\mathbf{Q})$ is the one written in the absolute frame of reference but shifted with the relative velocity $\mathbf{w}$, that is as follows,

$$\mathbf{F}_c(\mathbf{Q}) = \begin{pmatrix} \rho(\mathbf{u}-\mathbf{w}) \\ \mathbf{m} \otimes (\mathbf{u}-\mathbf{w}) + p\mathbb{I} \\ (\mathbf{u}-\mathbf{w})(\rho E) + p\mathbf{u} \end{pmatrix}, \tag{2.2}$$

the source term includes the Coriolis force in the momentum equation

$$\mathbf{S}(\mathbf{Q}, \Omega) = \begin{pmatrix} 0 \\ -\rho\Omega \times \mathbf{u} \\ 0 \end{pmatrix}, \tag{2.3}$$

and finally the viscous flux

$$\mathbf{F}_v(\mathbf{Q}) = \begin{pmatrix} 0 \\ \tau(\mathbf{u}) \\ \kappa\nabla T + \tau(\mathbf{u}) \cdot \mathbf{u} \end{pmatrix}, \text{ with } \tau(\mathbf{u}) = \mu\Big[(\nabla\mathbf{u} + \nabla\mathbf{u}^T) - \frac{2}{3}\nabla \cdot \mathbf{u}\mathbb{I}\Big]. \tag{2.4}$$

The control parameters of the flow system are the Reynolds number $Re_\infty$, which is the ratio between inertia and viscous forces, the Prandtl number $Pr$, which is the ratio between kinematic viscosity $\nu \equiv \mu/\rho$ and thermal diffusivity $\kappa$, and the Mach number $M_\infty$, which is the ratio of the flow velocity and the speed of sound $c_\infty$:

$$Re_\infty = \frac{\rho_\infty U_\infty L}{\mu}, \; Pr = \frac{\mu}{\rho\kappa}, \; M_\infty = \frac{U_\infty}{c_\infty} \tag{2.5}$$

In the configuration of the flow past a cylinder, fig. 1 (a), the reference length $L$ is the diameter of the cylinder, while in the two others the reference length is the chord of the plate (fig. 1 (b)) and the airfoil (fig. 1 (c)) respectively. In the transonic flow past an airfoil the dynamic viscosity $\mu$ is replaced by the sum of the dynamic molecular viscosity and the dynamic turbulent viscosity $\mu + \mu_t$ where $\mu_t$ is obtained using the Spalart–Allmaras turbulence model using the compressibility and Edwards correction.

In order to model the aeroelastic motion of a wing, we simply consider a wing section. The bending mode is represented as free movement in the perpendicular direction to the incoming flow, labeled heaving, while torsion is modeled through a rotational degree of

 

freedom, labeled pitching. Both structural degrees of freedom are treated as a spring-mass-damper system: heaving is emulated by a vertical spring, and pitching by a torsional spring, as shown in fig. 1. Here, the pitching angle is defined in the mathematically positive direction, opposite to the commonly defined *pitch-up* angle of attack, with $\alpha = -\theta$. Both springs are mounted at the center of gravity, $x_{cg} = 0$, that is, the elastic center coincides with the center of gravity. We have made this choice to simplify the analysis, but it does not change the main conclusions. The system of ordinary differential equations is as follows:

$$\begin{aligned} m\frac{\partial^2 h}{\partial t^2} + C_h\frac{\partial h}{\partial t} + K_h h &= L(\mathbf{Q}) = \Big[\int_{\Gamma_{fs}} \big(-p\mathbb{I} + \tau(\mathbf{u})\big)\mathbf{n}\,\mathrm{d}\mathbf{x}\Big]\cdot \mathbf{R}^T(\theta)\mathbf{e}_y \\ I_{ea}\frac{\partial^2 \theta}{\partial t^2} + C_\theta\frac{\partial \theta}{\partial t} + K_\theta(\theta-\theta_s) &= M(\mathbf{Q}) = \Big[\int_{\Gamma_{fs}} \mathbf{x}\wedge\big(-p\mathbb{I} + \tau(\mathbf{u})\big)\mathbf{n}\,\mathrm{d}\mathbf{x}\Big]\cdot \mathbf{e}_z \end{aligned} \tag{2.6}$$

Here, $m$ is the mass of the structure, $I_{ea}$ is the moment of inertia around the elastic center, and the coefficients $K_h$, $K_\theta$ , $C_h$, and $C_\theta$ are the stiffness and damping coefficients, respectively. The angle $\theta_s$ is the pre-stress pitching angle, which represents the pre-stressed state of the system when the angle of attack is not null, that is, $\theta_s = -\alpha_0 - M(\mathbf{Q}_0)/K_\theta$.

$$\begin{aligned} \frac{\partial^2 h}{\partial t^2} + 2\zeta_h\Big(\frac{\Omega}{U^*}\Big)\frac{\partial h}{\partial t} + \Big(\frac{\Omega}{U^*}\Big)^2 h &= \frac{1}{\overline{m}}\frac{2}{\rho_\infty U_\infty^2 L}\Big[\int_{\Gamma_{fs}} \big(-p\mathbb{I} + \tau(\mathbf{u})\big)\mathbf{n}\,\mathrm{d}\mathbf{x}\Big]\cdot \mathbf{R}^T(\theta)\mathbf{e}_y \\ \frac{\partial^2 \theta}{\partial t^2} + 2\zeta_\theta\Big(\frac{1}{U^*}\Big)\frac{\partial \theta}{\partial t} + \Big(\frac{1}{U^*}\Big)^2(\theta-\theta_s) &= \frac{1}{\overline{m}r_\theta^2}\frac{2}{\rho_\infty U_\infty^2 L^2}\Big[\int_{\Gamma_{fs}} \mathbf{x}\wedge\big(-p\mathbb{I} + \tau(\mathbf{u})\big)\mathbf{n}\,\mathrm{d}\mathbf{x}\Big]\cdot \mathbf{e}_z \end{aligned} \tag{2.7}$$

where as in the VIV problem of the cylinder, we simply consider the heaving $h$ motion. In eq. (2.2) we introduced the rigid-body velocity $\mathbf{w}$ which is defined as follows

$$\mathbf{w} \equiv \mathbf{R}(\theta)^T\big(-\mathbf{U}_\infty, \dot{h}\big) + \dot{\theta}\mathbf{e}_z \wedge \mathbf{x}, \tag{2.8}$$

where the first term accounts for the relative translational velocity, the second term for the heaving motion and the last term accounts for the rotation of the body. Here $\mathbf{R}(\theta)$ is a rotation matrix used to project the translational velocity onto the rotating axes. Finally, the fluid system is complemented with the following boundary conditions. An adiabatic no-slip, that is, $\mathbf{u} = \mathbf{w}$, boundary condtion is imposed at the body wall. At the inlet we impose a constant density $\rho_\infty$ and null velocity field $\mathbf{u} = \mathbf{0}$. Whereas at the outlet we impose a constant pressure $p_\infty = r\rho_\infty T_\infty$, where $r$ is the ideal gas constant of air and $T_\infty = 288.15K$.

In order to determine the onset of self-sustained oscillations, we consider the linearization of eq. (2.1) and eq. (2.7), which can be written in a compact formulation as follows,

$$\begin{aligned} &\Big(\mathcal{R}(\lambda)\Big)^{-1}\hat{\mathbf{q}} \equiv \Big(\lambda\mathbf{B} + D\mathbf{F}|_{\mathbf{q}_0}\Big)\hat{\mathbf{q}} = \mathbf{m}_\theta\theta + \mathbf{m}_{\dot\theta}\dot\theta + \mathbf{m}_{\dot h}\dot h \\ &\lambda\theta = \dot\theta, \quad \lambda h = \dot h \\ &\lambda\dot\theta + 2\zeta_\theta\Big(\frac{1}{U^*}\Big)\dot\theta + \Big(\frac{1}{U^*}\Big)^2\theta = \frac{1}{\overline{m}r_\theta^2}C_M(\hat{\mathbf{q}}) = \frac{1}{\overline{m}r_\theta^2}\mathbf{c}_m^T\hat{\mathbf{q}} \\ &\lambda\dot h + 2\zeta_h\Big(\frac{\Omega}{U^*}\Big)\dot h + \Big(\frac{\Omega}{U^*}\Big)^2 h = \frac{1}{\overline{m}}C_L(\hat{\mathbf{q}}) = \frac{1}{\overline{m}}\mathbf{c}_L^T\hat{\mathbf{q}} \end{aligned} \tag{2.9}$$

The operator $D\mathbf{F}|_{\mathbf{q}_0}$ is the linearised operator around the steady-state, which herein is obtained with algorithmic differentiation, so it corresponds to the discrete linearisation. Similarly, operators $\mathbf{m}_\theta$, $\mathbf{m}_{\dot\theta}$ and $\mathbf{m}_{\dot h}$ are the linearised operators with respect to the structural degrees of freedom. The expression of the moment and lift coefficients $(C_M(\hat{\mathbf{q}}), C_L(\hat{\mathbf{q}}))$ is provided in the RHS of eq. (2.9), and the operators $\mathbf{c}_L^T$ and $\mathbf{c}_m^T$ are the

linear mappings between the perturbed state $\hat{\mathbf{q}}$ and the corresponding force or moment coefficient.

An efficient method to determine the eigenvalues of eq. (2.9) consists in the factorisation of the fluid system with respect to the structural degrees of freedom and to use the superposition principle to reconstruct the RHS of the structural equations, that is,

$$\begin{gathered}\mathbf{c}_L^T\hat{\mathbf{q}} = \mathbf{c}_L^T\sum_i \mathcal{R}(\lambda)\mathbf{m}_i, \quad \mathbf{c}_m^T\hat{\mathbf{q}} = \mathbf{c}_m^T\sum_i \mathcal{R}(\lambda)\mathbf{m}_i \text{ for } i = [\theta, \dot{\theta}, \dot{h}] \\ \text{where } Z_L^i(\lambda) = -\mathbf{c}_L^T\mathcal{R}(\lambda)\mathbf{m}_i, Z_m^i(\lambda) = -\mathbf{c}_m^T\mathcal{R}(\lambda)\mathbf{m}_i,\end{gathered} \tag{2.10}$$

which leads to the resolution of the following characteristic polynomial,

$$H(\lambda) = \begin{vmatrix} \lambda^2 + \Big(2\zeta_h\big(\frac{\Omega^*}{U^*}\big) + \frac{Z_L^{\dot{h}}(\lambda)}{\overline{m}}\Big)\lambda + \big(\frac{\Omega^*}{U^*}\big)^2 & \frac{Z_L^{\theta}(\lambda) + \lambda Z_L^{\dot{\theta}}(\lambda)}{\overline{m}} \\ \frac{\lambda Z_m^{\dot{h}}(\lambda)}{r_\theta^2\overline{m}} & \lambda^2 + \Big(2\zeta_\theta\big(\frac{1}{U^*}\big) + \frac{Z_L^{\dot{\theta}}(\lambda)}{\overline{m}}\Big)\lambda + \big(\frac{1}{U^*}\big)^2 \end{vmatrix}. \tag{2.11}$$

The zeros of $H(\lambda)$ correspond to the eigenvalues of eq. (2.9). However, this process is not significantly more efficient than the direct computation of the eigenvalues of eq. (2.9). In order to determine the zeros of $H(\lambda)$ one needs to solve as many as structural degrees of freedom, three in our case, for each $\lambda \in \mathbb{C}$, as it was done by Sabino (2022).

However, the procedure can be considerably improved if one determine the transfer functions $Z_L^i(\mathrm{i}\omega)$ and $Z_m^i(\mathrm{i}\omega)$ for $i = [\theta, \dot{\theta}, \dot{h}]$, also known as impedances, along the real axis, that is, for $\lambda = \mathrm{i}\omega$ for $\omega \in \mathbb{R}$. Then, we reconstruct the complex form of the transfer functions using rational interpolation within the Loewner framework (Benner *et al.* 2017, Ch. 8). The Loewner framework provides a rigorous mathematical foundation for analytical continuation from measured frequency response data into the complex plane, making it particularly suited for dynamical systems identification. Its theoretical justification stems from tangential interpolation theory and realization theory for linear time-invariant (LTI) systems, where the rank property of the structured Loewner matrix directly reveals the minimal system order (Mayo & Antoulas 2007). Such a procedure, offers very good results in a thin region around the real axis where the transfer functions have been computed. Another advantage of this approach is that now one not only has an expression of $H(\lambda)$ but also $\dfrac{dH(\lambda)}{d\lambda}$, which enables fast computations of the eigenvalues using the Newton method.

Let us summarise the numerical procedure:

- Compute the transfer functions $Z_L^i(\mathrm{i}\omega)$ and $Z_m^i(\mathrm{i}\omega)$ for $i = [\theta, \dot{\theta}, \dot{h}]$, for $\omega \in \mathbb{R}$.
- Perform a rational interpolation following the Loewner framework, that is, compute $\tilde{Z}_L^i(\lambda), \tilde{Z}_m^i(\lambda)$ from $Z_L^i(\mathrm{i}\omega)$ and $Z_m^i(\mathrm{i}\omega)$ and determine $H(\lambda)$ using the rational interpolators.
- Determine the zeros of eq. (2.11) with the Newton method using the rational interpolators of the transfer functions, that is,

$$\delta\lambda_{n+1} = -\Big(\frac{dH(\lambda)}{d\lambda}\Big)^{-1}H(\lambda_n) \text{ with } \lambda_{n+1} = \lambda_n + \delta\lambda_{n+1} \tag{2.12}$$

In addition, for the computation of $\mathrm{EP}_n$ exceptional points, it is required that

$$\frac{d^jH(\lambda)}{d\lambda^j} = 0 \text{ for } j = 1, \ldots, n-1 \tag{2.13}$$

| Case | $U^*$ $\frac{U_\infty}{L\sqrt{K_\theta/I_{ca}}}$ | $\Omega$ $\sqrt{\frac{K_h/m}{K_\theta/I_{ca}}}$ | $\zeta_h$ $\frac{C_h}{2\sqrt{mK_h}}$ | $\zeta_\theta$ $\frac{C_\theta}{2\sqrt{I_{ca}K_\theta}}$ | $r_\theta$ $\sqrt{\frac{I_{ca}}{mL^2}}$ | $x_\theta$ $\frac{x_{cg}}{L}$ | $\tilde{m}$ $\frac{m}{1/2\rho_f L^2}$ | Re $\frac{\rho_f U_\infty L}{\mu}$ | $M_\infty$ $\frac{U_\infty}{c_\infty}$ |
|---|---|---|---|---|---|---|---|---|---|
| Configuration (a) | $10^{-2}-1$ | 1.0 | $D_s\frac{U^*}{\Omega}$ | – | – | 0 | 2.0 | 50 | 0.1 |
| Configuration (b) | $10^{-2}-10^{1}$ | 0.8 | 0 – 0.2 | 0.05 | 0.290 | 0 | $10^3$ | 2900 | 0.1 |
| Configuration (c) | $0.5-10^{1}$ | 0.8 | 0 – 0.2 | 0.0 – 0.2 | 0.6 | 0 | $10^3$ | $3.2\cdot10^6$ | 0.73 |

Table 1. Values of dimensionless parameters and definition. For the cylinder the damping parameter $D_s$ is varied between $[0, 1]$.

In such a case the eigenvalue condition $H(\lambda) = 0$ is complemented with the $\mathrm{EP}_n$ condition eq. (2.13) and it can be solved using a Newton update as for eq. (2.12).

## 3. Results

### 3.1. *Vortex-Induced-Vibrations for the flow past a circular*

We analyse the interplay between the fluid and VIV instabilities past a freely vertically moving circular cylinder at a $Re = 50$. The transfer function is represented in fig. 2 (a-b) for several values of the growth rate $\sigma = [0, -0.02, -0.04]$. The criterion for neutrality of the eigenvalue, that is, $\lambda = \mathrm{i}\omega$ is the following,

$$\underbrace{\mathrm{Re}\big(Z_L^{\dot{h}}(\mathrm{i}\omega)\big)}_{\text{aerodynamic damping}} = -2\zeta_h\frac{\Omega}{U^\star} = -D_s, \qquad \underbrace{\Big(\overbrace{\overline{m}+\frac{\mathrm{Im}\big(Z_L^{\dot{h}}(\mathrm{i}\omega)\big)}{\omega}}^{\text{added mass}}\Big)}_{\text{effective mass}}\omega^2 = \left(\frac{\Omega}{U^*}\right)^2. \tag{3.1}$$

That is, the aerodynamic damping must counterbalance the effect of the structural damping whereas the effective inertia due to the added mass must match the structural stiffness ($K_s = \left(\frac{\Omega}{U^*}\right)^2$). These two cases are represented in fig. 2 (a-b). The case $D_s = 0$ is represented with a dark blue line, in this case we can observe two intersections, one at a low frequency ($\omega_{LF}$) which corresponds to the critical frequency of the fluid mode and a second at a higher frequency ($\omega_{HF}$), which corresponds to the frequency where the heaving mode becomes unstable. In the second case, $D_s = 1$ which is represented with a dark green line, we can also observe two intersections at two very close frequencies. However, in this case both intersections belong to the fluid mode, while the heaving mode always remains stable. These two cases exemplify the behaviour on two opposite sides of the EP. For the first case, $D_s = 0$ which is represented in fig. 2 (c), the growth rate curves cross and the frequency curves are repelled. In contrast, for the second case where $D_s = 1$ and that is represented in fig. 2 (d), the growth rate curves are repelled and the frequency curves cross.

This phenomenon is further explored in fig. 2 (e), which represents the path of both modes for several values of the structural damping parameter $D_s = \{0, 0.8, 0.9, 1\}$ as a function of the reduced velocity. Therein, we can clearly observe a saddle-node at around $(\omega_{EP}, \sigma_{EP}) \approx (0.82, -0.02)$. For the values of the structural damping $D_s = \{0, 0.8\}$ the heaving mode becomes unstable and follows a trajectory to the right of the EP, while the fluid mode remains to the left of the EP and its growth rate decreases with $U^*$. For the highest values of the structural damping, $D_s = \{0.9, 1\}$, the heaving mode remains stable

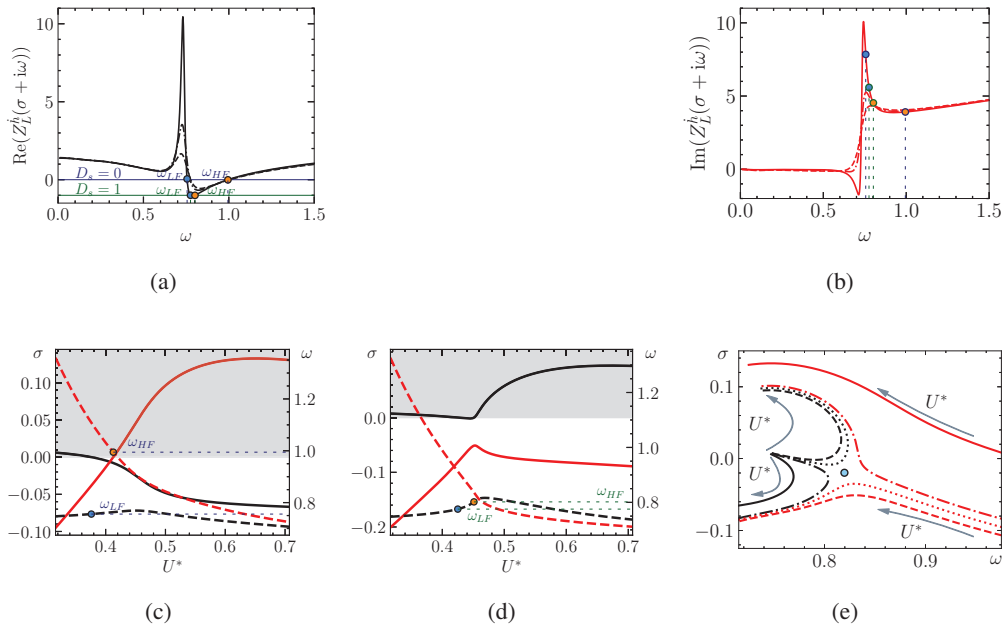


Figure 2. (a-b) Evolution of the transfer function $Z_L^{\dot{h}}$ with respect to the pulsation $\omega$. The real part is represented in black (a) and the imaginary in red (b). Three growth rates $\sigma$ are represented: $\sigma = 0$ (solid), $\sigma = -0.02$ (dashed) and $\sigma = -0.04$ (dash-dotted). (c) Evolution of the growth rate for $D_s = \zeta_h = 0$ for the fluid mode (black solid) and the heaving mode (red solid); the corresponding frequencies are shown with dashed lines. (d) The same as the middle figure but for $D_s = 1$. (e) Representation of path followed by the eigenvalues for increasing $U^*$ for the fluid mode (black) and heaving mode (red) for $D_s = 0$ (solid), $D_s = 0.8$ (dash-dotted), $D_s = 0.9$ (dotted) and $D_s = 1.0$ (dashed). The exceptional point is represented with a light blue marker.

all along its trajectory and the growth rate of the fluid mode increases with the reduced velocity. For frequencies smaller than the one of the EP ($\omega < \omega_{EP}$), the fluid mode (resp. heaving mode) follows a similar trajectory to the heaving mode (resp. fluid mode) at lower structural damping.

This exchange is further exemplified in fig. 3. It represents the trajectory of eigenvalues along closed loops in the parameter space, in particular, along ellipses: $D_s = D_{s,EP} + r_{D_s}\cos(\theta)$ and $U^* = U^* + r_{U^*}\sin(\theta)$. It reveals the manifold structure of the exceptional point, in particular it shows that its winding number is half, that is, winding around the EP once induces a exchange of modes, while winding twice around the EP returns to the same eigenvalue branch. Thus, it is clear that the naming convention of heaving and fluid mode is just a convention, and it is arbitrary near a EP.

### 3.2. *Flutter instability for the flow past a thin plate*

In this section we explore the aeroelastic instabilities for the laminar flow past a thin plate (Moulin 2020). Figure 4 (a-b) shows the evolution of the two elastic modes as a function of the reduced velocity for $\zeta_h = 0$ (solid) and $\zeta_H = 0.03$ (dashed). The red lines represent the path of the heaving mode, and the black lines represent the evolution of the pitching mode. As it was the case for the VIV instability past the circular cylinder in section 3.1, the naming convention is somehow arbitrary in the region of the parameter space near the EP, that is when the two eigenvalue paths are attracted. Figure 4 displays the saddle-node structure that is observed around the EP. For values of the structural damping lower than

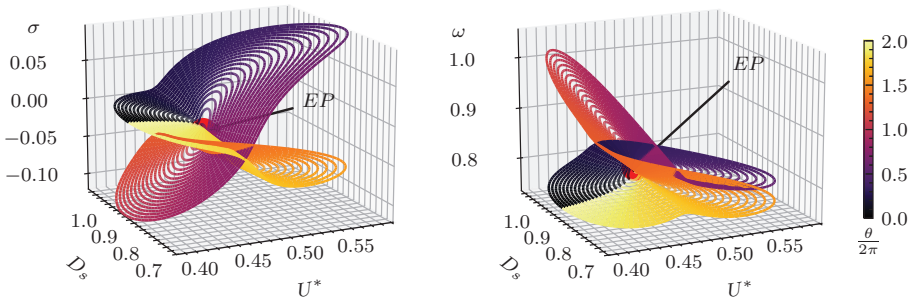


Figure 3. Manifold structure of the EP. It has been computed using individual trajectories along ellipses in the parameter space: $D_s = D_{s,EP} + r_{D_s}\cos(\theta)$ and $U^* = U^*_{EP} + r_{U^*}\sin(\theta)$ for $\theta \in [0, 4\pi]$, $r_{Ds} \in [0.001, 0.2]$ and $r_{U^*} \in [0.01, 0.1]$. The manifold is parametetrised by $\theta$ which is colour-coded. The EP is represented by a red circular marker.

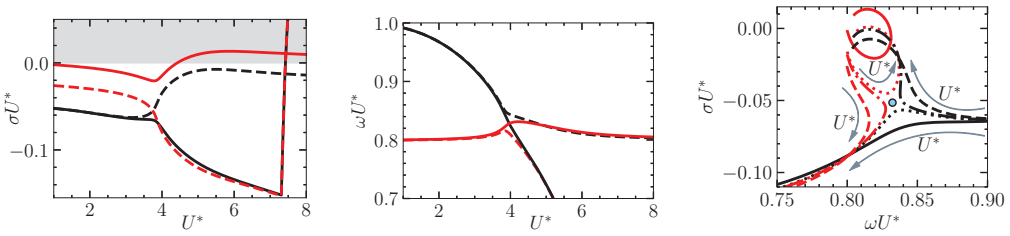


(a) (b) (c)

Figure 4. Evolution of the growth rate (a) and frequency (b) of the two elastic modes: heaving (red) and pitching (black) as a function of the reduced velocity for $\zeta_h = 0$ (solid) and $\zeta_h = 0.03$ (dashed). (c) Representation of path followed by the eigenvalues for increasing $U^*$ for the pitching mode (black) and heaving mode (red) for $\zeta_h = 0$ (solid), $\zeta_h = 0.0175$ (dotted), $\zeta_h = 0.02$ (dash-dotted) and $\zeta_h = 0.03$ (dashed). The exceptional point is represented with a light blue marker.

$\zeta_{h,EP}$ the branch of the heaving mode becomes unstable and the pitching mode remains stable for a wide range of the reduced velocity but it eventually becomes unstable at the divergence reduced velocity, around $U^*_D \approx 7.4$. For $\zeta_h > \zeta_{h,EP}$ the growth rate of the branch of the pitching mode increases for reduced velocities higher than the ones of the $U^*_{EP}$ and its frequency $\omega U^* \approx 0.8$, which corresponds to the one of the heaving mode, and in this the growth rate and frequency of the heaving branch decreases for a wide range of the reduced velocity until the divergence velocity $U^*_D \approx 7.4$ where it is destabilised. Such a mode-exchange occurs in the neighbourhood of the EP.

In order to demonstrate the mode-exchange, we represent the manifold structure of the EP in fig. 5. As in the VIV case discussed in section 3.1 it corresponds to a simple EP with a winding number equal to a half, that is, it takes two turns to return to the initial position. A single turn induces a mode-exchange. The important difference with the VIV case, it is the nature of the two modes. In this example, it corresponds to two aeroelastic modes, while in the case of the cylinder it is the coupling between a fluid and an aeroelastic mode. However, in both cases the underlying structure of the EP is the same.

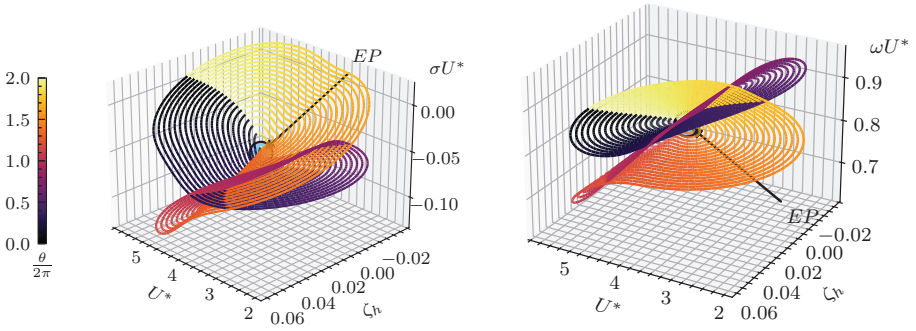


Figure 5. Manifold structure of the EP. It has been computed using individual trajectories along ellipses in the parameter space: $\zeta_h = \zeta_{h,EP} + r_{\zeta_h}\cos(\theta)$ and $U^* = U^*_{EP} + r_{U^*}\sin(\theta)$ for $\theta \in [0, 4\pi]$, $r_{U^*} \in [0.01, 2]$ and $r_{\zeta_h} \in [0.001, 0.05]$. The manifold is parametetrised by $\theta$ which is colour-coded. The EP is represented by a light blue circular marker.

### 3.3. *Transonic flutter instability past a OAT-15a airfoil*

In this last example, we illustrate the phenomenon of flutter in the transonic regime and in particular how two exceptional points drive the phenomenon known as *transonic dip* in aeroelasticity (Plath 2024, Sec. 1.2.2). To illustrate this phenomenon, we have selected the flow past the OAT15a airfoil at $M = 0.73$, $Re = 3.2 \cdot 10^6$ and $\alpha = 3.5°$, which has been previously studied in the fixed configuration by Sartor *et al.* (2015); Paladini *et al.* (2019), among others.

Figure 6 displays the spectrum for the structural values listed in table 1 (Conf. 3), $\zeta_h = 0.04273$, $\zeta_\theta = 0.0159$ and $U^* = 1$. The naming convention follows their behaviour at small reduced velocity, in particular if the displacement (resp. vertical velocity) is dominantly due to heaving, pitching motion or if it is small in comparison to the flow perturbations. The displacement (resp. velocity is represented) by red (resp. black) arrows on the right panel, where the norm of the mode has been normalised such the Chu's energy of the flow field is unitary. The left figure shows three leading eigenvalues, the fluid or buffet, the pitching and heaving modes represented with the blue, black and red markers respectively.

This configuration is further explored in fig. 7, which follows the path of the three leading eigenvalues while increasing the reduced velocity $U^*$, represented with the grey arrows. On fig. 7 (a) displays the selected configuration of damping parameters, and it shows two exceptional points of second order ($EP_2$). The first $EP_2^{f,h}$ leads to the interaction / exchange between the fluid and heaving mode and the second $EP_2^{f,p}$ between the pitching and fluid mode. The other four panels show the eigenvalue loci while varying the reduced velocity but with perturbed damping parameters, $\zeta_h = 0.04273 + r\cos(\theta)$, $\zeta_\theta = 0.0159 + r\sin(\theta)$ for $r = 0.0159$. On the panel (b) we can observe a mode exchange between the fluid and pitching mode around the exceptional point ($EP_2^{f,p}$) and the heaving branch is weakly deflected around the first exceptional point ($EP_2^{f,h}$). The panel (c) is very similar to the original one (a) but the interaction between the pitching and fluid mode is weaker and they do not exchange. On the panel (d) there is a mode exchange between the fluid and heaving mode around $EP_2^{f,h}$, and a strong interaction between the heaving and the pitching branches. Finally, on the panel (e) we have two mode switchings: first the heaving and fluid modes are swapped in a region close to around $EP_2^{f,h}$ and then there is a second mode

 

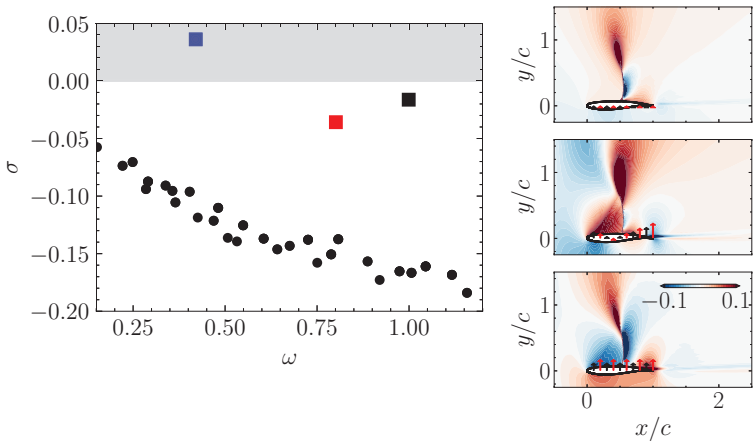


Figure 6. Spectrum for the configuration values listed in table 1 (Conf. 3) for $\zeta_h = 0.04273$, $\zeta_\theta = 0.0159$ and $U^* = 1$. The blue squared marker highlights the fluid mode, displayed on the top figure of the right panel. The pitching mode is represented with the black squared marker and on the middle figure of the right panel. The red squared marker represents the heaving mode, which is displayed on the bottom figure of the right panel. The red (resp. black) arrows of the right panel represent the vertical displacement (resp. velocity).

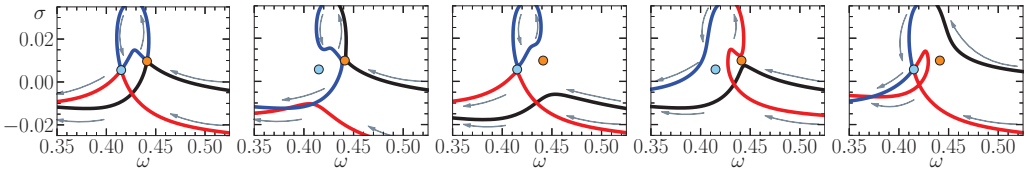


Figure 7. Veering phenomenon of the three leading eigenvalues: black line (pitching mode), red line (heaving mode) and blue line (fluid mode) around two exceptional points represented by two circle markers (blue and orange). Subfigure (a) is computed for $\zeta_h = 0.04273$, $\zeta_\theta = 0.0159$. Subfigures (b-e) are computed for damping parameters $\zeta_h = 0.04273 + r\cos(\theta)$, $\zeta_\theta = 0.0159 + r\sin(\theta)$ for $r = 0.0159$ and $\theta = 0$ for (b), $\theta = \pi/2$ for (c), $\theta = \pi$ for (d) and $\theta = 3\pi/2$ for (e). The remaining parameters are summarised in table 1. The grey arrows indicate the the direction of increasing $U^*$.

exchange between the pitching and heaving branches; that is for large $U^*$ the fluid, heaving, and pitching branches behave as the heaving, pitching, and fluid mode, respectively.

The existence of two $EP_2$ nearby in the parameter space suggests the existence of a $EP_3$, that is, a degenerate point where the three modes coalesce. This phenomenon is explored in figure fig. 8 (a), that shows the evolution of the two aforementioned exceptional points while varying $\Omega^*$. It shows that the two branches of $EP_2$ converge towards a point around $\Omega^* \approx 0.897$. For larger values of $\Omega^*$, while keeping $r_\theta = 0.6$ and $\overline{m} = 10^3$ there are no $EP_2$, so in a sense the $EP_3$ is the organizing centre of the linear dynamics leading to the mode switching phenomena. We have partially tracked the evolution of the $EP_3$ in the parameter space $(r_\theta, \overline{m})$.

In order to demonstrate the mode-exchange around the $EP_3$, we represent the manifold structure of the EP in fig. 9. In contrast to the previous visualisations of $EP_2$, which are codimension two, that is we can encircle $EP_2$ with a circle, an $EP_3$ is codimension four and it has to be encircled with a four-dimensional sphere ($S^3$). In fig. 9 we show a partial view of this encircling and we evidence the fact that we need to encircle the $EP_3$ three times in order to return to the initial position, while a turning around once or twice induces

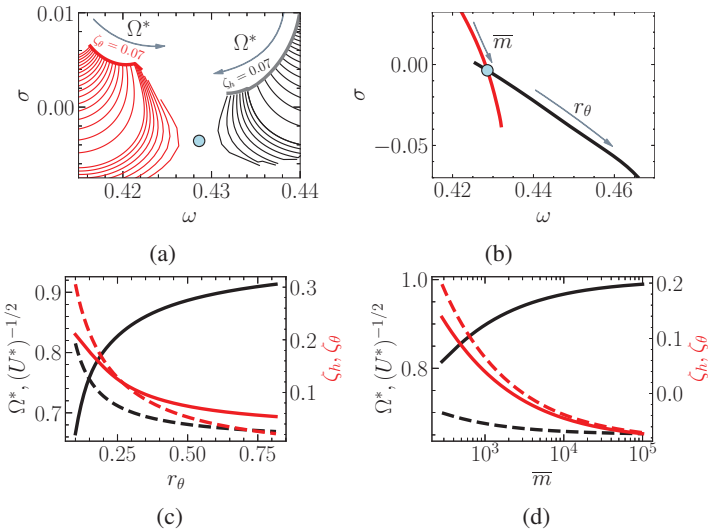


Figure 8. (a) Evolution of the $EP_2^{h,f}$ (thin red) as a function of $(\Omega^*, \zeta_\theta)$ and $EP_2^{p,f}$ (thin black) as a function of $(\Omega^*, \zeta_h)$ with the upper computed limt of the damping parameter indicated with a thick line. The $EP_3$ is represented with a circle blue marker. (b) Represents the evolution of the $EP_3$ for varying reduced mass or $r_\theta$ while keeping the other constant. Evolution of the $EP_3$ as a function of $(r_\theta, \overline{m} = 10^3)$ (c) and as function of $(r_\theta = 0.6, \overline{m})$ (d).

a single or a double mode exchange. Encircling two $EP_2$ induces a similar sequence of mode-swapping, which justifies the analysis of the $EP_3$ in order to understand the sequence of mode exchanges and to label it as an organising centre.

## 4. Conclusion

This study has established exceptional points as a fundamental and organising feature in the linear stability spectrum of fluid-structure interaction systems. Through a consistent numerical and analytical framework applied to three archetypal configurations—vortex-induced vibration, incompressible plate flutter, and transonic airfoil flutter—we have demonstrated that the non-Hermitian nature of the coupled fluid-structure operator naturally gives rise to these spectral singularities.

In the VIV and plate flutter cases, the interaction between modes (fluid/structural or between two structural modes) creates second-order exceptional points ($EP_2$). These points act as topological pivots in parameter space, around which eigenvalue branches veer and exchange identities, a phenomenon characterised by a half-integer winding number. The stability landscape is thus fundamentally reshaped near an EP, where conventional modal labeling breaks down and the system exhibits enhanced sensitivity to parameters.

The transonic flutter configuration reveals a richer structure, where the close interplay between fluid (buffet), pitching, and heaving modes leads to the formation of two nearby $EP_2$s. These coalesce at a specific parameter set, giving rise to a third-order exceptional point ($EP_3$), where three eigenvalues and their eigenvectors simultaneously degenerate. This $EP_3$ acts as an organising centre for the complex mode-swapping patterns observed and is intrinsically linked to the pronounced loss of stability characteristic of the transonic dip.

The presence of EPs underscores that linear stability analyses in FSI must account for the possibility of eigenvalue degeneracies beyond the standard diagonalisable case.

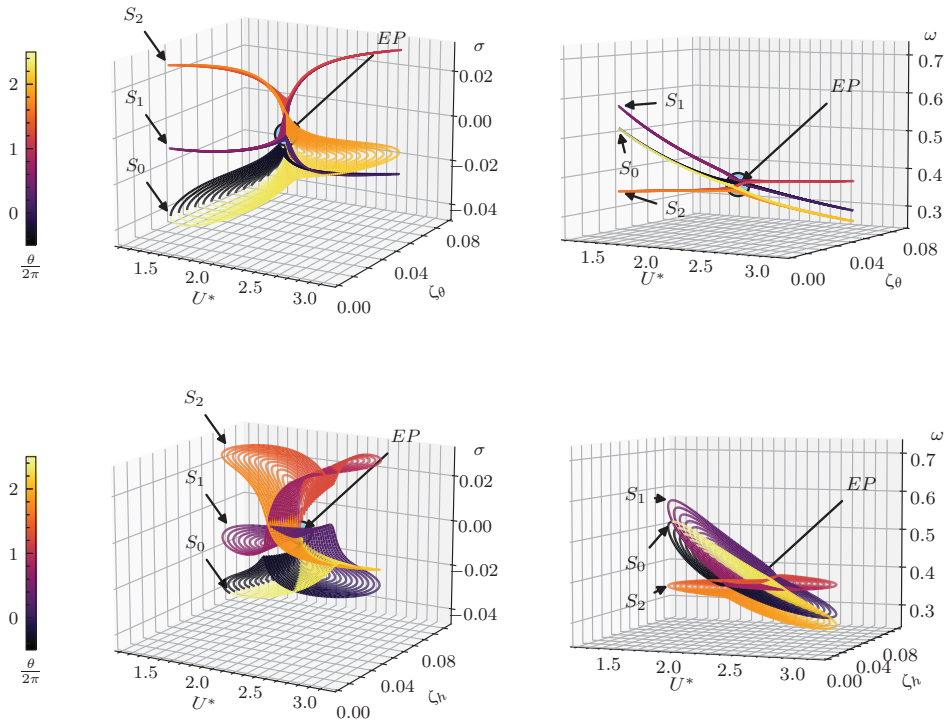


Figure 9. Manifold structure of the EP. It has been computed using individual trajectories along ellipses in the parameter space: $\zeta_h = \zeta_{h,EP} + r_{\zeta_h}\cos(\theta)$ and $U^* = U^*_{EP} + r_{U^*}\sin(\theta)$ for $\theta \in [0, 4\pi]$, $r_{U^*} \in [0.01, 2]$ and $r_{\zeta_h} \in [0.001, 0.05]$. The manifold is parametetrised by $\theta$ which is colour-coded. The EP is represented by a light blue circular marker.

The associated extreme parameter sensitivity and mode-swapping phenomena have direct implications for predicting flutter boundaries and for designing robust control strategies. Future work should explore exploiting the topological properties of EPs for novel flow control and energy harvesting paradigms, and investigate their role in nonlinear FSI dynamics and larger-scale dynamical systems.

## References


Achilleos, Vassos, Theocharis, Georgios, Richoux, Olivier & Pagneux, Vincent 2017 Non-hermitian acoustic metamaterials: Role of exceptional points in sound absorption. *Physical Review B* **95** (14), 144303.

Aurégan, Yves & Pagneux, Vincent 2017 Pt-symmetric scattering in flow duct acoustics. *Physical review letters* **118** (17), 174301.

Benner, Peter, Ohlberger, Mario, Cohen, Albert & Willcox, Karen 2017 *Model reduction and approximation: theory and algorithms*. SIAM.

Bergholtz, Emil J, Budich, Jan Carl & Kunst, Flore K 2021 Exceptional topology of non-hermitian systems. *Reviews of Modern Physics* **93** (1), 015005.

Bonnefis, Paul, Sierra-Ausin, Javier, Fabre, David & Magnaudet, Jacques 2024 Path instability of deformable bubbles rising in newtonian liquids: a linear study. *Journal of Fluid Mechanics* **980**, A19.

Casel, Mario & Ghani, Abdulla 2024*a* A novel method for stable thermoacoustic system design based on exceptional points-part i: Conceptualization. *Combustion and Flame* **267**, 113559.

Casel, Mario & Ghani, Abdulla 2024*b* A novel method for stable thermoacoustic system design based on exceptional points-part ii: Application to laminar and turbulent flame configurations. *Combustion and Flame* **267**, 113558.

Doppler, Jörg, Mailybaev, Alexei A, Böhm, Julian, Kuhl, Ulrich, Girschik, Adrian, Libisch, Florian, Milburn, Thomas J, Rabl, Peter, Moiseyev, Nimrod & Rotter, Stefan 2016 Dynamically encircling an exceptional point for asymmetric mode switching. *Nature* **537** (7618), 76–79.

Feng, Liang, Wong, Zi Jing, Ma, Ren-Min, Wang, Yuan & Zhang, Xiang 2014 Single-mode laser by parity-time symmetry breaking. *Science* **346** (6212), 972–975.

Ghani, Abdulla & Polifke, Wolfgang 2021 An exceptional point switches stability of a thermoacoustic experiment. *Journal of Fluid Mechanics* **920**, R3.

Heiss, Walter D 2012 The physics of exceptional points. *Journal of Physics A: Mathematical and Theoretical* **45** (44), 444016.

Helbig, Tobias, Hofmann, Tobias, Imhof, S, Abdelghany, M, Kiessling, T, Molenkamp, LW, Lee, CH, Szameit, A, Greiter, M & Thomale, R 2020 Generalized bulk–boundary correspondence in non-hermitian topolectrical circuits. *Nature Physics* **16** (7), 747–750.

Humbert, Sylvain C & Orchini, Alessandro 2025 Symmetry-breaking induced exceptional points in the thermoacoustic spectrum of annular combustors. *Journal of Fluid Mechanics* **1009**, R5.

Jouin, Antoine, Ciola, Nicola, Cherubini, Stefania & Robinet, Jean Christophe 2024 Detuned secondary instabilities in three-dimensional boundary-layer flow. *Physical Review Fluids* **9** (4), 043901.

Kern, J Simon, Lupi, Valerio & Henningson, Dan S 2024 Floquet stability analysis of pulsatile flow in toroidal pipes. *Physical Review Fluids* **9** (4), 043906.

Li, Xiaopeng, Yu, Ziqi, Iizuka, Hideo & Lee, Taehwa 2022 Experimental demonstration of extremely asymmetric flexural wave absorption at the exceptional point. *Extreme Mechanics Letters* **52**, 101649.

Matsushima, Kei & Yamada, Takayuki 2025 Exceptional points and defective resonances in an acoustic scattering system with sound-hard obstacles. *Proceedings of the Royal Society A* **481** (2320), 20250230.

Mayo, AJ & Antoulas, Athanasios C 2007 A framework for the solution of the generalized realization problem. *Linear algebra and its applications* **425** (2-3), 634–662.

Mensah, Georg A, Magri, Luca, Silva, Camilo F, Buschmann, Philip E & Moeck, Jonas P 2018 Exceptional points in the thermoacoustic spectrum. *Journal of Sound and Vibration* **433**, 124–128.

Miri, Mohammad-Ali & Alu, Andrea 2019 Exceptional points in optics and photonics. *Science* **363** (6422), eaar7709.

Moulin, Johann 2020 On the flutter bifurcation in laminar flows: linear and nonlinear modal methods. PhD thesis, Institut polytechnique de Paris.

Orchini, Alessandro, Silva, Camilo F, Mensah, Georg A & Moeck, Jonas P 2020 Thermoacoustic modes of intrinsic and acoustic origin and their interplay with exceptional points. *Combustion and Flame* **211**, 83–95.

Paladini, Edorado, Beneddine, Samir, Dandois, Julien, Sipp, Denis & Robinet, Jean-Christophe 2019 Transonic buffet instability: From two-dimensional airfoils to three-dimensional swept wings. *Phys. Rev. Fluids* **4**, 103906.

Plath, Matthias 2024 Numerical aeroelastic stability of transonic laminar airfoils. PhD thesis, Université Paris-Saclay.

Sabino, Diogo 2022 Aeroelastic instabilities of an airfoil in transitional flow regimes. PhD thesis, Université Paul Sabatier-Toulouse III.

Sartor, Fulvio, Mettot, Clément & Sipp, Denis 2015 Stability, receptivity, and sensitivity analyses of buffeting transonic flow over a profile. *Aiaa Journal* **53** (7), 1980–1993.

Schaefer, Felicitas, Guo, Shuai & Polifke, Wolfgang 2021 The impact of exceptional points on the reliability of thermoacoustic stability analysis. *Journal of Engineering for Gas Turbines and Power* **143** (2), 021010.

Schmid, Peter J 2007 Nonmodal stability theory. *Annu. Rev. Fluid Mech.* **39** (1), 129–162.

Shi, Chengzhi, Dubois, Marc, Chen, Yun, Cheng, Lei, Ramezani, Hamidreza, Wang, Yuan & Zhang, Xiang 2016 Accessing the exceptional points of parity-time symmetric acoustics. *Nature communications* **7** (1), 11110.

Trefethen, Lloyd N, Trefethen, Anne E, Reddy, Satish C & Driscoll, Tobin A 1993 Hydrodynamic stability without eigenvalues. *Science* **261** (5121), 578–584.

Wiersig, Jan 2020 Review of exceptional point-based sensors. *Photonics research* **8** (9), 1457–1467.

Xiong, Lei, Nennig, Benoit, Aurégan, Yves & Bi, Wenping 2017 Sound attenuation optimization using metaporous materials tuned on exceptional points. *The Journal of the Acoustical Society of America* **142** (4), 2288–2297.

Yao, Shunyu & Wang, Zhong 2018 Edge states and topological invariants of non-hermitian systems. *Physical review letters* **121** (8), 086803.

Zhou, Hengyun, Peng, Chao, Yoon, Yoseob, Hsu, Chia Wei, Nelson, Keith A, Fu, Liang, Joannopoulos,

John D, Soljačić, Marin & Zhen, Bo 2018 Observation of bulk fermi arc and polarization half charge from paired exceptional points. *Science* **359** (6379), 1009–1012.

Zhu, Weiwei, Fang, Xinsheng, Li, Dongting, Sun, Yong, Li, Yong, Jing, Yun & Chen, Hong 2018 Simultaneous observation of a topological edge state and exceptional point in an open and non-hermitian acoustic system. *Physical review letters* **121** (12), 124501.

# Can turbulence explain the formation of void regions in clouds?

Javier Sierra-Ausin,[1] Alain Pumir,[1] Mohsen Bagheri,[2,3] Kim Ye Won,[2,3]
Eberhard Bodenschatz,[2,3] Bernard Mehlig,[4] and Kristan Gustavsson[4]

[1] *Laboratoire de Physique, ENS de Lyon, Université de Lyon 1 and CNRS, 69007 Lyon, France*
[2] *Max Planck Institute for Dynamics and Self-Organization, 37077 Göttingen, Germany*
[3] *Institute for the Dynamics of Complex Systems, University of Göttingen, Friedrich-Hund-Platz 1, Göttingen, D-37077 Germany*
[4] *Department of Physics, Gothenburg University, Gothenburg, SE-40530 Sweden*

(Dated: January 11, 2026)

Fluid particles transported by incompressible turbulent flows become uniformly distributed in space. In contrast, inertial particles can be unevenly distributed in the flow. Although in clouds, small droplets have a very small inertia, we observe the presence of voids, i.e. small regions where droplets are essentially absent. This is consistent with the results of numerical simulations, which reveal the presence of voids even when the inertia of the particles is very small.We explain this unexpected manifestation of fluid inertia by the effect of vortices of moderate intensity, which are sufficiently persistent in time to expel droplets. Our results explain the extreme sensitivity of void formation on the inertia of particles.

Dust particles in circumstellar accretion disks [1], respiratory droplets in exhaled air [2], or small water droplets in atmospheric clouds [3–5] are transported by a turbulent fluid, although their weak inertia prevents them from following exactly the flow. In incompressible turbulent flows, tracer particles, in the absence of any inertial effects follow the flow, and their spatial distribution must remain or become homogeneous. A remarkable effect of particle inertia is that it could lead to inhomogeneous spatial distribution, even if the flow is incompressible [6]: particles heavier than the fluid are centrifuged out of vortical regions in the turbulent fluid. This could lead to the accumulation of particles in certain regions of the flow, which may in turn facilitate collisions, a process that favors the formation of rain drops by aggregation of smaller droplets [4, 7, 8]. In practice, however, the weakness of the droplet inertia makes it questionable whether this effect could be play any role in for cloud microphysics [9]. However, recent experiments in cloudy conditions have shown the sporadic appearance of voids in clouds [10], and recent measurements in clouds also provided evidence for weak clustering of small droplets [11, 12].

In a cloud physics context, it has been extensively documented that entrainment and mixing of dry air from air outside the cloud can generate substantial inhomogeneities in the droplet distribution inside the cloud [13], therefore providing a potential explanation for the observation of voids. More recently, numerical simulations of suspensions of particles with low inertia have shown the existence of void regions in the flow in an otherwise completely homogeneous suspension [14, 15].

The ambiguous understanding of the inertial effects of small particles largely stems from the lack of high-resolution *in-situ*data needed to resolve cloud microphysics [5, 9] and from the limited attention given to low-Stokes-number particles (St $< 0.1$) in both experimental [16–19] and numerical [20–22] studies. Recent advances in high-resolution airborne *in-situ* measurement systems, however, now allow direct characterization of cloud microphysics in real atmospheric conditions, including the behavior of low-Stokes-number particles.

Here, we ask whether the effects of inertia could be the reason for the formation of voids in clouds. To this end, we used *in-situ* measurements of cloud droplets in turbulent clouds, giving access to particle sizes and to the properties of turbulence. Figure 1 shows representative *in situ* PIV images from the EUREC$^4$A campaign [23] at increasing Stokes numbers. Void regions are frequently observed within the cloud, particularly at larger Stokes numbers.

Our observations indicate that small cloud droplets, of radius of the order $5 - 20\mu$m, with a very inertia (quantified by small Stokes numbers St $\sim 10^{-2}$) can exhibit inhomogeneous spatial distributions, and that the presence of these inhomogeneities strongly depends on the Stokes number itself. The sizes of these regions can be as large as $\sim$ 2cm, which corresponds to approximately $\sim 30\eta$, where $\eta$ is the Kolmogorov size, i.e. the size of the smallest eddies in the flow.

Numerically, we observe that voids can also form in a suspension of weakly inertial particles in a direct numerical simulation (DNS) of turbulent flow. In fact, we demonstrate that the statistics of voids obtained from the field campaign and from DNS, as measured by the probability density function (PDF) of Voronoi sizes [18], agree very well. Further analysis of the numerical results allow us to explain the formation of voids by a cumulative expulsion of weakly inertial particles by regions of strong vorticity. Interestingly, we demonstrate that the mechanism leading to the expulsion observed in clouds is not due to the most intense vortices, which are too rare, but rather to vortices of intermediate strength, which are persistent enough in time to empty regions of size $\sim 30\eta$. Our analysis also explain the sensitivity of the void forma-

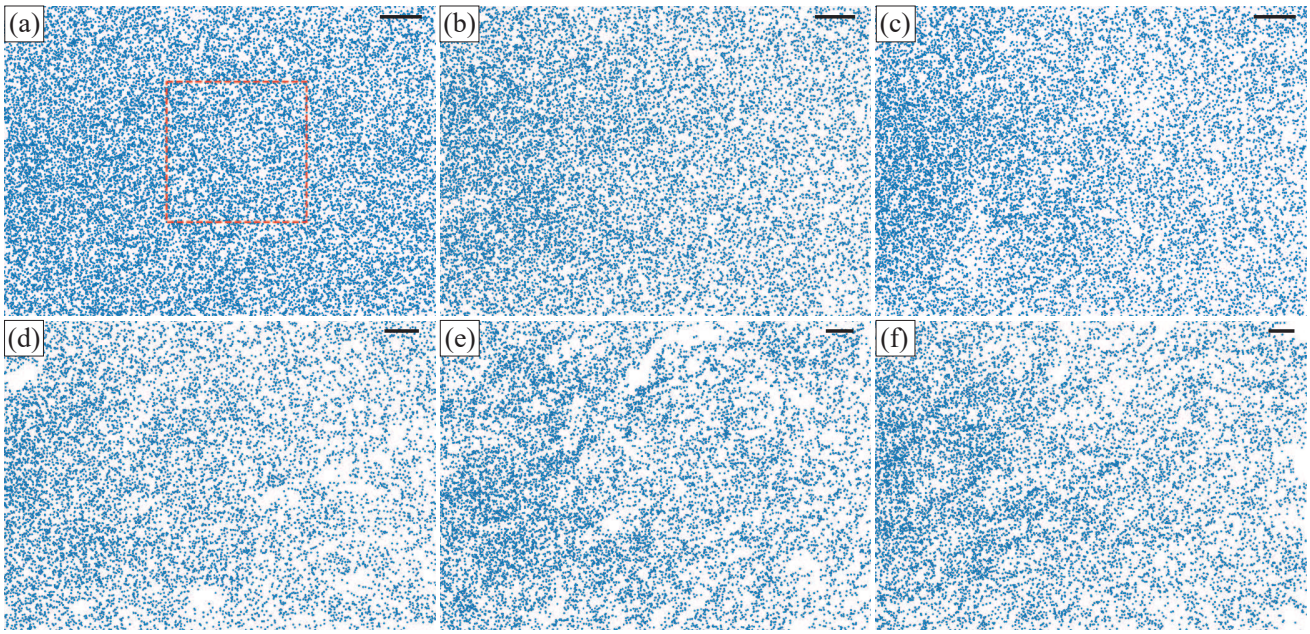


FIG. 1: Representative particle images with an increase in the Stokes number observed during the EUREC$^4$A campaign. ⟨St⟩: (a) 0.013 (0.97), (b) 0.025 (1.00), (c) 0.035 (1.03), (d) 0.045 (1.04), (e) 0.056 (1.11), (f) 0.085 (1.27). $\langle St \rangle$ is a time-averaged Stokes number; each image corresponds to the frame with median value of a each St range. Values in parentheses are inhomogeneity indices from the Voronoi cell area distribution (see Figure 3). The Stokes number and Voronoi cell area are calculated based on the square region shown in the (a) with red dashed lines. The physical scale of the image is 13.6 × 9.8 $cm^2$. The images were generated from the particle positions, each represented with a radius of 0.3 mm, and a scale bar corresponding to $15\eta$ is provided.

tion process on particle inertia, measured by the Stokes number.

In our study, we consider the motion of small particles or radius $a$, located at a position $\mathbf{x}_p$ and moving with a velocity $\mathbf{v}$ in a turbulent fluid, with velocity $\mathbf{u}$ at the location of the particles. In the limit of very small particle Reynolds number, $\mathrm{Re}_p = |\mathbf{u} - \mathbf{v}|a/\nu \ll 1$, the equations of motion reduce to:

$$\frac{d\mathbf{v}}{dt} = \frac{1}{\tau_p}(\mathbf{u}(\mathbf{x}_p) - \mathbf{v}) \ , \quad \frac{d\mathbf{x}_p}{dt} = \mathbf{v} \, , \tag{1}$$

where $\tau_p = \frac{2}{9}\frac{\rho_p}{\rho_f}\frac{a^2}{\nu}$ is the relaxation time of the particle. In a turbulent flow, the time of the fastest eddies is the Kolmogorov time, $\tau_K = (\nu/\epsilon)^{1/2}$, where $\epsilon$ is the rate of turbulent energy dissipation per unit mass of the fluid. The dimensionless ratio $\mathrm{St} = \tau_p/\tau_K$ compares the relaxation time of the particle $\tau_p$ and the time of the fastest eddies, and measures the inertia of the particles. In atmospheric flows, the values of St are found to be of the order of $\sim 0.01$ for realistic values of $a$ and of $\epsilon$ [9]. These low values suggest that the velocity of the particle adjusts in a short time to the velocity of the fluid when one considers eddies of amplitude $\sim 1/\tau_K$. However, extremely intense vorticity fluctuations develop in the flow, with magnitudes orders of magnitude larger than the typical fluctuation, an effect which could potentially play a role in generating spatially inhomogeneous particle distributions.

Those observation results give us the idea that despite od the small Stokes number, the Voronoi index increases as the Stokes number. Method to calculate the stokes number [**?** ]

Figure 2 presents two examples of *in situ* PIV measurements obtained during cloud-kite observations in the EUREC$^4$A campaign [27]. The two measurements were conducted at similar altitudes (approximately 1 km). Compared to FL12, FL6 exhibits approximately twice the droplet number concentration, consistent with a stronger influence of continental aerosol sources. In contrast, FL12 is characterized by a Stokes number approximately four times larger than that of FL6. Moreover, the Stokes number in FL12 shows substantial fluctuations, including within the cloud-core region where entrainment and mixing are expected to be minimal. These fluctuations are associated with pronounced spatial inhomogeneity in the droplet distribution.

To examine whether this sensitivity to the Stokes number is representative of the full dataset, all available PIV measurements are grouped into six Stokes number bins, as summarized in Table I. Only cloud-core regions, identified by approximately steady particle number density

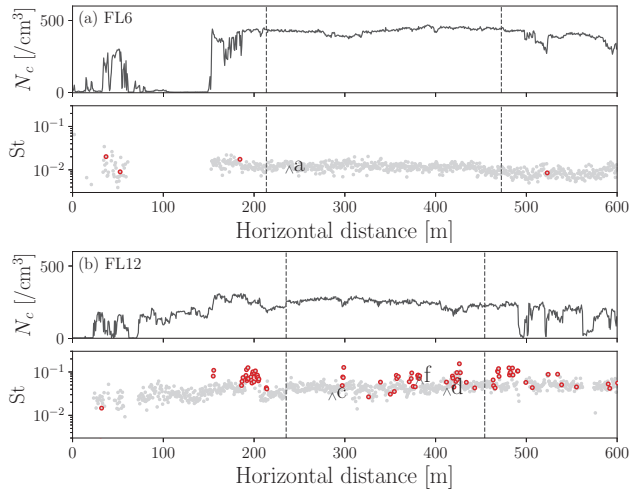


FIG. 2: Particle number concentration ($N_c$) and St along the horizontal distance of the clouds from EUREC$^4$A campaign. (a) February 4 at 18:43 (FL6), (b)) February 12 at 22:54 (FL12). In the St plot, the red markers denote points corresponding to inhomogeneity indices from the Voronoi cell area distribution larger than 1.

(e.g., indicated by the dashed vertical lines in Fig. 2), are included in the analysis in order to minimize the effects of entrainment and mixing.

, processing curves for each bin.

voids depends mostly on the turbulence from the 4th bins epsilon varies an order of 10 while the mean diameter still remains in same. The Reynolds number not related to the deviation of the right tails in Voronoi area distribution. It is mostly come from the turbulence, not the droplet size, unlikely reported

compare the exp with DNS. The probability density functions of normalized Voronoi cell areas are shown in Figure 3. The distribution obtained for F4 (blue circles) follows a Poisson-Voronoi distribution (shown as black dashed lines). In comparison, the distribution for F12 (red triangles) exhibits heavy tails. The deviation begins at $2.5\,\langle A\rangle$, and corresponds to a probability level of $\sim 10^{-3}$. It reaches a maximum at $\sim 2.8\,\langle A\rangle$ and then decreases until $14.1\langle A\rangle$ which corresponds to 7.5, 8.4, and $42.3\eta^2$, respectively.

The values of St and Sv are small, consistent with Table 1 in [9]. The experiments shown here therefore amply confirm that voids can form in clouds, with droplets of very small inertia, and are also consistent with recent DNS observations [15], and our own simulations, which we will discuss later. The results also point to a sensitivity on St. How to explain these observations, given in particular the remark that the Stokes numbers considered are small, and between St $\approx 0.01$ (F4) and St $\approx 0.033$ (F12) is the question we consider in turn.

TABLE I: Parameter values for measurements. Dissipation rate per unit mass $\varepsilon$. Droplet diameter $d$. $\langle\rangle$: time-averaged value. R$_\lambda$ is range between 170 to 2110. The data are collected from nine independent PIV measurements during the EUREC$^4$A campaign, including flights Flight 6 and Flight 12 [**?** ], comprising a total of 1740 image sets.

| St$_{min}$ | St$_{max}$ | $\langle$St$\rangle$ | $\langle$Sv$\rangle$ | $\langle\varepsilon\rangle$ [m$^2$/s$^3$] | $\langle R_\lambda\rangle$ | $\langle d\rangle$ [$\mu$m] |
|---|---|---|---|---|---|---|
| 0.005 | 0.020 | 0.013 | 0.253 | 0.011 | 1210 | 12.9 |
| 0.020 | 0.030 | 0.025 | 0.374 | 0.016 | 1180 | 16.4 |
| 0.030 | 0.040 | 0.035 | 0.399 | 0.022 | 1620 | 17.6 |
| 0.040 | 0.050 | 0.045 | 0.446 | 0.026 | 1720 | 19.2 |
| 0.050 | 0.068 | 0.056 | 0.414 | 0.040 | 1660 | 19.4 |
| 0.070 | 0.155 | 0.085 | 0.325 | 0.091 | 1590 | 19.2 |

Our analysis is based on the fact that inertia leads to a difference between the velocities of the fluid, $\boldsymbol{v}_\mathrm{p}$, and of the particles, $\boldsymbol{u}$ [6]. Namely, for small Stokes number St$=\tau_\mathrm{p}/\tau_\mathrm{K}\ll 1$, the equation for the dynamics of particles, Eq. (1), can be simply approximated by advection in an effective particle-velocity field [6] $\dot{\boldsymbol{x}}=\boldsymbol{v}_\mathrm{p}$ with $\boldsymbol{v}_\mathrm{p}=\boldsymbol{u}-\tau_p \mathrm{D}\boldsymbol{u}/\mathrm{D}t$. Effectively, $\boldsymbol{v}_\mathrm{p}$ differs from $\boldsymbol{u}$ by a quantity proportional to St, and is a compressible field: $\boldsymbol{\nabla}\cdot\boldsymbol{v}_\mathrm{p}=-\tau_\mathrm{p}\mathrm{tr}\mathbb{A}^2=-\tau_\mathrm{p}(\mathrm{tr}\mathbb{S}^2-\mathrm{tr}\mathbb{O}^T\mathbb{O})$, where we denote by $\mathbb{A}$ the velocity gradient tensor, and $\mathbb{S}\equiv(\mathbb{A}+\mathbb{A}^T)/2$ and $\mathbb{O}\equiv(\mathbb{A}-\mathbb{A}^T)/2$ its symmetric and antisymmetric components. Inertial droplets tend to avoid sinks of the effective velocity field $\boldsymbol{v}_\mathrm{p}$ i.e. vortical regions with large values of $\omega=|\boldsymbol{\omega}|$ [6, 28].

The number density $n(\boldsymbol{x}_t,t)$ of droplets advected by $\boldsymbol{v}_\mathrm{p}$, evolves according to [7, 29]

$$n(\boldsymbol{x}_T,T) = n_0\exp\Big[-\int_{-T}^{0}\mathrm{d}t'\,\boldsymbol{\nabla}\cdot\boldsymbol{v}_\mathrm{p}(t')\Big] = n_0\exp\Big[\mathcal{I}_T(\boldsymbol{x}_0)\Big], \quad (2)$$

where:

$$\mathcal{I}_T(\boldsymbol{x}_0)=\mathrm{St}\times\tau_K\int_{-T}^{0}\mathrm{d}t'\,\mathrm{tr}\mathbb{A}^2(t') \;=\mathrm{St}\times\mathcal{I}'_T(\boldsymbol{x}_0)\,, \quad (3)$$

the integral in Eq. (3) being integrated along a particle trajectory. Having in mind the limit of small St, we focus on tracer particles [7]. For typical fluctuations of the velocity gradient, $\mathrm{tr}\mathbb{A}^2=(\mathrm{tr}\mathbb{S}^2-\omega^2/2)$ is of order $\tau_K^{-2}$, which suggests that for a duration of order $\sim 10\tau_K$, the integral $\mathcal{I}'_T\lesssim 10$. This estimate implies that the integral $\mathcal{I}_T(\boldsymbol{x}_0)$ remains small, so $n(\mathbf{x}_T,T)$ should remain close to $n_0$. For this reason, particles with St $\sim 0.01$ are expected to be almost uniformly distributed [9]. This makes it difficult to understand the origin of the inhomogeneities in the distribution of droplets, clearly seen in Figs. (2,3).

The shortcoming of the argument above is that very strong fluctuations of the velocity gradient tensor appear in the flow [30], carried in particular by very intense vortex tubes, where the values of tr$(\mathbb{A}^2)$ are very negative.

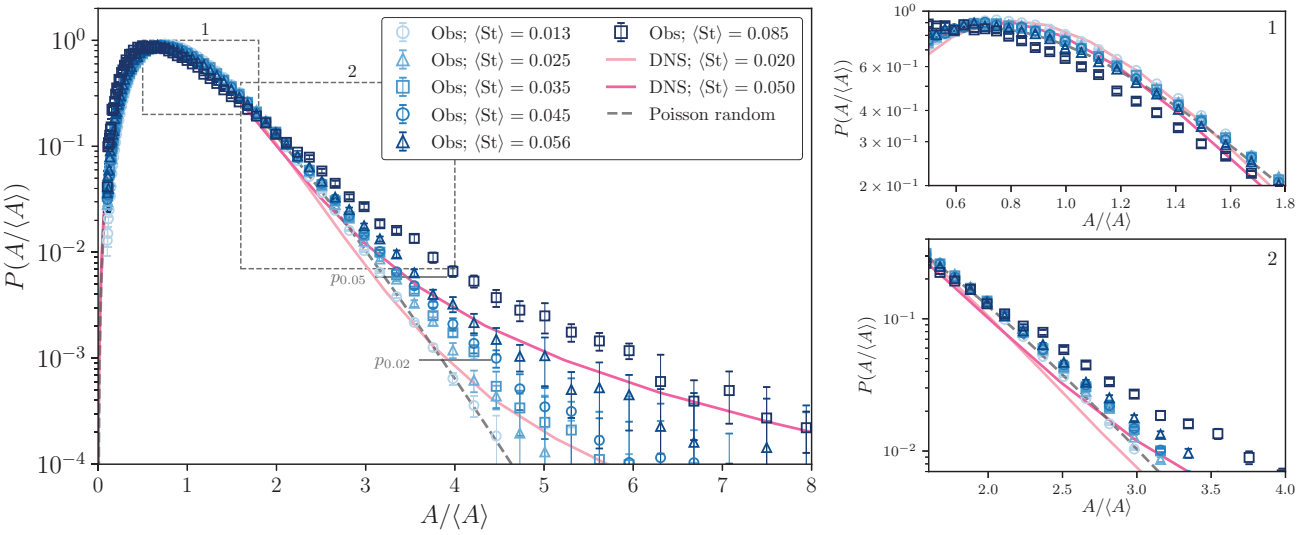


FIG. 3: PDF of the area of Voronoi cells from observations (symbols) and from DNS at $R_\lambda = 170$. The values of $\langle \mathrm{St}\rangle$ are indicated in the legend. The dashed line corresponds to the PDF of Voronoi areas for a set of random points [24–26]. The two pale horizontal lines correspond to probability, $p_{St}$, such that the distribution of $A/\langle A\rangle$ in the DNS differ, at the given value St by $\sim 8\%$ from the random distribution.

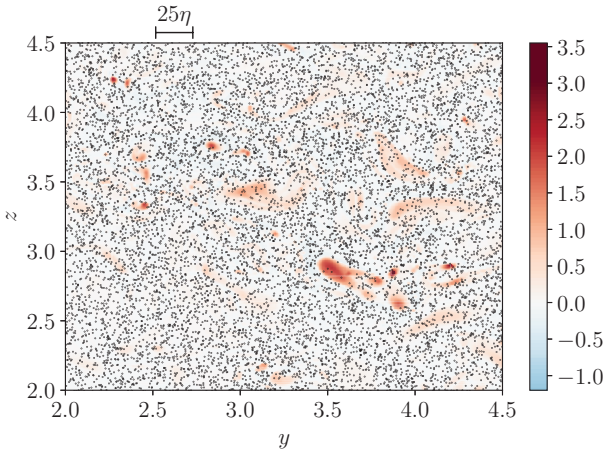


FIG. 4: Voids in the spatial distribution of particles in a direct numerical simulation of a turbulent flow at moderate Reynolds number ($R_\lambda = 170$), and St = 0.02, Sv = 0. Shown are particle positions (black dots) in a thin slice of the three-dimensional configuration space. The highly depleted regions of the flow correspond to large values of the the integral (3), indicated in red, see the color bars.

These features invalidate the expectation that $\mathcal{I}$ is necessarily small when St $\sim 0.01$, although the most intense vortex tubes are not the main reason why voids form.

To study the relation between void formation and the value of the integral $\mathcal{I}_T$ in a turbulent flow, we performed DNS of homogeneous isotropic turbulence by solving the Navier-Stokes equations at moderate Reynolds with the code GHOST [31]. The simulations were run at moderate resolution, up to $1024^3$ grid points, and covered a range of values of the Taylor-scale based Reynolds number [32] up to $R_\lambda \sim 200$. This is much smaller than in cloud measurements (Fig. 2), where $\mathrm{Re}_\lambda \lesssim 10^3$, but sufficient to analyze void at small St. Starting with a large number of inertial particles, at $St \approx 0.02$, our visualization of the particle distribution reveals the existence of regions of low particle density, as shown in Fig. 4. The characteristic scale of these voids is $\sim 25\eta_K$, generally consistent with the observations in clouds,shown in Fig. 2. To characterize more precisely the statistics of voids, Fig. 3 shows the PDF of the areas of Voronoi cells throughout all the flow. The results suggest that one observes cells larger than expected from a random distribution of points with a probability of order $\sim 10^{-4}$ for St = 0.02 (blue curve). On the other hand, the distribution of size of Voronoi areas for St = 0.05 (red line) is very close to the corresponding distribution for experimental data at St = 0.047. Overall, there is a full consistency between the experimental and the numerical results, strongly suggesting that the origin of the voids can be attritbuted to the expulsion of weakly inertial droplets from vorticies in the flow.

One of the remarkable aspects is that the formation of voids depends very sensitively on St for values of the order of St $\gtrsim 10^{-2}$. Even for the value St = 0.02, it is important to notice that the most intense events in the flow, with a vorticity 10 times larger than the *rms* of vorticity fluctuations, is less than $10^{-6}$. This leads to the

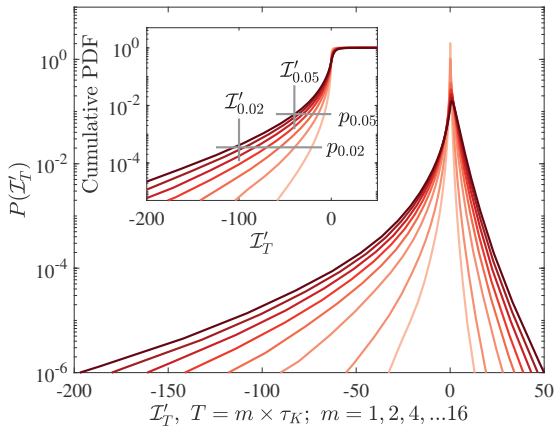


FIG. 5: PDF of the integral $\mathcal{I}'_T$, defined by Eq. (3). The PDFs are shown at values of $T/\tau_K$ equal to 1, and $2 \times n$ for $1 \leq n \leq 8$. As $T$ increases, strong negative values of $\mathcal{I}'_T$ become more probable, although the distribution tends to saturate at large times. The inset shows the cumulative PDF for $T/\tau_K = 2 \times n$, for $1 \leq n \leq 16$. The Reynolds number of the flow is $R_\lambda = 170$. Along with the two probabilities $p_{\rm St}$ identified in Fig. 3, the two pale vertical lines correspond to $\mathcal{I}'_{\rm St} = -2/{\rm St}$, for which the integral in Eq. (3) is equal to -2.

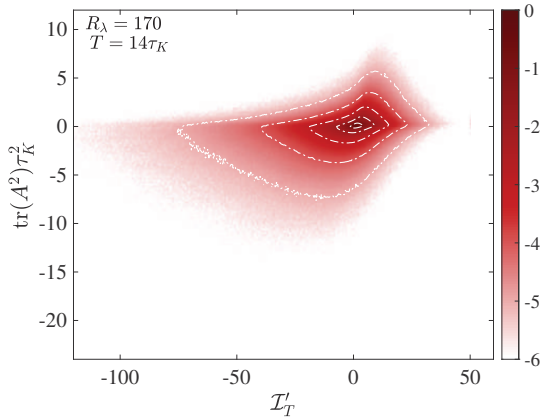


FIG. 6: Joint PDF of $-\mathcal{I}'_T\tau_K$ at $T = 14\tau_K$ (horizontal) $\mathrm{tr}(\mathbb{A}^2)\tau_K^2$ (horizontal). A strong value of the integral $-\mathcal{I}'_T$, necessary to form a void, does not correlate very strongly with regions of intense vorticity, which correpond to negative values of $Q$. The Reynolds number of the flow is $R_\lambda = 170$.

conclusion that the voids are not formed by the intense vortices in the flow, such that $\omega^2\tau_p^2 \approx 1$, as those vortices are much rarer than voids at the values of St considered. Fig. 5 shows the PDF of $\mathcal{I}'_T$ in a flow at $R_\lambda = 170$, as one follows the motion of tracers at times $T = 2n\tau_K$ for $1 \leq n \leq 7$, down to a probability $\sim 10^{-6}$. The figure shows a very dramatic growth of the negative tail as the time $T = n\tau_K$ increases. At short times, values of $\mathcal{I}'_T$ can reach values as large as $\sim -50$ with a probability $\gtrsim 10^{-4}$, reflecting the presence of very strong vortices – stronger vortices also exist in the flow, although with a much smaller probability. The positive side of the distribution of $\mathcal{I}'_T$ reflects strong fluctuations of the strain, $\mathrm{tr}\mathbb{S}^2$, which favor an increase in the density of heavy particles [6]. The growth of the positive tails is significantly more limited than that of the negative tails, which implies that the formation of regions of high density is limited. It is worth noting that for $T/\tau_K \gtrsim 14$, the distribution of $\mathcal{I}'_T$ does not change very much. We also compare the distribution of the Voronoi cell areas between the DNS and the experiments. We notice that the PDFs remain essentially constant when integrating the equations of motion forward in time, for a time $T \gtrsim 15\tau_K$. This time is of the order of $15\tau_K \sim 2.5\lambda_1^{-1}$, where $\lambda_1$ is the largest Lyapunov exponents for the tracer advection problem ($d\boldsymbol{x}/dt = \boldsymbol{u}$) [33]. In the following, we will keep a value of $T = 16\tau_K$.

The values of ${\rm St} \times \mathcal{I}'_T$ at the grid points are indicated by the color in Fig. 4. We observe that the regions with a low density of particles correlate with regions where ${\rm St} \times \mathcal{I}'_T$ is large, colored in red. In comparison, strong correlation of ${\rm St} \times \mathcal{I}'_T$ are very rare, and significantly less intense. Fig. 4 suggests that voids are associated with values of ${\rm St} \times \mathcal{I}'_T \lesssim 2$. In fact, we observe that the probability that ${\rm St} \times \mathcal{I}'_T$ is larger than $\sim 2$ is comparable to the probability of voids, as measured by the PDF of the area of Voronoi cells shown in Fig. 3.

We notice that the picture we are drawing does not explicitly rely on the most intense vortices at the location and time of the voids. The requirement for the integral $\mathcal{I}'_T$ to become large is that in the time interval $[-T, 0]$, the Lagrangian trajectory $\boldsymbol{x}(t)$ has experienced large fluctuations of the vorticity, sufficient to integrate to a very large value. As a consequence, the correlation between the integral $\mathcal{I}'_T(\boldsymbol{x})$ and the enstrophy, $|\omega|^2$, is not particularly strong, as soon as $T/\tau_K \gtrsim 5$, as revealed by Fig. 6 Again, we stress that very large values of $\omega_i\omega_i > 100\tau_K^{-2}$, which occur with a probability $\lesssim 10^{-8}$, cannot explain the formation of the voids observed with a much higher probability.

We have associated the observation of voids for values of St as small as ${\rm St} \approx 0.02$ to the distribution of the integral $\mathcal{I}_T$, which can reach very negative values, ensuring that particles can be expelled from regions of the flow. In comparison, large values of $\mathcal{I}'_T$ can also form, up to $\mathcal{I}'_T \approx 50$, see Fig. 5. The resulting values of $\mathcal{I}_T \equiv {\rm St}\mathcal{I}'_T$ are much of the order of $\approx 50{\rm St}$, suggests a significant increase of the density $n(\boldsymbol{x}_T, T)$, as predicted by Eq. (3). In fact, our analysis of the pair correlation function, in the spirit of [12], reveals clustering in the regions where $\mathcal{I}_T$ is appreciable. This aspect, which will be the subject of a separate publication, indicates that our approach allows us to describe weak, but measurable inhomogeneities in

the distribution of particles transported by turbulence. In this letter, we have shown that the presence of strong vorticity fluctuations in a turbulent flow can explain the formation of heterogeneities in a suspension of weakly inertial particles, such as droplets in a cloud. In fact, our DNS results reproduce quantitatively the distribution of Voronoi areas observed in the flow, see Fig. 3, and in particular the dependence on the Stokes numbers of the particles. The formation of voids can be explained by approximating the velocity of inertial particles by the simplified expression introduced in [6], and keeping track of the expulsion experienced by particles as the flow evolves. Importantly, the voids observed in the simulation are not due to the most intense vortices in the flow, which are too rare, but rather by intermediate vortices which are persistent enough. The results also explain the strong dependence of the expulsion mechanism on the Stokes number of the particles. Thus, turbulence itself may induce heterogeneities of the distribution of small, very weakly inertial droplets in a cloud. The interplay between these effects and entrainment and mixing of outside air [13] remains to be more fully explored.


[1] T. Birnstiel, F. M., and A. Johansen, *Space Sci. Rev.* **205**, 41 (2016).

[2] M. L. Pöhlker, C. Pöhlker, O. O. Krüger, J.-D. Förster, T. Berkemeier, W. Elbert, J. Fröhlich-Nowoisky, U. Pöschl, G. Bagheri, E. Bodenschatz, J. A. Huffman, S. Scheithauer, and E. Mikhailov, *Rev. Mod. Phys.* **95**, 045001 (2023).

[3] R. A. Shaw, *Annu. Rev. Fluid Mech.* **35** (2003).

[4] G. Falkovich, A. Fouxon, and M. Stepanov, *Nature* **419** (2002).

[5] E. Bodenschatz, S. Malinowski, S. R. A., and S. F., *Science* **327** (2010).

[6] M. R. Maxey, *J. Fluid Mech.* **174**, 441 (1987).

[7] G. Falkovich and A. Pumir, *Phys. Fluids* **16**, L47 (2004).

[8] A. Pumir and M. Wilkinson, *Annu. Rev. Condens. Matter Phys.* **7** (2016).

[9] W. W. Grabowski and P. Vaillancourt, *J. Atmosph. Sci.* **56**, 1433 (1999).

[10] K. Karpińska, J. F. E. Bodenschatz, S. P. Malinowski, J. L. Nowak, S. Risius, T. Schmeissner, R. A. Shaw, H. Siebert, H. Xi, H. Xu, and E. Bodenschatz, *Atmos. Chem. Phys.* **19**, 4991 (2019).

[11] M. L. Larsen, R. A. Shaw, A. B. Kostinski, and S. Glienke, *Phys. Rev. Lett.* **121** (2018).

[12] B. Thiede, M. J. Larsen, F. Nordsiek, O. Schlenczek, E. Bodenschatz, and G. Bagheri, *submitted* (2025).

[13] J. M. Yeom, I. Helman, P. Prabhakaran, J. C. Anderson, F. Yang, R. A. Shaw, and W. Cantrell, *Proc. Nat. Acad. Sci.* **120**, 2307354120 (2023).

[14] T. Oujia, K. Matsuda, and K. Schneider, *J. Fluid Mech.* **905** (2020).

[15] J. Matsuda, K. Yoshimatsu, and K. Schneider, *Phys. Rev. Lett.* **132** (2024).

[16] S. Sumbekova, A. Cartellier, A. Aliseda, and M. Bourgoin, *Physical Review Fluids* **2**, 024302 (2017).

[17] A. J. Petersen, L. Baker, and F. Coletti, *Journal of Fluid Mechanics* **864**, 925 (2019).

[18] R. Monchaux, M. Bourgoin, and A. Cartellier, *Physics of Fluids* **22**, 103304 (2010).

[19] E. W. Saw, R. A. Shaw, S. Ayyalasomayajula, P. Y. Chuang, and A. Gylfason, *Physical review letters* **100**, 214501 (2008).

[20] H. Yoshimoto and S. Goto, *Journal of Fluid Mechanics* **577**, 275 (2007).

[21] L. Baker, A. Frankel, A. Mani, and F. Coletti, *Journal of Fluid Mechanics* **833**, 364 (2017).

[22] P. J. Ireland, A. D. Bragg, and L. R. Collins, *Journal of Fluid Mechanics* **796**, 617 (2016).

[23] B. Stevens, S. Bony, D. Farrell, F. Ament, A. Blyth, C. Fairall, J. Karstensen, P. K. Quinn, S. Speich, C. Acquistapace, F. Aemisegger, A. L. Albright, H. Bellenger, E. Bodenschatz, K.-A. Caesar, R. Chewitt-Lucas, G. de Boer, J. Delanoë, L. Denby, F. Ewald, B. Fildier, M. Forde, G. George, S. Gross, M. Hagen, A. Hausold, K. J. Heywood, L. Hirsch, M. Jacob, F. Jansen, S. Kinne, D. Klocke, T. Kölling, H. Konow, M. Lothon, W. Mohr, A. K. Naumann, L. Nuijens, L. Olivier, R. Pincus, M. Pöhlker, G. Reverdin, G. Roberts, S. Schnitt, H. Schulz, A. P. Siebesma, C. C. Stephan, P. Sullivan, L. Touzé-Peiffer, J. Vial, R. Vogel, P. Zuidema, N. Alexander, L. Alves, S. Arixi, H. Asmath, G. Bagheri, K. Baier, A. Bailey, D. Baranowski, A. Baron, S. Barrau, P. A. Barrett, F. Batier, A. Behrendt, A. Bendinger, F. Beucher, S. Bigorre, E. Blades, P. Blossey, O. Bock, S. Böing, P. Bosser, D. Bourras, P. Bouruet-Aubertot, K. Bower, P. Branellec, H. Branger, M. Brennek, A. Brewer, P.-E. Brilouet, B. Brügmann, S. A. Buehler, E. Burke, R. Burton, R. Calmer, J.-C. Canonici, X. Carton, G. Cato Jr., J. A. Charles, P. Chazette, Y. Chen, M. T. Chilinski, T. Choularton, P. Chuang, S. Clarke, H. Coe, C. Cornet, P. Coutris, F. Couvreux, S. Crewell, T. Cronin, Z. Cui, Y. Cuypers, A. Daley, G. M. Damerell, T. Dauhut, H. Deneke, J.-P. Desbios, S. Dörner, S. Donner, V. Douet, K. Drushka, M. Dütsch, A. Ehrlich, K. Emanuel, A. Emmanouilidis, J.-C. Etienne, S. Etienne-Leblanc, G. Faure, G. Feingold, L. Ferrero, A. Fix, C. Flamant, P. J. Flatau, G. R. Foltz, L. Forster, I. Furtuna, A. Gadian, J. Galewsky, M. Gallagher, P. Gallimore, C. Gaston, C. Gentemann, N. Geyskens, A. Giez, J. Gollop, I. Gouirand, C. Gourbeyre, D. de Graaf, G. E. de Groot, R. Grosz, J. Güttler, M. Gutleben, K. Hall, G. Harris, K. C. Helfer, D. Henze, C. Herbert, B. Holanda, A. Ibanez-Landeta, J. Intrieri, S. Iyer, F. Julien, H. Kalesse, J. Kazil, A. Kellman, A. T. Kidane, U. Kirchner, M. Klingebiel, M. Körner, L. A. Kremper, J. Kretzschmar, O. Krüger, W. Kumala, A. Kurz, P. L'Hégaret, M. Labaste, T. Lachlan-Cope, A. Laing, P. Landschützer, T. Lang, D. Lange, I. Lange, C. Laplace, G. Lavik, R. Laxenaire, C. Le Bihan, M. Leandro, N. Lefevre, M. Lena, D. Lenschow, Q. Li,

G. Lloyd, S. Los, N. Losi, O. Lovell, C. Luneau, P. Makuch, S. Malinowski, G. Manta, E. Marinou, N. Marsden, S. Masson, N. Maury, B. Mayer, M. Mayers-Als, C. Mazel, W. McGeary, J. C. McWilliams, M. Mech, M. Mehlmann, A. N. Meroni, T. Mieslinger, A. Minikin, P. Minnett, G. Möller, Y. Morfa Avalos, C. Muller, I. Musat, A. Napoli, A. Neuberger, C. Noisel, D. Noone, F. Nordsiek, J. L. Nowak, L. Oswald, D. J. Parker, C. Peck, R. Person, M. Philippi, A. Plueddemann, C. Pöhlker, V. Pörtge, U. Pöschl, L. Pologne, M. Posyniak, M. Prange, E. Quiñones Meléndez, J. Radtke, K. Ramage, J. Reimann, L. Renault, K. Reus, A. Reyes, J. Ribbe, M. Ringel, M. Ritschel, C. B. Rocha, N. Rochetin, J. Röttenbacher, C. Rollo, H. Royer, P. Sadoulet, L. Saffin, S. Sandiford, I. Sandu, M. Schäfer, V. Schemann, I. Schirmacher, O. Schlenczek, J. Schmidt, M. Schröder, A. Schwarzenboeck, A. Sealy, C. J. Senff, I. Serikov, S. Shohan, E. Siddle, A. Smirnov, F. Späth, B. Spooner, M. K. Stolla, W. Szkółka, S. P. de Szoeke, S. Tarot, E. Tetoni, E. Thompson, J. Thomson, L. Tomassini, J. Totems, A. A. Ubele, L. Villiger, J. von Arx, T. Wagner, A. Walther, B. Webber, M. Wendisch, S. Whitehall, A. Wiltshire, A. A. Wing, M. Wirth, J. Wiskandt, K. Wolf, L. Worbes, E. Wright, V. Wulfmeyer, S. Young, C. Zhang, D. Zhang, F. Ziemen, T. Zinner, and M. Zöger, *Earth System Science Data* **13**, 4067 (2021).

[24] J.-S. Ferenc and Z. Neda, *Physica A: Statistical Mechanics and its Applications* **385**, 518 (2007).

[25] H. J. Hilhorst, *Journal of Statistical Mechanics: Theory and Experiment* **2009**, P05007 (2009).

[26] A. Gabrielli, *Journal of Statistical Mechanics: Theory and Experiment* **2009**, N07001 (2009).

[27] B. Stevens, S. Bony, D. Farrell, F. Ament, A. Blyth, et al., *Earth System Science Data* **13**, 4067 (2021).

[28] G. Haller and T. Sapsis, *Physica D* **573-583**, 254501 (2008).

[29] E. Balkovsky, G. Falkovich, and A. Fouxon, *Phys. Rev. Lett.* **86**, 2790 (2001).

[30] D. Buaria, A. Pumir, E. Bodenschatz, and P. K. Yeung, *New J. Physics* **21**, 043004 (2019).

[31] P. Mininni, D. Rosenberg, R. Reddy, and A. Pouquet, *Parallel Comput.* **37** (2011).

[32] S. B. Pope, *Turbulent flows*, 2000.

[33] P. L. Johnson and C. Meneveau, *Physics of Fluids* **27**, 085110 (2015).